The Thalanga sequence – Facies Architecture, Geochemistry, Alteration and Metamorphism of Felsic Volcanics Hosting the Thalanga Massive Sulphide Deposit (Early Ordovician, Northern Queensland, Australia)

by

Holger Paulick

MSc (Geology), Technical University of Berlin, Germany

UNIVERSITY OF TASMANIA

School of Earth Sciences

Submitted in fulfilment of the requirements for the degree of Doctor of Philosophy

University of Tasmania

July 1999

This thesis contains no material which has been accepted for a degree or diploma by the University or any other institution and, to the best of my knowledge and belief, no material previously published or written by another person except where due acknowledgment is made in the text of the thesis.

Authority of access:

This thesis is not to be made available for loan or copying until January 2000. Following that time the thesis may be made available for loan and limited copying in accordance with the *Copyright Act 1968*.

Holger Paulick

Abstract

The Thalanga sequence is a felsic, lava-dominated, submarine volcanic succession in the Cambro-Ordovician Mount Windsor Subprovince (northern Queensland, Australia). The sequence consists of altered rhyolite lavas, syn-volcanic intrusions and volcaniclastic facies (footwall), conformably overlain by a lithologically diverse unit (Favourable Horizon) containing the Thalanga massive sulphide deposit, succeeded by a volcano-sedimentary facies association dominated by weakly altered dacite lavas (hangingwall). This package is ~400 to ~800 m thick, has a subvertical dip due to regional deformation and youngs towards the south. Massive, Zn-Pb-Cu-rich sulphide-ore lenses (total 6 Mt) are stratiform, occur over a strike length of ~3 km and are invariably underlain by a broad, continuous alteration zone which extends at least 300 m into the footwall.

Regional metamorphism in the Thalanga area generated upper greenschist facies (450 to 500°C; ≤3.5 kbar), foliated biotite-muscovite±chlorite assemblages. Subsequent contact metamorphism, associated with the intrusion of a voluminous, post-tectonic diorite pluton, was of similar metamorphic grade.

Six drill core cross sections (total 15 km of core) in the Thalanga mine area and one outcrop section located 5 km to the west of the deposit have been studied. Reconstruction of the facies architecture indicates that the massive sulphides formed in a below-storm-wave-base depositional environment on top of an elevated, lava-dominated, rhyolitic volcanic centre. Effusive eruptions persisted after formation of the massive sulphide lenses but involved compositionally and texturally distinct dacite. A modern analogue for the setting of the Thalanga deposit is the PACMANUS hydrothermal field on the crest of the dacite lava-dominated Pual Ridge in the eastern Manus back-arc basin (Papua New Guinea).

Rhyolite in the footwall alteration zone includes both genuine volcaniclastic facies and apparent clastic facies formed by domainal or multi-stage hydrothermal alteration of coherent rhyolite. A comparison of the distribution of clastic and coherent facies with the geometry of pyrite-rich, intensely altered, discordant zones in the footwall suggests that intense hydrothermal fluid flow was independent of the facies arrangement.

Alteration facies at Thalanga are texturally and mineralogically diverse and ten different facies have been defined on the basis of dominant mineral assemblages and general alteration intensity. Alteration facies representing moderate to intense

hydrothermal alteration (quartz-K-feldspar, disseminated tremolite, quartz-pyrite, chlorite-pyrite, carbonate-chlorite-tremolite and phyllosilicate-rich, mottled alteration facies) are exclusive to the footwall. The mottled facies, characterised by muscovite-biotite-chlorite±pyrite assemblages, represents the bulk of the footwall alteration zone and is related to diffuse upflow of hydrothermal fluids causing destruction of primary feldspar, formation of hydrothermal phyllosilicates and precipitation of pyrite. It envelopes discordant zones of quartz-pyrite alteration facies connected to massive sulphides in the Favourable Horizon. Variations in the distribution of some alteration facies along strike suggest that parts of the hydrothermal system experienced particular alteration processes. Low intensity alteration facies (epidote, phyllosilicate, and albite alteration and hematite dusting) are common in the hangingwall dacite and probably represent the results of diagenetic alteration and low-grade sub-seafloor metamorphism.

The geochemical effects of alteration were examined using whole rock major and trace element data and electron microprobe analyses of chlorite, biotite and muscovite. Mass balance calculations show that hydrothermal alteration in the footwall is characterised by substantial gains in Fe, S and Mg and Na loss. Furthermore, most alteration facies gained Si, and K was conserved or added during hydrothermal activity. The concentrations of Ba, Rb, Sr, As and Bi vary according to qunatitative differences in major mineral phases among alteration facies (eg. abundances of barite, muscovite, alkali feldspar, plagioclase, tremolite, epidote and pyrite). Light REE were added to footwall rhyolite during hydrothermal alteration whereas heavy REE remained immobile. In general, Eu was progressively leached from the footwall with increasing intensity of hydrothermal alteration.. The geochemical data and in particular the Mg-rich character of the footwall alteration zone indicate that the hydrothermal fluids at Thalanga were seawater-derived.

Several compositional features of the footwall alteration zone show systematic changes with distance from the ore defining a geochemical halo. These geochemical proximity indicators may assist in prospect- and mine-scale exploration for VHMS deposits in similar geological settings.

Acknowledgments

This PhD project was supervised by Drs Jocelyn McPhie and Bruce Gemmell at the Centre for Ore Deposit Research (CODES, School of Earth Sciences, University of Tasmania, Hobart, Australia) and I am thankful for their guidance through the course of the study. It would not have been possible to undertake this research without Jocelyn's exceptional support during the early stage of preparations for my temporary relocation from Germany to Australia in 1994/95. In this context I would like to express my gratitude to Profs Gerhard Franz and Eberhard Klitzsch (Technical University of Berlin, Germany) for their help and advice.

During my time in Hobart, Jocelyn provided much advice on scientific matters and the art of writing and also managed to examine chapters quickly when time was limited. Furthermore, I would like to thank her for the interest and encouragement in the study of coloured pumices from Sudan.

Financial and logistical support for this project was provided by the German Academic Exchange Society (DAAD), the Department of Employment, Education and Training Australia (OPRS Scholarship), the Centre for Ore Deposit Research, AMIRA project P439 and RGC Exploration. I wish to thank RGC staff at Thalanga and Charters Towers, particularly Walter Herrmann, Colin Kendall, Ian Warland, Haydn Hadlow, Craig Miller and Leanne Carr, for discussions, advice and assistance during core logging at Thalanga.

It would not have been possible to assemble the analytical data necessary for this study without the help of several people namely Phil Robinson (XRF analysis), Ashley Townsend (ICP-MS analysis), David Steele (microprobe, University of Tasmania), Prof Gerhard Franz and Mr Galbert (microprobe, Technical University of Berlin), Simon Stevens (lapidary), Nilar Hlaing and Zohrey Adabi (sample preparation for XRF and ICP-MS analysis).

I am indebted to Walter Herrmann and Anthea Hill for the introduction to Thalanga geology and I would also like to thank Profs Ross Large and Clive Burrett for their continued interest in the progress of my studies. Dr Dima Kamenetsky, Dr Ron Berry,

Prof Gerhard Franz and Walter Herrmann read drafts of chapters dealing with geochemistry and metamorphism which is very much appreciated. June Pongratz was a great help in sorting out computer and printing related problems and provided much support in the very final stage of thesis production. Rohan Wolfe offered expert advice on 'Freehand 5.5' and other matters of life. Steve Hunns was a source of constant constructive criticism and an excellent flatmate.

I would like to thank my fellow post-grads at CODES and the School of Earth Sciences, and particularly my 'cubicle comrades' John Dunster, Mohammad Adabi, Peter Winefield, David 'Rowdy' Rawlings, Tony Webster and Phisit 'Meng' Limtrakum, for their company, support and 'Friday night entertainment'. Rowdy and Tony introduced me to the intricacies of 'Australian humour' which took a little while to recognise as such.

Special thanks are due to my family in Berlin and to Dr Annett Uhmann for their patience and undwindling support during the entire course of this project. I am also extremely grateful for Annetts assistance during the final stage of thesis preparation which included dealing with the unformatted references, folding of maps and figures and preparing a formidable rock catalogue single-handedly. Thank you very much.

Table of contents

Appendix

- **Tables:**

- **Reprint**:

Paulick H. and McPhie, J. (1999) Facies architecture of the felsic lava-dominated host sequence to the Thalanga massive sulphide deposit, Lower Ordovician, northern Queensland. Australian Journal of Earth Sciences, *46*, 391-405.

- **Pocket:**

Drill hole logs and geological interpretation of section 1 (Far West Thalanga)

Drill hole logs and geological interpretation of section 2 (West Thalanga)

Drill hole logs and geological interpretation of section 3 (Central Thalanga)

Drill hole logs and geological interpretation of section 4 (Central Thalanga)

Drill hole logs and geological interpretation of section 5 (East Thalanga)

Drill hole logs and geological interpretation of section 6 (East Thalanga)

List of figures

List of Tables

List of Abbreviations

AAS:	Atomic absorption spectrophotometry
act:	actinolite
aggr:	aggregate
ALS:	Australian Laboratory Services Pty. Ltd.
altn:	alteration
analabs	Analabs Pty. Ltd.
ba:	barite
bio:	biotite
bx:	breccia
carb.:	carbonate
carb/tre:	carbonate and/or tremolite or actinolite
Cc:	calcite
chl:	chlorite
cpy:	chalcopyrite
CTC:	carbonate-tremolite-chlorite
diss:	disseminated
dk:	dark
Dol:	dolerite
epi:	epidote and/or zoisite
fsp:	feldspar
gal:	galena
irreg.:	irregular
M:	massive
mag.:	magnetite
med:	medium
mod.:	moderately
phen:	phenocrysts
phyl:	phyllosilicate
PPL:	plain polarised light
psclst:	pseudoclastic
psmorphs:	pseudomorphs
px:	pyroxene
py:	pyrite
qtz:	quartz
ser:	sericite
SM:	semi-massive
SMS:	semi-massive sulphide
sph:	sphalerite
sst:	sandstone
TS:	thin section
tx:	texture
vol/c:	volcaniclastic
XRF	X-ray fluorescence analysis

1 Introduction

Volcanic hosted massive sulphide (VHMS) deposits are an important source of base metals (Zn, Cu and Pb) and may also contain substantial Ag and Au. In general, VHMS deposits have been compared and contrasted using characteristics such as metal content and metal ratios, structure of the ore body and composition of the host-rock sequence. Accordingly, a variety of classification schemes have been proposed based on geotectonic setting (Sillitoe, 1973; Sawkins, 1976), host-rock lithology (Klau & Large, 1980; Morton & Franklin, 1987) and major ore element chemistry (Hutchinson, 1973; Solomon, 1976; Lydon, 1988; Large, 1992). The stratiform, Early Ordovician, Thalanga massive sulphide deposit consists of polymetallic ore lenses hosted by a submarine, felsic volcanic sequence and may be classified as a Zn-Pb-Cu-type or Kuroko type VHMS deposit.

VHMS deposits occur throughout the geological time-scale and are typically hosted by volcanic successions formed in submarine basins. It is inferred that present-day hydrothermal fields on the ocean floor, associated with black smokers and actively forming massive sulphides, represent a modern analogue for the geological environment of massive sulphide mineralisation in the past. However, most of the modern hydrothermal systems occur on mafic oceanic crust whereas VHMS deposits are commonly hosted by felsic-dominated sequences (Solomon, 1976). Recent discoveries of active hydrothermal fields located on felsic, submarine volcanic structures probably represent the closest modern analogue to many ancient massive sulphide deposits including Thalanga (PACMANUS, Manus Basin, Binns & Scott, 1993; JADE, Okinawa Trough, Halbach et al., 1993).

World-class VHMS ore bodies (containing tens to hundreds of Mt of ore), occur in Spain and Portugal (Iberian Pyrite Belt), Russia (Ural Mountains), Sweden (Skellefte and Bergslagen Districts), Canada (Abiti, Noranda and Bathurst Mining Camps) and Australia (Mount Read Volcanics, Tasmania). Large (1992) lists 30 significant VHMS deposits (with $\geq$1 Mt of ore) on the Australian continent ranging in age from early Archean to Permian with an estimated total metal content of ~20 Mt (combined Cu, Pb and Zn). These deposits show a wide spectrum of characteristics in terms of ore body geometries, ore mineralogies and metal ratios. However, there are significant similarities, including features such as metal zonation, alteration mineralogy, alteration chemistry, sulphur

isotope characteristics, ore textures and host volcanic relationships. Most deposits are located in Western Australia (Archean), Tasmania (Cambrian), northern Queensland (Cambro-Ordovician), and southeastern Australia (Silurian) (Fig. 1.1a). The Cambrian to Ordovician was an important time for VHMS formation in Australia and deposits of this age contain a total of ~12 Mt of metal (Fig. 1.1b). The largest deposits occur in Tasmania (Mount Lyell, Rosebery and Hellyer) whereas deposits in northern Queensland are significantly smaller (Table 1.1).

Table 1.1: Total resource data for Cambrian to Ordovician VHMS deposits > 1 Mt in Australia

deposit	Size (Mt)	Cu (%)	Pb (%)	Zn (%)	Au (ppm)	Ag (ppm)
West Tasmania (Mount Read Volcanics)						
Mount Lyell:						
Lyell Blow	5.6	1.3	nr	nr	2.0	61.0
Prince Lyell	87.6	0.9	nr	nr	0.3	2.0
North Lyell	5.1	5.3	nr	nr	0.4	33.0
Royal Tharsis	1.5	1.5	nr	nr	0.5	2.8
Cape-Horn	1.4	1.4	nr	nr	0.4	3.3
Crown Lyell III	2.1	1.4	nr	nr	0.3	4.1
Crown Lyell OC	1.1	1.4	nr	nr	0.5	3.9
Lyell Comstock	2.4	2.4	nr	nr	0.7	5.2
Rosebery	19.4	0.7	5.0	16.2	2.9	155.0
Hercules	2.6	0.4	5.2	16.7	2.7	159.0
Que River	3.1	0.6	7.5	13.5	3.4	200.0
Hellyer	16.0	0.4	7.0	13.0	2.3	160.0
Northern Queensland (Mount Windsor Subprovince and Balcooma)						
Reward	1.5	5.0	nr	nr	1.5	nr
Balcooma	3.5	3.0	nr	nr	3.0	nr
Liontown	2.0	0.5	2.3	6.6	0.9	50.0
Dry River South	1.5	1.1	3.4	9.4	0.8	97.0
Thalanga	6.6	1.8	2.6	8.4	0.4	69.0

from: Large (1992); except Thalanga (1998 resource estimate); nr: not recorded

The subject of this thesis is the geological setting of the Thalanga VHMS deposit, the largest massive sulphide occurrence in northern Queensland. The deposit was mined from 1990 to 1998 and can be described as a metamorphosed, Zn-Pb-Cu-Ag-Au ore body with a pronounced sheet-like geometry consisting of several, partly connected, thin (generally ≤10 m), stratiform lenses of pyrite-sphalerite-galena-chalcopyrite with variable gangue assemblages. The host-rock sequence (Thalanga sequence) consists of footwall rhyolite which is moderately to intensely altered below the ore bodies and a weakly altered succession dominated by dacite in the hangingwall.

Fig. 1.1: Distribution, age and metal contents of Australian VHMS deposits (from Large, 1992).

(a) Location and age of major Australian VHMS deposits (modified from Large, 1992). Ages shown in *italic* (*Archean*), **bold** (**Cambrian and Ordovician**) and plain (Silurian, Devonian and Permian) font.

(b) Metal content (combined copper, lead and zinc) of Australian VHMS deposits (modified from Large, 1992). The Cambrian to Ordovician represents the most important time for VHMS-style mineralisation in Australia yielding world-class deposits in western Tasmania (Mount Read Volcanics) and smaller deposits in northern Queensland (Mount Windsor Subprovince and Balcooma).

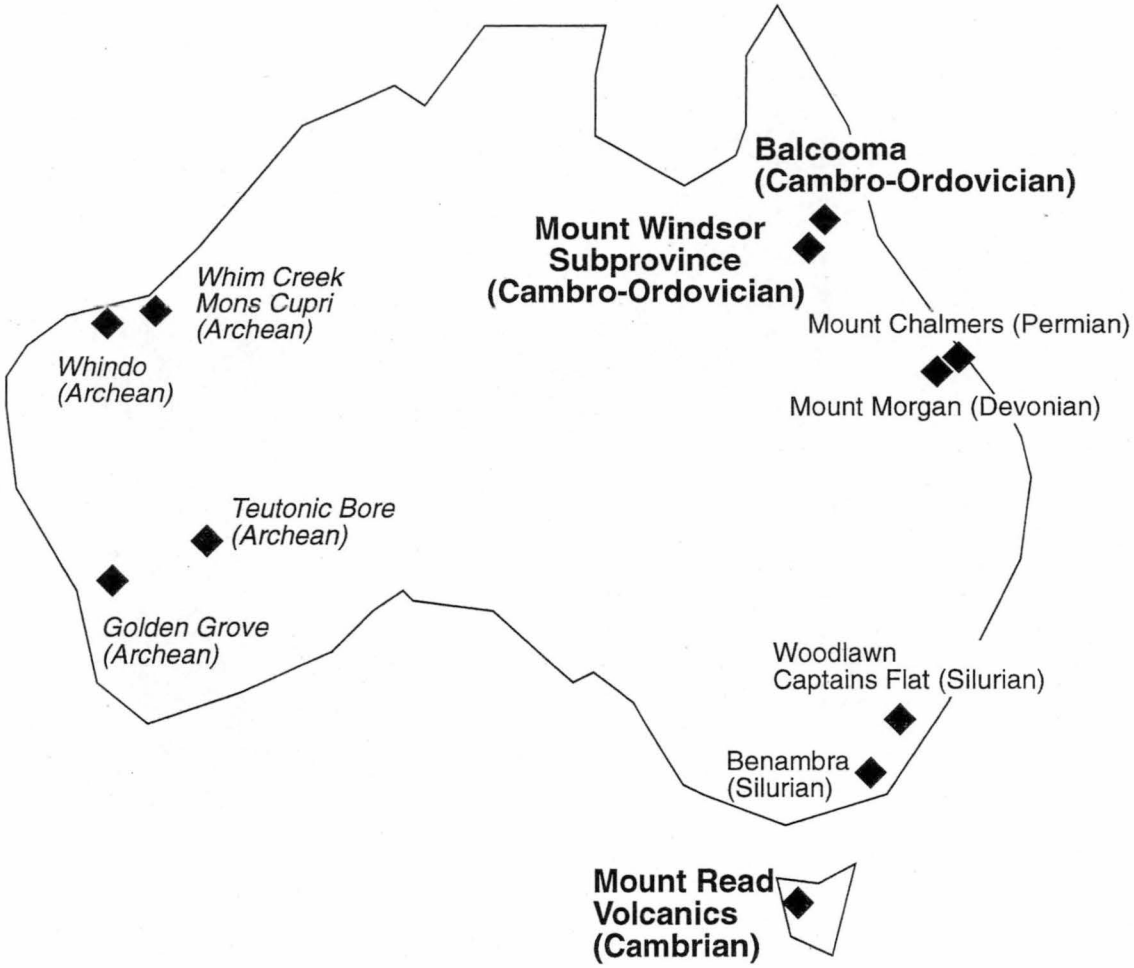

Fig. 1.1a

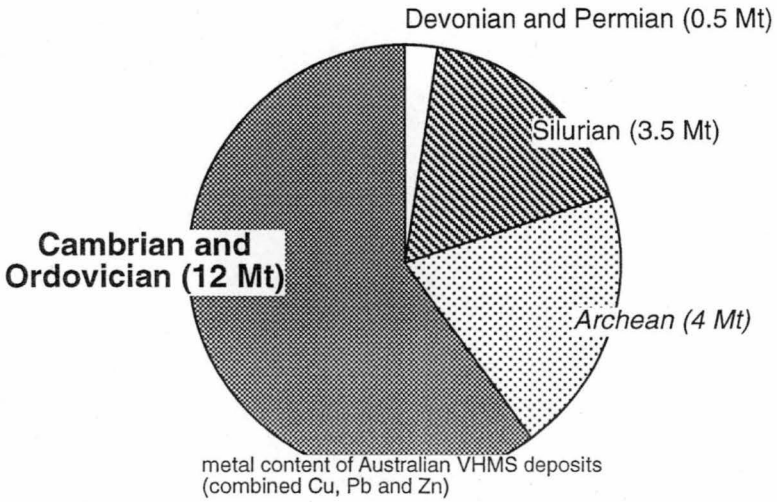

Fig. 1.1b

1.1 Aims

This thesis is concerned with the facies architecture of the felsic volcanic host-rock sequence to the Thalanga deposit and the zonation and geochemical features of the hydrothermal alteration system. Specifically, this study aims to

- constrain the conditions of regional and contact metamorphism in the Thalanga area,
- reconstruct the volcanic facies architecture of the Thalanga sequence,
- define alteration facies based on texture and mineralogy and reconstruct the geometry of the mineralising hydrothermal system,
- investigate possible relationships between volcanic facies architecture and the geometry of the hydrothermal system,
- determine the primary geochemistry of footwall rhyolite and hangingwall dacite and consider implications for petrological interpretations,
- characterise the geochemical changes associated with hydrothermal alteration,
- identify any geochemical indicators of proximity to the massive sulphides which could be applied in base metal exploration.

Due to the scarcity of natural outcrop in the Thalanga mine area most of the geological information for this research was obtained from diamond drill core. The facies architecture of the Thalanga sequence has been reconstructed by linking data from a series of cross sections along strike of the deposit. Volcanic facies interpretation has been difficult in footwall rhyolite below the ore body because primary textures have been variably modified due to hydrothermal alteration and metamorphism. Allen (1988) demonstrated that domainal or multi-stage alteration can generate apparent clastic textures in coherent facies of felsic lavas and intrusions. Similar features have been observed at Thalanga and specific textural criteria were established in order to discriminate coherent facies with 'pseudoclastic' textures from genuine volcaniclastic facies in the footwall alteration zone. The influence of primary volcanic facies on the pathways of hydrothermal fluids has been assessed by comparing the volcanic facies architecture of footwall rhyolite with the geometry of the footwall alteration zone.

Hydrothermal alteration has produced texturally and mineralogically diverse assemblages which define a semi-conformable, stratabound footwall alteration zone in rhyolite below the Thalanga ore body. Definition of mapable alteration facies based on

distinctive mineral assemblages, textures and general intensity of alteration allowed reconstruction of the geometry of alteration zones. Geochemical analyses including major, trace and rare earth elements were used to characterise the geochemical changes associated with each alteration facies whereas data for least-altered samples of footwall rhyolite and hangingwall dacite were used to investigate the primary geochemistry of the Thalanga sequence. Mass balance calculations were performed in order to identify the net geochemical changes associated with alteration at Thalanga.

The geochemical halo of the Thalanga deposit was outlined by investigating systematic changes in whole rock and mineral composition correlated with distance from the massive sulphides. From these data a set of geochemical proximity indicators were determined.

The results of this study provide constraints on the geological environment and conditions of massive sulphide formation at Thalanga and have implications for VHMS ore genesis models and for mineral exploration. This approach shows that integrating volcanic facies analysis with geochemistry and alteration studies is an effective way to build a better understanding of VHMS deposits in ancient, metamorphosed successions. This thesis represents an example of the usefulness of an integrated approach in the study of VHMS deposits by combining different disciplines of geological research which are commonly pursued independently.

1.2 Regional geology of the Mount Windsor Subprovince

The Thalanga deposit is located close to the western end of the Cambro-Ordovician Mount Windsor Subprovince, an EW trending, elongate belt of deformed marine sedimentary and volcanic rocks in northern Queensland (Fig. 1.2). The area is characterised by a peneplain landscape with a bushland savanna vegetation and has a dry, tropical climate with rainfall restricted to the summer months (December to February). Discontinuous outcrop over a distance of ~160 km exposes a grossly conformable stratigraphic succession with a subvertical, south-facing dip and a thickness up to 10 km (Henderson, 1986; Berry et al., 1992). Granitoid intrusions of the Ordovician to Devonian Lolworth-Ravenswood batholith occupy the northern margin of the

Fig. 1.2: Simplified geological map of northern Queensland.

This map shows the distribution of Precambrian basement rocks and major Cambrian to Devonian structural blocks in the region (from Stolz, 1995 after Day et al., 1975).

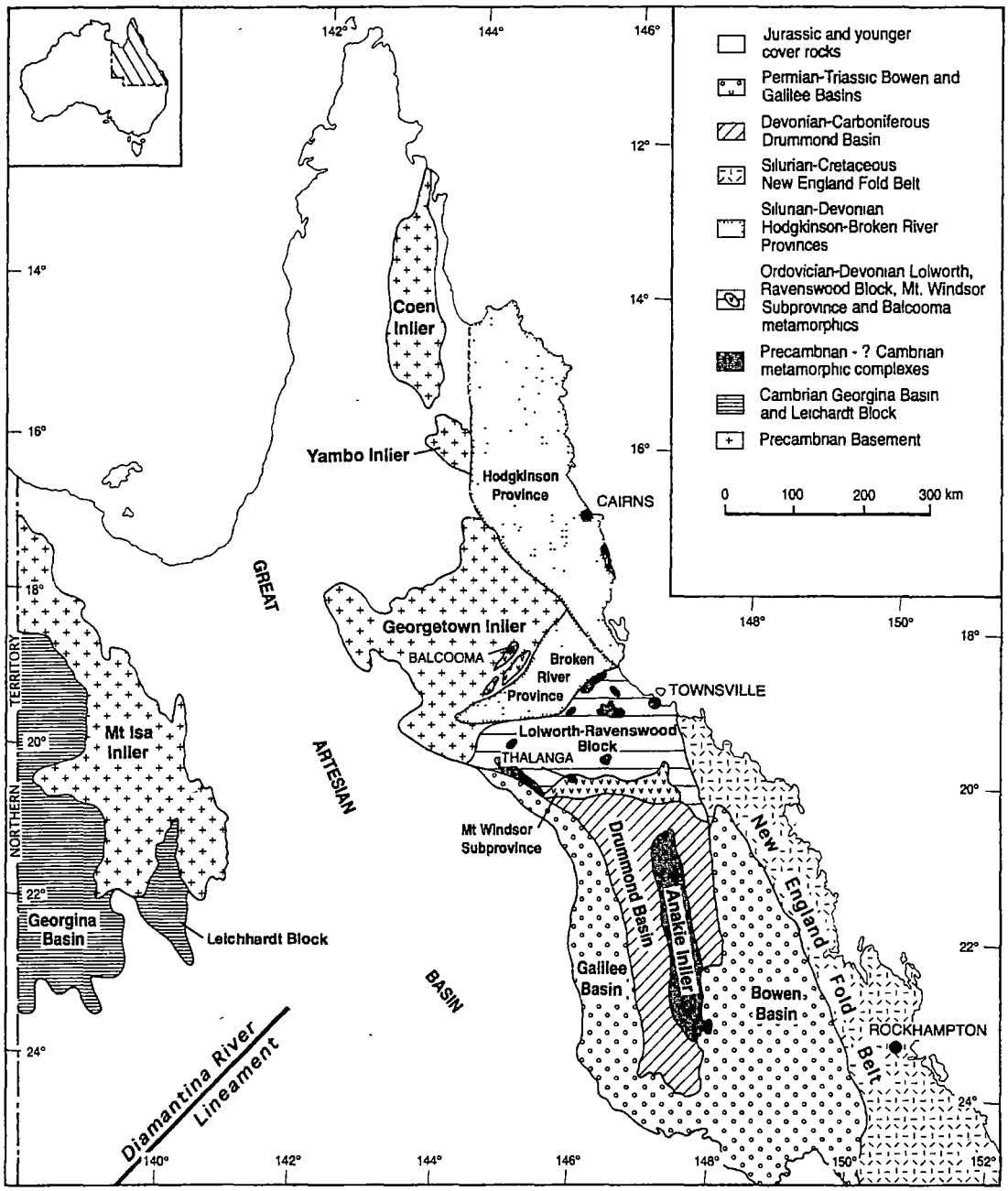
Jurassic and younger cover rocks
Permian-Triassic Bowen and Galilee Basins
Devonian-Carboniferous Drummond Basin
Silurian-Cretaceous New England Fold Belt
Silurian-Devonian Hodgkinson-Broken River Provinces
Ordovician-Devonian Lolworth, Ravenswood Block, Mt. Windsor Subprovince and Balcooma metamorphics
Precambrian - ? Cambrian metamorphic complexes
Cambrian Georgina Basin and Leichardt Block
Precambrian Basement
0 100 200 300 km
Coen Inlier
Yambo Inlier
Hodgkinson Province
CAIRNS
GREAT
ARTESIAN
BASIN
Georgetown Inlier
BALCOOMA
Broken River Province
TOWNSVILLE
Lolworth-Ravenswood Block
THALANGA
Mt Isa Inlier
Mt Windsor Subprovince
Drummond Basin
Anakie Inlier
New England Fold Belt
Georgina Basin
Leichhardt Block
Galilee Basin
Bowen Basin
ROCKHAMPTON
Diamantina River Lineament
NORTHERN TERRITORY
142°
144°
146°
148°
150°
152°
140°
12°
14°
16°
18°
20°
22°
24°

Fig. 1.2

subprovince. To the south, the succession is unconformably overlain by Devonian to Carboniferous sedimentary formations of the Drummond Basin (Fig. 1.2).

1.2.1 Stratigraphy of the Seventy Mile Range Group

The Cambro-Ordovician succession in the Mount Windsor Subprovince has been divided into four conformable formations which together constitute the Seventy Mile Range Group (Henderson, 1986; Fig. 1.3). The Puddler Creek Formation (PCF) at the base of the Seventy Mile Range Group consists of dominantly continental-derived, lithic sandstone and greywacke interbedded with siltstone. Basaltic to andesitic intrusions and lavas of alkaline affinity are abundant in the upper part of the PCF. The overlying Mount Windsor Formation (MWF) consists mainly of rhyolitic lavas and intrusions and monomictic, rhyolitic volcaniclastic facies. The stratiform massive sulphide deposit at Thalanga occurs at the top of the MWF. The overlying Trooper Creek Formation (TCF) comprises a variety of sedimentary and volcanic lithofacies and shows prominent lateral facies variations. The volcanic facies have andesitic, dacitic and rhyolitic compositions and include lava, syn-volcanic intrusions and volcaniclastic mass-flow units. The non-volcanic facies principally consists of sand- and siltstone turbidites, and massive to laminated black mudstones. In addition, silica-ironstones ('jaspers') and massive sulphide deposits occur within the TCF (eg. Liontown, Highway-Reward and Waterloo, Fig. 1.3). Most of these deposits are relatively small (<1 Mt to 2 Mt; Berry et al., 1992) and currently sub-economic. At present, mining is restricted to the Cu-Au rich ore body at Highway-Reward. The Rollston Range Formation overlies the TCF and consists of fossiliferous sandstone, siltstone and siliceous mudstone. In most parts of the Mount Windsor Subprovince the Seventy Mile Range Group is covered by up to 100 m of sandstone and conglomerate of the Tertiary Campaspe Formation.

Age

The age of the Seventy Mile Range Group most likely spans the Cambrian-Ordovician boundary (Fig. 1.3b). Zircons from rhyolite lavas of the MWF have been dated by SHRIMP U-Pb and yielded crystallisation ages of 481±5 and 485±5 Ma (Early Ordovician; Perkins et al., 1993). Palaeontological dating based on graptolites in the TCF

Fig. 1.3: Regional geology and stratigraphy of the Seventy Mile Range Group.

(a) Regional geology of the Seventy Mile Range Group in the western part of the Mount Windsor Subprovince (from Huston et al., 1995 after Henderson, 1986). Thalanga and several other base metal sulphide deposits and prospects are shown (Berry et al., 1992).

(b) Generalised stratigraphic column for the Seventy Mile Range Group in the Mount Windsor Subprovince (modified from Large, 1992). Ages are based on:

[1)] Graptolites from the TCF (Mount Windsor area) and the Rollston Range Formation (Mount Windsor and Sunrise Spur area) (Henderson, 1983).

[2)] Zircon crystallisation ages (Perkins et al., 1993) for rhyolite samples from the Thalanga railway cutting and near Liontown station. Original data were measured against the SL 13 standard and ages presented here are recalculated in accordance with recommendations of Black et al. (1997).

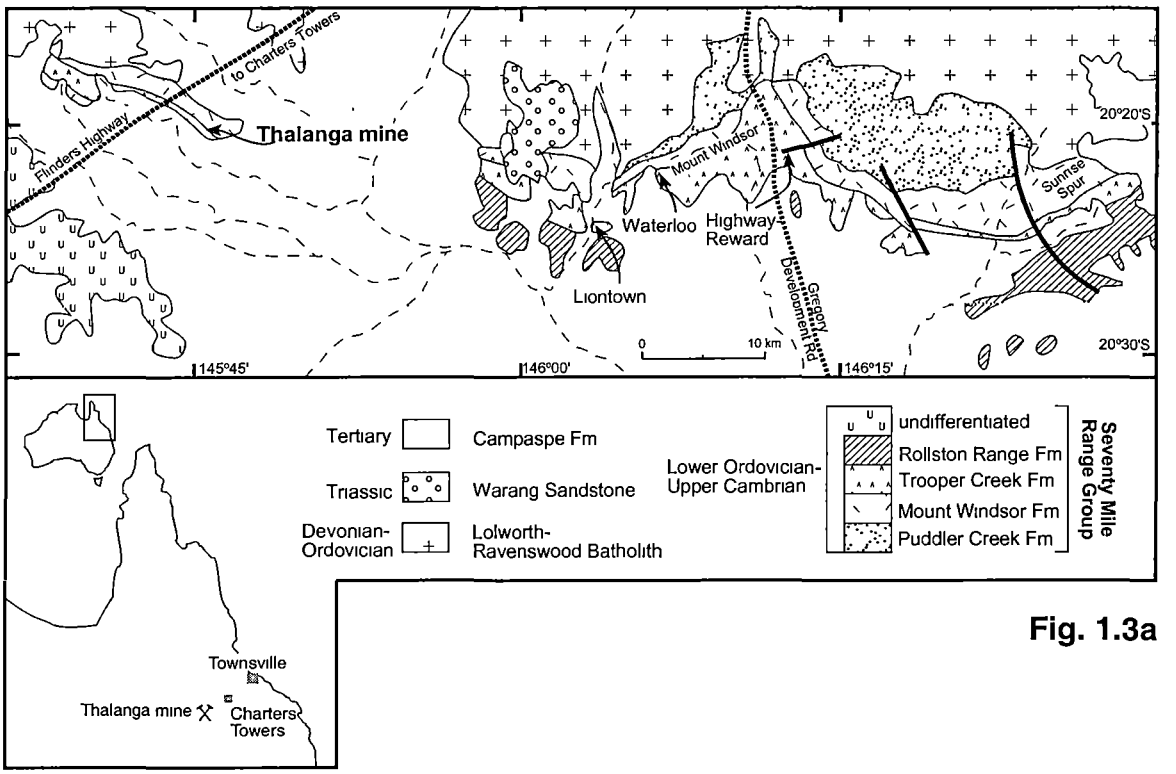

Fig. 1.3a

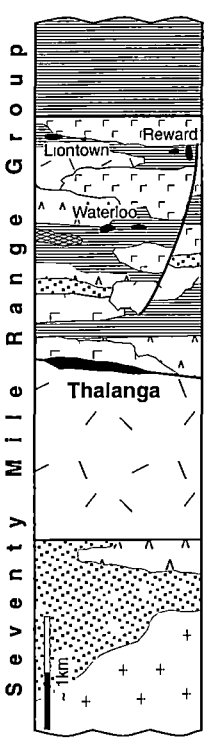

Formation	Age	Lithology
Rollston Range Formation	**Early Ordovician** (Bendigonian-Chewtonian, fossils [1])	sandstone, siltstone and mudstone
Trooper Creek Formation	**Early Ordovician** (Lancefieldian 2-Lancefieldian 3, fossils [1])	andesitic, dacitic and rhyolitic lavas, intrusions and associated breccia, mudstone, siltstone, sandstone; pumice-lithic breccia; silica ironstone; massive sulphide
Mount Windsor Formation	**Early Ordovician** (481 ± 5 Ma and 485 ± 5 Ma; SHRIMP dating [2])	rhyolitic lavas and intrusions, monomictic rhyolitic breccia (minor sandstone)
Puddler Creek Formation	**? Late Cambrian**	sandstone and greywacke; alkali basalt and trachyandesite lavas and sills
Lolworth-Ravenswood Batholith		basal contact intruded by the Lolworth-Ravenswood Batholith

Fig. 1.3b

constrain its age to Lancefieldian (Early Ordovician; Henderson, 1983). Consequently, the stratigraphic position of the Thalanga deposit at the top of the MWF is Early Ordovician in age. It is inferred that the sedimentary facies association of the PCF underlying the MWF was deposited during the Cambrian.

Depositional environment

The presence of turbidites, suspension-settled mudstone and graptolite and pelagic trilobite fossils (Henderson, 1983) implies that most of the succession was deposited in a below-wave-base, relatively deep marine environment. The sedimentary facies association at Thalanga is dominated by mudstone and graded mass-flow units which is consistent with this general interpretation. However, shallow water facies have recently been identified in the TCF close to the Highway-Reward massive sulphide deposits (Doyle, 1997), indicating that water depths varied spatially and temporally.

Tectonic setting

The geochemical and Nd isotope characteristics of volcanics in the Mount Windsor Subprovince indicate that they were emplaced in a continental back-arc basin (Stolz, 1995). In a model for the tectono-magmatic evolution of the Mount Windsor Subprovince (Fig. 1.4), Stolz (1995) inferred that sediments of the PCF were deposited on an attenuated passive continental margin during the Neo-proterozoic? to Upper Cambrian. A change in the tectonic regime caused the onset of subduction and development of a back-arc basin on continental crust leading to the emplacement of alkaline andesites in the top part of the PCF. Subsequently, substantial melting of the continental lithosphere produced the quartz-phyric rhyolites of the Mount Windsor Formation. Volcanics in the TCF have compositional characteristics indicative of a magma source that was generated, or modified at least partially, by subduction-related processes.

Fig. 1.4: A model for the tectonic evolution of the Mount Windsor Subprovince from the Neoproterozoic? to Early Ordovician (from Stolz, 1995).

This model is based on geochemical and isotopic data for various volcanic rocks from the Seventy Mile Range Group.

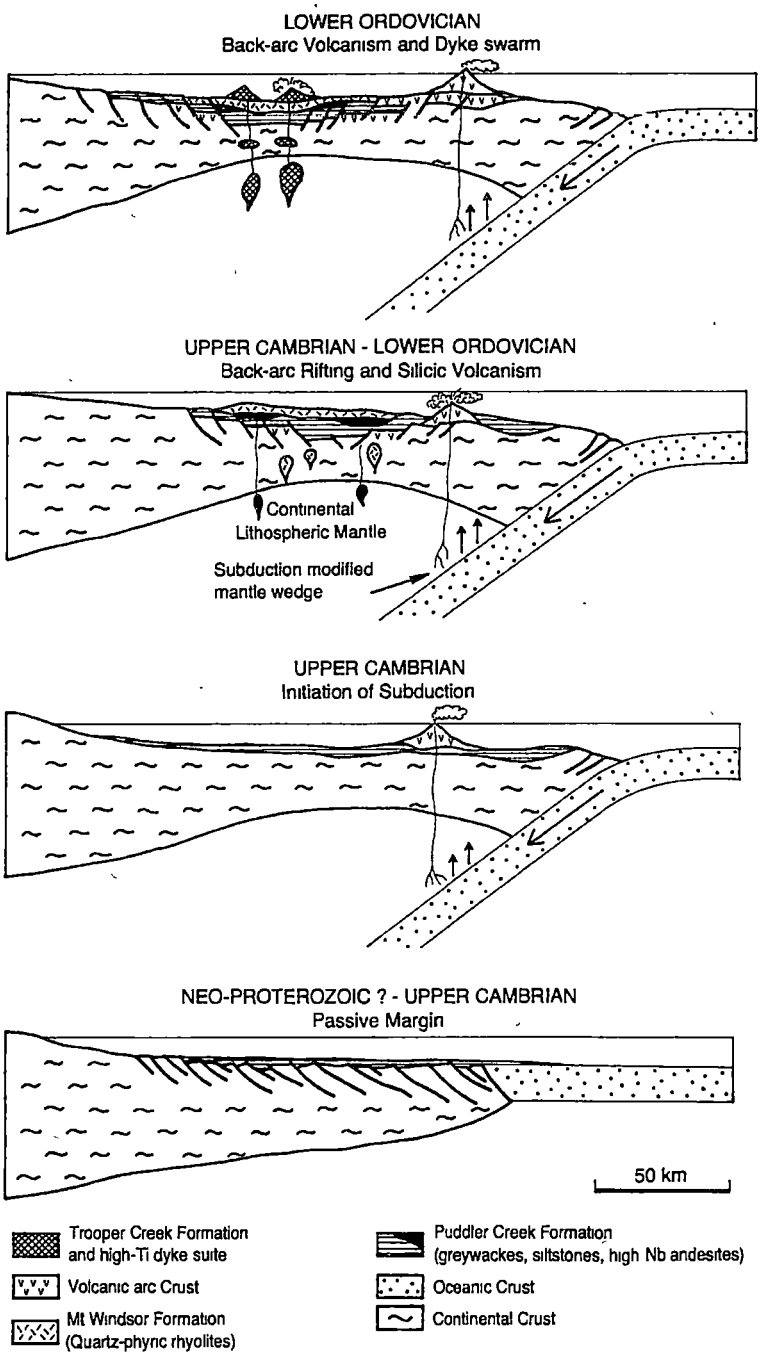
LOWER ORDOVICIAN
Back-arc Volcanism and Dyke swarm
UPPER CAMBRIAN - LOWER ORDOVICIAN
Back-arc Rifting and Silicic Volcanism
Continental
Lithospheric Mantle
Subduction modified
mantle wedge
UPPER CAMBRIAN
Initiation of Subduction
NEO-PROTEROZOIC ? - UPPER CAMBRIAN
Passive Margin
50 km
Trooper Creek Formation
and high-Ti dyke suite
Volcanic arc Crust
Mt Windsor Formation
(Quartz-phyric rhyolites)
Puddler Creek Formation
(greywackes, siltstones, high Nb andesites)
Oceanic Crust
Continental Crust

Fig. 1.4

Regional deformation and metamorphism

The subprovince has been deformed by up to four major events (D1 to D4, Berry et al., 1992). However, early faults (D1) that occur locally in the Mount Windsor Subprovince have not been recognised at Thalanga. Regional deformation (D2) was associated with relatively low pressure regional metamorphic assemblages, ranging from sub-greenschist grade in the east to upper greenschist grade in the west, and produced a near vertical axial plane penetrative cleavage (S2). The Mount Windsor Subprovince is interpreted to represent a single, south-facing limb of a large, E-W trending, upright D2 syncline. Two later phases of faulting (D3 and D4) could be associated with the emplacement of unfoliated (post-D2) Siluro-Devonian intrusions. These post-kinematic plutons have hornfels facies contact metamorphic aureoles which commonly contain cordierite. The aureoles are readily recognisable in the eastern part of the Mount Windsor Subprovince where prograde contact metamorphism exceeded the grade of the earlier regional metamorphism.

1.3 Geology of the Thalanga VHMS deposit

The Thalanga deposit is situated at the foot of the eastern end of a low, northwest trending, strike ridge (Thalanga Range), flanked to the north, east and south by an extensive peneplain (Fig. 1.5). Outcrop in the vicinity of the deposit is poor and most of the geological interpretation in the area is based on observations from RAB/Percussion holes, diamond drill holes and mine development.

A hematite-limonite gossan above the Central Thalanga ore lens was discovered in 1975 by Penarroya (Aust) Pty Ltd (Hartley, 1984; Herrmann, 1995). Mining commenced in 1989 under a joint venture of Pancontinental Mining Ltd, Outokumpu Australia Pty Ltd and Agip Australia; later Pancontinental was the sole owner of the mine. Thalanga became part of the RGC group in 1995. After the initial development of an open pit to access the supergene enrichment zone, primary massive sulphides were extracted by underground developments. Mining operations ceased in June, 1998 due to the depletion of reserves. From 1990 to 1998 a total of 4,707,607 t of supergene and primary massive sulphide ore were milled and concentrated on site and transported to port via the nearby Mount Isa-Townsville railway line. The total mineral resource (including past production and in-

ground resources) was estimated in June 1998 as 6.6 Mt @ 1.8% Cu, 2.6% Pb, 8.4% Zn, 69g/t Ag and 0.4g/t Au (data provided by Phil Jay, RGC Thalanga Pty Ltd, September 1998).

1.3.1 Stratigraphy

The Thalanga deposit occurs at the top of MWF rhyolites (thickness: 500 to 1000 m) and below a volcano-sedimentary succession dominated by dacites (TCF, thickness: >500 m). The stratigraphic interval that includes the ore body is referred to as the Favourable Horizon. In this thesis, the footwall rhyolites, the lithologies of the Favourable Horizon and the hangingwall succession are collectively referred to as the 'Thalanga sequence'. In a vertical long projection of the Favourable Horizon, the Thalanga ore body has an arcuate shape over a strike extent of about 3000 m and the main ore lenses are referred to as East, Central and West Thalanga (Fig. 1.5). The ore lenses have sheet-like geometries ranging in thickness from <1 m to about 25 m with an average of about 5 m. Small satellite massive sulphide bodies occur to the west (West 45) and the east (Far East & Orient) of the main Thalanga deposit.

At Thalanga, phenocryst assemblages have been used to discriminate among the lithofacies and also provide a good indication of composition. Rhyolites in the footwall (MWF) are quartz ± feldspar-phyric whereas dacites in the hangingwall (TCF) are feldspar-phyric (or aphyric). These texturally defined groups correlate well with geochemical subdivisions based on immobile element ratios (Chapter 6).

On a regional scale, the stratigraphic boundary between the MWF and the TCF was assigned by Henderson (1986) to the basal contact of the lowermost dacite. At Thalanga, the contact between the TCF and the MWF is at the basal contact of the first occurrence of dacite clast-bearing breccia units or dacite lava overlying the massive sulphides. Consequently, the Favourable Horizon is part of the MWF. It should be noted that quartz-phyric rhyolite clasts occur in some polymictic breccia in the TCF.

The footwall of the massive sulphides consists of rhyolite lavas, syn-volcanic intrusions and resedimented rhyolitic breccia units (MWF) which show variable degrees of textural, mineralogical and geochemical modification as a result of hydrothermal alteration, deformation and metamorphism.

The Favourable Horizon conformably overlies footwall rhyolite and consists of diverse facies with marked lateral variations. It ranges in thickness between 5 and 50 m in the Thalanga mine area and includes coarse quartz-feldspar crystal-rich volcaniclastic facies ('Quartz-Eye Volcaniclastics'), coarsely quartz-feldspar-phyric rhyolite sills, rare rhyolitic breccia, massive to semi-massive sulphides, carbonate-tremolite-chlorite rocks, massive to semi-massive barite, silica-ironstone and laminated or massive grey-brown mudstone.

The hangingwall (TCF) consists of a volcano-sedimentary succession dominated by dacite with patchy or vein controlled alteration which is generally not texturally destructive.

1.3.2 Intrusions

Two large plutons in the vicinity of the Thalanga deposit were identified by geomagnetic surveys and intersected by drilling (Fig. 1.5). A foliated (pre-D2) granitoid is located to the north of the Thalanga ore body and in East Thalanga, an unfoliated (post-D2) diorite intrusion cross cuts the stratigraphy. The diorite has a garnet-bearing contact metamorphic aureole and its apophyses are commonly present in drill core from East Thalanga. Relatively thin (<1 m to 5 m), post-D2 dikes and sills of dolerite and basalt occur locally.

1.3.3 Structure

The structural geology of the Thalanga area was examined in detail by Hill (1996) and Fig. 1.6 illustrates the results of that study. The Thalanga sequence was deformed during regional deformation (D2) and a strong, bedding parallel foliation (S2) developed in incompetent, phyllosilicate-rich rocks such as sedimentary and volcaniclastic facies in the hangingwall and in the altered, phyllosilicate-rich footwall rhyolite. Foliated biotite, commonly in assemblages including quartz, muscovite and chlorite, are ubiquitous in altered rhyolite and pelitic sedimentary and volcaniclastic facies, indicating metamorphic conditions of upper greenschist grade. The ore lenses of West, Central and East Thalanga are separated by NNE striking normal faults ('pre-D3 structures' of Hill, 1996). Displacement along ENE trending faults during a younger deformation event (D3, Hill

Fig. 1.5: Geological map of the Thalanga mine area.

This map shows the location of cross sections through the Thalanga sequence examined for this thesis. Parts of the MWF are exposed in outcrop along the Thalanga Range but its contact with the PCF is covered by the Tertiary Campaspe Formation and has been inferred from RC drilling to the north and northwest of the mine. The contact between the PCF and the MWF is only exposed in outcrop close to the Flinders Highway. The inset shows a vertical long projection of the Thalanga ore lenses and the location of the drill core based cross sections. The outcrop section uses a railway cutting 5 km west of the Thalanga mine. Grid references refer to AMG (Australian Map Grid).

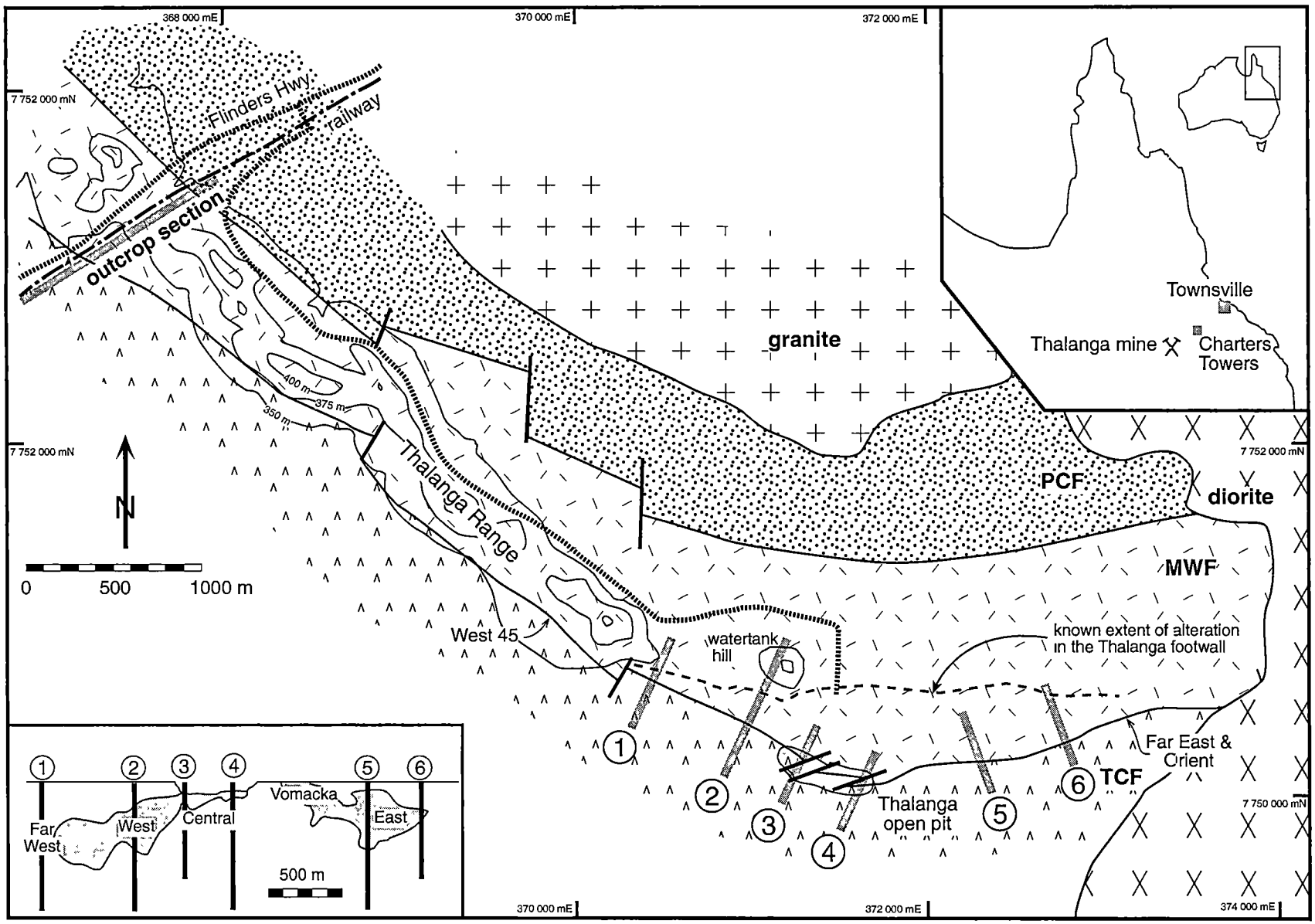
368 000 mE
370 000 mE
372 000 mE
374 000 mE
7 752 000 mN
7 750 000 mN
Flinders Hwy
railway
outcrop section
granite
400 m
375 m
350 m
Thalanga Range
West 45
watertank hill
known extent of alteration in the Thalanga footwall
PCF
diorite
MWF
TCF
Far East & Orient
Thalanga open pit
Townsville
Thalanga mine
Charters Towers
N
0
500
1000 m
Far West
West
Central
Vomacka
East
500 m
1
2
3
4
5
6

Fig. 1.5

1996) moved footwall rhyolite into an apparent hangingwall position above the Favourable Horizon in Central Thalanga (Fig. 1.5). The change in strike of the Thalanga sequence from northwest (West Thalanga) to northeast (East Thalanga) is due to sub-vertical open folding (wavelength >10 km, N-striking axial plane) which formed after regional folding and prior to D3-faulting (Hill, 1996).

1.4 Previous research

1.4.1 Mount Windsor Subprovince

Major studies on aspects of the geology of the Mount Windsor Subprovince include papers presented by Henderson (1983, 1986), Berry et al. (1992) and Stolz (1995). Henderson (1986) demonstrated that the Cambro-Ordovician volcano-sedimentary succession of the Seventy Mile Range Group represents a distinctive subprovince within the Charters Towers Province and divided the sequence into four conformable formations. Berry et al. (1992) provided a description of the structural history of the Mount Windsor Subprovince and the geology of the massive sulphide deposits. Stolz (1995) presented geochemical and isotopic evidence for the tectonic evolution of the subprovince, from an attenuated passive, continental margin to a subduction-related, back-arc rift setting. Detailed deposit-scale studies on VHMS deposits in the Mount Windsor Subprovince have been published by Kay (1987; Highway deposit), Mulholland (1991; Magpie deposit), Beams et al. (1990; Reward deposit) and Huston et al. (1995, Waterloo and Agincourt deposits).

Several research projects on geological problems in the Mount Windsor Subprovince were completed at the CODES Special Research Centre (formerly Key Centre), University of Tasmania. These include Herrmann (1994, genesis of massive carbonate-tremolite-chlorite rocks at Thalanga), Miller (1996, geology of the Liontown deposit) and Doyle (1997, volcanic setting of the Highway-Reward deposit). A detailed study on the genesis of the Thalanga massive sulphide deposit was completed by Hill (1996). Other on-going projects include a geochemical study of the Waterloo deposit (Thomas Monecke, PhD project) and a project on the regional volcanic facies architecture of the Seventy Mile Range Group (Kirsten Simpson, PhD project).

Fig. 1.6: Schematic block models of the main deformation events at Thalanga (from Hill, 1996).

The massive sulphide deposit is represented with a hatched pattern. Depth to hinge of F_2 syncline is unknown.

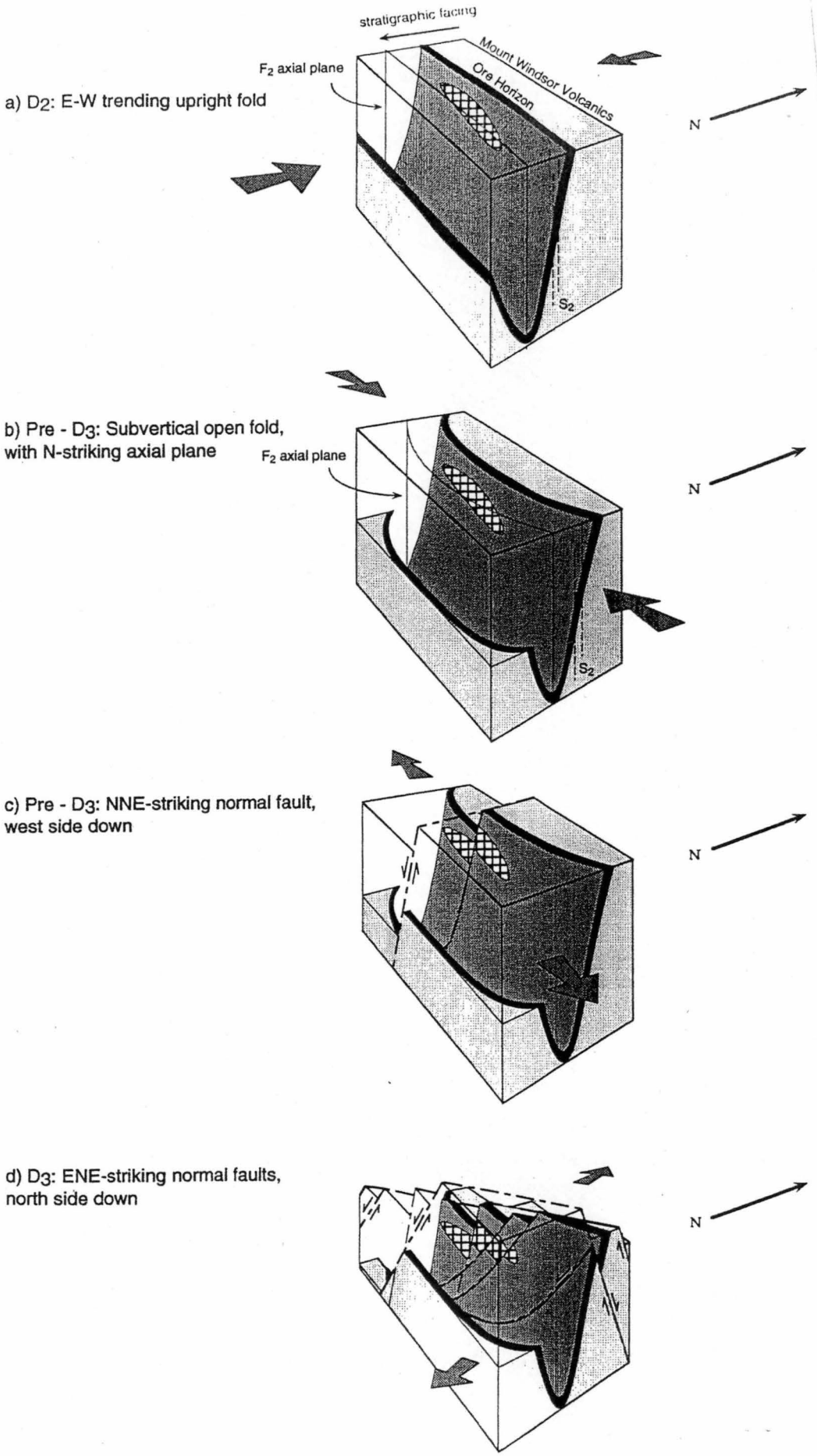
stratigraphic facing
Mount Windsor Volcanics
Ore Horizon
F2 axial plane
a) D2: E-W trending upright fold
S2
N
b) Pre - D3: Subvertical open fold,
with N-striking axial plane
F2 axial plane
S2
N
c) Pre - D3: NNE-striking normal fault,
west side down
N
d) D3: ENE-striking normal faults,
north side down
N

Fig. 1.6

1.4.2 Thalanga

The results of the initial exploration phase at Thalanga are documented in Gregory et al. (1990) and references therein. Based on data from about 100 exploration diamond drill holes, the exploratory decline, cross-cuts and underground drilling in Central Thalanga, it was concluded that the mineralisation was of syn-genetic origin and that massive sulphides were deposited onto the seafloor from dense saline solutions.

In a major study on the Thalanga deposit, Hill (1996) investigated the origin of the massive sulphides and associated massive to semi-massive carbonates, the volcanic facies association of the Favourable Horizon and the structural geology of the Thalanga area. The focus of the study was the geology of the Favourable Horizon and the spatial relationship between massive sulphides and the immediate host rocks. Hill (1996) concluded that the deposit was of syn-genetic origin but that the massive sulphides formed predominantly by sub-seafloor replacement of coarse quartz-bearing volcaniclastic units (Quartz-Eye Volcaniclastics or QEV) and carbonate-chlorite-rich alteration assemblages (now carbonate-chlorite-tremolite-rich rocks). Sulphur isotopes indicated that the hydrothermal solutions contained dissolved igneous sulphur and Cambro-Ordovician seawater sulphur that had been inorganically reduced during hydrothermal convection.

Hill (1996) also demonstrated that the Thalanga massive sulphides have been strongly recrystallised and partially remobilised during regional deformation (D2). Locally, structural repetition and thickening of the massive sulphides occurred along younger faults (D3) which are oriented at a low angle to stratigraphy.

Massive carbonate-chlorite-tremolite-rich rocks in the Favourable Horizon of West Thalanga were initially interpreted to represent metamorphosed calcareous exhalites (Gregory et al., 1990). However, in a detailed geochemical study, Herrmann (1994) showed that these rocks have immobile element ratios similar to footwall rhyolite and concluded that they represent metamorphosed equivalents of intensely carbonate-chlorite altered footwall rhyolite rather than genuine exhalites.

1.5 Approach and methods

The principal aims of this study are to examine the volcanic facies architecture of the felsic host rock sequence to the Thalanga massive sulphide deposit, the geometry of the alteration system and geochemical modifications related to hydrothermal alteration and the conditions of regional and contact metamorphism. This was achieved by constructing six cross sections using diamond drill holes and examination of one outcrop cross section 5 km to the west of the Thalanga mine.

In the outcrop section, the entire MWF and a large portion of the TCF are exposed. In the mine area, the stratigraphic thickness of the Thalanga sequence, represented in drill hole cross sections, ranges from 300 to 700 m and includes the upper ~ 150 to 450 m of the footwall (including outcrop on watertank hill in West Thalanga, Fig. 1.5), 5 to 50 m of the Favourable Horizon and ~ 200 to 250 m of the hangingwall. The down-dip extent of the cross sections in the mine area varies between 600 and 900 m.

1.5.1 Drill hole coverage

Due to the limited outcrop in the Thalanga mine area, the project relied strongly on diamond drill core logging. Drilling was targeted at the Favourable Horizon and intercepted variable stratigraphic thicknesses of the footwall and hangingwall. Cross sections were located mainly where relatively long drill holes (up to 1000 m of drill core), collared up to 300 m stratigraphically above or below the Favourable Horizon, were available. Each cross section is based on 4 to 6 drill holes covering variable stratigraphic thicknesses and down-dip extent (Table 1.2). In total, ~15,000 m of core from 33 diamond drill holes were examined. Graphic logs and detailed lithological descriptions of these drill holes are presented in the Appendix.

Although diamond drill core provides continuous one-dimensional 'outcrop', there are some problems in its use for geological interpretations. At Thalanga, drill holes projected onto cross sections may in fact deviate laterally by ± 50 m from the position of the section (± 80 m in section 4). Therefore, the geology and facies relationships shown on the cross sections are based on information from a slice through the Thalanga sequence up to 150 m thick (Fig. 1.7). Furthermore, drill holes may be up to several hundred metres apart in the down-dip direction of the cross sections (Fig. 1.8) and some

Fig. 1.7: Locations of drill hole cross sections in the Thalanga mine area and surface projections of drill holes logged for this study.

Note that the drill holes may deviate laterally away from the sections by ±50 m. Therefore, the geological interpretations of these cross sections represent slices rather than true two dimensional sections through the Thalanga sequence.

(a) Thalanga mine area showing the locations of cross sections examined for this study and the orientation of the West and East Thalanga mine grid. Also shown are the surface projections of TH471 which intersects the contact between footwall rhyolite and the diorite intrusion, and underground drill hole E3204SD50 which intersects mudstone with cordierite porphyoblasts in the Favourable Horizon. Open circles indicate collar position.

(b) Surface projection of the drill holes logged and sampled for this study in West and Central Thalanga and locations of sections 1 (19450E), 2 (20080E), 3 (20460E), and 4 (20800E).

(c) Surface projection of the drill holes logged and sampled for this study in East Thalanga and locations of sections 5 (31980E), and 6 (32380E).

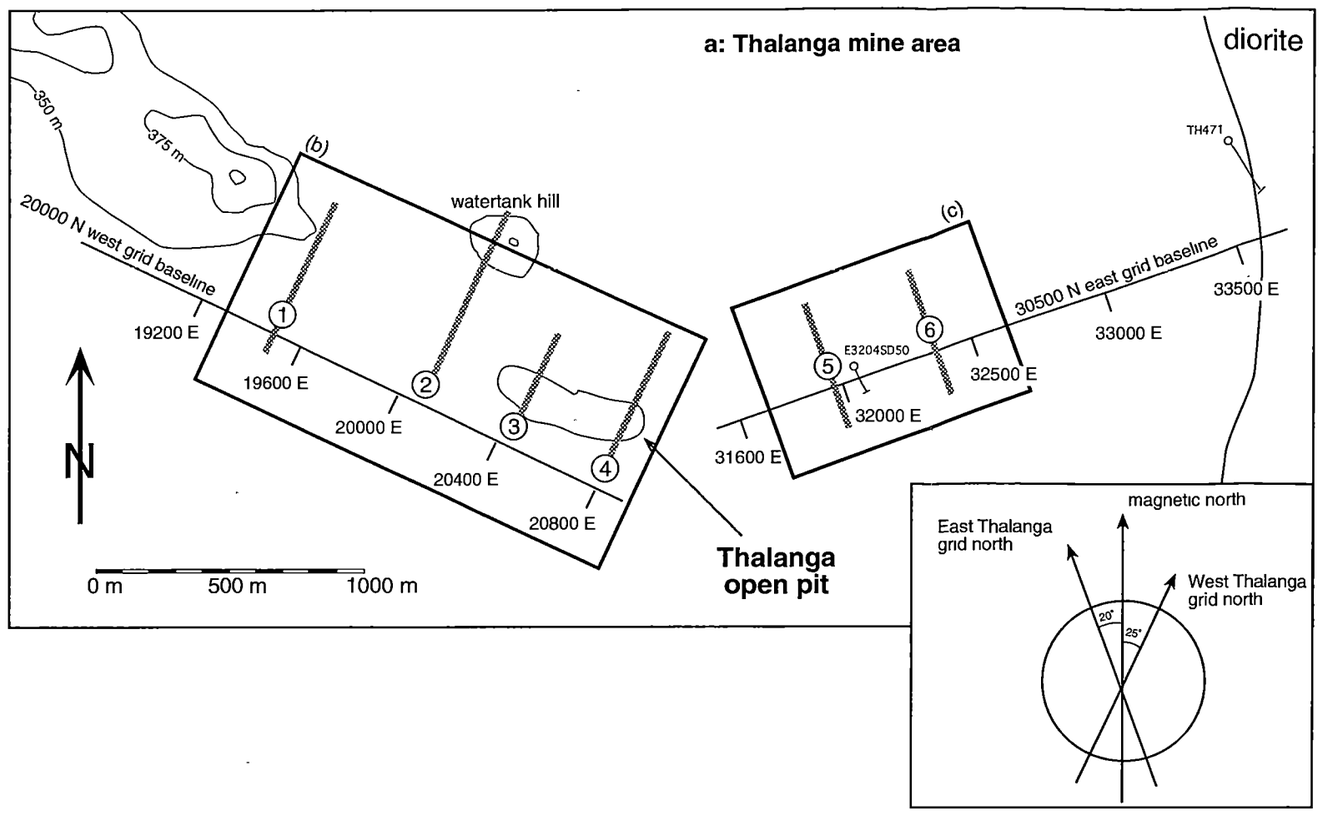
a: Thalanga mine area
diorite
350 m
375 m
(b)
watertank hill
20000 N west grid baseline
19200 E
19600 E
20000 E
20400 E
20800 E
0 m
500 m
1000 m
N
Thalanga
open pit
(c)
TH471
30500 N east grid baseline
33500 E
33000 E
32500 E
32000 E
31600 E
E3204SD50
magnetic north
East Thalanga
grid north
West Thalanga
grid north
20°
25°

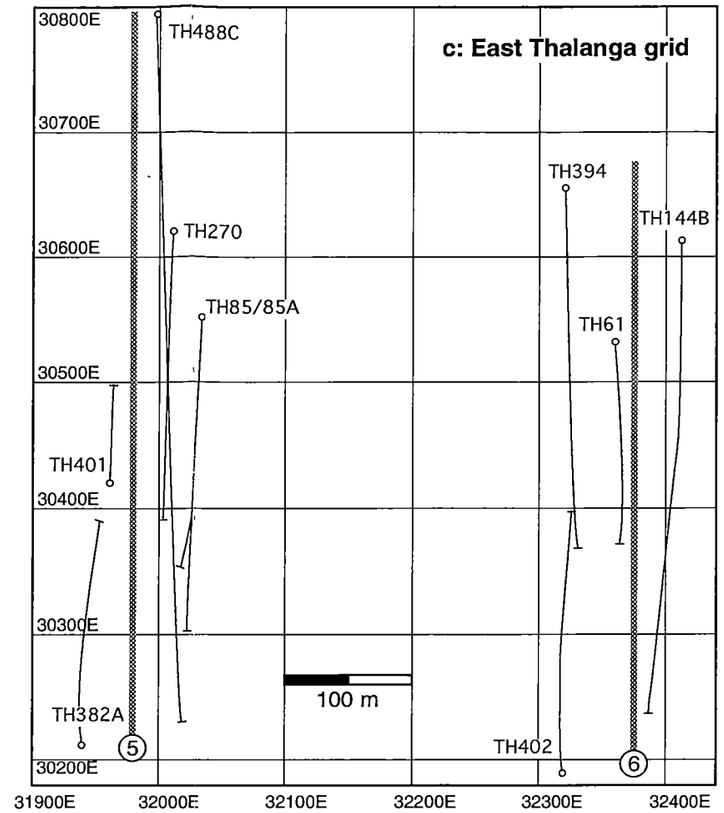
c: East Thalanga grid
30800E
30700E
30600E
30500E
30400E
30300E
30200E
TH488C
TH270
TH85/85A
TH401
TH382A
TH394
TH144B
TH61
TH402
100 m
31900E
32000E
32100E
32200E
32300E
32400E

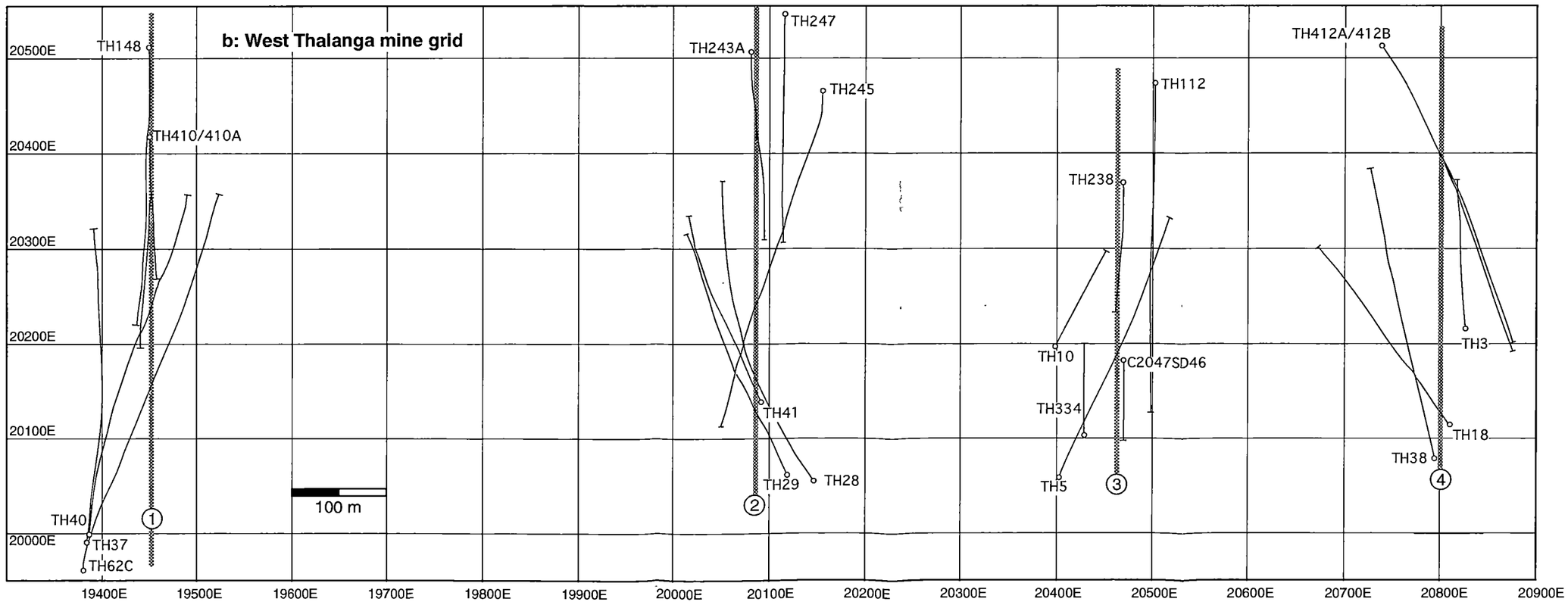
b: West Thalanga mine grid
20500E
20400E
20300E
20200E
20100E
20000E
TH148
TH410/410A
TH40
TH37
TH62C
100 m
TH247
TH243A
TH245
TH41
TH29
TH28
TH112
TH238
TH10
TH334
TH5
C2047SD46
TH412A/412B
TH3
TH18
TH38
19400E
19500E
19600E
19700E
19800E
19900E
20000E
20100E
20200E
20300E
20400E
20500E
20600E
20700E
20800E
20900E

Fig. 1.7

Table 1.2: Summary of logged diamond drill holes

Sections through the Thalanga sequence in the mine area											
cross section		stratigraphic thickness intersected		diamond drill holes (footwall and FH)		total for footwall and FH	diamond drill hole (hangingwall)		total for hangingwall	total for section
mine grid	location	footwall and FH	hangingwall	name	length [m]		name	length [m]		
19450E ± 60	**section 1 (Far West)** just west of main western ore lens	~270m	~250m	TH148	550		TH37	500		
				TH410	440		TH40	590		
				TH410A	300	Σ1290m	TH62C	950	Σ2040m	Σ3330m
20080E ± 60	**section 2 (West)** through main West Thalanga ore lens	~230m	~230m	TH234A	350		TH28	530		
				TH245	550		TH29	320		
				TH247	310	Σ1210m	TH41	600	Σ1550m	Σ2760m
20460E ± 50	**section 3 (Central)** western part of Central Thalanga lens	~280m	~120m	part of TH5	300		part of TH5	200		
				TH112	650		TH334	150		
				TH238	260	Σ1210m	C2047SD46	120	Σ470m	Σ1680m
20800E ± 80	**section 4 (Central)** eastern part of Central Thalanga lens	~300m	~100m	TH3	200		part of TH18	170		
				part of TH18	230		part of TH38	100		
				part of TH38	300					
				TH412A	580					
				TH412B	750	Σ2060m			Σ270m	Σ2330m
31980E ± 50	**section 5 (East)** through main East Thalanga ore lens	~300m	~200m	TH85	600		TH382A	500		
				TH85A	300		TH401	130		
				TH270	380					
				TH488C	1050	Σ2330m			Σ630m	Σ2960m
32380E ± 50	**section 6 (East)** just east of East Thalanga ore lens	~200m	~220m	TH61	280		TH402	400		
				TH144B	700					
				TH394	500	Σ1480m			Σ400m	Σ1880m
										Σ 14940m

FH: Favourable Horizon

Fig. 1.8: Cross sections 1 to 6 through the Thalanga sequence showing the drill hole coverage in the down-dip dimension.

The down-dip extent of the section varies substantially, depending on the availability of deep drill holes. Northings on sections refers to the mine grid; 1000 RL (surface) equals 330 m above sea level. Tick marks on drill holes are 50 m apart. Massive sulphides are shown in black. Thick, dashed lines are D3 faults. Thin line represents the stratigraphic contact between MWF and TCF; the Favourable Horizon containing the massive sulphides is included in the MWF.

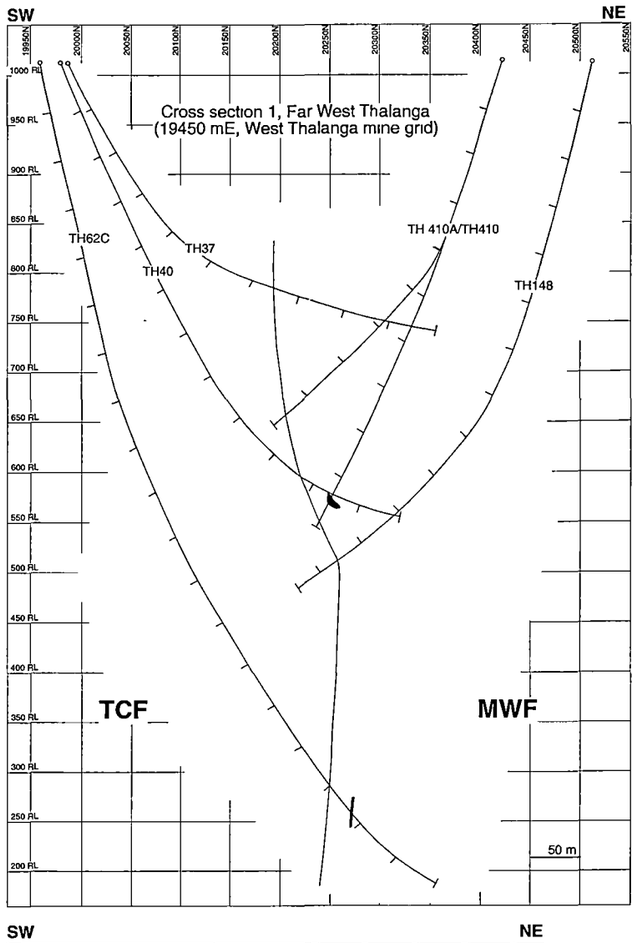
SW
NE
Cross section 1, Far West Thalanga
(19450 mE, West Thalanga mine grid)
TH62C
TH37
TH40
TH 410A/TH410
TH148
TCF
MWF
50 m

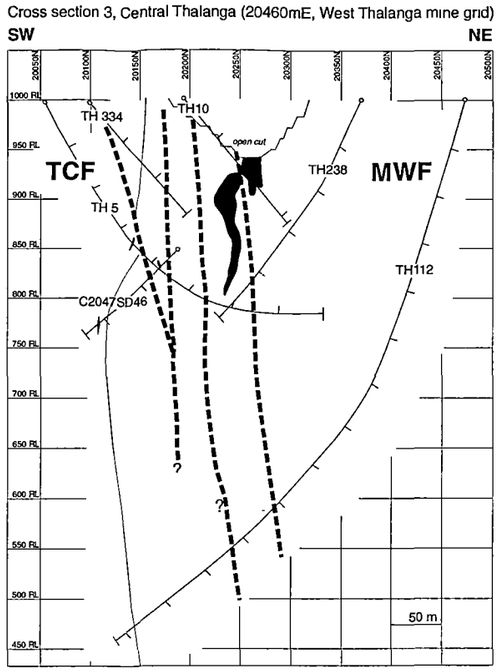
Cross section 3, Central Thalanga (20460mE, West Thalanga mine grid)
SW
NE
TH 334
TH10
open cut
TH238
TH 5
TH112
C2047SD46
TCF
MWF
50 m

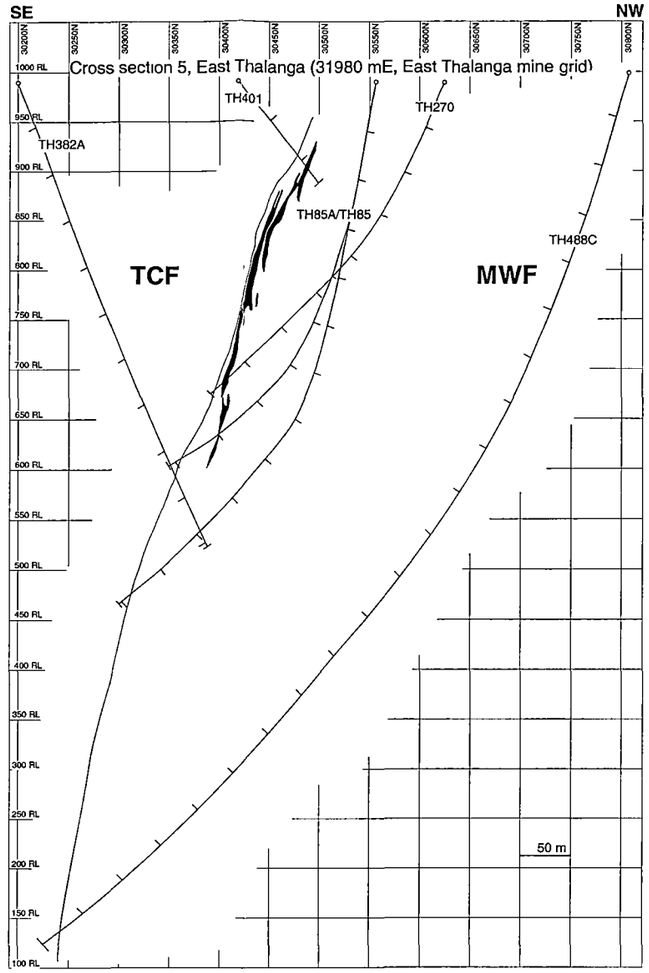
SE
NW
Cross section 5, East Thalanga (31980 mE, East Thalanga mine grid)
TH401
TH270
TH382A
TH85A/TH85
TH488C
TCF
MWF
50 m

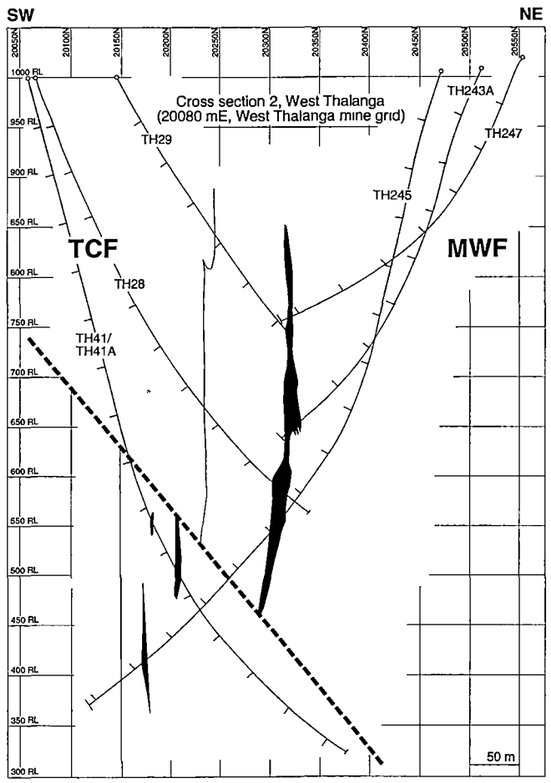
SW
NE
Cross section 2, West Thalanga
(20080 mE, West Thalanga mine grid)
TH243A
TH247
TH29
TH245
TH28
TH41/
TH41A
TCF
MWF
50 m

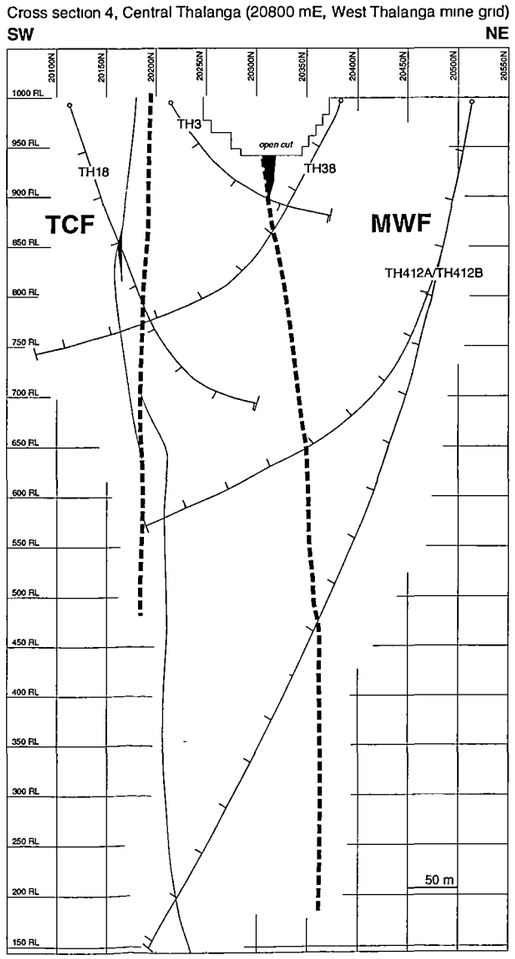
Cross section 4, Central Thalanga (20800 mE, West Thalanga mine grid)
SW
NE
TH3
open cut
TH18
TH38
TH412A/TH412B
TCF
MWF
50 m

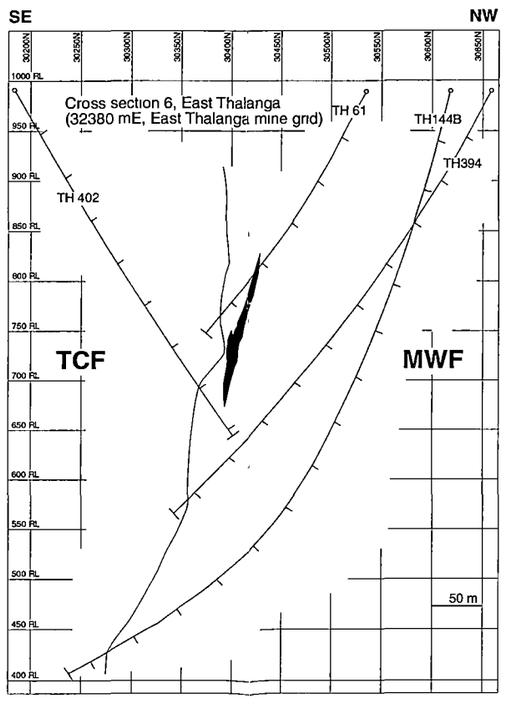
SE
NW
Cross section 6, East Thalanga
(32380 mE, East Thalanga mine grid)
TH 61
TH144B
TH394
TH 402
TCF
MWF
50 m

Fig. 1.8

lithological contacts might have been missed. Notwithstanding these limitations the drill hole data have allowed detailed examination of the lithological diversity, facies architecture and alteration zonation in the Thalanga sequence.

1.5.2 Facies analysis and alteration logging

The different lithofacies present in the Thalanga sequence have been identified and characterised in order to correlate units between drill holes, interpret their mode of emplacement and develop a general facies model for the volcanological evolution of the Thalanga area. This part of the project was primarily based on observations of hand specimen and thin section textures and contact relationships. The descriptive terminology proposed by McPhie et al. (1993, p. 9 and 10) has been applied in naming the lithofacies. Several types of rhyolites and dacites have been identified by 'phenocryst logging' (systematic recording of the mineralogy, abundance and size range of phenocrysts).

Identification of primary lithofacies was particularly challenging in the footwall alteration zone below the massive sulphides. Alteration commonly imparted an apparent clastic textures onto the altered footwall rhyolite and specific textural criteria have been developed in order to distinguish coherent rhyolite facies with pseudoclastic textures from genuine volcaniclastic facies (Chapter 5).

The mineralogy, abundance and distribution of non-primary minerals (including alteration minerals and metamorphic equivalents of alteration minerals) was systematically recorded during drill core examination (graphic logs of drill holes in the Appendix). These alteration logs and observational data from thin sections of variably altered rocks in the Thalanga sequence provided the basis for the definition of different types of alteration referred to as 'alteration facies' (Chapter 7).

1.5.3 Geochemical analyses

About 180 samples were selected for geochemical analyses including altered and least-altered examples of different types of rhyolite and dacite identified in the Thalanga sequence. These were analysed for major and trace elements by XRF analyses and ICP-MS. A sub-set of the samples was selected for REE analysis. The methods applied for

sample preparation and measurement procedures are detailed in the Appendix together with the tabulated data. The data reveal the geochemical effects of hydrothermal alteration in the footwall alteration zone and show that several elements, including Ti and Zr were immobile (Chapters 6 and 8).

Several samples containing garnet-bearing mineral assemblages, which are scarce in the Thalanga sequence, were analysed by electron microprobe analysis in order to constrain the peak conditions of metamorphism in the Thalanga area using thermobarometric calculations (Chapter 4). Furthermore, changes in the mineral chemistry of muscovite, chlorite and biotite were examined in a series of samples of altered footwall rhyolite from one drill hole in West Thalanga (TH247, section 2) (Chapter 8). The data and a description of analytical procedures are documented in the Appendix.

1.6 Thesis outline

This thesis is organised in a series of chapters which deal with specific aspects of this study. The general features of the various lithofacies present in the Thalanga sequence and the textural and mineralogical effects of alteration are introduced in Chapter 2.

The conditions of regional and contact metamorphism in the Thalanga area are constrained using evidence from metamorphic mineral assemblages, metamorphic textures and thermobarometric calculations based on microprobe data from garnet bearing samples (Chapters 3 and 4). Chapter 4 also includes a detailed discussion of the mineral chemistry of muscovite, chlorite, biotite and garnet at Thalanga.

The volcanic facies architecture of the Thalanga sequence is reconstructed in Chapter 5 which includes a detailed assessment of volcanic facies interpretation in the footwall alteration zone and the use of phenocryst logging as a tool for discriminating different types of volcanics.

The geochemical data are presented in Chapter 6 which is predominantly concerned with the characteristics of the primary geochemistry of Thalanga volcanics and possible petrogenetic implications.

Chapter 7 deals with the various styles and mineralogy of alteration at Thalanga and ten different alteration facies are defined on the basis of textural and mineralogical features and general intensity of alteration. The geochemical effects of alteration in the footwall rhyolite and hangingwall dacite are examined in detail in Chapter 8. Chapter 9 provides a detailed discussion of the results of facies analysis and the examination of alteration at Thalanga and includes a comparison with other VHMS deposits. The conclusions of this research project are summarised in the final chapter of this thesis (Chapter 10).

2 The Thalanga sequence - Introduction to lithofacies and alteration

In this chapter, the principal geological features of the Thalanga sequence are described with emphasis on the main lithofacies in the footwall, Favourable Horizon and hangingwall including the principal styles of alteration. In the following chapters, particular aspects of this research project (metamorphism, volcanic facies analysis, alteration and geochemistry) will be addressed in the context of this framework.

2.1 Footwall

The footwall to the Thalanga deposit consists of a succession of rhyolitic lavas, resedimented monomictic rhyolite breccia and minor syn-volcanic intrusions ranging in thickness between ~550 m in the outcrop section to ~1000 m below the massive sulphides. Several different types of rhyolite can be distinguished based on consistent differences in quartz and feldspar phenocrysts (Chapter 5). Coherent and volcaniclastic facies of footwall rhyolite are readily distinguishable in least-altered successions which have not been affected by hydrothermal alteration such as the outcrop section (Fig. 2.1a, b; Fig. 5.5). In contrast, facies recognition is difficult in the footwall alteration zone below the massive sulphides because primary volcanic textures have been greatly modified by hydrothermal alteration (Fig. 2.1 c, d). This zone underlying the Thalanga deposit is laterally continuous and extends for more than 300 m into the footwall (Fig. 2.2). It is texturally and mineralogically diverse and includes various mineral assemblages indicating silicic, pyritic, phyllosilicate-dominated and calcareous alteration. Accordingly, several alteration facies have been defined on the basis of dominant mineral assemblages and alteration intensity (Chapter 7). The lateral contacts of the footwall alteration zone are gradational over several tens of metres and generally characterised by increasing abundances of muscovite, chlorite and biotite, destruction of feldspar phenocrysts and occurrences of disseminated pyrite.

The bulk of the footwall alteration zone is represented by phyllosilicate-rich, feldspar-destructive alteration which is accompanied by disseminated pyrite. The abundance and relative proportions of muscovite, chlorite, biotite and quartz typically vary on hand specimen scale, giving rise to the characteristic mottled appearance of this alteration facies and widespread apparent clastic textures in the footwall alteration zone (Fig. 2.1c). Allen (1988) described similar textures in hydrothermally altered, coherent

Fig. 2.1: Examples of primary and secondary textures of footwall rhyolite and textures of massive and semi-massive sulphides.

(a) Least-altered, quartz-feldspar-phyric, coherent rhyolite with an evenly porphyritic texture (sample TH247-74.50, section 2; see Fig. 7.5b for sample location). Selective staining of the sample with sodium cobaltinitrate shows that many feldspar phenocrysts are K-rich and that K-feldspar is also abundant in the quartzofeldspathic groundmass.

(b) Monomictic rhyolite breccia in the outcrop section is poorly sorted, clast- to matrix-supported and clasts may be locally arranged in a jig-saw fit manner. These textures and gradational contacts with coherent facies support the interpretation that this facies represents in situ and resedimented, syn-eruptive autoclastic breccia (lens cap is 5 cm in diameter).

(c) Coherent rhyolite with apparent clastic textures is common below the Thalanga deposit. This rock shows evenly distributed quartz phenocrysts and is interpreted as coherent facies of rhyolite lava which experienced domainal or multi-stage hydrothermal alteration leading to the development of muscovite-rich and chlorite-rich groundmass domains. Such rocks are common in the footwall alteration zone and may be easily mistaken as volcaniclastic facies. The textural criteria applied to distinguish 'apparent' and genuine volcaniclastic facies are discussed in detail in Chapter 5 (sample TH410-169.90).

(d) Intensely altered rhyolite immediately below the ore body, showing quartz- and pyrite-rich alteration. Quartz phenocrysts are the only preserved original feature in such intensely altered rhyolite (sample TH394-454.80).

(e) Typical massive sulphide ore from Central Thalanga with coarsely recrystallised, dark red-brown sphalerite locally containing bands of pyrite (sample CT-91-45, UTas catalogue number 133306, sample courtesy of Anthea Hill).

(f) Typical banded massive sulphide ore from Central Thalanga with alternating sphalerite and pyrite-rich layers. The banding of sphalerite and pyrite defines the S2 foliation which developed as a result of D2 regional deformation (sample TH1, UTas catalogue number 133314, sample courtesy of Anthea Hill).

(g) Semi-massive sulphides with a gangue assemblage of carbonate-chlorite-tremolite from West Thalanga. The textures of such rocks provide evidence that the sulphides replaced of pre-existing carbonate-rich assemblages (Hill, 1996) (sample TH139A-298.3, UTas catalogue number 133442, scale is 1 cm, sample courtesy of Anthea Hill).

(h) Semi-massive sulphides overprinting coarse quartz crystal-rich volcaniclastic facies (QEV) from East Thalanga (sample TH401-103.7).

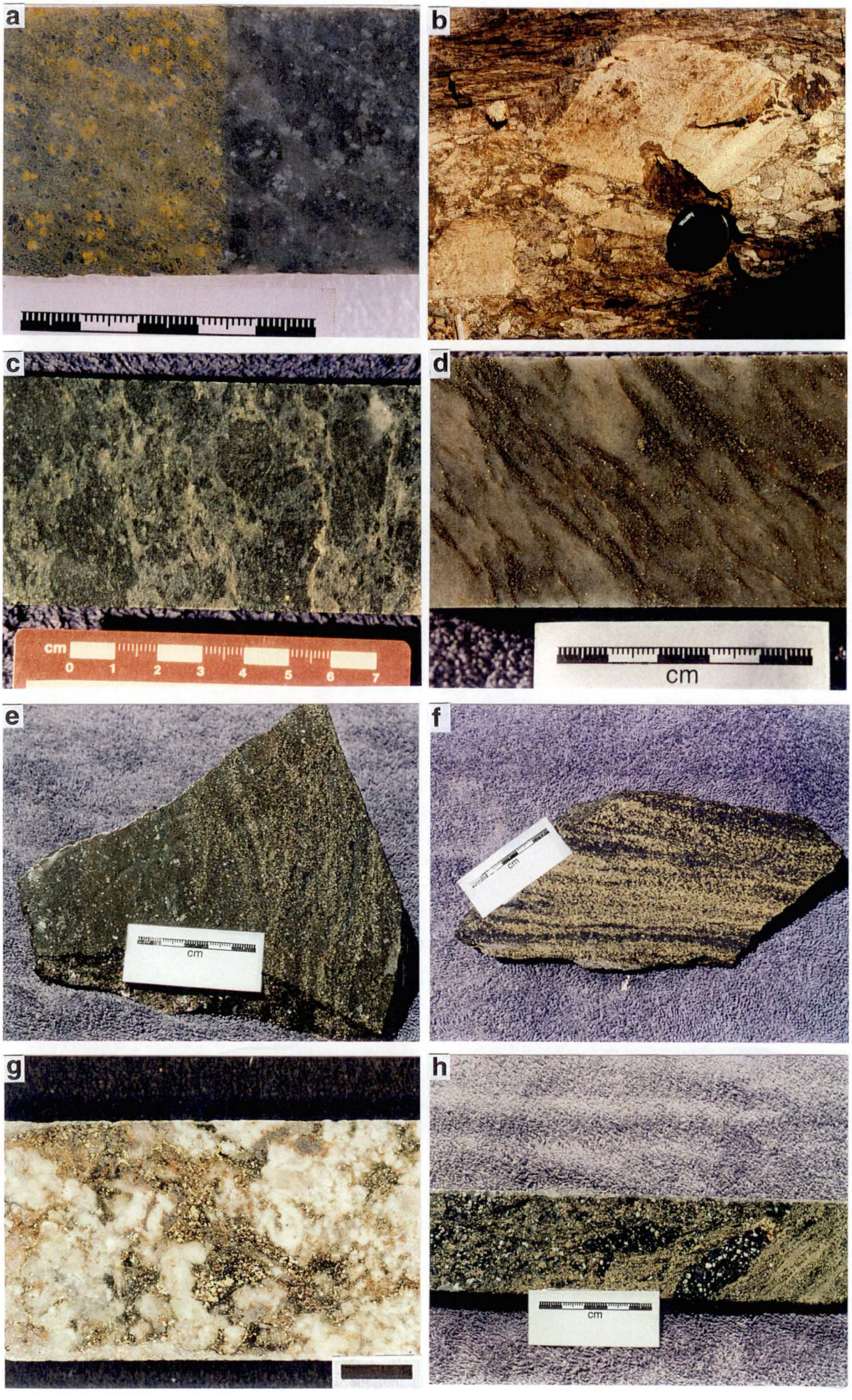

Fig. 2.1

facies of rhyolitic lavas, domes, and cryptodomes in the footwall to the Benambra VHMS deposits and presented textural criteria for distinguishing coherent facies with superimposed pseudoclastic textures from genuine clastic facies. These textural criteria have been developed and adapted to solve the problem of distinguishing coherent from clastic facies in the rhyolitic footwall alteration zone at Thalanga (Chapter 5).

The mottled alteration facies envelopes discordant zones of intense quartz- and pyrite-rich alteration which also occupy stratiform zones of up to ~50 m thickness located directly below the massive sulphides (Fig. 2.1d; 2.2). The discordant zones of intense quartz-pyrite alteration intersect the Favourable Horizon at a low angle (20° to 50°) and are generally connected to the ore lenses. The cause and significance of this orientation is enigmatic, however, by comparison of the volcanic facies interpretation with the alteration facies allowed assessment of the degree to which hydrothermal fluid flow was controlled by primary permeability contrasts between clastic and coherent facies in the footwall rhyolite (Chapter 5, 7 and 9).

2.2 Favourable Horizon

The massive sulphide-bearing Favourable Horizon at Thalanga ranges between <1 to 50 m in thickness and consists of a laterally variable lithofacies association. The contact with the underlying footwall rhyolite is typically gradational or obscured due to intense alteration.

In the mine area, the Favourable Horizon comprises variable assemblages of:

- Massive or banded sulphides (pyrite-sphalerite-galena ±chalcopyrite ±magnetite ±pyrrhotite) (Fig. 2.1e, f);
- Semi-massive, disseminated to patchy sulphides (dominantly sphalerite, galena and chalcopyrite) in a gangue of carbonate-tremolite-chlorite (Fig. 2.1g) or distinctive quartz crystal-rich volcaniclastic units (Fig. 2.1h);
- Sulphide-poor carbonate-tremolite-chlorite rocks which are almost exclusive to West Thalanga (section 2); these rocks were formerly regarded as exhalites (Gregory et al., 1990), however, recent research has shown that they represent metamorphosed, intensely chlorite-carbonate altered footwall rhyolite (Herrmann, 1994);
- Massive to semi-massive barite, usually with some disseminated sulphides and quartz-barite rocks (especially common in the up-dip fringes of West Thalanga and the Vomacka ore lenses) (Fig. 2.3a, Fig. 1.5);
- Minor silica-ironstones, mainly in the distal or upper fringes of ore lenses and also to the west of the mine (Fig. 2.3b);

Fig. 2.2: Schematic representation of facies organisation in the Thalanga area.

A more detailed model for the volcanological evolution of the Thalanga sequence based on volcanic facies analysis is presented in Chapter 5 (Fig. 5.6). Coarsely quartz-feldspar-phyric rhyolite represents the 'Quartz-Eye Porphyry' facies of Hill (1996) and is referred to as rhyolite type 4 in Chapter 5.

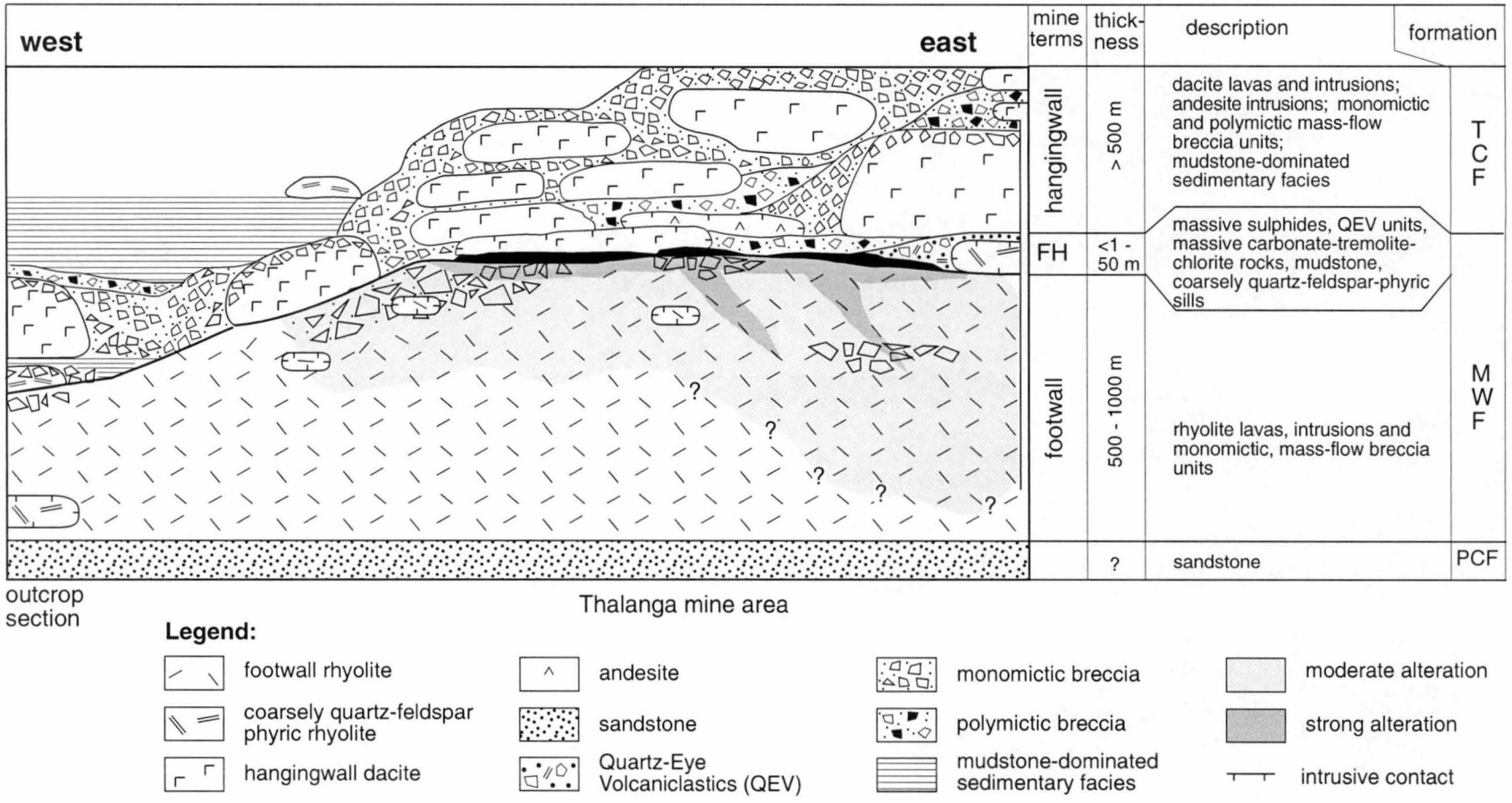
west
east
mine terms
thick-ness
description
formation
hangingwall
> 500 m
dacite lavas and intrusions; andesite intrusions; monomictic and polymictic mass-flow breccia units; mudstone-dominated sedimentary facies
TCF
massive sulphides, QEV units, massive carbonate-tremolite-chlorite rocks, mudstone, coarsely quartz-feldspar-phyric sills
FH
<1 - 50 m
footwall
500 - 1000 m
rhyolite lavas, intrusions and monomictic, mass-flow breccia units
MWF
?
sandstone
PCF
outcrop section
Thalanga mine area
Legend:
footwall rhyolite
coarsely quartz-feldspar phyric rhyolite
hangingwall dacite
andesite
sandstone
Quartz-Eye Volcaniclastics (QEV)
monomictic breccia
polymictic breccia
mudstone-dominated sedimentary facies
moderate alteration
strong alteration
intrusive contact

Fig. 2.2

- Massive or laminated mudstone; some beds are graded with quartz-feldspar crystal-rich, sandy bases;
- Coarse, massive to thickly-bedded quartz crystal-rich volcaniclastic mass-flow units (Quartz-Eye Volcaniclastics; Hill, 1996, Fig. 2.3c) which are locally mineralised (Fig. 2.1h);
- Unaltered to weakly altered, coherent, coarsely quartz-feldspar-phyric rhyolite sills (Fig. 2.3d).

2.3 Hangingwall

The hangingwall to the Thalanga deposit (>300 m stratigraphic thickness) is dominated by weakly altered, variably feldspar-phyric dacite lavas and intrusions but also contains diverse monomictic and polymictic volcaniclastic breccia and mudstone-dominated sedimentary facies, minor andesite intrusions, and rare, coarsely quartz-feldspar-phyric rhyolite. There are substantial and systematic changes in the composition and facies arrangement of the hangingwall along strike. Different types of dacite, which can be distinguished based on differences in phenocryst populations and immobile element ratios, are dominant in East, Central and West Thalanga and the proportion of sedimentary facies increases to the west of the deposit (Fig. 2.2, Fig. 5.5). In the mine area, massive sulphides are typically directly overlain by texturally unaltered to weakly altered feldspar-phyric to aphyric coherent dacite.

In Central and West Thalanga, the hangingwall includes andesite sills (10 to 30 m thick) and in section 1 a coherent, coarsely quartz-feldspar-phyric rhyolite of uncertain emplacement mode occurs ~150 m stratigraphically above the Favourable Horizon (Fig. 2.2). Monomictic and polymictic breccias of mostly dacitic derivation vary in composition and abundance along strike (Fig. 2.3e, Fig. 5.5). Sedimentary facies dominated by massive to laminated mudstone interbedded with feldspar crystal-bearing turbidites, are an important component of the hangingwall to the west of the mine area and in section 1 (Fig. 2.3f).

Alteration in the hangingwall is substantially weaker than in the footwall alteration zone and feldspar phenocrysts are generally preserved. Sulphides are absent except for rare occurrences in dacite immediately above the ore lenses (eg. TH10 section 3, Appendix). Coherent facies of the hangingwall dacite commonly shows weak alteration in

Fig. 2.3: Examples of lithofacies in the Favourable Horizon and the hangingwall to the Thalanga deposit.

(a) Close-up of massive quartz-barite sample from Central Thalanga. These rocks occur locally on the fringes of the Thalanga deposit (sample TH5-165.5, scale is 1 cm).

(b) Silica-ironstones occur on the fringes of the massive sulphide deposit and locally within the Favourable Horizon along the Thalanga Range (sample THRW20).

(c) Quartz and feldspar crystal-rich volcaniclastic sandstone from the Favourable Horizon. This facies has been locally overprinted by semi-massive sulphides indicating that sub-seafloor replacement processes were important during mineralisation (Fig. 2.1h) (sample TH401-101.10).

(d) Coarsely quartz- and feldspar-phyric rhyolite sills occur within the Favourable Horizon in East Thalanga (sample E3212SI18-45, UTas catalogue number 133423, scale is 1 cm, sample courtesy of Anthea Hill).

(e) Polymictic breccia from the hangingwall in Central Thalanga. This facies contains two different types of dacite clasts (grey, moderately feldspar-phyric dacite type 2 and white-pinkish, poorly feldspar-phyric dacite type 1) set in a foliated, phyllosilicate-rich matrix (sample TH5-28.0).

(f) Laminated mudstone from the hangingwall in section 1 to the west of the West Thalanga ore lens (sample TH40-44.0).

(g) Dacite from the hangingwall to the Thalanga deposit showing substantial hematite alteration (red colouration) and epidote alteration (green minerals in the groundmass). This figure shows an example of poorly-feldspar phyric dacite with very fine feldspar phenocrysts (<1 mm, dacite type 1, Chapter 5). Bulk rock geochemistry indicates that this sample did not experience albite alteration since values for K_2O and Na_2O are within the range expected for unaltered, felsic volcanics (K_2O = 4.14 wt.%; Na_2O = 3.19 wt.%) (sample TH402-321.0, scale bar in cm).

(h) Albite altered, highly feldspar-phyric dacite with abundant, fine feldspar phenocrysts (≤1 mm) from the hangingwall (dacite type 3, Chapter 5). Even though this dacite sample appears unaltered in hand specimen, the bulk rock geochemical analysis clearly indicates that albite alteration has taken place (K_2O = 0.11 wt.%; Na_2O = 7.75 wt.%) (sample TH18-89.70, scale bar in cm).

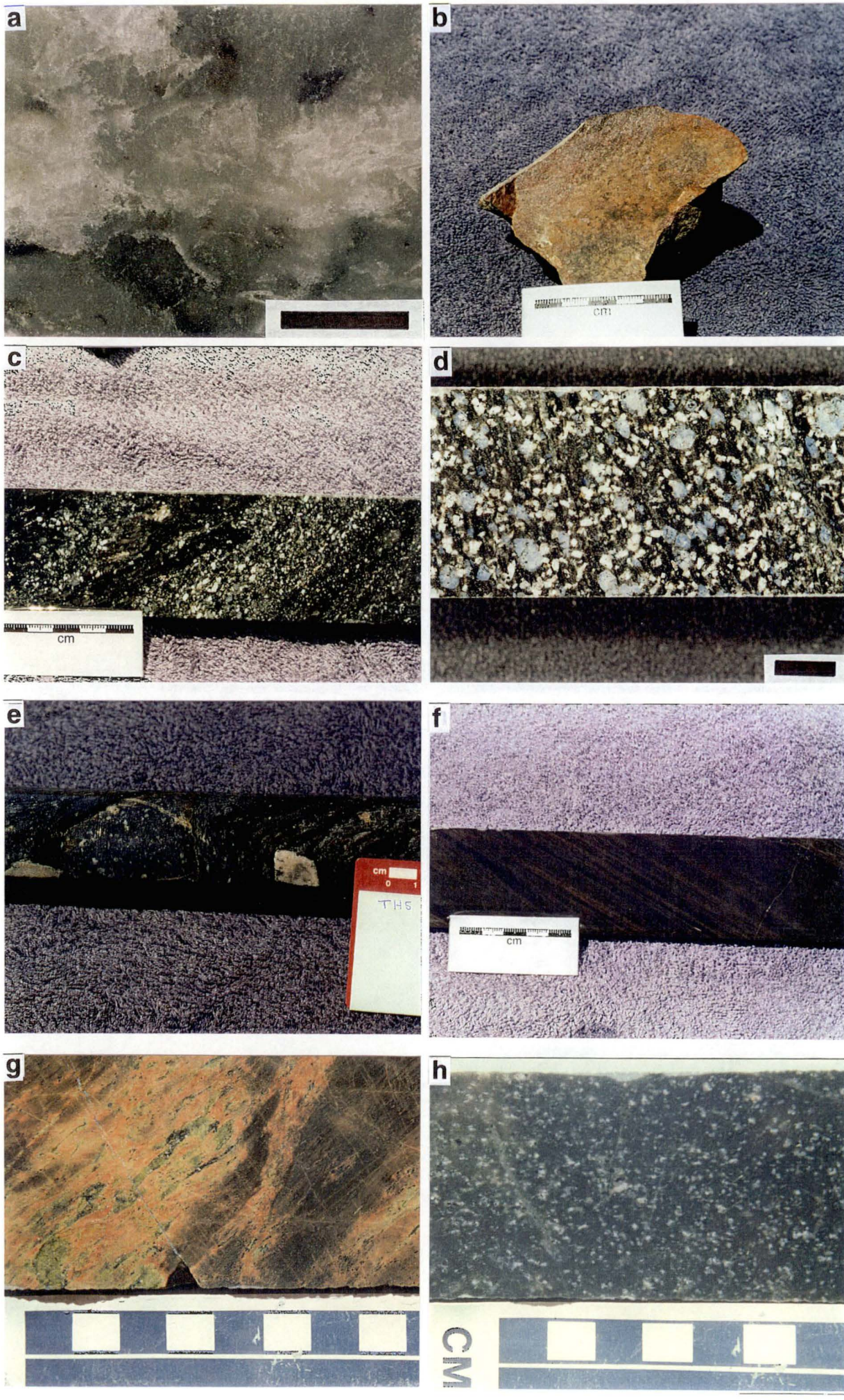

Fig. 2.3

the form of hematite dusting, causing a prominent red colouration of the groundmass, and patchy to vein-controlled epidote alteration. These two types of alteration often occur together in altered hangingwall dacite (Fig. 2.3g).

Many texturally unaltered hangingwall dacites experienced substantial Na-enrichment due to albite alteration which is difficult to recognise in hand specimen (Fig. 2.3g). As will be discussed in Chapter 6, hangingwall dacites typically have elevated Na_2O concentrations (5 to 8 wt.%) whereas their K_2O and CaO contents are low (<1 wt.%), which, together with petrographic evidence, clearly indicates that albite alteration occurred.

2.4 Summary

The Thalanga sequence consists of a felsic-lava dominated volcano-sedimentary succession which shows significant variations in thickness and lithofacies composition along strike. The lithofacies arrangement in the hangingwall, although dominated by variably feldspar-phyric dacites, varies substantially between East, Central and West Thalanga. The Favourable Horizon, which hosts the massive sulphides in the mine area, shows marked lithological diversity. It conformably overlies the comparatively monotonous rhyolitic footwall which is strongly altered below the Thalanga deposit.

The extensive footwall alteration zone occupies a broad, laterally continuous area below the massive sulphides and is characterised by texturally and mineralogically diverse alteration. The bulk of the footwall alteration zone is occupied by phyllosilicate-dominated, feldspar-destructive alteration which envelopes discordant zones of more intense quartz- and pyrite-rich alteration. These discordant zones terminate at the Favourable Horizon and are commonly connected to massive sulphides. In contrast, the hangingwall dacites, directly overlying massive sulphides, are unaltered to weakly altered.

3 Metamorphism of the Thalanga sequence

This chapter is concerned with the textural and mineralogical effects of metamorphism in the Thalanga area. Mineral assemblages observed in the various lithofacies are documented and discussed in terms of implications for the metamorphic history. The likely pre-metamorphic mineralogical compositions of the various rock types in the Thalanga sequence and possible metamorphic mineral reactions are inferred. Textural evidence is presented in order to demonstrate that metamorphism was isochemical and not associated with significant element mobility.

3.1 Introduction

3.1.1 Metamorphism in the Mount Windsor Subprovince

The Cambro-Ordovician, volcano-sedimentary succession of the Mount Windsor Subprovince was metamorphosed under greenschist facies conditions during regional deformation (D2) which was associated with the development of a pervasive cleavage (S2) (Middle to Late Ordovician; Berry et al., 1992). Regional isograds defined by mapping of metamorphic minerals and mineral assemblages show that the grade of regional metamorphism increases from sub-greenschist facies in the east to upper greenschist facies in the west of the subprovince (Fig. 3.1). Berry et al. (1992) also reported andalusite in samples from the Waddys Mill area (to the west of Thalanga), indicating relatively low pressure conditions for the regional metamorphism and deformation. Locally, a second stage of metamorphism occurred, associated with the emplacement of unfoliated (post-D2) intrusions of the Lolworth-Ravenswood batholith (Middle Silurian to Early Devonian; Hutton et al., 1994). In the east, these contact metamorphic aureoles consist of hornfels with cordierite, biotite and actinolite overgrowing the main tectonic foliation. The effects of contact metamorphism are difficult to recognise in the western part of the subprovince due to the higher grade of regional metamorphism.

Fig. 3.1: Regional variations in metamorphic grade in the Mount Windsor Subprovince.

Substantial variations in metamorphic grade are evident from mapping of syn-kinematic and post-kinematic isograds in the western (A) and central (B) part of the Mount Windsor Subprovince (from Berry et al., 1992).

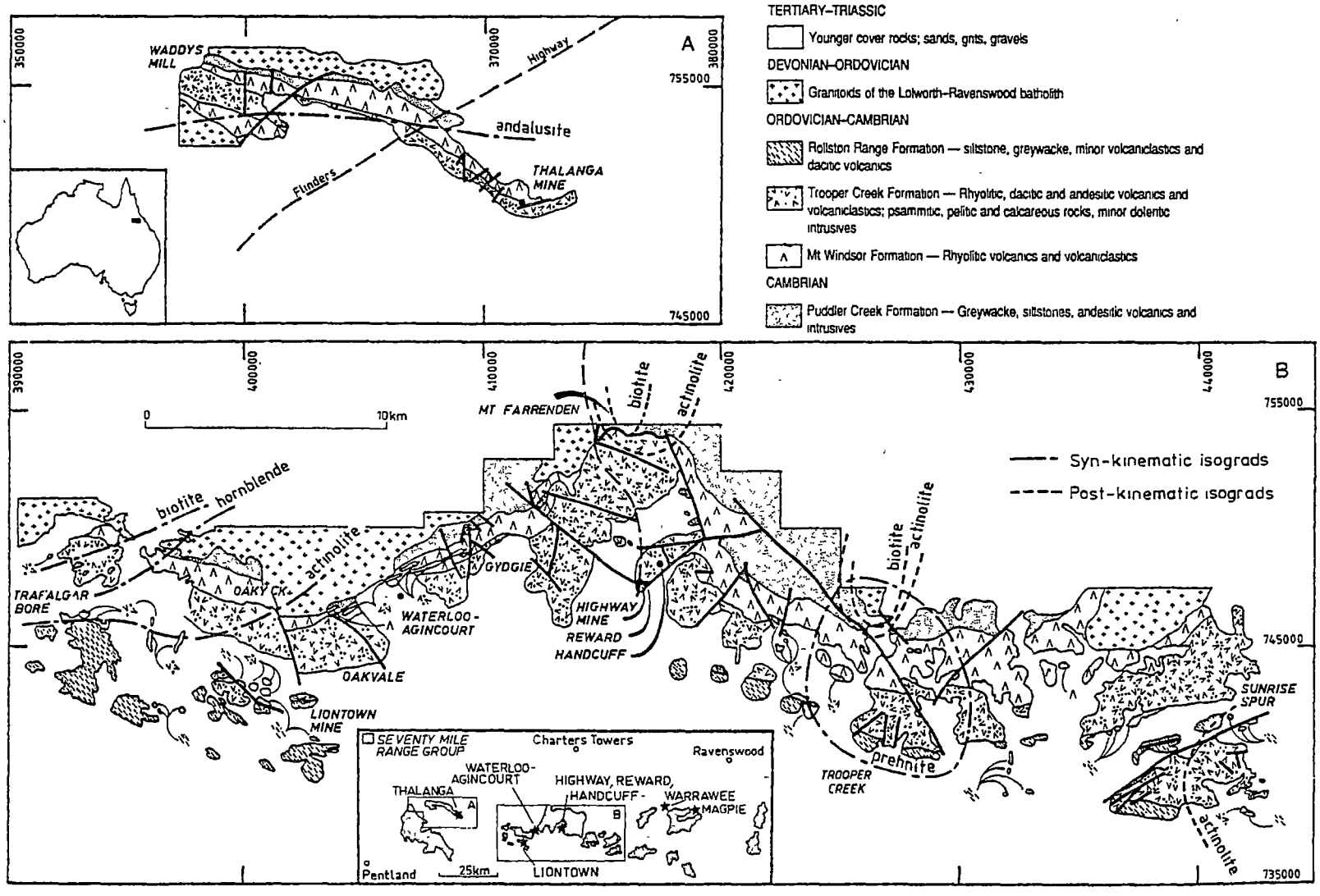
A
350000
370000
380000
755000
745000
WADDYS MILL
Highway
andalusite
Flinders
THALANGA MINE
TERTIARY–TRIASSIC
Younger cover rocks; sands, grits, gravels
DEVONIAN–ORDOVICIAN
Granitoids of the Lolworth–Ravenswood batholith
ORDOVICIAN–CAMBRIAN
Rollston Range Formation — siltstone, greywacke, minor volcaniclastics and dacitic volcanics
Trooper Creek Formation — Rhyolitic, dacitic and andesitic volcanics and volcaniclastics; psammitic, pelitic and calcareous rocks, minor dolentic intrusives
Mt Windsor Formation — Rhyolitic volcanics and volcaniclastics
CAMBRIAN
Puddler Creek Formation — Greywacke, siltstones, andesitic volcanics and intrusives
B
390000
400000
410000
420000
430000
440000
755000
745000
735000
0
10km
MT FARRENDEN
biotite
actinolite
biotite
hornblende
actinolite
TRAFALGAR BORE
OAKY CK
WATERLOO - AGINCOURT
GYDGIE
HIGHWAY MINE
REWARD
HANDCUFF
OAKVALE
LIONTOWN MINE
biotite
actinolite
prehnite
TROOPER CREEK
SUNRISE SPUR
actinolite
Syn-kinematic isograds
Post-kinematic isograds
SEVENTY MILE RANGE GROUP
Charters Towers
Ravenswood
WATERLOO-AGINCOURT
HIGHWAY, REWARD, HANDCUFF
THALANGA
WARRAWEE
MAGPIE
A
B
Pentland
25km
LIONTOWN

Fig. 3.1

3.1.2 Metamorphism at Thalanga

The various lithofacies in the Thalanga area show diverse textural and mineralogical features which are inferred to be controlled by pre-metamorphic compositional differences. Coherent facies of quartz-feldspar-phyric rhyolite laterally adjacent to the footwall alteration zone has a quartzofeldspathic groundmass with minor muscovite ± biotite ± chlorite. These rocks show brittle fractures and no cleavage indicating that they behaved competently during regional deformation and did not develop the S2 foliation due to the paucity of phyllosilicates. Similarly, coherent facies of siliceous, feldspar-phyric hangingwall dacite above the Thalanga deposit are also typically unfoliated due to the scarcity of phyllosilicates in the quartz- and feldspar-rich groundmass. In contrast, pelitic sedimentary facies (phyllite), which is common in the hangingwall, is strongly foliated and contains abundant, aligned biotite, muscovite and chlorite, defining the S2 fabric. These textural and mineralogical differences are inferred to be due to primary differences in mineralogy and competency between coherent facies of unaltered felsic lavas and clay-rich sediments.

The Thalanga massive sulphides are underlain by a laterally extensive zone occupied by variably altered rhyolite which contains muscovite, biotite, chlorite and minor disseminated pyrite (≤3 vol.%). Phyllosilicate-rich altered rhyolite is typically strongly foliated, indicating that these mineral assemblages equilibrated during regional deformation and metamorphism. Pyrite-rich zones, representing intense alteration, occur immediately below the massive sulphides in the Favourable Horizon. The lateral contacts between altered rhyolite and the surrounding 'unaltered' rhyolite are gradational and marked by a gradual increase in the abundance of muscovite, biotite and chlorite, successive destruction of feldspar phenocrysts and occurrence of disseminated pyrite. The gradational character of lateral contacts and preserved quartz phenocrysts in the footwall alteration zone indicate that the rhyolite in the surrounding country rock represents the 'unaltered' equivalents to altered rhyolite below the massive sulphides. Furthermore, immobile element geochemistry shows that all samples of footwall rhyolite, regardless of alteration intensity, have the same Ti/Zr ratio (3.9 ± 0.4; n=113, Chapter 6 and 8).

Thus, the rhyolite below the massive sulphides was affected by hydrothermal alteration associated with mineralisation which caused the formation of various

phyllosilicates, the destruction of feldspar and precipitation of pyrite. Rhyolites adjacent to the footwall alteration zone was less influenced by hydrothermal activity and consequently, the mineralogical composition is dominated by quartz and feldspar, which is typical for unaltered felsic volcanics.

There is no indication of significant hydrothermal alteration in the hangingwall since texturally unaltered feldspar is ubiquitous and sulphides are extremely scarce. Therefore, hydrothermal alteration associated with massive sulphide mineralisation is inferred to have occurred prior to the emplacement of the hangingwall dacite and, hence, long before the metamorphism of the Thalanga sequence. This interpretation is supported by geochemical data showing that the altered footwall rhyolite experienced various compositional changes including Mg-, Fe-, and S-enrichment and Na-depletion. These geochemical features are exclusive to the footwall alteration zone and absent in the hangingwall dacite and 'unaltered' rhyolite.

In the following, the term 'least-altered' is used to refer to rocks which are regarded as having a mineralogical and geochemical composition which approximates the original composition of the fresh volcanic rocks in the Thalanga sequence. This term is preferred instead of 'unaltered' because minor compositional modifications could have occurred during diagenesis or low-grade seafloor alteration processes (eg. silicification and/or mobility of Na and K; Lipman, 1965) which may be difficult to recognise in hand specimen, thin section or in the geochemical data.

It should be noted that calc-silicate minerals (epidote, zoisite, actinolite and tremolite) occur locally in the altered footwall rhyolite, hangingwall sedimentary facies and in the hangingwall dacite. Furthermore, massive rocks consisting predominantly of calcite, tremolite and chlorite are a characteristic lithofacies of the Favourable Horizon in West Thalanga (section 2; Figs. 1.5, 5.5 and 7.5 and Appendix) where they typically represent the gangue to semi-massive sulphides (Fig. 2.1g). Rare occurrences of massive calc-silicate rocks, consisting predominantly of calcite, epidote and actinolite have been observed in the hangingwall (section 1 Figs. 1.5, 5.5 and 7.5; logs of drill holes TH37 and TH40 in the Appendix).

At Thalanga, the strong, very steeply dipping regional foliation (S2) is commonly defined by aligned biotite-muscovite±chlorite in phyllosilicate-rich rocks such as altered rhyolite in the footwall and phyllites in the hangingwall. However, decussate crystals of

chlorite and biotite, cross cutting the S2 foliation, are common in East Thalanga indicating that these minerals recrystallised during contact metamorphism associated with the voluminous, post-D2 diorite pluton to the east of the Thalanga deposit.

3.2 Metamorphic mineral assemblages and textures in different lithofacies of the Thalanga sequence

3.2.1 Phyllite

Phyllite is common in the hangingwall to the west of the Thalanga deposit where a mudstone-dominated sedimentary facies occurs (graphic logs for section 1 and the outcrop section, Fig. 5.5 and Appendix). Furthermore, the matrices of many volcaniclastic breccia and sandstone units in the hangingwall are also fine-grained and phyllosilicate-rich. Both the mudstone facies and matrices consist dominantly of fine (<50 μm), equigranular quartz-muscovite-biotite±chlorite assemblages, with aligned phyllosilicate crystals defining the S2 foliation (Fig. 3.2a,b). Locally, phyllites contain accessory phases such hornblende, feldspar, actinolite and/or carbonate. In some samples, chlorite crystals have an oblique orientation to the S2 foliation (Fig. 3.2c) which is interpreted as evidence that chlorite locally recrystallised during contact metamorphism.

Rare pelitic hornfels with abundant, largely pseudomorphed, cordierite porphyoblasts (1 to 4 cm in diameter) has been observed in the Favourable Horizon in East Thalanga (Fig. 3.2d). The extensively pinitised cordierite is interpreted as a product of contact metamorphism and occurs with muscovite, phlogopite and quartz.

Patches and bedding parallel intervals (5 to 20 cm thickness) of quartz-actinolite ±epidote±chlorite assemblages occur locally within the phyllite in the hangingwall (section 1, Fig. 3.2e). These intervals contain actinolite sheaves which are slightly deformed, possibly indicating late syn-D2 crystal growth (Fig. 3.2f). These domains are biotite-free and may contain minor carbonate, muscovite and/or feldspar and rare hornblende-garnet assemblages.

Fig. 3.2: Metamorphic textures and mineral assemblages of phyllites.

(a) Phyllite in the Thalanga sequence generally consist of foliated biotite, muscovite and chlorite in assemblage with fine-grained quartz (sample TH40-37.40, hangingwall, PPL, scale bar is 100 μm).

(b) Foliated biotite- and chlorite-rich matrix of a phyllitic, volcaniclastic unit containing feldspar crystals (f) and siliceous dacite clasts (d). Note that the foliation is wrapped around the edge of the siliceous dacite clast indicating a significant contrast in competence between the matrix and the clast (sample TH5-28.25, hangingwall, PPL, scale bar is 500 μm).

(c) Phyllite from Central Thalanga (section 4) with chlorite crystals (c) oriented obliquely with respect to the S2 foliation defined be aligned muscovite and biotite. This texture indicates that the chlorite recrystallised after D2, probably during contact metamorphism associated with the intrusion of the diorite pluton (sample TH38-403.4, hangingwall, PPL, scale bar is 500 μm).

(d) Hand specimen of pelitic hornfels with abundant, variably pinitised cordierite porphyroblasts (cd) from the Favourable Horizon in East Thalanga (sample E3204SD50-57.90;~ 1300 m to the west of the diorite intrusion; scale bar is 1 cm).

(e) Hand specimen of phyllite in the hangingwall of Far West Thalanga (section 1) with a bedding parallel quartz-actinolite-rich layer. The differences in chemical composition between the phyllosilicate-rich layer and the actinolite-rich layer are illustrated in Fig. 3.7 (sample TH37-138.50).

(f) Abundant actinolite bundles occur in the quartz-actinolite-rich layer in sample TH37-138.50 (Fig. 3.2e). These bundles are slightly sheared and aligned actinolite crystals define the S2 foliation (PPL, scale bar is 100 μm).

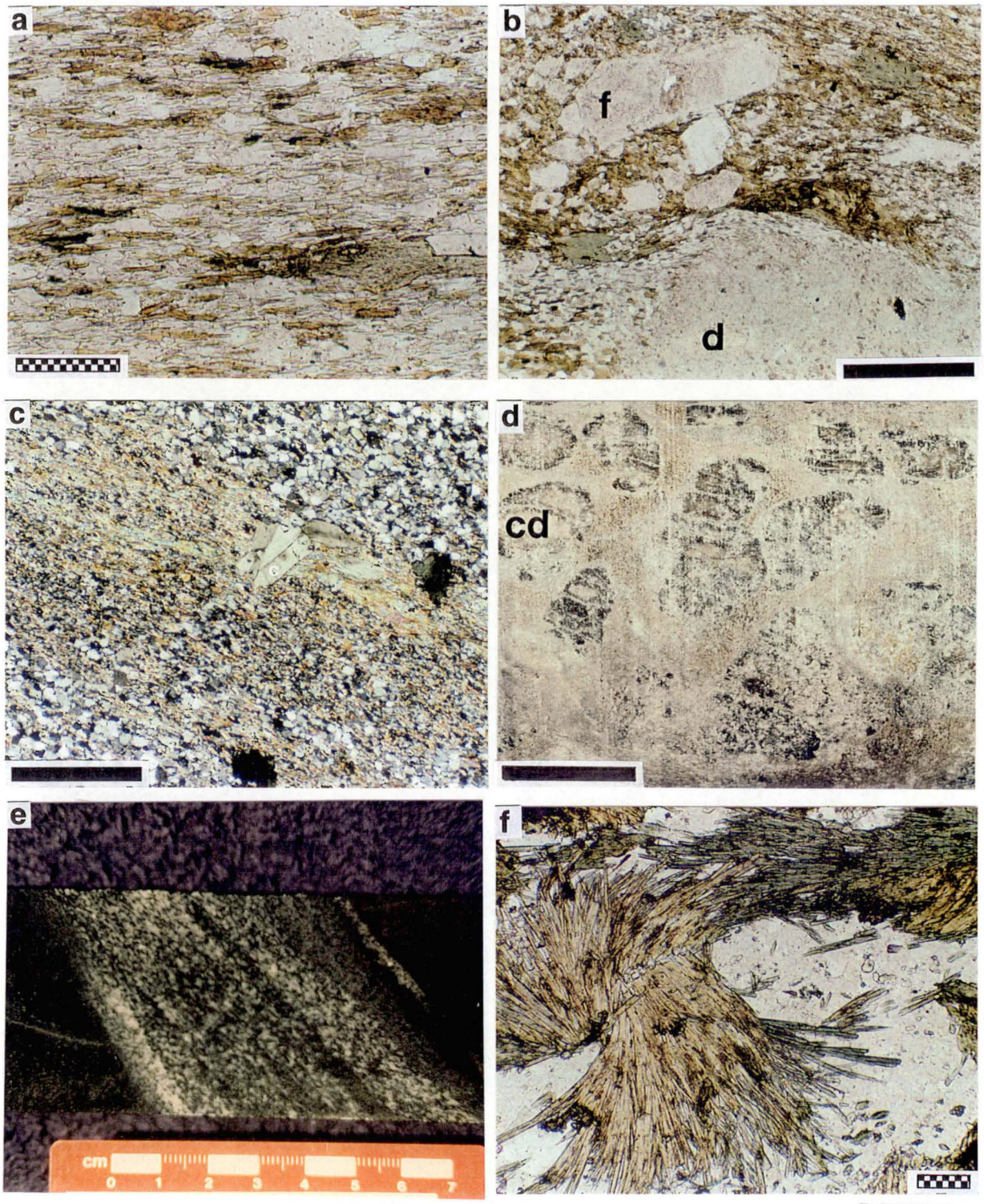

Fig. 3.2

Locally, garnet occurs in phyllite and a prominent example is represented by a quartz-free laminae of garnet-biotite-carbonate-muscovite in a sample of compositionally layered phyllite (sample TH40-67.0, Fig. 3.3). Several, mineralogically distinctive, thin beds and laminae observed in thin section probably correspond to primary compositional differences between single layers (Fig. 3.3a to d). Garnets are restricted to a narrow, biotite-rich lamina (~1 mm wide) where they form a necklace of aligned, equigranular, euhedral crystals (0.7 to 1.3 mm in diameter, Fig. 3.3b). These garnets are interpreted to have formed during regional metamorphism because of their euhedral shapes, which contrast markedly with anhedral, poikiloblastic garnets in the contact metamorphic aureole of the diorite intrusion, and their remoteness from the diorite pluton (Chapter 4). Inclusions of muscovite and biotite, which are aligned parallel to the S2 foliation in the surrounding matrix, are common in the central parts of these garnets. It is possible that the S2 foliation developed very early during regional deformation in incompetent rocks such as phyllosilicate-rich mudstone. The garnets may have begun to crystallise at a slightly later stage during D2, overgrowing this foliation.

The garnet-rich lamina is separated from an amphibole- and epidote-rich domain by a ~1 cm wide layer which consists of equigranular quartz (± biotite ± carbonate) (Fig. 3.3). The amphibole is dark bluish green and intimately intergrown with pleochroic (green-pale yellow) chlorite (Fig. 3.3c). An assemblage of epidote-biotite-quartz flanks the amphibole-chlorite aggregate. Another distinctive layer in sample TH40-67.0 consists of biotite and quartz (Fig. 3.3d).

3.2.2 Hangingwall dacite

Coherent dacite and dacite clasts in volcaniclastic breccia units in the hangingwall to the Thalanga deposit are variably feldspar-phyric (now mainly albite) and generally unfoliated. They have a fine-grained quartzofeldspathic groundmass typically with minor biotite ±muscovite ± chlorite commonly forming semi-connected networks (Fig. 3.4a).

Locally, alkali feldspar phenocrysts are partially replaced by biotite, indicating that they were consumed in the biotite-forming metamorphic reaction (Fig. 3.4b). Relatively coarse, blocky muscovite occurs locally and may have formed by recrystallisation of fine-grained white mica (Fig. 3.4c). In relatively phyllosilicate-rich dacite, the S2 foliation is defined by biotite which is overgrown by chlorite crystals in some samples in East Thalanga (Fig. 3.4d).

Fig. 3.3: Texture of garnet-bearing layered phyllite from the hangingwall in section 1 (Far West Thalanga, sample TH40-67.0).

Sample TH40-67.0 consists of thin beds and laminae with strikingly different mineralogical composition. This indicates that primary compositional differences controlled the development of distinctive metamorphic mineral assemblages.

(a) Sketch of the thin section of sample TH40.67.0.

(b) Photomicrograph of laminae consisting of garnet, biotite and minor calcite (quartz absent). Note that garnets are organised in a necklace-like manner and are strictly exclusive to this lamina (PPL, scale bar is 500 μm).

(c) A ~2 cm wide layer of fine-grained quartz separates the garnet-rich lamina from a domain that consists partly of a quartz-biotite-epidote assemblage and partly of a hornblende-chlorite-quartz assemblage (PPL, scale bar is 100 μm; e: epidote; a: actinolite; c: chlorite).

(d) Adjacent to the hornblende-rich layer is a thin bed that consists of quartz, biotite and minor feldspar (f) crystal relics (PPL, scale bar is 500 μm).

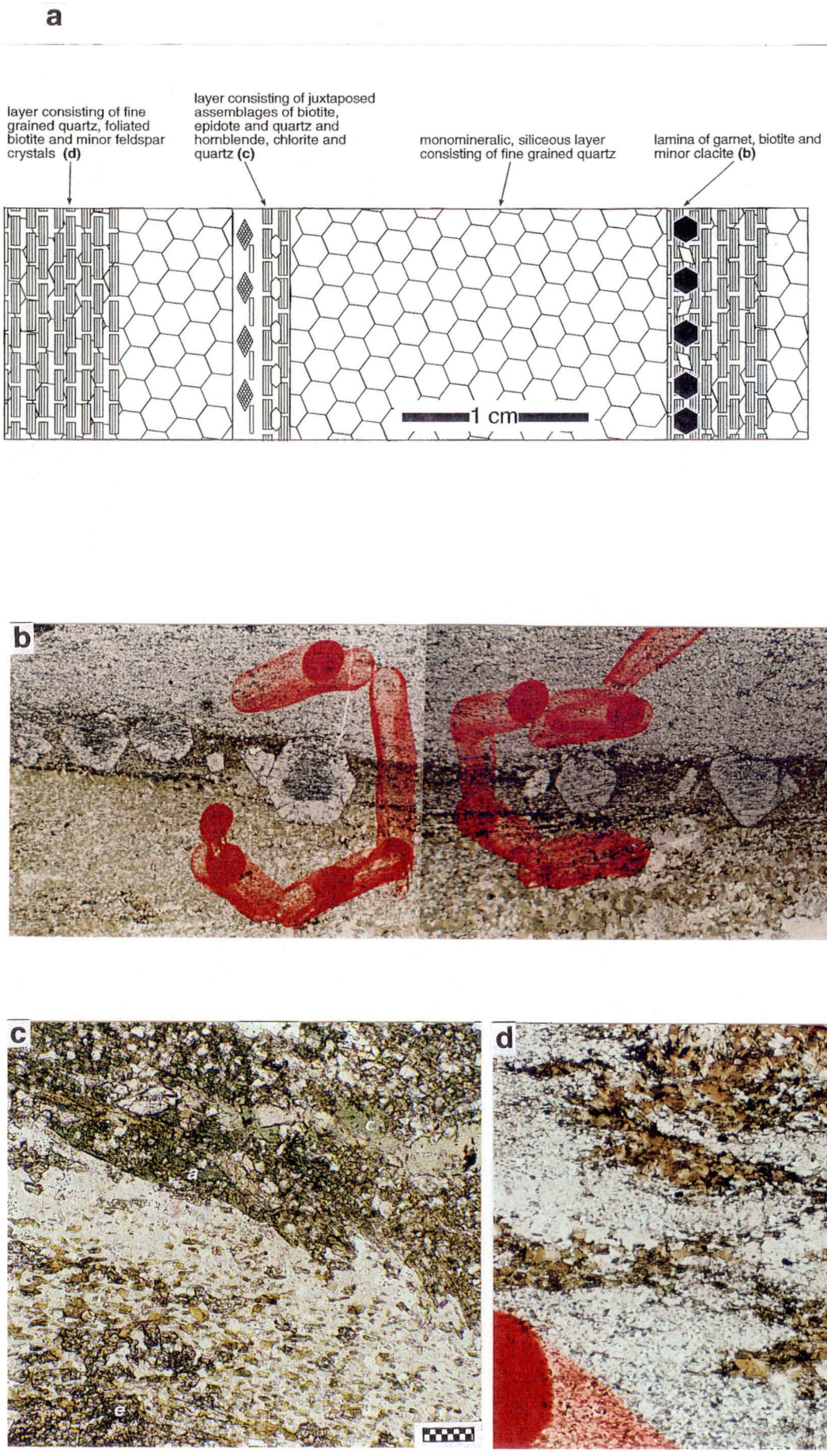
a
layer consisting of fine grained quartz, foliated biotite and minor feldspar crystals (d)
layer consisting of juxtaposed assemblages of biotite, epidote and quartz and hornblende, chlorite and quartz (c)
monomineralic, siliceous layer consisting of fine grained quartz
lamina of garnet, biotite and minor clacite (b)
1 cm
b
c
a
e
d
f

Fig. 3.3

Calc-silicate minerals, especially epidote and actinolite, are fairly common in the hangingwall dacite. Epidote veins often have a selvedge of disseminated epidote in the surrounding quartz-feldspar-rich groundmass (Fig. 3.4e). Epidote also occurs in patchy domains and may be associated with biotite, chlorite, carbonate, actinolite and/or hornblende.

Acicular actinolite is locally disseminated in the quartzofeldspathic groundmass of coherent dacite, together with chlorite and/or epidote as well as minor carbonate and/or biotite (Fig. 3.4f). Locally, actinolite and epidote are partially replacing feldspar phenocrysts, indicating that plagioclase breakdown was involved in the actinolite- and epidote-forming reaction (Fig. 3.4g, h).

3.2.3 Footwall rhyolite

Within the footwall alteration zone, foliated muscovite, chlorite and biotite are ubiquitous and commonly accompanied by minor pyrite (<1-3 vol.%). They are interpreted to represent the metamorphic equivalents of phyllosilicates formed in the footwall alteration zone during the circulation of hydrothermal solutions. Muscovite, biotite and chlorite crystals are usually aligned, defining the S2 foliation in the western part of Thalanga, whereas decussate textures are common in East Thalanga (Fig. 3.5a, b).

The abundance of muscovite, chlorite and biotite in the altered footwall rhyolite is variable and can be regarded as a relative measure of alteration intensity. Feldspar phenocrysts are progressively replaced with increasing alteration intensity. In some samples, biotite occurs around remnants of alkali feldspar phenocrysts suggesting that alkali feldspar was also consumed during the metamorphic biotite-forming reaction (Fig. 3.5c). Intimate intergrowth of biotite and chlorite is a common feature (Fig. 3.5d). Such aggregates may have consisted of interlayered chlorite and muscovite prior to metamorphism and biotite may have formed by a reaction involving both precursor minerals. This reaction could have proceeded until the muscovite was consumed (exhaustion of the alkali metal source).

Fig. 3.4: Metamorphic textures and mineral assemblages of dacites.

(a) Dacites in the hangingwall to the Thalanga deposit are feldspar-phyric (f; now mainly albite) and have a siliceous, quartzofeldspathic groundmass. Minor biotite within the groundmass forms interconnected, network-like textures (TH18-138.80, hangingwall, PPL, scale bar is 500 μm).

(b) Some hangingwall dacites contain abundant, foliated biotite which is locally replacing alkali feldspar phenocrysts (f; sample TH28-60.60, PPL, scale bar is 500 μm).

(c) Muscovite is common as a minor, fine interstitial phase in the groundmass of hangingwall dacites. Sample TH61-287 shows relatively coarse muscovite (m) with biotite aligned in the S2 foliation (PPL, scale bar is 500 μm).

(d) Locally, hangingwall dacites contain abundant biotite, muscovite and chlorite which are generally aligned parallel to S2 (arrow). In sample TH402-119.20, biotites are foliated whereas chlorite (c) crystals have an oblique orientation with respect to the foliation. This indicates that chlorite recrystallised during contact metamorphism (PPL, scale bar is 500 μm).

(e) Epidote is common in hangingwall dacite and occurs in veins (v) and disseminated (arrow) within the quartzofeldspathic groundmass. Both styles of epidote occurrence are present in a hand specimen of sample TH62C-679.50 (scale bar is 1 cm).

(f) Acicular actinolite (a) is common in the siliceous groundmass of hangingwall dacites in East Thalanga. Fine, needle-shaped crystals disseminated in the quartzofeldspathic groundmass are typical (sample TH382A-400; scale bar is 500 μm; F: feldspar phenocryst).

(g) Locally, feldspar phenocrysts (f) are partially replaced by actinolite (a) and/or epidote (e). This indicates that feldspar may have been involved in the actinolite-forming reaction. Sample TH62C-825.25 of hangingwall dacite also contains abundant disseminated epidote (PPL, scale bar is 500 μm).

(h) Image shown in Fig. 3.4g under crossed nicols.

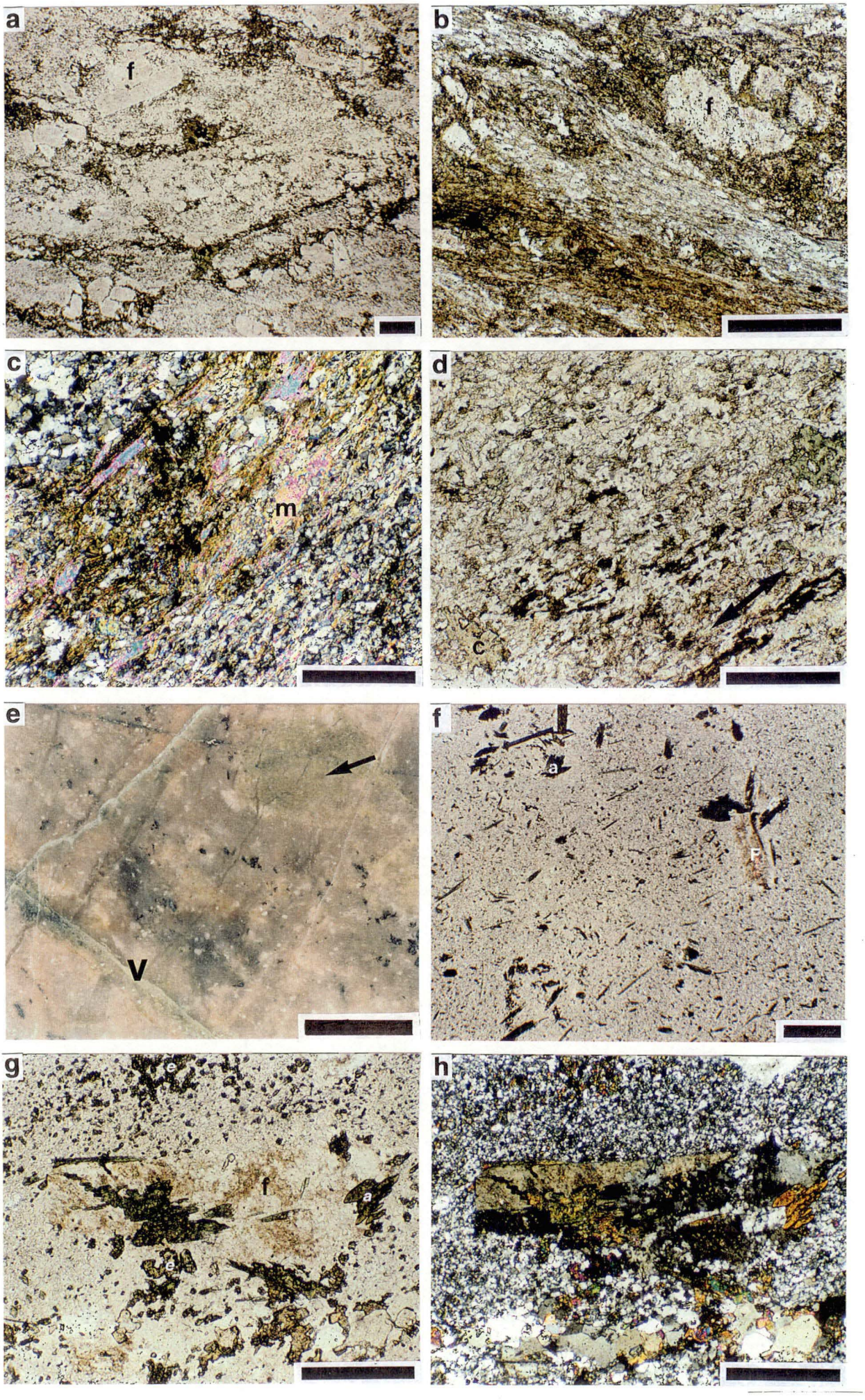

Fig. 3.4

Locally, minor garnets occur within chlorite-rich parts of the altered rhyolite in East Thalanga. These include relatively large (up to 5 mm), anhedral, garnet poikiloblasts in an assemblage with chlorite, muscovite and quartz within chlorite-rich apparent clasts of domainally altered rhyolite (Fig. 3.5e; Chapter 4 and Fig. 4.2). These domains are surrounded by an apparent matrix consisting of quartz, muscovite, biotite and minor chlorite. The preferential occurrences of garnets in the chlorite-rich domains indicates that their compositional characteristics favoured garnet crystallisation rather than formation of biotite which is common in the apparent matrix. Garnets are absent in altered rhyolite in Central and West Thalanga.

Altered rhyolite with patchy domains of disseminated calc-silicate minerals (epidote, zoisite, actinolite and tremolite) occurs locally in the footwall alteration zone. This indicates that some altered rhyolites contained carbonate, most likely of hydrothermal origin, prior to metamorphism. Assemblages with calc-silicate minerals include quartz-epidote-actinolite±muscovite±chlorite (Fig. 3.5f) and tremolite-quartz-epidote (Fig. 3.5g); tremolite-rich rhyolite close to the Favourable Horizon in West Thalanga (section 2, Fig. 1.5) locally grade into massive chlorite-tremolite-carbonate rock (Fig. 3.5h). Locally, tremolite replaces quartz phenocrysts, indicating that SiO_2 was consumed during the tremolite-forming metamorphic reaction (Fig. 3.5 g, h).

3.2.4 Massive calc-silicate rocks

Massive rocks consisting of calcite, dolomite, tremolite, actinolite, epidote, quartz, chlorite, biotite and muscovite occur in the Favourable Horizon in West Thalanga (sections 1 and 2) and in one horizon overlying a dacite lava dome in the hangingwall about 150 m above the Favourable Horizon (section 1, Fig. 1.5 and Fig. 5.5 and Appendix).

Massive carbonate-chlorite-tremolite-rich rocks (CCT rocks) occur in the Favourable Horizon of West Thalanga (section 2) (Fig. 3.6a, b). The relative proportions of these minerals vary substantially and carbonate (calcite and dolomite)-dominated, tremolite-dominated and chlorite-dominated end-members can be distinguished (Herrmann, 1994). Minor phases are muscovite, epidote, zoisite, barite, quartz, diopside (Fig. 3.6c), sphalerite and pyrite.

Fig. 3.5: Metamorphic textures and mineral assemblages of altered footwall rhyolite.

(a) Fine-grained muscovite, biotite and chlorite are ubiquitous in altered footwall rhyolite. These minerals are generally aligned parallel to the S2 foliation in western parts of Thalanga (sample TH247-169, PPL, scale bar is 100 μm; q: quartz phenocryst).

(b) In contrast to the strongly foliated texture of altered rhyolite, typical for the western parts of Thalanga, decussate chlorite and biotite are common in East Thalanga. This is most likely an effect of contact metamorphism associated with the emplacement of the voluminous diorite pluton to the east of Thalanga (sample TH144B-296.85, PPL, scale bar is 500 μm).

(c) In moderately altered rhyolite, relics of alkali feldspar phenocrysts (f) are often partially replaced by biotite. This indicates that feldspar was involved in the biotite forming reaction during metamorphism (sample TH410-312.85, PPL, scale bar is 100 μm).

(d) Intimate intergrowth of chlorite (c) and biotite (b) is commonly observed in the groundmass of altered rhyolite (sample TH247-219, PPL, scale bar is 100 μm).

(e) Large garnets occur locally in domainally altered rhyolite in East Thalanga. These garnet occurrences (arrow) are restricted to lensoidal chlorite-rich domains defining apparent clasts (AC) which are commonly surrounded by a quartz-muscovite-rich apparent matrix (AM) (hand specimen of sample TH394-262.80, section 6, East Thalanga; scale bar is 1 cm).

(f) Assemblages of chlorite (c), epidote (e) and actinolite (a) locally occur in the groundmass of weakly altered footwall rhyolite (sample TH112-404.30, PPL, scale bar is 500 μm; q: quartz phenocryst).

(g) Disseminated epidote (e) and bundles of tremolite (t) are a prominent features in some parts of the footwall alteration zone. The intergrowth of tremolite with quartz phenocrysts (arrow) indicates that quartz was consumed by the tremolite-forming reaction (TH148-569.10, crossed nicols; scale bar is 500 μm).

(h) Gradational contact from altered, tremolite-bearing rhyolite with preserved quartz phenocrysts (q) to massive CCT rock in the Favourable Horizon (West Thalanga, section 2). This image shows the contact zone between altered rhyolite and massive CCT rock with disseminated sphalerite (s). Note that tremolite crystals (t) are intergrown with quartz phenocrysts (arrow) which indicates that quartz was consumed by the tremolite-forming reaction (sample TH41A-575.25, PPL, scale bar is 500 μm).

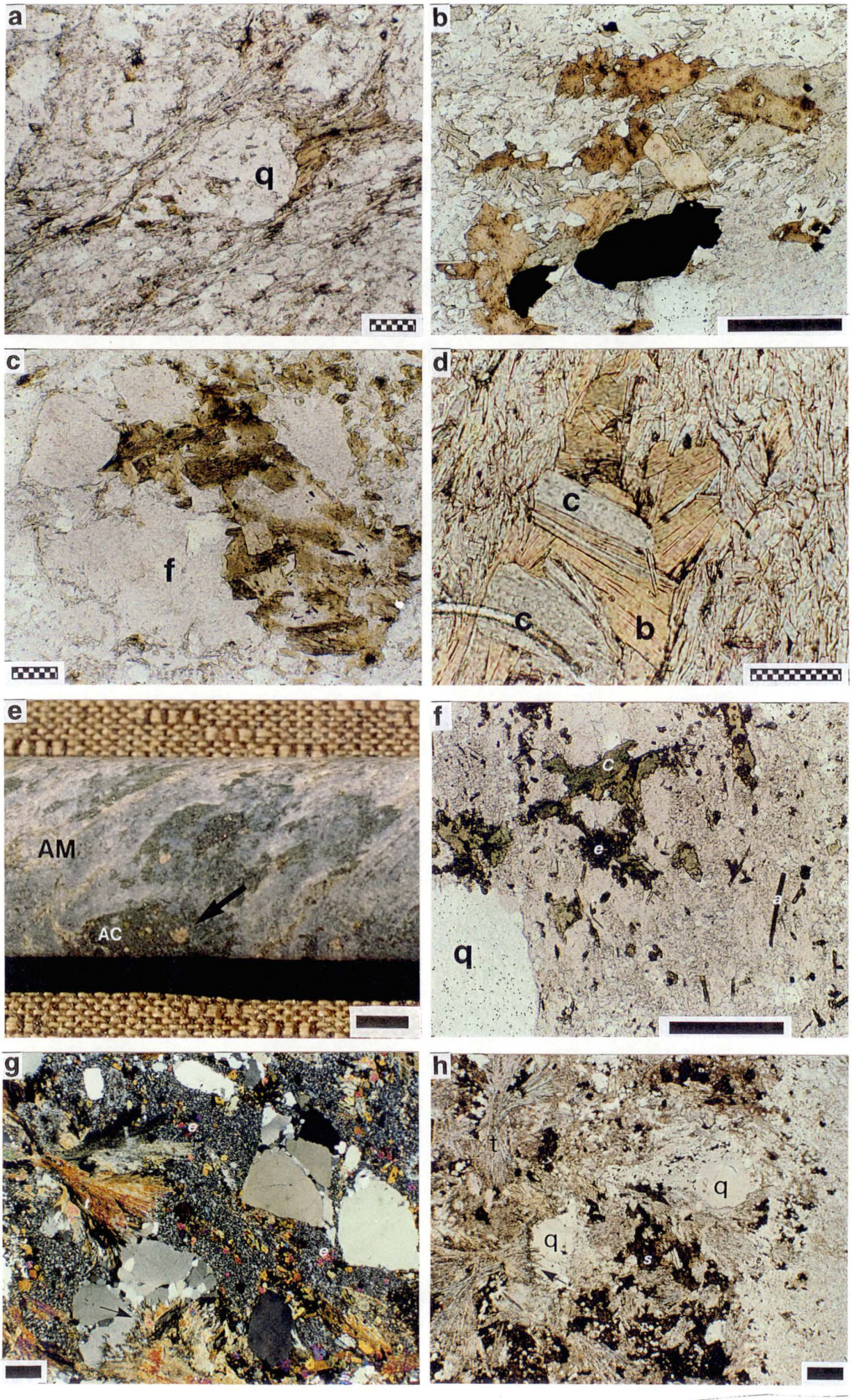

Fig. 3.5

The CCT rocks lack quartz crystals which are otherwise common in the Favourable Horizon. Any relic primary textures have been destroyed by recrystallisation and formation of new minerals during metamorphism. Although initially interpreted as exhalites (Gregory et al., 1990), detailed geochemical studies indicated that CCT rocks probably represent intense alteration of footwall rhyolite (Herrmann, 1994). This interpretation is supported by the gradational character of contacts with tremolite-rich altered rhyolite that has recognisable quartz phenocrysts (Fig. 3.5h). In section 1, (Fig. 1.5; drill hole log of TH37, Appendix) minor occurrences of massive calc-silicate rocks in the Favourable Horizon consist of calcite-epidote-quartz assemblages (Fig. 3.6d).

The massive calc-silicate units in the hangingwall are generally quartz-dominated. They consist of quartz-epidote-actinolite or quartz-biotite-epidote-actinolite; additional phases such as calcite, chlorite and/or muscovite occur locally (Fig. 3.6 e-g). Minor calcite-rich intervals in this unit consist of calcite-quartz-epidote±chlorite assemblages (Fig. 3.6h).

The variations in the metamorphic mineral assemblages among calc-silicate rocks in the Thalanga sequence reflect compositional differences that existed prior to metamorphism. The abundance of tremolite in CCT rocks of the Favourable Horizon in West Thalanga indicates that these units contained Ca- and Mg-bearing phases (dolomite and/or a mixture of calcite and chlorite) prior to metamorphism.

Calc-silicate rocks with assemblages of quartz-epidote-actinolite±biotite probably contained some Ca- and Fe-bearing phases such as calcite and Fe-rich chlorite. If carbonate was less abundant than quartz, then most of the carbonate would have been consumed in the epidote- and/or actinolite-forming reactions. Massive calc-silicate rocks consisting of calcite-epidote-quartz assemblages may have had relatively Fe- and Mg-poor bulk rock geochemical compositions which precluded the formation of actinolite or tremolite during metamorphism.

Fig. 3.6: Metamorphic textures and mineral assemblages of massive calc-silicate rocks

(a) Massive calc-silicate rocks in the Favourable Horizon of section 2 (West Thalanga) consist of carbonate (calcite and dolomite), chlorite (c) and tremolite (t) (sample TH28-502.85, crossed nicols, scale bar: 500 μm).

(b) Some massive calc-silicate rocks in the Favourable Horizon of West Thalanga consist entirely of radiating, intergrown tremolite crystals (hand specimen of sample HPTH-1 from West Thalanga, courtesy of W. Herrmann).

(c) Massive calc-silicate rocks from the Favourable Horizon of West Thalanga contain rare diopside (d) with tremolite (t) (sample TH245-675.8, PPL, scale bar is 500 μm).

(d) Minor occurrences of calc-silicate rocks in the Favourable Horizon of Far West Thalanga (section 1) consist of quartz (q), epidote (e) and calcite (sample TH410-503.10, crossed nicols, scale bar is 500 μm).

(e) Massive calc-silicate rocks from the hangingwall in Far West Thalanga (section 1) are variable in composition. Sample TH37-189.1 (~150 m stratigraphically above the Favourable Horizon) consists of quartz, calcite (c), epidote (e) and actinolite (a) which represents the most common assemblage (PPL, scale bar is 500 μm).

(f) Image shown in Fig. 3.6e under crossed nicols.

(g) Sample TH37-193.0 represents the biotite-rich end-member of the massive calc-silicate rocks in the hangingwall. It consists of quartz, biotite, calcite, epidote (e), actinolite (a) and chlorite (c) (PPL, scale bar 500 μm).

(h) Sample TH37-190.20 represents the carbonate-dominated end-member of massive calc-silicate rocks in the hangingwall. It consists of carbonate, chlorite (c), epidote (e) and quartz (q) (PPL, scale bar is 500 μm).

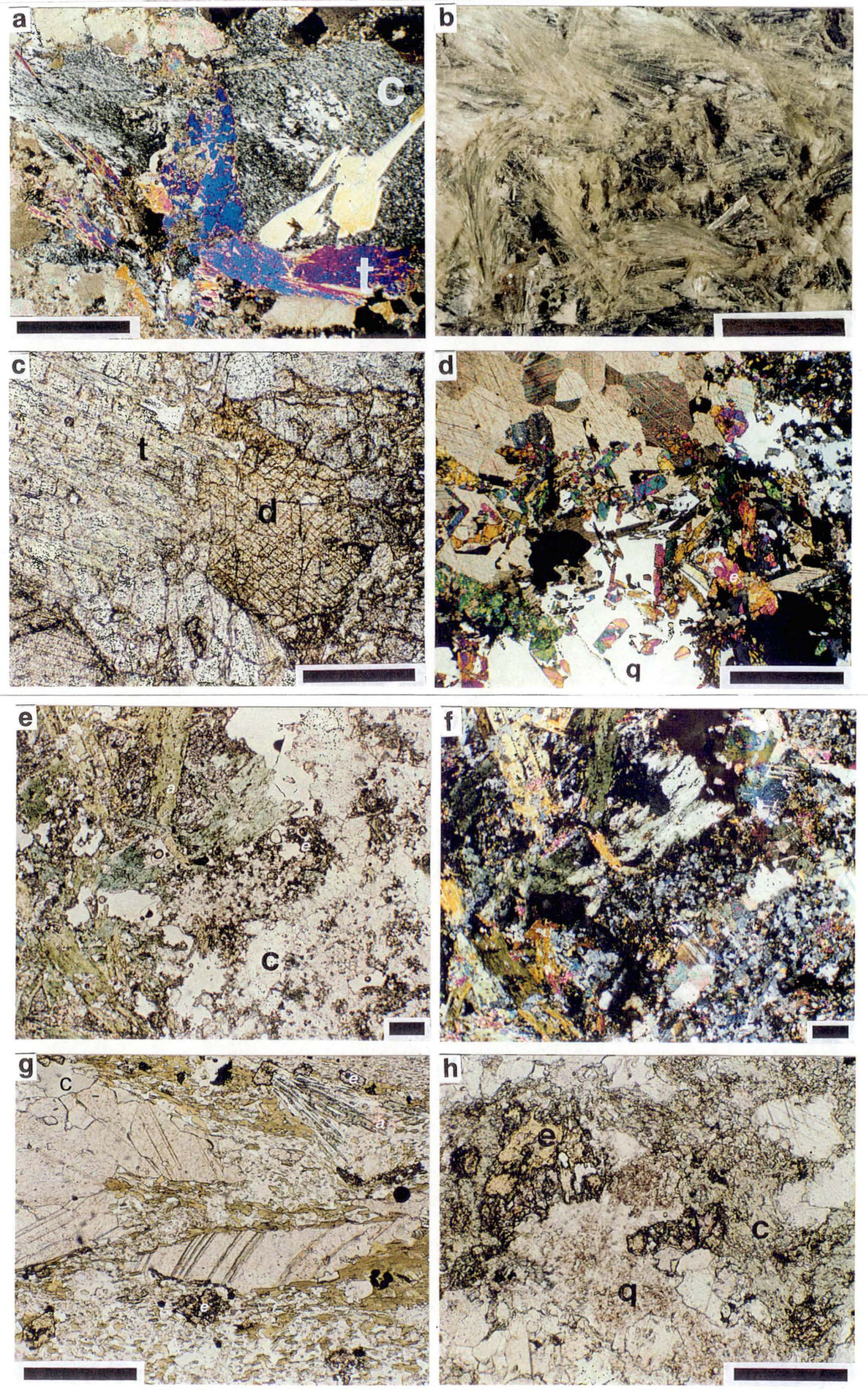

Fig. 3.6

3.2.5 Massive sulphides

Following is a brief summary of the observations and interpretations presented by Hill (1996) who studied the mineral assemblages and textures of the Thalanga massive sulphides in considerable detail. The main sulphide minerals are pyrite, sphalerite, galena and chalcopyrite which are locally accompanied by minor tetrahedrite-tennantite, magnetite and/or arsenopyrite. Quartz, barite, chlorite, calcite, dolomite, tremolite and muscovite are the principal gangue minerals in the massive sulphide lenses.

In most parts of the deposit, the massive to banded polymetallic sulphides are coarsely recrystallised to crystal aggregates with sharp grain boundaries and triple point grain contacts. This indicates that the sulphides were subjected to thermal annealing during metamorphism which has overprinted and destroyed any primary sulphide textures. However, textures that might have formed during D2 or later deformation events are recognisable.

It is evident that some chalcopyrite, galena and sphalerite were remobilised during regional metamorphism and deformation. Piercement structures generated during D2 in the competent hangingwall dacites directly overlying massive sulphides, and other dilational sites such as tension gashes and boudin necks, are filled with chalcopyrite and dark red-brown, Fe-rich sphalerite. Pressure shadows of euhedral pyrite or quartz are occupied by remobilised chalcopyrite and galena which also occur along brittle fractures in massive pyrite zones.

Alternating pyrite-rich and sphalerite-rich bands are a common feature of the ore and may have formed by isoclinal folding of primary massive sulphide bands, diffusive mass transfer during metamorphism, or shearing during tectonic deformation.

The textures observed in the massive sulphides at Thalanga are typical for metamorphosed VHMS deposits and have been described in a number of deposits of similar metamorphic grade (eg. Vokes & Craig, 1993).

3.3 Discussion

Facies control on variations in metamorphic mineral assemblages in the Thalanga sequence

In the Thalanga area, textural and mineralogical changes associated with metamorphism vary significantly depending on the pre-metamorphic composition of the rocks (Table 3.1). Siliceous, least-altered rhyolite shows brittle fractures and contains scarce interstitial muscovite, chlorite and biotite in a quartzofeldspathic groundmass. Due to the stability of quartz-feldspar assemblages under a wide range of P-T conditions, and the paucity of phyllosilicates, recrystallisation during metamorphism was largely inhibited and a foliation did not develop. Instead, these rocks responded to regional deformation by brittle failure.

In contrast, phyllosilicate-rich altered rhyolite has a groundmass containing variable proportions of muscovite, biotite and chlorite which are commonly foliated. The differences in mineralogy and texture between altered and least-altered rhyolite are interpreted to reflect the compositional changes in the footwall alteration zone during hydrothermal activity prior to metamorphism.

Metamorphic mineral assemblages in the quartzofeldspathic groundmass of the hangingwall dacite vary among biotite-, actinolite- and epidote-dominated end-members. These minerals commonly represent <10 vol.% of the rock and feldspar phenocrysts are typically texturally unaltered. Differences in bulk rock composition among the hangingwall dacites may be responsible for variations in metamorphic mineral assemblages and it may be inferred that epidote and/or actinolite crystallised in dacites which experienced some carbonate alteration prior to metamorphism whereas biotite formed in dacites which were relatively Ca-poor.

Phyllites in the hangingwall consist of foliated assemblages of quartz-muscovite-biotite±chlorite. However, layers of strikingly different mineralogy (mainly quartz and actinolite) occur locally within this facies and indicate that some layers contained substantial amounts of carbonate prior to metamorphism.

Evidence for isochemical metamorphism

The contrasting mineral assemblages and textures in phyllites, massive calc-silicate rocks,

hangingwall dacites, least-altered rhyolites and altered rhyolites indicate that the development of metamorphic mineral assemblages was controlled by the pre-existing local rock composition. Recombination of chemical components to form new, metamorphic mineral assemblages occurred on a mm- to cm-scale and did not transgress pre-existing boundaries between compositionally different rock domains. Textural observations that lend support to this interpretation include:

- exclusive occurrence of large, poikiloblastic garnets in chlorite-rich domains of domainally altered rhyolite in East Thalanga;
- development of strikingly different metamorphic mineral assemblages on a cm- to mm-scale in compositionally layered phyllites (sample TH40-67.0; Fig. 3.3); and
- occurrences of discrete, bedding parallel intervals (3 - 20 cm) consisting of quartz-actinolite±epidote assemblages within the mudstone-dominated facies in the hangingwall.

These textural observations indicate that pre-metamorphic variations of local bulk rock composition controlled the crystallisation of particular metamorphic mineral assemblages and that regional and contact metamorphic recrystallisation was isochemical in the Thalanga area. Sedimentation processes produced compositionally different beds within the sedimentary succession and domainal or multi-stage hydrothermal alteration processes generated mineralogical and compositional heterogeneity in the footwall rhyolite.

The geochemical differences between an actinolite-rich interval and the directly adjacent phyllite in sample TH37-138.50 were determined by XRF analyses. The data show that the actinolite-rich interval contains ~3 times more CaO and substantially less K_2O than the adjacent phyllite (Fig. 3.7). Furthermore, the concentrations of Ba and Rb, which are commonly substituted into micas replacing K, are also relatively low in the actinolite-rich interval. Since all other chemical components have similar concentrations in both domains, variations in CaO and K_2O must have controlled the crystallisation of actinolite rather than biotite in some intervals within mudstone-dominated sedimentary facies in the hangingwall. These geochemical variations may be due to differences in the abundances and relative proportions of clay minerals, quartz and calcite in the pre-metamorphic precursors of these sedimentary beds.

Fig. 3.7: Comparison of the geochemical composition of pelitic phyllite and an intercalated actinolite-rich interval.

The composition of an actinolite-rich interval and the adjacent pelitic phyllite was determined by X-Ray Fluorescence (XRF) analyses using splits of sample TH37-138.50 (Fig. 3.2e). Comparison of the concentrations of major elements and selected trace elements show that the phyllosilicate-rich part of the sample is enriched in potassium and trace elements that substitute for potassium in micas (Ba and Rb) whereas the actinolite-rich interval is substantially enriched in calcium. All other elements have similar concentrations in both parts of sample TH37-138.50.

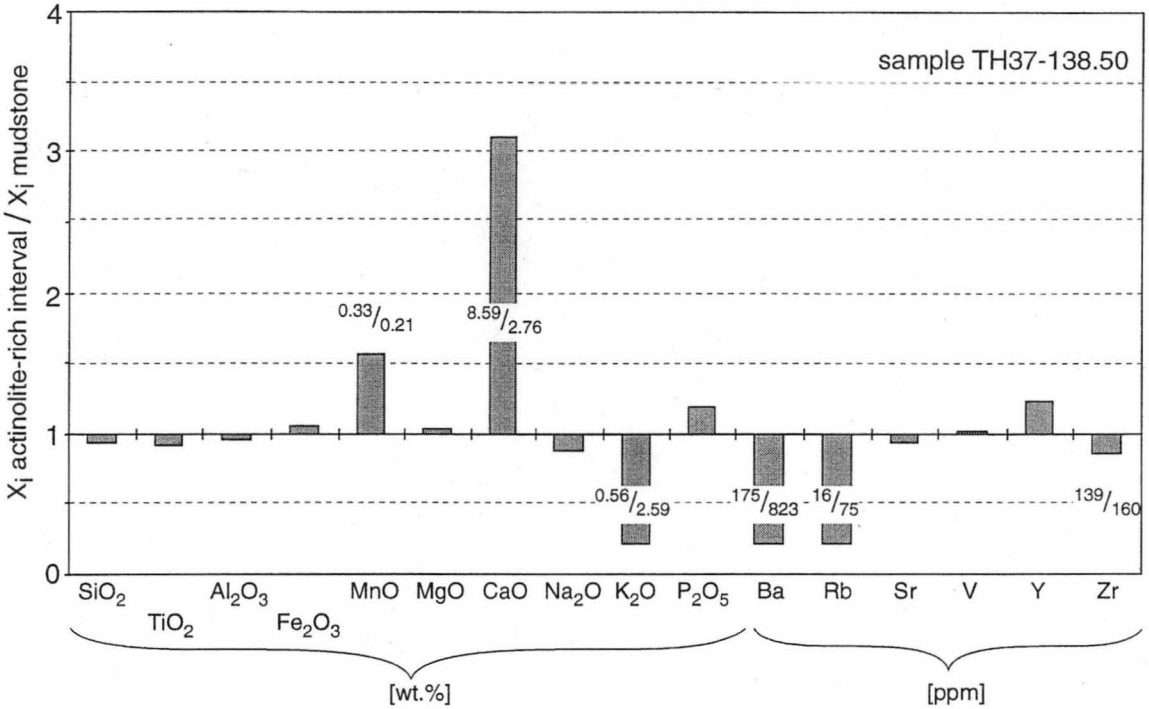
sample TH37-138.50
X_i actinolite-rich interval / X_i mudstone
4
3
2
1
0
0.33/0.21
8.59/2.76
0.56/2.59
175/823
16/75
139/160
SiO2
TiO2
Al2O3
Fe2O3
MnO
MgO
CaO
Na2O
K2O
P2O5
Ba
Rb
Sr
V
Y
Zr
[wt.%]
[ppm]

Fig. 3.7

Possible metamorphic reactions and likely precursor mineral assemblages

Muscovite, chlorite and biotite are abundant in the altered rhyolite and interpreted to represent the metamorphic equivalents of phyllosilicate minerals formed during hydrothermal alteration associated with mineralisation (Table 3.1). Hydrothermally altered rocks associated with modern massive sulphide deposits on the seafloor contain abundant clay minerals (typically smectite and illite) and chlorite (eg. Goodfellow et al., 1993; Ridley et al., 1994; Turner et al., 1993; Honnorez et al., 1998). These phases can be intimately intergrown and mixed-layer minerals with smectite-illite or chlorite-smectite composition have been documented (Alt & Jiang, 1991). Hydrothermal K-rich white mica has been reported from altered felsic volcanics in the Manus Basin (Binns & Scott, 1993) and the Okinawa Trough (Halbach et al., 1993) and in basalts below the TAG hydrothermal field (Honnorez et al., 1998).

It is inferred that hydrothermal phyllosilicates in the Thalanga footwall included Mg- and K- bearing phases which were unstable under the P-T conditions of greenschist facies metamorphism. Re-equilibration was achieved by metamorphic reactions which included the formation of new, metamorphic phases. Biotite is interpreted to have formed exclusively during metamorphism because P-T conditions of alteration in VHMS environments are too low for biotite crystallisation ($<<1$ kbar and ≤ 350 °C) and it is not known to occur in hydrothermally altered rocks associated with modern seafloor massive sulphide deposits. Furthermore, biotite is rare in least-altered rhyolite where it occurs as small grains within the quartzofeldspathic groundmass and therefore it can be concluded that biotite was not a primary phenocryst phase in footwall rhyolite.

It is possible that muscovite and chlorite originally formed during hydrothermal alteration at Thalanga and that re-equilibration of these minerals during metamorphism was achieved by recrystallisation and cation exchange reactions. The biotite-forming reaction probably involved muscovite and chlorite and textural evidence (Fig. 3.5c) also suggests that feldspar phenocrysts were consumed during biotite crystallisation (K-feldspar + chlorite => biotite).

Least-altered rhyolite outside of the footwall alteration zone has a groundmass consisting of quartz and feldspar with minor interstitial muscovite, biotite and chlorite. These phyllosilicates may represent the metamorphic equivalents of minor clay minerals formed during interaction of cold seawater and the groundmass of the rhyolite which

probably consisted of glassy and devitrified domains.

Metamorphic assemblages including calc-silicate minerals (epidote, zoisite, tremolite and actinolite) occur throughout the sequence. However, variations in their abundance and relative proportions are substantial, ranging from minor disseminated epidote in the quartzofeldspathic groundmass of siliceous dacite or rhyolite to massive calc-silicate rocks. It is important to note that tremolite, which is locally disseminated in the altered footwall rhyolite, has not been observed in the hangingwall. Instead, epidote and actinolite are the principal calc-silicate minerals in the hangingwall dacite and hangingwall sedimentary facies. This indicates that the footwall rhyolite, which originally contained very little magnesium and calcium (composition of least-altered rhyolite, Chapter 6, Table 6.1) locally became substantially enriched in these elements during hydrothermal alteration. In contrast, occurrences of actinolite- and/or epidote-bearing assemblages indicate high Fe/(Fe + Mg) ratios for the bulk rock composition of some hangingwall lithologies. The presence of feldspar-actinolite-chlorite assemblages in the hangingwall dacite indicates that actinolite may have formed by dewatering reactions during metamorphism involving minor pre-metamorphic chlorite (plagioclase + Fe-rich chlorite => albite + actinolite + H_2O).

Disseminated epidote is common and locally abundant in the hangingwall dacite and minor occurrences have been observed in the footwall rhyolite. Epidote veins are present in the footwall, hangingwall and occasionally within apophyses of the diorite pluton in East Thalanga (section 6; Chapter 7, Fig. 7.7 and Appendix). Epidote group minerals are stable under a wide range of condition (Deer et al., 1992) and the origin of epidote at Thalanga is uncertain. In general, sub-seafloor metamorphism is inferred to be the main process of epidote formation in basalt-dominated ophiolite sequences where rocks consisting entirely of epidote (epidosites) are common (Schiffman et al., 1990). In this case, the circulation of seawater through oceanic crust is the cause of epidote formation. Mafic volcanics contain significant Ca and Fe in pyroxene, amphibole and plagioclase and these minerals are readily altered due to hydration. In contrast, felsic volcanics contain little original Ca and Fe and crystallisation of epidote requires addition of these components from a hydrothermal fluid. Therefore, it could be argued that epidote at Thalanga may have a hydrothermal origin. However, it is also possible that epidote

formed during regional and/or contact metamorphism at Thalanga by metamorphic reactions involving hydrothermal carbonate and chlorite.

The mineral assemblages observed in the phyllites are largely metamorphic and most likely equivalent to original components such as fine-grained clays, volcanic ash (including glass and crystal fragments) and possibly biogenic particles. The occurrences of thin actinolite-rich beds imply that significant carbonate accumulated locally.

Massive CCT rocks in the Favourable Horizon of West Thalanga have been interpreted to represent intensely altered footwall rhyolite, based mainly on geochemical evidence (Herrmann, 1994). In some altered rhyolite tremolite has replaced quartz phenocrysts (Fig. 3.5 g, h), so the absence of quartz phenocrysts in CCT rocks could be related to SiO_2 consumption during the tremolite-forming reaction. It is inferred that CCT rocks contained substantial hydrothermal dolomite and/or a mixture of calcite and chlorite prior to metamorphism and that all the original quartz in the altered rhyolite was consumed during metamorphic mineral reactions.

Table 3.1: Metamorphic mineral assemblages in various lithofacies of the Thalanga sequence and inferred precursor compositions

lithofacies	mineral assemblages	inferred composition prior to metamorphism
least-altered rhyolite	• quartz-feldspar with minor muscovite±biotite(±chlorite)	weakly altered rhyolite; muscovite, chlorite and biotite formed by reaction involving ?diagenetic phyllosilicates
altered rhyolite	• quartz-muscovite±feldspar • quartz-muscovite-biotite±feldspar • quartz-muscovite-biotite-chlorite±pyrite(rare large garnet) • quartz-pyrite-muscovite±biotite • chlorite-pyrite-muscovite-quartz (rare garnet) • muscovite-epidote-quartz±actinolite±biotite±chlorite±carbonate • quartz-epidote-actinolite±muscovite(±chlorite±carbonate±biotite) • tremolite-quartz-epidote ±muscovite±carbonate±chlorite±sphalerite	variably altered footwall rhyolite with hydrothermal phyllosilicates, carbonates and sulphide minerals biotite, garnet, tremolite and actinolite crystallised during metamorphism; muscovite, chlorite and epidote may have formed during alteration or metamorphism
dacite	• quartz-feldspar-biotite-chlorite±sercite (±carbonate±zoisite±garnet) • quartz-feldspar-epidote±biotite±chlorite±carbonate±actinolite • quartz-feldspar-actinolite±chlorite±epidote±carbonate	weakly altered dacite (?sub-seafloor metamorphism) with variable proportions of phyllosilicates (?clays) and carbonate (and ?epidote)
phyllite	• quartz-muscovite-biotite±chlorite(±carbonate±zoisite) • quartz-biotite±epidote±chlorite(±actinolite±carbonate) • quartz-actinolite±epidote±chlorite(±carbonate) • (rare: garnet-biotite-carbonate; garnet-hornblende-quartz(chlorite-biotite); cordierite-biotite-chlorite-muscovite)	sedimentary material including phyllosilicates and volcanic glass ± feldspar and quartz crystal fragments; rock intervals with calc-silicates may have formed from a precursor which contained carbonate
massive calc-silicate rocks	• quartz-epidote±biotite±actinolite±carbonate±chlorite±muscovite • carbonate-quartz-epidote±chlorite±tremolite±zoisite±biotite±sericte • carbonate-tremolite-chlorite • tremolite±carbonate±muscovite±quartz±chlorite±epidote±sphalerite (±diopside)	chemical facies of variable composition, abundant tremolite-rich rocks in the Favourable Horizon in West Thalanga suggest Ca-rich precursor with a high X_{Mg} (dolomite and/or calcite-chlorite-rich); massive, calcareous, epidote-rich rocks in Far West Thalanga (section 1, Favourable Horizon and hangingwall) probably had a more siliceous precursor with a low X_{Mg}

3.4 Summary

The Thalanga sequence was affected by regional and contact metamorphism which substantially modified the original mineralogy and texture of altered footwall rhyolite, sedimentary facies and calc-silicate rocks. The least-altered footwall rhyolite and hangingwall dacite show only minor features attributable to changes during metamorphism due to the dominance of quartz and feldspar in these rocks and competent behaviour during regional deformation.

Regional deformation during D2 imparted a steeply dipping cleavage (S2) on phyllosilicate-rich rocks in the Thalanga sequence, such as sedimentary facies in the hangingwall and altered rhyolite in the footwall. The abundance of biotite crystals defining the S2 foliation indicates that deformation took place under upper greenschist facies conditions.

The emplacement of a voluminous, post-D2 diorite pluton, which cross cuts the stratigraphic sequence to the east of the Thalanga deposit, was associated with contact metamorphism. Textural features attributable to contact metamorphism, such as decussate chlorite and biotite crystals and occurrences of large (up to 5 mm), anhedral garnet poikiloblasts in chlorite-rich domains of altered rhyolite, are restricted to East Thalanga.

Certain metamorphic minerals and mineral assemblages are restricted to particular rock types or compositionally distinctive domains within altered rhyolite or sedimentary facies. This indicates that differences in pre-metamorphic compositions controlled the development of metamorphic mineral assemblages and that isochemical metamorphic equilibration occurred on a mm- to cm-scale.

4 Mineral chemistry and constraints on the P-T conditions of regional and contact metamorphism

In this chapter microprobe analyses of muscovite, biotite, chlorite and garnet from different lithofacies in the Thalanga sequence are presented and compositional variations are discussed in detail. Garnet-bearing assemblages were analysed from the contact zone with the diorite pluton, altered rhyolite in East Thalanga and dacite breccia and layered phyllite from the hangingwall in Far West Thalanga (section 1). Compositional data from garnet-biotite and garnet-chlorite assemblages in these samples have been used to constrain the conditions of regional and contact metamorphism.

4.1 Regional and contact metamorphic garnet-bearing assemblages in the Thalanga sequence

Garnet-bearing assemblages are important because they provide an opportunity to estimate the temperature conditions during metamorphism using compositional data obtained by microprobe analysis (eg. Ferry & Spear, 1978). In general, garnet crystals are rare at Thalanga, however, they occur locally in chlorite-rich domains in the footwall rhyolite in East Thalanga and in biotite-rich domains in the hangingwall sedimentary facies in Far West Thalanga. Garnet porphyroblasts are comparatively abundant (~10 vol.%) in a 1.5 m wide contact zone with the voluminous diorite pluton east of the Thalanga deposit which was intersected by drill hole TH471.

In East Thalanga, domainally altered footwall rhyolite occasionally contain large (up to 5 mm), anhedral garnets with abundant quartz inclusions. A gradual increase in the abundance of garnets (from <0.1 vol.% to ~1 vol.%) can be observed approaching the contact with the diorite pluton in TH471 which clearly indicates that they crystallised during contact metamorphism. The anhedral morphologies of garnet poikiloblasts and the abundance of groundmass inclusions indicate that the duration of conditions suitable for garnet growth may have been short, preventing the development of euhedral crystals. This is consistent with conditions expected for a short-lived thermal anomaly associated with the intrusion of magma.

Relatively small (up to ~1 mm), euhedral garnet porphyroblasts occur locally in sedimentary and volcaniclastic facies in the hangingwall of section 1 (~3.5 km to the west of the diorite pluton). Mineral assemblages include garnet-biotite-chlorite-quartz and garnet-biotite-calcite-muscovite. These garnets are interpreted to have formed during regional metamorphism because of their association with foliated biotite, the remoteness

Fig. 4.1: Location of samples selected for microprobe analyses from the Thalanga sequence.

Garnet-bearing samples (G1 to G6) were analysed from Far West Thalanga (section 1), East Thalanga (section 5 and 6) and from the contact metamorphic aureole of the diorite pluton. The compositions of muscovite, chlorite and biotite were determined in least-altered to intensely altered rhyolite sampled in drill hole TH247 (12 samples, section 2). Least-altered rhyolite in the outcrop section contains minor muscovite, biotite and chlorite which were analysed in two samples.

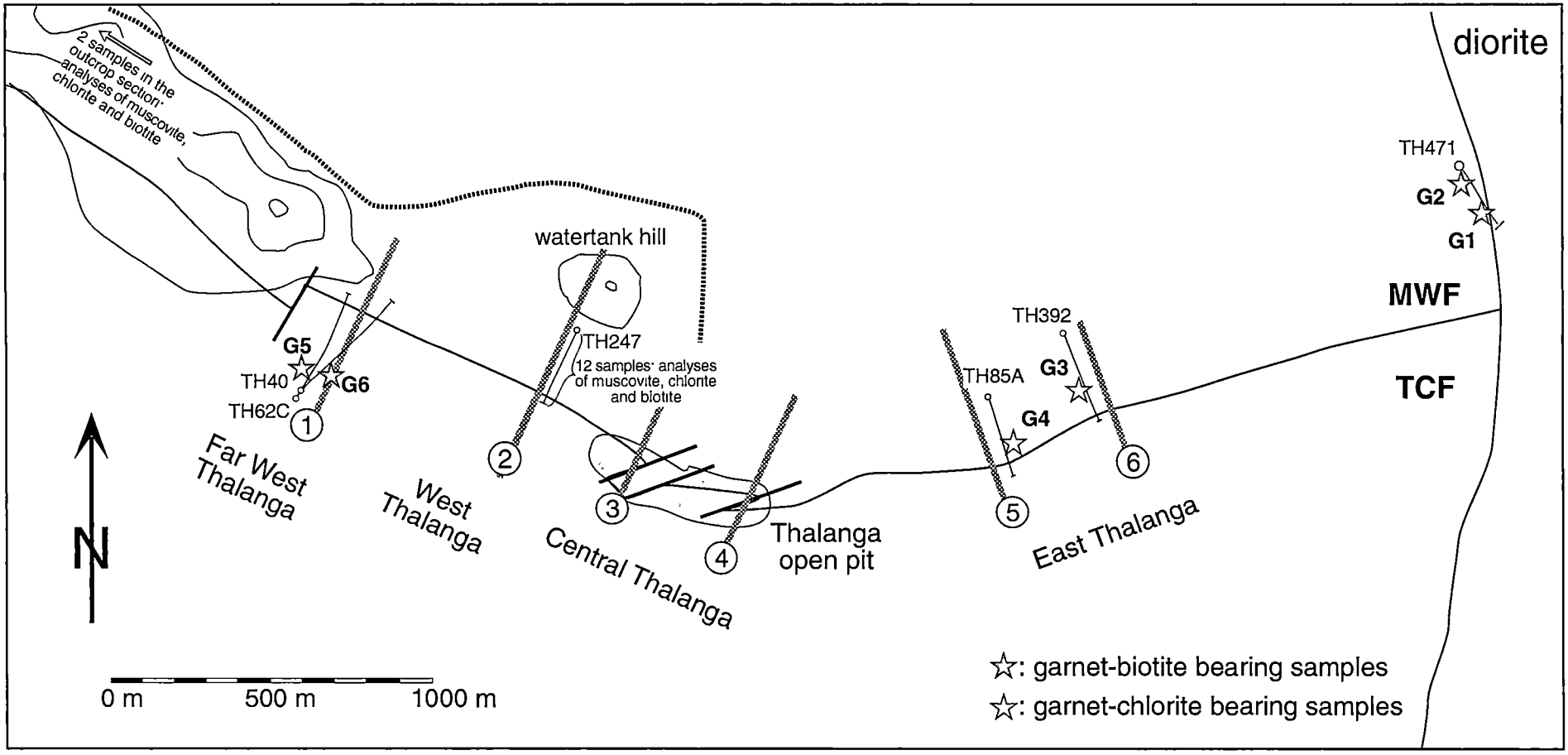
2 samples in the outcrop section: analyses of muscovite, chlorite and biotite
watertank hill
TH247
12 samples: analyses of muscovite, chlorite and biotite
G5
G6
TH40
TH62C
1
2
3
4
5
6
Far West Thalanga
West Thalanga
Central Thalanga
Thalanga open pit
East Thalanga
TH392
TH85A
G3
G4
TH471
G2
G1
diorite
MWF
TCF
N
0 m
500 m
1000 m
☆: garnet-biotite bearing samples
☆: garnet-chlorite bearing samples

Fig. 4.1

from the diorite pluton, and their euhedral shapes. The euhedral shapes of these garnet crystals indicate that elevated P-T conditions prevailed for a significant period of time which is consistent with circumstances expected for regional metamorphism.

Six garnet-bearing samples from various stratigraphic and along-strike positions within the Thalanga sequence were selected to determine the peak conditions of regional and contact metamorphism (Fig. 4.1; Table 4.1). The compositions of garnet, biotite, chlorite and muscovite were determined in the contact zone with the diorite pluton (sample G1, TH471-159.50, Fig. 4.2a-c) and in garnet-bearing rhyolite at ~30 m from the contact (sample G2, TH471-104, Fig. 4.2d). In addition, the composition of poikiloblastic garnet in a paragenesis with chlorite and muscovite from section 6 (sample G3, TH394-262.80, Fig. 4.2e; ~1200 m to the west of the intrusion) was determined. These data were used to estimate the temperature conditions of contact metamorphism.

Tiny euhedral garnets (<0.3 mm in diameter) occur in chlorite-pyrite-rich footwall rhyolite in East Thalanga (section 5, sample G4, TH85A-384, Fig. 4.2f). It is uncertain if these crystals formed during regional or contact metamorphism. Euhedral garnet porphyroblasts in compositionally layered phyllite (sample G5, TH40-67.0, Fig. 4.2g) and in a dacite breccia (sample G6, TH62C-142, Fig. 4.2h) from the hangingwall in Far West Thalanga (section 1) are inferred to have equilibrated with the surrounding biotite during regional metamorphism.

4.2 Mineral chemistry

Compositional data were obtained for mineral assemblages in the 6 garnet-bearing samples (Table 4.1; Fig. 4.2). Furthermore, chlorite, biotite and muscovite were analysed in 12 samples from one diamond drill hole in West Thalanga (section 2; TH247) and two samples of least-altered rhyolite from the outcrop section (Fig. 4.1). The compositions of calcite and tremolite were determined in an intensely altered rhyolite sampled close to the Favourable Horizon in West Thalanga (sample TH247-361.30). Epidote, amphibole and minor calcite were analysed in one sample of layered phyllite from the hangingwall (sample G5).

Microprobe analyses of garnet-bearing samples were performed with a Camebax Microbeam instrument at the Zentrallabor für Elektronenmikroskopie (Technische Universität Berlin, Germany). Samples from TH247 and the outcrop section were analysed at the Central Science Laboratory (CSL, University of Tasmania, Hobart, Australia). The analytical results and conditions of measurements are given in the Appendix. In the following, the data are presented and interpreted with an emphasis on

Fig. 4.2: Textures of garnet-bearing assemblages in the Thalanga sequence.

(a) A garnet hornfels occupies the immediate contact zone with the diorite pluton. (hand specimen of sample G1 [TH471-159.50], ~0.3 m from the contact; scale bar is 1 cm).

(b) Abundant, euhedral garnets occur in a biotite-muscovite-quartz-rich groundmass of a garnet hornfels at the contact zone with the diorite pluton (sample G1, PPL, scale bar is 500 μm).

(c) Relatively large garnets in the contact zone with the diorite pluton contain inclusions of muscovite, biotite and quartz. An inclusion of intergrown biotite and chlorite occurs in one garnet (arrow). This assemblage could represents a relic of the groundmass that existed prior to peak metamorphism. Chlorite is absent from the groundmass of the hornfels and chlorite was possibly consumed during the garnet-forming reaction (sample G1, PPL, scale bar is 100 μm).

(d) Altered rhyolite sampled at ~30 m from the diorite pluton contains minor poikiloblastic garnets with abundant inclusions (quartz, feldspar, muscovite, biotite) and anhedral, ragged crystal shapes (sample G2 [TH471-104], PPL, scale bar is 500 μm).

(e) Large garnet poikiloblasts with chlorite and muscovite occur in domainally altered footwall rhyolite in East Thalanga (section 6, sample G3 [TH394-262.80], section 6; scale bar is 500 μm; image of hand specimen in Fig. 3.5e).

(f) Rarely, small garnet crystals (g) occur in chlorite-pyrite-rich rhyolite in East Thalanga (section 5, sample G4 [TH85A-384], PPL, scale bar is 500 μm).

(g) Garnet crystals occur locally in the layered phyllite in the hangingwall of Far West Thalanga (section 1). In sample G5 (TH40-67.0) a necklace of garnet crystals occurs in one specific lamina with biotite and calcite whereas quartz is absent (Fig. 3.3; PPL, scale bar 500 μm).

(h) Siliceous dacite clasts in monomictic breccia units in the hangingwall of Far West Thalanga (section 1) generally contain minor biotite (±chlorite) which forms interconnected networks. Locally, euhedral garnet crystals occur in biotite-rich domains (sample G6 [TH62C-142], PPL, scale bar is 500 μm).

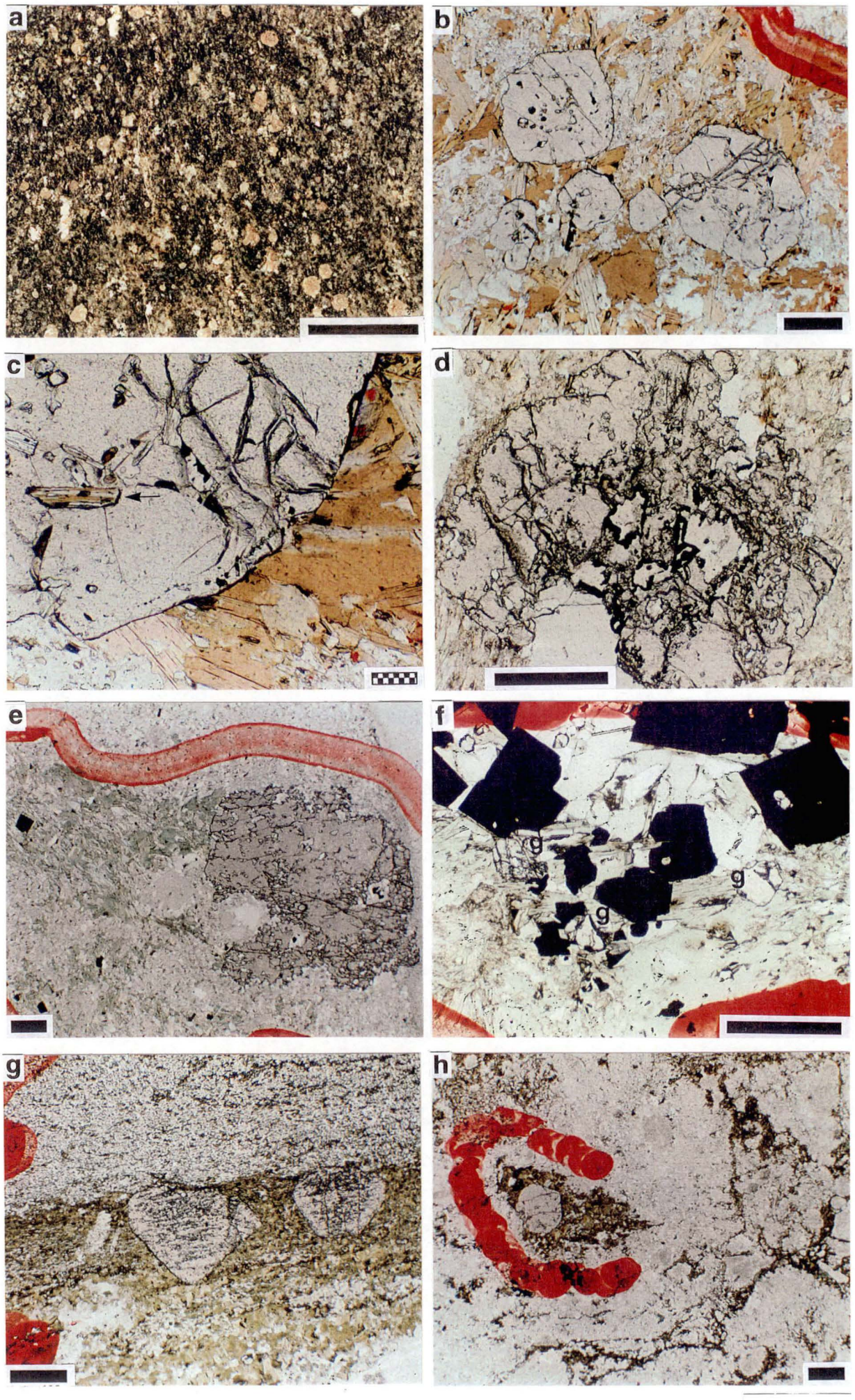

Fig. 4.2

Table 4.1: Summary of petrographic characteristics of garnet-bearing samples from the Thalanga sequence

gt-bearing sample	sample name	location	distance from diorite	rock type	assemblage	garnets (shape, size, inclusions)	sample description
G1	TH471-159.50	proximal to diorite pluton	0.5 m	garnet hornfels (diorite contact zone)	gt-bio-mus	euhedral, 150 µm to 1400 µm, abundant qtz, mus, bio, (chl), (opaque) inclusions	Dark brown, pelitic hornfels with abundant garnet porphyroblasts. Groundmass consists of light brown biotite, muscovite, quartz, plagioclase and opaque minerals.
G2	TH471-104	proximal to diorite pluton	30 m	altered rhyolite	gt-bio-chl-mus	anhedral, 1800 µm to 2200 µm, poikilitic: abundant qtz, mus and opaque inclusions	Altered rhyolite with minor, large garnet poikiloblasts. Groundmass consists of variable proportions of biotite, chlorite, muscovite and quartz.
G3	TH394-262.80	East Thalanga (section 6)	~1200 m	domainally altered rhyolite	gt-chl-mus	anhedral, 4000 µm, poikilitic: abundant qtz and mus inclusions	Domainally altered rhyolite with chlorite-rich domains (apparent clasts or 'blotches') and quartz-muscovite-rich domains (apparent matrix; cf. **Fig. 3.5e**). Scare, large, garnet poikiloblasts are restricted to chlorite-rich domains. Biotite is present only in the surrounding chlorite-poor domain associated with muscovite, quartz and minor chlorite.
G4	TH85A-384	East Thalanga (section 5)	~1600 m	chlorite-pyrite-rich rhyolite	gt-chl-mus	euhedral or fractured, 160 - 220 µm, inclusion-free	Chlorite-and pyrite-rich, altered rhyolite with small garnets. Garnets occur with chlorite, muscovite, quartz and pyrite. Biotite is absent. Formation of garnet instead of biotite may have been favoured by high bulk rock concentrations of Fe, Mn, and Al and low K concentration (FeO = 18.7 wt.%; MnO = 0.33 wt.%; Al_2O_3 = 14.7 wt.%; Na_2O = 0.09 wt.%; K_2O = 1.0 wt.%; K_2O/Al_2O_3 = 0.07; XRF analysis; cf. Appendix).
G5	TH40-67.0	Far West Thalanga (section 1)	~3500 m	layered phyllite	gt-bio-cc	euhedral, 900 to 1300 µm, foliated mus ± bio inclusions in central parts	Layered phyllite consisting of several texturally and mineralogically distinctive layers (**Fig. 3.3**). Garnets are restricted to a narrow lamina (~1 mm wide) of foliated, dark brown-green biotite ± calcite forming a necklace of aligned, equigranular, euhedral crystals (**Fig. 3.3b, Fig. 4.2 g**). Other distinctive laminae consist of hornblende-chlorite, epidote-chlorite-quartz, quartz (± biotite ± carbonate) and biotite-quartz.
G6	TH62C-142	Far West Thalanga (section 1)	~3500 m	dacite breccia	gt-bio-chl	euhedral, 820 µm, minor qtz inclusions	Monomictic breccia with abundant, siliceous dacite clast. An interconnected, irregular network of brown to olive-green biotite ± chlorite occurs in the quartzofeldspathic groundmass of dacite clasts. Rare garnet is surrounded by biotite crystal aggregates.

Abbreviations: bio: biotite, cc: calcite, chl: chlorite, gt: garnet

illustrating variations in mineral composition. Systematic changes in the composition of chlorite and biotite, which correlate with distance from the mineralised Favourable Horizon in West Thalanga, are discussed in Chapter 8.

4.2.1 Muscovite

The basic structural components of mica are composite sheets in which a layer of octahedrally coordinated cations is sandwiched between two identical layers of linked (Si, Al)O_4 tetrahedra. Muscovite is a di-octahedral white mica with Al^{3+} being the dominant cation in the octahedral position. The large, 12-fold coordinated site between the sheets is mainly occupied by K^+ cations.

The ideal chemical composition of muscovite can be expressed as:

$K_2Al_4[Si_6Al_2O_{20}](OH)_4$.

In this ideal muscovite, Al^{3+} is the only cation in the octahedral sites and charge balance constraints demand that one octahedral position for every two Al[6] is vacant. However, substantial compositional variations are common in natural muscovites and the principal isomorphous replacements are as follows:

For K (X-position): Na, Rb, Ba

For Al[6] (Y-position): Mg, Fe^{2+}, Fe^{3+}, Mn, Li, Cr, Ti, V

For OH: F.

Furthermore, (Si_6Al_2) in the tetrahedral position can vary to (Si_7Al) (Deer et al., 1992). Substitution of Na for K leads toward the composition of paragonite. The name phengite describes muscovite with some Mg and Fe cations in octahedral sites which were incorporated into the crystal structure by a coupled substitution of (Mg, Fe^{2+})[6], Si[4] $\Leftrightarrow$ Al[4], Al[6] (Tschermak's exchange).

Muscovites were analysed in samples of altered footwall rhyolite, least-altered rhyolite and in the garnet-rich diorite contact zone and data were normalised using 22 oxygens as the basis for formula calculation. The majority of the analysed muscovites have Si[4]:Al[4] ratios greater than 3 : 1 and show some substitution of Mg and Fe for Al in octahedral sites. Deviation from the ideal muscovite composition is also indicated by the number of cations in the octahedral Y-position which is generally higher than in the ideal formula (range 4.02 to 4.38). Because of the small grain size of the muscovite crystals (commonly <10 μm) some analyses may be affected by contamination due to overlap with other minerals. In particular, analyses with high Mg and Fe concentrations are possibly due to contamination by adjacent (or underlying) chlorite or biotite crystals.

Fig. 4.3: Variation diagrams illustrating the compositional diversity of muscovite at Thalanga.

(a) Na [pfu] vs. K [pfu]

(b) Ba + Ti [pfu] vs. vacancies in the X-position [pfu]

(c) F [pfu] vs. Fe [pfu]

(d) Fe [pfu] vs. Mg [pfu]

(e) Si [pfu] vs. Mg + Fe [pfu]

(f) Al[6] [pfu] vs. Mg + Fe [pfu]

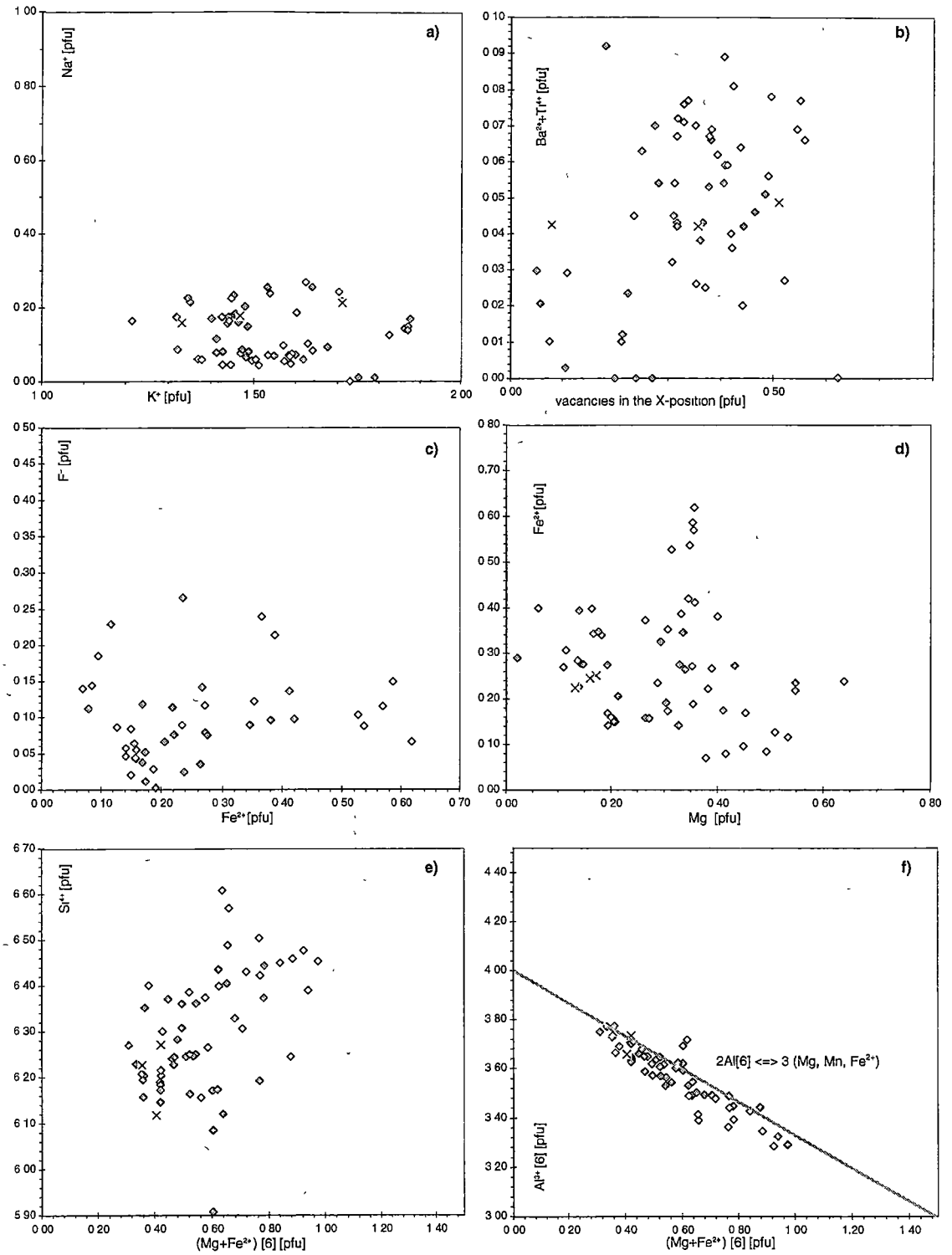

Legend:
composition of muscovite in samples of

- × diorite contact zone
- ◇ altered rhyolite
- ◇ least altered rhyolite

Fig. 4.3

The data show that K is the dominant cation in the X position and Na values are low and variable. Muscovites in least-altered rhyolite have <0.05 Na pfu (per formula unit) whereas muscovites in altered rhyolite have a wider range in Na content (0 to 0.22 pfu; Fig. 4.3a). The occupation of the X position in the muscovites is generally incomplete and up to 0.5 sites in the X-position may be vacant (Fig. 4.3b). Such vacancies can be related to the substitution of Ti^{4+} or Ba^{2+} but the concentrations of these elements are low and there is no correlation between the amount of these cations and the number of vacant X-sites (Fig 4.3b). Alternatively, the site vacancies may be related to the substitution of trivalent Fe or a hydromuscovite component ($K^+ \Leftrightarrow H_3O^+$).

Fluorine contents of muscovites in altered and least-altered rhyolite were measured for samples analysed at the CSL. There is a significant spread in the data showing that the muscovites contain up to 0.25 pfu of F (Fig. 4.3c) which could be incorporated into muscovite by a simple $OH^- \Leftrightarrow F^-$ substitution. The range of F concentrations in samples of altered rhyolite is only slightly larger than in least-altered rhyolite.

The amount of Mg and Fe^{2+} cations varies substantially and unsystematically (Fig. 4.3d). Muscovites in least-altered rhyolites have a narrow range of Mg contents (0.28 to 0.4 pfu) but variable Fe^{2+} contents (0.24 to 0.64 pfu). Muscovites from the diorite contact zone are fairly homogeneous and lower in their Fe^{2+} and Mg contents than muscovites in least-altered rhyolite. Muscovites of altered rhyolite show a relatively large compositional variability (0.1 to 0.6 pfu for Mg; 0.05 to 0.4 for Fe^{2+} pfu). The manganese concentration in muscovites is generally <0.1 wt.% and <<0.1 pfu.

The substitution of divalent cations into muscovite can be balanced by replacement of two Al[6] with three (Mg, Fe^{2+})[6] or by Tschermak's exchange. A positive correlation between the number of Mg + Fe^{2+} and Si cations should exist if the introduction of (Mg,Fe^{2+})[6] was coupled with an exchange of Si for Al in the tetrahedral position. However, the Thalanga data set shows that this is not the case (Fig. 4.3e). In contrast, a plot of (Mg + Fe^{2+})[6] versus Al[6] shows that the increase of divalent cations is correlated with a decrease in Al[6] (Fig. 4.3f). The slope of the correlation trend (0.666) is consistent with the interpretation that three (Mg, Fe^{2+})[6] were introduced into the muscovite structure for every two Al^{3+}[6], thereby filling vacant octahedral sites. However, a similar trend could be expected if the data represent partially mixed analyses of muscovite and adjacent biotite or chlorite grains, which, given the small size of muscovite crystals, is the more likely interpretation.

4.2.2 Biotite

The structure of biotite is similar to that of muscovite except that the octahedral sites are completely filled by divalent cations; therefore biotite can be described as a tri-octahedral mica. The ideal chemical composition of biotite, representing a solid solution of annite and phlogopite, can be expressed as:

$K_2(Mg, Fe)_6[Si_6Al_2O_{20}](OH)_4$.

However, in natural biotite there is appreciable substitution of Al for (Mg, Fe) in octahedral sites balanced by Al for Si in tetrahedral sites (Tschermak's exchange). Other common substitutions are:

For K (X-position): Na, Ca, Ba, Rb

For octahedral sites (Y-position): Mn, Ti, Fe^{3+}, Li

For OH: F

At Thalanga, biotite was analysed in samples of least-altered rhyolite, altered rhyolite, the garnet-rich diorite contact zone, dacite breccia and layered phyllite. Calculations of chemical formulae were performed on the basis of 22 oxygens.

The X-position in biotites from Thalanga is occupied by 1.7 to 2 K pfu (Fig. 4.4a) leaving ≤ 0.3 sites vacant. The biotite is sodium-poor containing less than 0.05 Na pfu. Vacancies in the X-position can result from incorporating Ti^{4+} into the biotite structure but Fig. 4.4a shows no trend to support this interpretation. Biotite in altered rhyolite is relatively Ti-poor ($\leq$0.12 Ti pfu) whereas biotite from all other lithofacies commonly contains slightly more Ti (commonly ~0.2 pfu).

Fluorine concentrations of biotite in samples of altered and least-altered rhyolite show a large spread. Contents of F < 0.2 pfu are restricted to least-altered rhyolite (Fig. 4.4b) whereas one intensely altered, quartz-pyrite-rich rhyolite contains biotite with 1.5 to 1.8 F pfu (detection limit: 0.3 wt.%, 0.2 pfu) which may be classified as fluoro-phlogopite. Biotites in other samples of altered rhyolite range between 0.2 and 1 F pfu, largely overlapping with biotites of least-altered rhyolite. There is a general negative correlation between fluorine and iron which is in agreement with the F-Fe avoidance rule (Munoz, 1984). Chlorine concentrations in biotites are close to or below the detection limit (0.05 wt.%).

The octahedral positions in biotite are mainly occupied by variable proportions of iron and magnesium. Biotite in dacite breccia from the hangingwall is Fe-rich (close to 4 Fe pfu) whereas samples of altered rhyolite contain Mg-rich biotite (up to 5 Mg pfu) (Fig. 4.4c). Least-altered rhyolite contains biotite with about equal proportions of Fe and Mg. Biotite in altered rhyolite show a wide range in relative proportions of Fe and Mg.

Fig. 4.4: Variation diagrams illustrating the compositional diversity of biotite at Thalanga.

(a) Ti [pfu] vs. K [pfu]

(b) F [pfu] vs. Fe [pfu]

(c) Fe [pfu] vs. Mg [pfu]

(d) Al[6] [pfu] vs. Mg + Fe + Mn [pfu]

(e) Al[6] [pfu] vs. vacancies in the Y position [pfu]

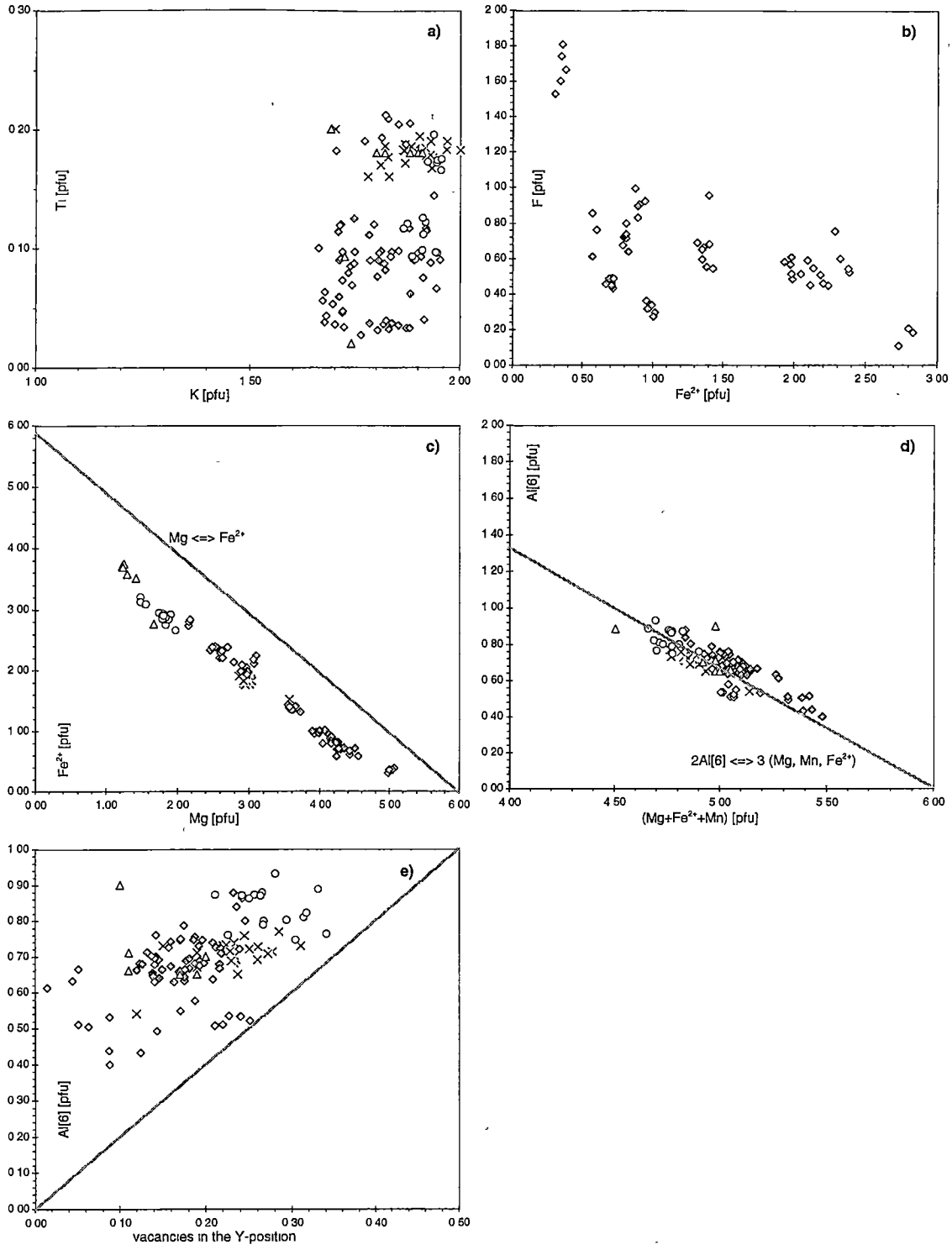

Legend:
composition of biotite in samples of

- × diorite contact zone
- ◇ altered rhyolite
- ◇ least altered rhyolite
- ○ layered phyllite
- △ dacite beccia

Fig. 4.4.

The tightly constrained negative correlation between the abundance of Fe and Mg cations indicates a simple substitution of Mg[6] $\Leftrightarrow$ Fe^{2+}[6]. However, the total of these cations in the Y-position is less than the ideal number of 6 (even if Mn cations are included which are generally $\leq$0.1 pfu) and some of these positions are occupied by Al[6].

There is a substantial amount of Al in octahedral coordination in the biotites, ranging from 0.4 to 0.9 pfu (Fig. 4.4d). The well constrained negative correlation between Al[6] and (Mg+Fe^{2+}+Mn)[6] has a slope of ~0.666, suggesting that octahedral Al was substituted into the biotite structure by replacement of two Al[6] for three (Mg+Fe^{2+}+Mn)[6]. This substitution would introduce one vacant site in the Y-position for every 2 Al[6] in order to maintain the overall charge balance. Therefore, a plot of Al[6] versus the number of vacant sites in the Y-position should show a positive trend with a slope of ~2. However, such a trend is not apparent (Fig. 4.4e) and all analysed biotites contain a higher amount of Al[6] than expected if all Al[6] was introduced by simple replacement of divalent octahedral cations. This indicates that Al[6] replacement was also influenced by some other substitution or that the additional Al is due to contamination of the analyses by fine-grained muscovite.

4.2.3 Chlorite

Common chlorite consists of talc-like layers (with linked tetrahedral-octahedral-tetrahedral sheets) which are separated by brucite-like sheets with cations in octahedral coordination. The composition may be represented in a structural formula such as:

$(Mg, Fe^{2+}, Fe^{3+}, Mn, Al)_{12}[(Si, Al)_8O_{20}](OH)_{16}$.

In the octahedral position (Y-position), divalent cations may also include Ni and Zn and some Cr may replace Fe^{3+} or Al. In general, chlorite has a total of ~12 octahedral cations per formula unit, however in some cases this number is $\leq$10 due to extensive replacement of three (Y^{2+})[6] for two Al^{3+}[6] and one site vacancy (Y^{2+}[6] = divalent cation in octahedral site).

Chlorite analyses from least-altered rhyolite, altered rhyolite, the diorite contact zone, dacite breccia and layered phyllite were recalculated on the basis of 28 oxygens. All chlorites contain close to 12 cations pfu in the octahedral position which is characteristic for tri-octahedral chlorites. They contain significant Al (total number of Al cations between 4 and 6) which is fairly evenly balanced between tetrahedral and octahedral positions.

Fig. 4.5: Variation diagrams illustrating the compositional diversity of chlorite at Thalanga.

(a) Al[4] [pfu] vs. Al[6] [pfu]

(b) Al[6] - Al[4] [pfu] vs. vacancies in the Y-position

(c) Si [pfu] vs. Mg + Fe + Mn [pfu]

(d) Fe [pfu] vs. Mg [pfu]

(e) Mn [pfu] vs. Mg/(Mg + Fe)

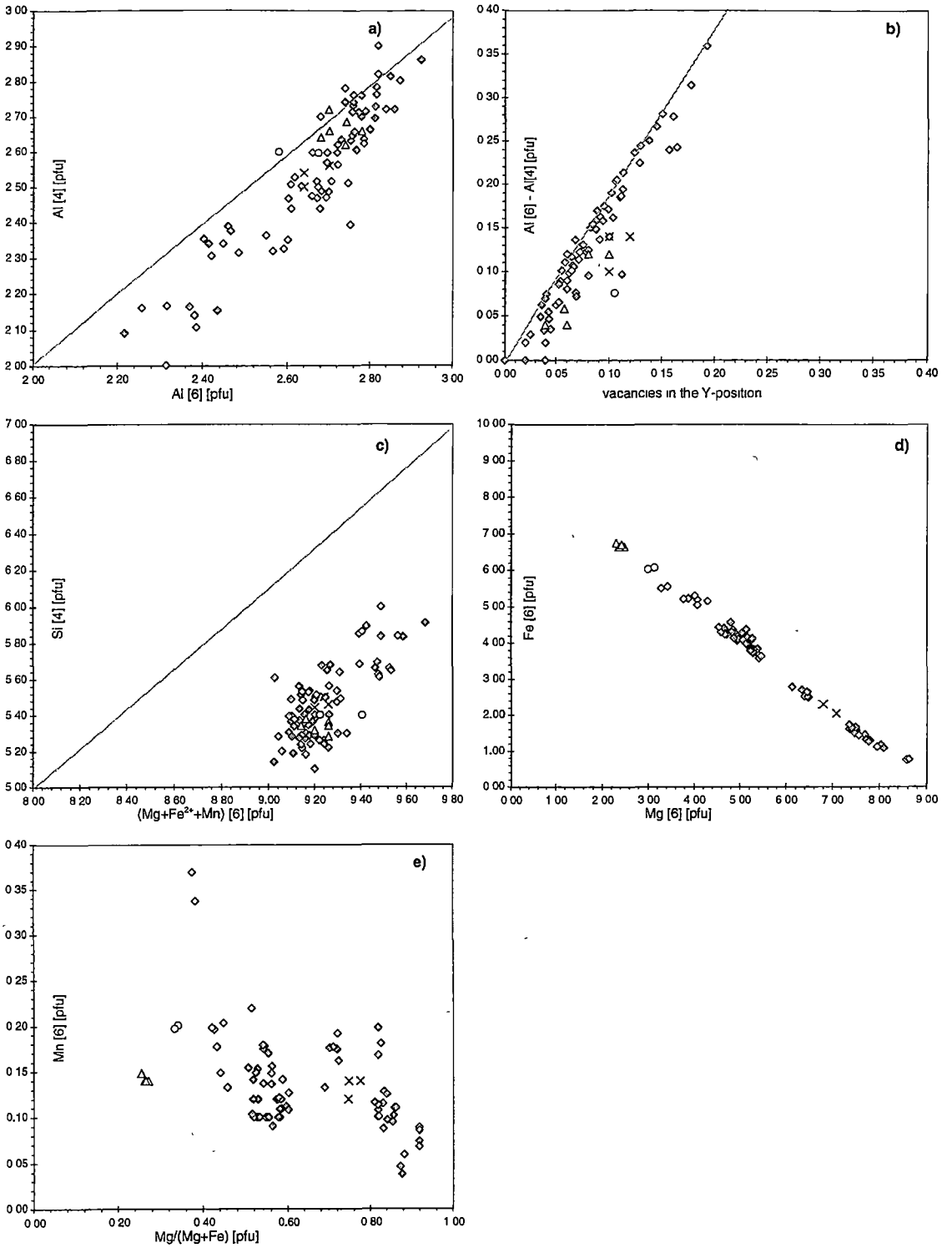
a)
Al [4] [pfu]
Al [6] [pfu]
b)
Al [6] - Al[4] [pfu]
vacancies in the Y-position
c)
Si [4] [pfu]
(Mg+Fe2++Mn) [6] [pfu]
d)
Fe [6] [pfu]
Mg [6] [pfu]
e)
Mn [6] [pfu]
Mg/(Mg+Fe) [pfu]
Legend:
composition of chlorite in samples of
× diorite contact zone
◇ altered rhyolite
◇ least altered rhyolite
○ layered phyllite
△ dacite beccia

Fig.: 4.5

There is a positive correlation between Al[4] and Al[6] which suggests that a coupled substitution of Al^{3+} for Si^{4+} in tetrahedral positions and Al^{3+} for (Mg, Fe^{2+}) in octahedral positions occurred (Fig. 4.5a). However, in most chlorites there is more Al[6] than expected if Al occupation of octahedral sites was solely controlled by such a coupled substitution of the Tschermak's type. This additional amount of Al[6] may be introduced by replacement of divalent cations in the octahedral position. In this case, the total number of cations in the octahedral position should decrease systematically, because one site vacancy is generated for every two Al[6] replacing three (Y^{2+})[6]. The number of Al[6] cations not accounted for by Tschermak's exchange can be obtained by subtracting the amount of Al[4] from the number of Al in octahedral positions. The amount of Al cations derived by this operation ranges between 0 and 0.35 and there is a strong positive correlation with the number of vacant sites in the Y-position (Fig. 4.5b). The trend has a slope of ~2 which is consistent with the interpretation that additional Al cations were introduced into the Y position by replacement of divalent cations. If most of the Al[6] was related to Tschermak's exchange there should be positive correlation between Si[4] and the total of divalent cations in the Y-position. However, only a broad positive correlation between tetrahedral Si and octahedral (Mg, Fe^{2+}, Mn) exists (Fig. 4.5c). This is consistent with the interpretation that the amount of (Mg, Fe^{2+}, Mn)[6] was variably reduced due to the substitution: $2Al^{3+}[6] \Leftrightarrow 3$ (Mg, Fe^{2+}, Mn)[6]. However, it should be noted that similar trends could be expected if some of the analyses were contaminated by fine-grained muscovite which would also increase the amount of measured Al relative to divalent cations.

The relative proportions of iron and magnesium cations in chlorite range from nearly pure clinochlore (Mg-rich end-member) to chamosite (Fe-rich end-member) with Mg/(Mg+Fe) <0.3 (Fig. 4.5d). A tightly constrained linear trend indicates a simple replacement of Mg[6] $\Leftrightarrow$ (Fe^{2+})[6]. Dacite breccia in the hangingwall contains the most iron-rich chlorite and chlorite in layered phyllite and least-altered rhyolite also contains more Fe than Mg pfu (5 - 6 Fe pfu; 3 - 4 Mg pfu). Samples of altered rhyolite contain chlorite with a comparatively large range in the proportions of iron and magnesium cations (4.5 - 0.5 Fe pfu; 4.5 - 9.5 Mg pfu).

In general, chlorites from Thalanga contain between 0.1 and 0.2 Mn pfu except for Mg-rich chlorites from altered rhyolite which have less than 0.1 Mn pfu (Fig. 4.5f). Chlorites with the highest Mg[6] content are virtually Mn-free. The Zn content of chlorites was measured in samples of altered and least-altered rhyolite but concentrations are generally below the detection limit (0.19 wt.%; Table A7 in the Appendix).

4.2.4 Garnet

Garnet is an orthosilicate with tetrahedral, octahedral and 8-fold coordinated sites. The chemical composition is usually expressed in molecular proportions of several end-members. Common end-members include:

pyrope $Mg_3Al_2Si_3O_{12}$

almandine $Fe^{2+}{}_3Al_2Si_3O_{12}$

spessartine $Mn_3Al_2Si_3O_{12}$

grossular $Ca_3Al_2Si_3O_{12}$

andradite $Ca_3(Fe^{3+}, Ti)_2Si_3O_{12}$

uvarovite $Ca_3Cr_2Si_3O_{12}$.

The composition of garnet crystals from Thalanga can be expressed in molecular proportions of the end-members pyrope (pyr), grossular (gro), almandine (alm) and spessartine (spes). Overall, almandine and spessartine are the dominant components with combined concentrations ranging between ~60 mol.% and 90 mol.% (Fig. 4.6a, b).

Garnets from the immediate contact zone with the diorite pluton (sample G1) probably formed under the highest temperatures reached during contact metamorphism. The seven garnet crystals analysed commonly show a zonation with pyrope concentrations of up to 20 mol.% in the centre (Fig. 4.6a; 4.7a). In all analyses, spessartine is the component with the highest concentration (commonly between 45 and 50 mol.%) followed by almandine (35 to 40 mol.%). The grossular component is always < 5 mol.%. Spessartine, almandine and grossular concentrations increase in the marginal parts of single crystals where pyrope concentrations are relatively low (~8 mol.%). This zonation is well developed in relatively large garnets (≥1 mm) but weaker for smaller garnets which may have been reset by diffusion during retrogression. However, apparently small garnet crystals in thin sections may well represent sections through peripheral parts of larger garnets.

Relatively large anhedral garnet poikiloblasts in altered rhyolite sampled at ~ 30 m from the contact with the diorite show weakly developed compositional zoning with concentrations of almandine and spessartine close to 45 mol.% and a pyrope content of ~6 mol.% (sample G2, Fig. 4.7b).

A garnet poikiloblast with a diameter of ~4 mm in sample G3 (East Thalanga, section 6, ~1200 m to the west of the diorite pluton) shows a symmetric zonation (Fig. 4.7c). In the inner core, almandine and spessartine have approximately the same concentration (~45 mol.%). In an outer core zone, spessartine increases to 48 mol.% whereas almandine decreases to 42 mol.%. Approaching the rim, the trend reverses and

Fig. 4.6: Composition of garnets in the Thalanga sequence illustrated in ternary diagrams.

The garnets of the 6 samples analysed (G1 to G6) consist mainly of spessartine and almandine. However, garnets in layered phyllite of the hangingwall contain about equal proportions of grossular, spessartine and almandine. The core zones of garnets in the diorite contact zone contain up to 20 mol.% pyrope.

(a) Molecular proportions of pyrope, spessartine and almandine in garnets from Thalanga.

(b) Molecular proportions of almandine, spessartine and grossular in garnets from Thalanga.

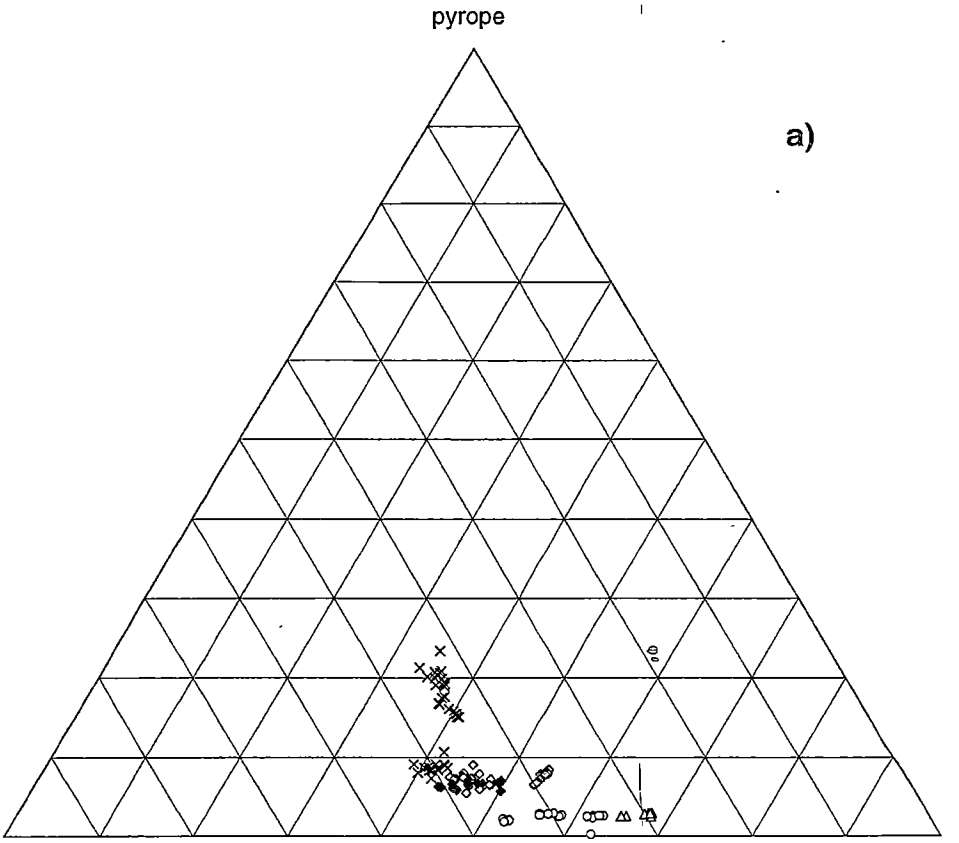

Legend:
composition of garnet in samples of:

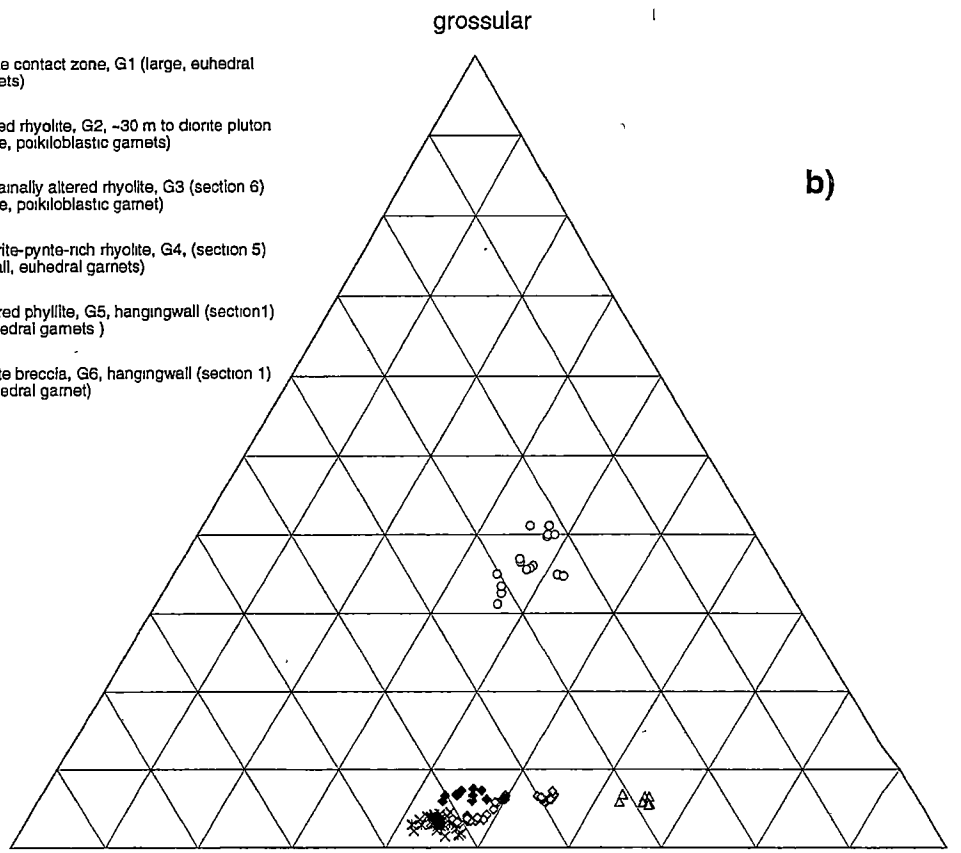

× diorite contact zone, G1 (large, euhedral garnets)

◇ altered rhyolite, G2, ~30 m to diorite pluton (large, poikiloblastic garnets)

◆ domainally altered rhyolite, G3 (section 6) (large, poikiloblastic garnet)

◇ chlorite-pyrite-rich rhyolite, G4, (section 5) (small, euhedral garnets)

○ layered phyllite, G5, hangingwall (section1) (euhedral garnets)

△ dacite breccia, G6, hangingwall (section 1) (euhedral garnet)

Fig. 4.6

Fig. 4.7: Internal compositional variability of representative garnet crystals from the Thalanga sequence.

Microprobe analyses show that some garnet crystals are compositionally zoned. Abbreviations such as 'gtC1' refer to a particular garnet crystal and analyses tabulated in the Appendix are labelled accordingly.

(a) Composition of euhedral garnet in diorite contact zone (sample G1)

(b) Composition of poikiloblastic garnet in altered rhyolite (sample G2)

(c) Composition of poikiloblastic garnet in domainally altered rhyolite (sample G3)

(d) Composition of small garnet in chlorite and pyrite-rich altered rhyolite (sample G4)

(e) Composition of euhedral garnet in layered phyllite (sample G5)

(f) Composition of euhedral garnet in dacite breccia (sample G6)

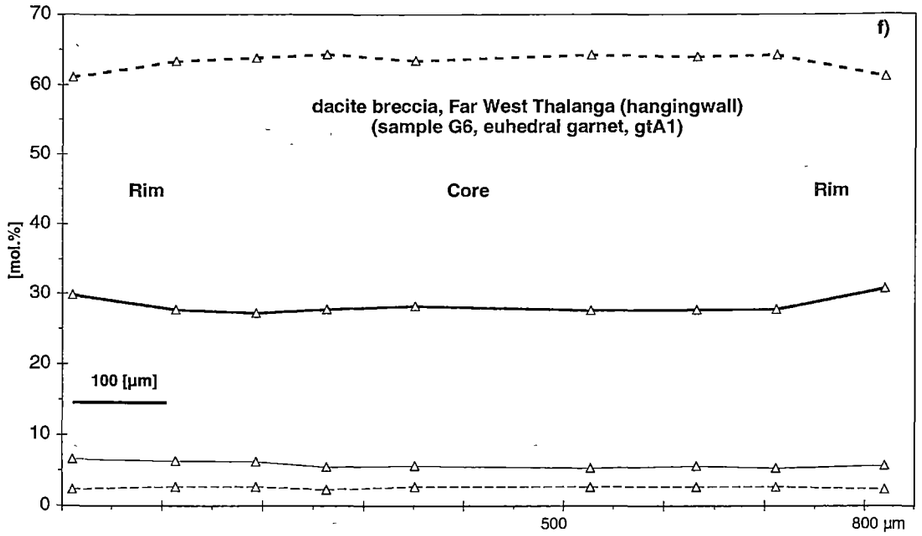
f)
dacite breccia, Far West Thalanga (hangingwall)
(sample G6, euhedral garnet, gtA1)
Rim
Core
Rim
[mol.%]
100 [µm]
500
800 µm

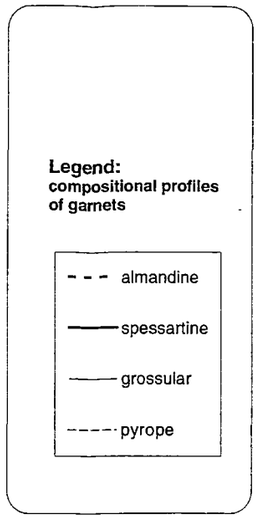
Legend:
compositional profiles
of garnets
almandine
spessartine
grossular
pyrope

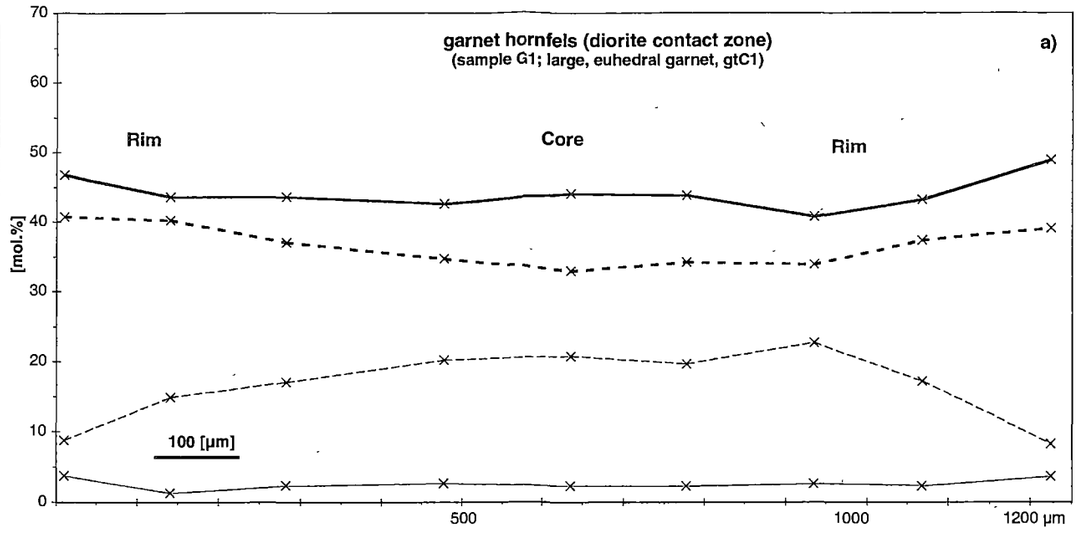
garnet hornfels (diorite contact zone)
(sample G1; large, euhedral garnet, gtC1)
a)
Rim
Core
Rim
[mol.%]
100 [µm]
500
1000
1200 µm

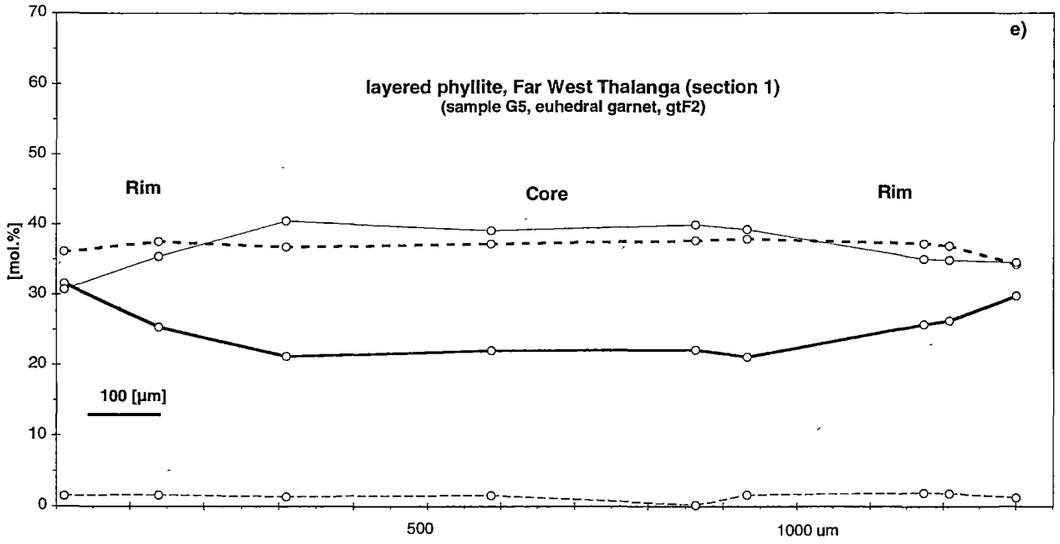
e)
layered phyllite, Far West Thalanga (section 1)
(sample G5, euhedral garnet, gtF2)
Rim
Core
Rim
[mol.%]
100 [µm]
500
1000 um

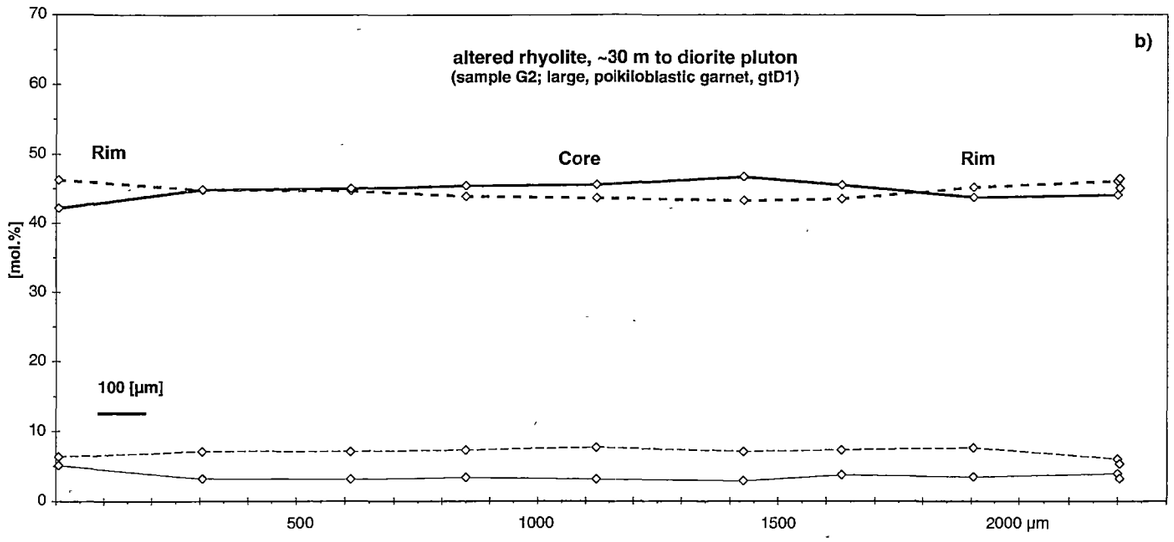
b)
altered rhyolite, ~30 m to diorite pluton
(sample G2; large, poikiloblastic garnet, gtD1)
Rim
Core
Rim
[mol.%]
100 [µm]
500
1000
1500
2000 µm

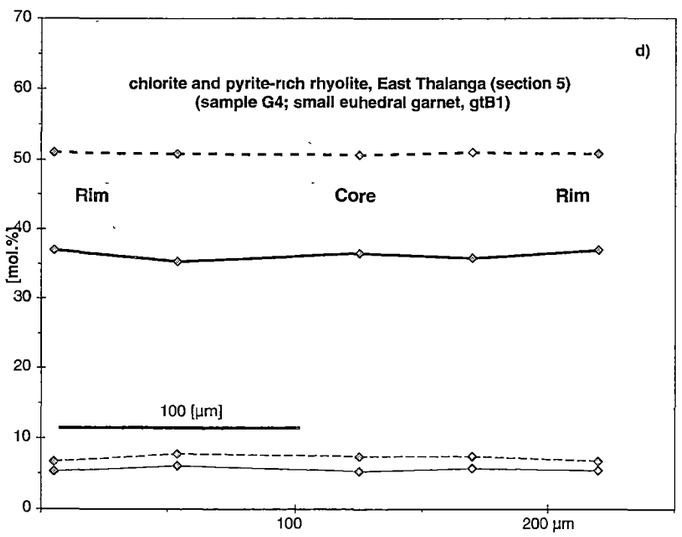
d)
chlorite and pyrite-rich rhyolite, East Thalanga (section 5)
(sample G4; small euhedral garnet, gtB1)
Rim
Core
Rim
[mol.%]
100 [µm]
100
200 µm

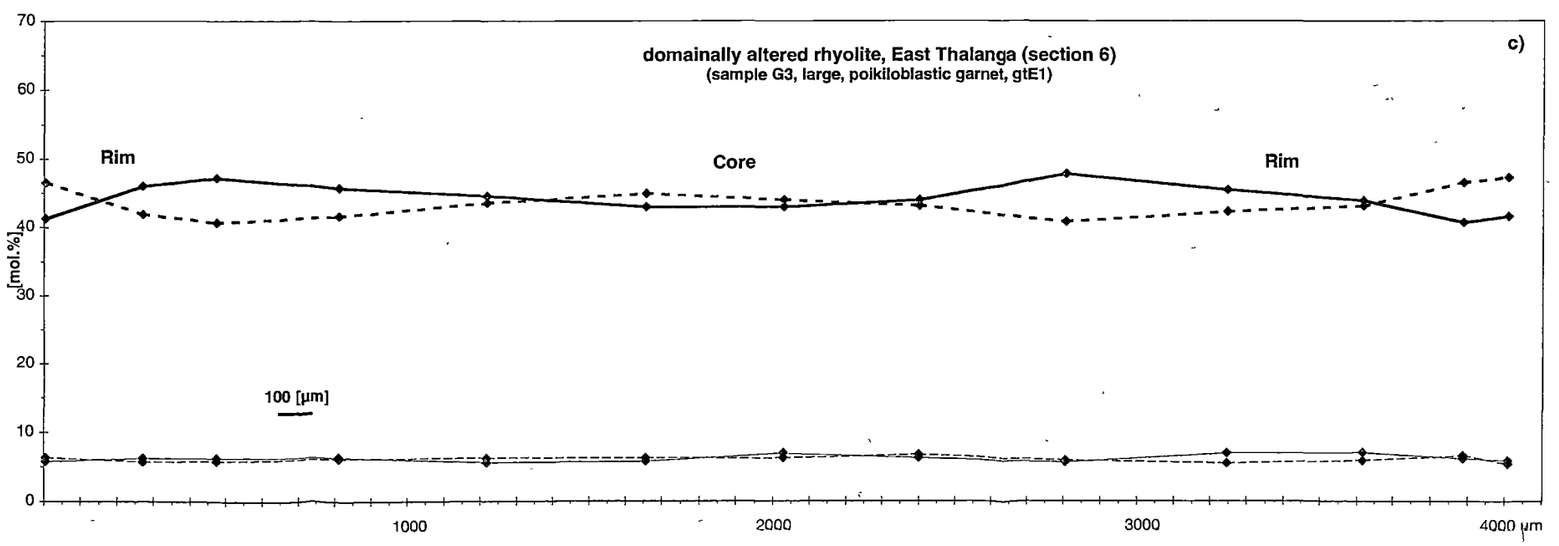
c)
domainally altered rhyolite, East Thalanga (section 6)
(sample G3, large, poikiloblastic garnet, gtE1)
Rim
Core
Rim
[mol.%]
100 [µm]
1000
2000
3000
4000 µm

Fig. 4.7

almandine increases to 48 mol.% whereas spessartine decreases to 42 mol.%. The concentrations of grossular and pyrope are constant throughout the crystal (~5 mol.%).

Small (<0.3 mm) euhedral garnets from a chlorite- and pyrite-rich altered rhyolite in East Thalanga (section 5) are unzoned and can be characterised as spessartine-rich almandine (average: $alm_{50}spes_{37}gro_5pyr_7$, sample G4, Fig. 4.7d).

Grossular-rich, euhedral garnets in a layered phyllite (sample G5) occur in a lamina consisting of biotite and calcite (quartz absent). The high grossular content in the core zone of these compositionally zoned crystals ($alm_{37}spes_{20}gro_{40}pyr_3$, Fig. 4.6b; 4.7f) is an indication that pre-metamorphic calcite was involved in the garnet-forming reaction. The rims of these zoned garnets contain about equal proportions of grossular, spessartine and almandine ($alm_{36}spes_{31}gro_{31}pyr_2$).

The euhedral garnet in a biotite-rich domain within dacite breccia (sample G6) has an average composition of $alm_{60}spes_{30}gro_7pyr_3$. It is homogeneous in composition except for a slight increase in spessartine and decrease in almandine content on the outermost margin (Fig. 4.7e).

4.2.5 Amphibole, epidote and calcite

Sample G5 (TH40-67.0)

Amphibole, epidote and calcite were analysed in sample G5 (layered phyllite, section 1) (Fig. 3.3). Amphibole crystals with blue-green pleochroic colours occur with Fe-rich chlorite and in contact with an epidote-biotite-quartz domain (Fig. 3.3c). They are iron-rich (Fe/Fe+Mg: 0.7) and show substantial substitution of Al for Si in the tetrahedral position. The concentrations of Na^+ and K^+ (totals of 0.43 to 0.5 pfu) can be accounted for by a substitution of Al^{3+} for Si^{4+} (ie. $Na^+[12]$, $Al^{3+}[4] \Leftrightarrow Si^{4+}[4]$). These amphiboles are best classified as ferro-hornblende with substantial tschermakite and edenite components. Their average composition is:

$(Na_{0.28}, K_{0.19})\ Ca_{1.94}(Fe_{2.89}, Mg_{1.38}, Mn_{0.10}, Ti_{0.04}, Al_{0.76})\ [Al_{1.52}, Si_{6.48}\ O_{23}]\ (OH)_2$.

Epidote crystals in an epidote-biotite-quartz domain adjacent to the hornblende-chlorite aggregate (Fig. 3.3c) are homogeneous in composition, with ~60 mol.% of one of the octahedral sites (M3) occupied by Fe. Minor concentrations of MnO (0.26- 0.31 wt.%) were also measured. An average formula can be expressed as:

$Ca_{1.93}Al_2(Al_{0.33}, Fe_{0.60}, Mn_{0.02}, Ti_{0.01})\ Si_{2.97}O_{12}(OH)$.

Carbonate occurs in one specific lamina in association with foliated, Fe-rich biotite and grossular-rich garnet (Fig. 3.3b). It is calcite with minor MnO, FeO and MgO, and the composition is: $Ca_{1.90}Mg_{0.01}Mn_{0.06}Fe_{0.03}CO_3$.

Sample TH247-361.30

Tremolite, calcite and chlorite were analysed in sample TH247-361.30 which represents a zone of intense calcareous alteration with patchy, semi-massive sulphides in West Thalanga (section 2). The tremolite has a nearly pure end-member composition, the associated chlorite is almost pure clinochlore and the calcite contains >1.90 Ca pfu. The chemical composition of the tremolite can be expressed as:

$Ca_{2.01}\ (Mg_{4.84}\ Fe^{2+}_{0.11}\ Al_{0.02}\ Mn_{0.03})\ [Al_{0.12}\ Si_{7.88}\ O_{23}]\ [(OH)_{1.86}\ F_{0.14}]$.

4.3 Thermobarometry

Estimates of temperature and pressure conditions during equilibrium crystallisation of coexisting minerals can be calculated from compositional data obtained by electron microprobe analysis. The principal prerequisites for such calculations are that the minerals represent an equilibrium assemblage and that appropriate reaction models have been calibrated.

The ratio in which chemical elements are partitioned between certain minerals can be expressed by the distribution coefficient (K_D). The value of K_D for any given mineral reaction is variably dependant on the prevailing pressure and temperature conditions during reaction. If the K_D for a mineral reaction is principally temperature-controlled it can be potentially used to estimate temperature conditions under which the reaction occurred. Likewise, a mineral reaction with a primarily pressure dependant K_D may hold potential for application as a geobarometer. Numerous mineral reactions have been proposed as thermometers and barometers (eg. Spear, 1993, p. 525). In general, calibration of mineral reactions relies strongly on the results of petrological experiments. However, thermobarometers have also been calibrated empirically using mineral assemblages in rocks, for which the P-T conditions of equilibration are known from independent evidence (eg. Dickenson & Hewitt, 1986). Furthermore, it is possible to calculate distribution coefficients of mineral reactions using internally consistent thermodynamic data sets.

4.3.1 The garnet-biotite ion exchange thermometer

The cation exchange reaction involving Fe and Mg between garnet and biotite (ie. Fe-garnet + Mg-biotite ⇔ Mg-garnet + Fe-biotite) is the basis of garnet-biotite thermometry. The K_D of this reaction is strongly temperature dependent and a multitude of calibrations of this reaction for application as a geothermometer can be found in the

literature (eg. Ferry & Spear, 1978; Perchuk & Lavrent'eva, 1983; Bhattacharya et al., 1992; Kleemann & Reinhardt, 1994). The temperature dependence of the partitioning of Fe and Mg between garnet and biotite was first studied experimentally by Ferry and Spear (1978). However, these experiments were performed with pure, synthetic almandine-pyrope and annite-phlogopite solid solutions and the calibration of this thermometer should not be used for garnets with X_{Ca+Mn} >0.2 and biotites with X_{Al+Ti} >0.15. Garnet and biotite from Thalanga are outside these limits. In a second major experimental study of synthetic and natural starting materials of variable composition, Perchuk and Lavrent'eva (1983) developed an alternative calibration. In addition, there have been numerous recalibrations of the garnet-biotite thermometer (eg. Bhattacharya et al., 1992). There is disagreement over the influence of cations other than Mg and Fe on the calibrations and the application of ideal or non-ideal mixing models.

In a comparative study, Kleemann and Reinhardt (1994) applied 11 published garnet-biotite thermometers to the original experimental data of Ferry and Spear (1978) and Perchuk and Lavrent'eva (1983). They found substantial discrepancies between the calculated and measured temperatures (up to 200 °C). A statistical treatment of the calculated temperatures shows that most calibrations fail to reproduce one or both of the experimental data sets in a satisfactory manner. Kleemann and Reinhardt (1994) concluded that the influence of octahedral Ti and Al in biotite on temperature calculations is significant and propose a thermometer based on the activity model for Ca-Mg-Fe-Mn garnets of Berman (1990) and a new activity model for biotite. When applied to all experimental data, this thermometer had the highest accuracy.

Because garnets at Thalanga are spessartine-rich and biotites contain significant Al[6] it is important to use a calibration of the garnet-biotite thermometer that takes these variables into account. Therefore, garnet-biotite thermometry was performed with the calibration of Kleemann and Reinhardt (1994).

4.3.2 The garnet-chlorite ion exchange thermometer

The exchange of Fe and Mg cations between chlorite and garnet was empirically calibrated as a geothermometer using results from garnet-biotite geothermometry. The chlorite-garnet calibration originally proposed by Dickenson and Hewitt (1986) was modified by Laird (1988). This calibration was applied to low pressure facies pelitic schists and the results of chlorite-garnet and biotite-garnet geothermometry were found to be in good agreement (Holdaway et al., 1988).

4.3.3 The garnet-biotite-muscovite-plagioclase barometer

A garnet-muscovite-biotite-plagioclase barometer was proposed by Ghent and Stout (1981) to enable the calculation of pressure estimates for meta-sedimentary rocks lacking an Al_2SiO_5 polymorph. The reactions studied were:

pyrope + grossular + muscovite $\Leftrightarrow$ 3 anorthite + phlogopite and

almandine + grossular + muscovite $\Leftrightarrow$ 3 anorthite + annite.

These reactions are pressure sensitive due to the change in Al coordination from 6 to 4 and the Mg and Fe coordination from 8 to 6. The calculated equilibrium constant equations for the Mg and Fe end-member equilibria were applied to a variety of natural samples from different metamorphic facies. This calibration provided pressure estimates which compared well with pressures estimated from garnet-plagioclase-Al_2SiO_5-quartz equilibria.

A variety of other calibrations of the garnet-muscovite-biotite-plagioclase barometer are based on internally consistent thermodynamic data sets and/or empirical calibrations against the garnet-plagioclase-Al_2SiO_5-quartz geobarometer (eg. Hoisch, 1990; Powell & Holland, 1988; Hodges & Crowley, 1985).

4.3.4 Results of thermobarometric calculations

The computer program 'Thermobarometry 2.1' (Spear & Kohn, 1998) was used to calculate lines of equal K for a number of mineral assemblages. This program returns the calculated temperatures and pressures as a table and plots the respective lines on a P-T diagram. The program allows the application of a multitude of calibrated barometers and thermometers to one data set.

Barometry

The pressure conditions of regional metamorphism in the Mount Windsor Subprovince were previously constrained to $\leq$3.5 kbar by occurrences of andalusite in pelitic sedimentary rocks of the Puddler Creek Formation close to Waddys Mill (8 km to the north-west of Thalanga) (Fig. 4.1; Berry et al., 1992; Holdaway, 1971). In the Thalanga mine area, neither andalusite nor any other Al_2SiO_5 polymorph have been observed possibly reflecting unfavourable bulk rock compositions (ie. more iron and magnesium and less aluminium than in true pelites).

A pressure estimate for contact metamorphic recrystallisation has been calculated based on co-existing garnet-muscovite-plagioclase-biotite in the contact zone with the

diorite pluton. Garnets in sample G1 show significant compositional zoning and it is inferred that the garnet margins crystallised in equilibrium with the surrounding groundmass. Therefore, the composition of a garnet margin was used in the calculation. Data for muscovite and biotite are averages (n=25 for biotite; n=3 for muscovite), and one plagioclase was analysed in the groundmass. Using a variety of calibrations for this barometer, a radiating array of lines of equal K are obtained (Fig. 4.8a). However, the lines converge at ~3 to 3.5 kbar and ~470 °C where they are intersected by a line of equal K for the garnet-biotite thermometer. This indicates that contact metamorphism occurred under relatively low pressure conditions, similar to that of regional metamorphism.

Thermometry

In order to estimate the peak temperature conditions of garnet crystallisation during contact metamorphism, the garnet core composition with the highest pyrope content was selected from sample G1 (diorite contact zone). Analyses of 25 groundmass biotites show very little compositional variation indicating that diffusion rates within the biotite crystals were high enough to allow for complete homogenisation. Peak metamorphic temperatures were calculated from the composition of garnet cores and groundmass biotite, whereas the composition of a garnet margin was used to estimate the temperature when garnet and biotite last equilibrated during the retrogressive stage of contact metamorphism. Assuming pressures of 2-4 kbar, the peak metamorphic temperatures can be estimated to have been in the order of 750 °C. Temperatures calculated with the composition of the garnet crystal margin are in the range of 480 °C (Fig. 4.8b).

Garnets sampled at a distance of ~30 m from the contact with the diorite pluton (sample G2) are fairly homogenous in composition, however the marginal parts show a slight enrichment of almandine over spessartine (Fig. 4.7e). The compositions of the garnet margin and the garnet core were used for the calculations. Groundmass biotite shows very little compositional variability and an average (n=6) was used for the calculations. Temperature estimates of 540 °C were obtained using the composition of the garnet core and 510 °C using the composition of garnet margin (Fig. 4.9a).

The large poikiloblastic garnet in sample G3 shows systematic but minor internal compositional variation in its spessartine and almandine contents (Fig. 4.7c). It occurs in an assemblage with chlorite and muscovite and based on calibrations of the Fe-Mg exchange between garnet and chlorite, a temperature estimate for their last equilibration can be calculated. Using the composition of the garnet rim and an average for the groundmass chlorite (n=5), temperatures in the range of 490 to 520°C have been obtained by three different calibrations (Fig. 4.10a).

In sample G4, very small, compositionally homogeneous garnet crystals with pyrite, muscovite and chlorite. Using an average for the garnet composition (n=13) and an average for the chlorite in the groundmass (n=5), temperature estimates ranging between 460 and 490 °C have been calculated by three different calibrations (Fig. 4.10b).

Garnets in sample G5 (layered phyllite) are restricted to one specific lamina where they occur with foliated biotite and calcite. The garnets are compositionally zoned (Fig. 4.7e) and the composition of the core and the margin were used for garnet-biotite thermometry. Biotite is homogeneous in composition and an average (n=10) was used for the calculations. Temperatures of ~440 °C were calculated for both garnet compositions (Fig. 4.9b).

In sample G6, an euhedral, almandine-rich garnet occurs in an assemblage with biotite and minor chlorite. The garnet shows weak compositional zoning (Fig. 4.7f) and analyses from its core and margin were used for the calculations. Groundmass biotite is homogeneous in composition and an average (n=10) was calculated. The calculated temperature estimates are in the range of 480 to 500 °C (Fig. 4.9c).

4.4 Conditions of regional and contact metamorphism

Garnet-bearing mineral assemblages are scarce in the Thalanga sequence, indicating that garnet was not a stable metamorphic phase in most of the rocks. This indicates that garnet crystallised only locally where the bulk rock geochemical composition was favourable. Minor garnet is known to crystallise locally during prograde metamorphism before conditions reach the garnet isograd *sensu stricto* (Yardley, 1989; Spear, 1993) because the temperature of garnet formation is significantly reduced in manganese- and/or calcium-rich rocks (Spear, 1993, p. 353). This is consistent with the general spessartine-rich and locally grossular-rich composition of garnets at Thalanga.

The temperature conditions of regional metamorphism have been constrained by garnet-biotite thermometry on samples from the hangingwall in section 1 (~3500 m west of the diorite pluton). The results range between 480 and 500 °C for a sample of dacite breccia whereas an estimate of around 440 °C was obtained from grossular-rich garnet in layered phyllite (Fig. 4.11).

Fig. 4.8: Results of thermobarometric calculations of coexisting mineral assemblages in the diorite contact zone.

For comparison, the stability fields for Al_2SiO_5 polymorphs (Holdaway, 1971) are shown with grey lines.

(a) Results of garnet-plagioclase-muscovite-biotite barometry and garnet-biotite thermometry using the composition of groundmass biotite, muscovite and plagioclase and the composition of garnet margin.

Keq line 2: garnet-biotite Fe-Mg exchange thermometry (calibration of Kleemann & Reinhardt, 1994)

garnet-plagioclase-muscovite-biotite equilibria barometry:

Keq line 5: calibration of Ghent and Stout (1981) - Fe end-member

Keq line 6: calibration of Ghent and Stout (1981) - Mg end-member

Keq line 7: calibration of Hodges and Crowley (1985) - Fe end-member

Keq line 8: calibration of Powell and Holland (1988)

Keq line 10: calibration of Hoisch (1990) - Fe end-member

Keq line 11: calibration of Hoisch (1990) - Mg end-member

(b) Results of garnet-biotite thermometry (calibration of Kleemann & Reinhardt, 1994) using the composition of garnet margin, garnet core and groundmass biotite.

Keq line 1: garnet core - groundmass biotite

Keq line 2: garnet margin - groundmass biotite

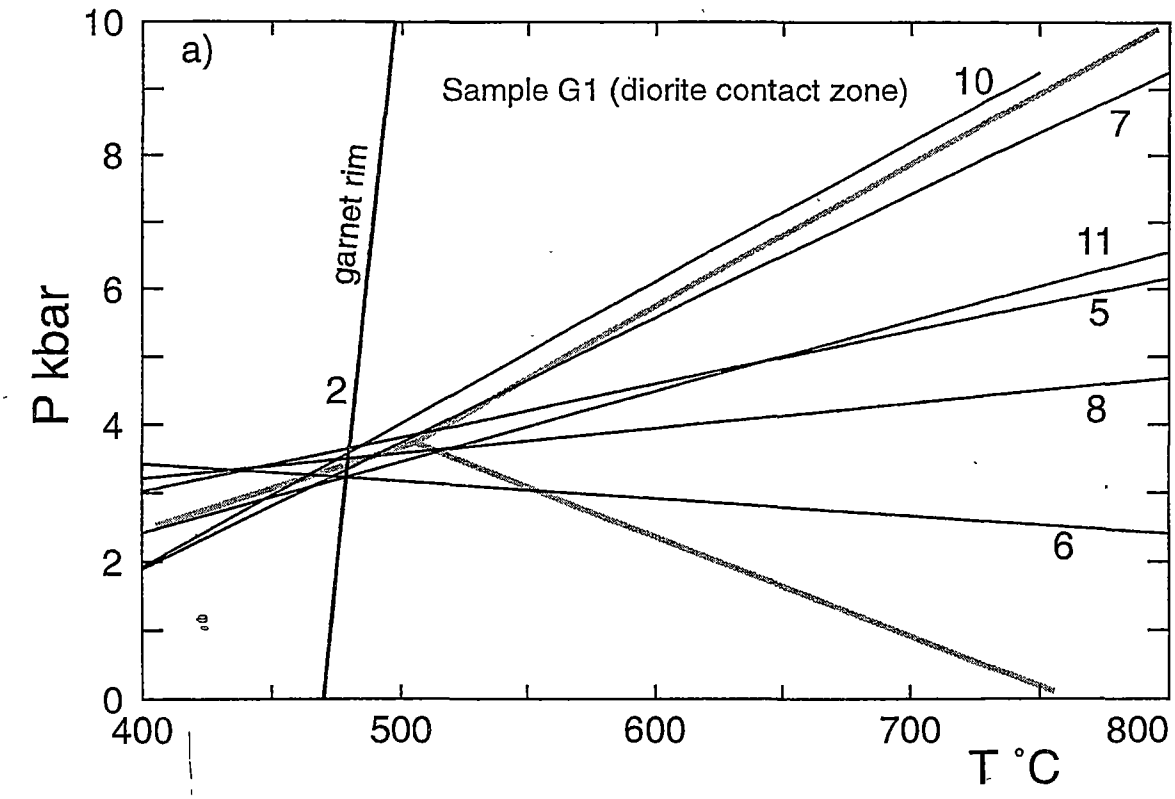

X_{Ca+Mn} garnet rim: 0.44

X_{Ca+Mn} garnet core: 0.43

$X_{Al[6]+Ti}$ groundmass biotite: 0.15

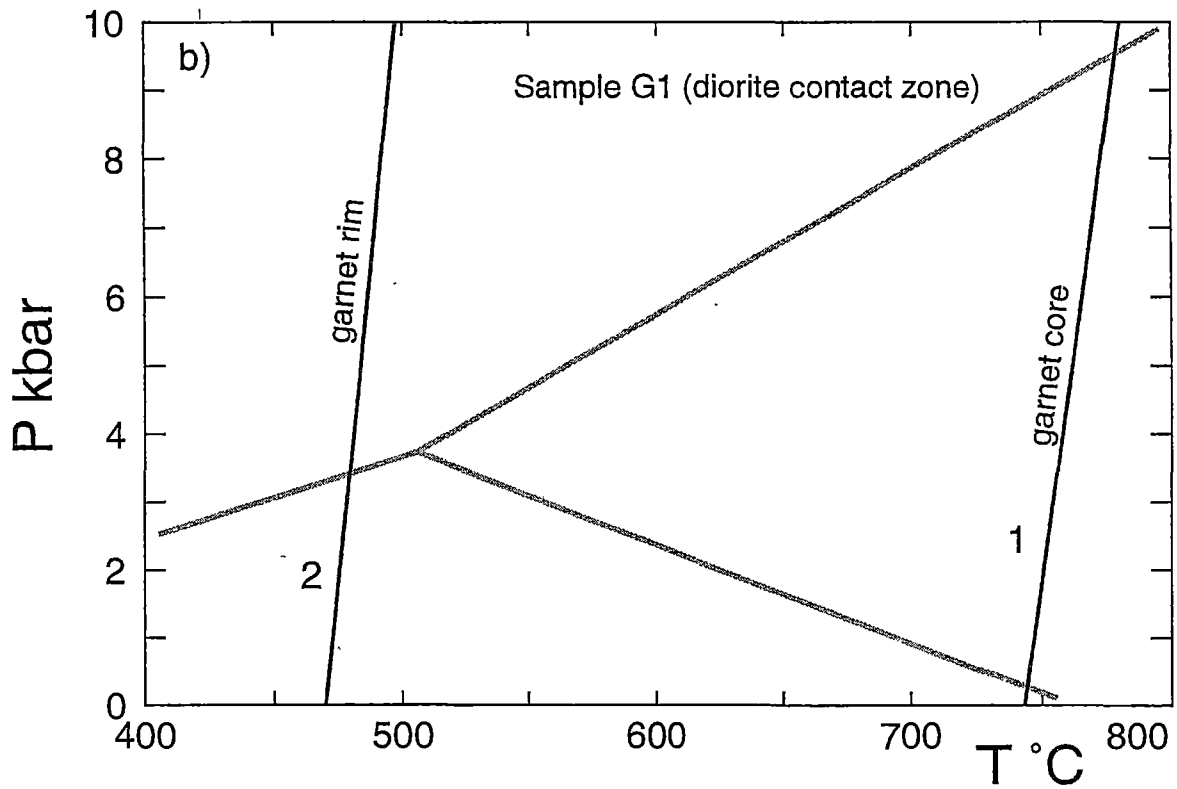

Fig. 4.8

Fig. 4.9: Results of garnet-biotite thermometry.

For comparison, the stability fields for Al_2SiO_5 polymorphs (Holdaway, 1971) are shown with grey lines (calibration of Kleemann & Reinhardt, 1994).

(a) Sample G2: altered rhyolite sampled at ~ 30 m from diorite contact.

Keq line 1: garnet core - groundmass biotite

Keq line 2: garnet margin - groundmass biotite

(b) Sample G5: layered phyllite from the hangingwall (Far West Thalanga, section 1).

Keq line 1: garnet core - groundmass biotite

Keq line 2: garnet margin - groundmass biotite

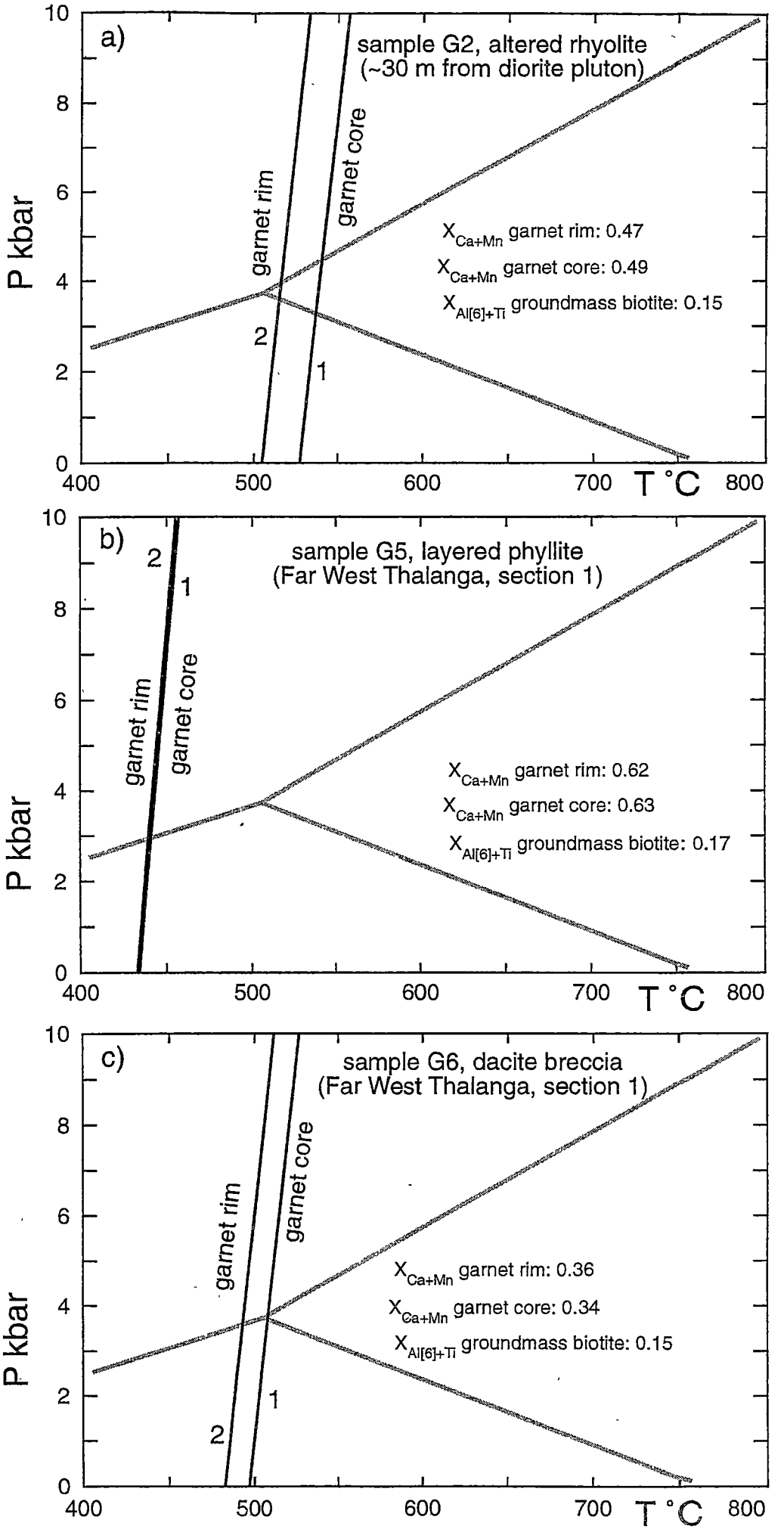
a)
sample G2, altered rhyolite
(~30 m from diorite pluton)
garnet rim
garnet core
X_{Ca+Mn} garnet rim: 0.47
X_{Ca+Mn} garnet core: 0.49
$X_{Al[6]+Ti}$ groundmass biotite: 0.15
2
1
P kbar
T °C
b)
sample G5, layered phyllite
(Far West Thalanga, section 1)
garnet rim
garnet core
X_{Ca+Mn} garnet rim: 0.62
X_{Ca+Mn} garnet core: 0.63
$X_{Al[6]+Ti}$ groundmass biotite: 0.17
2
1
P kbar
T °C
c)
sample G6, dacite breccia
(Far West Thalanga, section 1)
garnet rim
garnet core
X_{Ca+Mn} garnet rim: 0.36
X_{Ca+Mn} garnet core: 0.34
$X_{Al[6]+Ti}$ groundmass biotite: 0.15
2
1
P kbar
T °C

Fig. 4.9

Fig. 4.10: Results of garnet-chlorite thermometry.

For comparison, the stability fields for Al_2SiO_5 polymorphs are shown with grey lines (Holdaway, 1971).

(a) Sample G3: domainally altered rhyolite in East Thalanga (section 6).

garnet margin - groundmass chlorite:

Keq line 1: modified calibration of Dickenson and Hewitt (1986) (Laird, 1988)

Keq line 2: modified calibration of Dickenson and Hewitt (1986) (Laird, 1988) with Hodges and Spear (1992) garnet model

Keq line 3: modified calibration of Dickenson and Hewitt (1986) (Laird, 1988) with Berman (1990) garnet model

(b) Sample G4: chlorite- and pyrite-rich altered rhyolite in East Thalanga (section 5).

garnet - groundmass chlorite:

Keq line 1: modified calibration of Dickenson and Hewitt (1986) (Laird, 1988)

Keq line 2: modified calibration of Dickenson and Hewitt (1986) (Laird, 1988) with Hodges and Spear (1992) garnet model

Keq line 3: modified calibration of Dickenson & Hewitt (1986 (Laird, 1988) with Berman (1990) garnet model

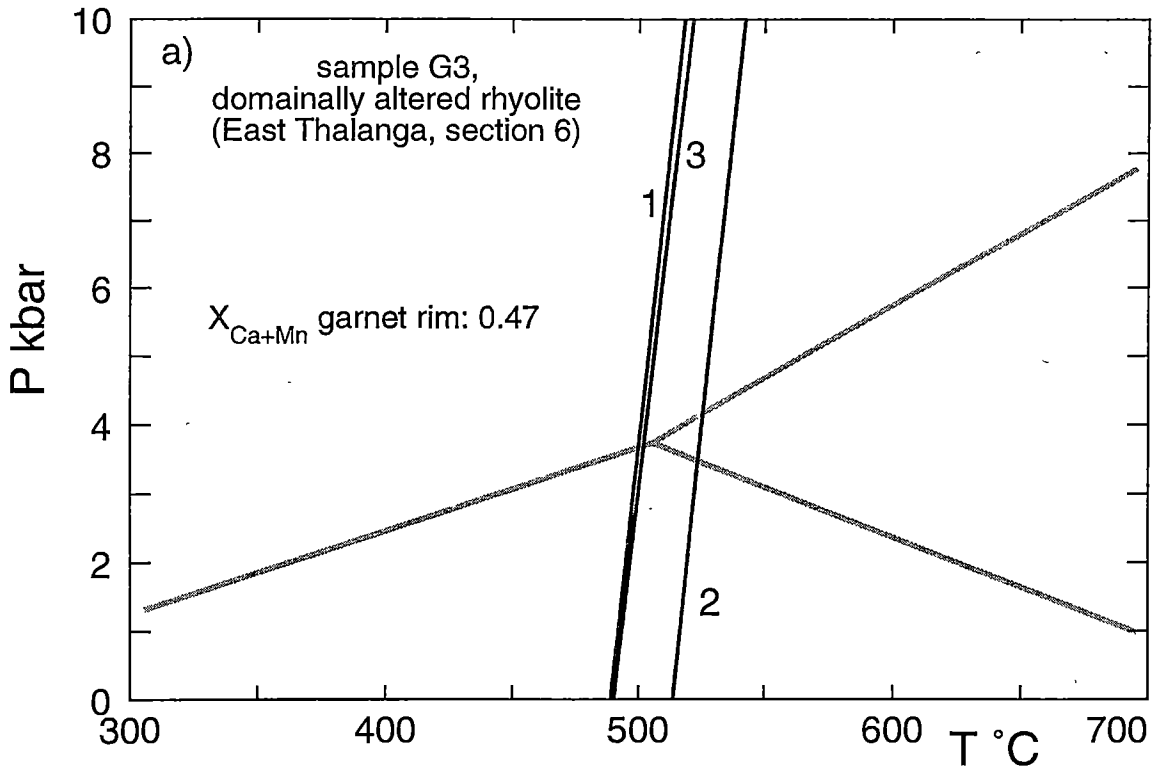
a)
sample G3,
domainally altered rhyolite
(East Thalanga, section 6)
X_{Ca+Mn} garnet rim: 0.47
1
2
3
P kbar
T °C
0
2
4
6
8
10
300
400
500
600
700

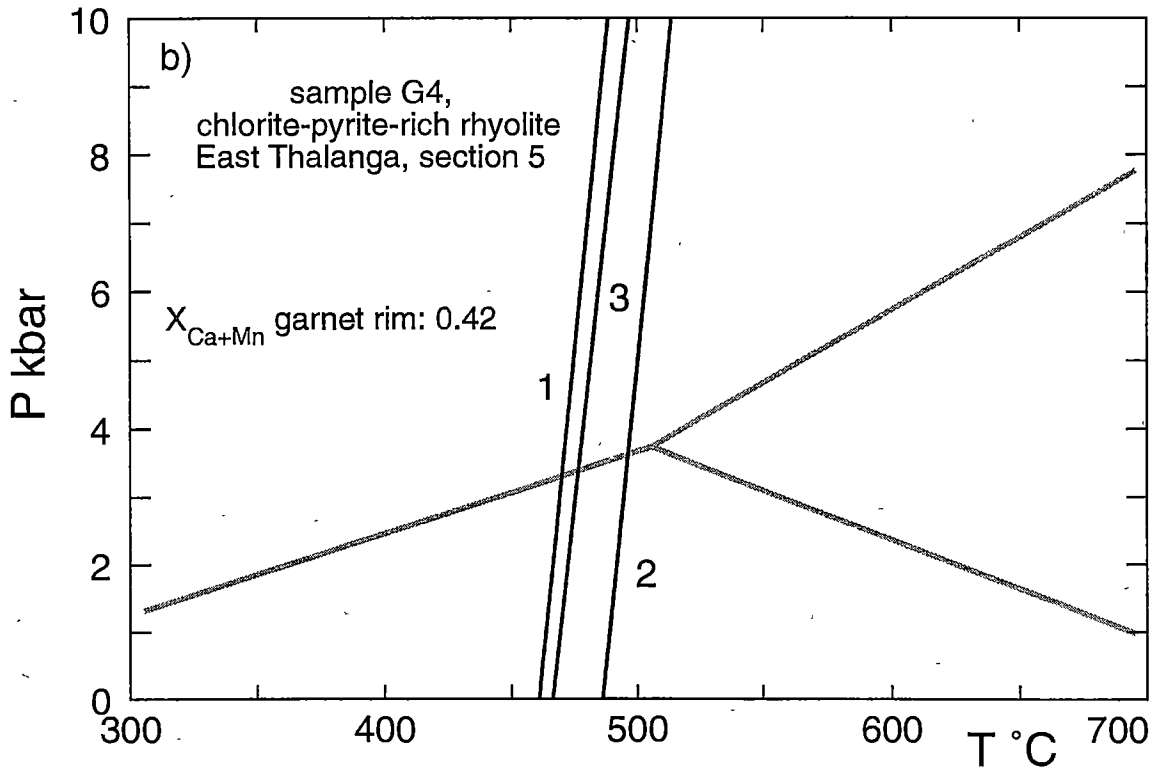
b)
sample G4,
chlorite-pyrite-rich rhyolite
East Thalanga, section 5
X_{Ca+Mn} garnet rim: 0.42
1
2
3
P kbar
T °C
0
2
4
6
8
10
300
400
500
600
700

Fig. 4.10

Very small garnets (<0.3 mm) formed in intensely altered, chlorite-pyrite-rich rhyolite (sample G4) under comparable temperature conditions (~480 °C). This suggests that these texturally similar garnets crystallised contemporaneously during the peak regional metamorphism. It is important to note that garnet-biotite and garnet-chlorite thermometry on altered and unaltered rocks in the Thalanga sequence yield comparable results. Hence, compositional differences between mineral assemblages generated during hydrothermal alteration in the footwall rhyolite and mineral assemblages unrelated to hydrothermal activity in the hangingwall did not affect equilibration during metamorphism. This is an interesting result since other studies on metamorphosed host sequences to VHMS deposits have found that the stability fields of metamorphic mineral assemblages in altered rocks and unaltered rocks differed significantly due to substantial changes in whole rock composition associated with hydrothermal activity (Zaleski et al., 1991).

The rare diopside crystals observed in some CCT rocks in West Thalanga (section 2; Fig. 3.6c) may be related to a reaction such as tremolite + calcite + quartz => diopside + CO_2 + H_2O which occurs at temperatures between 450 and 500 °C at low X_{CO_2} and 2 kbar (Slaughter et al., 1975; Fig. 5.8 in Yardley, 1989). These temperatures are similar to estimates of the conditions of regional metamorphism.

Results from barometric calculations based on a garnet-biotite-muscovite-plagioclase assemblage from the diorite contact zone indicate a pressure of 3 to 3.5 kbar for contact metamorphism. These relatively low P conditions are consistent with rare occurrences of cordierite porphyroblasts in pelitic hornfels in the Favourable Horizon of East Thalanga (Fig. 3.2d). This pressure estimate indicates that no significant uplift occurred between regional and contact metamorphism. Peak contact metamorphic temperatures reached 750 °C in the diorite contact zone (Fig. 4.11) which may reflect the temperature of the diorite melt during emplacement. Large poikiloblastic garnet in the immediate contact metamorphic aureole (~30 m from the diorite contact) formed at temperatures of 510 to 540 °C. Texturally similar garnets in altered rhyolite (sample G3) in the footwall of East Thalanga crystallised at slightly lower temperatures (500 to 520 °C, Fig. 4.11). These results indicate that that the diorite pluton developed a ~1200 m wide contact metamorphic aureole which was heated to temperatures of ≤500 °C. The absence of poikiloblastic garnets in Central and West Thalanga (> 2000 m to the west of the intrusion) indicates that temperatures were well below 500 °C during contact metamorphism in these areas.

Fig. 4.11: Variations in metamorphic temperatures with distance from the diorite pluton.

Metamorphic temperatures have been calculated from garnet-biotite and garnet-chlorite assemblages sampled at different localities in the Thalanga mine area. Garnet-bearing samples from section 1 (~3500 m to the west of the diorite pluton) are interpreted to represent assemblages which formed during regional metamorphism. Garnets in the diorite contact zone and the contact metamorphic aureole appear to have crystallised at slightly higher temperatures than garnets of regional metamorphic origin.

Fig. 4.12: Conditions of regional and contact metamorphism at Thalanga.

The thermobarometric results indicate that the Thalanga sequence was metamorphosed under middle to upper greenschist grade conditions during regional deformation. Contact metamorphism reached slightly higher temperatures than regional metamorphism in East Thalanga. Peak contact metamorphic temperatures (~750 °C) were restricted to the diorite contact zone (diagram modified from Yardley, 1989, p. 50).

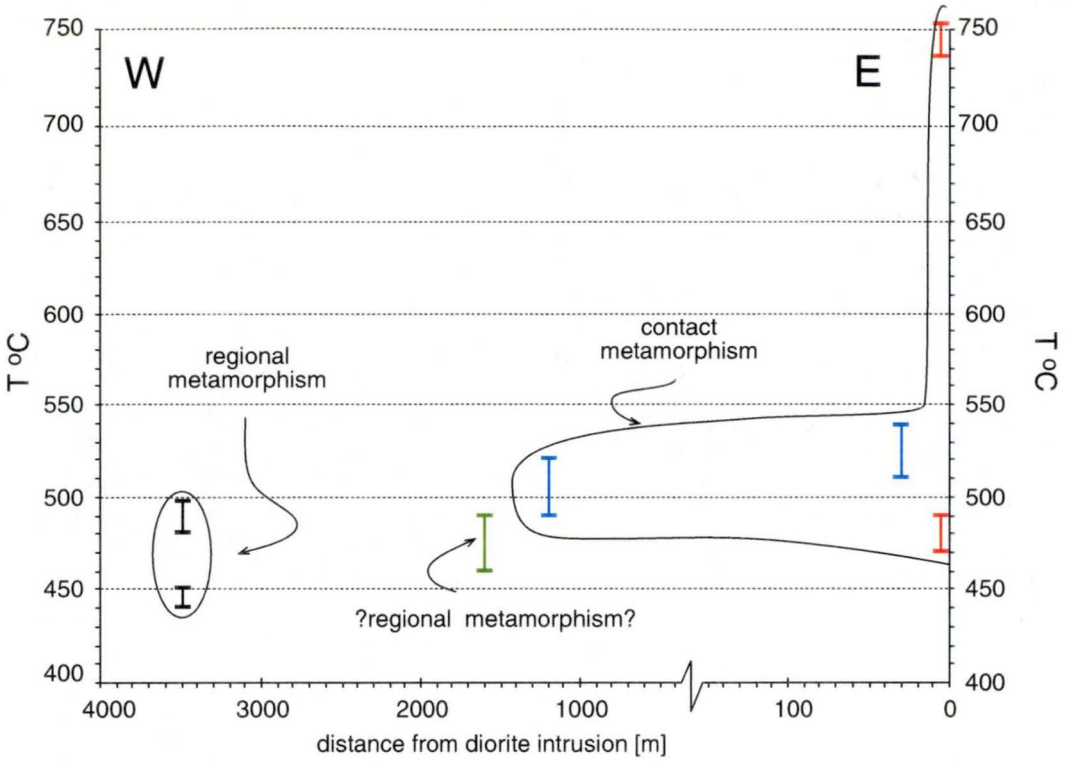

Fig. 4.11

Legend:

- garnet hornfels (diorite contact zone)
- moderately altered rhyolite (footwall)
- intensely altered, chlorite- and pyrite-rich rhyolite (footwall)
- weakly altered dacite beccia and phyllite (hangingwall)

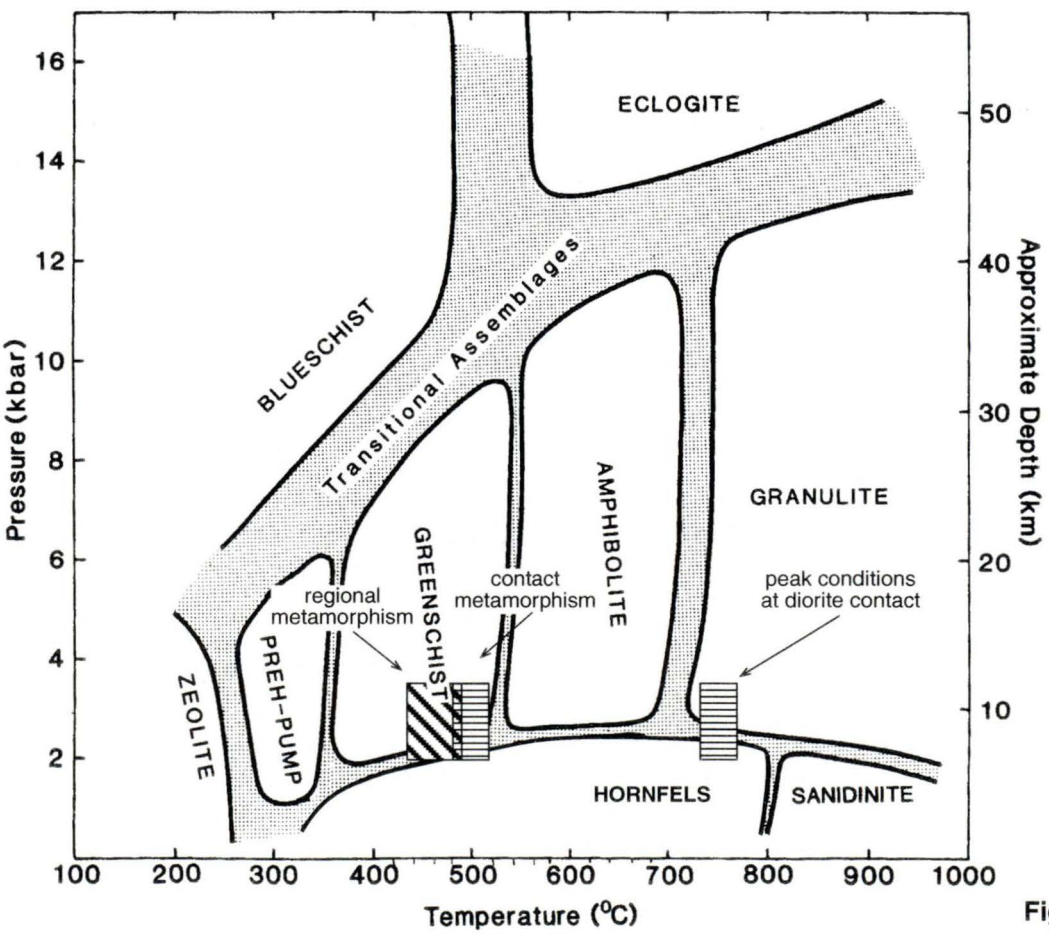

Fig. 4.12

4.5 Summary

The Thalanga sequence experienced regional and contact metamorphism under upper greenschist facies pressure and temperature conditions. Regional deformation (D2) imparted a steeply dipping cleavage (S2) on phyllosilicate-rich rocks in the Thalanga sequence which is defined by aligned biotite, chlorite and muscovite crystals. The compositions of coexisting euhedral garnets and groundmass biotite in sedimentary facies in the hangingwall of section 1 (Far West Thalanga) indicate peak temperatures of 480 to 500 °C (Fig. 4.12). Pressure conditions during regional metamorphism are constrained to ≤3.5 kbar by occurrences of andalusite in pelitic sedimentary rocks to the north-west of Thalanga (Berry et al., 1992).

The intrusion of a voluminous, post-D2 diorite pluton, which cross cuts the stratigraphic sequence to the east of the Thalanga deposit, was associated with contact metamorphism. Large (up to 5 mm), anhedral, garnet poikiloblasts occur locally in altered rhyolite within the contact metamorphic aureole. Peak temperatures in the diorite contact zone reached ~750 °C and a ~1200 m wide contact metamorphic aureole with temperatures ≥500 °C developed in the surrounding country rock. The pressure conditions of contact metamorphism have been constrained by calculations based on the garnet-biotite-muscovite-plagioclase barometer showing that contact metamorphism occurred under low-pressure conditions similar to those for regional metamorphism (~3 to 3.5 kbar). This indicates that no significant uplift occurred in the time between the regional and the contact metamorphic event.

The calculated temperatures from garnet-biotite and garnet-chlorite assemblages show that regional and contact metamorphism at Thalanga was of similar grade (Fig. 4.12), however, temperatures in the contact metamorphic aureole slightly exceeded the peak temperature of regional metamorphism.

5 Facies architecture of the Thalanga sequence

This chapter describes the facies architecture of the Thalanga sequence and explains the textural criteria used to discriminate primary from apparent textures in the footwall alteration zone. Facies analysis is based on data given in graphic logs and accompanying descriptions of all drill holes logged from sections 1 to 6 during this study (Appendix). The various volcanic and sedimentary facies of the Thalanga sequence are described, documenting substantial facies variations which were previously unrecognised (Figs. 5.1 to 5.4). The principal facies and facies relationships identified on each of the cross sections have been summarised by interpretive, true-thickness graphic logs (Fig. 5.5). Most of this chapter has been presented as a paper in the Australian Journal of Earth Sciences (Paulick & McPhie, 1999; Appendix).

5.1 Introduction

The facies architecture of submarine volcanic successions that host massive sulphide ore deposits has been the focus of research aimed at characterising environments favourable for mineralisation (eg. Cas, 1992; Allen, 1992; McPhie & Allen, 1992; Allen et al., 1996a, 1996b). A critical component of this research is the identification and interpretation of primary textures formed during eruption and emplacement but subsequently modified during diagenesis, hydrothermal alteration and metamorphism (eg. Allen, 1988, 1992; McPhie et al., 1993). Facies interpretation of the Thalanga sequence is difficult because of its inherent complexity, strong reliance on drill core observations and additional complications introduced by alteration and deformation.

The reconstruction of the facies architecture of the Thalanga host succession is based on textural interpretation and volcanic facies analysis of six drill core cross sections in the Thalanga mine area and one outcrop section about 5 km to the west of the ore body (Fig. 1.5). The stratiform Thalanga massive sulphide lenses are located on top of rhyolite lavas, syn-volcanic intrusions and resedimented breccia units (MWF) and are overlain by a dacite-dominated volcano-sedimentary succession (TCF).

The entire MWF (~550 m thick) and a large portion of the TCF are exposed in the outcrop section. The thickness of the MWF increases to ~1000 m in the Thalanga mine area (Fig. 1.5). The stratigraphic thickness shown in the drill core cross sections ranges from 300 to 700 m and includes the upper ~150 to 450 m of the footwall (extended using outcrop on watertank hill), 5 to 50 m of the Favourable Horizon and ~200 to 250 m of the hangingwall. Using textural criteria, coherent and clastic facies have been distinguished in altered parts of the footwall. By comparing the geometry of intensely altered zones

with the distribution of coherent and clastic facies of rhyolite in the footwall, it has been possible to assess whether volcanic facies influenced or controlled hydrothermal fluid flow.

Furthermore, it has been possible to distinguish different types of rhyolite and dacite based on characteristic phenocryst assemblages. In the hangingwall (TCF), different types of locally derived monomictic and polymictic breccia units have been recognised based on their clast populations. Sedimentary facies in the hangingwall are dominated by black, massive to laminated mudstone and mass-flow emplaced, feldspar crystal-bearing turbidites which are characteristic facies of below-wave base subaqueous settings. A submarine environment for the Thalanga area is indicated by occurrences of graptolite and trilobite fossils described by Henderson (1983) in laterally equivalent sequences in the Mount Windsor area (Fig. 1.3a). Variations in the spatial arrangement of lithofacies in the Thalanga sequence along strike have been used to constrain the palaeotopography and geology of the site of ore formation.

5.2 Rhyolite and dacite types in the Thalanga sequence

5.2.1 Petrography of rhyolite and dacite

Coherent rhyolite and dacite in the Thalanga sequence have an evenly porphyritic texture (Figs. 5.1 and 5.2). Coherent rhyolite is variably quartz-feldspar-phyric and, outside of the footwall alteration zone, has a quartzofeldspathic groundmass with minor interstitial sericite, biotite and rare chlorite. Locally preserved perlitic fractures and spherulites indicate that groundmasses were originally partly glassy and partly crystalline (Fig. 5.3a). Hangingwall dacite is feldspar-phyric and commonly unaltered or weakly altered, with a cryptocrystalline groundmass consisting of quartz and feldspar. Quartz-filled amygdales and relic perlitic textures are locally present in the dacite.

The mineralogy, abundance, size range and relative proportions of phenocrysts in felsic lavas have been successfully used for correlating separate emplacement units in ancient and modern volcanic successions. De Rosen-Spence et al. (1980) demonstrated that separate Archean rhyolite lavas in the Noranda area (Canada) maintained characteristic quartz and feldspar phenocryst assemblages over extents up to 10 km. In a major study of a Tertiary rhyolitic volcanic field (Taylor Creek Rhyolite), Duffield and Dalrymple (1990) identified 20 separate rhyolite domes and lavas based on contact relationships and characteristics of the phenocryst populations.

At Thalanga, four types of rhyolite and three types of dacite can be distinguished based on phenocryst logging (systematic recording of mineralogy, size range, abundance and distribution of phenocrysts) (Table 5.1; Fig. 5.1). These texturally defined types correlate with geochemical subdivisions based immobile element ratios (Chapter 6). The footwall in the mine area is dominated by weakly to intensely altered, poorly to moderately porphyritic rhyolite type 1 (1-5 vol.% phenocrysts, <1 to 2 mm). Rhyolite type 1 contains quartz and feldspar phenocrysts (Fig. 5.1a, b) although feldspars are progressively replaced by sericite and biotite with increasing intensity of alteration and are generally obliterated in zones of moderate to strong alteration. Rhyolite type 2 is highly porphyritic with 7-15 vol.% quartz and feldspar phenocrysts mainly in the 1-5 mm size range (Fig. 5.1c, d). It occurs below rhyolite type 1 in East Thalanga and West Thalanga and is unaltered to moderately altered. Rhyolite type 3 occurs predominantly in the outcrop section. It is unaltered to weakly altered, moderately quartz-phyric (5-10 vol.%, 1 to 2 mm) but contains only minor feldspar phenocrysts (<1 vol.%) (Fig. 5.1e, f). Rhyolite type 4 is characterised by abundant, coarse quartz and feldspar phenocrysts (40-50 vol.%, 3-8 mm) and is common in the Favourable Horizon of East Thalanga (Fig. 5.1g, h).

Consistent differences in feldspar phenocryst size range and abundance allow three types of dacite to be distinguished in the hangingwall (Table 5.1, Fig. 5.2). Dacite type 1 is poorly porphyritic (<1 vol.%) with fine (<1 mm) feldspar phenocrysts and locally appears aphyric. Dacite type 2 is moderately porphyritic (1-5 vol.%) with feldspar phenocrysts mainly in the 1 to 3 mm size range whereas dacite type 3 is highly porphyritic (8-15 vol.%) with fine feldspar phenocrysts ($\leq$1 mm).

Fig. 5.1: Macroscopic and microscopic textures of least-altered rhyolite types 1 to 4 (MWF).

Scale bar for hand specimens: 5 mm, scale bar for photomicrographs: 1 mm.

(a) Rhyolite type 1 with ~2 % quartz and feldspar phenocrysts (mainly ≤1 mm in diameter) (hand specimen of sample TH5-339.0; Central Thalanga).

(b) Rhyolite type 1 with euhedral quartz and feldspar phenocrysts in a microcrystalline groundmass (photomicrograph of sample TH5-339.0, crossed nicols).

(c) Rhyolite type 2 with ~10 % quartz and feldspar phenocrysts (mainly 1 to 3 mm in diameter) (hand specimen of sample TH412B-674.50; Central Thalanga).

(d) Rhyolite type 2 with quartz phenocrysts (1 to 2 mm in diameter) and feldspar phenocrysts (<1 mm) in a fine-grained groundmass (photomicrograph of sample TH412B-674.50, crossed nicols).

(e) Rhyolite type 3 with ~8 % quartz phenocrysts mainly ≤1 mm in diameter. Feldspar phenocrysts are scarce in rhyolite type 3 (hand specimen of sample THRW3, outcrop section).

(f) Rhyolite type 3 with quartz phenocrysts ≤1 mm in diameter (photomicrograph of sample THRW3, PPL).

(g) Rhyolite type 4 with a highly porphyritic texture (~25 % phenocrysts) and coarse quartz and feldspar phenocrysts (mainly 2 to 5 mm in diameter) in a microcrystalline groundmass (hand specimen of sample THRW7, outcrop section).

(h) Rhyolite type 4 with coarse quartz phenocrysts (~4 mm in diameter) and sericitised feldspar phenocrysts in a microcrystalline groundmass. Quartz phenocrysts show prominent resorption textures (arrow) (photomicrograph of sample THRW7, crossed nicols).

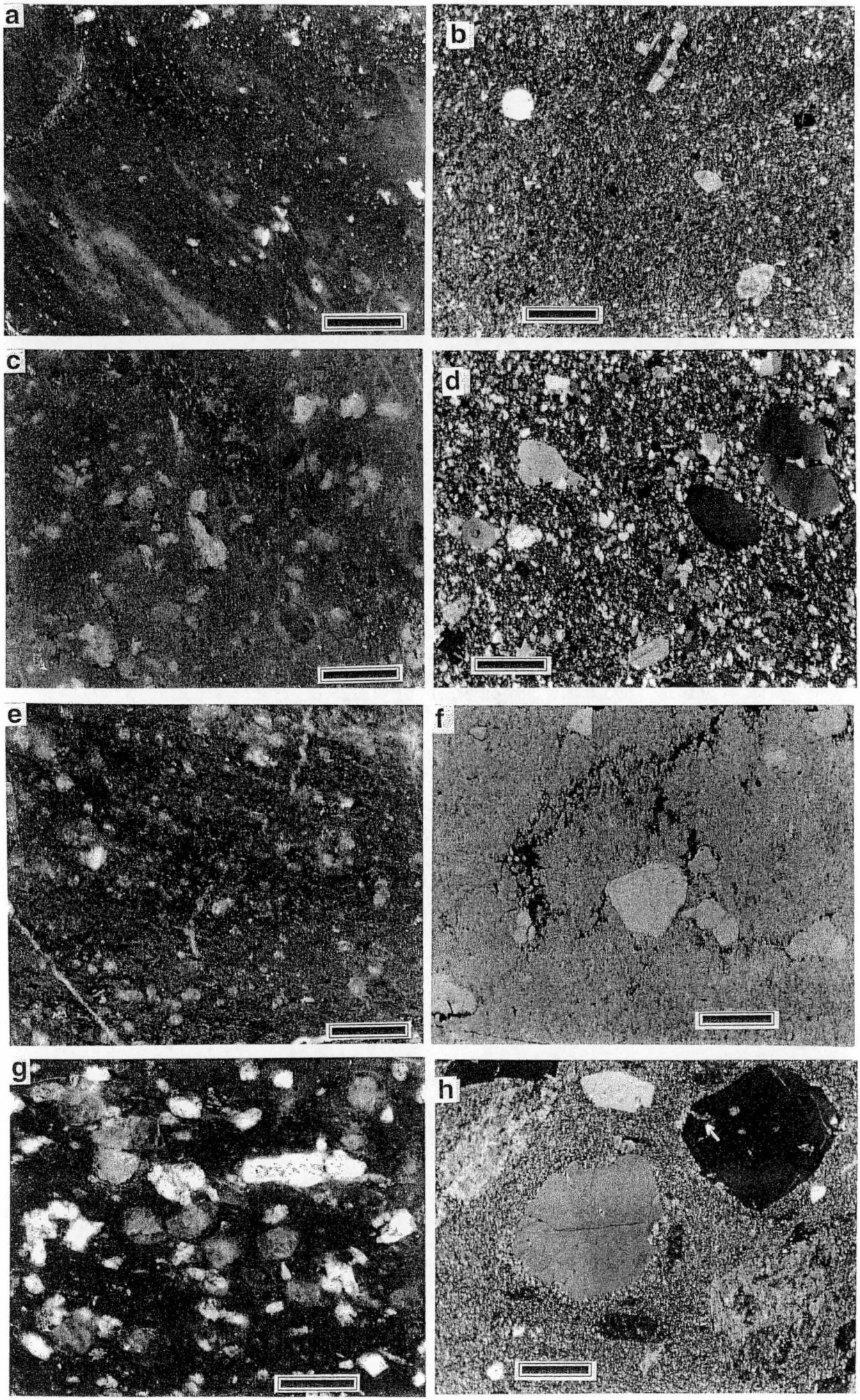

Fig. 5.1

Fig. 5.2: Macroscopic and microscopic textures of least-altered dacite types 1 to 3 (TCF).

Scale bar for hand specimens: 5 mm, scale bar for photomicrographs: 1 mm).

(a) Dacite type 1 with rare feldspar phenocrysts (<1 mm in diameter) (hand specimen of sample TH401-89.40, East Thalanga).

(b) Dacite type 1 with rare feldspar phenocrysts (~0.2 mm in diameter) in a groundmass of quartz, feldspar and biotite. (photomicrograph of sample TH401-89.40, crossed nicols).

(c) Dacite type 2 with ~5 % feldspar phenocrysts (mainly 1 to 2 mm in diameter) (hand specimen of sample TH28-304.50, West Thalanga).

(d) Dacite type 2 with ~5% feldspar phenocrysts in a fine-grained, quartzofeldspathic groundmass (photomicrograph of sample TH28-304.50, crossed nicols).

(e) Dacite type 3 with ~10 % feldspar phenocrysts (mainly <1 mm in diameter) (hand specimen sample TH402-102.70, East Thalanga).

(f) Dacite type 3 with ~10% feldspar phenocrysts (<1 mm in diameter) in a feldspar-rich, microcrystalline groundmass (photomicrograph of sample TH402-102.70, crossed nicols).

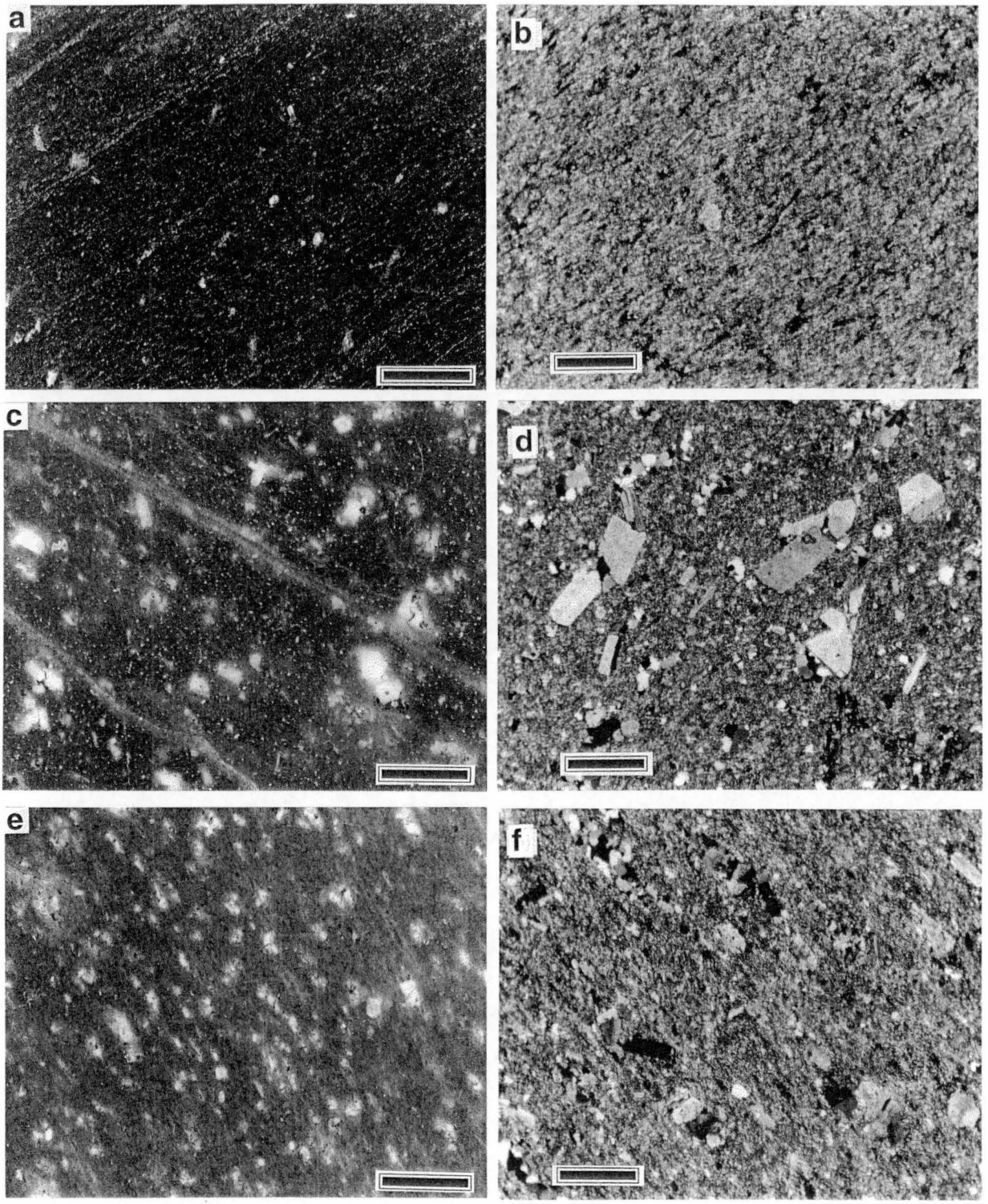

Fig. 5.2

Table 5.1: Rhyolite and dacite types in the Thalanga sequence

	phenocrysts			Ti/Zr[1]	alteration	distribution and estimated dimensions[2]
	type	size [mm]	modal %			
rhyolite type 1	qtz, fsp[3]	< 1 - 2	1 - 5	3.9 ± 0.4 (n = 92)	weak to strong	top of MWF in mine area; lava (150-200 m thick, >1000 m wide, >3000 m long), minor syn-volcanic intrusions
rhyolite type 2	qtz, fsp	mainly 2-3 (up to 5)	7 - 15	4.3 ± 0.5 (n = 9)	moderate to unaltered	MWF; below rhyolite type 1 in mine area, lava (>250 m thick, >300 m wide, >3000 m long), rare syn-volcanic intrusions
rhyolite type 3	qtz, (fsp)	1 - 2	5 - 10	3.9 ± 0.4 (n = 12)	weak to unaltered	MWF; common in outcrop section, several lavas (50-150 m thick), rare syn-volcanic intrusions (section 1)
rhyolite type 4[4]	qtz, fsp	mainly 3 - 8	40 to 50	Variable 8 - 16	weak to unaltered	MWF: intrusions (≤50 m thick); Favourable Horizon: intrusions and lavas (≤50 m thick); TCF: ?intrusion/lava (section 1)
dacite type 1	(fsp)	< 1	< 1	12.4 ± 0.4 (n = 11)	weak to unaltered	TCF; lava in East Thalanga (100-150 m thick, >1000 m wide, >500 m long)
dacite type 2	fsp	1-3	1 - 5	11 ± 1 (n = 11)	weak to unaltered	TCF; West and Central Thalanga: several lavas (≤50 m thick, >550 m wide, ?>1000 m long); Far West and outcrop section: domes (150-180 m thick, >300 m wide)
dacite type 3	fsp	≤ 1	8-15	19 ± 1 (n = 18)	weak to unaltered	TCF; sills (10-50 m thick, >500 m wide, >500 m long)

fsp: feldspar; qtz: quartz. [1] Calculated arithmetic means and standard deviation. [2] Based on facies interpretation of cross sections, width: down dip extent, length: extent along strike. Due to the spacing of drill holes and cross sections these estimates may in reality include several emplacement units of the same rock type. [3] Feldspar pseudomorphs in weakly altered rhyolite; feldspar phenocrysts are generally obliterated in moderately to strongly altered rhyolite. [4] Equivalent to Quartz-Feldspar Porphyry of Hill (1996) and Quartz-Eye Porphyry in mine terminology

5.2.2 Volcanic facies interpretation in the footwall alteration zone

The footwall alteration zone below the Thalanga massive sulphide deposit has a stratabound geometry. The contacts between altered and least-altered rhyolite are gradational and marked by changes in the mineralogy, texture and chemical composition of the rocks. Specifically, the amount of sericite, chlorite and biotite in the rhyolite groundmass increases and feldspar phenocrysts are replaced progressively by sericite and biotite. Rhyolite with apparent clastic textures consisting of patchy, wispy to irregular quartz-rich and phyllosilicate-rich (sericite, biotite, and chlorite in variable proportions) groundmass domains are characteristic of the footwall alteration zone. This style of mottled alteration has complicated discrimination of coherent from clastic facies in the

footwall. However, quartz phenocrysts were apparently largely unaffected by alteration and are still preserved even in intensely altered footwall rhyolite. Where the primary volcanic textures have been most strongly altered, the characteristics of the quartz phenocryst population (abundance, size range and distribution) have proven invaluable in identification of different facies, emplacement units and rhyolite types. In particular, genuine monomictic rhyolite breccia displays marked and consistent differences in quartz crystal abundance and/or size range between clasts and matrix (Fig. 5.3b). In contrast, coherent facies with apparent clastic textures are in fact evenly porphyritic, with similar phenocryst abundances and sizes in apparent matrix and apparent clast domains. Furthermore, genuine monomictic rhyolite breccia may show normal grading and may contain clasts with internal laminar or banded fabrics in random orientation (eg. rotated, flow laminated clasts; Table 5.2, Fig. 5.3c,d).

Large parts of the footwall were initially thought to be pyroclastic (eg. tuffs and lapilli tuffs; Wills, 1985; Gregory et al., 1990) due to the apparent prominence of fiamme and other clastic textures. However, more recent research (Hill, 1996; Paulick, 1997) has shown that the apparently clastic textures result from domainal hydrothermal alteration of glassy or partly glassy coherent facies (Allen, 1988). Prior to alteration, the groundmass of felsic lavas and intrusions typically consists of glassy and crystalline (eg. spherulitic) domains. During diagenesis, glass is readily altered to zeolites, clays or feldspar whereas crystalline domains may recrystallise but otherwise remain relatively stable. Therefore, the primary distribution of crystalline versus glassy domains strongly influences textural and mineralogical changes during the initial stages of hydrothermal alteration. Apparent clastic textures defined by phyllosilicate-rich and phyllosilicate-poor domains such as those at Thalanga may in some cases represent formerly glassy and formerly crystalline domains respectively, within the coherent parts of felsic lavas and intrusions. Furthermore, domainal and multi-stage alteration processes may also lead to the development of apparent clastic texture in coherent facies with homogeneous primary texture (Allen, 1988).

Fig. 5.3: Textures of coherent rhyolite and rhyolitic breccia facies from the footwall alteration zone (MWF).

(a) Least-altered rhyolite type 1 with quartz (q) and feldspar (f) phenocrysts in a groundmass with relic perlitic texture (sample TH62C-882.05, Far West Thalanga, PPL, scale bar: 500 μm).

(b) Monomictic rhyolite breccia with a poorly porphyritic, siliceous rhyolite clast (c) in a phyllosilicate-rich and quartz crystal-rich matrix (m) (sample TH85-100.90, East Thalanga, scale bar: 1 cm).

(c) Clast-supported, monomictic rhyolite breccia with rotated, flow laminated clasts (sample TH38-58.0, Central Thalanga).

(d) Laminated, siliceous mudstone top of normally graded, monomictic rhyolite breccia unit (sample TH247-256.0)

(e) Coherent rhyolite facies with abundant siliceous kernels (relic perlite?) in phyllosilicate-rich domain. The siliceous kernels could be mistaken for quartz phenocrysts (sample TH247-230.50, West Thalanga).

(f) Sericite-rich altered, coherent rhyolite with strong foliation. Siliceous kernels (k) (relic perlite?) between phyllosilicate-rich bands resemble quartz phenocrysts (q) in hand specimen. (sample TH243A-249.20, West Thalanga, PPL).

(g) Anastomosing bands of phyllosilicate encircling kernels of siliceous groundmass in weakly altered rhyolite. This texture may represent an early, incipient stage of 'pseudophenocryst' formation (TH410-125.10, Far West Thalanga).

(h) Rhyolite-mudstone breccia (facies C) with mudstone clasts showing internal lamination (TH247-251.70, West Thalanga).

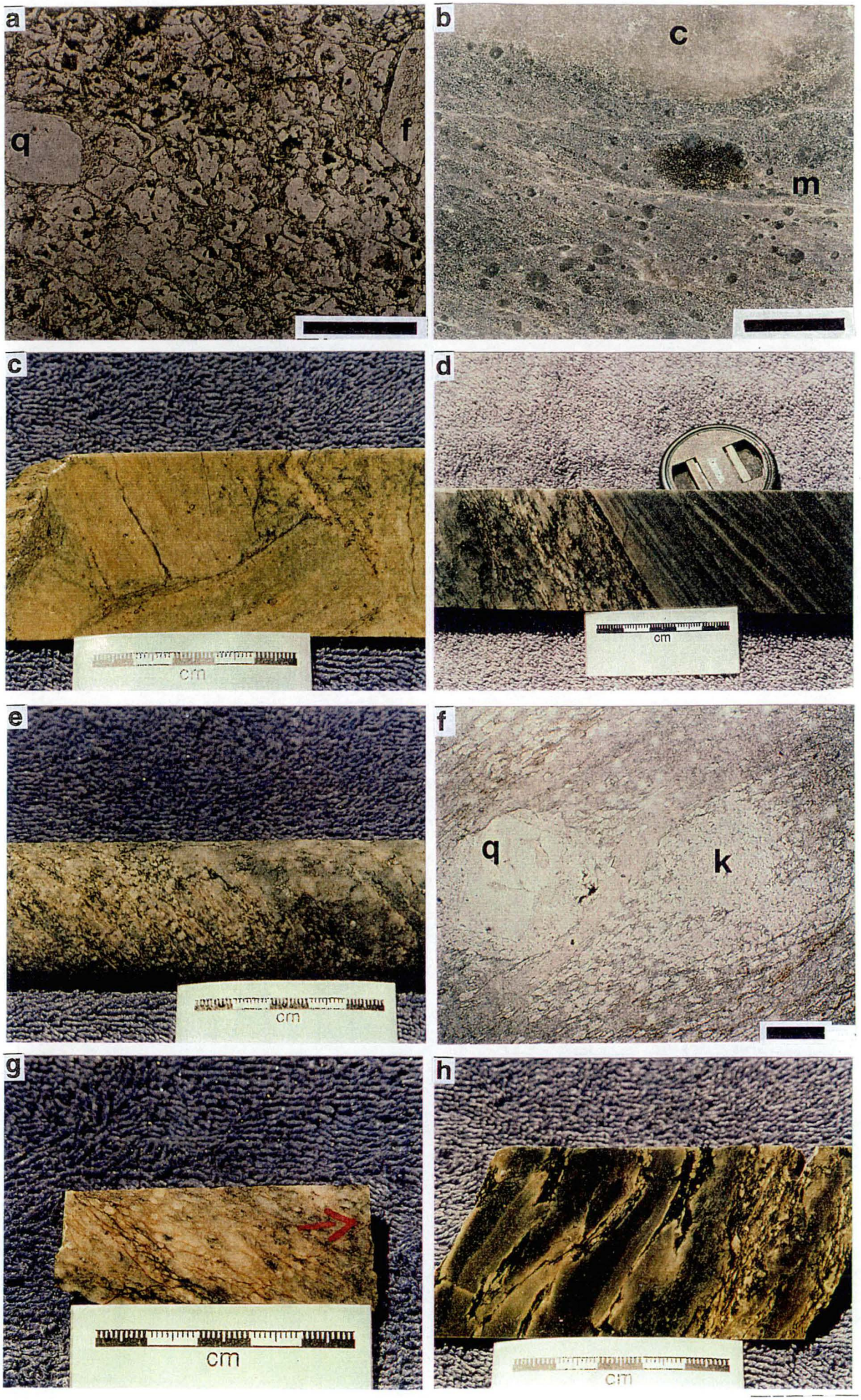

Fig. 5.3

Table 5.2: Criteria applied to discriminate monomictic clastic facies and coherent facies in the altered, rhyolitic footwall to the Thalanga massive sulphide deposit

	internal texture and organisation[a)]	top contact [a)]
coherent facies	• evenly porphyritic • euhedral phenocrysts • internal fabric (eg. flow lamination) with uniform or systematic orientation • massive, ungraded units	• sharp → lava or intrusion • sharp with chilled margins, overlying sediments disturbed and/or baked → intrusion • gradation into mixed, sediment-matrix-supported monomictic breccia with abundant jig-saw fit textures → intrusion • gradation from coherent to jigsaw-fit, monomictic breccia to normal graded, monomictic breccia → lava overlain by in-situ and resedimented autoclastic facies
monomictic rhyolitic clastic facies	• consistent differences in crystal size range and abundance between clasts and matrix, or else evenly porphyritic • euhedral or broken crystals • clasts with internal fabrics in random orientation • graded units → resedimented autoclastic facies • massive units → in situ autoclastic facies	• sharp, undisturbed → depositional • sharp, irregular → erosional • gradational into overlying unit → depositional

[a)]: description → interpretation

5.2.3 Critical evaluation of the use of phenocryst logging

The use of phenocryst populations as a means of discrimination of coherent and clastic facies in altered volcanic successions depends on the assumptions that (1) the coherent facies indeed had an evenly porphyritic texture prior to alteration and (2) the characteristics of the phenocryst population were not substantially modified during alteration, deformation and metamorphism. Observations made during this study suggest that both conditions are met at Thalanga and demonstrate that careful, systematic phenocryst logging can be a powerful tool in facies interpretation of altered, quartz-phyric, rhyolitic successions.

Lavas typically contain a specific assemblage of phenocrysts which are uniformly dispersed throughout one emplacement unit (McPhie et al., 1993). In most cases, these phenocryst assemblages represent the products of magma crystallisation prior to eruption (or shallow intrusion). Syn-eruptive nucleation and growth of crystals is restricted to microlite and spherulite formation. The melt (or parts of it) may solidify as a volcanic glass if cooling is rapid enough. Size and/or density sorting of phenocrysts is not likely to occur during effusive eruptions of felsic magmas because most felsic melts

typically have high viscosities and only slightly lower density than phenocrysts (especially quartz and feldspar) (Murase & McBirney, 1973; McBirney & Murase, 1984).

However, substantial heterogeneities in the phenocryst assemblages of felsic lavas may result from incomplete mixing of two or more texturally distinctive magmas (magma mingling) immediately prior to eruption or during emplacement. The resulting textures include compositional flow banding and swirls, schlieren or blobs of one magma hosted within another magma (Sampson, 1987; Seaman et al., 1995). Mingling can produce heterogeneity in phenocryst populations on scales ranging from cm to several metres and could be difficult to identify in drill core in an altered and deformed succession. However, in the Thalanga sequence, intervals of rhyolite with uniform phenocryst populations are very thick (m to several tens of m). In addition, in sections through least-altered rhyolite, the contact between units with contrasting phenocryst populations are generally either sharp or marked by volcaniclastic facies. Therefore, it can be inferred that phenocrysts populations in the rhyolites of the MWF were not affected by syn-eruptive magma mingling.

The texture of coherent rhyolite is substantially modified in the footwall alteration zone below the Thalanga ore body. Hydrothermal alteration affected the texture and mineralogical composition of groundmasses and also led to the destruction of feldspar phenocrysts. In contrast, quartz phenocrysts appear to have been largely unaffected by hydrothermal alteration and subsequent deformation and metamorphism. However, some quartz phenocrysts show undulous extinction and in-situ brecciation in strongly altered and foliated rocks which is probably a result of strain during regional deformation. In addition, some quartz phenocrysts are overgrown by a rim of fine quartz grains along their margins. These modifications are minor and logging of the abundance, size range and distribution of quartz phenocrysts has been instrumental in facies interpretation of the altered footwall rhyolite.

Careful textural observations with the hand lens are required for phenocryst logging because, on superficial inspection, the distribution of quartz phenocrysts may appear to be uneven, especially in domainal altered, coherent rhyolite. Quartz phenocrysts are easily recognised in a dark, phyllosilicate-rich groundmass but harder to distinguish in domains with a white or grey, siliceous groundmass. Furthermore, phyllosilicate-rich domains may contain round to lensoidal remnants of siliceous groundmass encircled by foliated sericite, biotite and/or chlorite which in hand specimen superficially resemble genuine quartz phenocrysts (Fig. 5.3 e, f). Such 'pseudophenocrysts' may represent the remnants of perlite kernels surrounded by phyllosilicates occupying the original arcuate,

perlitic cracks. Extensive alteration could have caused a progressive isolation of remnant siliceous kernels by successive replacement of the original groundmass. In some altered rhyolite, initial stages of the 'encircling' of small, round to lensoidal siliceous groundmass domains by arcuate-shaped phyllosilicate bands can be observed which may represent relics of original perlitic texture (Fig. 5.3g). The examination of thin sections has proven essential for facies recognition in the footwall alteration zone in order to confirm interpretations based on textural observations of hand specimen.

5.3 Volcaniclastic and non-volcanic sedimentary facies in the Thalanga sequence

A variety of volcaniclastic and non-volcanic sedimentary lithofacies occur in the Thalanga sequence. The description, classification and interpretation of these facies (Table 5.3) is mainly based on detailed examination of diamond drill holes. Graphic logs and lithological descriptions are presented in the Appendix (sections 1 to 6, back pocket).

In general, lavas and intrusions in the Thalanga sequence are composed of the various rhyolite and dacite types described above and are dominated by coherent facies; in situ and resedimented autoclastic facies are less abundant. Other volcaniclastic facies in the Thalanga sequence include monomictic and polymictic breccia and volcaniclastic sandstone of variable composition (Table 5.3). In the footwall, normally graded rhyolitic breccia beds are typically monomictic but a rhyolite-mudstone breccia facies (facies C) is also present (Fig. 5.3h). These facies are interpreted as syn-eruptive, resedimented autoclastic breccia, mainly comprising hyaloclastite and resedimented talus.

Breccia units in the hangingwall dominantly contain clasts of dacite type 1 or dacite type 2. Locally, some rhyolite fragments and quartz crystals are also present. Clasts of dacite type 3 or of andesite have not been observed in hangingwall facies. Silicified dacite type 1 clasts with preserved tube pumice textures are fairly common (Fig. 5.4 a, b). Dacite type 2 clasts are generally grey, siliceous and massive but some are pumiceous or perlitic (Fig. 5.4 c).

In the hangingwall, monomictic breccia units contain either dacite type 1 or dacite type 2 clasts. Locally, monomictic dacite type 2 breccia contains abundant pumice clasts. Polymictic dacite breccia with pumiceous dacite type 1 and perlitic dacite type 2 clasts is present in Central Thalanga (facies D). Polymictic dacite-rhyolite breccia (facies E) also occurs in the hangingwall and shows systematic changes in clast population along strike. Polymictic breccia composed of dacite 1 and rhyolite fragments occurs in East Thalanga

Table 5.3: Volcaniclastic and non-volcanic sedimentary facies in the Thalanga sequence

facies	description	interpretation
monomictic breccia facies		
A: in situ monomictic breccia	monomictic, non-graded, poorly sorted, clast- to matrix-supported, gradational contact with coherent facies of identical composition, *thickness: 1 - 20 m **clasts:** up to 50 cm, blocky, polyhedral or irregular, locally perlitic, internal foliations in clasts in random orientation, jig-saw fit texture **matrix:** same as clasts, *phyllitic or siliceous, crystals evenly distributed, – crystal fragments [domainal altered in situ rhyolite breccia and domainal altered coherent rhyolite are difficult to discriminate in footwall alteration zone]	in situ autobreccia and hyaloclastite
B: graded or bedded monomictic breccia	monomictic, normally graded, poorly sorted, matrix- to clast-supported, commonly sharp top and base, thickness: mostly 3 - 20 m (up to 40 m) **clasts:** generally 1-10 cm, locally finer, locally abundant perlitic or pumiceous clasts, blocky, polyhedral, lensoidal (deformed into foliation) or irregular, internal foliations in clasts in random orientation **matrix:** phyllitic or siliceous, quartz – feldspar crystals (rhyolite breccia) or feldspar crystals (dacite breccia with uneven distribution, crystal fragments	resedimented autoclastic breccia
polymictic breccia facies		
C: rhyolite-mudstone breccia	poorly quartz-(feldspar)-phyric rhyolite clasts or siliceous mudstone clasts in a quartz -(feldspar) -rich matrix, normally graded, matrix-supported, commonly sharp top and base, thickness: mostly 5 - 20 m (up to 30 m) **clasts:** 1-5 cm, rhyolite (siliceous, blocky to irregular), mudstone (wispy to blocky, locally with preserved internal lamination) **matrix:** phyllitic, quartz (+feldspar) crystals (5-10%, † 1 - 2 mm) with uneven distribution, crystal fragments	resedimented rhyolitic hyaloclastite and/or talus from rhyolite lavas/domes + mudstone intraclasts
D: polymictic dacite breccia	dacite 1 clasts (white, siliceous, commonly pumiceous with relict tube vesicle texture) in a feldspar -rich matrix – perlitic dacite 2 clasts, normally graded, matrix-supported, sharp top and base, thickness: 3 - 20 m **clasts:** >1 - 5 cm white, siliceous dacite 1 clasts, 2 - 20 cm perlitic dacite 2 clasts common in some units **matrix:** phyllitic with abundant, unevenly distributed, feldspar crystals (15 - 20%, † 1 - 2mm)	resedimented partly pumiceous hyaloclastite and/or talus from dacite lavas/domes
polymictic dacite-rhyolite breccia facies		
E1: polymictic dacite 1 - rhyolite breccia	dacite 1 clasts in quartz-bearing matrix – rhyolite clasts, normally graded or non-graded, matrix-supported, sharp contacts, thickness: <1 - 8 m (units with rhyolite clasts: †16 m) **clasts:** 5-10% dacite 1: relic tube pumice clasts or grey, siliceous, non-vesicular clasts, up to 10 cm, blocky to lensoidal (deformed into foliation), sharp, planar margins, minor rhyolite 1 or rhyolite 2 clasts **matrix:** phyllitic (biotite-rich), rarely siliceous, foliated, quartz crystals (1-5% ,1 - 2 mm, blue in some units) and feldspar crystals (<1-3%, †1 - 2mm), crystals unevenly distributed	resedimented hyaloclastite and/or talus derived from dacite 1 lava/dome + accidental rhyolite fragments
E2: polymictic dacite 1 - dacite 2 - rhyolite breccia	dacite 1 and dacite 2 clasts in quartz-bearing matrix – rhyolite clasts, normally graded, matrix-supported, poorly sorted, sharp contacts, thickness: 8 - 18 m **clasts:** 5-10% dacite 1: non-vesicular and relic pumice clasts (<1 - 15 cm), blocky to lensoidal or irregular, 5 - 20% dacite 2: grey siliceous non-vesicular or perlitic clasts (<1 to 10 cm), blocky, polyhedral, minor rhyolite type 2 or type 4 clasts (<1 - 4 cm) **matrix:** phyllitic (biotite-rich), foliated, blue quartz crystals (1-10%, <1 - 3 mm) and feldspar crystals (2-5%, 1 - 2 mm), crystals unevenly distributed	resedimented hyaloclastite and/or talus derived from dacite lavas/domes + accidental rhyolite fragments
E3: polymictic dacite 2 - rhyolite breccia	dacite 2 clasts in a quartz-bearing matrix – rhyolite clasts, normally graded or non-graded, matrix-supported, poorly sorted, sharp contacts, thickness: 10 - 17 m **clasts:** 10 - 20% grey siliceous dacite 1 clasts (<1 - 5 cm), blocky, massive or flow-laminated, rare rhyolite type 1 and type 4 clasts **matrix:** phyllitic (biotite-rich), foliated, blue quartz crystals (1-5%, <1 - 3 mm) and feldspar crystals (1-5%, 1 - 2 mm), crystals unevenly distributed	resedimented hyaloclastite and/or talus derived from dacite 2 lavas/domes + accidental rhyolite fragments
Quartz-Eye Volcaniclastics (QEV)		
F: coarse quartz crystal-rich sandstone/breccia	normally graded or non-graded, matrix-supported, thickness: usually 2 - 7 m (up to 20 locally <1 m) **components:** abundant, commonly blue quartz crystals, abundance and grain size variable on cm-scale within one unit (10 - 80%, generally 20-50%, 2-8mm, locally up to 15mm), feldspar crystals present in most units (1 - 20%, 1 - 5 mm), –rhyolite 4 clasts and/or minor rhyolite 1 clasts, common mudstone intraclasts (black biotite-chlorite-rich or light grey sericite-quartz-rich), rare massive sulphide clasts **matrix:** generally phyllitic (sericite-rich), foliated, locally siliceous, locally sulphide-rich (mineralised) [QEV may grade laterally or vertically to normally graded quartz -bearing sandstone with finer(†1 - 4 mm) and less abundant crystals]	resedimented rhyolitic debris with locally incorporated lithic fragments
volcaniclastic sandstone facies		
G1: graded quartz sandstone	normally graded, single and multiple, medium to thick beds, grain- to matrix-supported **components:** 10 - 50% quartz crystals (1 - 5 mm, locally blue), –rare rhyolite and/or rare mudstone intraclasts **matrix:** phyllitic and foliated grading to siliceous mudstone at the top	crystal-rich turbidite, rhyolitic provenance, ?post-eruptive
G2: graded feldspar - quartz sandstone	normally graded, grain-supported, very thick beds (1 - 3 m) **components:** 40 - 50% feldspar crystals (1-3 mm), 30-40% quartz crystals (1-5 mm, grey or bluish), black mudstone intraclasts **matrix:** siliceous or biotite- and chlorite-rich	crystal-rich, high density turbidite, ?syn- to post-eruptive
G3: graded feldspar sandstone	normally graded, medium to thin beds, minor very thick (1-4 m) feldspar crystal-rich units, grain- to matrix-supported, interbedded with mudstone **components:** 10 - 50% feldspar crystals († 1 - 2 mm), minor dacite 2 granules, rare scoriaceous fragments **matrix:** phyllitic (sericite-rich), foliated	volcaniclastic turbidite, mixed provenance, post-eruptive
mudstone facies		
H1: mudstone	grey or brown, phyllitic, massive or laminated, pale sericite+quartz-rich and dark biotite+quartz-rich laminae, sparse fine quartz and feldspar crystals, rare siliceous quartz+feldspar -phyric clasts which may be water-settled pumice clasts, intervals are <1 m to several metres thick	hemipelagic sediment
H2: mudstone + volcaniclastic sandstone	mudstone facies similar to H1 intercalated with thin to thick beds of feldspar sandstone (G3) facies and rarely with quartz-feldspar sandstone (G2), silica-ironstone or carbonate (I), or monomictic dacite 2 breccia (B) facies, intervals are 50 - 80 m thick	hemipelagic sediment and syn- to post-eruptive volcaniclastic turbidites
chemical facies		
I: siliceous and calcareous facies	massive to bedded silica-ironstone (quartz-magnetite-hematite), quartz-barite, carbonate-chlorite-tremolite sulfides, carbonate-epidote-actinolite(–quartz –barite– chlorite), thickness: generally < 1 m	chemical precipitates

*phyllitic: dominantly composed of sericite-biotite-chlorite in variable proportions, +:thickness ranges of breccia facies refer to single beds

(facies E1). In Central Thalanga, polymictic breccia contains dacite type 1 and dacite type 2 clasts (facies E2; Fig. 5.4d) whereas in West Thalanga, dacite type 1 clasts are absent (facies E3). A distinctive volcaniclastic facies characterised by abundant, coarse (usually blue) quartz crystals and a variety of clast types (rhyolite type 1, rhyolite type 2, massive sulphide and mudstone intraclasts) is common in the Favourable Horizon and often associated with massive sulphides (facies F, Quartz-Eye Volcaniclastics, Fig. 5.4e). Volcaniclastic sandstones with abundant volcanic quartz or quartz+feldspar crystals (facies G1 and G2, Fig. 5.4f, g) are interpreted to be of syn- (?to post-) eruptive origin.

Grey to brown, massive to laminated mudstone occurs locally in the Favourable Horizon and is common in the hangingwall to the west of the mine. Intervals of mudstone intercalated with medium to thinly bedded, feldspar-bearing turbidites (facies G3, Fig. 5.4h) is a typical facies association.

The chemical facies (facies I) includes silica-ironstone, quartz-barite and carbonate-calc-silicate rocks representing rocks of uncommon mineralogy and composition in the Thalanga sequence. All of these rock types have previously been considered to have formed as hydrothermal exhalites (Gregory et al., 1990), however, more recent research by Herrmann (1994) has shown that massive carbonate-chlorite-tremolite rocks in the Favourable Horizon in West Thalanga most likely represent metamorphosed, intensely carbonate-chlorite altered footwall rhyolite. The origin of the various rock types (eg. exhalative versus replacement) included in facies I is outside the scope of this study. They are regarded here as members of one facies.

5.4 Comparison of facies associations in seven cross sections through the Thalanga sequence

The cross sections and outcrop section have been converted to true-thickness graphic logs that summarise the volcanic facies and alteration intensity (Fig. 5.5). The geological cross sections and logs of diamond drill holes studied are presented in the Appendix. These show that in general terms, the Thalanga sequence is a felsic, lava-dominated, proximal succession which conformably overlies (PCF), and grades upwards into (top of TCF), a mudstone-dominated sedimentary facies association. Syn-volcanic intrusions are an important but subordinate part of the succession.

Fig. 5.4: Textures of volcaniclastic and non-volcanic sedimentary facies in the Thalanga sequence.

(a) Silicified dacite type 1 pumice clast with delicate, fibrous internal texture interpreted to represent tube vesicles (facies E1) (sample TH402-348.90, East Thalanga, TCF, scale bar: 1 cm).

(b) Dacite type 1 pumice clast with fibrous internal lamination interpreted to be tube vesicles (facies E2) (photomicrograph of sample TH38-406.40, Central Thalanga, TCF, scale bar: 500 μm).

(c) Perlitic dacite type 2 clast with a feldspar phenocryst that had been broken at the margin of the clast (arrow). The perlitic texture indicates that this clast was originally glassy (facies D) (photomicrograph of sample C2047-112.75, Central Thalanga, TCF, scale bar: 500 μm).

(d) Polymictic breccia containing rhyolite type 4 and siliceous dacite type 1 ?pumice clasts (facies E2) (sample TH334-61.60, Central Thalanga, TCF).

(e) Examples of Quartz-Eye volcaniclastic facies (facies F) from the Favourable Horizon in East Thalanga. Note uneven distribution of coarse, commonly blue quartz crystals and siliceous mudstone intraclasts (m) (samples TH61-216.20 and TH61-237.50).

(f) Quartz crystal-rich sandstone from the footwall in East Thalanga. Coarse, quartz-crystal-rich base of one bed is overlying the fine-grained, siliceous top of the underlying bed. The low-angle orientation of the contact with respect to the long axis of core is due to the steep orientation of the drill hole collar with regard to stratigraphy (sample TH144B-151.70).

(g) Feldspar and quartz crystal-rich sandstone from the hangingwall in Far West Thalanga (~ 300 m above the Favourable Horizon) (sample TH37-22.30).

(h) Bedded mudstone-dominated sedimentary facies with intercalated graded beds of feldspar-bearing turbidites from the in the hangingwall in Far West Thalanga (facies H2) (sample TH37-70.70).

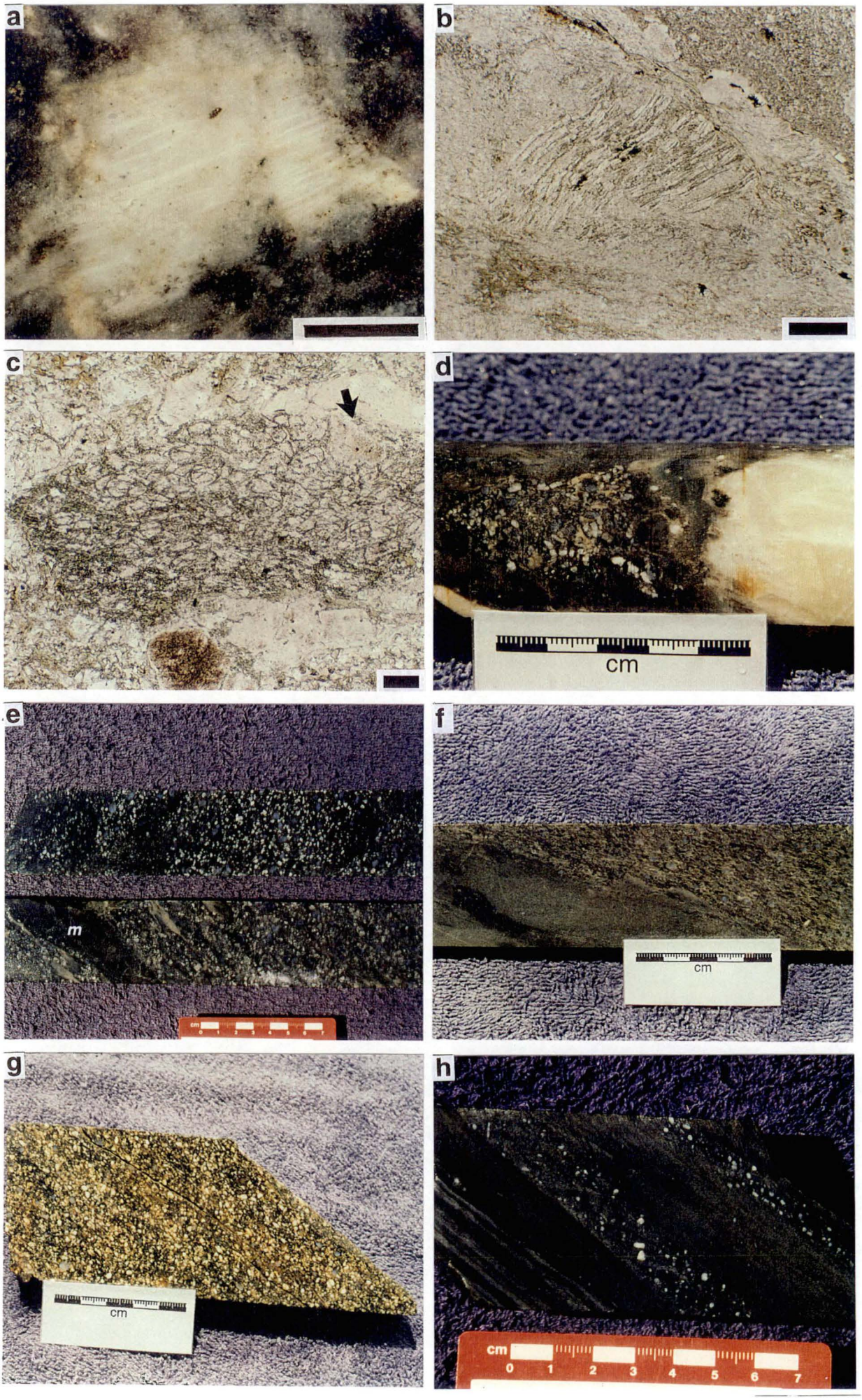

Fig. 5.4

In the following sections, the facies architecture of the Thalanga sequence is described in terms of the principal facies present in the footwall, Favourable Horizon and hangingwall, and the lateral variations in the facies associations that occur between the mine area and the outcrop section.

5.4.1 Footwall

In the outcrop section, the MWF consists mainly of rhyolite type 3 lavas (50-150 m thick) which are dominated by coherent facies; in situ and resedimented autoclastic breccia facies are minor. The PCF at the base of the section consists of thinly bedded mudstone which includes a small silica-ironstone lens. Rhyolite type 4 intrusions occur in the top part of the PCF and in the basal part of the MWF. Rhyolite type 1 and 2 lavas are minor components.

In the Thalanga mine area, the upper part of the MWF consists of unaltered to strongly altered rhyolite types 1 and 2. The ore body occurs on top of rhyolite type 1 lava (150 to 200 m thick) dominated by coherent facies in Central and East Thalanga (sections 3-6) whereas resedimented syn-eruptive rhyolitic breccia (facies B and C) is the immediate footwall to massive sulphides in West Thalanga. Unaltered rhyolite type 1 syn-volcanic intrusions into moderately to strongly altered rhyolite breccia have been identified in the upper parts of Far West (section 1) and Central (section 3) Thalanga. In East and West Thalanga (sections 1, 2, 5 and 6), lower parts of the footwall (~200 to 250 m below the Favourable Horizon) consist mainly of unaltered to moderately altered rhyolite type 2 lava (> 250 m thick), with subordinate resedimented autoclastic breccia (facies B) and quartz crystal-rich sandstone turbidites (facies G1). In Central Thalanga (section 4), rhyolite type 2 intrudes moderately altered rhyolite type 1 lava, the base of which has not been intersected. In contrast to its predominance in the outcrop section, rhyolite type 3 is absent in the upper part of the MWF in the Thalanga mine area except for one intrusion with a peperitic top contact in Far West Thalanga (section 1).

5.4.2 Favourable Horizon

The Favourable Horizon conformably overlies rhyolite (type 1 or 3) and consists of a lithologically diverse facies association with marked lateral facies variations. It includes coarse quartz-feldspar crystal-rich volcaniclastic facies (Quartz-Eye Volcaniclastics or QEV, facies F), rhyolite type 4 intrusions, rare rhyolite type 1 resedimented autoclastic breccia, massive to semi-massive sulphides, carbonate-tremolite-chlorite rocks, massive to semi-massive barite, silica-ironstones and laminated or massive grey-brown mudstones.

In the outcrop section, the Favourable Horizon consists of laminated grey-brown mudstone, quartz-feldspar crystal-rich sandstone, minor siliceous mudstone and a single 40-m thick, rhyolite type 4 lava. The top part of the mudstone contains quartz-feldspar-phyric siliceous clasts up to 5 cm across which may be water-settled pumice clasts.

In the mine area, the Favourable Horizon is dominated by the QEV which contains minor rhyolite clasts (types 4 and 1), mudstone intraclasts and rare massive sulphide clasts (Hill, 1996). Rhyolite type 4 intrusions (possibly including minor partially extrusive units) are common in East Thalanga (section 6) and also occur in Central Thalanga to the west of section 3 (Hill, 1996, not shown in Fig. 5.5). Hill (1996) concluded that the QEV was predominantly derived from an unknown rhyolite source in the vicinity of the Thalanga deposit because (1) the QEV locally contain quartz crystals that are significantly coarser (up to 15 mm) than phenocrysts in rhyolite type 4, and (2) intrusive (peperitic) contacts between coherent facies of rhyolite type 4 and QEV predominate. In East Thalanga (section 6), the QEV is the immediate host to the massive sulphides whereas rhyolite type 4 intrusions are unaltered and not associated with the ore. This observation also suggests that there was a time lag between QEV emplacement (syn-mineralisation) and rhyolite type 4 intrusion (post-mineralisation).

Carbonate-tremolite-chlorite rocks that represent metamorphosed intense alteration of footwall rhyolite (Herrmann, 1994) are common in West Thalanga (section 2) but scarce elsewhere. In West Thalanga, carbonate, tremolite and chlorite are also the dominant gangue minerals in massive sulphides. Silica-ironstones occur in places in the distal and upper fringes of ore lenses and intercalated with laminated or massive grey-brown mudstone in the Favourable Horizon to the west of the mine along the Thalanga Range (Duhig et al., 1992).

Massive to semi-massive barite also occurs locally on the fringes of the ore body in particular along the up-dip and western termination of the West Thalanga ore lens and the western margin of the East Thalanga ore lens (Hill, 1996). They range in thickness from <1 m to ~3 m and may extend for up to 150 m in the down-dip or along-strike direction. These rocks consist dominantly of variable proportions of fine-grained (<50 μm) quartz and barite; other minerals (eg. muscovite, biotite, sphalerite) vary in abundance from negligible to common (10 - 20 vol.%). Semi-massive sulphide with barite-rich gangue are also present in some marginal parts of the ore lenses and typically grade laterally into quartz- and barite-rich rocks. Locally, top and base contacts of massive to semi-massive barite are gradational to altered rhyolite, sedimentary facies or chemical facies which suggests that they may have formed by sub-seafloor replacement processes. However, some units have sharp and conformable stratigraphic contacts (eg. TH5, section 3,

Appendix) and may therefore represent chemical sediments deposited onto the palaeo-seafloor.

5.4.3 Hangingwall

The hangingwall to the massive sulphides (TCF) is unaltered to weakly altered and dominated by dacitic lavas, although there are marked changes in the composition and facies associations along strike. In East Thalanga, dacite type 1 lava (100-150 m thick, >1000 m wide and >500 m long) immediately overlies the Favourable Horizon (sections 5 and 6). Polymictic breccia (facies E1) with dacite type 1 clasts in a quartz crystal-bearing matrix occurs below and above this massive lava. This facies locally contains rhyolite clasts and extends westward through to Central Thalanga (sections 3 and 4) but not beyond. East Thalanga (section 5) also includes another variety of polymictic breccia with dacite type 1 clasts in a feldspar-rich matrix (facies D). However, clasts of dacite types 2 or 3 are not present in volcaniclastic units in East Thalanga.

In the west, dacite type 2 is predominant in the hangingwall. Dacite type 2 lava ?domes (150 to 180 m thick) overly the Favourable Horizon in Far West Thalanga (section 1) and the outcrop section. In section 1, the dacite type 2 dome is flanked by a thick interval of monomictic resedimented pumiceous autoclastic breccia (facies B). An equivalent association is present in West Thalanga (section 2) where a series of dacite type 2 lavas, each <50 m thick, is intercalated with resedimented autoclastic breccia (facies B). Polymictic breccia units occurring in these two sections and in the outcrop section contain dacite type 2 (and rhyolite) clasts but no dacite type 1 or dacite type 3 clasts (facies E3). In contrast, polymictic breccia with both dacite type 1 and dacite type 2 clasts (± rhyolitic components) is common in Central Thalanga (facies D and E2).

Dacite type 3 intrusions with sharp, chilled margins and peperitic top contacts occur in East, West and Central Thalanga. Although clearly post-dating dacite type 1, dacite type 2 and deposition of associated monomictic and polymictic breccia, the peperitic contacts indicate that emplacement was syn-volcanic. In West Thalanga (section 2), a dacite type 3 sill (15 to 60 m thick, >500 m wide, length unknown) intruded parallel to the Favourable Horizon just above the mineralisation and displaced quartz crystal-rich sandstone (distal equivalent of QEV, facies G1) intercalated with laminated mudstone into the hangingwall. A dacite type 3 feeder dike occurs in the footwall of East Thalanga (section 5). Minor andesite sills with sharp, chilled contacts, post-date dacitic volcanism and locally intrude the hangingwall.

Fig. 5.5: Graphic logs for the Thalanga sequence in the outcrop section ~5 km west of Thalanga mine and in 6 sections in the Thalanga mine area.

Positions of sections are shown on Figure 1.5. Tick marks are 50 m apart, true stratigraphic thickness.

The outcrop section in the railway cutting was mapped during this study and the graphic log was extended into the TCF based on mapping by Hill (1996) on the southeastern side of the Thalanga Range.

These simplified graphic logs of the facies associations in the Thalanga mine area are based on detailed lithofacies logging of 4 to 6 diamond drill holes per section drilled at variable angles to stratigraphy. The total of length of drill core examined per section varies between 1700 m and 3300 m (Table 1.2). Graphic logs and description of lithofacies of drill holes are presented in the Appendix together with the interpreted geological cross sections simplified in these stratigraphic logs.

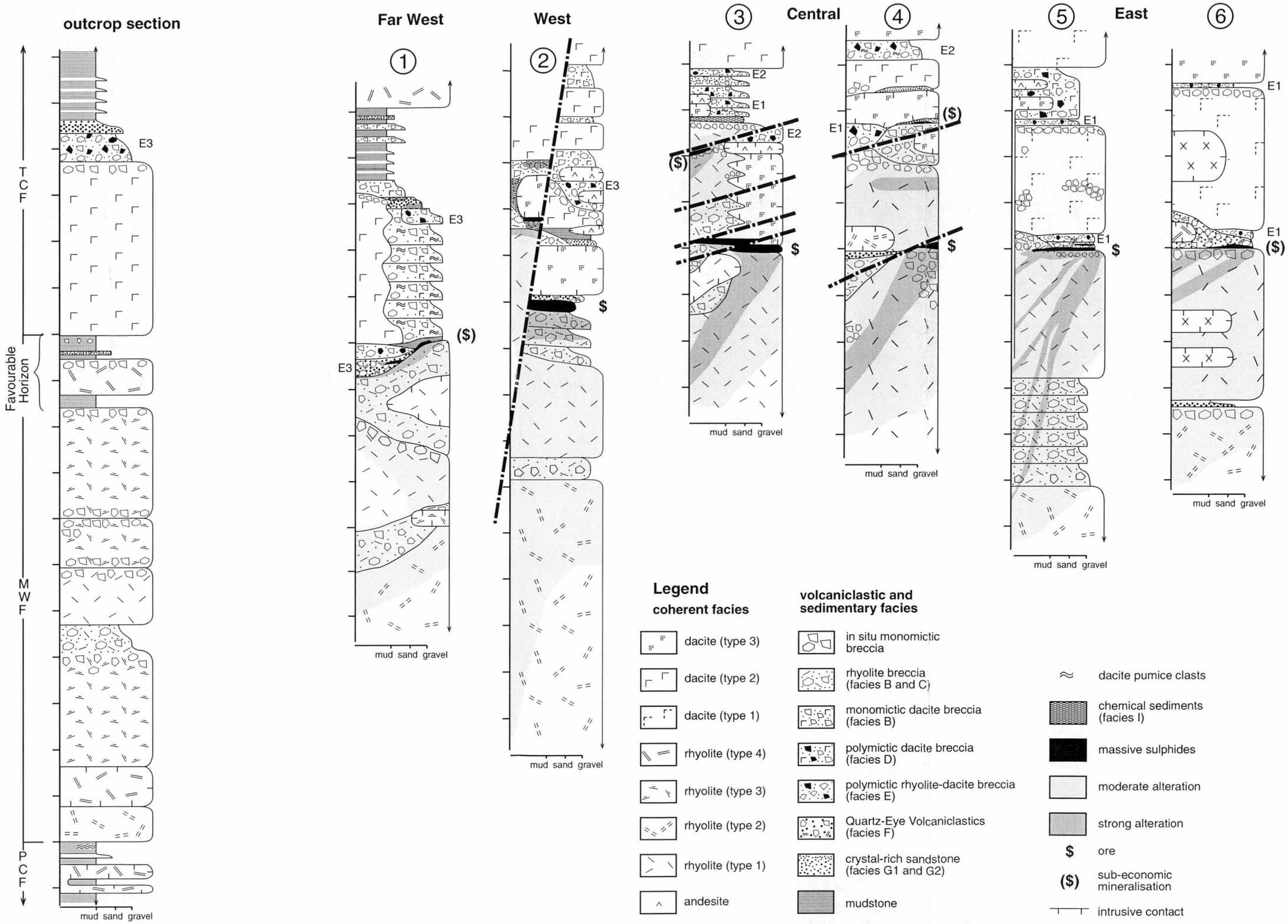
outcrop section
Far West
West
Central
East
1
2
3
4
5
6
T C F
Favourable Horizon
M W F
P C F
E1
E2
E3
($)
$
mud sand gravel
Legend
coherent facies
dacite (type 3)
dacite (type 2)
dacite (type 1)
rhyolite (type 4)
rhyolite (type 3)
rhyolite (type 2)
rhyolite (type 1)
andesite
diorite
volcaniclastic and sedimentary facies
in situ monomictic breccia
rhyolite breccia (facies B and C)
monomictic dacite breccia (facies B)
polymictic dacite breccia (facies D)
polymictic rhyolite-dacite breccia (facies E)
Quartz-Eye Volcaniclastics (facies F)
crystal-rich sandstone (facies G1 and G2)
mudstone
mudstone interbedded with volcani-clastic sandstone (facies H2 includes facies G3)
dacite pumice clasts
chemical sediments (facies I)
massive sulphides
moderate alteration
strong alteration
$ ore
($) sub-economic mineralisation
intrusive contact
D3 - fault

Fig. 5.5

These observations indicate that mass-flow-transported clasts in the various polymictic breccia facies were derived locally from coeval dacite lavas and domes, and to a lesser extent, from exposed parts of rhyolites. The limited lateral extents of the different polymictic breccia facies and their close spatial association with particular dacite types suggest that the mass flows were confined to local depressions (no more than a few hundred metres in maximum extent) that were probably defined by constructional volcanic features such as the steep margins of lavas and domes.

A different facies association occurs in the upper part of the hangingwall in Far West Thalanga (section 1) and the outcrop section. Above the dacite type 2 lava/?dome (150 to 180 m thick), the sequence is dominated by mudstone and thinly bedded feldspar-rich turbidites (facies H2), but includes subordinate monomictic dacite type 2 breccia (facies B), polymictic breccia with dacite type 2 clasts (facies E3) and quartz-feldspar crystal-rich sandstone (facies G2). Thus, this area was a depocentre receiving mass-flow transported clastic input from at least two sources: a ?distal extra-basinal source for the turbidites, and a more local source, most likely the adjacent dacite type 2 lava/?dome.

In the Far West Thalanga hangingwall section (section 1) silica-ironstone and massive calcareous rocks (carbonate-epidote-actinolite, facies I) are partially hosted within crystal-rich sandstone and occur 150 m above the Favourable Horizon, laterally adjacent to the top of the dacite type 2 lava/?dome. The Far West Thalanga hangingwall section is also exceptional in the presence of an interval of coherent rhyolite type 4 (uncertain mode of emplacement), 250 m above the Favourable Horizon, overlying laminated, grey-brown mudstone.

5.5 Discussion

5.5.1 Evolution of the Thalanga sequence

The Thalanga mine area was a submarine felsic volcanic centre dominated by the products of effusive eruptions, comprising lavas and domes, together with lava- or dome-derived, mass-flow-emplaced clastic units and syn-volcanic intrusions. Prior to mineralisation at Thalanga, the volcanism was rhyolitic (rhyolite types 1 and 2) (Fig. 5.6a). The thickening of the MWF in the mine area could be due to the restricted emplacement of the rhyolites, although the composition of the lower part of section is unknown. The crest of this volcanic centre could have been up to 500 m above the adjacent area to the west, assuming that the top surface of the underlying PCF was roughly horizontal. This relief could have been constructed by high-aspect-ratio lavas and

Fig. 5.6: Model for the evolution of the Thalanga sequence. Legend for symbols given on Figure 5.5.

(a) In the Thalanga mine area, a topographically high volcanic centre was constructed by lavas of rhyolite types 1 and 2. A laterally extensive, footwall alteration zone enveloping zones of intense alteration associated with pyrite veining developed in the upper 200 to 300 m of the lavas. QEV (facies F) emplacement was coeval with mineralising hydrothermal activity. In the outcrop section, the equivalent interval consists mainly of well bedded mudstone enclosing rhyolite type 4 lava. Minor rhyolitic syn-volcanic intrusions were emplaced in the footwall alteration zone and the Favourable Horizon after hydrothermal alteration and mineralisation had largely ceased.

(b) Effusive eruptions continued after mineralisation and dacite types 1 and 2 were extruded in East and West Thalanga respectively. These events also generated significant thicknesses of dacitic autobreccia, resedimented autoclastic breccia and polymictic volcanic breccia. Dacite type 3 and andesite intruded the hangingwall in East, West and Central Thalanga at a later stage. To the west, extrusion of dacite 2 was followed by deposition of a mudstone-dominated sequence that received sporadic mass-flow-transported input (eg. feldspar crystal-rich turbidites, facies H2) from a distal?, extra-basinal source.

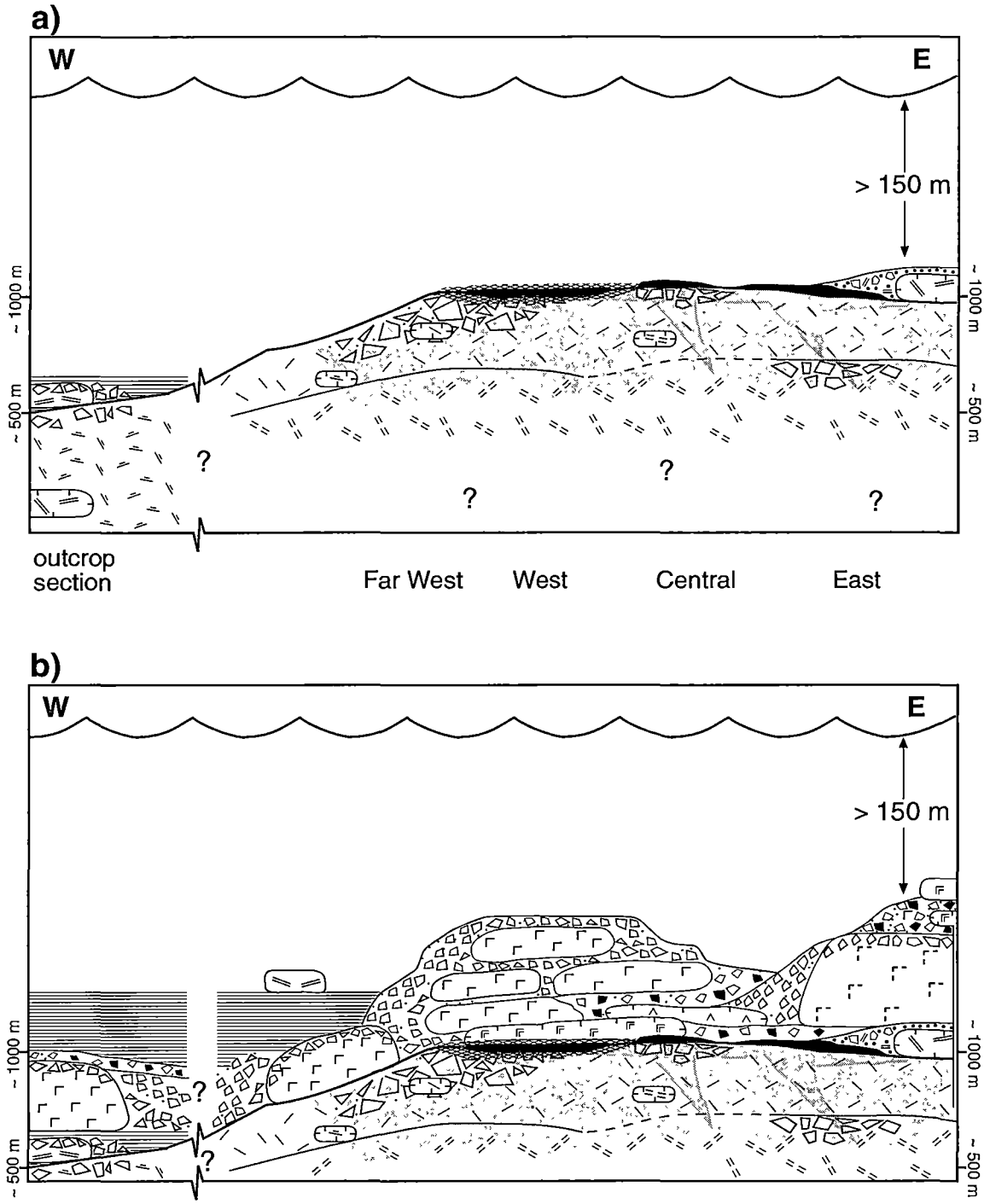
a)
W
E
> 150 m
~ 1000 m
~ 500 m
~ 1000 m
~ 500 m
?
?
?
?
outcrop section
Far West
West
Central
East
b)
W
E
> 150 m
~ 1000 m
~ 500 m
~ 1000 m
~ 500 m
?
?

Fig. 5.6

domes. Monomictic rhyolitic resedimented autoclastic breccia that is common in the footwall towards the west (sections 1 and 2) probably accumulated on the flanks of the rhyolitic edifice. Deposition of QEV units in the Favourable Horizon on the top of the rhyolite ridge/plateau indicates the presence of local depressions and knolls (probably tens to a few hundreds of metres in extent and <20 m relief), which could be attributable to irregularities in the surface structure of the rhyolite lavas (subaerial rhyolites, eg. Fink, 1980). Accumulation of the QEV was largely synchronous with massive sulphide formation.

The Thalanga mine area remained a centre of effusive volcanism and topographically high during TCF emplacement, in contrast to the area to the west (Fig. 5.6b). The massive sulphides at Thalanga were buried by dacite lavas, syn-volcanic intrusions and thick, mass-flow-emplaced volcanic breccias composed of locally derived clasts, while hemipelagic mudstone and turbidite sand, partly derived from an unknown, distal? source, accumulated in the laterally equivalent area to the west. The topographically high Thalanga mine area did not receive this mass-flow transported sedimentary input from external sources.

Although the volcanic activity continued to be dominated by effusive eruptions after the mineralisation, there was a marked shift from rhyolitic to dacitic compositions and the hangingwall was supplied by a quartz phenocryst-free magma reservoir. Quartz crystals and rhyolite lava clasts that occur in polymictic, mass-flow-emplaced units in the hangingwall above the massive sulphides were probably locally derived from exposed rhyolite of the MWF. However, the presence of coherent rhyolite type 4 in the hangingwall of section 1 indicates that minor rhyolitic volcanism continued in the Thalanga area after mineralisation.

5.5.2 A modern analogue - the Pual Ridge, Papua New Guinea

A modern analog for the Thalanga massive sulphide deposit and its setting on a submarine, felsic topographic high is the PACMANUS hydrothermal field in the eastern Manus back-arc basin north of New Britain (Papua New Guinea). Several hydrothermally active areas and sulphide deposits occur at 1,630 m below sea level (bsl), near the top of the 20 km long, 1 to 1.5 km wide, dominantly dacitic Pual Ridge which rises 400 to 600 m

above the surrounding ocean floor (Binns & Scott, 1993). The lavas range from weakly to highly vesicular, and are poorly porphyritic (plagioclase, pyroxene and magnetite phenocrysts) with groundmasses composed of glass and plagioclase and pyroxene microlites. The lavas of the Pual Ridge range in composition from andesite to rhyodacite following a calc-alkaline fractionation trend. However, dacite lavas are dominant above 1800 m bsl and their surfaces are described as "extremely hummocky with jagged protuberances that are commonly several metres high" (Binns & Scott, 1993, p. 2227). Abundant autoclastic breccia, mainly in situ and resedimented hyaloclastite, has also been observed. Talus breccia produced by mass wasting is particularly abundant on the flanks of Pual Ridge whereas the crest of the ridge has an irregular topography and consists of knolls (rising 20 to 50 m above the surrounding area) and local basins (<300 m maximum extent).

5.5.3 Relationship between hydrothermal activity and rhyolitic volcanism

The hydrothermal system that generated the Thalanga base metal deposit became active during emplacement of the footwall rhyolites. However, the presence of unaltered rhyolite intrusions in the footwall indicates that the rhyolitic volcanism outlived the hydrothermal activity and massive sulphide formation. The deposition of the QEV in the Favourable Horizon was apparently coeval with mineralisation because the QEV contains massive sulphide clasts and locally hosts the mineralisation (Hill, 1996). Nevertheless, monomictic rhyolite mass-flow-emplaced breccia units in the footwall mark previously unrecognised palaeo-seafloor positions within the MWF that are potentially prospective for exhalative base metal sulphides produced during earlier, separate or related stages of the Thalanga hydrothermal activity.

In an attempt to assess whether volcanic facies controlled or influenced the Thalanga hydrothermal system, the facies arrangement in the footwall was compared with the sites of most intense fluid flow as indicated by zones of strong alteration. Such a comparison shows that the zones of intense alteration do not coincide either with particular facies boundaries or facies types, and instead, clearly cross cut the facies arrangement (eg. sections 3-6, Fig. 5.5; see also geological cross sections and drill hole logs in the Appendix or Figs. 7.5 to 7.7). The present-day oblique orientation of zones of intense alteration may be largely due to shearing during regional folding (D2) and it is

possible that the original orientation of these zones was more or less normal to stratigraphy. Even so, it is clear that neither particular facies types nor particular emplacement units were preferred sites for hydrothermal fluid flow. In the absence of recognisable early (pre-D2) tectonic features, such as syn-volcanic faults, the mechanism of focussing hydrothermal fluid flow at Thalanga remains enigmatic.

5.6 Summary

The Thalanga massive sulphide ore body overlies a ~1000 m thick succession of rhyolitic lavas, syn-volcanic intrusions and monomictic mass-flow units which thins significantly to the west. The ore body formed on top of an elevated rhyolitic volcanic centre constructed by the products of effusive eruptions in a subaqueous, below storm-wave-base depositional environment. This is similar to the setting of the PACMANUS hydrothermal field in the eastern Manus Basin (Papua New Guinea) which occurs at ~1,600 m bsl on the top of a 400 to 600 m high ridge composed predominantly of dacitic lava.

Several types of rhyolite in the footwall and dacite in the hangingwall have been distinguished by phenocryst logging even though primary textures have been modified by hydrothermal alteration. In addition, careful textural observations have allowed discrimination of genuine from false clastic facies in the strongly altered footwall lavas and intrusions, and recognition of mass-flow-emplaced units that indicate palaeo-seafloor positions within the rhyolitic footwall.

The mineralising hydrothermal system at Thalanga was active during rhyolitic volcanism but ceased before the final stages of rhyolite emplacement. The emplacement of QEV in the Favourable Horizon appears to have been largely coeval with mineralisation. However, the coarse-quartz crystal-rich volcaniclastic facies is not restricted either to the Favourable Horizon nor to the mine area, being present in the hangingwall and well to the west of the mine.

Zones of strong alteration in the footwall are well defined and delineate positions of intense hydrothermal fluid flow. These zones cut across emplacement units and are not confined to particular facies types. Thus it appears that controls other than volcanic facies were important in focussing the Thalanga hydrothermal system.

6 Constraints on the primary geochemistry of Thalanga volcanic units

The geochemical composition of volcanic units in the Thalanga sequence reflects a variety of processes related to magmatic evolution, diagenesis, sub-seafloor metamorphism and hydrothermal alteration associated with mineralisation. This chapter is concerned with the characterisation of the primary geochemical composition and interpretation of a general petrological model.

In total, 180 samples, representing the principal lithofacies in the Thalanga sequence, have been analysed during this study. These include altered and least-altered samples of the different types of rhyolite and dacite which were defined petrographically (Chapter 5). Data for rhyolite type 4 were supplemented with analyses presented in Hill (1996). For simplicity, rhyolite types 1, 2 and 3 are collectively referred to as 'footwall rhyolite' and dacite types 1, 2 and 3 as 'hangingwall dacite'.

The geochemical data-set consists of bulk rock XRF analyses of major, minor and trace elements; rare earth elements (REE) were determined for a representative sub-set of samples. The analytical procedures are described in the Appendix and the data are presented in Table A4.

6.1 Introduction

VHMS deposits are commonly associated with felsic host rocks in bimodal volcanic sequences (Mosier et al., 1983; Franklin et al., 1981) and the petrogenesis of these volcanics has been the subject of numerous research projects (eg. MacGeehan & MacLean, 1980; Sillitoe, 1982; Lesher et al., 1986; Swinden, 1991; Lentz & Goodfellow, 1992; Barrie et al., 1993; Syme & Bailes, 1993; Stolz, 1995). These studies have characterised the tectonic setting of potentially prospective volcanic sequences using geochemical and isotopic evidence (Galley, 1995). In general, it has been inferred that VHMS deposits have formed preferentially in extensional tectonic environments.

The interpretation of magmatic affinities, possible source characteristics and likely tectonic environments of ancient volcanics is a difficult task. Most major elements commonly used for classification of fresh, modern volcanics are mobile during alteration and metamorphism (Rollinson, 1993) and especially alkalis and silica are readily mobilised even during circulation of cold meteoric or marine waters through fresh, glassy volcanics (Lipman, 1965). Therefore, the identification of immobile element signatures of volcanic rocks from known tectonic settings has long been a major goal in igneous

petrology (eg. Pearce & Cann, 1973, Winchester & Floyd, 1977, Rollinson, 1993, p. 171-215). A variety of diagrams using high field strength elements (HFSE), such as Ti, Zr, Y, Nb, P and Th, for the discrimination of basalts from different tectonic settings has been proposed and applied to ancient volcanic sequences. However, the uncritical use of such diagrams may lead to spurious interpretations because trace element concentrations in igneous rocks are a function of a variety of processes which may, or may not, be unique to specific tectonic setting.

In a recent review on the lithogeochemistry of VHMS districts, Barrett & MacLean (1997) concluded that massive sulphide formation occurred preferentially in three settings associated with extension:

- rifting of continental crust in marine basins behind a continental margin volcanic arc (examples: Bathurst Mining Camp, Canada, Lentz & Goodfellow, 1992; Mount Windsor Subprovince, Australia, Stolz, 1995),
- rifting of continental crust in an intraplate-setting due to upwelling of the asthenosphere producing peralkaline rhyolites and alkaline basalts (example: Prays Mountains, Wales, Leat et al., 1986), and
- rifting of mature arcs where subduction-related effects on volcanism are important and involvement of continental crust in magma genesis is limited (examples: Kuroko deposits, Japan, Dudàs et al., 1983; Myra Falls, Canada, Barrett & MacLean, 1997).

Lentz (1998) also concluded that VHMS deposits formed in various extensional tectonic settings and suggested that Zr/Y and $(La/Yb)_N$ ratios could be useful in discriminating barren and potentially prospective volcanic provinces.

The Zr/Y ratio has been regarded as an indicator of magmatic affinities of altered, ancient, felsic volcanic successions (Lesher, et al., 1986; MacLean & Barrett, 1993; Barrett & MacLean, 1997; Lentz, 1998). In general, tholeiitic felsic volcanics have relatively low Zr/Y ratios (2 to 4) whereas calc-alkaline affinities are indicated by Zr/Y ratios >7; intermediate values (4 to 7) can be classified as transitional. The increase in Zr/Y ratios is interpreted to reflect the compatible behaviour of Y in calc-alkaline suites. The compatibility of Y (and heavy REE) has been related to hornblende fractionation and/or hornblende restite formation (eg. Arth & Barker, 1976; Pearce, 1982; Henderson, 1984; Sisson, 1994).

The petrology and tectono-magmatic evolution of the Mount Windsor Subprovince was examined on a regional scale by Stolz (1995) using bulk rock geochemical analyses (including REE) and Nd isotopes of representative, least-altered volcanics from the PCF, MWF and TCF. Stolz (1995) inferred that these volcanics were emplaced in a continental

back-arc setting and proposed a model for the evolution of the subprovince (Fig. 1.4). Continental-derived clastic sedimentary facies of the PCF were deposited on an attenuated passive continental margin during the Neoproterozoic to Cambrian. In the Late Cambrian to Early Ordovician, back-arc extension was initiated and accompanied by the first phase of volcanism. This event is represented by alkaline basalts and andesites in the top part of the PCF which were derived from subcontinental, lithospheric mantle. Subsequently, rhyolites (MWF), derived from extensive partial melting of the sub-continental lithosphere, were emplaced on top of the PCF. Continued volcanism produced the mafic to felsic volcanic succession of the TCF. Mafic units of the TCF have a subduction-related geochemical signature similar to modern back-arc basalts whereas felsic units were influenced by assimilation of continental crust.

6.2 Geochemistry of Thalanga volcanic units

6.2.1 Major element mobility during alteration

The different types of rhyolite and dacite identified on the basis of consistent differences in phenocryst populations (Chapter 5) each show marked variations in major element concentrations (Tables 6.1 and 6.2), suggesting that the compositions have been strongly modified after emplacement as a result of alteration. The term 'alteration' is used to refer to any post-depositional modification in the composition of the rocks which may be the result of a variety of processes including diagenesis, sub-seafloor metamorphism or hydrothermal alteration.

On variation diagrams such as the TAS diagram (Na_2O+K_2O versus SiO_2, Le Maitre et al., 1989, Fig. 6.1a), which is commonly used for the classification fresh volcanic rocks, the data points are widely scattered. Analyses of rhyolite type 1 from the altered, immediate footwall to massive sulphides in the mine area, vary between 55 and 85 wt.% SiO_2 and 2 to 10 wt.% $K_2O + Na_2O$. Rhyolites type 2 and 3 are generally weakly altered and their analyses plot mainly in the field for rhyolite. Samples of rhyolite type 4 and hangingwall dacite (types 1 to 3) also plot mainly in the field for rhyolite. These unsystematic variations indicate that original SiO_2, Na_2O and K_2O concentrations were substantially modified during alteration and that geochemical classification based on these major elements in invalid.

Fig. 6.1: Major element geochemistry of Thalanga volcanic units: TAS-diagram, S versus SiO_2 and S versus FeO.

(a) The TAS diagram ($Na_2O + K_2O$ versus SiO_2) is commonly used for the classification of fresh, modern volcanic rocks (Le Maitre et al., 1989). The data for the Thalanga volcanic units show a wide and unsystematic distribution which indicates that alkalis and silica were mobile during alteration.

(b) The effects of hydrothermal alteration on footwall rhyolites are clearly apparent in a diagram of S versus SiO_2. S concentration >0.5 wt.% are common in analyses of rhyolite type 1. The S contents of hangingwall dacites and rhyolite type 4 are generally <0.01 wt.% (detection limit).

(c) The high concentrations of S in altered rhyolite type 1 correlate with the abundance of pyrite observed in drill core and with the measured FeO concentrations. However, elevated FeO values are also related to other alteration processes such as the formation of chlorite.

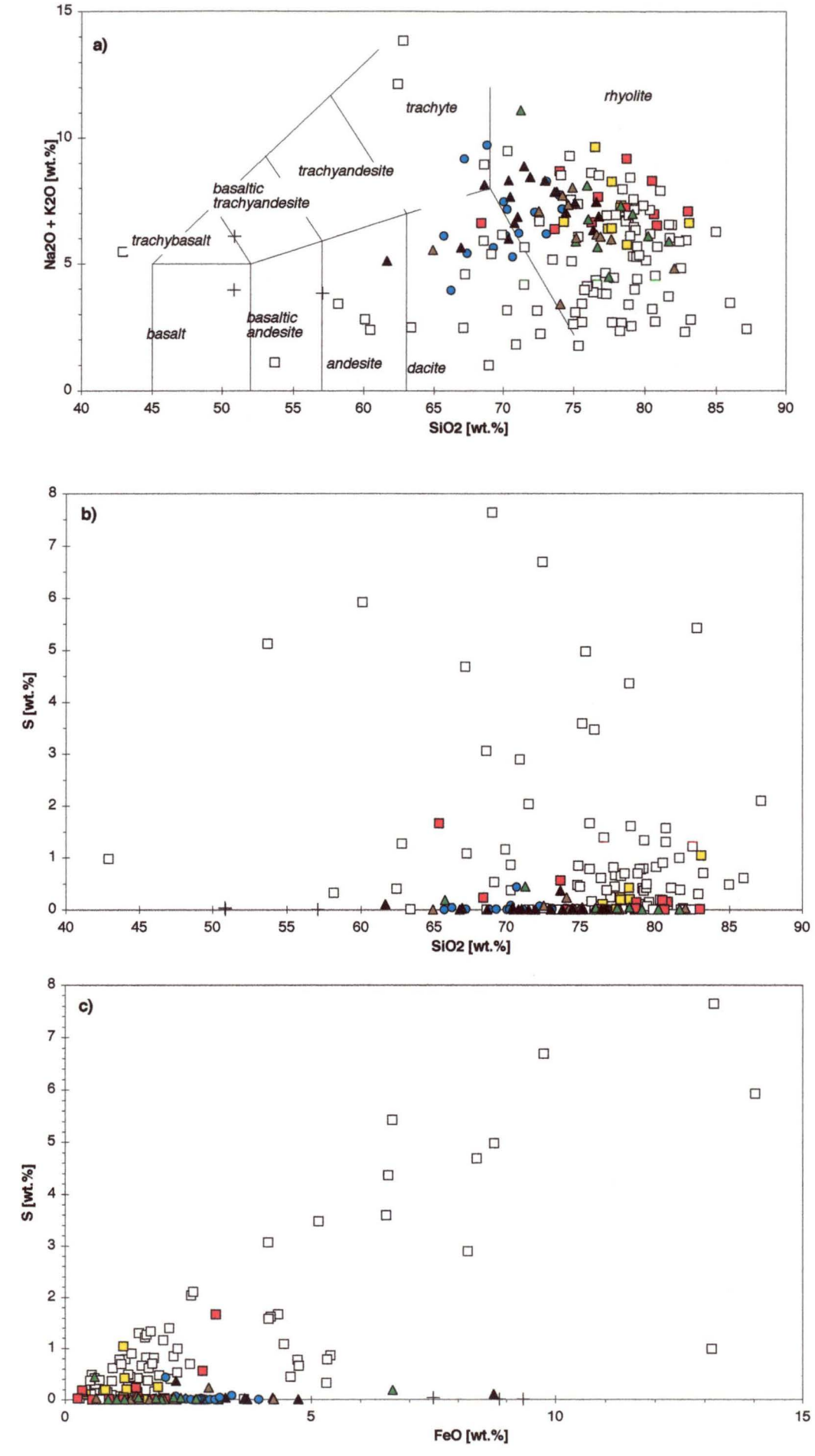
a)
trachyte
rhyolite
trachyandesite
basaltic
trachyandesite
trachybasalt
basaltic
andesite
basalt
andesite
dacite
Na2O + K2O [wt.%]
SiO2 [wt.%]
b)
S [wt.%]
SiO2 [wt.%]
c)
S [wt.%]
FeO [wt.%]
rhyolite 1
rhyolite 2
rhyolite 3
rhyolite 4
dacite 1
dacite 2
dacite 3
andesite

Fig. 6.1

Elevated S concentrations in the footwall rhyolite are a clear indication of substantial geochemical modifications related to hydrothermal activity associated with massive sulphide formation (Fig. 6.1b). Most samples of rhyolite type 1 contain >0.5 wt.% S and values >1 wt.% are common. In contrast, S concentrations in the hangingwall dacite, andesite and rhyolite type 4 are mainly below the detection limit (<0.01 wt. %). Enrichment in S in the footwall alteration zone is reflected by the presence of pyrite and a positive correlation between S and FeO (Fig. 6.1c). However, FeO enrichment is also associated with other alteration processes including the formation of chlorite.

Assuming that least-altered footwall rhyolites had Na_2O concentrations between 3 and 5 wt.%, and MgO contents <0.5 wt.% Figure 6.2a indicates that hydrothermal alteration in the footwall was associated with decreasing concentrations of Na_2O whereas MgO was enriched and values >2 wt.% are common. In contrast, hangingwall dacites are generally Na_2O-rich and their MgO contents are relatively low. The high Na_2O contents of the dacites are coupled with comparatively low K_2O concentrations which is consistent with widespread albite alteration in the hangingwall (Chapters 7 and 8) (Fig. 6.2b). Footwall rhyolites show extreme variability in K_2O concentrations, ranging between 1 and 8 wt.%. Rhyolite type 4 has Na_2O concentrations mainly between 2 and 5.5 wt.% suggesting that changes to their original alkali concentrations were relatively minor.

A diagram comparing total concentration of alkalis (Na_2O + K_2O) with the K_2O ratio ($100*K_2O/[Na_2O + K_2O]$) was developed by Hughes (1973) in order to identify the effects of Na- and K-metasomatism on the geochemical composition of common volcanic rocks (Fig. 6.2c). Hughes (1973) used the term 'metasomatism' to describe geochemical changes during sub-seafloor metamorphism associated with removal and/or introduction of elements; in this sense, 'metasomatism' is essentially synonymous with 'alteration'. The diagram shows a field for fresh igneous rocks with about equally balanced K_2O and Na_2O concentrations. On this diagram, the data from Thalanga are widely spread implying that alkali concentrations of most samples were modified by alteration. Dacites in the hangingwall suffered variable degrees of sodic metasomatism (albite alteration) whereas rhyolites in the footwall experienced potassic metasomatism. However, some samples of each volcanic rock type defined at Thalanga plot within the 'igneous field' and their concentrations of alkalis may approximate the original Na_2O and K_2O values.

Fig. 6.2: Major element geochemistry of Thalanga volcanic units: MgO versus Na_2O, K_2O versus Na_2O and 'Hughes diagram'.

(a) MgO versus Na_2O. Alteration of footwall rhyolites was associated with decreasing Na_2O concentrations and increasing MgO. Rhyolites with 3 to 5 wt.% Na_2O have low MgO values and probably represent least-altered samples. MgO concentrations are low in the hangingwall dacites and Na_2O values range mainly between 4 and 7 wt.%.

(b) Na_2O versus K_2O. High Na_2O concentrations of hangingwall dacites are correlated with low K_2O contents indicating Na-enrichment due to albite formation. Footwall rhyolites show an extremely wide range of K_2O values (1 to 8 wt.%).

(c) Diagram for $K_2O + Na_2O$ versus K_2O ratio ($100 * K_2O/[K_2O+Na_2O]$) ('Hughes diagram'). Analyses of hangingwall dacites plot in the field indicating Na-metasomatism whereas data for footwall rhyolites plot in the field for K-metasomatism and also show a general depletion in alkali elements. Some samples of each volcanic rock type plot within the field for fresh, modern igneous rocks (Hughes, 1973).

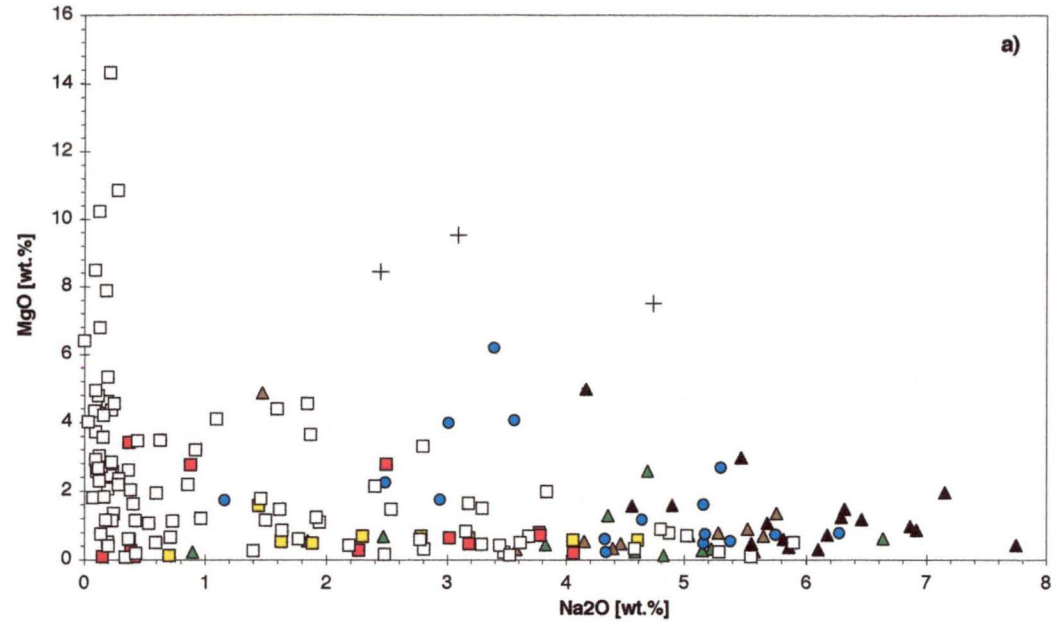

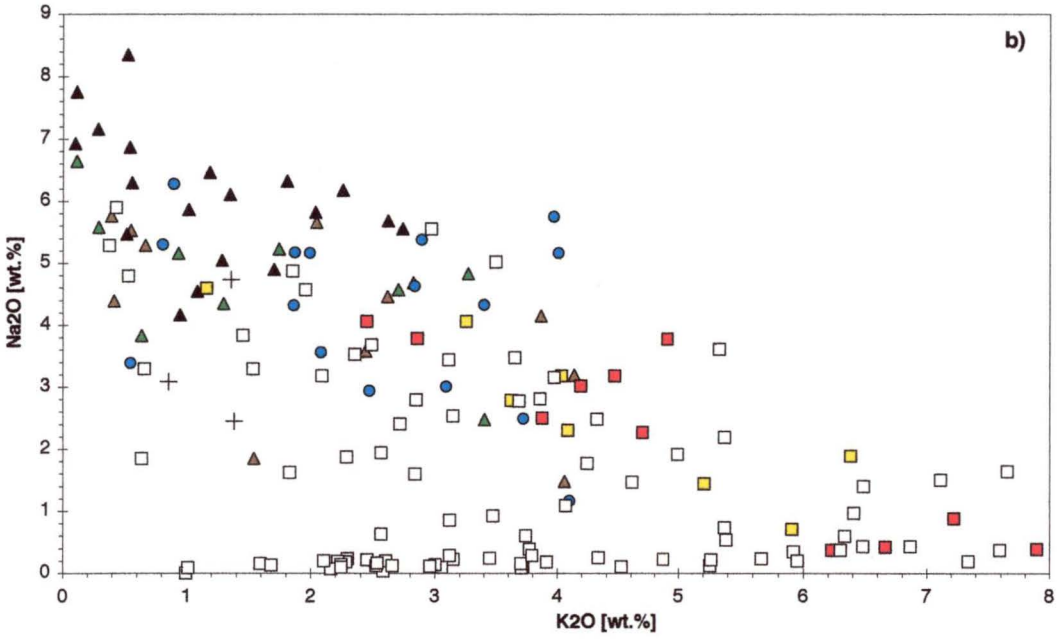

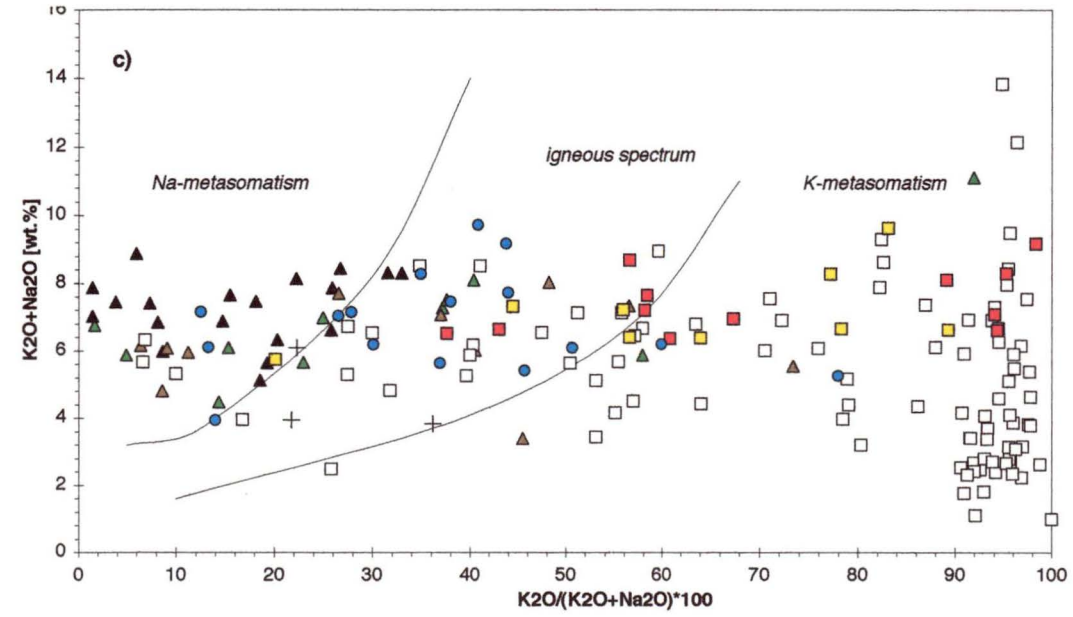

□rhyolite 1 □rhyolite 2 ■rhyolite 3 ●rhyolite 4 ▲dacite 1 ▲dacite 2 ▲dacite 3 +andesite

Fig. 6.2

These variations in the geochemistry of rhyolites and dacites at Thalanga indicate that their major element compositions were variably modified after emplacement. However, footwall rhyolites and hangingwall dacites show different trends in most diagrams indicating that they were affected by different alteration processes. The comparatively high values of S, MgO and FeO in many samples of footwall rhyolite indicate that they were hydrothermally altered during mineralising hydrothermal activity (Reed, 1997; Scott, 1997). In contrast, concentrations of these elements are low in hangingwall dacites which, however, show comparatively elevated Na_2O values. This feature is consistent with albite alteration as a result of sub-seafloor metamorphism (Hughes, 1973; Humphris & Thompson, 1978). The effects of alteration are further examined and discussed in Chapters 7, 8 and 9.

6.2.2 Immobile element geochemistry

In contrast to the wide scatter in the major element data, HFSE of the Thalanga volcanic units show consistent and systematic trends on variation diagrams. This suggests that HFSE were immobile during alteration and metamorphism at Thalanga, as has been found in studies of other VHMS successions (eg. Finlow-Bates & Stumpfl, 1981; MacLean & Kranidiotis, 1987; Barrett & MacLean, 1994b).

Footwall rhyolite, rhyolite type 4 and the different types of hangingwall dacite can be distinguished by their distinctive Ti/Zr ratios (Fig. 6.3a). The data show that rhyolite types 1 to 3 have a consistent Ti/Zr ratio of 4 (Fig. 6.3a; Table 6.1) despite the extreme compositional variability in terms of major elements. The highly correlated positive trend ($r=0.93$), and the fact that the line of best fit passes through the origin of the diagram, indicate that Ti and Zr were immobile during hydrothermal alteration (MacLean & Barrett, 1993; MacLean, 1990). The variations in TiO_2 and Zr concentrations at a constant Ti/Zr ratio are interpreted to result from mass changes associated with removal or addition of mobile components causing relative enrichment or depletion of immobile elements. The amount of mass change can be determined by mass balance calculations which are presented and discussed in Chapter 8.

The Ti/Zr ratios of rhyolite type 4 from the MWF vary between 8 and 12 with an average of ~10 (Table 6.1). In contrast, one sample of rhyolite type 4 from the hangingwall (TCF) has a Ti/Zr ratio of 15.7 (sample TH62C-46). The three petrographically defined types of dacite in the hangingwall have distinct Ti/Zr ratios and show less variability in TiO_2 and Zr concentrations than footwall rhyolite. The positive trends for analyses of dacite type 1 and dacite type 2 are highly correlated and Ti/Zr ratios

Fig. 6.3: Immobile geochemistry of Thalanga volcanic units: TiO_2 versus Zr and Zr/TiO_2 versus Nb/Y.

(a) In a plot of TiO_2 versus Zr, several highly correlated linear trends are apparent. Rhyolite types 1, 2 and 3 have a consistent Ti/Zr ratio of ~4 whereas dacite types 1, 2 and 3 have significantly higher Ti/Zr ratios. These linear trends indicate that TiO_2 and Zr were immobile during alteration and that changes in their concentration at constant Ti/Zr ratio are related to overall mass changes. Andesites have high Ti/Zr ratios which are consistent with their mafic composition.

(b) Fields for altered volcanics on a Zr/TiO_2 versus Nb/Y diagram (Winchester & Floyd, 1977). The data for rhyolite types 1, 2 and 3 plot in the field for rhyolites whereas data for rhyolite type 4 and dacite types 1, 2 and 3 plot in the field for rhyodacite/dacite. Analyses of andesite plot in the field for andesitic and basaltic rocks.

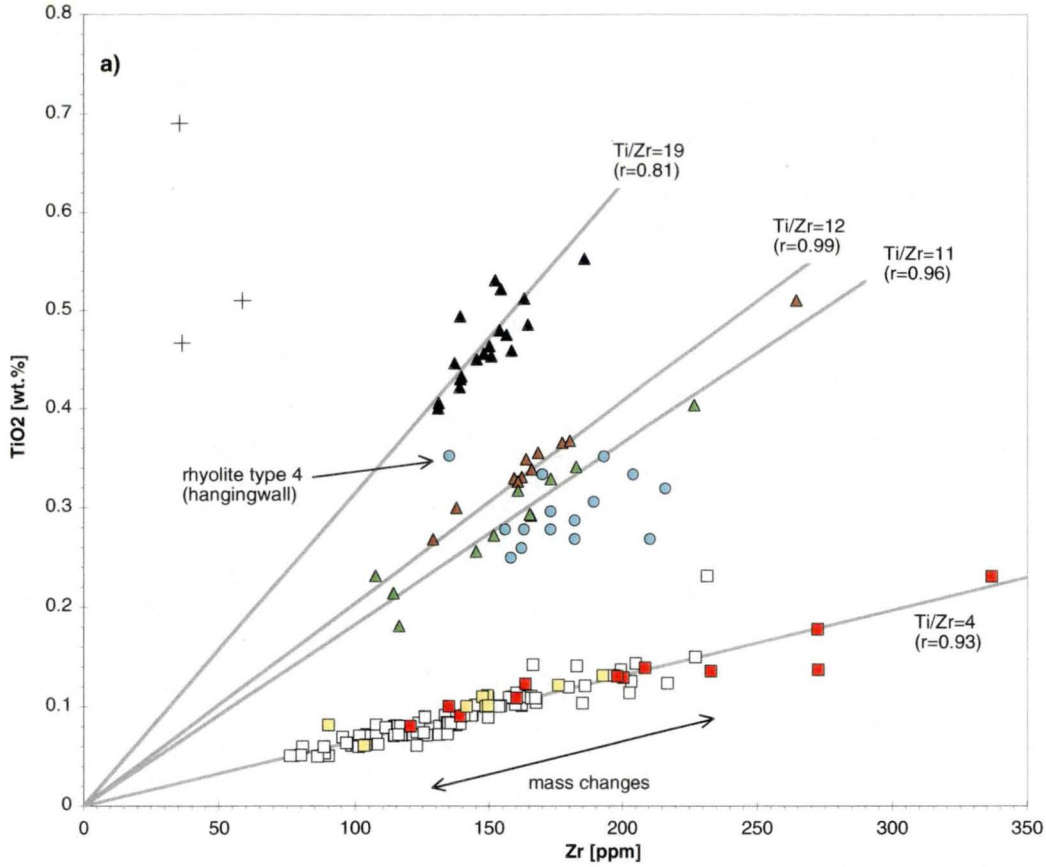

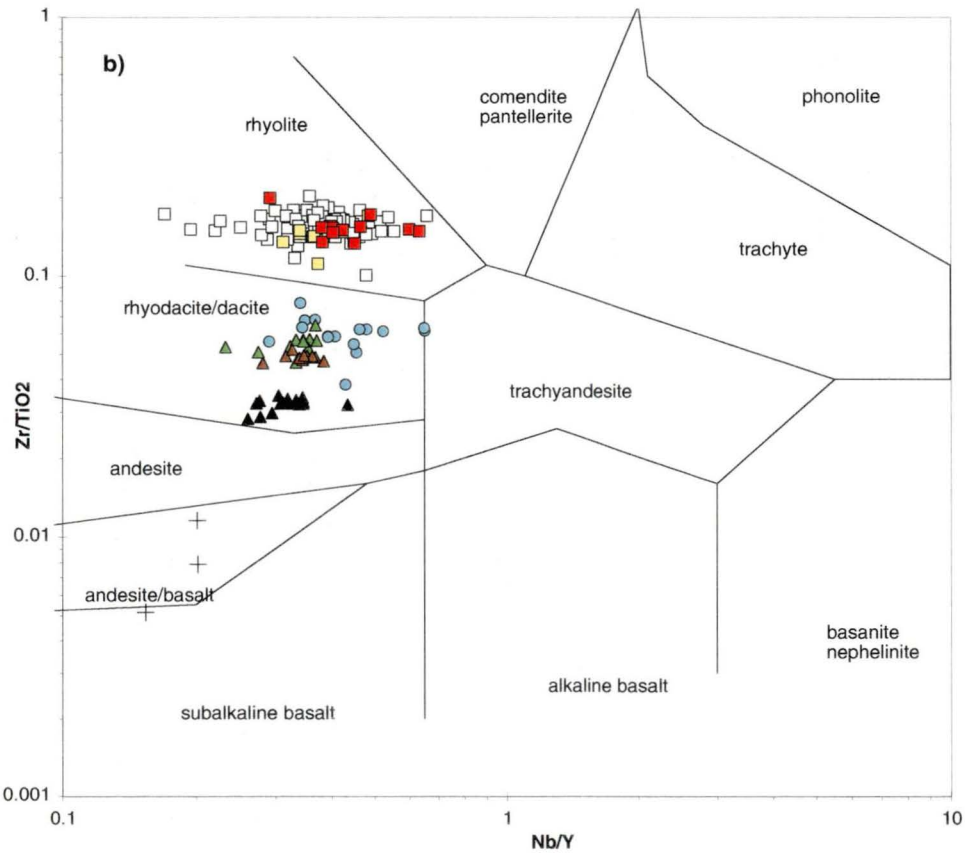

□ rhyolite 1 □ rhyolite 2 ■ rhyolite 3 ○ rhyolite 4 △ dacite 1 △ dacite 2 ▲ dacite 3 + andesite

Fig. 6.3

are fairly similar (12.4 ± 0.4 and 11 ± 1, respectively). In contrast, dacite type 3 contains significantly more TiO_2 and has a higher Ti/Zr ratio (19 ± 1; Table 6.2). Andesites from the hangingwall have the highest Ti/Zr ratios in the Thalanga sequence, consistent with their mafic composition.

A plot of Zr/TiO_2 versus Nb/Y was designed by Winchester & Floyd (1977) in order to distinguish variably differentiated volcanic rocks using HFSE instead of potentially mobile major elements. In this diagram, all the data for footwall rhyolite plot in the field for rhyolite (Fig. 6.3b). Analyses of hangingwall dacite and rhyolite type 4 have lower Zr/TiO_2 than footwall rhyolite and may be classified as rhyodacites or dacites. Andesites plot in the basaltic or andesitic field. All volcanic rocks at Thalanga have low Nb/Y ratios characteristic of subalkaline volcanic suites. This diagram shows that the classification of Thalanga volcanic units based on phenocryst populations is largely consistent with their geochemical signature in terms of HFSE ratios. However, rhyolite type 4 has a somewhat less felsic composition than the footwall rhyolite, even though it contains an extremely high proportion of quartz and feldspar phenocrysts.

On a regional scale, volcanic units belonging to different formations in the Mount Windsor Subprovince can be discriminated in a plot of Th versus TiO_2 (Stolz, 1995). This is also the case for the rhyolites and the dacites in the Thalanga sequence (Fig. 6.4a). Samples of rhyolite types 1, 2 and 3 have relatively low Ti/Th ratios and plot in the field assigned to the MWF whereas hangingwall dacites have Ti/Th ratios characteristic for the TCF. Data for rhyolite type 4 are limited because Th was only rarely analysed by Hill (1996). Most samples have high Th and low TiO_2 concentrations, characteristic of MWF, however, Ti/Th ratios are somewhat elevated compared to footwall rhyolite. One analysis of rhyolite type 4 from the hangingwall (sample TH62C-46) has a Ti/Th ratio comparable to hangingwall dacite and plots in the field for the TCF.

In previous studies concerned with the petrogenesis of VHMS successions, Zr versus Y diagrams have been used to identify volcanic suites with different magmatic affinities (MacLean & Barrett, 1993; Barrett & MacLean, 1997; Lentz, 1998). Data from the Thalanga sequence show significant variability on such a diagram (Fig. 6.4b). Samples of rhyolite type 1 are extremely variable but plot mainly in the tholeiitic field whereas analyses of rhyolite type 2 fall on the boundary between the tholeiitic and transitional fields. Samples of rhyolite type 3 have Zr and Y concentrations which plot exclusively in the transitional field. Samples of rhyolite type 4 have transitional Zr/Y ratios but some data points fall within the calc-alkaline field. Hangingwall dacites have a comparatively restricted range of Zr/Y ratios (~5 to 6) and plot in the transitional field (Table 6.2).

Fig. 6.4: Immobile element geochemistry of Thalanga volcanic units: Th versus TiO_2 and Zr versus Y.

(a) On a regional scale, volcanic units of different formations in the Mount Windsor Subprovince can be distinguished on a Th versus TiO_2 variation diagram (Stolz, 1995). At Thalanga, data for rhyolites plot in the field assigned to MWF rhyolites except for one rhyolite type 4 occurring in the hangingwall which plots in the field for the TCF. Data for dacite types 1, 2 and 3 and andesite plot in the field for the TCF. Note that rhyolite types 1, 2 and 3 have fairly similar, low Ti/Th ratios whereas samples of rhyolite type 4 have somewhat higher values.

(b) Fields assigned to tholeiitic, calc-alkaline and transitional magmatic affinities have been defined by Barrett & MacLean (1997) based on Zr/Y ratios. On a Zr versus Y plot, the data for Thalanga volcanic units show a large spread. Data for rhyolites may indicate that magmatic affinities changed from dominantly tholeiitic for rhyolite type 1 to transitional for rhyolite types 2, 3 and 4. Dacite types 1, 2 and 3 plot in a confined area in the transitional field.

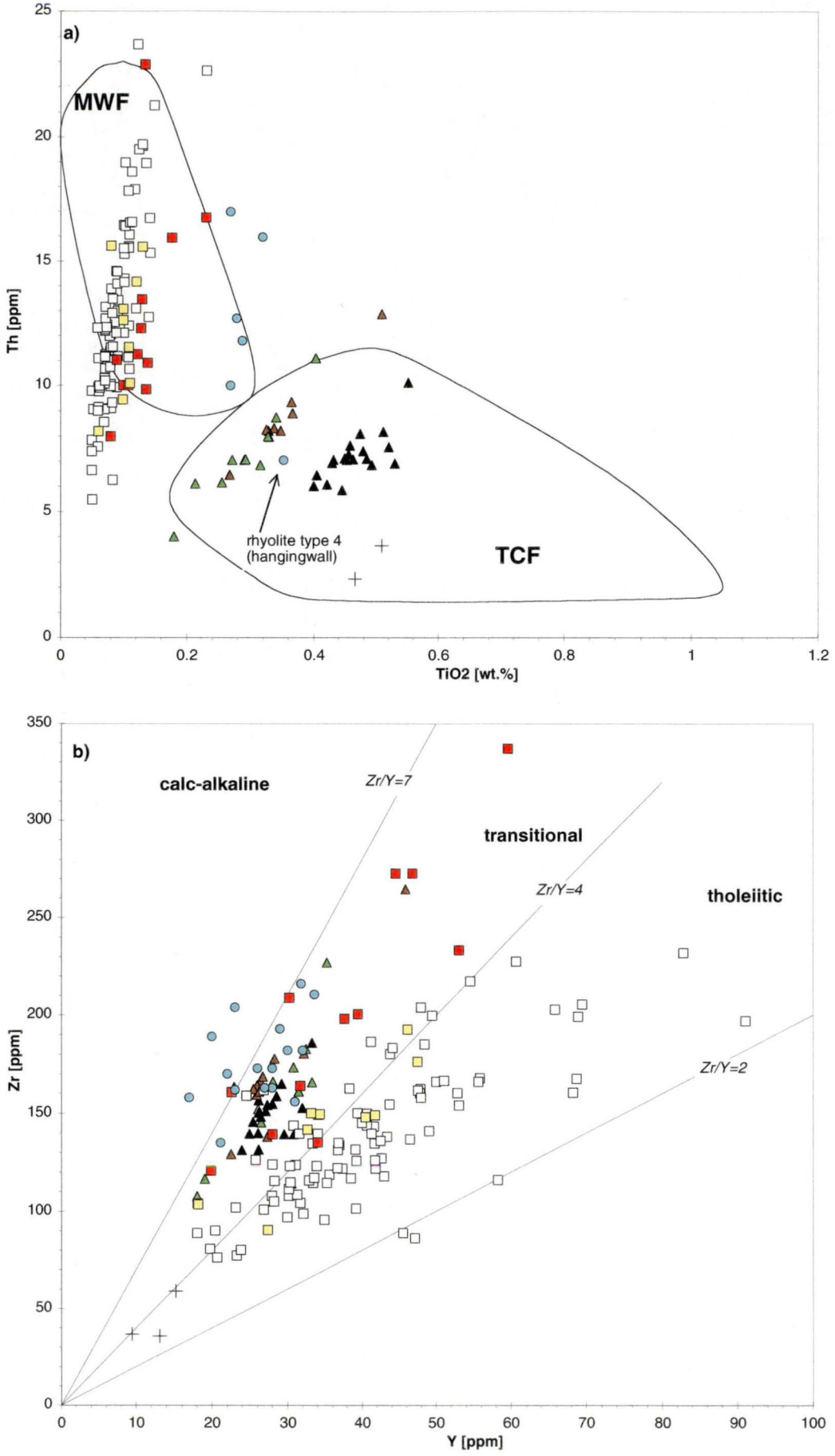
a)
MWF
TCF
rhyolite type 4
(hangingwall)
Th [ppm]
TiO2 [wt.%]
b)
calc-alkaline
transitional
tholeiitic
Zr/Y=7
Zr/Y=4
Zr/Y=2
Zr [ppm]
Y [ppm]
rhyolite 1
rhyolite 2
rhyolite 3
rhyolite 4
dacite 1
dacite 2
dacite 3
andesite

Fig. 6.4

6.2.3 Composition of least-altered rhyolites and dacites

Least-altered samples of the different types of dacite and rhyolite were identified using petrographic and geochemical criteria. Petrographically, rhyolites and dacites with preserved feldspar phenocrysts and quartzofeldspathic groundmasses containing minimal amounts of phyllosilicates were considered as least-altered. This criterion is based on the observation that originally glassy groundmasses in felsic volcanics devitrify to assemblages of quartz and feldspar (Lofgren, 1971; Smith, 1960). However, even though feldspar phenocrysts in the dacites are, in general, texturally unaltered, geochemical analyses indicate that these rocks commonly experienced Na-enrichment (albite alteration) (Fig. 6.2c). Therefore, selection of least-altered samples based on petrographical criteria alone is not sufficient.

Geochemical analyses of least-altered rhyolite are characterised by low MgO contents (< 1 wt.%), low S concentrations (< 0.05 wt.%), low CaO contents (< 2 wt.%) and intermediate K_2O ratios (>25 and <60) which are typical features of fresh, modern felsic volcanic rocks (Le Maitre, 1976). The same criteria were applied to identify least-altered dacite except for a higher level of CaO (< 3 wt.%) to allow for the higher abundance of plagioclase. This selection process showed that 2 to 5 samples of each type of dacite or rhyolite may be regarded as least-altered and averages of these analyses are presented in Tables 6.1 and 6.2. In contrast to the compositional range encompassed by variably altered samples of rhyolite and dacite, the compositions of the least-altered equivalents are typical for common, high-silica, felsic volcanics (ie. high concentrations of SiO_2, K_2O, Na_2O and incompatible trace elements; low concentrations of Fe_2O_3, MgO, CaO and compatible trace elements; Le Maitre et al., 1989).

REE data

The REE data for andesite and least-altered equivalents of the various dacite and rhyolite types were normalised against chondrite and plotted in REE diagrams. In general, REE are considered to be immobile during alteration and low grade metamorphism, however it has been demonstrated that some REE may become mobile under certain conditions in the hydrothermal environment (Campbell et al., 1984; Whitford et al., 1988; MacLean, 1988; Schade et al., 1989; Chapter 8). Here, the data for least-altered samples are presented, in order to examine the primary characteristics of REE patterns and to consider their petrogenetic implications.

Table 6.1: Compositional range of rhyolites in the Thalanga sequence and composition of least altered equivalents

	rhyolite type 1				rhyolite type 2				rhyolite type 3				rhyolite type 4				rhyolite 4 (HW)
	range of analyses	average n=93	standard deviation	least altered 1)	range of analyses	average n=8	standard deviation	least altered 2)	range of analyses	average n=12	standard deviation	least altered 3)	range of analyses	average n=15	standard deviation	least altered 4)	(one analysis)
SiO2 [wt.%]	37.2 to 87.2	75.2	8.1	77.9	74.3 to 83.1	77.9	2.5	78.8	65.3 to 83.0	76.4	5.3	77.3	65.7 to 74.0	70.0	2.6	72.1	74.2
TiO2	0.05 to 0.23	0.09	0.03	0.11	0.06 to 0.13	0.10	0.02	0.10	0.08 to 0.23	0.13	0.04	0.14	0.25 to 0.35	0.29	0.03	0.30	0.35
Al2O3	6.8 to 21.4	12.0	2.8	12.2	8.4 to 15.0	12.0	1.8	11.6	8.3 to 19.6	12.8	3.4	12.3	13.5 to 16.5	14.9	1.0	14.5	13.6
Fe2O3	0.33 to 28.1	3.88	4.93	1.37	0.47 to 2.10	1.38	0.52	1.61	0.29 to 3.42	1.50	1.05	1.52	2.02 to 5.98	3.32	0.94	2.73	2.75
MnO	<0.01 to 0.50	0.06	0.09	0.02	<0.01 to 0.04	0.03	0.01	0.03	<0.01 to 0.10	0.03	0.03	0.03	0.03 to 0.14	0.05	0.03	0.04	0.05
MgO	0.08 to 14.3	2.43	2.51	0.50	0.13 to 1.57	0.66	0.41	0.65	0.10 to 3.40	1.04	1.20	0.56	0.24 to 6.20	1.92	1.69	0.57	0.79
CaO	<0.01 to 13.2	0.73	2.00	0.46	0.03 to 1.44	0.57	0.59	0.44	<0.01 to 1.44	0.39	0.45	0.65	0.92 to 7.20	2.15	1.53	1.53	0.98
Na2O	<0.01 to 5.9	1.38	1.59	4.04	0.71 to 4.59	2.32	1.21	3.51	0.15 to 4.06	2.07	1.53	3.56	1.16 to 5.75	4.12	1.31	5.16	6.27
K2O	0.38 to 13.1	3.81	2.27	3.21	1.16 to 8.0	4.80	2.07	3.12	2.45 to 9.02	5.37	2.03	3.77	0.55 to 4.10	2.64	1.12	3.03	0.90
P2O5	<0.01 to 0.05	0.02	0.01	0.01	0.01 to 0.02	0.02	0.004	0.02	0.01 to 0.06	0.03	0.02	0.02	0.05 to 0.20	0.08	0.04	0.06	0.07
LOI	0.3 to 15.7	2.6	2.5	0.5	0.5 to 1.6	0.8	0.4	0.7	0.4 to 3.8	1.3	1.2	0.7					0.7
S	<0.01 to 18.2	1.71	2.89	0.05	<0.01 to 1.04	0.29	0.36	0.15	<0.01 to 1.66	0.33	0.53	0.06	<0.01 to 0.43	0.08	0.14	0.03	0.01
Ba [ppm]	97 to 23,000	1,515	2,704	559	204 to 1,930	1,134	545	907	388 to 3,200	1,162	867	649	288 to 6,930	1,422	1,593	1183	430
Cu	<1 to 35,120	495	3,712	2	2 to 350	61	121	23	2 to 148	20	42	4	2 to 123	33	45	21	63
Pb	3 to 5,320	157	628	11	5 to 240	51	79	9	5 to 365	46	101	8	6 to 400	61	98	59	10
Zn	8 to 25,000	779	2,947	50	32 to 1,160	189	390	47	6 to 214	70	69	77	42 to 2,300	316	563	154	46
Cr	<1 to 220	7	30	1	<1 to 3	2	1	2	<1 to 6	3	1	<1	2 to 190	56	47	101	3
Nb	8 to 40	15	4	14	9 to 20	13	3	13	12 to 26	16	5	14	9 to 13	11	1	11	9
Ni	<1 to 20	2	2	2	<1 to 2	2	1	1	<1 to 3	2	1	1	3 to 8	5	2	<5	3
Rb	13 to 319	103	56	72	43 to 164	110	39	78	41 to 272	136	65	93					19
Sr	2 to 401	50	54	68	33 to 95	62	24	67	19 to 84	46	19	57					59
Th	5 to 24	13	4	13	8 to 16	13	3	10	8 to 23	13	4	12	10 to 17	13	3	12	7
V	<1 to 38	3	6	<1	<1 to 4	2	1	1	<1 to 1	3	1	<1	14 to 19				31
Y	18 to 91	40	14	36	18 to 48	36	10	33	20 to 60	37	12	39	17 to 34	27	5	24	21
Zr	76 to 232	138	35	157	90 to 193	144	34	138	121 to 337	203	66	218	156 to 216	180	19	177	135
Ag	<0.1 to 54	1.5	6.6	0.1	<0.1 to 0.7	0.2	0.2	<0.1	<0.1 to 0.9	0.2	0.2	0.3	<1				0.2
As	<1 to 64	6.8	10.1	1.9	<1 to 19.2	3.0	6.6	1.1	<1 to 100	11.2	28.1	1.0	<1 to 110	19.0	28.0	14.0	1.4
Bi	<0.1 to 413	7.4	42.8	0.2	<0.1 to 2.2	0.6	0.7	0.3	<0.1 to 6.8	1.0	1.9	1.8	0.2 to 0.5	0.3	0.2	0.3	0.1
Cd	<0.1 to 49	1.9	6.8	0.1	<0.1 to 5.9	1.1	2.0	0.2	<0.1 to 1.7	0.4	0.5	0.6					0.1
Cs	<0.1 to 4.9	1.0	0.9	0.8	0.3 to 1.1	0.6	0.3	0.6	0.2 to 1.9	1.1	0.6	1.0					1.3
Mo	<0.1 to 74	4.4	9.8	0.2	<0.1 to 7.0	2.0	3.0	0.3	0.2 to 31	4.6	9.0	0.5					0.1
Sb	<0.1 to 39	1.0	4.1	0.2	0.2 to 0.9	0.3	0.3	<0.1	<0.1 to 1.5	0.4	0.4	0.3					0.1
Tl	<0.1 to 21	1.6	2.8	0.5	<0.1 to 1.2	0.6	0.4	0.3	0.3 to 8.7	1.8	2.3	0.8					0.1
U	0.8 to 6.2	2.9	1.1	2.3	1.5 to 3.9	2.6	0.7	2.3	2.1 to 5.9	3.4	1.1	3.6					2.6
Ti/Zr	3.0 to 6.0	3.9	0.4	4.1	3.5 to 5.4	4.2	0.5	4.2	3.0 to 4.5	3.9	0.4	3.8	7.6 to 11.8	9.8	1.0	10.2	15.7
Zr/Y	1.8 to 6.4	3.6	0.8	4.6	3.3 to 5.7	4.1	0.8	4.2	4.0 to 7.1	5.5	0.9	5.6	6.3 to 6.8	6.5	0.4	7.6	6.4
Ti/Th	29 to 80	43	9	50	31 to 63	49	9	59	35 to 83	64	13	70	95 to 174	138	31	150	300
Nb/Y	0.17 to 0.66	0.38	0.07	0.41	0.31 to 0.48	0.38	0.05	0.39	0.29 to 0.63	0.44	0.10	0.38	0.29 to 0.65	0.44	0.11	0.48	0.43
K2O-ratio	7 to 100	76	26	44	20 to 89	66	22	47	38 to 98	71	22	51	13 to 78	39	17	37	13
REE:	(20 analyses)				(2 analyses)				(4 analyses)				(3 analyses)				
(La/Yb)N	3.09 to 15.8	6.79	2.80	3.09	3.9 to 7.2			7.2	1.24 to 3.96	3.09		3.96	7.01 to 9.87	8.01		7.1	5.15
Eu/Eu*	0.30 to 0.99	0.51	0.18	0.54	0.40 to 0.45			0.45	0.45 to 0.75	0.58		0.57	0.69 to 0.89	0.78		0.76	0.75

1) average of samples THWH4, THRW9, TH5-339 and TH394-142, REE data of sample THWH4 2) average of samples TH144B-34, TH247-74 and TH148-54, REE data of sample TH148-54 3) average of samples TH410-323, THRW10, THRW8, THRW5 and THRW5, REE data of sample THRW5
4) average of samples APH-28, APH-37, APH-1 and APH-39, REE data of sample APH-39 (from data documented in Hill, 1996 which only included a limited range of trace elements) Data for hangingwall (HW) rhyolite type 4, sample TH62C-46

Table 6.2: Compositional range of dacites in the Thalanga sequence and composition of least altered equivalents

	dacite type 1				dacite type 2				dacite type 3			
	range of analyses	average n=11	standard deviation	least altered 5)	range of analyses	average n=12	standard deviation	least altered 6)	range of analyses	average n=15	standard deviation	least altered 7)
SiO2 [wt.%]	64 9 to 82.0	74 9	3 9	**74.6**	65 7 to 81.7	76.1	4.4	**77.8**	61.7 to 76 8	70 0	3.8	**72.5**
TiO2	0.27 to 0 51	0.35	0 06	**0.35**	0 18 to 0 40	0 28	0 06	**0.32**	0.40 to 0.55	0.47	0.04	**0.49**
Al2O3	10 2 to 18.4	13 0	2.0	**13.0**	10 3 to 14 7	12.0	1 6	**12.1**	12.2 to 16.7	14.1	1 1	**13.9**
Fe2O3	0.71 to 4.72	2 25	1.00	**2.15**	0.67 to 7.40	2.32	1.84	**1.33**	1 41 to 9 71	3.45	1.87	**3.08**
MnO	0 01 to 0.15	0 06	0 04	**0.05**	<0.01 to 0.15	0 05	0.05	**0.01**	0 01 to 0 15	0.05	0.04	**0.04**
MgO	0.29 to 4.85	1 02	1 24	**0.57**	0 13 to 2 57	0 63	0.72	**0.23**	0 29 to 4.97	1.25	1.11	**0 59**
CaO	0.71 to 6 54	2 10	1.70	**1.43**	0.33 to 4.92	1 42	1 67	**0.57**	0 53 to 8 41	1.60	1.77	**0.75**
Na2O	1.47 to 5 76	4 12	1 41	**4.33**	0 89 to 6.64	4 38	1 56	**4.87**	4.16 to 8 35	6.07	1 06	**5.87**
K2O	0 39 to 4.14	2 07	1.41	**3.35**	0 11 to 10.21	2.49	2.82	**2.57**	0.10 to 2 74	1.19	0.81	**2.50**
P2O5	0.05 to 0.09	0 06	0.01	**0.06**	0 03 to 0 06	0 05	0.01	**0.06**	0 09 to 0 13	0.11	0.01	**0.11**
LOI	0.3 to 3.8	1.0	1 0	**0.5**	0 4 to 2 6	1 0	0 8	**0.6**	0.3 to 3.3	1.0	0 8	**0.4**
S	<0.01 to 0.23	0.08	0.09	**<0.01**	<0 01 to 0.44	0 11	0 16	**<0.01**	<0.01 to 0 36	0.07	0.12	**<0.01**
Ba [ppm]	51 to 1,300	490	356	**803**	23 to 8,360	1,250	2,394	**794**	18 to 1,300	508	350	**778**
Cu	2 to 26	6	7	**7**	3 to 46	15	15	**4**	<1 to 149	13	34	**5**
Pb	3 to 118	22	33	**10**	3 to 60	15	16	**7**	4 to 214	28	58	**110**
Zn	16 to 2,740	371	792	**41**	3 to 241	70	66	**46**	17 to 919	142	208	**211**
Cr	2 to 5	3	1	**2**	1 to 4	3	1	**2**	<1 to 4	2	1	**3**
Nb	8 to 15	10	2	**10**	6 to 13	9	2	**11**	7 to 11	9	1	**9**
Ni	<1 to 2	1	1	**<1**	1 to 3	2	1	**2**	<1 to 6	2	1	**1**
Rb	13 to 114	42	27	**54**	3 to 131	52	45	**50**	2 to 59	25	17	**38**
Sr	60 to 143	100	25	**92**	40 to 157	70	36	**45**	47 to 194	99	37	**64**
Th	6 to 13	9	2	**9**	1 to 11	7	3	**8**	6 to 10	7	1	**7**
V	4 to 29	9	7	**8**	2 to 9	5	3	**2**	12 to 41	26	7	**23**
Y	23 to 46	29	6	**27**	18 to 35	28	6	**30**	23 to 148	34	28	**29**
Zr	129 to 265	170	33	**169**	108 to 227	155	35	**174**	131 to 186	150	13	**149**
Ag	<0.1 to 0.9	0.1	0.1	**0.1**	<0 1 to 0 2	0 2	0.0	**0.2**	<0.1 to 0.9	0 2	0 2	**0.2**
As	<1			**<1**	<1 to 13.8	2 4	3 8	**1.0**	0 4 to 1.4	0 9	0.5	**<1**
Bi	<0 1 to 137	16 2	39 8	**<0.5**	<0 1 to 1 2	0.2	0 3	**<0.5**	<0.1 to 1.8	0 2	0.4	**1.0**
Cd	<0 1 to 30	4.0	9.0	**<0.1**	<0 1 to 1.5	0 4	0 5	**0.5**	<0 1 to 3 1	0 6	0.9	**0.7**
Cs	0 3 to 1 9	0.6	0.4	**0.4**	0.2 to 6.9	1 2	1 9	**0.6**	<0.1 to 3 5	0 7	0 8	**0.8**
Mo	<0.1 to 2.1	0.4	0 6	**<0.2**	<0.1 to 0 6	0 2	0 2	**0.3**	<0.1 to 2.0	0 5	0.5	**0.7**
Sb	<0 1 to 0 7	0 3	0.2	**0.3**	<0 1 to 0 6	0 2	0 2	**0.3**	<0 1 to 1 2	0 4	0 3	**0.3**
Tl	<0 1 to 1 0	0.3	0 3	**0.4**	<0 1 to 1 4	0.4	0.5	**0.3**	<0.1 to 0.8	0.3	0.3	**0.3**
U	1 4 to 2.9	2 1	0 5	**2.1**	1 3 to 2.7	1.9	0.4	**2.0**	0.7 to 3 5	1 7	0 6	**1.5**
Ti/Zr	11.6 to 13.0	12.4	0 4	**12.4**	9 3 to 12 9	11 0	0 9	**11.0**	17 4 to 21 3	18 7	1.0	**19.7**
Zr/Y	5.0 to 6 4	6 0	0 4	**6.3**	3 7 to 6 4	5 5	0.7	**5.7**	0 9 to 7 1	5 3	1 2	**5.2**
Ti/Th	235 to 255	244	6	**245**	210 to 1380	347	343	**244**	328 to 462	393	34	**421**
Nb/Y	0 28 to 0 39	0.34	0 03	**0.37**	0 23 to 0 37	0 33	0 04	**0.35**	0.06 to 0.44	0.31	0.07	**0.30**
K2O-ratio	6 to 73	33	21	**44**	2 to 92	32	26	**34**	1 to 33	16	10	**30**
REE:	(5 analyses)				(1 analysis)				(3 analyses)			
(La/Yb)N	3.52 to 16 8	7 61	5.38	**6.84**				**2.41**	2 47 to 4 29	3 43		**3.54**
Eu/Eu*	0.63 to 0.76	0.70	0 06	**0.66**				**0.87**	0 75 to 0.77	0 76		**0.77**

5) average of samples TH382A-356, TH401-89 and TH402-321, REE data of sample TH382A-356 6) average of samples TH28-139, TH28-304 and THFH4, REE data of sample TH28-304
7) average of samples TH10-17 and TH85-41 5, REE data of sample TH38-421

The petrologically most important features of chondrite-normalised REE diagrams for volcanic rocks are: the concentration of REE compared to the chondrite standard, the shape of the REE pattern (indicating relative enrichment or depletion of light, middle or heavy REE), and the presence or absence of a negative Eu anomaly. These features are interpreted to be controlled by the mineralogical composition of the magma source, conditions during partial melting and fractionation processes associated with magma evolution (Wilson, 1989; Rollinson, 1993).

Least-altered samples of rhyolite types 1, 2 and 3 have very similar REE patterns showing light REE (LREE) enrichment (La = 80 to 100 x chondrite, Fig. 6.5a) suggesting that they were derived from a single parental magma. These rhyolite types also have a pronounced negative Eu anomaly that may be related to fractional crystallisation of feldspar or to a process of partial melting during which feldspar was retained in the magma source. The REE pattern for rhyolite type 4 shows light REE enrichment of a similar magnitude but only a comparatively small negative Eu anomaly.

Andesite has a relatively low total REE content (La = 10 x chondrite) and is characterised by a smooth pattern with minor LREE enrichment. This is similar to the characteristics of mafic volcanics in the TCF on a regional scale (Stolz, 1995). Dacite types 2 and type 3 have higher concentrations of REE (La = 30 x chondrite) and their patterns are essentially parallel to the one for andesite except for a small negative Eu anomaly. In contrast, REE data for dacite type 1 show a comparatively large range in $(La/Yb)_N$-values (3.5 to 16.8, Table 6.2), a measure of LREE enrichment, and the pattern for least-altered dacite type 1 shows high LREE concentrations (La = 100 x chondrite).

The REE patterns of dacite types 2 and 3 suggest that these felsic volcanic units evolved from a mafic parental magma by fractional crystallisation. The small negative Eu anomaly of dacites is an indication of minor feldspar fractionation during magma evolution. The strong LREE enrichment of dacite type 1, which is comparable to the LREE enrichment observed for rhyolites of the MWF, may indicate that this magma was influenced by interaction with the continental crust.

Fig. 6.5: Chondrite-normalised REE pattern for andesite and least-altered felsic volcanic units of the Thalanga sequence.

Chondrite composition from Boynton (1984), as reported in Rollinson (1993).

(a) REE patterns of least-altered rhyolite types 1, 2, 3 and 4.

(b) REE patterns of andesite and least-altered dacite types 1, 2 and 3.

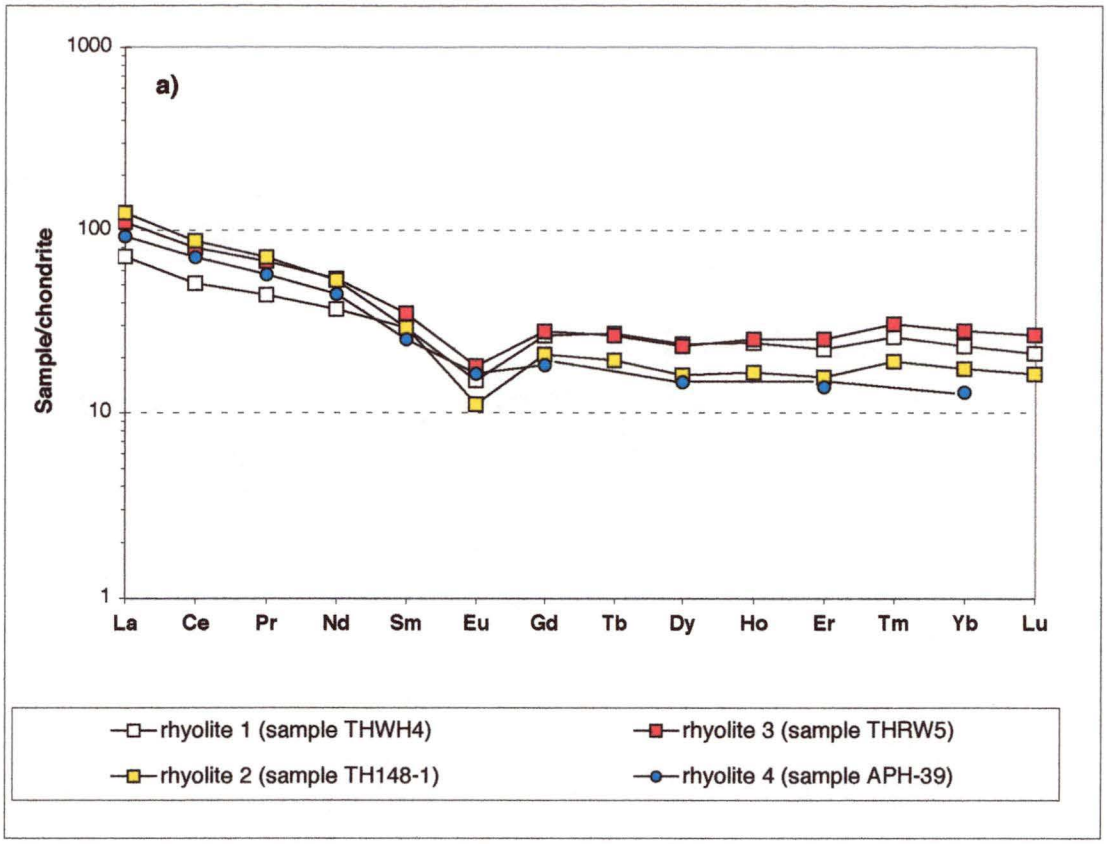
a)
1000
100
10
1
Sample/chondrite
La
Ce
Pr
Nd
Sm
Eu
Gd
Tb
Dy
Ho
Er
Tm
Yb
Lu
rhyolite 1 (sample THWH4)
rhyolite 3 (sample THRW5)
rhyolite 2 (sample TH148-1)
rhyolite 4 (sample APH-39)

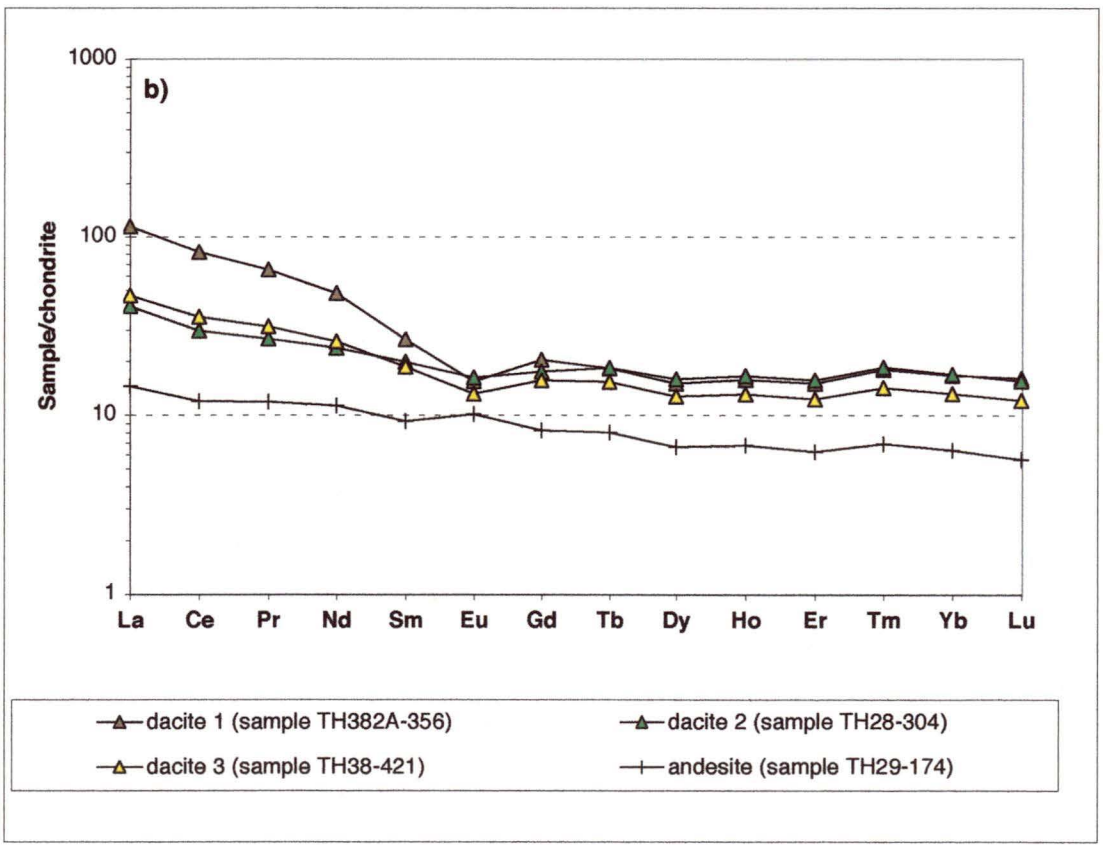
b)
1000
100
10
1
Sample/chondrite
La
Ce
Pr
Nd
Sm
Eu
Gd
Tb
Dy
Ho
Er
Tm
Yb
Lu
dacite 1 (sample TH382A-356)
dacite 2 (sample TH28-304)
dacite 3 (sample TH38-421)
andesite (sample TH29-174)

Fig. 6.5

Spiderdiagrams

Normalised multi-element diagrams (spiderdiagrams) are commonly used to compare the concentrations of large ion lithophile elements (LILE), HFSE and REE in mafic volcanics with the composition of the primitive, undifferentiated mantle or normal mid-ocean ridge basalt (N-MORB) (eg. Pearce, 1983). Spiderdiagrams comparing the composition of Thalanga volcanic units to N-MORB and the composition of the lower continental crust (LCC) (Wedepohl, 1995) are presented in Figures 6.6 and 6.7.

All four rhyolite types show very similar patterns on the N-MORB normalised spiderdiagram (Fig. 6.6a). The LILE (Rb, Ba and K) and light REE are strongly enriched compared to N-MORB. Some HFSE and heavy REE are moderately enriched; Y and Yb concentrations are similar in the rhyolites and N-MORB. Troughs exist for Nb, Sr, P and Ti with particularly strong relative depletion of P and Ti in rhyolite types 1, 2 and 3.

The pattern for andesite in the N-MORB normalised diagram is relatively smooth but shows marked troughs for Th and Nb (Fig. 6.6b). Concentrations of heavy REE, Ti, Zr and P are lower than in N-MORB. These features are similar to the patterns of other mafic volcanics in the TCF on a regional scale and comparable to the geochemical signatures of many modern, subduction-related, back-arc basalts (Stolz, 1995). The spiderdiagrams for dacite type 1, 2 and 3 are broadly similar and have ragged shapes with pronounced troughs for Sr, P and Ti. A minor negative deflection exists for Nb for dacite types 2 and 3 whereas dacite type 1 shows a significant trough for Nb due to its comparatively high concentrations of La and Ce.

All four rhyolite type are largely similar to the LCC for most elements (Fig. 6.7a). However, Sr, P and Ti are relatively depleted, especially in rhyolite types 1, 2 and 3. In contrast, the data for andesite show consistently lower concentrations than LCC with a somewhat irregular pattern (Fig. 6.7b). The dacites show generally similar patterns to those of the rhyolites, with less strongly developed troughs for P and Ti. However, dacite types 2 and 3 have relatively low LREE (La and Ce) contents compared to the LCC (Fig. 6.7b).

Fig. 6.6: Spiderdiagrams for andesite and least-altered felsic volcanic units of the Thalanga sequence normalised to the composition of N-MORB.

N-MORB composition from Saunders and Tarney (1984), as reported in Rollinson (1993).

(a) Spiderdiagrams of least-altered rhyolite types 1, 2, 3 and 4.

(b) Spiderdiagrams of andesite and least-altered dacite types 1, 2 and 3.

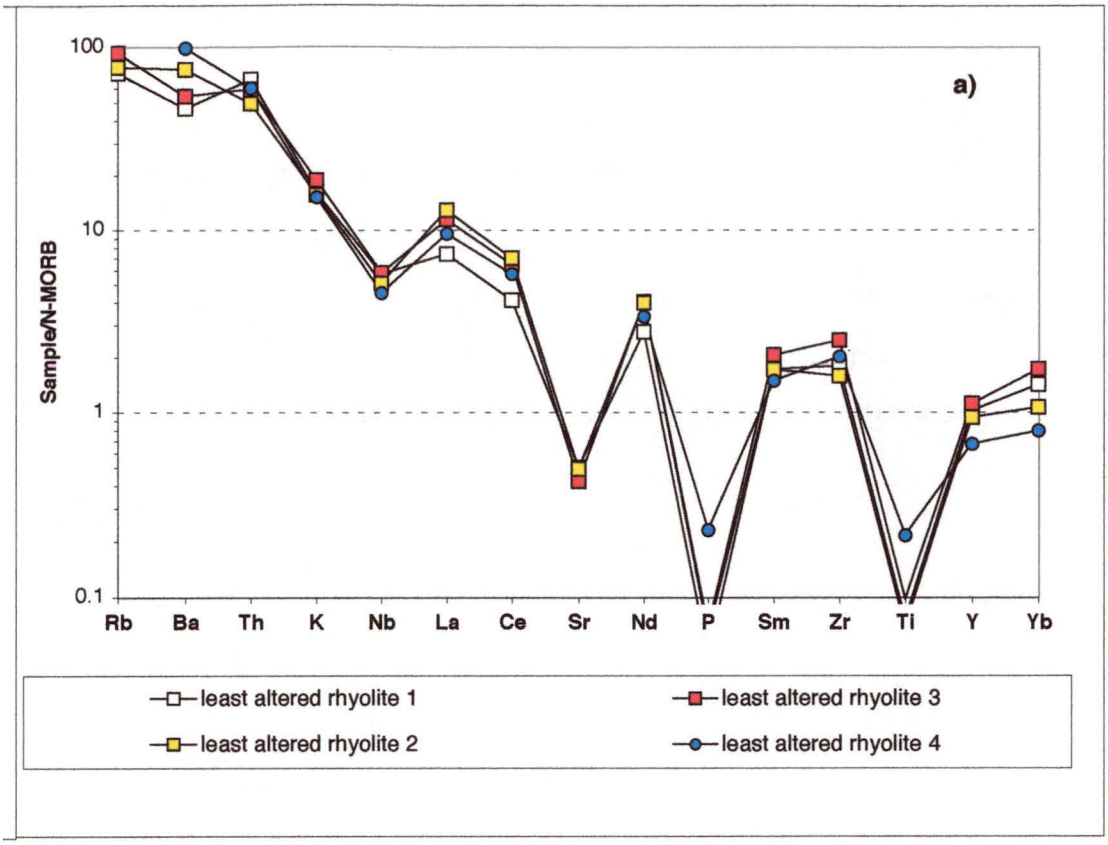
a)
100
10
1
0.1
Sample/N-MORB
Rb
Ba
Th
K
Nb
La
Ce
Sr
Nd
P
Sm
Zr
Ti
Y
Yb
least altered rhyolite 1
least altered rhyolite 3
least altered rhyolite 2
least altered rhyolite 4

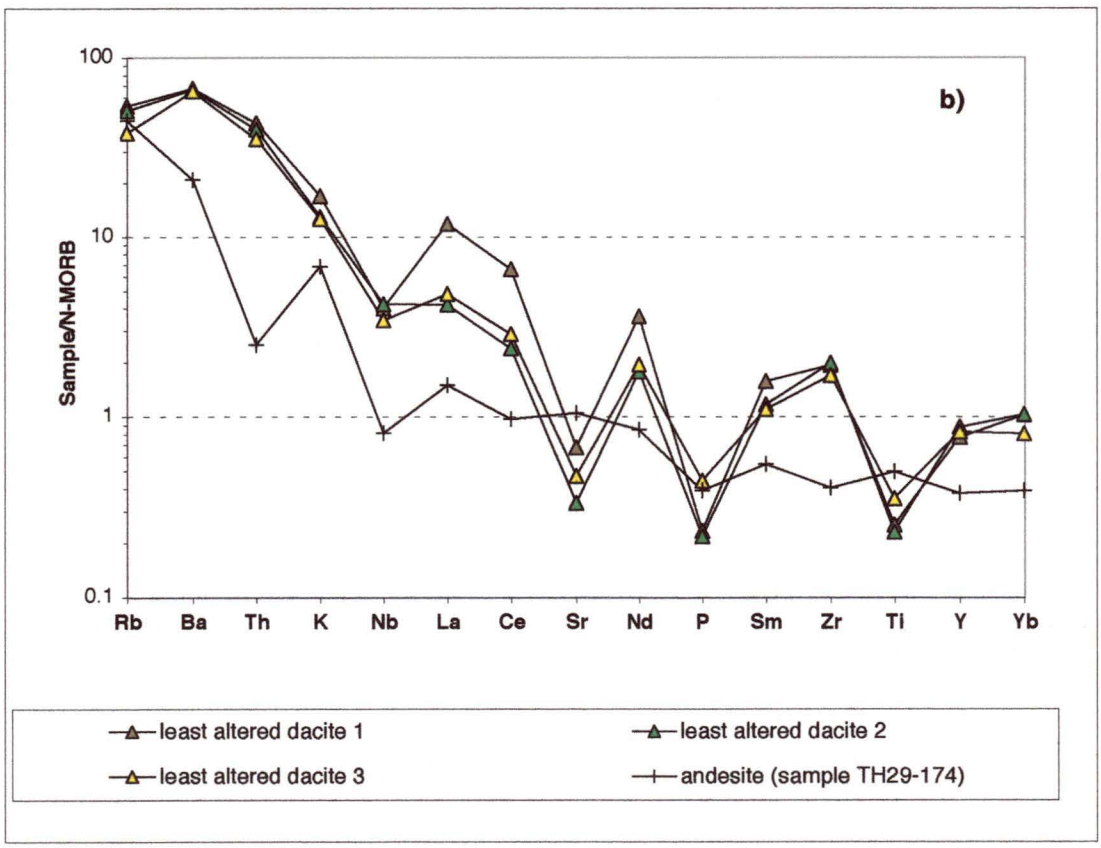
b)
100
10
1
0.1
Sample/N-MORB
Rb
Ba
Th
K
Nb
La
Ce
Sr
Nd
P
Sm
Zr
Ti
Y
Yb
least altered dacite 1
least altered dacite 2
least altered dacite 3
andesite (sample TH29-174)

Fig. 6.6

Fig. 6.7: Spiderdiagrams for andesite and least-altered felsic volcanic units of the Thalanga sequence normalised to the composition of the lower continental crust.

Lower continental crust (LCC) composition from Wedepohl (1995).

(a) Spiderdiagrams of least-altered rhyolite types 1, 2, 3 and 4.

(b) Spiderdiagrams of andesite and least-altered dacite types 1, 2 and 3.

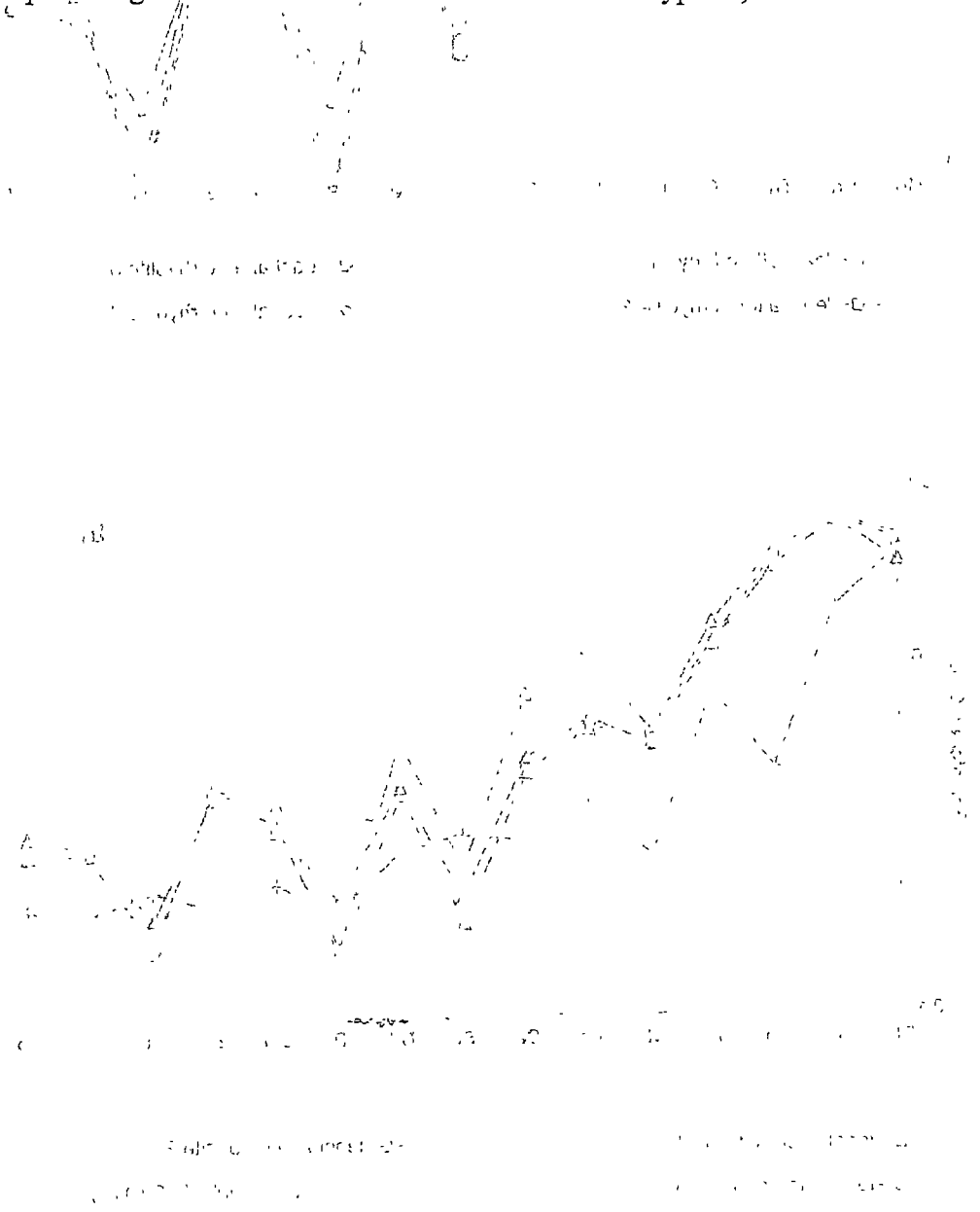

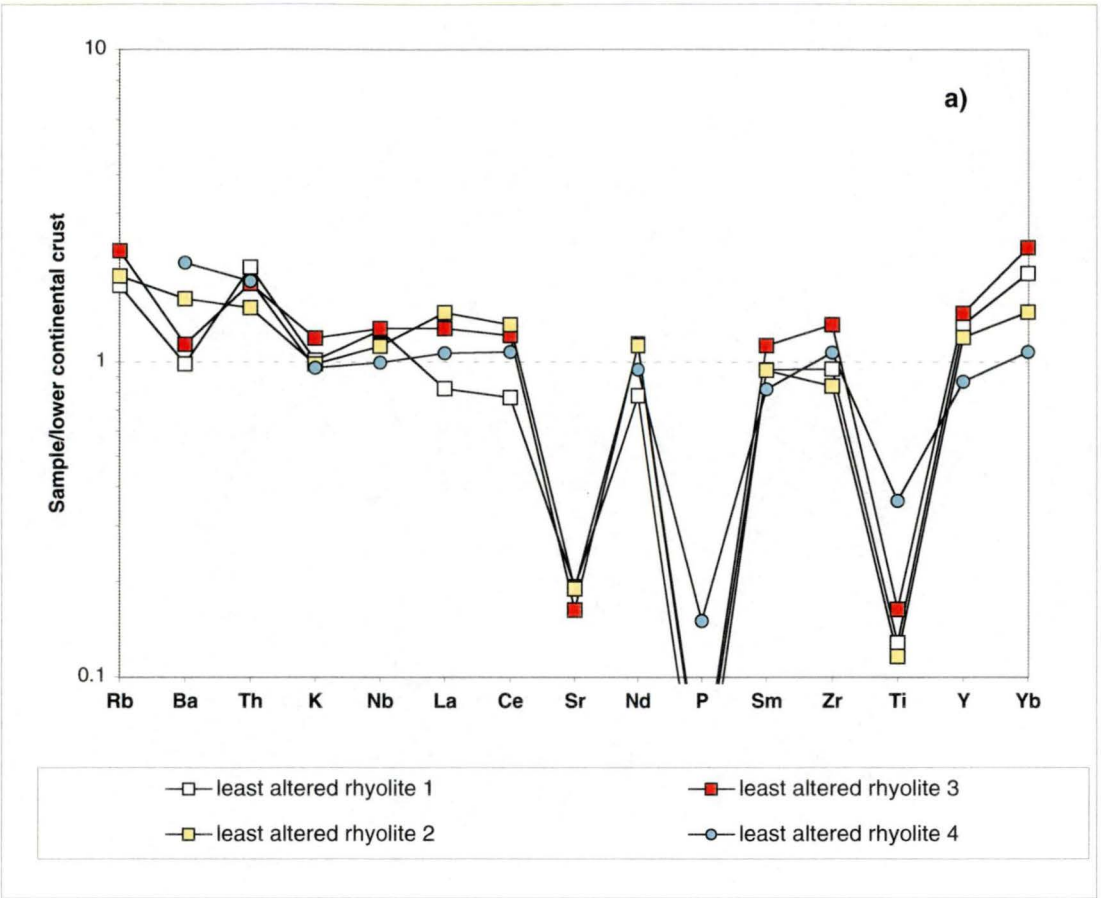
a)
10
1
0.1
Sample/lower continental crust
Rb
Ba
Th
K
Nb
La
Ce
Sr
Nd
P
Sm
Zr
Ti
Y
Yb
least altered rhyolite 1
least altered rhyolite 3
least altered rhyolite 2
least altered rhyolite 4

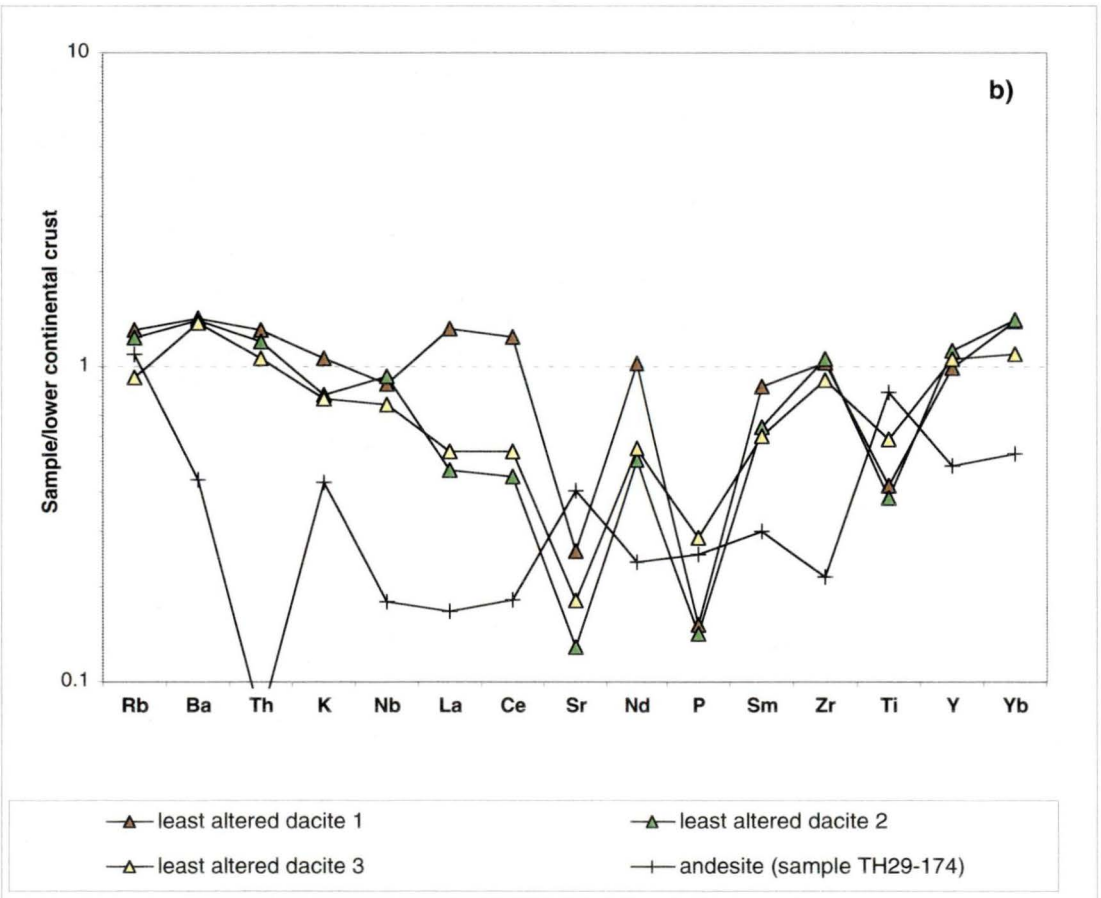
b)
10
1
0.1
Sample/lower continental crust
Rb
Ba
Th
K
Nb
La
Ce
Sr
Nd
P
Sm
Zr
Ti
Y
Yb
least altered dacite 1
least altered dacite 2
least altered dacite 3
andesite (sample TH29-174)

Fig. 6.7

6.3 Discussion

6.3.1 Comparison of geochemical characteristics and petrogenetic implications

The presented data show that the volcanic units of the Thalanga sequence have a number of important, primary geochemical features. These are generally consistent with the current model for the tectono-magmatic evolution of the Mount Windsor Subprovince (Stolz, 1995). The immobile element composition and the REE characteristics of footwall rhyolites and hangingwall dacites are similar to felsic volcanic rock of the MWF or the TCF on a regional scale. However, rhyolite type 4 in the Favourable Horizon (MWF) shows Ti/Zr-, Ti/Th-ratios which are intermediate between the values for footwall rhyolites and hangingwall dacites.

The quartz ± feldspar-phyric, highly siliceous footwall rhyolites in the Thalanga sequence belong to the regionally extensive, rhyolitic MWF which has been derived from extensive melting of continental lithosphere (Stolz, 1995). They are characterised by low Ti/Zr and Ti/Th ratios and have pronounced negative Eu anomalies. Their composition in terms of LILE, HFSE and REE is similar to the LCC except for strong relative depletion of Sr, P and Ti. These features could be interpreted as evidence for feldspar, apatite and Ti-oxide or Ti-Fe-oxide crystal fractionation or formation of a restite containing these minerals in the magma source.

In general, immobile element data indicate that the primary geochemical composition of footwall rhyolite was fairly homogeneous. However, differences in Zr/Y ratios among the rhyolite types suggest minor variations in magma genesis and evolution. It is possible that some of the variability in the Zr versus Y plot (Fig. 6.4b) is related to minor mobility of Y during alteration, however, the systematic differences in Zr/Y ratios between distinctive rhyolite types suggest that the variations reflect primary compositional features. Furthermore, Zr/Y ratios of least-altered equivalents conform with the general trends described above (Table 6.1). Consequently, the changes in the Zr/Y ratio of rhyolites probably result from compositional differences in the crustal magma source, variations in the degree of partial melting, differences in the mineralogical composition of the restite or processes related to magma evolution (assimilation, fractionation, magma mixing).

Samples of rhyolite type 4 have significantly higher Ti/Zr ratios than rhyolite types 1, 2 and 3 and are less SiO_2 -rich (72 wt.%, Table 6.1) than least-altered samples of the other rhyolite types. Furthermore, the coarse quartz phenocrysts of rhyolite type 4 show abundant resorption textures indicative of disequilibrium between the melt and quartz whereas quartz phenocrysts in rhyolite types 1, 2 and 3 are euhedral (Fig. 5.1).

These observations indicate that the petrogenetic evolution of rhyolite type 4 was different from that of the other rhyolite types.

On a regional scale, geochemical and isotopic data indicate that the mafic to felsic volcanic units of the TCF belong to one co-magmatic suite derived from an asthenospheric mantle source (Stolz, 1995). However, Nd-isotope evidence also show that some felsic members of the suite were variably contaminated through interaction with the continental crust. The REE data for hangingwall dacites at Thalanga are consistent with this model.

Dacite types 2 and 3 have REE pattens similar to those of andesite but show minor negative Eu anomalies and higher overall REE concentrations. Assuming that the andesite and dacite represent different stages of magmatic evolution, these REE patterns suggest that olivine, pyroxene and plagioclase were involved in fractional crystallisation. These minerals have small partition coefficients for REE elements, except Eu which is highly compatible in plagioclase. Dacite type 1 shows strong enrichment of LREE whereas the concentrations of heavy REE are similar to the values for dacite types 2 and 3. This LREE enrichment could be the result of interaction with continental crust similar in composition to the source of footwall rhyolites.

6.3.2 Speculation on the petrogenetic evolution of volcanic units in the Thalanga sequence

The primary geochemical characteristics of the footwall rhyolites show that they represent a compositionally largely homogeneous group. Nevertheless, the consistent petrographic differences in quartz and feldspar phenocryst abundance and size range among the rhyolite types 1, 2 and 3 indicate that they were derived from separate magma batches. These rhyolitic magmas, with distinctive phenocryst populations, may have evolved in a magma chamber that was periodically replenished with new batches of crustal melts. In this model, periodic eruption of rhyolite would successively tap magmas with slightly different phenocryst content giving rise to the different rhyolite types observed. In a similar fashion, the differences in Zr/Y ratio among the rhyolites could be related to variations in the composition of magmas supplied or compositional evolution within the magma chamber.

It is possible that towards the end of rhyolitic volcanism, abundant, coarse quartz and feldspar phenocrysts accumulated in the gradually cooling, residual magma. This highly viscous phenocryst-rich magma would be expected to have a bulk rock composition broadly similar to, or somewhat more felsic than, the composition of

previously erupted rhyolites type 1, 2 and 3. However, the data for least-altered rhyolite type 4 show that the groundmass probably has a relatively mafic composition and textural evidence indicates disequilibrium between quartz phenocrysts and melt. The SiO_2 content of the groundmass can be estimated by a simple calculation. Assuming that 25 vol.% of the rock is represented by quartz phenocrysts (100 wt.% SiO_2) and 25 vol.% by K-feldspar (65 wt.% SiO_2) the remaining 50 vol.% of groundmass must have a SiO_2 concentration of about 62 wt.% in order to obtain the total of 72 wt.% given by bulk rock analyses of least-altered rhyolite type 4 samples. This suggests that rhyolite type 4 may have been derived from a slightly different source or evolved following a different fractionation path than rhyolite type 1, 2 and 3. Further study, including analyses of melt inclusions in quartz phenocrysts and geochemical and isotopic analyses of groundmass separates are required in order to elucidate the petrogenesis of rhyolite type 4.

The geochemical features of hangingwall dacite and andesite indicate that they were derived from a different source than the rhyolites (asthenospheric mantle, Stolz, 1995). The shapes of REE patterns of dacite types 2 and 3 and andesite are similar except for the small, negative Eu anomaly present in the dacites. These features are consistent with a model involving fractional crystallisation of common crystal phases such as olivine, pyroxene and feldspar from a mafic parental magma. However, dacite type 1 probably experienced significant interaction with continental crust leading to variable enrichment of LREE. The aphyric texture of dacite type 1 suggests that the magma was relatively hot and/or vapour-rich compared to dacite types 2 and 3, and may have more readily assimilated country rocks.

The Z/Y ratios of hangingwall dacites and footwall rhyolites are <7 which is characteristic for volcanic sequences with tholeiitic or transitional magmatic affinities (Barrett & MacLean, 1997; Lentz, 1998). This is consistent with the interpretation of an extensional tectonic regime which has been previously proposed for the Mount Windsor Subprovince (Stolz, 1995). It is also similar to the Zr/Y values of other VHMS-hosting volcanic successions and satisfies one of the criteria for prospective volcanic belts suggested by Lentz (1998).

6.4 Summary

The Thalanga sequence is dominated by felsic volcanic units belonging to the MWF and TCF. The original bulk rock compositions have been significantly modified due to alteration. However, immobile elements and the composition of least-altered samples can be used to characterise the primary geochemistry of the Thalanga volcanic units. Importantly, immobile element ratios, such as Ti/Zr and Ti/Th, allow discrimination of different types of volcanics in the Thalanga sequence and immobile element ratio plots show that geochemical classification based on HFSE conforms with the field classification based on phenocryst populations.

The immobile element data and the composition of least-altered samples indicate that rhyolite types 1, 2 and 3 in the MWF represent a compositionally homogeneous group. However, variations in Zr/Y ratios suggest that minor primary compositional differences existed which could be related to magma genesis or magma evolution. It is suggested that the petrographically distinct rhyolite types 1, 2 and 3 are related to the periodic tapping of a magma chamber which evolved texturally and in terms of Zr and Y content.

REE data imply that hangingwall dacites may have evolved from a mafic parent magma by fractional crystallisation of olivine, pyroxene and plagioclase. However, LREE enrichment of dacite type 1 suggests that interaction of dacite magma with continental crust may have also occurred. This interpretation is consistent with Nd-isotope data for other felsic volcanic units in the TCF presented by Stolz (1995) which suggest that fractionation was typically associated with assimilation of continental crust.

7 Alteration and alteration facies

7.1 Introduction

In this chapter, the effects of alteration on the mineralogy and texture of footwall rhyolite and hangingwall dacite are examined and several alteration facies are defined based on dominant mineral assemblages and alteration intensity. These modifications may represent the result of a combination of processes, including diagenesis, sub-seafloor metamorphism and hydrothermal alteration associated with the formation of massive sulphides, that overprinted the various lithofacies in the Thalanga sequence after deposition. It is inferred that hydrothermal activity related to mineralising processes generated the moderate to intense alteration facies defining the footwall alteration zone below the Thalanga deposit. Weak alteration facies are common in the hangingwall dacites and the processes responsible for their formation are discussed in Chapter 9.

Alteration of host rocks is an integral part of hydrothermal processes associated with the formation of VHMS deposits. Chemical processes during fluid/rock interaction are complex and often result in substantial compositional and textural modifications. Hydrothermal alteration involves reactions of the fluid with the glassy or partially devitrified groundmass of volcanic rocks and destruction of phenocrysts such as plagioclase, alkali feldspar, pyroxene or olivine. Chemical components of the hydrothermal fluid may be incorporated into secondary, hydrothermal minerals such as chlorite, illite, smectite or other clay minerals which may form at the expense of volcanic glass, phenocrysts or crystalline groundmass. Hydrothermal processes are controlled by a number of variables including composition and mineralogy of the rock, characteristics of the fluid (eg. composition, pH, fO_2), temperature, pressure and water to rock ratio.

Commonly observed alteration assemblages in host successions of VHMS deposits may be referred to as sericitic, chloritic, silicic or carbonate alteration depending on the predominant hydrothermal minerals (Thompson & Thompson, 1996). At Thalanga, the altered rocks have been affected by upper greenschist facies metamorphism and converted to a variety of assemblages including muscovite-chlorite-biotite, tremolite-chlorite-calcite and albite-epidote-actinolite. These mineral assemblages represent the metamorphic equivalents of minerals formed during alteration. A discussion concerning the possible precursors of the various metamorphic assemblages in the Thalanga sequence is presented in Chapter 3 with a summary provided in Table 3.1.

The broad (~3,000 m along strike), phyllosilicate-rich and feldspar-destructive alteration zone below the Thalanga deposit is texturally, mineralogically and geochemically complex and extends at least 300 m stratigraphically into the footwall.

Contacts with the surrounding, least-altered rhyolite are gradational. The strata-bound or semi-conformable geometry of the Thalanga footwall alteration zone contrasts with discordant alteration pipes found beneath some Archean VHMS deposits in Canada (Hutchinson et al., 1982; Barrett & MacLean, 1994a), the Tertiary Kuroko deposits in Japan (Ohmoto & Skinner, 1983) and the Hellyer deposit in western Tasmania (Gemmell & Large, 1992). However, footwall alteration zones of several other Australian volcanic-hosted massive sulphide (VHMS) deposits are strata-bound or semi-conformable (Large, 1992). Examples of sheet-style VHMS deposits with strata-bound footwall alteration zones include the Rosebery, Mount Chalmers, Que River, Woodlawn and Thalanga deposits (Large, 1992).

In this chapter, the mineralogical and textural characteristics of alteration in the Thalanga sequence are described and a number of alteration facies that reflect variations in the intensity and conditions of alteration are defined. The distribution of alteration facies in cross sections through West, Central and East Thalanga are presented and discussed. The likely alteration processes and implications for the evolution of the Thalanga hydrothermal system are discussed in Chapter 9.

7.2 Logging alteration at Thalanga

Logging of alteration in diamond drill core involved recording the types, relative abundance and distribution of non-primary minerals (ie. alteration minerals and their metamorphic equivalents). This information allowed the definition of alteration facies. Abundance and approximate distribution of non-primary minerals are displayed as graphic strip logs alongside the lithofacies interpretation of the drill holes (eg. Fig. 7.1). Logs for all drill holes examined in sections 1 to 6 are presented in the Appendix. Estimates of abundances of sericite, chlorite and biotite, disseminated pyrite, pyrite veins, tremolite and carbonate, epidote and hematite are given. The main styles of alteration - pervasive, domainal, patchy and vein-style - are presented by different patterns. Estimates of mineral abundances based on examination of drill core hand specimen were checked against data from thin sections and corrected where necessary.

Fine-grained white mica is abundant in altered rhyolite and can be recognised in hand specimen and in thin section. The term 'sericite' has been used as a descriptive term for this phase, without reference to any particular mineral composition (Deer et al., 1992). However, microprobe analyses show that 'sericite' at Thalanga has the composition of muscovite (Chapter 4, Fig. 4.3). Chlorite and biotite were assigned to

Fig. 7.1: Example of a graphic drill hole log (DDH TH61, section 6) showing lithofacies characteristics, abundance and distribution of non-primary minerals, and interpreted alteration facies.

A brief description of the lithology and alteration is also provided. Logs for drill holes from sections 1 to 6 are assembled in the Appendix, together with the geological interpretations of the cross sections which are also illustrated in Figures 7.5 to 7.7.

TH61 - drill hole log (section 6, East Thalanga)

lithological log — estimate of mineral abundances

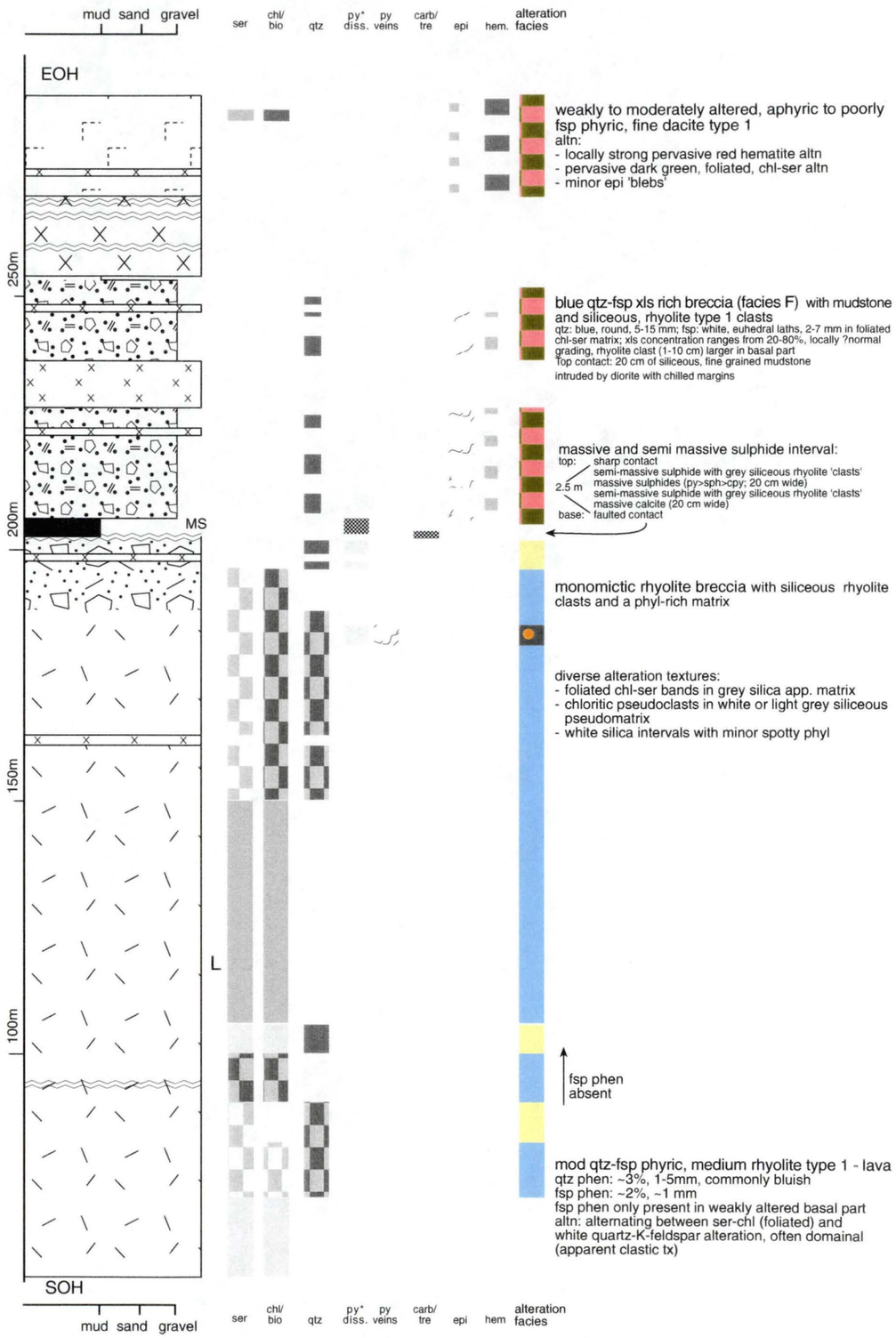

Legend

coherent facies

- dacite (type 3)
- dacite (type 2)
- dacite (type 1)
- rhyolite (type 4)
- rhyolite (type 3)
- rhyolite (type 2)
- rhyolite (type 1)
- andesite
- diorite

volcaniclastic and sedimentary facies

- in situ monomictic breccia (facies A)
- rhyolite breccia (facies B and C)
- monomictic dacite breccia (facies B)
- polymictic dacite breccia (facies D)
- polymictic rhyolite-dacite breccia (facies E1, E2, and E3)
- Quartz-Eye Volcaniclastics (facies F)
- quartz crystal-rich sandstone (facies G1)
- feldspar-quartz crystal-rich sandstone (facies G2)
- mudstone (facies H1)
- mudstone interbedded with volcaniclastic sandstone (facies H2 includes facies G3) (on section 1, Fig. 7.5a)

- dacite pumice clasts
- siliceous and calcareous facies (facies I)
- massive or semi-massive sulphides
- sharp contact
- intrusive contact (cross section)
- no line — gradational contact
- D3 - fault (cross section)
- fault (drill core logs)

alteration intensity - drill hole logs (as indicated by mineral abundances)

- weak alteration (3-10% for sericite, chlorite or biotite, 1-5% for disseminated pyrite)
- moderate alteration (10-20% for sericite, chlorite or biotite, 5-20% for disseminated pyrite, >75%for groundmass quartz)
- intense alteration (>20% for sericite chlorite or biotite, >20% disseminated pyrite and intense silicification)
- domainal alteration; weakly and moderately altered intervals/domains (cm to m scale)
- domainal alteration; moderately and intensely altered intervals/domains (cm to m scale)
- patchy alteration (weak, moderate or intense)
- some veins (~1-3 per core meter)
- abundant veins (3-10 per core meter)
- very abundant veins (>10 per core meter)

alteration facies

- mottled alteration facies
- quartz-K-feldspar alteration facies
- quartz-pyrite alteration facies
- chlorite-pyrite alteration facies
- disseminated-tremolite alteration facies
- carbonate-chlorite-tremolite alteration facies
- hematite dusting
- epidote alteration facies
- patchy epidote and hematite alteration facies

Fig. 7.1

one category ('chl/bio') during alteration logging because it was usually impossible to obtain reliable separate estimates for their relative abundances in hand specimen due to the intimate intergrowth of these two minerals. In some instances, the column for disseminated pyrite ('diss. py*') was used to show the combined abundance of several sulphide minerals, in which case the types of sulphides observed are marked on the log. 'Hematite dusting' refers to alteration involving fine, submicroscopic, disseminated hematite crystals that resulted in a bright red colouration of phyllosilicate-poor groundmasses in weakly altered dacites or rhyolites.

7.3 Alteration facies and alteration grade

The term 'alteration facies' is used in a strictly descriptive sense as proposed by Riverin and Hodgson (1980) and refers to rock units with characteristic mineralogical and textural features which can be identified during the course of mapping and drill core logging. The various alteration facies can be grouped according to alteration intensity which describes the abundance of non-primary minerals and the intensity of textural modifications of the rocks (Table 7.1). In least-altered quartz-feldspar-phyric rhyolite, plagioclase and alkali-feldspar phenocrysts are unaltered and the quartzofeldspathic groundmass locally contains remnant primary textures such as relic perlite and spherulites (Figs. 2.1a and 5.3a). Weak alteration is texturally undestructive and characterised in hand specimen by patchy or vein-controlled occurrences of phyllosilicates, epidote and hematite. In contrast, mottled alteration facies (moderate alteration intensity) is feldspar destructive and distinguished by a significant increase in muscovite, chlorite and biotite in the groundmass accompanied by minor disseminated pyrite. Intense pyritic alteration is usually associated with intense silicification of the groundmass and contains abundant disseminated pyrite and pyrite veins. In addition, intense calcareous alteration is represented by carbonate-chlorite-tremolite-rich rocks. The mineralogy of alteration facies at Thalanga is summarised in Table 7.1.

Table 7.1: Mineralogy of alteration facies at Thalanga

increasing alteration intensity

altn intensity:		weak				moderate			intense		
altn facies:	least altered	albite altn	hematite dusting	epidote altn	phyllosilicate[4] altn	diss. tre. altn	qtz-K-fsp altn	mottled altn	chl-carb-tre altn[5]	qtz-py altn	chl-py altn
quartz[1]	●●	●●	●●●	●●	●●	●●	●●●	●●	○	●●●	● to ●●
primary fsp[2]	●●	○	●	○ to ●	●	○	○				
K-feldspar[3]							●●				
albite		●●									
muscovite	●	○	●	●	● to ●●	○	○	●●	○	● to ●●	●
chlorite	○			○	○ to ●	○		●	●●		●●
biotite	○	○		○	●			●		○ to ●	
epidote	○			● to ●●		●			○		
actinolite				●							
tremolite						● to ●●			●●		
calcite				○ to ●		○ to ●			●●		
hematite			?●								
pyrite					○			● to ●●		●●	●●
sphalerite						○	○		○		

[1]: includes primary quartz (as phenocrysts and in the matrix) and hydrothermal quartz.
[2]: primary plagioclase and/or alkali-feldspar as phenocrysts and in the matrix.
[3]: K-feldspar in quartz-K-feldspar alteration facies is interpreted to represent a hydrothermal alteration product of primary feldspar.
[4]: variable proportions of muscovite, chlorite and biotite; footwall rhyolite is generally muscovite-dominated with minor pyrite; biotite-dominated in hangingwall dacite (no pyrite).
[5]: also contains barite locally.
○: rare; ◕: common; ● ●: abundant; ● ● ●: dominant
abbreviations: altn: alteration; carb: carbonate; chl: chlorite; K-fsp: K-feldspar, py: pyrite; qtz: quartz; tre: tremolite

7.3.1 Weak alteration

Weak alteration encompasses four different facies: *phyllosilicate alteration, epidote alteration, hematite dusting* and *albite alteration*. Phyllosilicate alteration in the footwall rhyolite is muscovite-dominated whereas biotite is the dominant mineral of this alteration facies in the hangingwall dacite. Albite alteration, hematite dusting and epidote alteration are particularly common in the phyllosilicate-poor hangingwall dacite but also occur sporadically in the footwall rhyolite. In general, feldspar phenocrysts are preserved in weakly altered rocks and primary volcanic textures can be identified occasionally.

Phyllosilicate alteration

The muscovite-dominated phyllosilicate alteration facies is common at the margins of the footwall alteration zone but is also present in the outcrop section 5 km to the west of the Thalanga deposit. Patchy remnants of original quartzofeldspathic groundmass and feldspar phenocrysts are generally present and boundaries with the least-altered rhyolite or moderately altered rhyolite are gradational (Fig. 7.2a). In the hangingwall, phyllosilicate alteration is biotite-dominated with disseminated biotite typically forming an interconnected network within the quartzofeldspathic groundmass of the dacites (Fig. 7.2b; Fig. 3.4a). In general, phyllosilicate-altered rhyolite and dacite contain less than ~10 vol.% combined muscovite, biotite and chlorite.

Epidote alteration

Epidote alteration is typically vein-controlled but also occurs as irregular patches in the quartzofeldspathic groundmasses of weakly altered dacite and rhyolite (Fig. 7.2c, d). Epidote is often associated with calcite or actinolite; however, minor muscovite, chlorite and biotite can also be present. Epidote alteration is particularly common in the hangingwall dacite and locally associated with hematite dusting, resulting in a characteristic red and green colouration of the rock (Fig. 2.3e). Epidote alteration is rare in the footwall and largely restricted to syn-volcanic rhyolite intrusions in West and Central Thalanga.

Fig. 7.2: Examples of weakly altered rhyolite and dacite.

(a) Weak phyllosilicate alteration in rhyolite is dominated by muscovite±biotite, typically showing a patchy distribution. Feldspar phenocrysts are preserved in remnant siliceous domains (s) of least-altered rhyolite. This alteration facies is common on the fringes of the footwall alteration zone and grades into mottled alteration facies. However, patches of phyllosilicate alteration occur sporadically within least-altered rhyolite outside of the footwall alteration zone and in the outcrop section (a: altered domain; sample TH243A-86.0; section 2).

(b) Phyllosilicate alteration in hangingwall dacite is biotite-dominated. Biotite (b) commonly forms interconnected networks within the quartzofeldspathic groundmass of the dacite. Sample TH40-68.50 represents a particularly clear example of phyllosilicate alteration of a siliceous dacite clast within monomictic dacite breccia (section 1).

(c) Epidote alteration (e) and hematite dusting (h) in the footwall rhyolite (samples TH112-370 [top], TH112-388.60 [middle], and TH112 404.40 [base]; section 3, Central Thalanga).

(d) Epidote alteration is abundant in the hangingwall dacite and may be accompanied by carbonate (arrow) and/or actinolite (sample TH62C-825.20).

(e) Hematite dusting is common is coherent facies of hangingwall dacite and may show pervasive, patchy or vein-controlled distribution (samples TH402-320.80, TH402-175.50, TH402-123.0 and TH402-88.30, left to right).

(f) Dacite in direct contact with an apophysis of the post-D2 diorite pluton has a red margin due to hematite dusting. It is suggested that thermal oxidation of iron oxide microcrysts (<1 μm) in the groundmass of the dacite may be responsible for the formation of hematite (d: dacite, dio: diorite; sample TH402-330.10).

(g) Epidote alteration and hematite dusting occur locally in post-D2 diorite intrusions. This indicates that these alteration facies may post-date hydrothermal activity at Thalanga (sample TH144B-392.80).

(h) Albite alteration in the hangingwall dacite has no reliable textural expression. Many albite-altered samples are texturally unaltered in hand specimen. Sample TH18-89.7 shows clear geochemical indications for albite alteration (Na_2O = 7.7 wt.%; K_2O = 0.1 wt.%; CaO = 1 wt.%; K_2O/K_2O+Na_2O = 0.01) but was logged as least-altered during drill core examination.

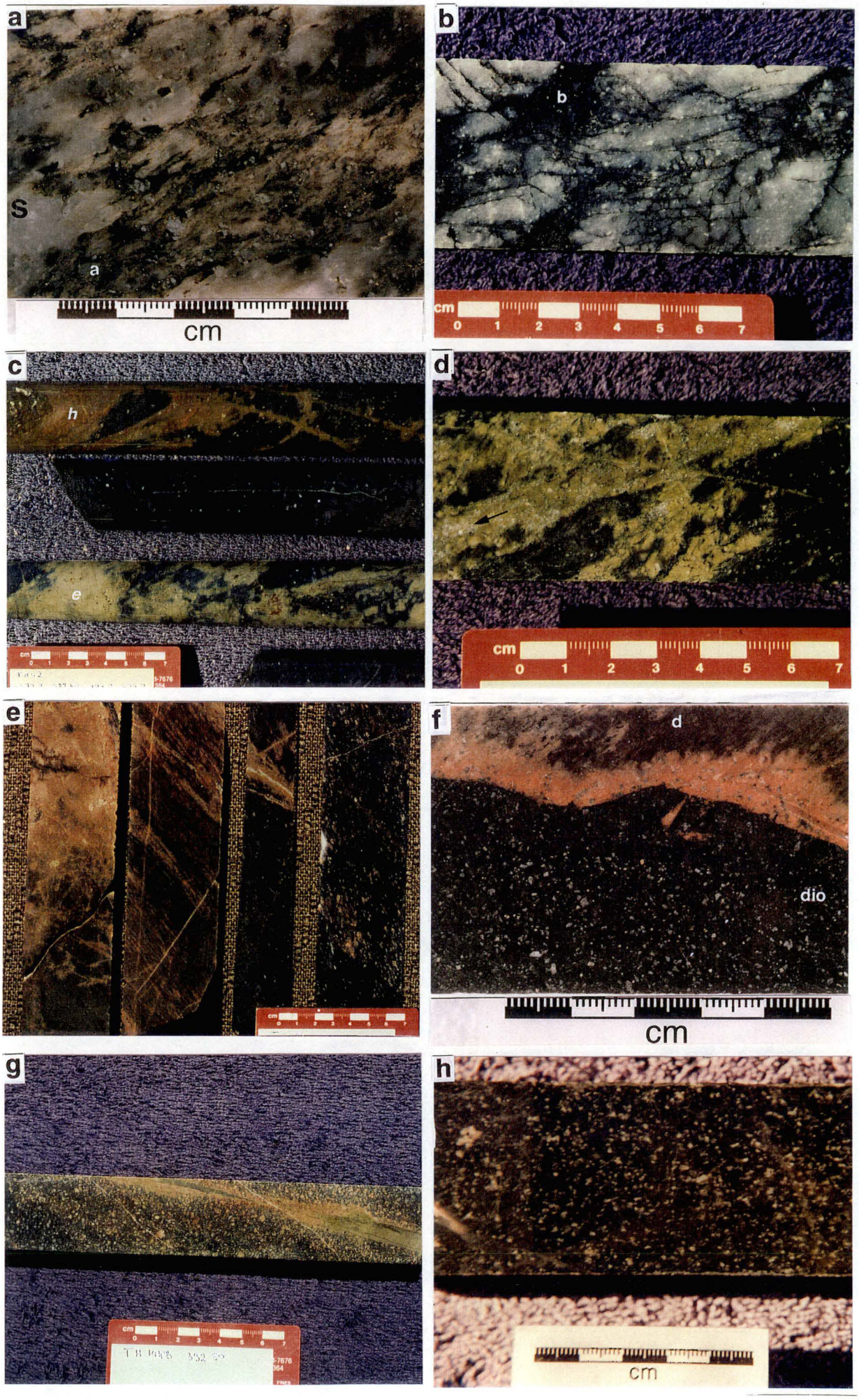

Fig. 7.2

Hematite dusting

Disseminated, submicroscopic hematite crystals are inferred to be the cause of red colouration of the siliceous, quartzofeldspathic groundmasses of weakly altered dacites (Fig. 7.2e). Locally, this type of alteration is also present in weakly altered rhyolite in the footwall (Fig. 7.2c). Hematite dusting occurs as selvedges along quartz veins or as patchy domains irregularly scattered through the rock. In thin section, red domains are mineralogically identical to the surrounding quartzofeldspathic groundmass except for a significant coarsening of quartz and feldspar groundmass crystals.

At one locality in the hangingwall, dacite in contact with a post-D2 diorite intrusion shows a 2 cm wide, red margin (Fig. 7.2f). This observation suggests that thermal oxidation of Fe-oxide microcrysts (<1 μm in diameter) resulted in the formation of hematite microcrysts causing the red colour. Furthermore, hematite dusting and epidote veins also occur locally in apophysae of the post-D2 diorite pluton in East Thalanga (Fig. 7.2g, Table 7.2).

Albite alteration

Hangingwall dacites are commonly Na_2O-rich (4 to 7 wt.%) and relatively K_2O-poor (2.8 to <0.1 wt.%) (Chapter 6) and consequently have low values for the K_2O-ratio ($100*K_2O/[Na_2O + K_2O]$) which is characteristic for Na-metasomatism (Hughes, 1973) (Fig. 6.2b,c). However, Na-enrichment did not result in any particular textural feature and hand specimens of the hangingwall dacite with low K_2O-ratio typically appear unaltered (Fig. 7.2h). In thin section, the feldspar phenocrysts of such samples are texturally unaltered and the groundmasses consist of microcrystalline, quartzofeldspathic assemblages. Phyllosilicates are a minor component and <3 vol.% fine biotite may occur within the groundmass.

A plot of CaO versus Na_2O (Fig. 7.3) shows that Na_2O-enrichment is not correlated with high CaO concentrations and therefore it is inferred that the anorthite component of feldspars in Na-rich hangingwall dacites is low. Hangingwall dacites with elevated CaO values are epidote-altered and have comparatively low Na_2O concentrations. These geochemical data and petrographic observations suggest that Na-enrichment in the hangingwall dacite is due albite alteration of feldspar phenocrysts and fine-grained feldspar crystals in the groundmass.

Fig. 7.3: Geochemistry of hangingwall dacite: Na_2O versus CaO.

A plot of Na_2O versus CaO shows that dacite samples with high sodium concentrations contain $\leq$ 1 wt.% CaO. This is consistent with the interpretation that the hangingwall dacite experienced widespread albite alteration reflected in low values for the K_2O-ratio (Fig. 6.2c).

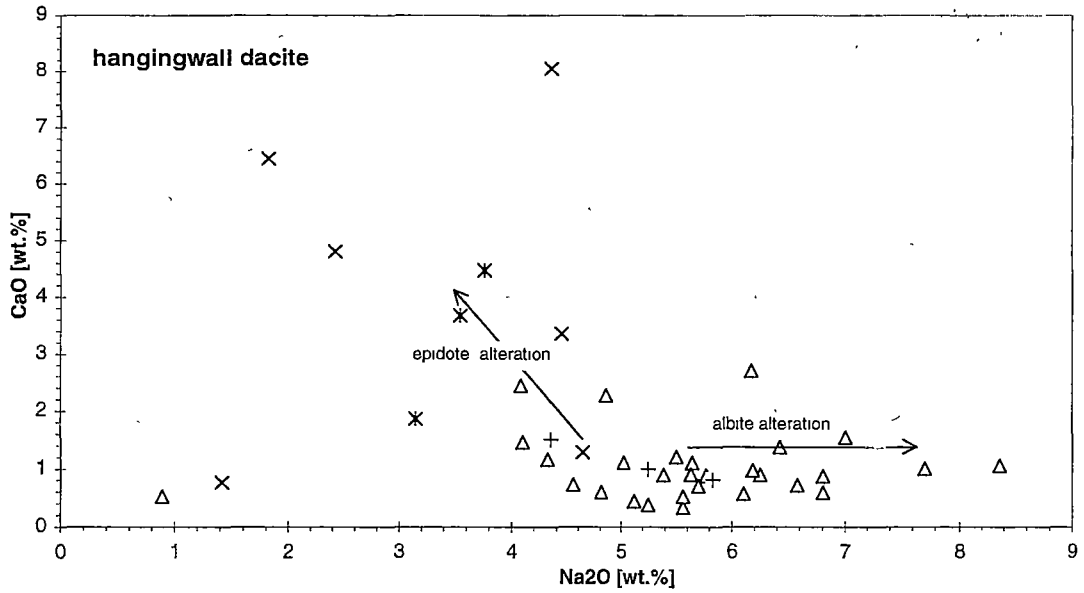

Legend:

×epidote alteration

+hematite dusting

⁎combined hematite dusting and epidote alteration

△texturally unaltered dacite and weak phyllosilicate alteration

Fig. 7.3

7.3.2 Moderate alteration

Alteration intensity increases in the main part of the Thalanga footwall alteration zone and is marked by a gradual increase in abundance of muscovite, biotite and chlorite in the groundmasses of rhyolites, disappearance of feldspar phenocrysts, occurrence of disseminated pyrite and substantial textural modifications. These features are characteristic of the mottled alteration facies. Moderate alteration also includes quartz-K-feldspar and disseminated tremolite alteration facies that occur preferentially on the fringes of the broad footwall alteration zone.

Mottled alteration

The bulk of the Thalanga footwall alteration zone consists of feldspar-destructive, phyllosilicate-dominated alteration facies which shows substantial textural variations and a generally mottled appearance (Fig. 7.4 a, b). This alteration facies is characterised by variable amounts and relative proportions of chlorite, muscovite, biotite and minor pyrite disseminated in the quartz-rich groundmass of altered rhyolite. Remnants of feldspar phenocrysts, pseudomorphed by biotite and muscovite, are rare. Typically, the abundance and relative proportions of muscovite, chlorite, biotite and quartz in the groundmass vary considerably on a hand specimen scale and textures which superficially resemble clastic volcanic facies are abundant (Fig. 7.4b; see also Figs. 2.1c and 4.7e). This feature, which is related to domainal or multi-phase alteration, is common in footwall alteration zones below VHMS deposits and has frequently led to the misinterpretation of altered footwall rocks as primary pyroclastic facies (Allen, 1988). Textural criteria used for discriminating genuine clastic facies from coherent facies with apparent clastic textures are presented in Chapter 5 and in Paulick & McPhie (1999).

Although the texture of the mottled alteration facies varies substantially, three main textural patterns occur. These include: strongly foliated textures in phyllosilicate-rich altered rhyolite (Fig. 7.4a), pseudoclastic textures with wispy, phyllosilicate-rich domains and lensoidal quartz-rich domains (Fig. 7.4b), and 'blotchy' textures with round to lensoidal chlorite-rich apparent clasts in a quartz-muscovite-rich apparent matrix (Fig. 4.7 e). These different textures probably represent variations in the combined effects of original, heterogeneous glassy versus crystalline domains in the coherent rhyolite, domainal and/or multi-phase hydrothermal alteration, and recrystallisation during regional and contact metamorphism.

Fig. 7.4: Examples of moderately to intensely altered rhyolite.
(scale in centimetres)

(a) Feldspar-destructive, mottled alteration facies is dominant in the footwall alteration zone and is characterised by variably abundant muscovite, chlorite and biotite representing metamorphic equivalents of hydrothermal phyllosilicates. Textures in the mottled alteration facies are variable on a hand specimen scale. This phyllosilicate-rich example was foliated during regional deformation (D2) (sample TH394-114.0; section 6).

(b) In the mottled alteration facies, relative abundances of quartz, muscovite, chlorite and biotite in the groundmasses commonly vary between separate domains. This image shows a typical example of coherent footwall rhyolite which has a groundmass consisting of quartz-rich and muscovite-biotite-rich domains (sample TH245-224.40; section 2). Such textures are easily mistaken as primary volcaniclastic textures. Criteria used to distinguish coherent facies with apparent clastic textures due to alteration from genuine volcaniclastic facies are discussed in Chapter 5. Other examples of the textural variability in the mottled alteration facies are documented in Figs. 2.1c and 4.7e.

(c) K-feldspar is abundant in the siliceous groundmass of quartz-K-feldspar alteration facies. This sample of quartz-K-feldspar alteration facies was partially treated with sodium cobaltinitrate in order to selectively stain K-feldspar crystals (method as described in Norman, 1974) (sample TH412B-645.30; section 4).

(d) Disseminated tremolite (t) alteration occurs as patches within altered rhyolite and is commonly accompanied by epidote (e) and calcite (cc) (sample TH247-325.20; section 2).

(e) Intense, quartz-pyrite alteration facies is characterised by abundant disseminated pyrite, pyritic veins and siliceous appearance. Phyllosilicates are variably abundant in this alteration facies and this sample shows a comparatively muscovite-rich variety (sample TH247-347.20; section 2).

(f) Quartz-pyrite alteration facies contains variably abundant muscovite and/or chlorite representing a continuous spectrum from muscovite-rich and chlorite-poor to chlorite-rich and muscovite-poor mineralogical composition. This type of relatively chlorite-rich quartz-pyrite alteration facies is particularly common in section 5 (West Thalanga) (sample TH85-204.0).

(g) In the chlorite-pyrite alteration facies, chlorite is very abundant in the groundmasses whereas quartz is depleted in comparison with least-altered rhyolite and other alteration facies. The presence of quartz phenocrysts, gradational contacts with mottled alteration facies and immobile element characteristic are crucial evidence for the identification of these rocks as intensely altered rhyolite (sample TH270-381; section 5).

(h) Massive to semi-massive carbonate-chlorite-tremolite alteration facies occurs close to, and within, the Favourable Horizon in section 2 (West Thalanga, Fig. 7.5b) and is characterised by pervasive chlorite (c) and carbonate alteration (cc) and radiating tremolite crystals (t) (sample TH245-674.80, section 2).

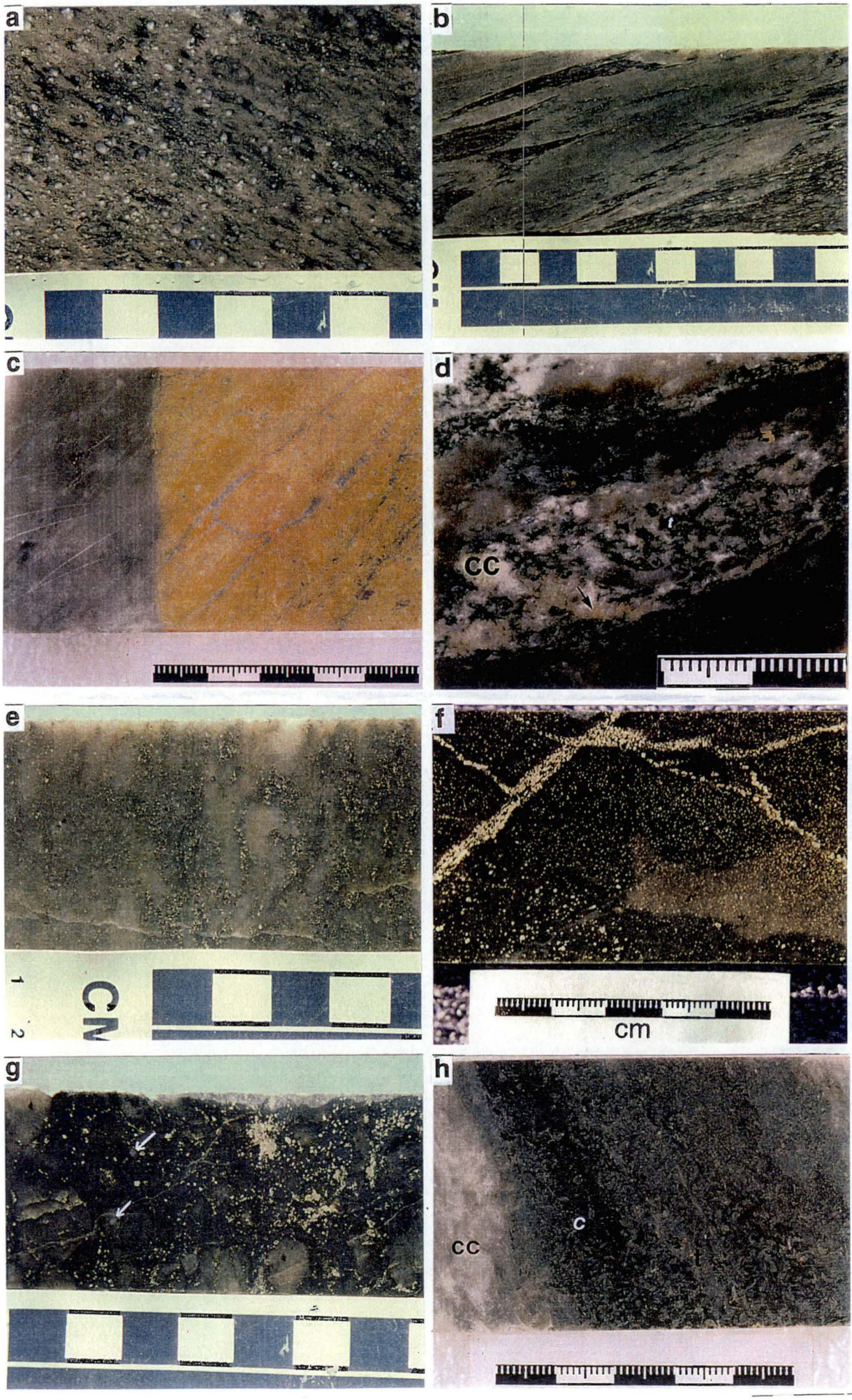

Fig. 7.4

Quartz-K-feldspar alteration

In hand specimen, this alteration facies is dominated by white, microcrystalline quartz and K-feldspar in the groundmasses of rhyolites (Fig. 7.4c). The presence of substantial K-feldspar is also indicated by geochemical data (Chapter 8, Fig. 8.1c). Rarely, blebs of sphalerite are also present.

Locally, overprinting relationships between mottled alteration facies and quartz-K-feldspar alteration facies have generated complex textures. Such textures include isolated, irregular patches or interconnected 'network-shaped' domains of white quartz within domains of muscovite-biotite-chlorite and massive quartz-K-feldspar domains that include patches of muscovite-biotite-chlorite assemblages.

Disseminated tremolite alteration

Patchy, tremolite-bearing domains occur sporadically in the footwall alteration zone. This alteration facies is characterised by tremolite-epidote±calcite assemblages disseminated in the groundmasses of altered rhyolites (Fig. 7.4d). Locally, tremolite has replaced quartz phenocrysts (Chapter 3, Fig. 3.5g, h) indicating that SiO_2 was consumed in the tremolite-forming metamorphic reaction. The disseminated tremolite alteration facies is inferred to be the metamorphic equivalent of hydrothermal carbonate-chlorite alteration.

7.3.3 Intense alteration

Intense alteration is characterised by substantial mineralogical and textural modification of the least-altered rhyolite, leaving only scarce evidence of the original composition and texture of the rocks. Intense pyritic alteration is mainly represented by quartz-pyrite alteration facies, however minor chlorite-pyrite alteration facies occurs locally in East Thalanga. Intense calcareous alteration is represented by carbonate-chlorite-tremolite-rich rocks. Contacts between intense alteration facies and surrounding moderate alteration are generally gradational.

Quartz-pyrite alteration

Primary groundmass textures and feldspar phenocrysts are obliterated in the intensely altered footwall rhyolites, however quartz phenocrysts are preserved. In the quartz-pyrite alteration facies, the groundmasses are quartz-rich with disseminated pyrite and pyrite veins and variably abundant muscovite, biotite and chlorite (~5 to ~15 vol.%). The proportions of muscovite and chlorite vary substantially and a continuous spectrum from

muscovite > chlorite to chlorite > muscovite is present (Fig. 7.4e, f). Discordant zones of the quartz-pyrite alteration facies cut across the mottled alteration facies in the footwall alteration zone and also form stratiform zones just below the massive sulphides.

Chlorite-pyrite alteration

The chlorite-pyrite alteration facies occurs exclusively close to, and just below, the Favourable Horizon in East Thalanga. This chlorite-rich alteration facies (~40 vol.% chlorite) is quartz-poor compared to least-altered rhyolite and other alteration facies, however, quartz phenocrysts are preserved (Fig. 7.4g). Muscovite is common in this alteration facies (~20 vol.%) whereas biotite is absent.

Carbonate-chlorite-tremolite alteration

Carbonate-chlorite-tremolite-rich rocks (Fig. 7.4h) commonly occur within, or close to, the Favourable Horizon in West Thalanga. These rocks were formerly regarded as exhalites but have been re-interpreted as metamorphosed equivalents of intense, carbonate-chlorite alteration formed in rhyolitic volcaniclastic facies, close to the palaeo-seafloor (Herrmann, 1994; Hill, 1996). Locally, gradational contacts with disseminated tremolite alteration facies can be observed (eg. drill hole TH41, Appendix section 2).

7.4 Spatial arrangement of alteration facies in cross sections

There are significant variations in the distribution and abundance of alteration facies in the 6 cross sections through the Thalanga sequence in West, Central and East Thalanga (Fig. 1.5). The geological interpretations of these sections, including primary lithofacies and alteration facies, are presented in Figures 7.5 to 7.7. Graphic logs and lithological descriptions of the diamond drill core examined for each section are documented in the Appendix. Lateral and vertical variations in the lithofacies of the Thalanga sequence are discussed in detail in Chapter 5 and summary logs for each section representing true stratigraphic thickness are presented in Figure 5.5. The spatial arrangement of alteration facies in cross sections 1 to 6 is described below and summerised in Table 7.2.

7.4.1 West Thalanga

In sections 1 and 2, footwall alteration is characterised by a strictly stratiform zone of quartz-pyrite alteration facies underlying the Favourable Horizon and a broad zone of mottled alteration facies (Fig. 7.5). The hangingwall consists of a variable lithofacies

association including dacite type 2 lavas, volcaniclastic breccia and sedimentary facies. Weak alteration, including hematite dusting and epidote alteration, are widespread in the hangingwall.

Section 1

The footwall alteration zone is comparatively thin in the down-dip part of section 1 where it extends for only ~50 m into the footwall rhyolite (Fig. 7.5a). In the up-dip part, mottled alteration facies is abundant, however, some parts of the rhyolite lavas and syn-volcanic intrusions were logged as least-altered or weakly altered with patchy epidote alteration and hematite dusting. Minor quartz-K-feldspar alteration facies and disseminated tremolite alteration facies can also be observed. Carbonate-rich units (facies I, Table 5.3) occur locally in the Favourable Horizon and in the hangingwall above a thick package of monomictic dacite type 2 breccia units, 150 m above the Favourable Horizon. Section 1 contains only minor occurrences of semi-massive sulphides which, together with the weakly developed footwall alteration zone, indicate that this area represents the western margin of the Thalanga hydrothermal system.

Section 2

Section 2 includes about 500 m of footwall and hangingwall stratigraphy and the West Thalanga ore lens (Fig. 7.5b). Coherent and clastic facies of the footwall rhyolite are present in about equal proportions and the immediate footwall below the Favourable Horizon consists of rhyolitic volcaniclastic units. The Favourable Horizon contains massive to semi-massive sulphides with calcareous gangue, carbonate-chlorite-tremolite alteration facies and minor QEV (facies F, Table 5.3). The hangingwall is occupied by dacite type 2 lavas, a dacite type 3 sill, an andesite intrusion and volcaniclastic units.

A stratiform zone of quartz-pyrite alteration facies underlies the massive sulphides and extends 10 to 50 m into the footwall and ~100 m down dip beyond the ore lens. Below this area of intense pyritic alteration is a broad zone of mottled alteration facies which has gradational contacts to least-altered rhyolite in the up-dip part of the section. In the down-dip part, zones of disseminated tremolite, quartz-K-feldspar and semi-massive carbonate-chlorite-tremolite alteration facies are present. Dacites in the hangingwall are least-altered to weakly altered and locally show epidote alteration and/or hematite dusting.

Fig. 7.5: Distribution of alteration facies in West Thalanga (sections 1 and 2).

The sections show the drill holes logged for this study, the interpreted lithofacies arrangement and alteration in the footwall and the hangingwall. Diamond drill hole (DDH) logs are given in the Appendix. The geometry of the ore lenses is based on mapping by Thalanga mine geologists (courtesy of RGC Ltd.). Tick marks on DDH are 50 m apart. Legend for lithofacies as in Figure 7.1 and in the Appendix.

(a) Geological interpretation of section 1.

(b) Geological interpretation of section 2.

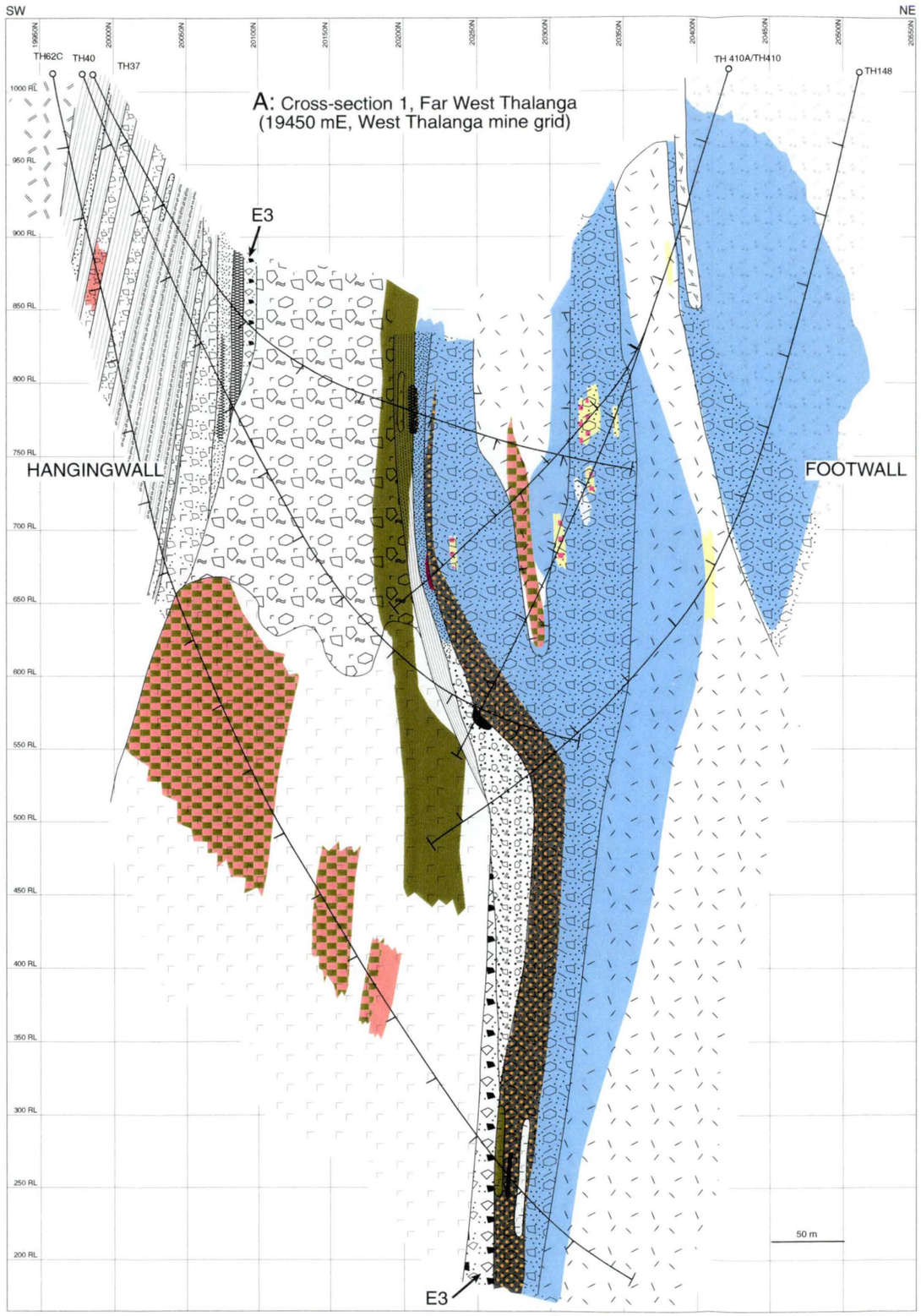

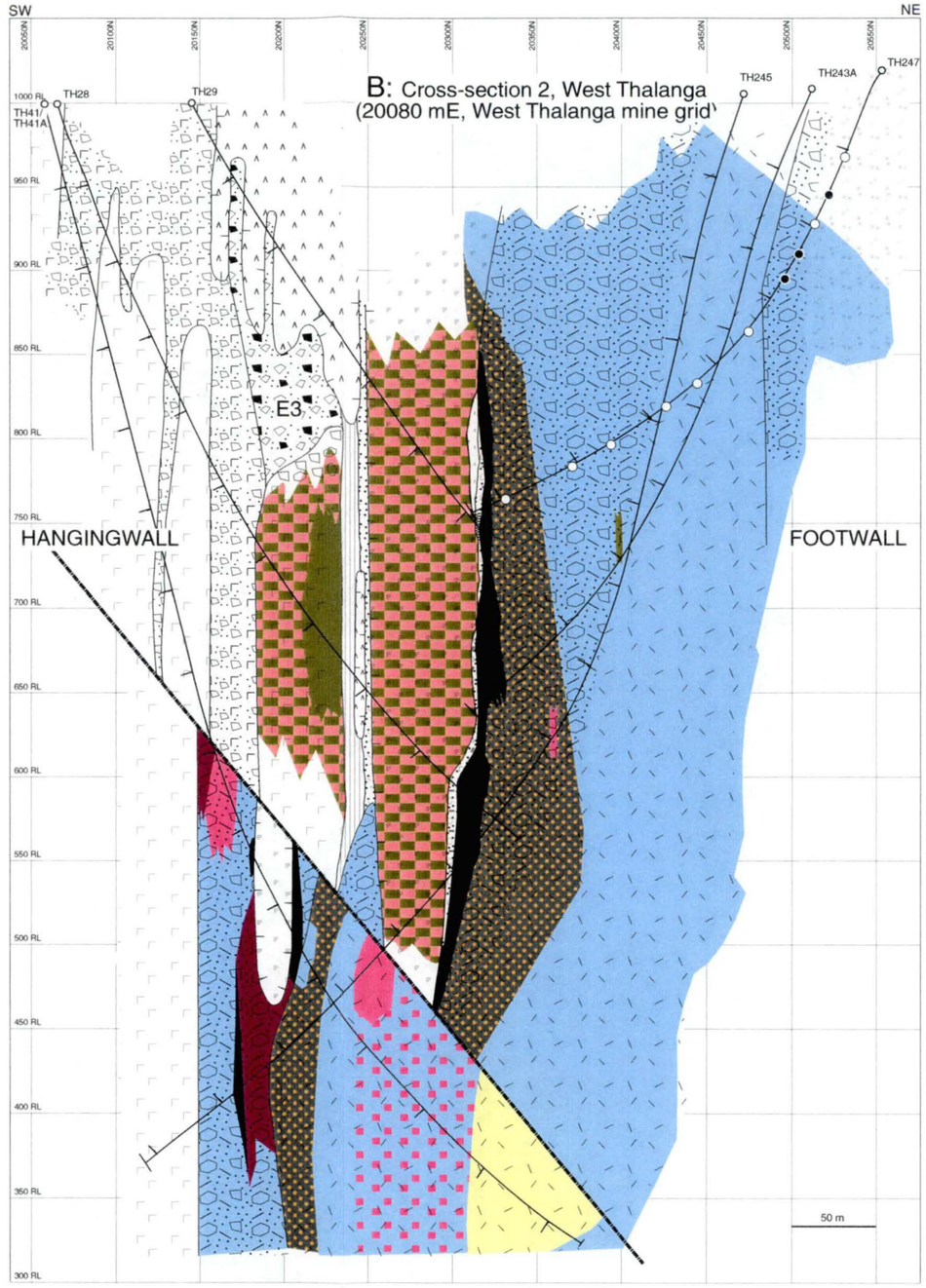

alteration facies

- least altered rocks, albite alteration and phyllosilicate alteration
- hematite dusting
- epidote alteration facies
- patchy epidote and hematite alteration facies
- mottled alteration facies
- quartz-pyrite alteration facies
- chlorite-pyrite alteration facies
- quartz-K-feldspar alteration facies
- disseminated-tremolite alteration facies
- carbonate-chlorite-tremolite alteration facies

● ○ sample locations for analyses presented in Fig. 8.12
(filled symbol: this study; open symbol: RGC Ltd.)

Fig. 7.5

7.4.2 Central Thalanga

In Central Thalanga, D3-faulting has moved altered footwall rhyolite into an apparent hangingwall position (Hill, 1996) and consequently, massive sulphides appear to be hosted by rhyolite (Fig. 7.6). The structure is particularly complex in section 3 where faulting has been intense. In Central Thalanga, discordant zones of quartz-pyrite alteration facies cross-cut coherent rhyolite and trend into massive sulphides in the Favourable Horizon.

Section 3

The structure of section 3 is very complex due to substantial D3 faulting (Fig. 1.3). About 100 m of footwall rhyolite has been transposed into an apparent hangingwall position (Fig. 7.6a). Furthermore, least-altered and weakly altered syn-volcanic intrusions of rhyolite type 1 are present in the footwall and dacite type 3 and andesite intrusions occur in the hangingwall. A discordant zone of quartz-pyrite alteration facies with a diameter ranging between 50 m and 100 m extends obliquely downwards for at least 200 m from the ore lens. This zone is enveloped by mottled alteration facies which grades into least-altered rhyolite in the up-dip part of the section. There are minor occurrences of quartz-K-feldspar, disseminated tremolite and carbonate-chlorite-tremolite alteration facies as well as epidote alteration and hematite dusting in the footwall. The hangingwall is not significantly altered except for local epidote alteration and hematite dusting in coherent dacite. The contact between footwall rhyolite and hangingwall dacite is occupied by a massive quartz-barite chemical facies (facies I) in some drill holes (TH5 and C2047SD46; drill hole logs in the Appendix).

Section 4

In section 4, about 150 to 180 m of variably altered footwall rhyolite has been moved into an apparent hangingwall position due to D3 faulting (Fig. 7.6b). A discordant zone of quartz-pyrite alteration facies extends for at least ~200 m into the footwall and is directly connected with massive sulphides. This discordant alteration zone has an orientation of ~40° with respect to stratigraphic dip. It is enveloped by mottled alteration facies which extends to a depth of ~800 m below the surface. However, the overall alteration intensity decreases in the lower part of the section where some zones of disseminated tremolite alteration facies, quartz-K-feldspar alteration facies and weakly altered footwall rhyolite occur. Least-altered syn-volcanic intrusions in this section are very weakly altered and probably post-date the main hydrothermal activity associated with mineralisation (Chapter 5).

Fig. 7.6: Distribution of alteration facies in Central Thalanga (sections 3 and 4).

The sections show the drill holes logged for this study, the interpreted lithofacies arrangement and alteration in the footwall and the hangingwall. Diamond drill hole (DDH) logs are given in the Appendix. The geometry of the ore lenses is based on mapping by Thalanga mine geologists (courtesy of RGC Ltd.). Tick marks on DDH are 50 m apart. Legend for lithofacies as in Figure 7.1 and in the Appendix.

(a) Geological interpretation of section 3.

(b) Geological interpretation of section 4.

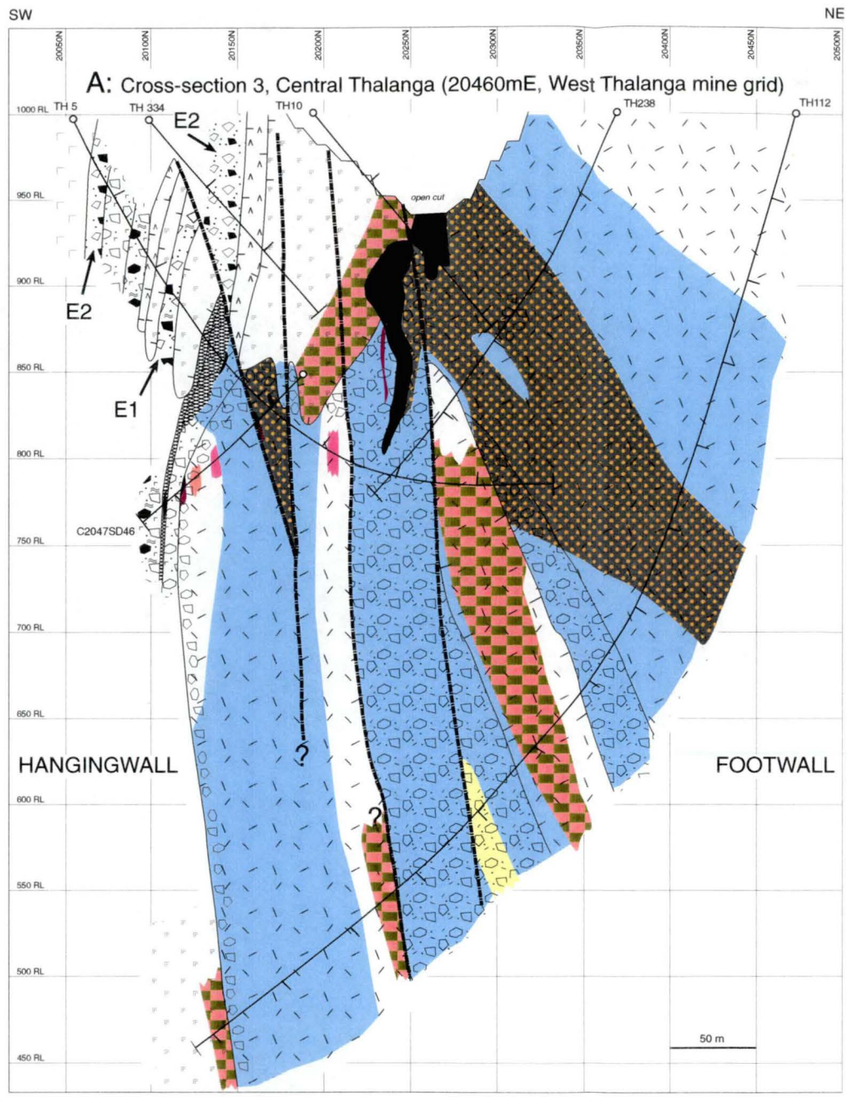

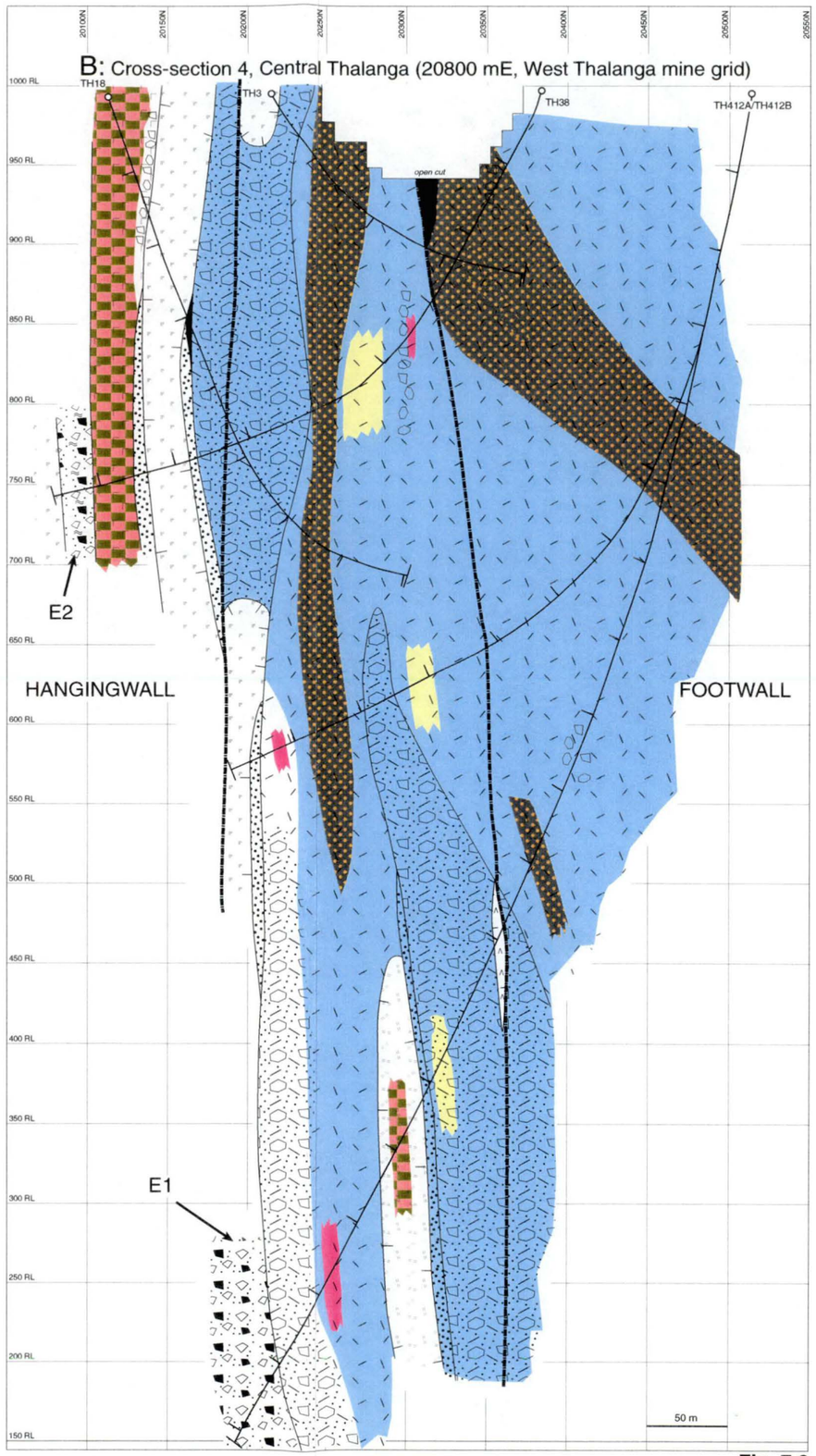

alteration facies

- least altered rocks, albite alteration and phyllosilicate alteration
- hematite dusting
- epidote alteration facies
- patchy epidote and hematite alteration facies
- mottled alteration facies
- quartz-pyrite alteration facies
- chlorite-pyrite alteration facies
- quartz-K-feldspar alteration facies
- disseminated-tremolite alteration facies
- carbonate-chlorite-tremolite alteration facies

Fig. 7.6

7.4.3 East Thalanga

In East Thalanga, discordant zones of quartz-pyrite alteration facies and have an orientation of 10° to 30° with respect to the Favourable Horizon (Fig. 7.7). The hangingwall is occupied predominantly by dacite type 1 lava with minor associated volcaniclastic facies. Apophyses of the post-D2 diorite pluton are common in section 6.

Section 5

Section 5 contains the main East Thalanga ore lens and about 550 m of footwall and hangingwall stratigraphy were intersected by exploration diamond drilling (Fig. 7.7a). The footwall consists of two voluminous rhyolite lavas and coherent rhyolite is predominant. Locally, mineralised, massive to normally graded QEV (facies F) is common in the Favourable Horizon.

A broad zone of mottled alteration facies below the Favourable Horizon grades into weakly altered or least-altered rhyolite in the up-dip part of the section and extends for at least 300 m into the footwall. Zones of quartz-K-feldspar alteration facies are common on the fringes of mottled alteration facies. In the up-dip part of the section, discordant zones of comparatively chlorite-rich quartz-pyrite alteration facies (Fig. 7.4f) cross-cut the footwall and lead up to massive sulphides. Similar discordant zones terminate in unmineralised Favourable Horizon in the lower part of the section. The chlorite-pyrite alteration facies dominates in the narrow stratiform zone directly underlying the massive sulphides and contacts between chlorite-pyrite alteration facies and quartz-pyrite alteration facies are gradational. The disseminated tremolite alteration facies is rare and restricted to the top part of the footwall rhyolite. The dacite type 1 lava in the hangingwall shows patchy to vein-controlled epidote alteration and/or hematite dusting.

Section 6

Section 6 contains the fringe of the East Thalanga ore lens and mottled alteration facies extends to a stratigraphic depth of at least 200 m into the footwall (Fig. 7.7b). In the up-dip part of the section, mottled alteration facies grades into least-altered rhyolite and quartz-K-feldspar alteration facies is common in this area. Discordant zones of quartz-pyrite alteration facies lead up to the Favourable Horizon but may have been disrupted by intrusions of post-D2 diorite in the down-dip part of the section. Epidote alteration and hematite dusting are widespread in dacite type 1 lava occupying the hangingwall but are also present in diorite intrusions. Furthermore, hematite dusting occurs in QEV (facies F) in the down-dip part of the section.

Fig. 7.7: Distribution of alteration facies in East Thalanga (sections 5 and 6).

The sections show the drill holes logged for this study, the interpreted lithofacies arrangement and alteration in the footwall and the hangingwall. Diamond drill hole (DDH) logs are given in the Appendix. The geometry of the ore lenses is based on mapping by Thalanga mine geologists (courtesy of RGC Ltd.). Tick marks on DDH are 50 m apart. Legend for lithofacies as in Figure 7.1 and in the Appendix.

(a) Geological interpretation of section 5.

(b) Geological interpretation of section 6.

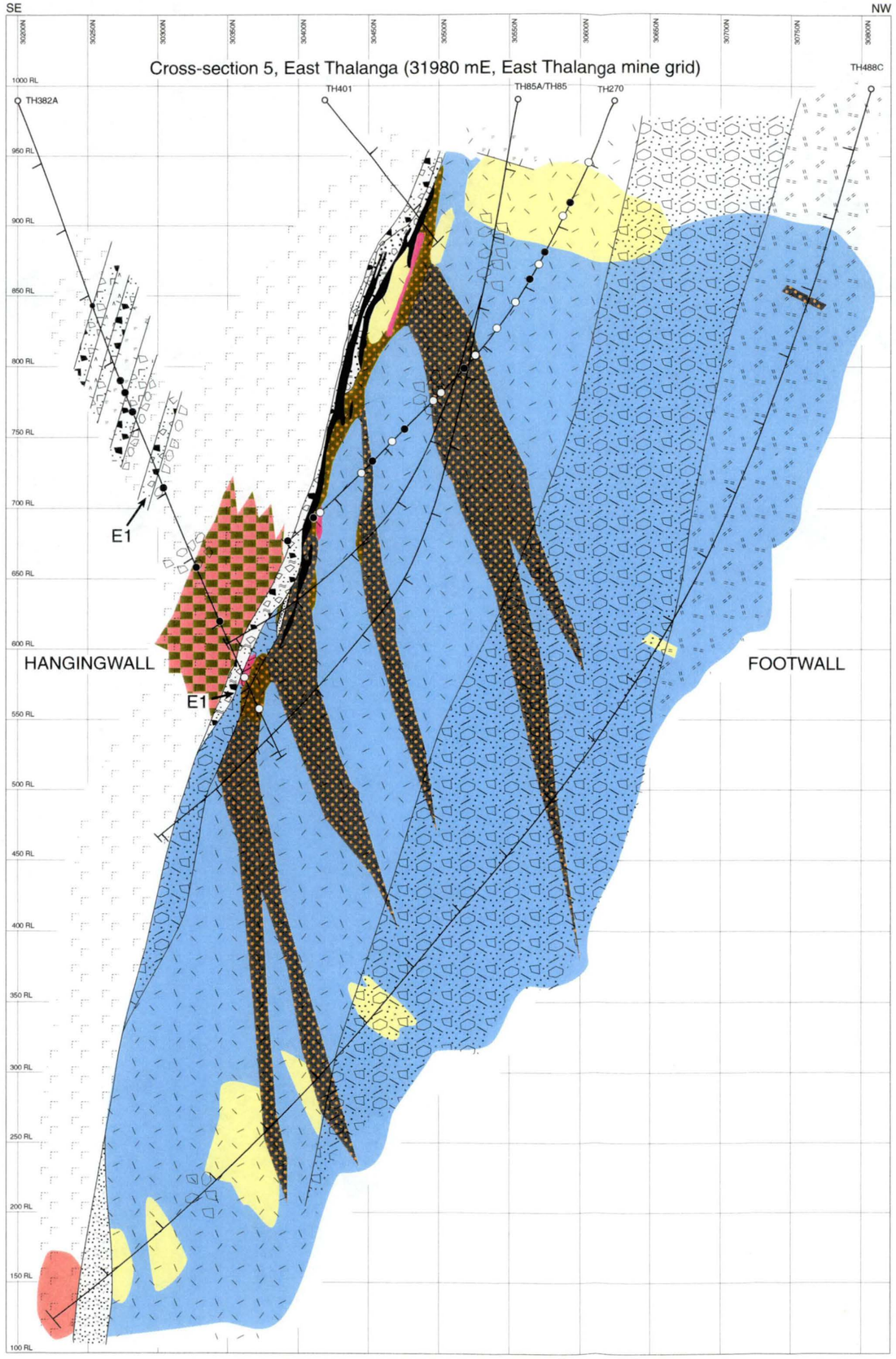

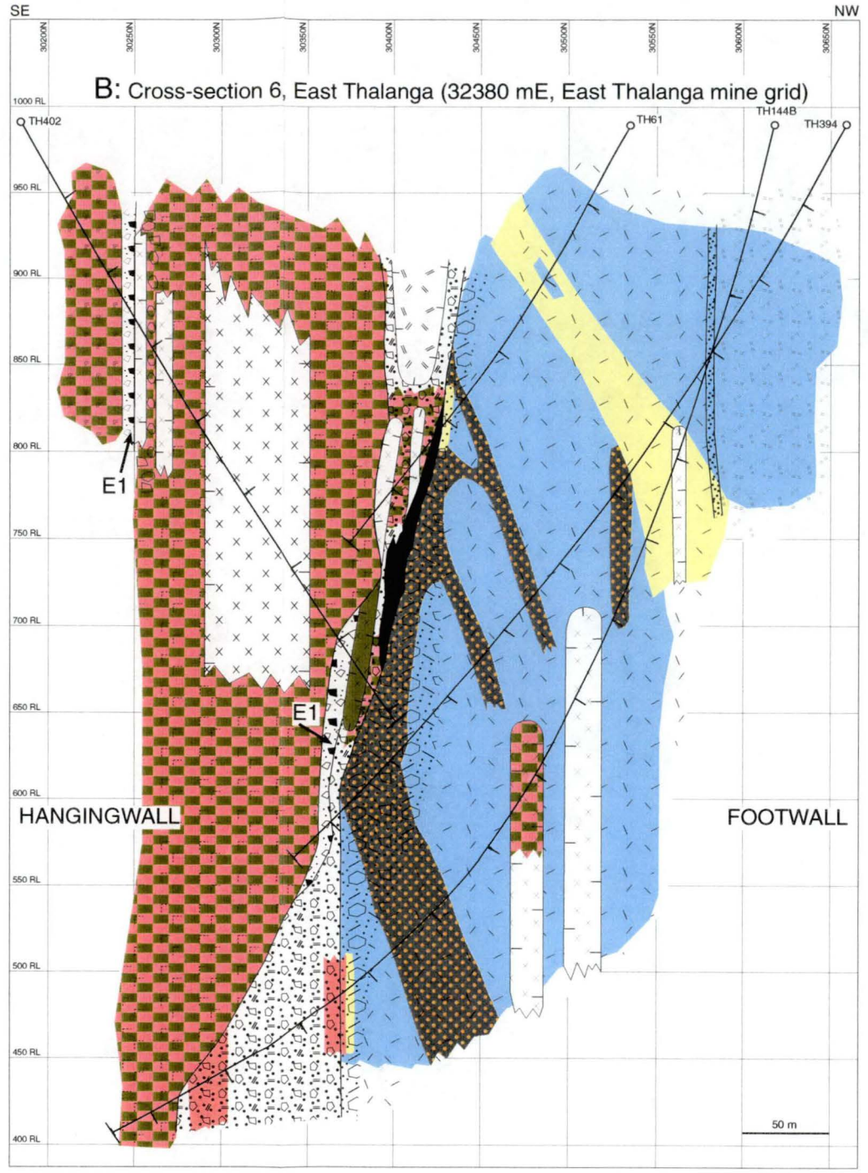

alteration facies

- least-altered rocks, albite alteration and phyllosilicate alteration
- hematite dusting
- epidote alteration facies
- patchy epidote and hematite alteration facies
- mottled alteration facies
- quartz-pyrite alteration facies
- chlorite-pyrite alteration facies
- quartz-K-feldspar alteration facies
- disseminated-tremolite alteration facies
- carbonate-chlorite-tremolite alteration facies

● ○ sample locations for analyses presented in Fig. 8.12 (filled symbol: this study; open symbol: RGC Ltd.)

Fig. 7.7

Table 7.2: Distribution of alteration facies at Thalanga

alteration intensity	alteration facies	footwall rhyolite	hangingwall dacite	post-D2 diorite
weak	phyllosilicate alteration	common	common	
weak	albite alteration	rare	abundant	
weak	hematite dusting	rare	common	rare
weak	epidote alteration	rare	common	rare
moderate	disseminated tremolite alteration	rare		
moderate	quartz-K-feldspar alteration	common		
moderate	mottled alteration	abundant		
intense	carbonate-chlorite-tremolite alteration	(in West Thalanga only) common		
intense	quartz-pyrite alteration	common		
intense	chlorite-pyrite alteration	(in East Thalanga only) common		

rare
common
abundant

7.5 Discussion

Distribution of alteration facies

Systematic logging of alteration facies in drill holes from 6 cross sections along the entire strike extent of the Thalanga deposit shows that alteration facies of moderate to high alteration intensity are restricted to the footwall, defining a broad, strata-bound alteration zone below the massive sulphides.

Cross sections through West, Central and East Thalanga show that the bulk of the footwall alteration zone is occupied by phyllosilicate-rich and feldspar-destructive mottled alteration facies which has gradational lateral contacts to surrounding least-altered rhyolite. This alteration facies occupies a broad zone which underlies massive sulphides along the entire strike extent of the deposit. It extends for ~3,000 m along strike, >1,000 m down-dip and 50 to >300 m stratigraphically into the footwall. The true maximum thickness of the footwall alteration zone is unknown. It is inferred that feldspar-destruction, formation of hydrothermal phyllosilicates and Mg-enrichment (indicated by the abundance of chlorite and biotite and geochemical data, Chapter 8) were the principal alteration processes in this zone.

Stratiform zones of pyritic alteration are located immediately below massive sulphides in all sections. They consist of quartz-pyrite alteration facies in West and Central Thalanga and are particularly prominent in section 2 where this zone reaches a maximum thickness of ~50 m (Fig. 7.5b). In East Thalanga (section 5, Fig. 7.7a) the intensely altered stratiform zone below the massive sulphides consists predominantly of chlorite-pyrite alteration facies.

Calcareous alteration facies (disseminated tremolite and carbonate-chlorite-tremolite alteration facies) are especially common close to, and within, the Favourable Horizon in section 2 (Fig. 7.5b), implying that significant hydrothermal carbonate and chlorite was precipitated in the near-seafloor environment in West Thalanga. In contrast, the disseminated tremolite alteration facies is rare in East Thalanga and restricted to the top part of the footwall rhyolite in section 5 (Fig. 7.7a). The carbonate-chlorite-tremolite alteration facies has not been observed in East Thalanga.

The restricted occurrences of chlorite-pyrite alteration facies at East Thalanga and the concentration of calcareous alteration facies in West Thalanga indicate that the conditions of alteration varied along strike of the deposit during the evolution of the hydrothermal system.

In contrast to the substantial textural and mineralogical modifications in the footwall

rhyolites, the hangingwall dacites are generally weakly altered (Table 7.2). Importantly, sulphides are extremely rare in the hangingwall, feldspar crystals are texturally preserved and phyllosilicate are generally a minor component (<10 vol.%) in coherent facies of dacite.

The weak alteration in the hangingwall may have occurred long after hydrothermal activity associated with the Thalanga deposit had ceased and could be due to background, sub-seafloor alteration processes. This interpretation is supported by the observation that there is no systematic increase in the abundance or intensity of phyllosilicate alteration, hematite dusting or epidote alteration in the proximity to the Favourable Horizon (Fig. 7.5 to 7.7 and drill hole logs in the Appendix). It is possible that weak alteration in the hangingwall was in part a result of small convective hydrothermal systems initiated by thermal anomalies associated with shallow, synvolcanic intrusions such as the dacite type 3 sills in West Thalanga. Similar settings for weak epidote alteration have been recognised by Harper (1995) in a mafic ophiolite succession. However, weak alteration could have also taken place during small-scale circulation of seawater in the subsurface during diagenesis.

Occurrences of epidote alteration and hematite dusting in post-D2 diorite intrusions in section 6 (West Thalanga, Fig. 7.7b) indicate that these alteration facies locally post-date regional deformation. This suggests that weak alteration was not linked to any particular large-scale hydrothermal event but may represent relatively minor hydrothermal activity which occurred sporadically during the geothermal history of the area

Controls on intense hydrothermal fluid flow

The mottled alteration facies envelops discordant zones of intense quartz-pyrite alteration facies which cross-cut the footwall. Their orientation varies between 20 and 50° with respect to stratigraphic dip. These zones are interpreted to represent the pathways of mineralising hydrothermal fluids because of their high concentrations of disseminated pyrite and pyrite veins and the observation that they are commonly connected to massive sulphides in the Favourable Horizon. A comparison of the distribution of coherent and volcaniclastic facies in the footwall with the geometry of discordant zones of quartz-pyrite alteration facies indicates that intense hydrothermal fluid flow during mineralisation was independent of the primary lithofacies arrangement (Chapter 5).

7.6 Summary

At Thalanga, 10 different alteration facies can be distinguished based on mineralogy, abundance and distribution of non-primary minerals. These include pyrite-rich, phyllosilicate-dominated, quartz-rich and calcareous mineral assemblages. The intensity of alteration can be estimated based on the overall degree of textural and mineralogical modification.

Mottled alteration facies (moderate alteration intensity), representing the bulk of the footwall alteration zone, is phyllosilicate-dominated, feldspar-destructive and accompanied by minor disseminated pyrite. It defines a broad, strata-bound alteration zone below the massive sulphides and commonly shows apparent clastic textures due to domainal or multi-stage alteration processes. Intense, pyrite-rich alteration occurs in discordant zones within the footwall alteration zone, interpreted as the pathways for ascending mineralising fluids, and in stratiform zones immediately below massive sulphides. Variations in the distribution of intense alteration facies along strike suggest that different alteration processes occurred in the footwall of East and West Thalanga during the evolution of the hydrothermal system.

Weak alteration is characterised by preservation of feldspar phenocrysts and primary textures and patchy to vein-controlled distribution of alteration minerals. Weak alteration is ubiquitous in the hangingwall dacites and is probably unrelated to hydrothermal processes associated with formation of the footwall alteration zone and mineralisation.

8 Alteration geochemistry and geochemical indicators of proximity to the Thalanga deposit

8.1 Introduction

This chapter is concerned with the geochemistry of the various alteration facies observed at Thalanga (Chapter 7) and the compositional effects of hydrothermal alteration. For this purpose, major and trace element data, including REE, are examined and estimates for mass changes are calculated. Furthermore, variations in the data with spatial distance from the Thalanga deposit are evaluated in order to identify geochemical parameters which distinguish altered rocks in the Thalanga mine area from the least-altered or weakly altered, surrounding country rocks. Several systematic compositional changes have been recognised which define a geochemical halo around the deposit and can be regarded as geochemical proximity indicators to massive sulphides at Thalanga.

Most of the geochemical data were obtained during this study and analytical procedures are described in the Appendix. Data for the carbonate-chlorite-tremolite alteration facies and rhyolite type 4 from the Favourable Horizon have been compiled from Herrmann (1994) and Hill (1996), respectively. Furthermore, some geochemical data on variably altered rhyolite made available by RGC Ltd. have been used (eg. Fig. 8.12).

8.2 Alteration geochemistry

8.2.1 Major element geochemistry and the Alteration Boxplot

The compositions of rhyolites from the footwall alteration zone are highly variable due to hydrothermal alteration. Most altered footwall rhyolites have major element compositions which are quite dissimilar to the common geochemical characteristics of fresh rhyolite (eg. elevated values for MgO, FeO and S; Chapter 6 and Appendix). Classification as rhyolite is based on the presence of quartz phenocrysts, gradational lateral contacts between the altered and least-altered rhyolite, with well preserved primary textures and immobile element data (Chapter 6, Figs. 6.3 and 6.4).

Altered footwall rhyolites show marked variations in the concentrations of sodium, calcium, magnesium and iron (Fig. 8.1a). Least-altered rhyolites are magnesium- and iron-poor and contain between 3 and 5 wt.% Na_2O + CaO which is within the range typical of fresh, modern felsic volcanics (Le Maitre et al., 1989). Increasing alteration intensity is coupled with a gradual decrease in Na_2O + CaO values and intensely altered

Fig. 8.1: Major element geochemistry of variably altered volcanic units at Thalanga: FeO + MgO versus Na_2O + CaO, S versus Na_2O + CaO and Carbonate-Chlorite-Pyrite Index versus Alteration Index (Alteration Boxplot).

(a) Na_2O + CaO versus FeO + MgO in rhyolite and dacite from Thalanga. Data from the footwall alteration zone are shown with symbols according to alteration facies. Alteration of the footwall rhyolite was associated with Na_2O + CaO depletion (except for calcareous alteration facies) and enrichment of MgO + FeO. In contrast, hangingwall dacites are Na-rich. Data for carbonate-chlorite-tremolite alteration facies and rhyolite type 4 from Herrmann (1994) and Hill (1996), respectively.

(b) Moderately to strongly altered footwall rhyolite contains significant sulphur due to pyrite alteration. Least-altered footwall rhyolite, rhyolite type 4 and hangingwall dacite are S-poor.

(c) Most of the various alteration facies present at Thalanga can be distinguished geochemically in the Alteration Boxplot (Large, 1996). See text for explanation.

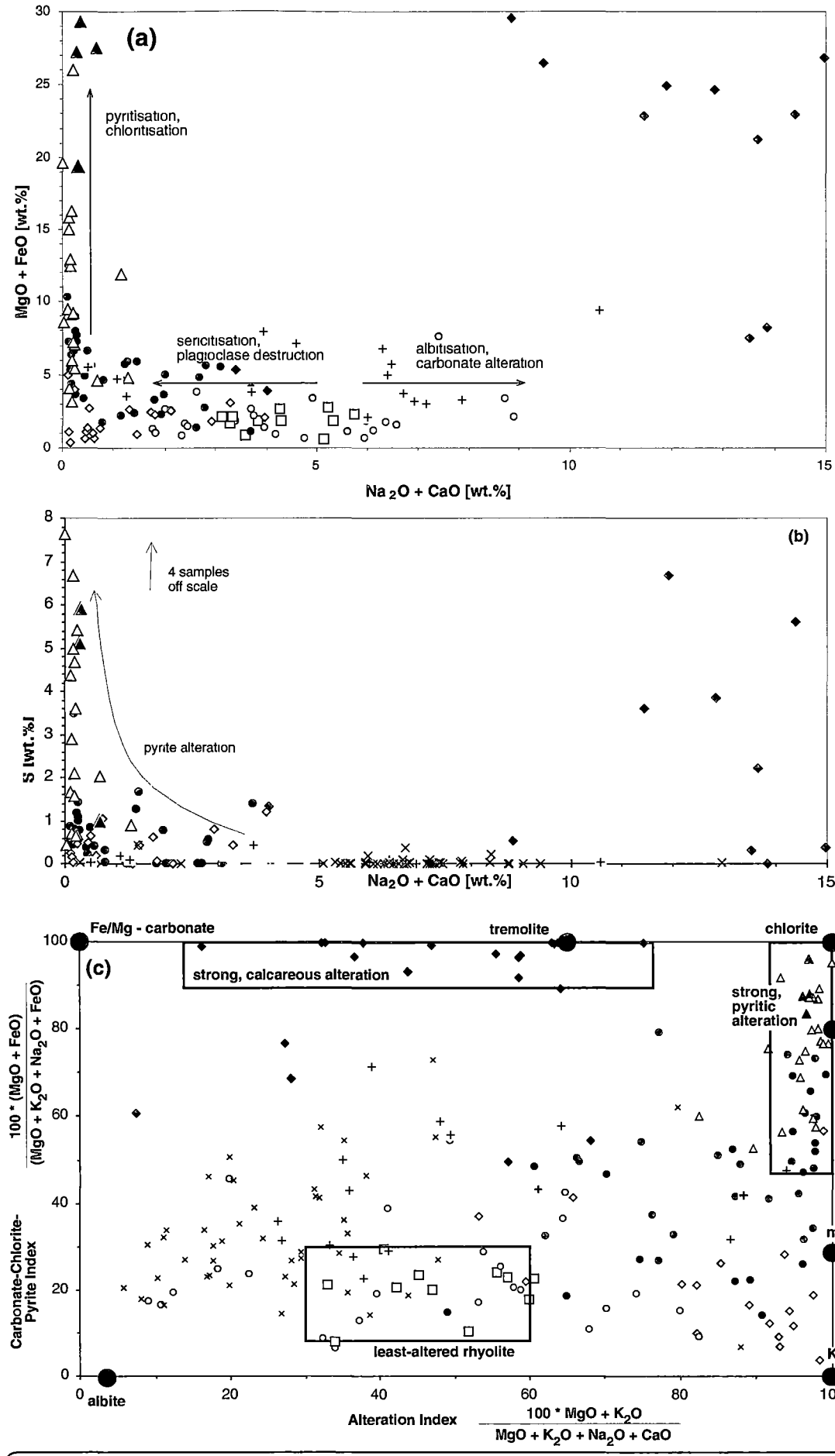
(a)
pyritisation, chloritisation
sericitisation, plagioclase destruction
albitisation, carbonate alteration
MgO + FeO [wt.%]
Na 2O + CaO [wt.%]
(b)
4 samples off scale
pyrite alteration
S [wt.%]
Na2O + CaO [wt.%]
(c)
Fe/Mg - carbonate
tremolite
chlorite
strong, calcareous alteration
strong, pyritic alteration
biotite
muscovite
K-feldspar
albite
least-altered rhyolite
100 * (MgO + FeO) / (MgO + K2O + Na2O + FeO)
Carbonate-Chlorite-Pyrite Index
Alteration Index 100 * MgO + K2O / MgO + K2O + Na2O + CaO
× hangingwall dacite
+ rhyolite type 4 in the Favourable Horizon
□ least-altered footwall rhyolite
○ weakly altered footwall rhyolite
◇ quartz-K-feldspar alteration facies
● mottled alteration facies
◆ carbonate-chlorite-tremolite alteration facies and disseminated tremolite alteration facies
△ quartz-pyrite alteration facies
▲ chlorite-pyrite alteration facies

Fig. 8.1

rhyolites have values <0.3 wt.%. This trend is indicative of plagioclase destruction and formation of muscovite, however, samples of quartz-K-feldspar alteration facies also have low Na_2O + CaO contents. Some samples of weakly altered rhyolite and disseminated tremolite alteration facies have elevated Na_2O + CaO concentrations, reflecting the presence of albite alteration and/or calcite. The carbonate-chlorite-tremolite alteration facies shows extreme calcium and magnesium enrichment and samples plot mainly in the upper right hand corner of Figure 8.1a. Intense, pyritic alteration is characterised by high MgO + FeO values commonly between 5 and 20 wt.% (maximum values: up to 30 wt.%), due to the presence of chlorite and pyrite. Samples of rhyolite type 4 have MgO + FeO values mainly between 3 and 7 wt.%. Their Na_2O + CaO content ranges between 7 and <1 wt.% and overlap with least-altered, weakly altered and moderately altered footwall rhyolite. Alteration logging showed that rhyolite type 4 was generally weakly altered which is consistent with the geochemical data. The hangingwall dacite is typically Na-rich due to widespread albite alteration and concentrations of MgO and FeO are comparatively low.

The depletion of Na_2O in the footwall is coupled with substantial S enrichment of moderately to intensely altered rhyolite, reflecting increasing pyrite abundance (Fig. 8.1b). The Ca-Mg-rich carbonate-chlorite-tremolite alteration facies locally contains barite and/or sphalerite and is variably enriched in sulphur. In contrast, S concentrations are close to, or below, the detection limit (0.01 wt.%) for the hangingwall dacite and rhyolite type 4.

Most alteration facies at Thalanga can be successfully discriminated in one diagram which utilises two multi-element ratios to monitor relative changes in the concentrations of MgO, FeO, K_2O, Na_2O and CaO (the Alteration Boxplot; Large, 1996) (Fig. 8.1c). The Alteration Index (AI = $100*[MgO+K_2O]/[MgO+K_2O+Na_2O+CaO]$; Ishikawa et al., 1976) quantifies calcium and sodium depletion and enrichment relative to magnesium and potassium. The AI increases as a result of plagioclase destruction, or chlorite, muscovite and K-feldspar alteration. In contrast, depletion of K_2O due to albite alteration or Ca-enrichment associated with calcareous alteration result in low AI values. The Carbonate-Chlorite-Pyrite Index (CCPI = $100*[MgO+FeO]/[MgO+FeO+Na_2O+K_2O]$; Large, 1996) measures total alkali depletion relative to magnesium and iron enrichment associated with chlorite and pyrite alteration. Furthermore, dolomite- and/or siderite-rich carbonate alteration is also characterised by high CCPI.

The least-altered footwall rhyolites have AI between 30 and 60 and CCPI between 10 and 30, reflecting relatively high, evenly balanced, primary concentrations of alkalis and low concentrations of FeO and MgO (Fig. 8.1c). Altered, pyrite-rich samples plot in

the upper right hand corner of Figure 8.1c (alteration index >90) due to substantial enrichment in magnesium and iron and depletion of sodium and calcium. Their large spread in CCPI is related to the amount and relative proportions of chlorite, biotite, muscovite and K-feldspar in single samples. Mottled alteration facies has intermediate AI and CCPI, partly overlapping with the fields for the least-altered rhyolite and pyrite-rich alteration facies. Samples of the carbonate-chlorite-tremolite alteration facies plot along the upper boundary of the diagram (CCPI >90) and the large spread in AI reflects the relative proportions of carbonate, chlorite and tremolite. Samples of the quartz-K-feldspar alteration facies overlap with samples of the mottled alteration facies and define a trend towards the composition of K-feldspar. A few samples of weakly altered rhyolite have low AI values (<20) which indicatives sodium and/or calcium enrichment and K_2O depletion. The hangingwall dacites have low values for both AI and CCPI which is consistent with widespread albite alteration. Samples of rhyolite type 4 show a wide distribution in the Alteration Boxplot, with data points overlapping with analyses of the hangingwall dacites, least-altered footwall rhyolites and mottled alteration facies. This is consistent with petrographic observations that suggest rhyolite type 4 is commonly texturally unaltered or weakly altered.

8.2.2 Base metal and trace element geochemistry

The concentrations of Cu, Pb, Zn and Ba in the various alteration facies, least-altered footwall rhyolite, hangingwall dacite and rhyolite type 4 are illustrated in Figure 8.2. In these diagrams, Na_2O was plotted on the x-axis because sodium depletion can be regarded as a general indicator of increasing alteration intensity in the footwall alteration zone.

The base metal contents of samples from the footwall alteration zone vary substantially. Intensely altered footwall rhyolites often have one order of magnitude higher Cu, Zn and Pb concentrations than least-altered equivalents. Samples of the carbonate-chlorite-tremolite alteration facies are especially enriched in base metals and Zn values > 1 wt.% are common. The chlorite-pyrite alteration facies is particularly Cu- and Zn-rich whereas base metal concentrations of the quartz-pyrite alteration facies are extremely variable (Fig. 8.2a to c). Base metal concentrations of the hangingwall dacite and rhyolite type 4 are generally within the range of the least-altered footwall rhyolite. Some samples are variably enriched in Cu, Pb and Zn, although a correlation with Na_2O concentrations is not apparent.

Fig. 8.2: Trace element geochemistry of variably altered volcanic units at Thalanga: Cu, Pb, Zn and Ba versus Na_2O.

Cu, Pb, Zn and Ba concentrations in samples of the least-altered and variably altered footwall rhyolite, rhyolite type 4 and hangingwall dacite. The data for Cu, Pb, Zn and Ba were plotted versus Na_2O because sodium depletion due to hydrothermal alteration is ubiquitous in the footwall alteration zone. Data for carbonate-chlorite-tremolite alteration facies and rhyolite type 4 from Herrmann (1994) and Hill (1996), respectively. Legend as for Figure 8.1.

(a) Cu versus Na_2O (b) Pb versus Na_2O

(c) Zn versus Na_2O (d) Ba versus Na_2O

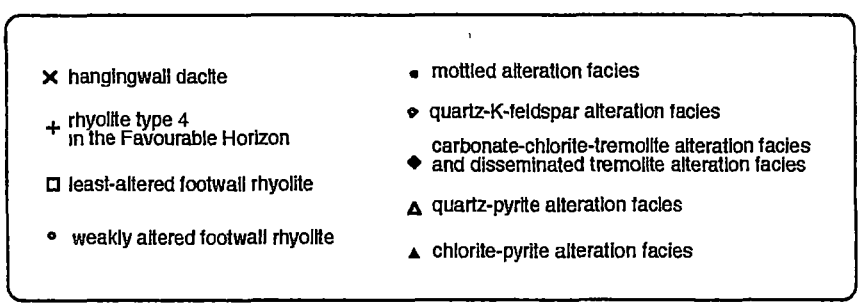

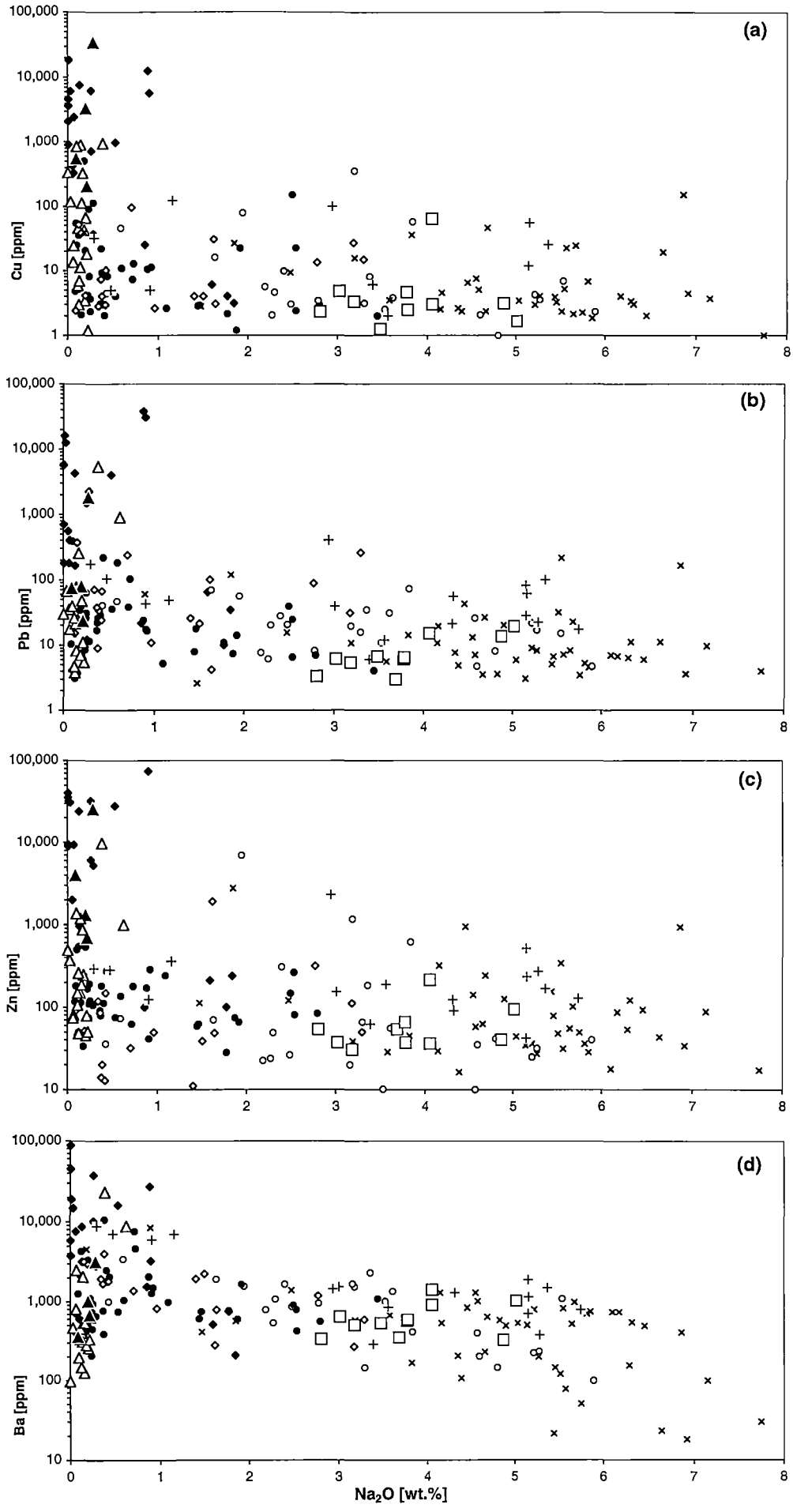
(a)
Cu [ppm]
100,000
10,000
1,000
100
10
1
(b)
Pb [ppm]
(c)
Zn [ppm]
(d)
Ba [ppm]
0
1
2
3
4
5
6
7
8
Na2O [wt.%]

Fig. 8.2

Several features indicate a strong mineralogical control on Ba enrichment or depletion (Fig. 8.2d). There is a general correlation between the decrease of Na_2O and an increase of Ba from the least-altered footwall rhyolite (~500 to 1,000 ppm) to some samples of moderately to intensely altered footwall rhyolite which contain 2,000 to >10,000 ppm Ba. The increase in Ba may be related to the formation of muscovite and K-feldspar replacing primary plagioclase and substitution of Ba for potassium. However, many samples of the quartz-pyrite alteration facies have relatively low Ba concentrations (within the range of the least-altered footwall rhyolite or lower). These low levels of barium suggest that these samples are relatively muscovite-(and K-feldspar)-poor. Extremely low values for barium occur in several Na-rich samples of the hangingwall dacite. This suggests that albitisation of feldspar crystals in the hangingwall dacite led to concurrent K and Ba depletion. Samples of the carbonate-chlorite-tremolite alteration facies are barium-rich (commonly ≥1 wt.%) which is related to occurrences of barite. Concentrations of Ba are relatively uniform in samples of rhyolite type 4 (1,000 to 2,000 ppm), however, some Na_2O-poor samples have elevated Ba values.

Figure 8.3 illustrates the trace element composition of variably altered footwall rhyolites and hangingwall dacites. The carbonate-chlorite-tremolite alteration facies and rhyolite type 4 are not included in these diagrams because appropriate data are not available (Herrmann, 1994 and Hill, 1996, respectively).

Concentrations of Rb in the footwall rhyolites (Fig. 8.3a) increase with decreasing Na_2O. This trend is consistent with an alteration process involving plagioclase destruction since Rb may be substituted for K in muscovite and K-feldspar. However, samples of the quartz-pyrite alteration facies deviate from this trend and have relatively low Rb contents. These samples have lower abundances of muscovite compared to the mottled alteration facies. The hangingwall dacites are comparatively Rb-poor reflecting K_2O depletion associated with albite alteration.

Data for Sr show considerable scatter, however, most moderately to intensely altered samples of the footwall rhyolite are relatively Sr-poor which is an indication of plagioclase destruction. Samples of the disseminated tremolite alteration facies have elevated Sr concentrations. The hangingwall dacite show a wide range of Sr values which is probably related to occurrences of epidote and carbonate (epidote alteration). These features are consistent with the interpretation that Sr has replaced Ca in Ca-bearing, non-primary minerals such as epidote, tremolite and carbonate.

Fig. 8.3: Trace element geochemistry of variably altered volcanic units at Thalanga: Rb, Sr, Tl, As, Bi, Mo and Sb versus Na_2O.

Rb, Sr, Tl, As, Bi, Mo and Sb concentrations in the least-altered footwall rhyolite, altered footwall rhyolite and hangingwall dacite. Legend as for Figure 8.1.

(a) Rb versus Na_2O

(b) Sr versus Na_2O

(c) Rb/Sr versus Na_2O

(d) Tl versus Na_2O

(e) As versus Na_2O

(f) Bi versus Na_2O

(g) Mo versus Na_2O

(h) Sb versus Na_2O

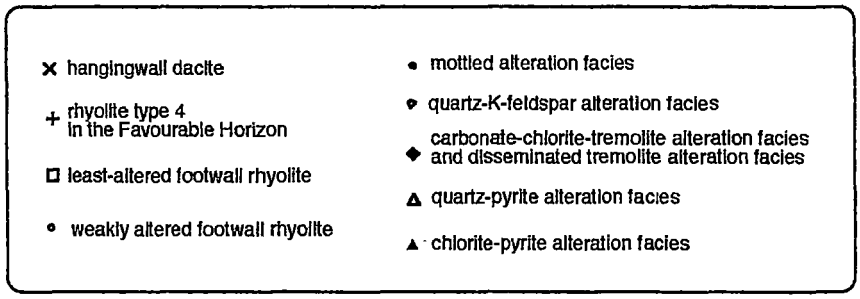

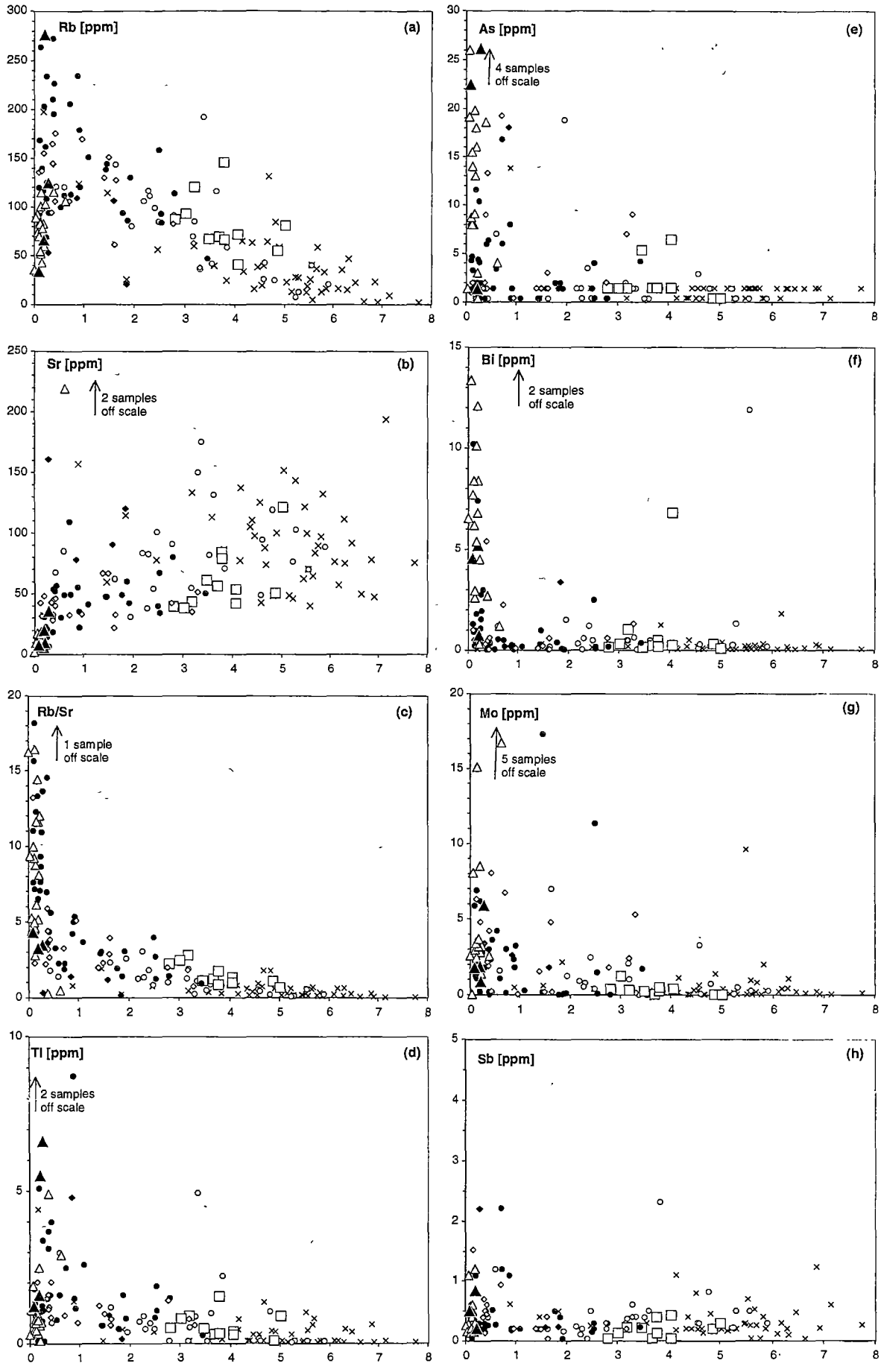
Rb [ppm]
(a)
As [ppm]
(e)
4 samples off scale
Sr [ppm]
(b)
2 samples off scale
Bi [ppm]
(f)
2 samples off scale
Rb/Sr
(c)
1 sample off scale
Mo [ppm]
(g)
5 samples off scale
Tl [ppm]
(d)
2 samples off scale
Sb [ppm]
(h)
Na2O [wt.%]
Na2O [wt.%]

Fig. 8.3

Increasing Rb/Sr ratios are correlated with depletion of Na_2O (Fig. 8.3c). In the mottled alteration facies, Rb/Sr values are slightly higher than in the least-altered footwall rhyolite (>2) and samples of the intense, pyritic alteration facies have a continuous range of values between 3 and 18. The hangingwall dacites have low Rb/Sr ratios ($\leq$1).

In general, Tl concentrations are close to, or below, the detection limit (0.5 ppm) but increase to values >2 ppm with decreasing Na_2O (Fig. 8.3d). However, samples of the intense, pyrite-rich alteration facies show a wide range in Tl concentrations and values <1 ppm are common. The hangingwall dacites have Tl concentrations below, or close to, the detection limit.

Variations in As, Bi and Mo contents are generally limited and within the range of the least-altered footwall rhyolite, except for the intense, pyrite-rich alteration facies (Fig. 8.3e to g). Analyses of the quartz-pyrite alteration facies show a wide, continuous range in As and Bi contents following a pattern which is largely similar to the trend for chlorite and pyrite alteration in Figure 8.1a. In general, As and Bi may substitute into pyrite and therefore, it is inferred that increasing concentrations of these elements are correlated with the abundance of pyrite. Elevated concentrations of Mo (>2 ppm) are common for samples of the quartz-K-feldspar, mottled and quartz-pyrite alteration facies. Concentrations of As, Bi and Mo are close to, or below, detection limit in hangingwall dacite. Concentrations of antimony in the footwall rhyolite and hangingwall dacite are generally close to the detection limit (0.5 ppm). Only a relatively small number of samples with Na_2O <1 wt.% contain >1 ppm Sb (Fig. 8.3h).

8.3 Mass balance calculations

Compositional changes related to alteration processes involving mass changes are obscured in the untreated analytical data due to the effect of closure, which is inherent in geochemical analyses expressed in weight percent (Aitchinson, 1984; Rollinson, 1993). For example, hydrothermal alteration leading to silicification of the footwall rhyolite, which was already SiO_2-rich prior to alteration, is difficult to recognise from the major element data. However, under certain conditions, absolute mass changes can be calculated if immobile elements can be identified and if the composition of the precursor to the altered rock can be estimated.

The problem of calculating mass changes associated with alteration has been addressed by numerous researchers and a variety of methods have been proposed (Gresens, 1967; Grant, 1986; MacLean & Kranidiotis, 1987; Huston, 1993; Madeisky & Stanley, 1993; Leitch & Lentz, 1994). In this study, mass changes were calculated using

the approach of MacLean & Kranidiotis (1987) which has been described and discussed in detail by MacLean (1990), MacLean & Barrett (1993) and Barrett & MacLean (1994).

This method relies on the concept that changes in the measured concentrations of immobile elements in a suite of altered rocks with a common precursor are controlled by the depletion and addition of mobile chemical components. For example, if the altered rock has a lower concentration of immobile elements than the precursor, it can be inferred that mass has been gained during alteration (Fig. 8.4a). Therefore, comparing the concentration of an immobile element in an altered sample to the concentration of the immobile element in the unaltered precursor returns a correction factor which can be used to calculated absolute mass changes. The correction factor is applied to the geochemical data for the altered sample in order to calculate a reconstituted concentration for each chemical component. The difference between this reconstituted concentration and the concentration in the precursor represents the absolute mass change of the component. Hence, the geochemical data for altered rocks may be recalculated for every single chemical component according to:

$$\Delta X_m = [(X_i^P / X_i^A) * X_m^A] - X_m^P$$

with

ΔX_m = absolute mass change of mobile component m

X_m^A = concentration of mobile component m in altered sample

X_m^P = concentration of mobile component m in precursor

X_i^A = concentration of immobile component i in altered sample

X_i^P = concentration of immobile component i in precursor

$[(X_i^P / X_i^A) * X_m^A]$ = reconstituted concentration.

At Thalanga, mass changes were calculated using Zr as the conserved immobile element because immobility is indicated by constant Ti/Zr ratios (below and Chapter 6). The averaged compositions of the least-altered samples of rhyolite types 1, 2 and 3 and dacite types 1, 2 and 3 are presented in Tables 6.1 and 6.2 and can be regarded as the best estimate for the respective precursors.

Criteria used for the identification of the least-altered samples include preservation of primary feldspar crystals, absence of pyrite and low abundances of non-primary minerals such as muscovite, chlorite, biotite, epidote and carbonate. Geochemically, least-altered rhyolites and dacites are characterised by low S, MgO and FeO contents and relatively high concentrations of Na_2O and K_2O with intermediate K_2O-ratio ($100*K_2O/[Na_2O + K_2O]$, Chapter 6).

Fig. 8.4: The effects of mass changes on the concentrations of immobile elements in altered rocks and evidence for immobility of Zr and TiO_2 at Thalanga.

(a) Schematic representation of the effects of mass changes on the concentrations of immobile elements (A and B). During hydrothermal alteration the mass of altered rocks may change relative to the precursor due to addition or removal of mobile chemical components. Consequently, the concentrations of immobile elements may vary but their ratios remain constant. See text for explanation.

(b) Variation diagram plotting TiO_2 versus Zr for variably altered footwall rhyolite and hangingwall dacite from Thalanga. This diagram is similar to Figure 6.3a. However, this diagram shows data according to alteration facies and the calculated precursor compositions of rhyolite types 1, 2 and 3 and dacite types 1, 2 and 3 are also plotted (Tables 6.1 and 6.2).

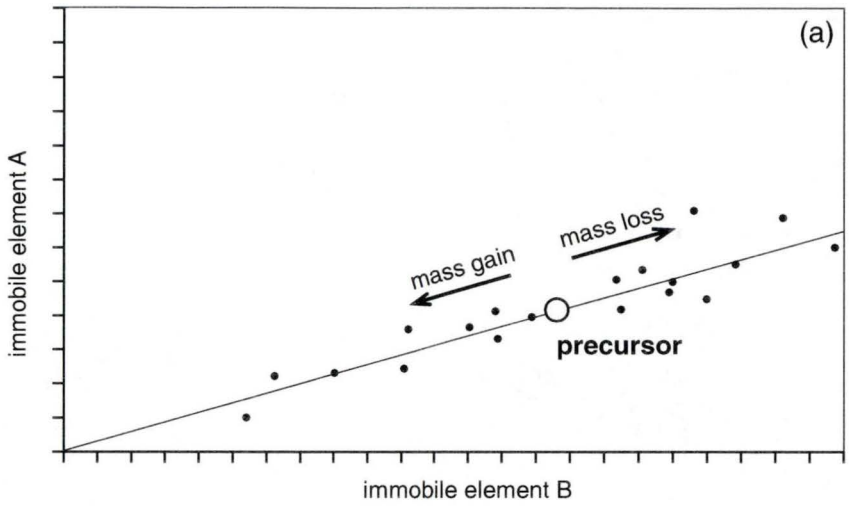

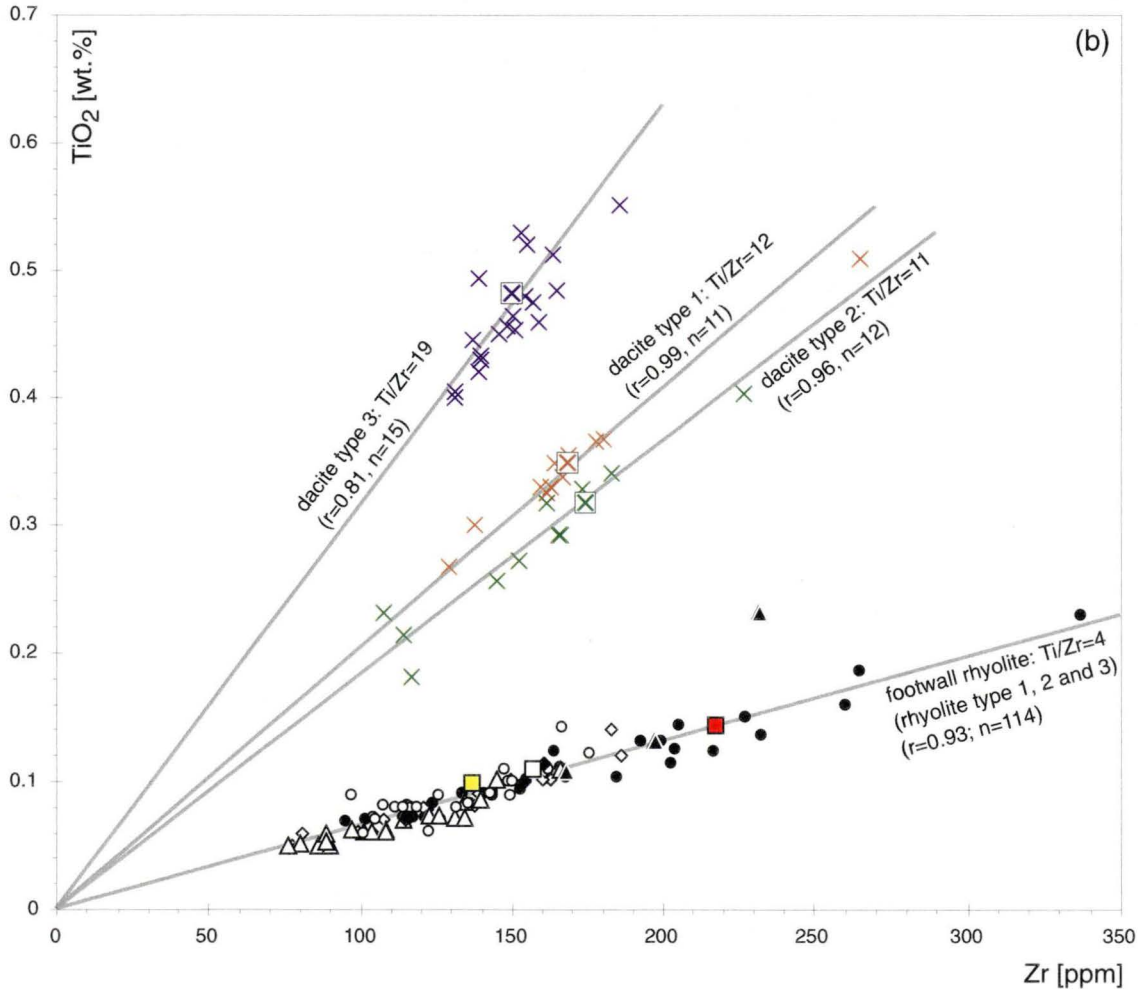

- precursor rhyolite type 1
- precursor rhyolite type 2
- precursor rhyolite type 3
- precursor dacite type 1
- precursor dacite type 2
- precursor dacite type 3
- weakly altered footwall rhyolite
- quartz-K-feldspar alteration facies
- mottled alteration facies
- disseminated tremolite alteration facies
- quartz-pyrite alteration facies
- chlorite-pyrite alteration facies

Fig. 8.4

Analyses of variably altered footwall rhyolite (rhyolite types 1, 2 and 3) define a positive correlation trend with a constant Ti/Zr ratio of ~ 4 (r = 0.93) on a diagram of TiO_2 versus Zr and the line of best fit can be extrapolated to intersect the origin of the diagram (Figs. 6.3a and 8.4b). This relationship satisfies the conditions for immobile behaviour during hydrothermal alteration proposed by MacLean & Barrett (1993). The positive correlation of TiO_2 and Zr is interpreted to be caused by mass changes during hydrothermal alteration related to variable removal or addition of mobile chemical components. As a result, the concentrations of TiO_2 and Zr are changing in equal proportions and therefore the ratio of these elements remains constant. Alternatively, this correlation trend could only be explained by an alteration process in which Ti and Zr were added or removed in exactly the same proportions. This is an unlikely scenario because Ti and Zr occur in minerals such as Ti-Fe-oxides and zircon which are difficult to dissolve even in highly concentrated acidic solutions. Furthermore, it is also unlikely that hydrothermal fluids would leach Zr and Ti from a rock at the same rate, as would be required in order to maintain a constant Ti/Zr ratio.

The spread of analyses for the variably altered footwall rhyolites and hangingwall dacites away from the data points of least-altered equivalents (ie. precursors) implies that significant mass changes occurred during alteration (Fig. 8.4b). It is also clear that the compositions of the least-altered rhyolite types 1, 2 and 3 differ somewhat in terms of Zr and TiO_2 concentrations even though they have essentially the same Ti/Zr ratio. This is an important observation because the value chosen for X_i^P strongly influences the calculation of mass changes. Consequently, the use of one averaged precursor composition based on all samples of the least-altered footwall rhyolite would result in spurious results and it is essential that analyses of altered footwall rhyolites are compared to the corresponding composition of the least-altered rhyolite type 1, 2 or 3.

At Thalanga, different textural and petrographic types of footwall rhyolite can still be recognised in the footwall alteration zone, and thus compared to the best possible estimate of their respective precursor compositions, avoiding the use of inappropriate Zr values for X_i^P in mass change calculations. The observation that the least-altered samples of different types of rhyolite may have different Zr and TiO_2 concentrations even though their Ti/Zr ratios are identical reinforces the importance of careful textural examination and volcanic facies analyses in the study of altered host rocks to massive sulphide deposits, especially in cases involving superficially homogeneous successions.

Fig. 8.5: Average mass changes of alteration facies in the footwall alteration zone and in hangingwall dacite.

(a) Average mass changes associated with alteration facies in the footwall alteration zone (mottled alteration facies: n = 37; quartz-pyrite alteration facies: n = 20; chlorite-pyrite alteration facies: n = 4; quartz-K-feldspar alteration facies: n = 19; disseminated tremolite alteration facies: n = 4). Data for carbonate-chlorite-tremolite alteration facies from Herrmann (1994; n = 15).

(b) Average mass changes associated with alteration facies in the hangingwall dacite (phyllosilicate alteration: n = 13; epidote alteration: n = 5; albite alteration: n = 15; hematite dusting [including samples with additional disseminated epidote]: n = 4).

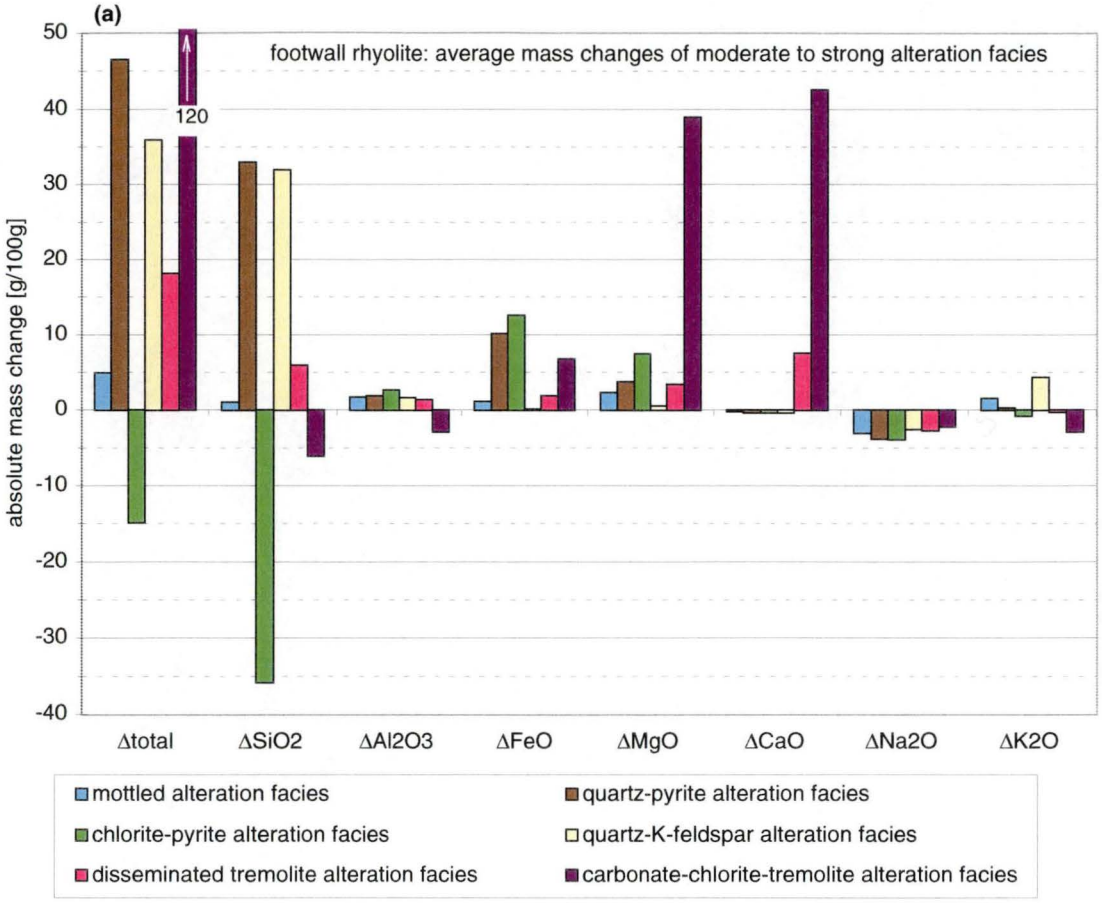
(a)
footwall rhyolite: average mass changes of moderate to strong alteration facies
absolute mass change [g/100g]
50
40
30
20
10
0
-10
-20
-30
-40
120
Δtotal
ΔSiO2
ΔAl2O3
ΔFeO
ΔMgO
ΔCaO
ΔNa2O
ΔK2O
mottled alteration facies
quartz-pyrite alteration facies
chlorite-pyrite alteration facies
quartz-K-feldspar alteration facies
disseminated tremolite alteration facies
carbonate-chlorite-tremolite alteration facies

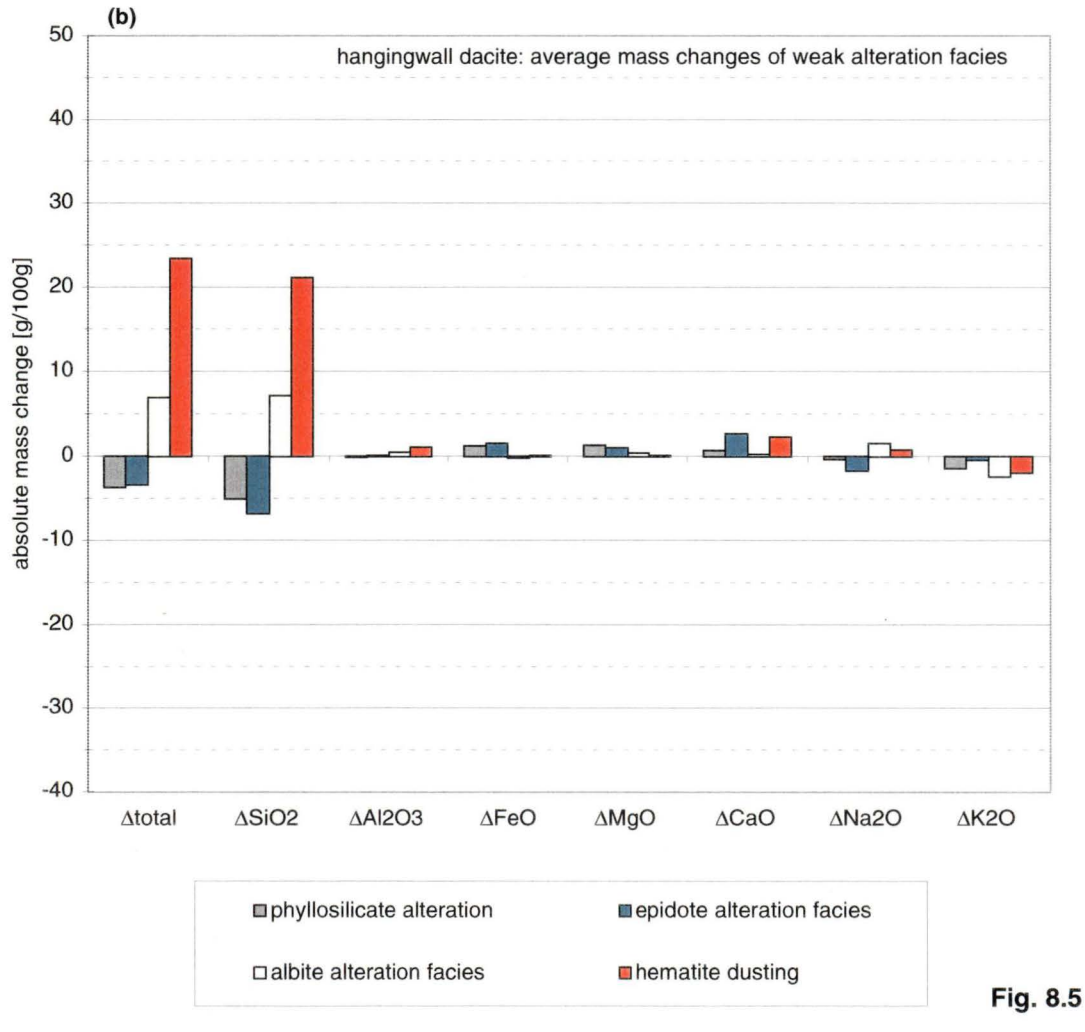
(b)
hangingwall dacite: average mass changes of weak alteration facies
absolute mass change [g/100g]
50
40
30
20
10
0
-10
-20
-30
-40
Δtotal
ΔSiO2
ΔAl2O3
ΔFeO
ΔMgO
ΔCaO
ΔNa2O
ΔK2O
phyllosilicate alteration
epidote alteration facies
albite alteration facies
hematite dusting

Fig. 8.5

8.3.1 Average mass changes of alteration facies

Absolute mass changes were determined for single samples by calculating the reconstituted concentration for each element and subtracting the respective concentration in the precursor. Hence, the effect of closure is overcome by applying an individual correction factor (X^P_{Zr}/X^A_{Zr}) to the data for each sample. Mass addition of a mobile element is indicated by $[(X^P_i/X^A_i)*X^A_m] > X^P_m$ whereas the reconstituted concentration is less than the concentration of the mobile element in the precursor if it was leached from the rock during alteration. Elements that were immobile during alteration should have ΔX_m values of zero.

Average mass changes of major elements for the various alteration facies in the footwall alteration zone and in the hangingwall are represented in Figure 8.5. The results show that moderate to intense alteration of footwall rhyolite was generally associated with significant total mass gain mainly in the form of SiO_2, FeO and MgO whereas near-total loss of Na_2O is ubiquitous (Fig. 8.5a). However, there are significant variations among the different alteration facies. For example, the chlorite-pyrite alteration is characterised by total mass loss due to leaching of SiO_2 (-35 g/100 g) which is partly balanced by substantial gains in FeO and MgO. In contrast, the quartz-pyrite alteration facies has gained SiO_2 (~35 g/100 g) and gains in FeO and MgO are somewhat smaller than for chlorite-pyrite alteration facies. Samples of the mottled alteration facies have strongly variable values for ΔSiO_2 (Fig. 8.6c) which, on average, suggest a small overall mass gain in silica. Mass gains in FeO, MgO and K_2O contribute to the comparatively small total mass gain for the mottled alteration facies. The quartz-K-feldspar alteration facies has gained ~ 30 g/ 100 g of total mass mainly in the form of SiO_2 and K_2O. The disseminated tremolite alteration facies shows a total mass gain, which is due to significant addition of MgO and CaO. Mass changes associated with carbonate-chlorite-tremolite alteration facies were examined by Herrmann (1994) who demonstrated that this facies represents altered footwall rhyolite which has lost SiO_2 (-6 g/100 g) and gained large amounts of MgO (39 g/100 g) and CaO (42 g/100 g) as well as Ba, S, CO_2 and base metals.

Weak alteration of the hangingwall dacite was associated with comparatively small mass changes (Fig. 8.5b). Phyllosilicate alteration is associated with total mass loss mainly in the form of SiO_2 (-5 g/100 g) and K_2O; however, FeO and MgO were added. Epidote alteration is also characterised by total mass loss due to negative ΔSiO_2 (-7 g/100 g), but has gained significant CaO, FeO and MgO. The loss in Na_2O is comparatively high for epidote alteration whereas K_2O remained largely unchanged. Total mass gain is associated with albite alteration which occurred in the form of SiO_2 and Na_2O mass

addition whereas most K_2O was lost during this type of alteration. Dacite samples with hematite dusting are characterised by the highest SiO_2 mass gains in the hangingwall (20 g/100 g), some gains in Na_2O and significant K_2O loss. Gains in CaO of this alteration facies are most likely attributable to minor disseminated epidote.

8.3.2 Mass change variation diagrams

The calculated mass changes show substantial variations among and within groups of the different alteration facies, as illustrated in variation diagrams plotting the results for ΔX_m of selected elements (Fig. 8.6). These variations are consistent with the observation that alteration at Thalanga is mineralogically and compositionally complex and boundaries between alteration facies are gradational.

A plot of ΔNa_2O versus ΔMgO (Fig. 8.6a) shows that Na_2O loss and MgO gain are widespread in the footwall alteration zone and that intensely altered rhyolite have lost nearly all the Na_2O that was originally in the rock (≥95 % relative loss compared to Na_2O concentration in the precursor, Table 6.1). Gains in Na_2O are common in the altered hangingwall dacite, consistent with widespread albite alteration. Data for the mottled alteration facies show variable Na_2O loss ranging from -0.2 g to -3.8 g/100 g and MgO gains up to 4 g/100 g. Samples of the chlorite-pyrite alteration facies have gained substantial amounts of MgO (4 g to 9 g/100 g) whereas MgO mass gains in the quartz-pyrite alteration facies are more variable (≤1 g to 11 g/100 g). The quartz-K-feldspar alteration facies is characterised by large Na_2O mass loss and little change in MgO.

A plot for the absolute mass changes of K_2O and FeO illustrates that K_2O contents remained largely unaffected by intense, pyritic alteration (Fig. 8.6b). The trend of FeO addition roughly follows the line of zero mass change for K_2O and ΔK_2O values vary erratically between 1 and -1. In contrast, variable K_2O and FeO addition is ubiquitous in the weakly to moderately altered footwall rhyolite. Samples of quartz-K-feldspar alteration facies are strongly enriched in K_2O gaining up to ~8g/100g K_2O, however, values for ΔFeO are low. The hangingwall dacites have lost variable amounts of K_2O and show erratic variations in ΔFeO.

These relationships show that K_2O, in contrast to Na_2O, was generally retained in, or added to, the footwall rhyolite during hydrothermal alteration at Thalanga. This is consistent with the observation that muscovite is a common phase in the altered rhyolite (Table 7.1), suggesting that muscovite was stable in most parts of the hydrothermal system during mineralising hydrothermal activity. K_2O addition in the footwall alteration zone is prominent in the quartz-K-feldspar alteration facies.

Fig. 8.6: Variation diagrams showing the calculated mass changes for single samples of alteration facies.

There are consistent differences among alteration facies however, they may occupy overlapping fields.

(a) ΔNa_2O versus ΔMgO

(b) ΔK_2O versus ΔFeO

(c) ΔFeO versus ΔSiO_2

(d) ΔK_2O versus Ba [ppm]

(e) ΔNa_2O versus Zn [ppm]

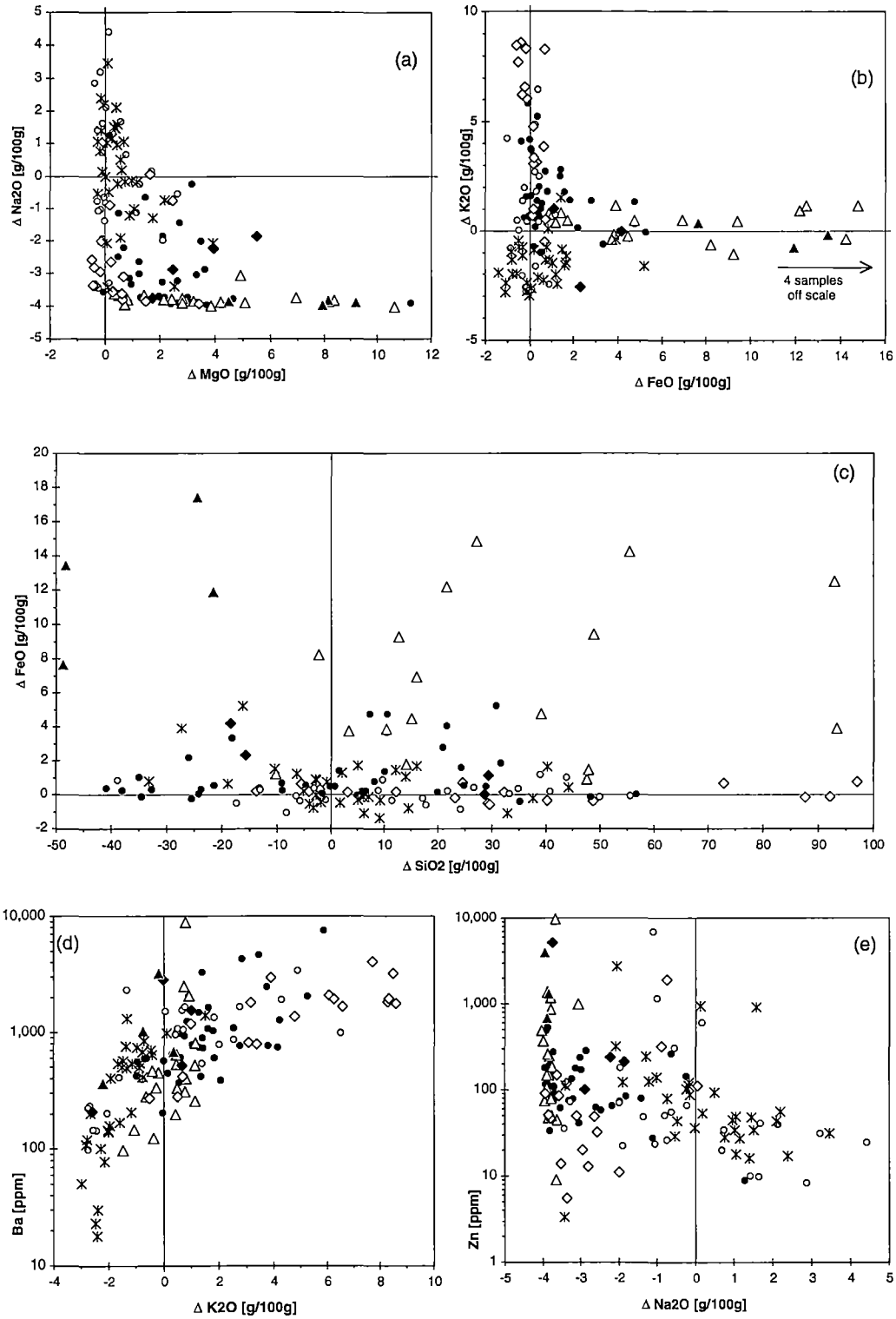

○ weakly altered footwall rhyolite	◆ disseminated tremolite alteration facies
◇ quartz-K-feldspar alteration facies	• mottled alteration facies
△ quartz-pyrite alteration facies	▲ chlorite-pyrite alteration facies
✳ altered hangingwall dacite	

Fig. 8.6

Large mass changes in SiO_2 are an important feature of alteration at Thalanga and parts of the footwall occupied by quartz-pyrite alteration facies have gained variable amounts of silica (mainly between 5 to 50 g/100 g; Fig. 8.6c). In contrast, the chlorite-pyrite alteration facies is characterised by depletion in SiO_2. Samples of the mottled alteration facies show a continuous range from substantial mass loss (-40 g/100 g) to substantial mass gain (50 g/100 g) indicating that SiO_2 was mobile on a large scale in the footwall alteration zone. The quartz-K-feldspar alteration facies is associated with large, in some cases extreme (>85 g/100 g), mass gains in SiO_2. The hangingwall dacite experienced variable mass gains and losses during alteration, indicating that silica was also a mobile chemical component under the conditions of weak alteration.

A strong correlation between absolute mass change of K_2O and barium concentration (in ppm) can be observed (Fig. 8.6d) supporting the interpretation that Ba has substituted for K in muscovite and K-feldspar. Loss of K_2O, which is particularly prominent in the albite-altered hangingwall dacites, correlates with extremely low Ba concentrations (<200 ppm). In contrast, the altered footwall rhyolites with positive ΔK_2O values are generally Ba-rich (>1000 ppm). A plot for mass changes of Na_2O and concentration of Zn (in ppm) shows that elevated Zn-values (>100 ppm) are almost exclusive to samples with Na_2O loss (Fig. 8.6e). However, the range of Zn content in intensely altered rhyolite, with near-total losses of Na_2O, is extremely wide.

8.4 Alteration and REE mobility

Chondrite-normalised REE patterns are used for geochemical classification and petrogenetic interpretation of ancient, metamorphosed volcanics (Chapter 6). This approach relies on the immobility of REE which, assuming low water/rock ratios and low to medium grade metamorphic conditions, is a reasonable assumption (Humphris, 1984). The effects of weathering on REE abundances are minimal and Michard (1989) demonstrated that hydrothermal solutions have between 5×10^2 and 10^6 times lower REE concentrations than the respective reservoir rock through which they have passed. Consequently, alteration is not expected to have major implications for REE chemistry unless water/rock ratios are high (Rollinson, 1993).

The behaviour of REE in footwall alteration zones of hydrothermal massive sulphide deposits has been the subject of considerable research (eg. Campbell et al., 1984; Whitford et al., 1988; MacLean, 1988; Schandl et al., 1995). These and other studies have shown that REE concentrations in altered volcanics are variably modified, compared to their respective precursors, indicating REE mobility under the conditions of

Fig. 8.7: Effect of total mass changes on the concentrations of REE.

This example shows data from the Delbridge massive sulphide deposit (Noranda mining camp, Canada) where REE were immobile during alteration (except for Eu). Overall REE depletion due to mass gains is characteristic for silicified samples whereas REE concentrations increased in samples which experienced mass loss. Figure from Barrett et al. (1993).

Fig. 8.8: Behaviour of LREE and HREE during hydrothermal alteration at Thalanga.

At Thalanga, light REE, such as La, were mobile during alteration whereas heavy REE (eg. Lu and Yb) were immobile.

(a) The positive correlation between Lu and Zr indicates that Lu was immobile during alteration.

(b) Variations in the concentration of Lu in altered rhyolite compared to the precursor are due total mass addition (causing relative Lu depletion) and total mass loss (causing relative Lu enrichment).

(c) Analyses of Yb and Lu show an extremely well correlated trend which indicates that both elements were immobile during alteration. The difference between the correlation factors for plots of Lu versus Yb and Lu versus Zr could be due to variable analytical precision of Zr measurements by XRF and REE analysis by high-resolution ICP-MS.

(d) In contrast to the highly correlated trend between Yb and Lu, the data points show substantial scatter in a plot of Lu versus La. This feature is interpreted to indicate that La was mobile during alteration at Thalanga.

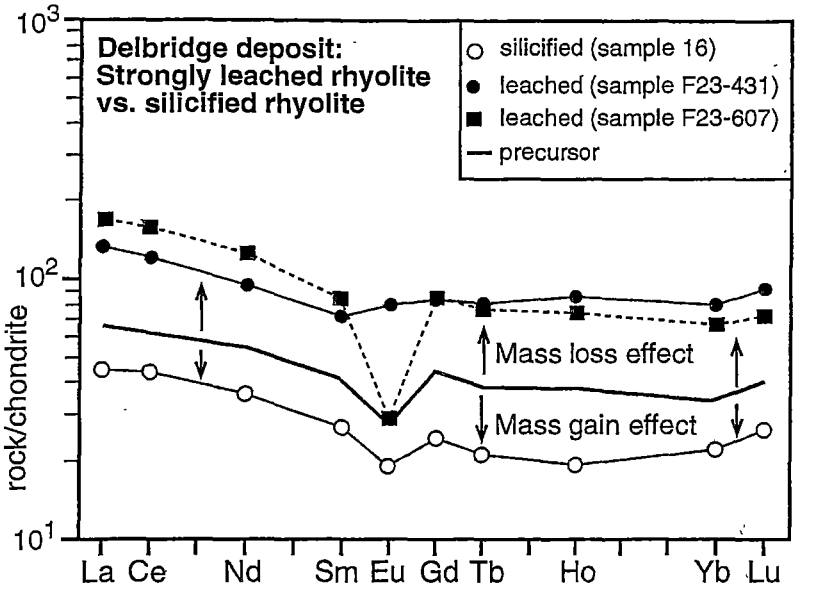

Fig. 8.7

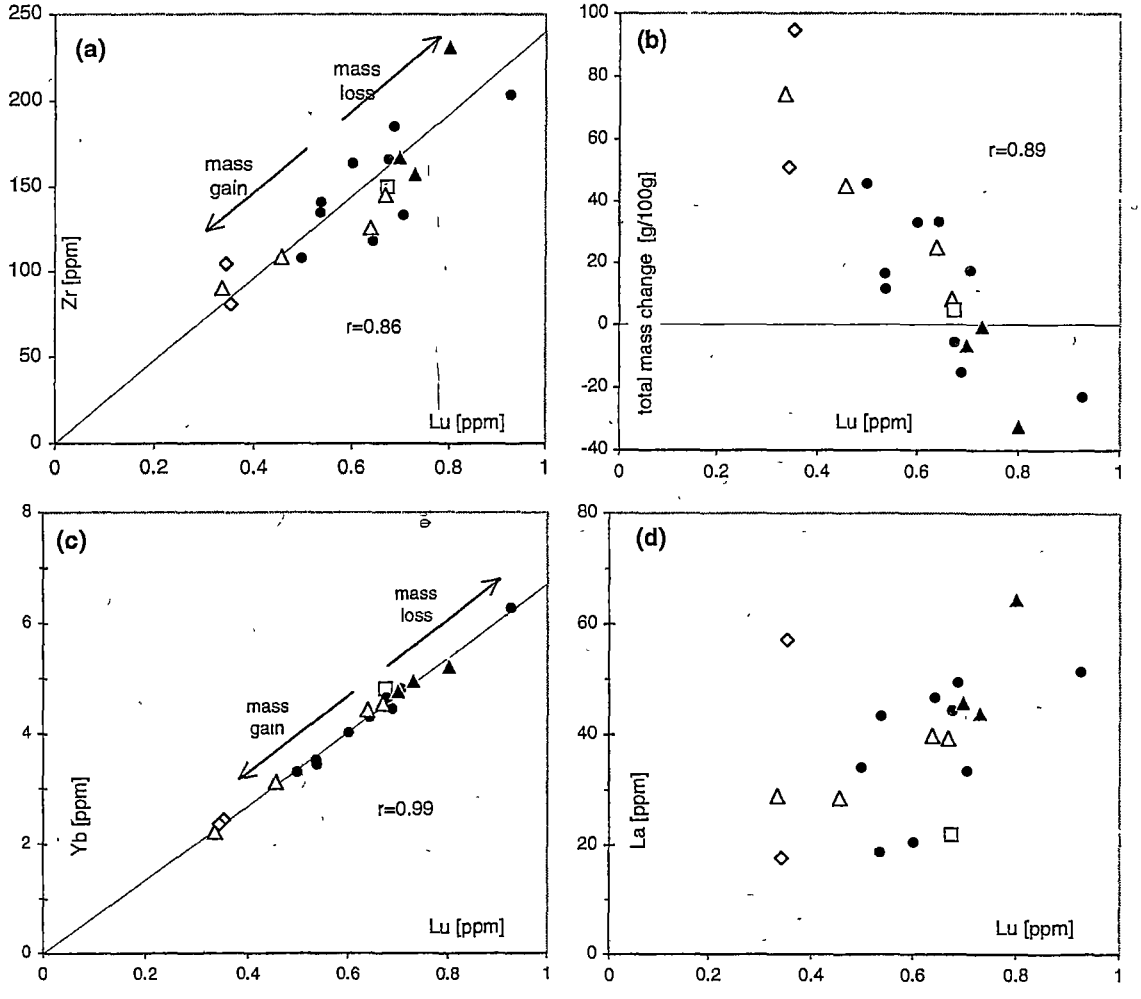

Legend:

□ precursor
◇ quartz-K-feldspar alteration facies
● mottled alteration facies
△ quartz-pyrite alteration facies
▲ chlorite-pyrite alteration facies

Fig. 8.8

mineralising hydrothermal alteration. Mobility of REE in this environment is probably a consequence of high water/rock ratios. Furthermore, the composition of the fluid, which may deviate substantially from the composition of seawater used in the relevant experiments, could also represent an important controlling factor. In general, mobility of REE increases from heavy REE to light REE and consequently, ratios such as Lu/La may change due to alteration (Campbell et al., 1984). Mobility of Eu is also an important feature in some alteration zones. For example, Eu-depletion in altered andesite compared to the least-altered precursor, represented by plagioclase-phyric andesite, is evident in the footwall to the Que River deposit (Tasmania, Australia), whereas other REE were immobile during alteration (Whitford et al., 1988). In this case, plagioclase destruction during hydrothermal activity is the likely cause of Eu leaching.

MacLean (1988) demonstrated that the concentrations of REE elements in altered rocks are influenced by mass changes associated with major element mobility. If all of the REE were immobile, their concentrations would change uniformly if mass was gained or lost during alteration, in a similar fashion as other immobile elements (eg. Zr). In this scenario, REE patterns of altered rocks have similar shapes to REE patterns of least-altered equivalents, however, in many cases they are displaced along the y-axis of chondrite-normalised diagrams according to overall mass gains and losses (Fig. 8.7, Barrett et al., 1993; Barrett & MacLean, 1994a).

Hence, changes in the concentrations of REE may be a function of two processes: (1) variable mobility of REE and (2) mass changes due to addition and depletion of major chemical components during hydrothermal activity. In order to isolate the effects of variable REE mobility, the data may be normalised to Lu, the most immobile of the REE, which removes the superimposed changes in REE concentration related to mass changes (MacLean, 1988; Ludden & Thompson, 1979).

Samples of altered rhyolite and least-altered volcanics of the Thalanga sequence were selected for REE analysis. The data for least-altered samples of the various types of rhyolite and dacite are presented and discussed in terms of petrological implications in Chapter 6. Here, the data for quartz-K-feldspar, mottled, quartz-pyrite and chlorite-pyrite alteration facies from the footwall alteration zone in East Thalanga are presented and compared to data of least-altered rhyolite type 1 (samples from drill holes TH270, TH85 and TH85A; Appendix).

The data show evidence for light REE (LREE) mobility whereas heavy REE (HREE) were immobile. A well constrained positive correlation between Zr and Lu, which can be extrapolated to intersect the origin of the diagram, indicates that both elements were immobile during alteration (Fig. 8.8a) (MacLean & Barrett, 1993). Changes

in the concentrations of Zr and Lu are interpreted to be caused by overall mass changes. Indeed, calculated total mass changes correlate well with Lu content, indicating that mass gain resulted in relative Lu depletion and mass loss caused enrichment of Lu compared to the precursor (Fig. 8.8b). A tightly constrained trend also exists for Lu and Yb concentrations which is interpreted as evidence for immobility of both elements (Fig. 8.8c). In contrast, substantial scatter can be observed in a diagram plotting Lu and La concentrations indicating that La/Lu ratios changed during alteration due to La mobility (Fig. 8.8d).

Plots of chondrite-normalised REE data show that the patterns for altered rhyolites are generally steeper than the pattern of the precursor and that $LREE_N/HREE_N$ ratios increased during alteration (Fig. 8.9). Furthermore, Eu-contents of altered samples were modified with some samples showing strongly developed negative anomalies whereas others display only a minor deflection in their REE pattern.

Analyses of the mottled alteration facies display the largest variations in the chondrite-normalised REE diagram (Fig. 8.9a). Heavy REE are generally depleted relative to the precursor whereas LREE are enriched and the size of the Eu anomaly is strongly variable. The quartz-K-feldspar alteration facies is depleted in HREE which correlates with large mass gains during this type of alteration. REE patterns for the quartz-pyrite alteration facies have very similar shapes and show variable depletion of HREE compared to the precursor (Fig. 8.9c). Light REE are uniformly enriched in the quartz-pyrite alteration facies and negative Eu anomalies are strongly developed. The chlorite-pyrite alteration facies is characterised by LREE enrichment and HREE concentrations which are similar to the precursor. Eu concentrations are relatively high and negative Eu anomalies are weakly developed.

The component of change in REE concentrations related to absolute mass changes caused by major element mobility was removed from the data by normalisation to Lu, which was immobile during alteration. This procedure reveals that LREE enrichment is ubiquitous (Fig. 8.10). However, the mottled alteration facies displays considerable and continuous spread in the magnitude of LREE addition with some samples overlapping with the precursor. Quartz-K-feldspar, quartz-pyrite and chlorite-pyrite alteration facies are uniformly enriched in LREE. Furthermore, these patterns show that Eu was depleted during quartz-pyrite alteration relative to the precursor whereas the chlorite-pyrite alteration facies is relatively Eu-enriched. The mottled alteration facies exhibits variable depletion and enrichment of Eu.

Fig. 8.9: Chondrite-normalised REE diagrams for variably altered footwall rhyolite.

Samples of mottled, quartz-K-feldspar, quartz-pyrite and chlorite-pyrite alteration facies from the footwall alteration zone in section 5 (East Thalanga) are compared to the rhyolite type 1 precursor. Data are normalised to chondritic abundances of Boynton (1984), as reported in Rollinson (1993).

(a) Mottled alteration facies

(b) Quartz-K-feldspar alteration facies

(c) Quartz-pyrite alteration facies

(d) Chlorite-pyrite alteration facies

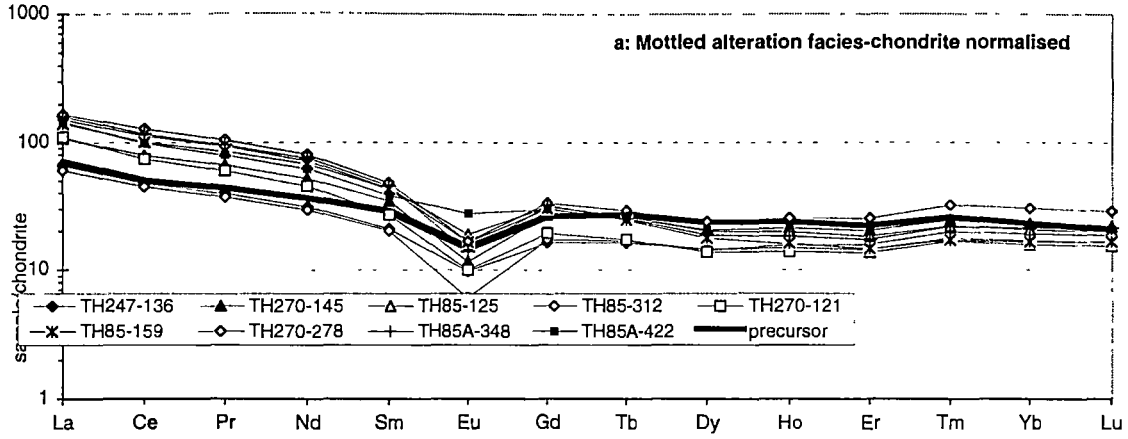
a: Mottled alteration facies-chondrite normalised
1000
100
10
1
sample/chondrite
TH247-136
TH270-145
TH85-125
TH85-312
TH270-121
TH85-159
TH270-278
TH85A-348
TH85A-422
precursor
La
Ce
Pr
Nd
Sm
Eu
Gd
Tb
Dy
Ho
Er
Tm
Yb
Lu

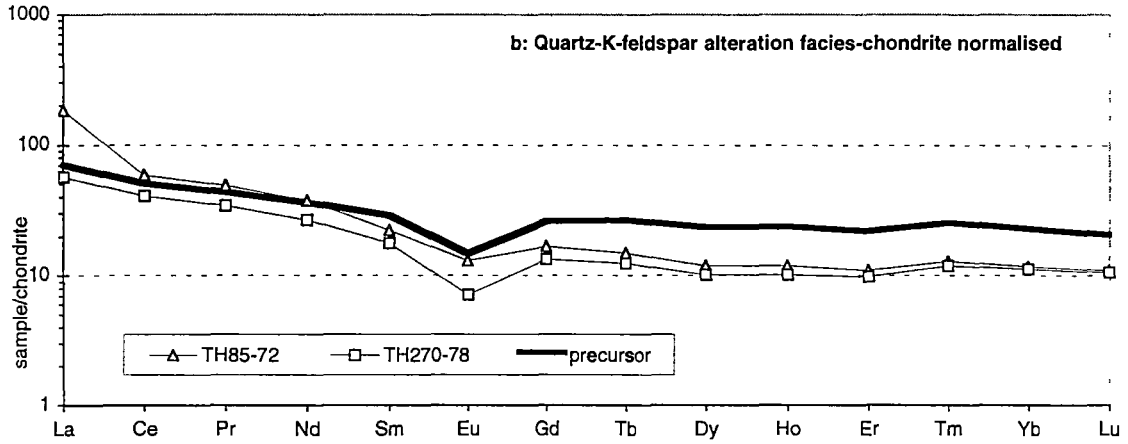
b: Quartz-K-feldspar alteration facies-chondrite normalised
1000
100
10
1
sample/chondrite
TH85-72
TH270-78
precursor
La
Ce
Pr
Nd
Sm
Eu
Gd
Tb
Dy
Ho
Er
Tm
Yb
Lu

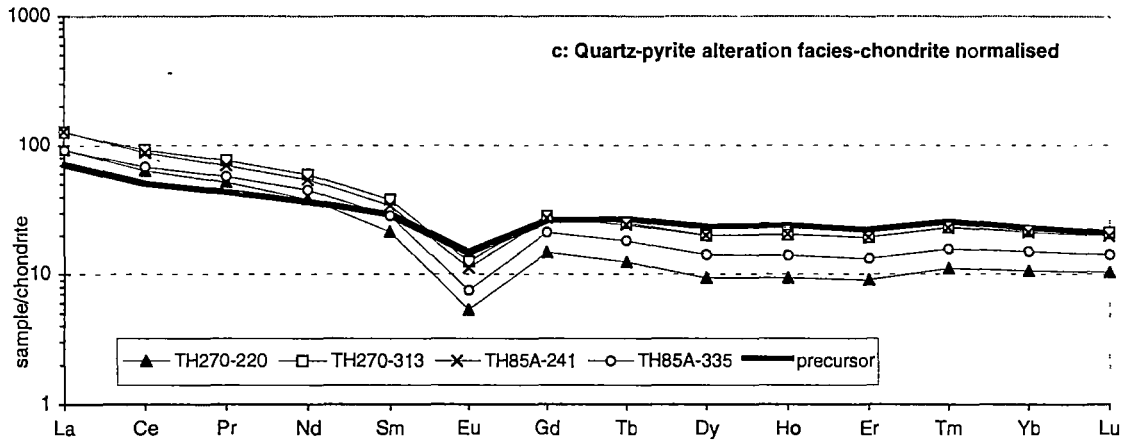
c: Quartz-pyrite alteration facies-chondrite normalised
1000
100
10
1
sample/chondrite
TH270-220
TH270-313
TH85A-241
TH85A-335
precursor
La
Ce
Pr
Nd
Sm
Eu
Gd
Tb
Dy
Ho
Er
Tm
Yb
Lu

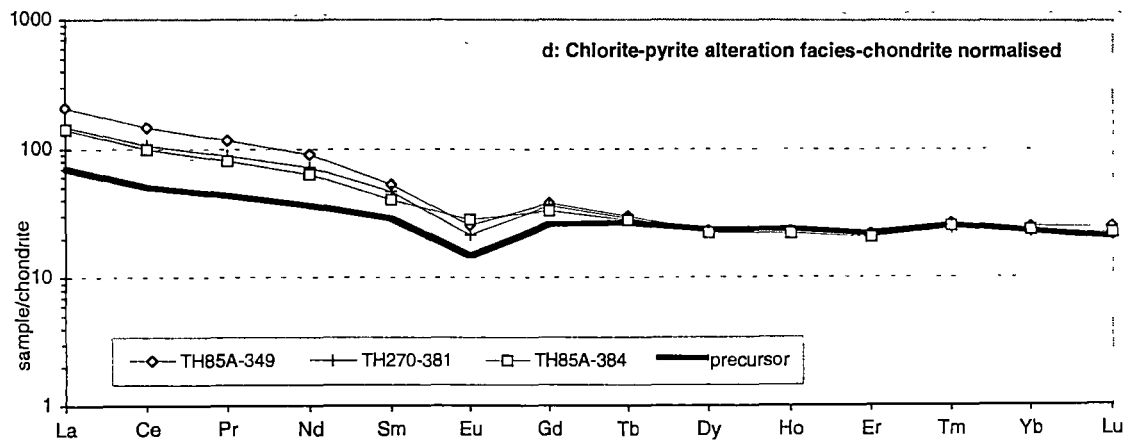
d: Chlorite-pyrite alteration facies-chondrite normalised
1000
100
10
1
sample/chondrite
TH85A-349
TH270-381
TH85A-384
precursor
La
Ce
Pr
Nd
Sm
Eu
Gd
Tb
Dy
Ho
Er
Tm
Yb
Lu

Fig. 8.9

Fig. 8.10: Chondrite- and Lu-normalised REE diagrams for variably altered footwall rhyolite.

Samples of mottled, quartz-K-feldspar, quartz-pyrite and chlorite-pyrite alteration facies from the footwall alteration zone in section 5 (East Thalanga) are compared to the rhyolite type 1 precursor.

(a) Mottled alteration facies

(b) Quartz-K-feldspar alteration facies

(c) Quartz-pyrite alteration facies

(d) Chlorite-pyrite alteration facies

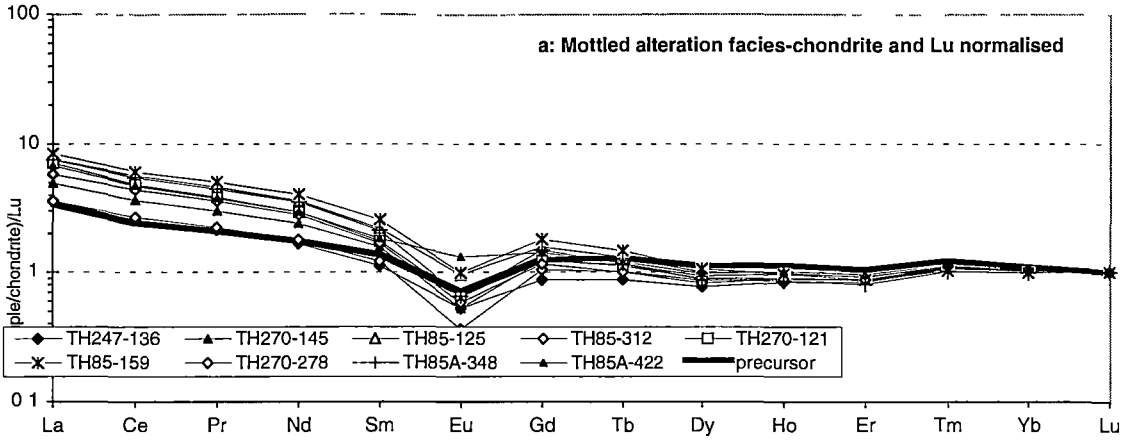
a: Mottled alteration facies-chondrite and Lu normalised
100
10
1
0 1
ple/chondrite)/Lu
TH247-136
TH270-145
TH85-125
TH85-312
TH270-121
TH85-159
TH270-278
TH85A-348
TH85A-422
precursor
La
Ce
Pr
Nd
Sm
Eu
Gd
Tb
Dy
Ho
Er
Tm
Yb
Lu

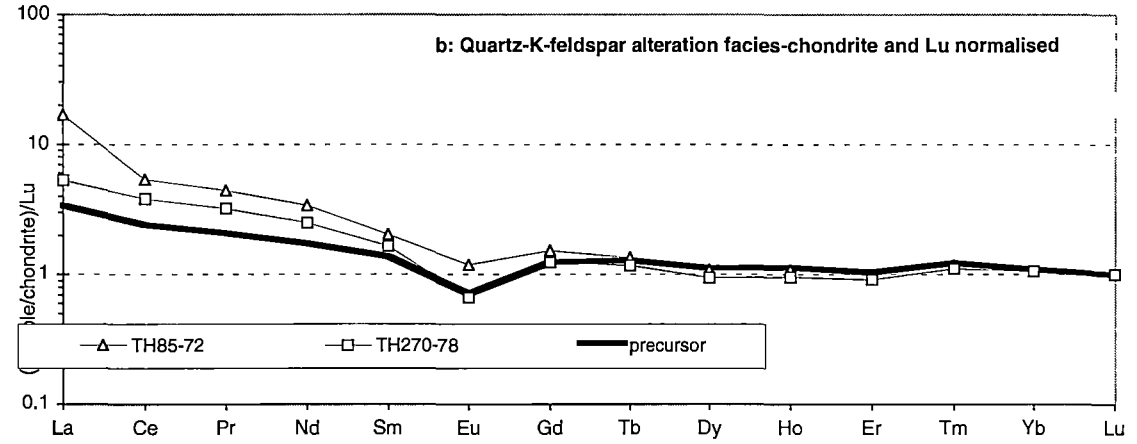
b: Quartz-K-feldspar alteration facies-chondrite and Lu normalised
100
10
1
0.1
le/chondrite)/Lu
TH85-72
TH270-78
precursor
La
Ce
Pr
Nd
Sm
Eu
Gd
Tb
Dy
Ho
Er
Tm
Yb
Lu

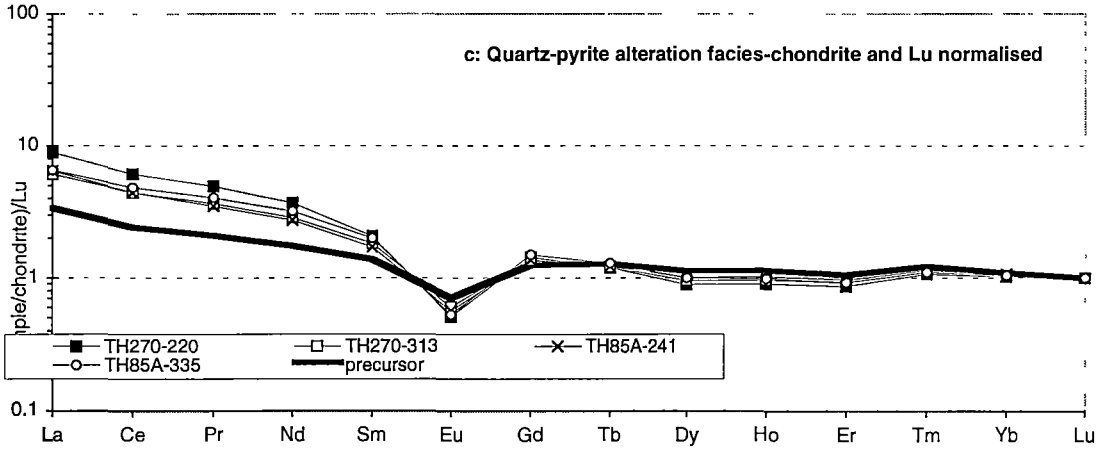
c: Quartz-pyrite alteration facies-chondrite and Lu normalised
100
10
1
0.1
nple/chondrite)/Lu
TH270-220
TH270-313
TH85A-241
TH85A-335
precursor
La
Ce
Pr
Nd
Sm
Eu
Gd
Tb
Dy
Ho
Er
Tm
Yb
Lu

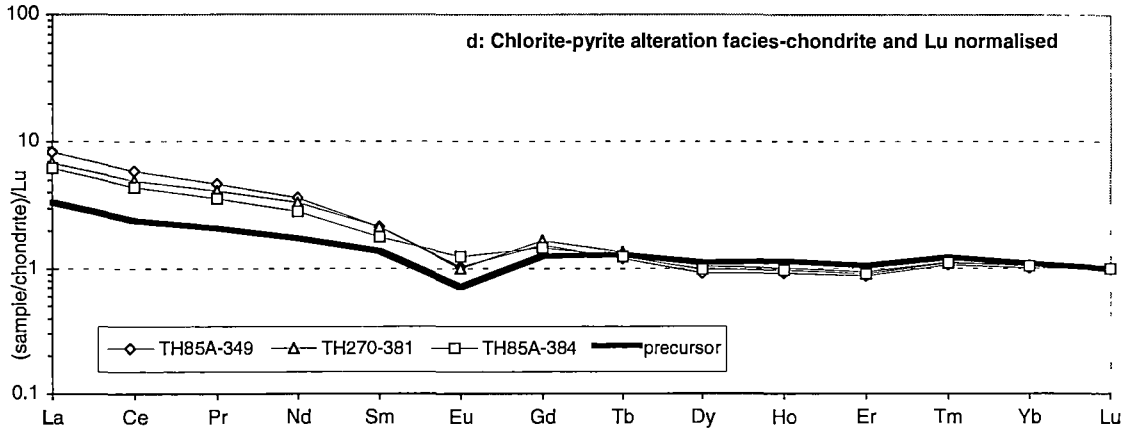
d: Chlorite-pyrite alteration facies-chondrite and Lu normalised
100
10
1
0.1
(sample/chondrite)/Lu
TH85A-349
TH270-381
TH85A-384
precursor
La
Ce
Pr
Nd
Sm
Eu
Gd
Tb
Dy
Ho
Er
Tm
Yb
Lu

Fig. 8.10

The interpretation of Eu mobility based on REE patterns is supported by the irregular scatter of data points in a variation diagram plotting the measured concentrations of Eu and Lu (Fig. 8.11a). This indicates that Eu was mobile within the footwall alteration zone. The net change in Eu content of single samples may be calculated from the Lu-normalised data by subtracting the values for the precursor. A positive correlation can be observed between Eu/Eu* and Eu net change, showing that samples with Eu loss have deeper negative Eu-anomalies than the precursor whereas elevated Eu/Eu* values are associated with Eu gains (Fig. 8.11b).

Changes in the magnitude of the Eu anomaly display an interesting relationship with the CCPI, a multi-element ratio measuring relative enrichment of MgO and FeO over Na_2O and K_2O (section 8.2). Samples of the quartz-K-feldspar, mottled and quartz-pyrite alteration facies define a general decreasing trend in Eu/Eu* with increasing CCPI (Fig. 8.11c). This indicates that Eu mobility due to alteration led to a deepening of the primary negative Eu anomaly with increasing alteration intensity. This relationship suggests that destruction of feldspar, in which Eu may be substituted, could be responsible for Eu leaching. However, samples of chlorite-pyrite alteration facies do not follow this trend and one sample of the mottled alteration facies also has a relatively high Eu/Eu* value. A possible explanation for this observation is discussed in section 8.6.

In summary, it can be demonstrated that the REE data for variably altered footwall rhyolites in East Thalanga show the effects of changes in REE concentrations due to (1) total mass changes associated with major element mobility, (2) addition of LREE to the quartz-K-feldspar, mottled, quartz-pyrite and chlorite-pyrite alteration facies and (3) mobility of Eu.

Fig. 8.11: Mobility of Eu during hydrothermal alteration at Thalanga.

(a) Data for Eu and Lu show substantial scatter indicating that Eu was mobile during hydrothermal alteration.

(b) Net addition of Eu was associated with increasing Eu/Eu* (ie. decreasing negative Eu anomaly) whereas Eu loss is correlated with decreasing Eu/Eu* (ie. increasing negative Eu anomaly). Net changes of Eu contents ($X_{Eu}^{altered\ sample} - X_{Eu}^{precursor}$) were calculated from the Lu-normalised data in order to exclude any effects of mass changes superimposed on the REE concentrations.

$Eu/Eu^* = Eu_N/\sqrt{(Sm_N * Gd_N)}$ (Taylor & McLennan, 1985).

(c) Eu/Eu* and CCPI are negatively correlated for the majority of the samples, indicating that increasing alteration intensity is correlated with increasing degree of Eu leaching. However, samples of the chlorite-pyrite alteration facies and one sample of mottled alteration facies do not conform with this trend. These samples (TH85A-422, TH85A-384, TH85A-349 and TH270-381) represent altered footwall rhyolite close to the Favourable Horizon which marks the position of the palaeo-seafloor during hydrothermal activity. Hence, anomalous Eu-enrichment seems to be restricted to the near-seafloor environment.

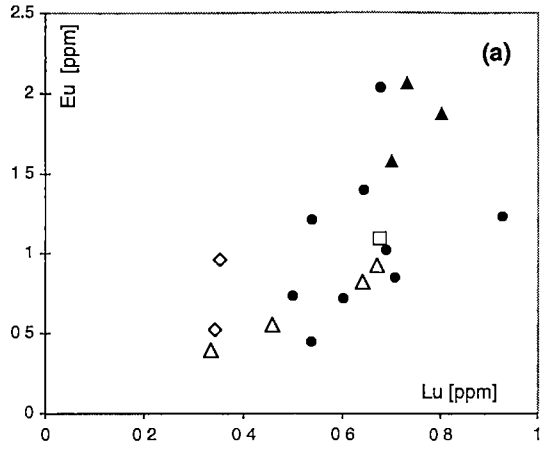
(a)
Eu [ppm]
Lu [ppm]
2.5
2
1.5
1
0.5
0
0
0.2
0.4
0.6
0.8
1

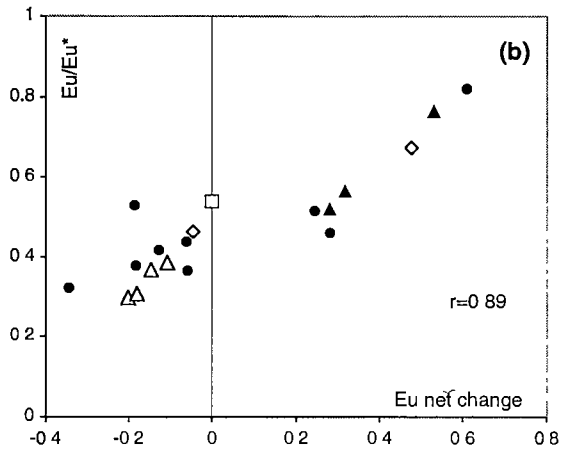
(b)
Eu/Eu*
Eu net change
r=0.89
1
0.8
0.6
0.4
0.2
0
-0.4
-0.2
0
0.2
0.4
0.6
0.8

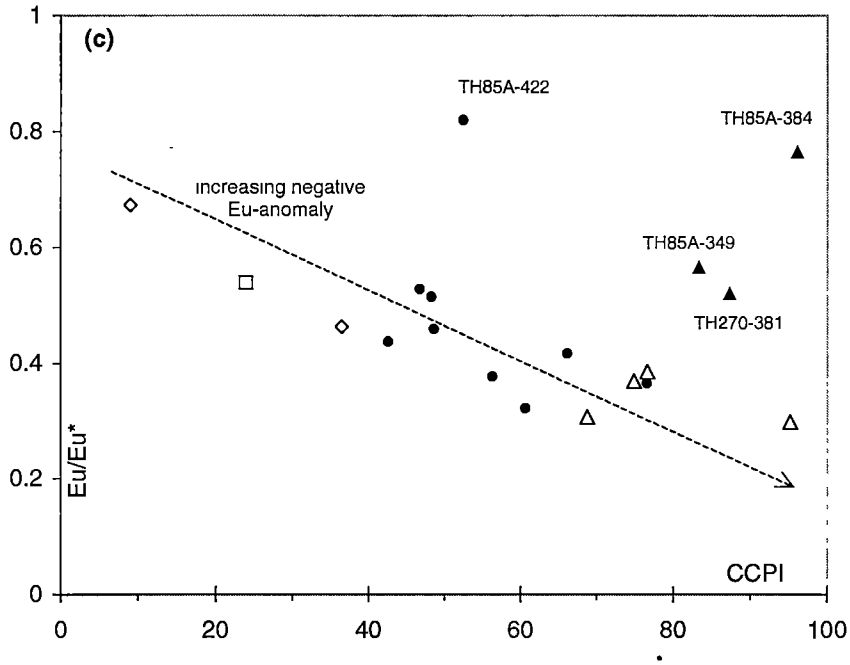
(c)
TH85A-422
TH85A-384
increasing negative
Eu-anomaly
TH85A-349
TH270-381
Eu/Eu*
CCPI
1
0.8
0.6
0.4
0.2
0
0
20
40
60
80
100

8.5 Geochemical halo of the Thalanga deposit

In this section, the composition of the footwall rhyolite and hangingwall dacite are examined in order to define systematic changes with distance from the Thalanga deposit. For this purpose, drill holes TH247 and TH270 were selected because they contain typical massive sulphides of West and East Thalanga and intersected substantial stratigraphic thicknesses of variably altered footwall rhyolite. Geochemical analyses of samples from these drill holes were made available by RGC Ltd., which substantially increased the density of data points. In order to examine the geochemical halo in the hangingwall dacite, drill hole TH382A was chosen because the hangingwall in East Thalanga consists mainly of one, thick dacite type 1 lava unit (Chapter 5, Fig. 5.5 and Fig. 7.7). The orientation of these drill holes with regard to the Favourable Horizon is variable and therefore drill hole depths do not reflect true stratigraphic position. Sample locations are indicated on drill hole traces in Figures 7.5 and 7.7.

Drill hole TH247 (West Thalanga) was collared in least-altered footwall rhyolite ~220 m below the Favourable Horizon and contains mainly mottled alteration facies overlain by quartz-pyrite alteration facies and massive sulphide with calcareous gangue (Fig. 8.12 and drill hole log in the Appendix, section 2). Drill hole TH270 in East Thalanga has a sub-parallel orientation to the Favourable Horizon for the upper 150 m of drill core and intersects zones of quartz-pyrite alteration which are comparatively chlorite-rich (Fig. 8.12 and drill hole log in the Appendix, section 5). This drill hole starts in weakly altered rhyolite ~120 m stratigraphically below the Favourable Horizon.

In the following, the variability of bulk rock geochemical data including major and trace elements are examined. Furthermore, microprobe analyses of chlorite and biotite from samples of TH247 are presented. Table 8.1 provides a summary of the principal results including a rating of the various geochemical parameters according to reliability as proximity indicators to the Thalanga deposit on a prospect and mine scale.

8.5.1 Footwall halo

Bulk-rock geochemistry

In general, data from TH247 and TH270 reflect the geochemical characteristics of the various alteration facies in the footwall which were discussed in section 8.2. However, some geochemical features show systematic changes correlated with distance from ore. In the following, trends in the data from drill holes TH247 and TH270 are compared in the light of their usefulness as ore-proximity indicators in the footwall to the Thalanga deposit.

Fig. 8.12: Geochemical proximity indicators to the Thalanga deposit.

The potential of various major and trace elements and element ratios to indicate proximity to the Thalanga deposit is illustrated using data from representative drill holes through the footwall alteration zone in East and West Thalanga (TH270 and TH247) and through the hangingwall dacite (TH382A). The graphic logs are substantially simplified (see Appendix for original graphic logs and detailed lithological descriptions). Colours and symbols for data points indicate alteration facies; see Figure 8.14 for legend. Geochemical data: this study and analyses provided by RGC Ltd.; see Figures 7.5 and 7.7 for sample locations (data are presented in Tables A4 and A5 in the Appendix).

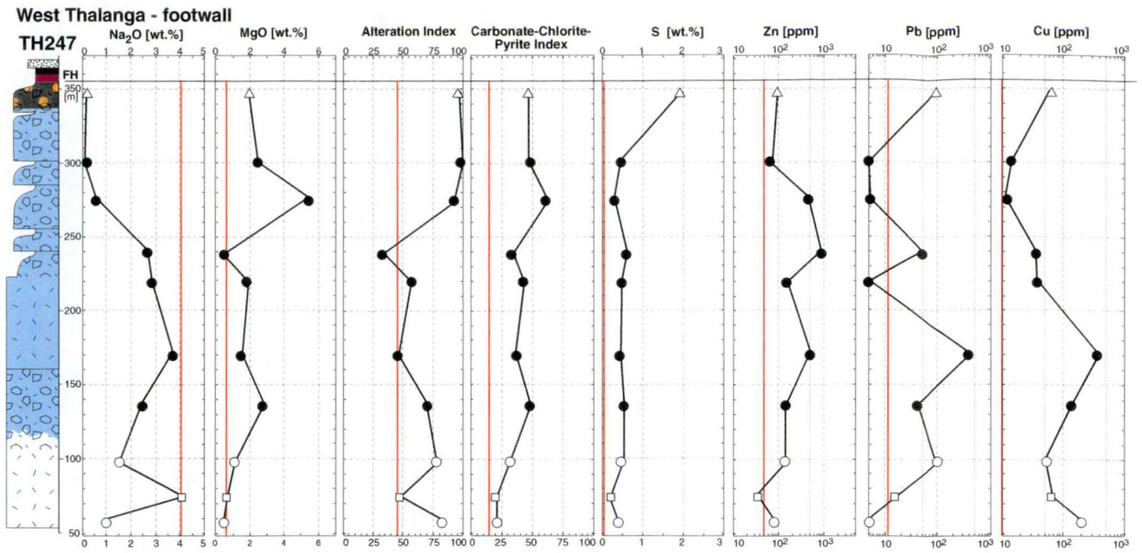
West Thalanga - footwall
TH247
Na2O [wt.%]
MgO [wt.%]
Alteration Index
Carbonate-Chlorite-Pyrite Index
S [wt.%]
Zn [ppm]
Pb [ppm]
Cu [ppm]
FH
[m]

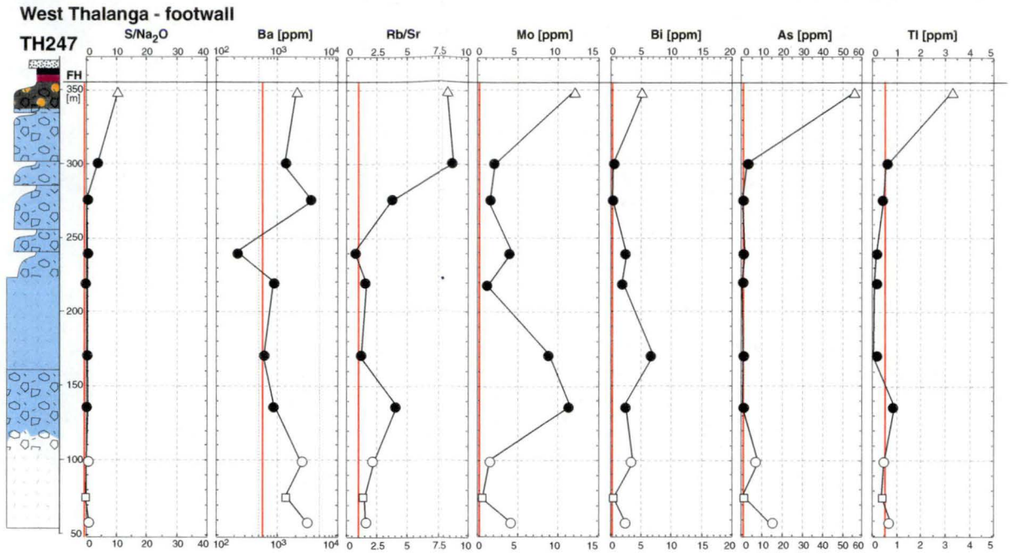
West Thalanga - footwall
TH247
S/Na2O
Ba [ppm]
Rb/Sr
Mo [ppm]
Bi [ppm]
As [ppm]
Tl [ppm]
FH
[m]

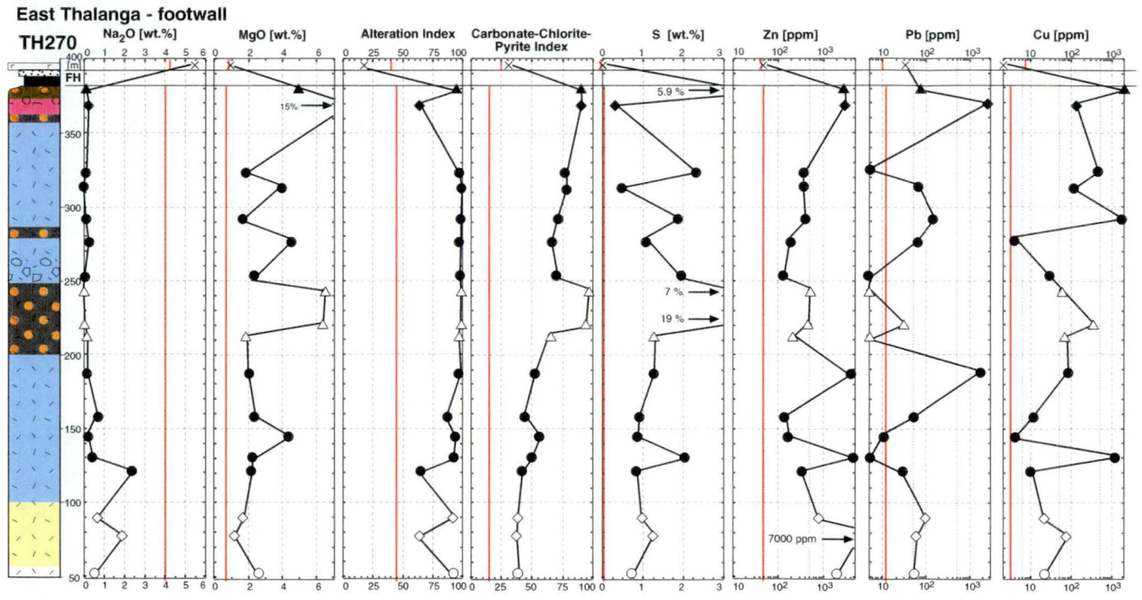
East Thalanga - footwall
TH270
Na2O [wt.%]
MgO [wt.%]
Alteration Index
Carbonate-Chlorite-Pyrite Index
S [wt.%]
Zn [ppm]
Pb [ppm]
Cu [ppm]
15%
5.9 %
7 %
19 %
7000 ppm
FH
[m]

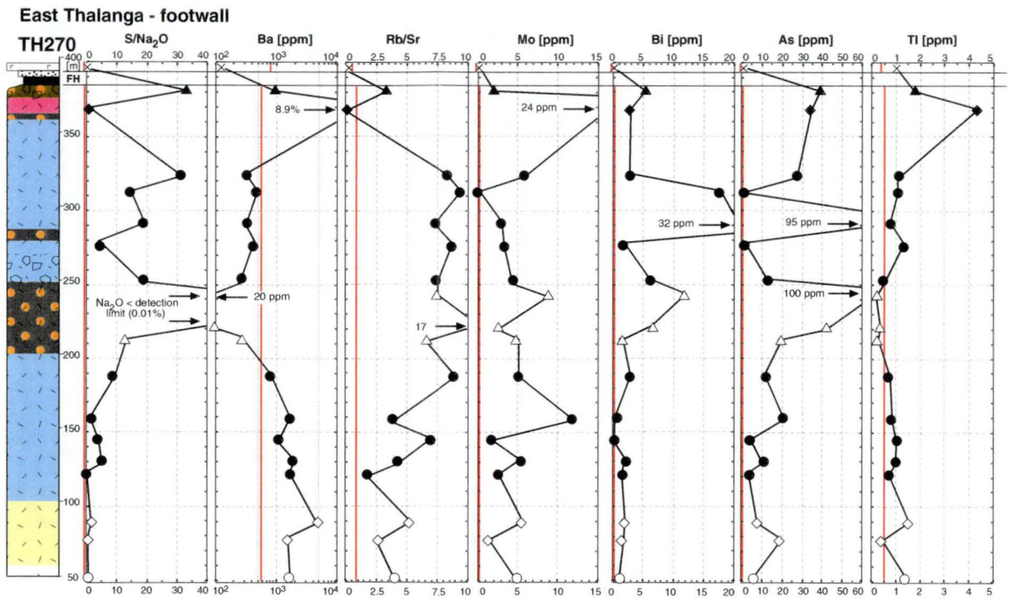
East Thalanga - footwall
TH270
S/Na2O
Ba [ppm]
Rb/Sr
Mo [ppm]
Bi [ppm]
As [ppm]
Tl [ppm]
8.9%
24 ppm
32 ppm
95 ppm
100 ppm
20 ppm
17
Na2O < detection limit (0.01%)
FH
[m]

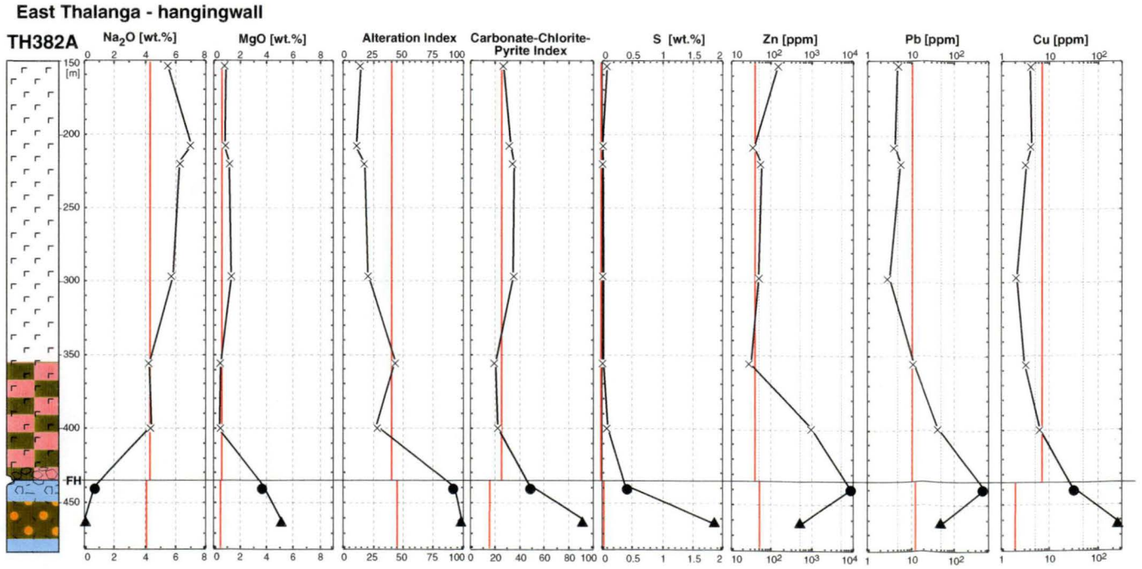
East Thalanga - hangingwall
TH382A
Na2O [wt.%]
MgO [wt.%]
Alteration Index
Carbonate-Chlorite-Pyrite Index
S [wt.%]
Zn [ppm]
Pb [ppm]
Cu [ppm]
FH
[m]

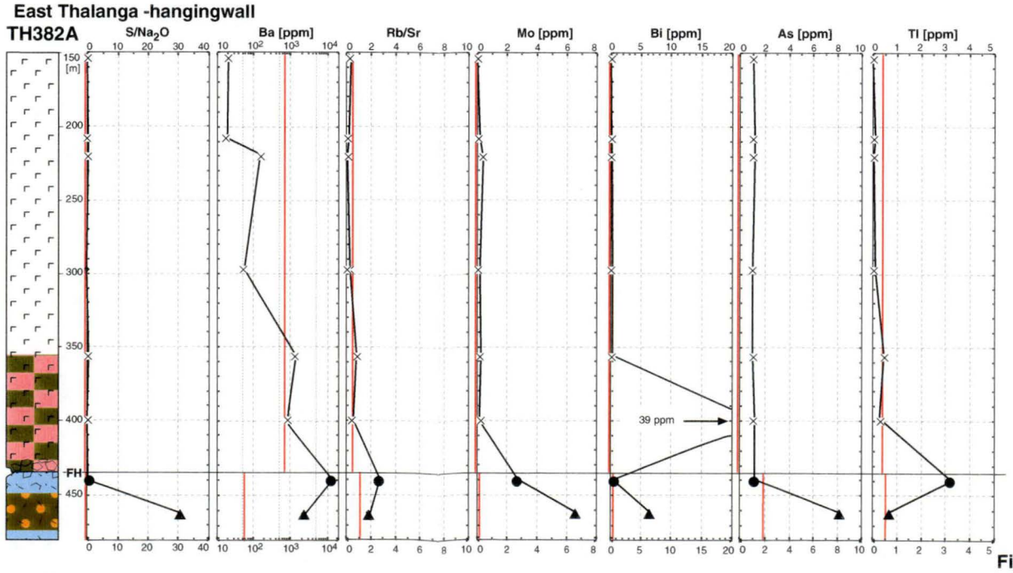
East Thalanga -hangingwall
TH382A
S/Na2O
Ba [ppm]
Rb/Sr
Mo [ppm]
Bi [ppm]
As [ppm]
Tl [ppm]
39 ppm
FH
[m]

Fig. 8.12

Major elements and alteration indices: The data from TH247 and TH270 indicate that the footwall alteration zones in East and West Thalanga differ somewhat in geochemical composition. In general, the footwall alteration zone in East Thalanga has higher values for MgO, S, AI and CCPI which is related to abundant zones of relatively chlorite-rich quartz-pyrite alteration facies (Fig. 8.12 and Figs. 7.5 and 7.7).

In TH247, the concentration of Na_2O decreases gradually towards the Favourable Horizon and values >2 wt.% are common in the lower part of the mottled alteration facies (Fig. 8.12). The concentration of MgO increases from background levels at the start of the hole (≤0.5 wt.%) to values around 2 wt.% in the central part of the alteration zone. Alteration Indices and CCPI are close to values typical for the least-altered rhyolite in the lower part of the mottled alteration facies but increase towards the Favourable Horizon. Sulphur concentrations are relatively low (≤0.5 wt.%) except for one sample of quartz-pyrite alteration facies just below the massive sulphides.

In TH270, Na_2O values are below 0.5 wt.% for most samples and AI >95 predominate (Fig. 8.12). A drop in AI just below the Favourable Horizon is correlated with a tremolite- and barite-rich sample of disseminated tremolite alteration facies. The pattern for S is somewhat erratic, although most samples have concentrations >1 wt.%, and one zone of chlorite-rich quartz-pyrite alteration facies has exceptionally high S values (7 and 19 wt.%). This zone is also marked by peaks in MgO concentrations. Despite the somewhat erratic pattern of MgO, the CCPI increases smoothly from close to background values at the start of TH270 to values >90 just below the ore.

Increase of MgO, S, AI and CCPI and depletion of Na_2O are characteristic geochemical features for the Thalanga footwall alteration zone. The potential of these parameters to be a guide in exploration is variable and controlled by the specific alteration facies present. In East Thalanga, the smooth increase in CCPI is an excellent guide to ore, due to intense Na_2O depletion and abundance of chlorite-rich quartz-pyrite alteration facies. In West Thalanga, a comparatively smooth trend in Na_2O depletion and a relatively subtle increase in CCPI (from 25 to 50) are reasonably well correlated with distance from the massive sulphides.

Base metals: The concentrations of base metals in altered rhyolite show erratic variations with comparable ranges in East and West Thalanga. Although values higher than background are predominant, there are numerous samples showing base metal concentrations within the range of the least-altered rhyolite. There are no consistent trends in the base metal data which could be used as a guide to the massive sulphides in East or West Thalanga. Consequently, analyses of Cu, Pb and Zn have a low potential as vectors to ore and, in some instances, may not reveal the former presence of a

mineralising hydrothermal system.

Trace elements: In general, the concentrations of barium show no consistent changes with distance from the Favourable Horizon. Nevertheless, Ba-rich samples in the vicinity of massive sulphides are potentially useful as mine-scale exploration vectors and correlate with local occurrences of barite. In East Thalanga, zones of the chlorite-rich quartz-pyrite alteration facies are marked by strong depletion in Ba. A general increase in the Rb/Sr ratio can be observed in East and West Thalanga, however there is considerable scatter and overlap with the range for the least-altered rhyolite. Just below the Favourable Horizon, the Rb/Sr ratio decreases dramatically in East Thalanga due to the presence of disseminated tremolite alteration facies. The concentrations of Mo, Bi and As are generally less than 1 ppm in the least-altered footwall rhyolite. In contrast, altered footwall rhyolites often contain several ppm to >10 ppm of these elements. In East Thalanga, the patterns are erratic and a correlation with distance from ore is not apparent. Spikes in the Mo, Bi and As concentrations are locally correlated with occurrences of pyrite-rich alteration facies. In West Thalanga, elevated values of Mo and As (>10 ppm) are restricted to the quartz-pyrite alteration facies immediately below massive sulphides. In general, Tl concentrations are close to, or below, the detection limit (<0.5 ppm) for all samples regardless of alteration facies. However, elevated Tl values (>3 ppm) occur in samples just below the Favourable Horizon in TH247, TH270 and TH382A.

In summary, Ba concentrations are strongly controlled by the mineralogy (ie. abundance of Ba bearing minerals such as muscovite, K-feldspar or barite) of alteration facies and may be enriched or depleted in the footwall alteration zone compared to least-altered footwall rhyolite. The Rb/Sr ratio is a good indicator of feldspar-destructive alteration and generally increases towards the Favourable Horizon in East and West Thalanga. However, occurrences of Ca-bearing, non-primary minerals (epidote, calcite and/or tremolite) have a strong effect on this ratio, causing substantial distortion of the trend in TH270. Anomalies in the concentrations of Mo, Bi and As distinguish the footwall alteration zone from the least-altered rhyolite and may be useful in regional- to prospect-scale base metal exploration. In contrast, elevated Tl values are restricted to samples immediately below, or laterally adjacent to, massive sulphides and may be regarded as a mine-scale vector to ore.

Mineral chemistry

Microprobe analyses of chlorite and biotite were presented and discussed in relation to the metamorphism of the Thalanga sequence in Chapter 4. Here, analyses of chlorite and biotite in samples of altered rhyolite from TH247 in West Thalanga and their compositional variations with regard to proximity to ore are examined. The abundances of chlorite and biotite in single samples vary substantially; they are relatively rare in least-altered rhyolite whereas samples of altered and least-altered rhyolite contain significant, but variable, amounts. However, chlorite and biotite from any single sample are homogeneous in composition.

Chlorite: Chlorites at Thalanga have close to 12 cations per formula unit (pfu) in octahedral positions and contain significant Al which is fairly evenly balanced between tetrahedral and octahedral positions (Fig. 4.11). The relative proportions of iron and magnesium cations vary substantially between samples and a continuous compositional range from nearly pure clinochlore (Mg-rich end-member) to chlorite with X_{Mg} (Mg/[Mg+Fe]) ~ 0.5 is present (Fig. 8.13a). A tightly constrained linear trend indicates a simple substitution of Mg[6] $\Leftrightarrow$ Fe^{2+}[6]. Least-altered rhyolites have accessory chlorite with high iron concentrations. Samples of the mottled alteration facies contain chlorites with a comparatively large range in the proportions of iron and magnesium cations (4.5 to 1 Fe pfu; 4.5 to 8 Mg pfu). Very Mg-rich chlorites occur in the quartz-pyrite alteration facies and in the carbonate-chlorite-tremolite alteration facies.

Biotite: The octahedral positions in biotites are occupied by variable proportions of iron and magnesium. Biotites of the mottled alteration facies are more Mg-rich than biotite in the least-altered and weakly altered rhyolite (Fig. 8.13b). Biotites with the highest X_{Mg} occur in the quartz-pyrite alteration facies. The well constrained correlation between the abundance of Fe and Mg cations indicates a simple substitution of Mg[6] $\Leftrightarrow$ Fe^{2+}[6]. The biotites also contain significant, but variable concentrations of fluorine. Fluorine contents of <0.2 pfu are restricted to the least-altered rhyolite from the outcrop section (Fig. 8.13c) whereas biotites in the quartz-pyrite alteration facies in West Thalanga (sample TH247-347) contain 1.5 to 1.8 pfu of F ($\cong$ 3.6 wt.%; detection limit: 0.3 wt.%). Biotites in the altered and least-altered rhyolite from TH247 have F contents in the range of 0.2 to 1 F pfu. In contrast, chlorine concentrations are always close to, or below, the detection limit (0.05 wt.%) (Table A6 in the Appendix).

Vectors to ore: Microprobe analyses from samples of TH247 in West Thalanga indicate that chlorites and biotites are homogeneous in composition on a thin section scale and that X_{Mg}^{chl} and X_{Mg}^{bio} increase systematically approaching the massive sulphides (Fig. 8.14).

Fig. 8.13: Compositional ranges of chlorite and biotite in samples of variably altered footwall rhyolite.

(a) The contents of Mg and Fe cations in chlorite vary systematically among samples of the least-altered and weakly altered footwall rhyolite, mottled alteration facies, quartz-pyrite alteration facies and carbonate-chlorite-tremolite alteration facies.

(b) The contents of Mg and Fe cations in biotite vary systematically among samples of the least-altered and weakly altered footwall rhyolite, mottled alteration facies and quartz-pyrite alteration facies.

(c) Biotites in the Thalanga footwall alteration zone are variably enriched in fluorine. The quartz-pyrite alteration facies contains particularly F- and Mg-rich biotite (fluoro-phlogopite).

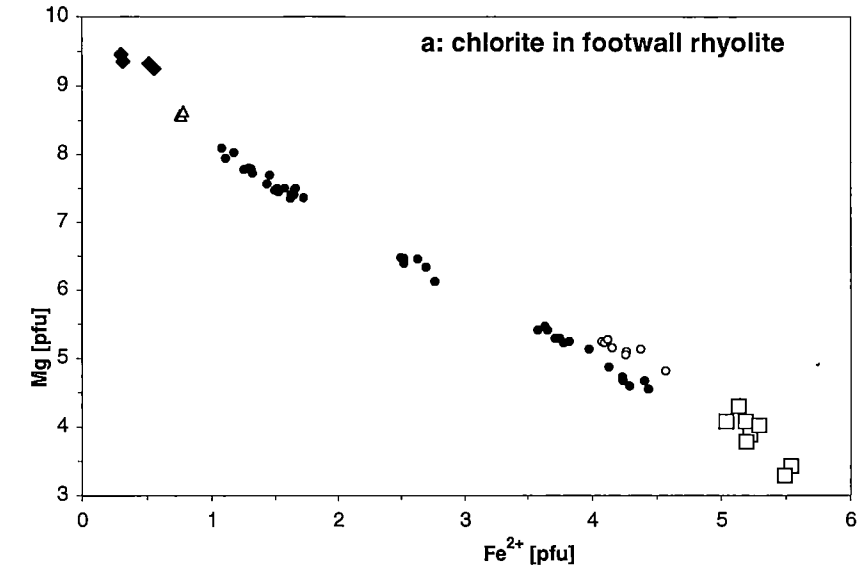

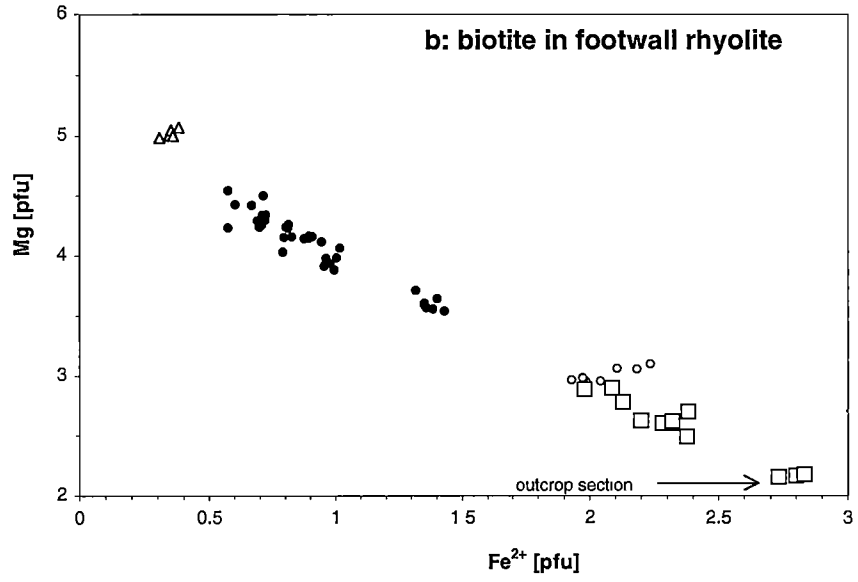

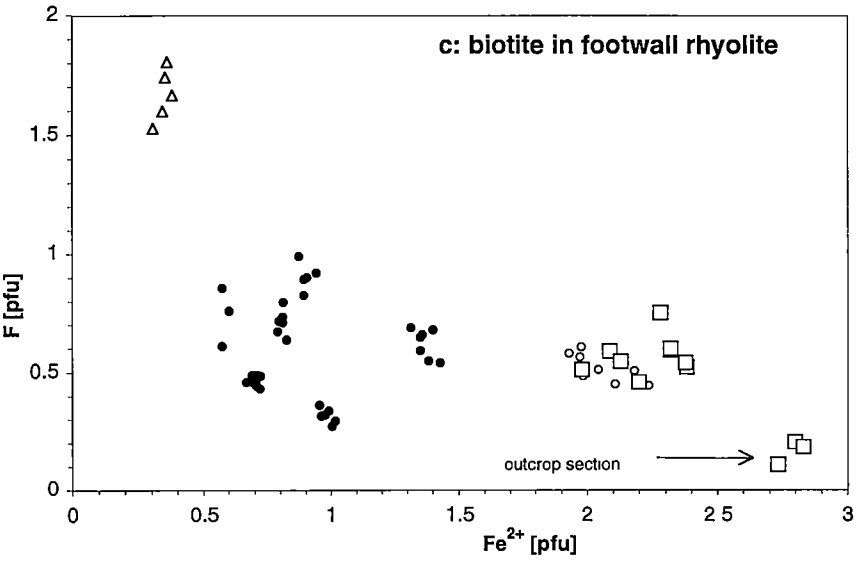

Legend:

□ least-altered footwall rhyolite

○ weakly altered rhyolite (phyllosilicate alteration)

● mottled alteration facies

△ quartz-pyrite alteration facies

◆ carbonate-chlorite-tremolite alteration facies

Fig. 8.13

The least-altered rhyolites at the start of drill hole TH247 have accessory chlorite with relatively high iron concentrations (X_{Mg}^{chl} = 0.45; Fig. 8.14a). However, approaching the ore position, X_{Mg}^{chl} increases steadily and the highest X_{Mg}^{chl} values (~0.96) are recorded in the carbonate-chlorite-tremolite alteration facies associated with semi-massive sulphides. The relative proportions of magnesium and iron in biotite also change substantially with increasing proximity to ore. The X_{Mg} of biotite increases gradually from 0.5 in the least-altered rhyolite to a maximum value of 0.95 just below the massive sulphides in the quartz-pyrite alteration facies (Fig. 8.14b).

8.5.2 Hangingwall halo

Bulk-rock composition

Hangingwall dacite type 1 in drill hole TH382A is relatively monotonous in geochemical composition (Fig. 8.12). However, high Na_2O values (5 to 7 wt.%) and AI <15 indicate substantial albite alteration in the upper part of the drill hole, whereas in the lower part of the hole Na_2O and AI are similar to the least-altered dacite type 1 (Table 6.2). Consequently, the decrease in Ba in the upper part of TH382A is probably related to potassium loss associated with albite alteration. It seems unlikely that the decrease in Na_2O from 7 to 4 wt.% and the increase in Ba towards the Favourable Horizon is related to the proximity of massive sulphides. Rather, the lower part of the dacite lava is comparatively less altered than the upper part because it experienced progressively less Na-enrichment and is similar in composition to least-altered samples of dacite type 1. However, dacite sampled ~20 m above the Favourable Horizon (TH382A-400) shows elevated concentrations of Zn, Pb and Bi compared to dacite higher up in the sequence (Fig. 8.12). This sample also contains anomalous sulphur (0.07 wt.%) which is unusual because, in general, dacite is sulphur-poor with values below detection limit (<0.01 wt.%). The enrichment in S, Zn, Pb and Bi may be related to localised, late stage activity of the Thalanga hydrothermal system.

Regionally, albite alteration is common in hangingwall dacite but its distribution within the stratigraphic sequence and along strike is not systematic. Albite alteration occurs in dacite overlying ore lenses and in sections without significant massive sulphide occurrences (eg. samples TH62C-680 and TH62C-142 in section 1). Hence, it appears that albite alteration was unrelated to the Thalanga hydrothermal system and it is not a general indicator of proximity to massive sulphides at Thalanga.

Fig. 8.14: Compositional changes of chlorite and biotite in altered footwall rhyolite with distance from massive sulphides in West Thalanga.

The X_{Mg} (Mg/[Mg+Fe]) of chlorite and biotite in samples of drill hole TH247 increases systematically approaching massive sulphides in the Favourable Horizon. The data show that the composition of chlorites and biotites are homogeneous on a thin section scale where different crystals have almost identical X_{Mg} values. Numbers in brackets: (number of analyses / number of crystals analysed) per thin section.

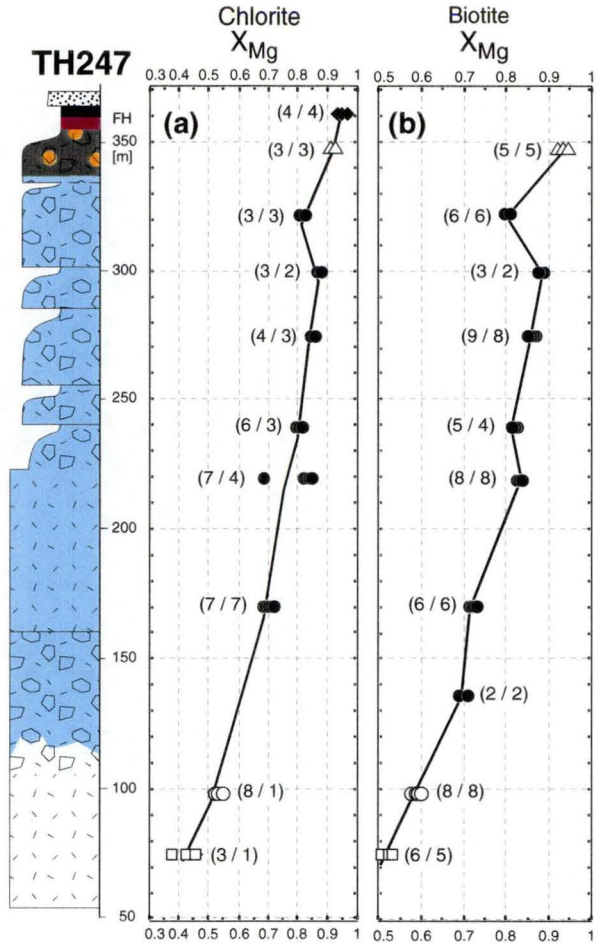

Fig. 8.14

Legend (Fig. 8.12 and Fig. 8.14):

alteration:

- weak alteration or least-altered rocks
- mottled alteration facies
- quartz-K-feldspar alteration facies
- disseminated tremolite alteration facies
- carbonate-chlorite-tremolite alteration facies
- quartz-pyrite alteration facies
- chlorite-pyrite alteration facies
- epidote alteration and hematite dusting

lithofacies:

- coherent facies of footwall rhyolite
- volcaniclastic facies of footwall rhyolite
- massive sulphide
- quartz-eye volcaniclastics (facies F)
- hangingwall volcano-sedimentary sequence dominated by coherent facies of dacite type 1 lava (cf. graphic log of TH382A in the Appendix for detail)

symbols:

- □ least altered footwall rhyolite
- ○ weakly altered footwall rhyolite
- ● mottled alteration facies
- ◇ quartz-K-feldspar alteration facies
- ◆ disseminated tremolite and carbonate-chlorite-tremolite alteration facies
- △ quartz-pyrite alteration facies
- ▲ chlorite-pyrite alteration facies
- × hangingwall dacite (type 1)
- — value for least-altered equivalent (Fig. 8.12)

Table 8.1: Geochemical proximity indicators to the Thalanga massive sulphide deposit

		Footwall rhyolite			vector potential		hangingwall dacite		vector potential	
		background	footwall alteration zone	proximal to ore	prospect scale	mine scale	background	proximal to ore	prospect scale	mine scale
Na_2O	[wt.%]	3 to 4	<3 to <1	<0.5	✓		5 to 7	4		(✓)[1)]
MgO	[wt.%]	<0.5	1 to 6	2 to >10	✓		≤1	<1		
S	[wt.%]	<0.5	<0.5 to >10	2 to >10	✓	(✓)	<0.5	<0.3		
S/Na_2O		<1	<1 to >10	≥10	(✓)	(✓)	<<1	<<1		
Rb/Sr		<2	<2 to >5	>5[2)]	(✓)	(✓)	<1	<1		
Al		30 to 60	60 to 100	95 to 100[2)]	✓	(✓)	20 to 40	20 to 40		
CCPI		25	50 to 90	50 to 90	✓	✓	20 to 30	20 to 30		
Ba	[ppm]	800 to >1000	<100 to >1000	>500 to >1%		(✓)	20 to 100	1000		(✓)[1)]
Zn	[ppm]	30 to 100	100 to >1000	100 to >1000	(✓)		50 to 100	1000		(✓)
Pb	[ppm]	<10 to 20	<10 to 500	>100	(✓)		5 to 10	100		(✓)
Cu	[ppm]	<10 to 50	10 to >1000	50 to >1000	(✓)		2 to 7	3 to 7		
Mo	[ppm]	<1	1 to >10	>10	✓	(✓)	<1	<1		
Bi	[ppm]	<0.5	1 to >10	>5	✓		<1	>10		(✓)
As	[ppm]	≤1	1 to >10	>30	✓	(✓)	<2	<2		
Tl	[ppm]	<0.5	<1	>3		✓	<0.5	≤0.5		
X_{Mg}^{bio}		0.5	0.55 to <0.9	>0.9	✓	✓				
X_{Mg}^{chl}		0.4 to 0.45	0.5 to <0.9	>0.9	✓	✓				

[1)]: lower Na_2O and Ba content in dacite proximal to massive sulphides indicate that these samples were not subjected to albite alteration. This feature is probably unrelated to the fact that these samples are proximal to ore.

[2)]: except for samples of carbonate-chlorite-tremolite alteration facies and disseminated tremolite alteration facies close to the Favorable Horizon which have low Al and low Rb/Sr.

Al: Alteration Index (Ishikawa, 1974)= 100 * $(MgO + K_2O)/(MgO + K_2O + CaO + Na_2O)$

CCPI: Carbonate-Chlorite- Pyrite Index (Large, 1996) = 100 * $(MgO + FeO)/(MgO + FeO + K_2O + Na_2O)$

✓: well developed geochemical anomaly, (✓) : locally developed geochemical anomaly or substantial scatter in the data

8.6 Discussion

The geochemistry of the footwall rhyolite was substantially modified during hydrothermal alteration and important compositional changes include enrichments in silica, iron, sulphur and magnesium and depletion of sodium. These features are consistent with the abundance of quartz, muscovite, chlorite, biotite and pyrite in the mottled alteration facies and quartz-pyrite facies, which, together, represent the bulk of the footwall alteration zone. The Mg-rich character of footwall alteration indicates that hydrothermal fluids associated with mineralisation at Thalanga were dominantly seawater-derived (cf. Reed, 1997).

Mass changes in the footwall alteration zone

Results of mass balance calculations show that silica was mobile during hydrothermal activity and that substantial silicification was associated with quartz-pyrite and quartz-K-feldspar alteration facies. Mass changes in silica in the mottled alteration facies are variable and mass balance results for single samples range between large losses and gains. On average, there was little silica addition to the mottled alteration facies suggesting that these mass changes could be due to internal redistribution of SiO_2 within the broad alteration zone below the Thalanga deposit. Silica was lost in chlorite-pyrite alteration facies which indicates that this type of alteration was associated with a silica-undersaturated hydrothermal fluid. Since the chlorite-pyrite alteration facies is limited to a narrow zone immediately below massive sulphides in section 5, it is inferred that these particular conditions of alteration were spatially and temporally restricted.

In contrast to the ubiquitous loss of sodium, potassium was conserved or enriched in the footwall alteration zone. The mottled and quartz-K-feldspar alteration facies have gained potassium during alteration whereas the pyrite-rich alteration facies show minor, erratic mass changes in K_2O.

Total mass changes are variable for the different alteration facies in the footwall and are generally controlled by the mass changes for SiO_2 (Fig. 8.5). The mottled alteration facies shows little total mass gain (5 g/100 g) whereas total gains for the quartz-pyrite and quartz-K-feldspar alteration facies are substantial (35 and 45 g/100 g, respectively). Calcareous alteration (carbonate-chlorite-tremolite and disseminated tremolite alteration facies) are characterised by large total mass gains attributable to addition of MgO and CaO.

Changes in the total mass of volcanic rocks may be related to replacement of glassy or devitrified groundmass with minerals of different density. Mass addition can also be accommodated by filling of primary cavities in coherent rhyolite such as vesicles,

lithophysae, vughs and quench fractures or intraclast space in clastic facies. However, mass changes may also lead to changes in rock volume causing compaction due to mass loss or expansion of rock volume due to mass gain. Substantial expansion of rock volume may be associated with large mass gains in rocks close to the near-seafloor environment, were confining pressures are relatively low. Exceptionally large total mass gains (~120 g/100 g, Fig. 8.6) have been calculated for the carbonate-chlorite-tremolite alteration facies which occurs near, or at the palaeo-seafloor in West Thalanga. It may be inferred that this alteration facies was generated by a process involving expansion of the rock volume.

Hydrothermal alteration and REE concentrations in altered footwall rhyolite

Mass changes also had an effect on the concentrations of REE. Altered samples which experienced mass gains have relatively low values for HREE such as Lu and Yb which were immobile during alteration. However, in addition to the effects of total mass change, enrichment of LREE occurred in the footwall. The amount of LREE addition varies among samples and among alteration facies. Some samples of mottled alteration facies have LREE values similar to the least-altered rhyolite (Fig. 8.10a). All the samples of altered rhyolite analysed for REE are from the upper part of the footwall alteration zone ($\leq$100 m below the palaeo-seafloor marked by the Favourable Horizon). One possibility is that LREE were leached from further down in the footwall and precipitated during interaction with rhyolitic country rock in the relatively shallow part of the hydrothermal system.

The identity of REE-bearing minerals responsible for the LREE enrichment at Thalanga is uncertain. However, LREE might be incorporated into cation exchange sites in clay minerals (Menzies et al., 1979). Since formation of hydrothermal phyllosilicates was clearly part of the alteration processes at Thalanga, it is plausible that substitution of LREE into such minerals may have caused the general increase in LREE/HREE ratio during alteration.

Judging from the variably developed Eu anomaly in chondrite- and Lu-normalised REE patterns, the behaviour of Eu appears to have been somewhat inconsistent during alteration. Nevertheless, there is a highly correlated relationship between Eu/Eu* and net change of Eu indicating that stronger negative Eu anomalies are due to Eu loss whereas high Eu/Eu* values are related to Eu gain (Fig. 8.11b). Interestingly, a well defined negative trend exists between the CCPI and Eu/Eu* for the majority of samples, indicating that increasing intensity of alteration was accompanied by Eu loss (Fig. 8.11c). However, samples of the chlorite-pyrite alteration facies and one sample of the mottled alteration facies do not follow this general trend but show elevated Eu/Eu* values (Fig. 8.11c). One possible explanation for this diverging behaviour of Eu may be suggested by

considering the spatial distribution of samples with regard to the mineralised Favourable Horizon in East Thalanga. Samples which follow the trend of Eu/Eu* decrease and CCPI increase are from depths ≥ 30 to 100 m stratigraphically below the massive sulphides whereas samples TH85A-384 and TH270-381 come from the chlorite-pyrite alteration facies directly below the Favourable Horizon (≤ 5 m). The chlorite-pyrite alteration facies is rare at deeper levels in the footwall and sample TH85A-349 represents an exceptional, 0.5 m wide interval of chlorite-pyrite-rich rhyolite ~40 m below massive sulphides (Fig. 7.7 and log of DDH TH85A in the Appendix). The sample of mottled alteration facies with elevated Eu/Eu* (sample TH85A-422) comes from volcaniclastic facies of rhyolite type 1 within the Favourable Horizon. Thus, it appears that Eu enriched samples are concentrated close to the palaeo-seafloor marked by the Favourable Horizon where conditions of alteration may have been different during hydrothermal activity compared to further down in the volcanic pile. Hence, it is possible that Eu which had been leached by hot, hydrothermal fluids in the deeper part of the footwall (30 to ≥100 m) may have been precipitated in the immediate sub-seafloor environment due to rapid cooling and/or mixing with ambient seawater and incorporated into hydrothermal clays or chlorite. Interestingly, metalliferous muds from the Red Sea. show positive Eu anomalies indicating that Eu-precipitation does occur in mineralising systems on the modern ocean floor (Calvez et al., 1988; Courtois and Treuil, 1977). However, in the Thalanga case, the data base is presently not comprehensive enough to draw any definitive conclusions on the processes controlling REE mobility during hydrothermal alteration.

Geochemical halo of the footwall alteration zone

At Thalanga, geochemical anomalies associated with hydrothermal alteration in the footwall can be detected at least 300 m below the Favourable Horizon and up to 100 m laterally beyond the mineralised position. However, most geochemical features of the altered rhyolites are strongly variable due to the mineralogical diversity of alteration. Therefore, geochemical patterns within the footwall are mainly controlled by the particular alteration facies present and straightforward trends with distance from ore are the exception rather than the rule. Nevertheless, several geochemical parameters are consistently different in the footwall alteration zone compared to the least-altered rhyolite and show trends correlated with distance from ore that may be useful in prospect-scale base metal exploration. These include elevated MgO, S, AI, CCPI, Rb/Sr, Mo, Bi, and As values and depletion in Na_2O.

Immediate proximity to ore is often indicated by elevated values for Ba, S, Mo, As, Tl, AI or CCPI just below, or laterally adjacent to, massive sulphides. It is remarkable that Tl, which generally has concentrations ≤0.5 to 1 ppm regardless of alteration facies,

commonly shows elevated concentrations (>3 ppm) close to, and within the Favourable Horizon. This suggests that Tl may be an important element for the identification of particular horizons within the stratigraphy which could be prospective for VHMS deposits. Interestingly, previous studies concerned with the geochemical halo of hydrothermal mineral deposits also recognised the importance of Tl as an indicator of proximity to ore (Ikramuddin et al., 1983; Möller et al., 1983).

In a similar fashion, the enrichment in Eu and elevated Eu/Eu* values for chlorite-pyrite and mottled alteration facies sampled close to the massive sulphides may be important for the identification of prospective sites in VHMS-related alteration zones. However, the data base is too limited to allow for any definite conclusions to be drawn.

Mineral chemistry of chlorite and biotite in footwall rhyolite

A very well constrained correlation exists between X_{Mg} of chlorite and biotite and distance from the West Thalanga ore lens. An important factor contributing to the trends (Fig. 8.14) is the homogeneous composition of chlorite and biotite on a thin section scale. This contrasts with data obtained for various phyllosilicates in drill core samples from the active TAG hydrothermal system (situated close to the mid-oceanic spreading ridge in the Atlantic Ocean) which show substantial small-scale variability and evidence for disequilibrium crystallisation (Honnorez et al., 1998). It is likely that hydrothermal phyllosilicates at Thalanga were also heterogeneous in composition originally but recrystallisation and equilibration of muscovite-biotite-chlorite assemblages during metamorphism resulted in chemical homogenisation.

The cause for the gradual increase in X_{Mg} of chlorite and biotite in altered rhyolite approaching the Favourable Horizon is not immediately apparent. It could be argued that the trends simply reflect an increasing influence of ambient seawater seeping into the volcanic strata. If this was the case, similar trends could be expected in a scenario where alteration is solely due to circulation of relatively cool seawater in the sub-surface and hot, metal-bearing hydrothermal fluids are absent. However, there are well constrained trends between increasing X_{Mg} of chlorite and biotite and increasing CCPI (Fig. 8.15) which indicate that the changes in X_{Mg} are a genuine feature of increasing intensity of hydrothermal alteration. This line of argument is supported by the general Mg-rich character of hydrothermal alteration at Thalanga which indicates that evolved seawater was the main component of the hydrothermal fluid.

Fig. 8.15: Comparison of whole rock Carbonate-Chlorite-Pyrite-Index and X_{Mg} of chlorite and biotite of altered footwall rhyolite.

The positive correlations between X_{Mg} of chlorite and biotite and CCPI, calculated from the respective bulk rock geochemical analyses, indicate that increasing X_{Mg} values are a result of increasing intensity of hydrothermal alteration.

(a) X_{Mg} (chlorite) versus CCPI

(b) X_{Mg} (biotite) versus CCPI

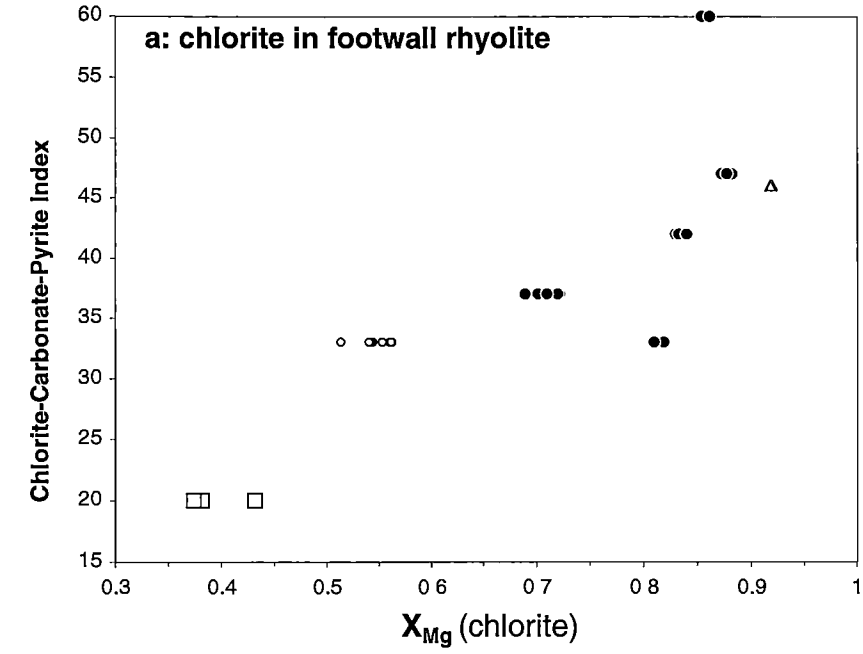

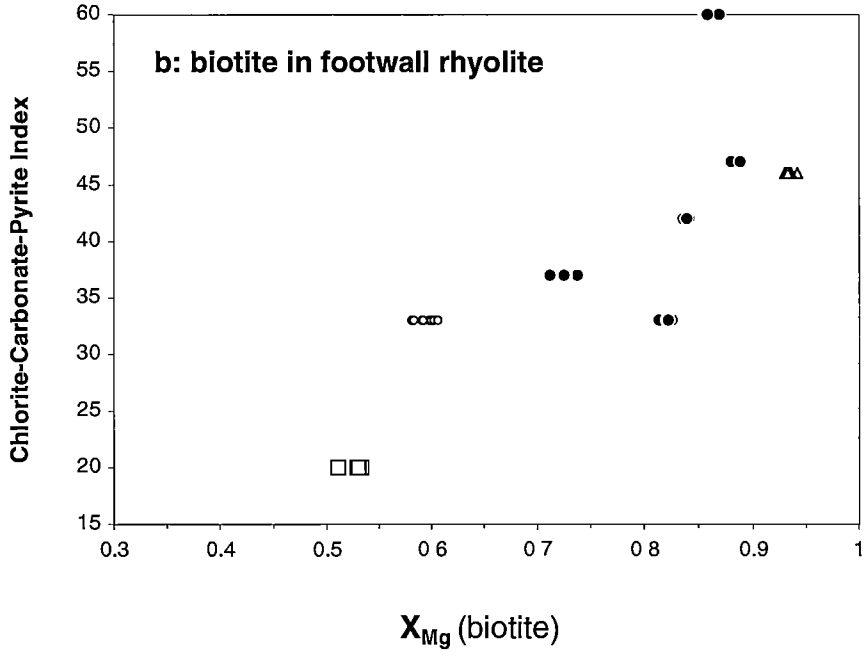

Legend:

□ least-altered footwall rhyolite

o weakly altered rhyolite (phyllosilicate alteration)

● mottled alteration facies

△ quartz-pyrite alteration facies

Fig. 8.15

An interesting compositional feature of biotites in the footwall alteration zone is their high fluorine content, especially in the quartz-pyrite alteration facies. With regard to the origin of the fluorine it is important to note that hydrothermal vent fluids are depleted in F relative to seawater (Von Damm et al., 1985). This suggests that seawater-derived fluids may loose F during interaction with the oceanic crust which could be incorporated into some hydrothermal phyllosilicates. Based on thermodynamic calculations Seyfried and Ding (1995) concluded that talc may represent a sink for F which may form during hydrothermal alteration of basalt. Another alternative is that the fluorine came from a magmatic source and that the hydrothermal fluid was a mixture of a fluorine-rich igneous and Mg-rich, seawater-derived fluids. However, additional Cl and F whole rock analyses, stable isotope data and fluid inclusion studies are required to confirm any involvement of a magmatic fluid phase. Such investigations, which could help to clarify the source of the hydrothermal fluids at Thalanga, were beyond the scope of this study.

Geochemistry of altered hangingwall dacite

Geochemical and mass changes in the hangingwall dacite are of a substantially smaller scale than in the footwall alteration zone and mainly involve mobility of silica and alkalies. Typically, samples of the hangingwall dacite have lost K_2O due to albite alteration. Furthermore, the geochemical data show that the hangingwall dacite is relatively poor in sulphur, iron, sulphur, base metals (Cu, Pb, Zn) and trace elements such as Ba, Rb, As, Bi and Mo. These features support the conclusion that the dacites were emplaced after hydrothermal activity associated with mineralisation had ceased and that the weak alteration of the hangingwall could be related to background seafloor alteration (diagenetic alteration and low-grade sub-seafloor metamorphism) post-dating hydrothermal activity.

Nevertheless, elevated Zn, Pb, Bi and S concentrations have been detected in one sample of dacite type 1 in section 5, ~20 m stratigraphically above massive sulphides (sample TH382A-400, Fig. 8.12). Hill (1996) established that minor sphalerite and galena were partially remobilised during deformation and emplaced locally in piercement structures in the lower parts of coherent hangingwall dacite in contact with massive sulphides. However, the basal contact of dacite type 1 lava in section 5 conformably overlies polymictic breccia (facies E1; drill core log of TH382A in the Appendix and Table 5.3) and brittle fractures filled with sulphides are not present. Consequently, it seems more likely that locally, minor hydrothermal activity was on-going during emplacement of dacite type 1 leading to weak alteration of the basal part of the lava and precipitation of minor sulphides.

8.7 Summary

The effects of alteration on the geochemical composition of the footwall rhyolite and hangingwall dacite have been examined using analyses of major, trace and rare earth elements. The principal results can be summarised as follows:

- the major element composition of the footwall rhyolite was substantially modified during hydrothermal alteration, the most prominent changes include sodium depletion and addition of silica, iron, magnesium and sulphur;
- most alteration facies present at Thalanga can be successfully discriminated geochemically in the Alteration Boxplot;
- mass balance calculations show that SiO_2 was a major mobile component during alteration; strong silicification was associated with pyritic alteration (quartz-pyrite alteration facies) but occurred also on the fringes of the hydrothermal system (quartz-K-feldspar alteration facies);
- potassium was conserved during intense, pyritic alteration and added in variable amounts to mottled and quartz-K-feldspar alteration facies;
- variations in the concentrations of trace elements such as Ba, Rb, Sr, As and Bi are interpreted to reflect strong mineralogical controls on their abundances;
- LREE and Eu were mobile during hydrothermal activity in the footwall alteration zone (LREE were added and Eu was variably depleted and enriched);
- several geochemical features of the footwall alteration zone show systematic changes correlated with distance from the mineralised Favourable Horizon and a number of ore proximity indicators have been identified (Table 8.1);
- alteration of the hangingwall dacite is weak and characterised geochemically by mobility of silica, widespread K_2O loss, Na_2O addition and localised CaO enrichment associated with epidote alteration;
- alteration in the hangingwall probably occurred after the principal hydrothermal activity had ceased;
- rare local occurrences of geochemical anomalies (elevated Zn, S and Bi) in the hangingwall dacite above ore in East Thalanga could be the result of minor, localised late-stage hydrothermal activity.

The geochemical data for the altered footwall rhyolite, especially the association of Mg-enrichment and pyritic alteration, indicate that hydrothermal fluids at Thalanga were seawater-derived.

9 Discussion: Volcanology and alteration of the Thalanga sequence and implications for massive sulphide mineralisation

In this chapter, the results of this study are summarised and genetic implications for massive sulphide mineralisation at Thalanga are discussed. The volcanic evolution of the Thalanga sequence has been constrained, providing important information on the geological environment of mineralisation. A model for the evolution of the Thalanga hydrothermal system is proposed by critical examination of the textural, mineralogical and geochemical evidence and comparison with other studies of VHMS-related alteration zones.

9.1 The environment of VHMS-style mineralisation

9.1.1 Volcanological setting of the Thalanga deposit

The Thalanga massive sulphide deposit is located at the top of a ~1,000 m-thick, rhyolitic lava-dominated succession which formed in a below-wave-base, submarine environment. This volcanic centre was constructional, rising up to 500 m above the surrounding area, during the time of massive sulphide formation (Chapter 5). Mineralisation appears to have occurred preferentially in localised shallow depressions (<20 m deep) which were also depocentres for coarse, quartz crystal-rich mass-flow emplaced units (QEV).

The PACMANUS hydrothermal field in the Manus basin (Papua New Guinea) represents a modern analogue for the Thalanga deposit. This field consists of several hydrothermally active areas and sulphide deposits at 1,630 m below sea level, near the top of a 20 km long, 1 to 1.5 km wide, ridge of dacite which rises 400 to 600 m above the surrounding seafloor (Binns & Scott, 1993).

The Thalanga mine area remained a centre of effusive volcanic activity after mineralisation and the hangingwall contains different types of dacite lavas and intrusions and locally-derived, monomictic and polymictic mass-flow-emplaced breccia units. In contrast, hemipelagic mudstone and turbidites, partly derived from an unknown ?distal source, accumulated in the laterally equivalent area to the west of the deposit. The topographically high Thalanga volcanic centre did not receive the mass-flow transported

sedimentary input from external sources.

This interpretation of the volcanic facies architecture, based on detailed facies analysis in seven cross sections, represents a substantial advance in the understanding of the geological setting of massive sulphide mineralisation at Thalanga. Volcanic facies recognition and interpretation involved detailed textural observations on hand specimen and thin section scale and comparison with published descriptions of the characteristics of other submarine, volcanic successions hosting massive sulphide deposits (eg. De Rosen-Spence et al., 1980; Allen, 1988, 1992, 1996a, 1996b; Morton et al., 1991; Cas, 1992; McPhie & Allen, 1992; Gibson et al., 1993; McPhie et al., 1993; Doucet et al., 1994). Correct distinction of primary from alteration-related textures is particularly important in such successions. Allen (1988) studied the textural effects of hydrothermal alteration on felsic volcanics and demonstrated that apparent clastic textures in altered silicic lavas at Benambra (Victoria, Australia) are the result of domainal and multi-stage hydrothermal alteration processes. Textural criteria for the discrimination of apparent and genuine volcaniclastic facies in altered volcanic sequences presented by Allen (1988) were adopted and developed for facies interpretation in the Thalanga footwall alteration zone (Chapter 5 and Paulick & McPhie, 1999). The footwall at Thalanga consists dominantly of altered coherent facies of rhyolite lavas, however rocks with apparent clastic textures, previously interpreted as 'pyroclastics' (Wills, 1985; Gregory et al., 1990), are very common. The textural evolution of the altered footwall rhyolite was controlled by various factors, including the primary textural heterogeneity (eg. distribution of glassy and crystalline groundmass domains), domainal alteration during hydrothermal activity, and recrystallisation during upper greenschist facies metamorphism and regional deformation.

9.1.2 Facies characteristics of submarine, felsic, lava-dominated volcanic centres

The Thalanga volcanic centre represents a felsic, non-explosive, submarine dome and lava complex and the footwall and hangingwall to the massive sulphides are dominated by rhyolite and dacite lavas, domes and syn-volcanic intrusions. The internal organisation of domes, cryptodomes and lavas is complex and variable and has been described in detail by several authors (Pichler, 1965; Yamagishi & Dimiroth, 1985; Kokelaar, 1982; Cas et al., 1990a; Kano et al., 1991; Allen, 1992; Cas, 1992; McPhie et al., 1993; Goto & McPhie,

1998). All three types of emplacement units consist of variable proportions of coherent facies and in situ or resedimented volcaniclastic facies. Volcaniclastic facies may include peperite, hyaloclastite, autobreccia and resedimented, syn-eruptive volcaniclastic debris. In general, domes and cryptodomes have high aspect-ratios; common lateral and vertical dimensions are both in the range of tens of m to >100 m. Laterally extensive submarine felsic lavas have thicknesses up to ~400 m and relatively low aspect ratios since they typically extend for several kilometres away from their vents (De Rosen-Spence et al., 1980; Cas, 1978, 1992).

At Thalanga, the maximum thicknesses of the various emplacement units range between ~50 and >250 m. Their lateral dimensions are difficult to constrain due to the wide spacing of drill holes and cross sections but estimated minimum extents are generally in the order of 500 m to 1,000 m (Table 5.1). Based on systematic changes in the lithofacies assemblages and geometry of the Thalanga sequence along strike a general facies model for submarine, felsic lava-dominated volcanic centres is suggested (Fig. 9.1).

The proximal facies association of such volcanic centres consists of a thick package of lavas, domes, cryptodomes and syn-volcanic intrusions dominated by coherent facies. Different lavas may be distinguishable on the basis of phenocryst assemblages and/or geochemical characteristics such as immobile element ratios. The volcaniclastic facies in this setting consist predominantly of in situ and/or resedimented lava-derived autoclastic breccia. Such breccias are typically monomictic. However, polymictic breccia, containing locally-derived clasts from several petrographically distinct lavas may also occur. The lateral extent of resedimented volcaniclastic breccia units is generally limited to confined, local depressions which are defined by constructional volcanic features such as steep margins of lavas and domes. The non-volcanic sedimentary facies are dominated by suspension-settled, laminated or massive hemipelagic mudstone. During periods of volcanic quiescence, laterally extensive, continuous horizons consisting of mudstone and mass-flow-emplaced, resedimented volcaniclastic units may form. Such facies may include chemical sediments such as silica-ironstones and are potential hosts for massive sulphides.

Fig. 9.1: Facies model for subaqueous, non-explosive felsic volcanic centres based on the volcanic facies architecture of the Thalanga sequence.

Proximal, medial and distal facies associations have been summarised on graphic logs. Recognition of stratigraphic levels indicating periods of relative volcanic quiescence is important because these horizons may be prospective for seafloor massive sulphide deposits.

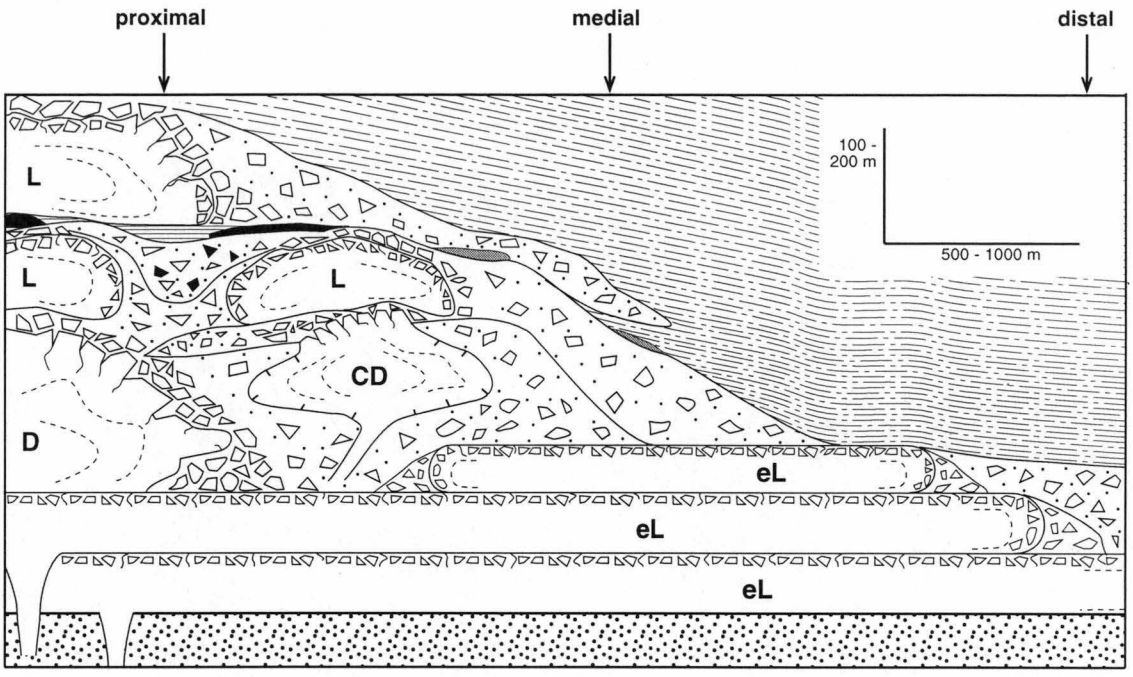

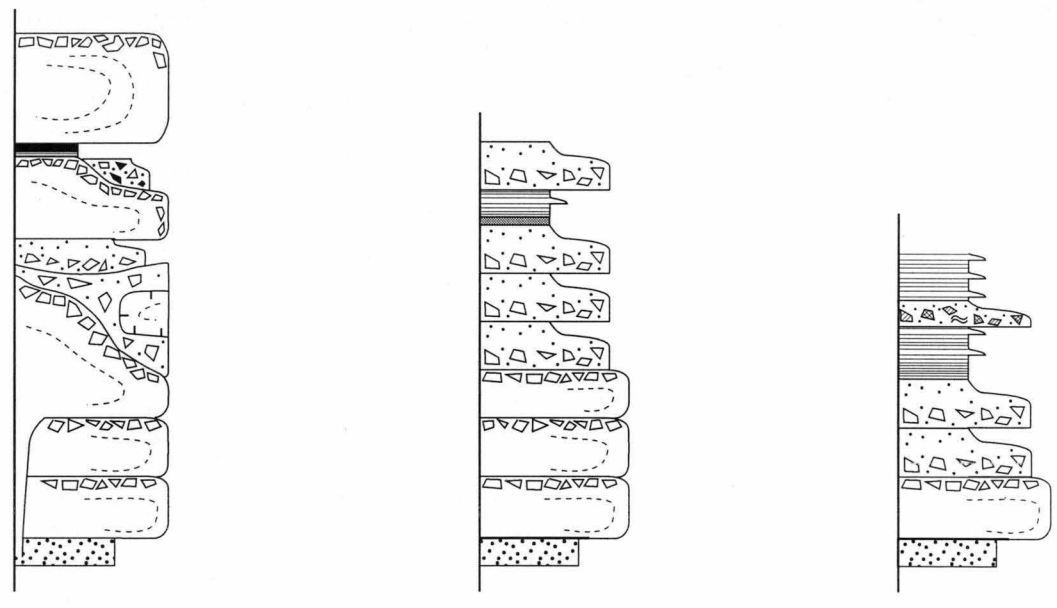

PROXIMAL MEDIAL DISTAL

volcanic facies

- in-situ volcaniclastic facies
- resedimented, syn-eruptive autoclastic facies
- CD: cryptodome; D: dome; eL: laterally extensive lava; L: short lava
- locally derived, polymictic breccia
- intrusive contact
- pre-volcanic facies

sedimentary facies

- mudstone
- turbidites
- mass-flow emplaced volcaniclastic breccia (eg. polymictic, pumice-rich breccia)

hydrothermal facies

- massive sulphide
- silica-ironstone

Fig. 9.1

In the medial facies association, the total thickness of volcanic units is somewhat less than in the proximal facies. Resedimented autoclastic breccia units are abundant, reflecting the importance of mass-flow processes on the flanks of the volcanic centre. Sedimentary facies may include turbidites derived from local or remote sources, especially in the upper part of the succession.

The most important feature of the distal facies association is the substantial increase in the abundance of sedimentary lithofacies, dominated by mudstone and turbidites, which are at least partially derived from extrabasinal sources. Although not observed in the Thalanga sequence, the distal facies association may also include syn- and post-eruptive volcaniclastic mass-flow units composed of various proportions of pumice, shards, crystals, crystal fragments and lithic clasts derived from explosive volcanic centres elsewhere in the basin. Mass-flows from foreign volcanic or sedimentary sources do not form deposits on the topographically elevated volcanic centre and are therefore absent in the proximal facies association. The distal facies may also include lavas consisting of variable proportions of coherent and volcaniclastic facies. Extensive outflow of felsic lavas is not common and may require special conditions that favour relatively low viscosity (eg. high temperatures, high volatile contents and high eruption rates) (Cas, 1978). However, the overall thickness of volcanic units is substantially reduced and it is inferred that lavas and lava-derived volcaniclastic facies become increasingly scarce with distance from the volcanic centre. Furthermore, any hiatus in eruptive activity at the volcanic centre may result in a substantial decrease of locally-derived, volcaniclastic facies in the distal facies association.

9.1.3 Water depth controls on eruption styles and formation of VHMS deposits

In reviewing styles of submarine volcanism and the geological setting of massive sulphide deposits, Cas (1992) concluded that deep submarine environments are especially favourable for VHMS mineralisation. This interpretation was based on the presence of sedimentary facies (hemipelagic mudstone and turbidites) indicating relatively deep-water settings in the host successions of various VHMS deposits, theoretical considerations concerning massive sulphide ore genesis (in particular the prevention of fluid boiling) and the analogy with modern, massive sulphide-bearing hydrothermal fields which occur in deep marine environments (>1,000 m water depth; Rona & Scott, 1993).

The ambient hydrostatic pressure influences the eruption styles (explosive versus effusive) of submarine magmas and is also an important controlling factor on the processes involved in the precipitation of sulphides from hydrothermal solutions. In order to generate instantaneous expansion of volatiles and explosive fragmentation during pyroclastic or phreatomagmatic eruptions the volatile pressure (P_V) must substantially exceed the ambient pressure (P_A). In the marine environment, the maximum water depth at which explosive volcanic eruptions are likely to occur (ie. where $P_A << P_V$) is controlled by a number of factors including hydrostatic pressure, magma composition, temperature, characteristics of the volatiles (including activities of volatile species and salinity), magma rise rate and character of the conduit (open or closed) (McBirney, 1963; Moore, 1965; Peckover et al., 1973; Wilson, 1980). McBirney (1963) demonstrated that H_2O has a low specific volume under confining pressure >200 bar and magmatic temperatures (≥800 °C), but the specific volume increases significantly at pressures <100 bar. This indicates that explosive volcanic eruptions are probably restricted to water depths <1,000 m, where volatile pressures may substantially exceed the ambient hydrostatic pressure. This depth estimate should be lower if other constraining factors are taken into account (eg. a_{CO_2} in the volatile phase, Wilson, 1980) and Cas (1992) concluded that the maximum water depths for subaqueous, explosive volcanic eruptions are in the range of 500 to 1,000 m. However, the maximum water depth at which explosive volcanic eruptions may occur is still a contentious issue and Lentz et al. (1999) argued that the importance of the salinity of magmatic fluids has been underestimated. Lentz et al. (1999) suggested that pyroclastic fragmentation may occur even at water depths >3,000 m if the magmatic fluid driving the explosions contains >1 wt.% NaCl.

Precipitation of sulphides from hydrothermal fluids is a complex process controlled by factors including fluid composition, fluid temperature, pH, oxidation-reduction state, and ambient pressure (eg. Henley & Ellis, 1983). The ambient pressure imposes constraints on fluid boiling. If boiling is prevented, which is likely to be the case in deep marine settings, massive sulphides may form on, or just below, the seafloor (eg. Drummond & Ohmoto, 1985). In contrast, if sulphide precipitation is related to fluid boiling in the subsurface disseminated stockwork deposits may form rather than seafloor massive sulphides.

The sedimentary facies association at Thalanga consists of mudstone and turbidites that are characteristic of below-wave-base, marine sedimentation. Furthermore, the presence of massive sulphide lenses, which formed at, or just below the palaeo-seafloor (Hill, 1996) indicates that water depths were high enough to prevent fluid boiling. The absence of locally sourced pyroclastic facies and the dominance of effusive volcanism are also consistent with a relatively deep marine setting where explosive volcanic activity was inhibited due to high ambient hydrostatic pressure. Collectively, these considerations imply that the Thalanga deposit probably formed in a deep submarine environment, at water depths in excess of 1,000 m.

Nevertheless, it should be noted that several studies concerned with the geological setting of massive sulphide formation have concluded that mineralisation occurred in 'shallow' environments (<<1,000 m water depth) (Sainty, 1992; Allen et al., 1996b; Halley & Roberts, 1997; Hunns & Zaw, 1997; Marani et al., 1997). The controls on massive sulphide formation in these settings are poorly understood, however, Halley & Roberts (1997) proposed that fluid chemistry, especially low-salinity fluids (possibly derived from a subaerial recharge zone), may have been important in the genesis of the Henty Au-rich massive sulphide deposit (Tasmania, Australia). Furthermore, Allen et al. (1996b) suggested that sub-seafloor replacement processes, occurring at depths up to 150 m below the time-equivalent palaeo-seafloor position was important in the formation of the relatively shallow (? <500 m) water VHMS deposits in the Skellefte district (Sweden).

9.1.4 Links between volcanism and hydrothermal activity

The spatial association of massive sulphides with a felsic, submarine effusive volcanic centre at Thalanga suggests that there may have been a genetic link between magmatism and mineralising hydrothermal activity. The large magma chamber that fed the compositionally fairly homogeneous rhyolitic eruptions may have also provided the heat required to sustain a vigorous hydrothermal system. Potentially, this magma could have also contributed to the chemical composition of fluids in the Thalanga hydrothermal system by mixing of a magmatic aqueous phase with seawater-derived fluids in the subsurface.

Discordant zones of intense alteration are connected to massive sulphides in the Favourable Horizon but do not coincide with particular facies boundaries or facies types and clearly cross-cut the facies arrangement in the footwall (Chapter 5). This indicates that factors other than primary differences in permeability between coherent and volcaniclastic rhyolite facies were important in concentrating hydrothermal fluid flow. Neither have any syn-volcanic faults been recognised. Thus, while magmatism and mineralisation can be generally linked, the mechanism of focusing fluid discharge during mineralising hydrothermal activity remains enigmatic.

9.1.5 Comparison with other volcanic successions hosting massive sulphide deposits

Submarine dome and lava complexes such as that hosting the Thalanga deposit have been identified as favourable environments for VHMS mineralisation (Cas, 1992). Other examples of VHMS deposits hosted in similar volcanic settings include the Hellyer, Que River and Benambra deposits in Australia (Waters & Wallace, 1992; Allen, 1988, 1992), the 'Noranda-type' VHMS deposits in Canada (eg. Millenbach, Amulet, Mattagami and Geco; Morton & Franklin, 1987) and the Kuroko deposits in Japan (Horikoshi, 1969; Sato et al., 1974; Ohmoto & Takahashi, 1983).

Archean Cu-Zn massive sulphide deposits in Canada with footwall and hangingwall successions consisting of felsic lavas, pillowed or massive mafic lavas and locally-derived volcaniclastic facies have been termed 'Noranda-type' deposits by Morton and Franklin (1987). Sedimentary facies consist of mudstone, turbidites and mass-flow-emplaced volcaniclastic units derived from extrabasinal sources. In situ pyroclastic facies have not been recognised, suggesting that explosive eruptions did not occur in the local environment. Morton and Franklin (1987) inferred that Noranda-type deposits formed in water depths >500 m.

The Hellyer deposit (Tasmania, Australia) formed in a deep, submarine environment on top of a 600 m thick succession dominated by pillowed and massive lavas of mafic to intermediate composition and associated volcaniclastic facies (Waters & Wallace, 1992). The ore occurs in the overlying mixed sequence, a diverse lithofacies association including dacite lavas and domes and polymictic, volcanic mass-flow units.

The mixed sequence is thickest in local depressions and is interpreted to represent a hiatus in volcanic activity (Waters & Wallace, 1992). The hangingwall comprises ~200 m of pillowed basaltic sills and black shale. The lithological diversity and lateral facies changes of the mixed sequence are similar to the character of facies associations in the Thalanga Favourable Horizon. Both the Favourable Horizon and the mixed sequence have been interpreted to represent a period of relative volcanic quiescence.

Allen (1992) reconstructed the geological setting of massive sulphide deposits at Benambra (Victoria, Australia) based on detailed facies interpretation of the altered and strongly deformed host-rock sequence. Felsic submarine volcanism generated extensive lavas, domes, cryptodomes and sills interleaved with hemipelagic mudstone and turbidites. The Benambra VHMS deposits formed in siltstone in the proximal facies of deep-marine volcanoes consisting of rhyolitic lavas, cryptodomes and syn-volcanic intrusions. Massive sulphides are overlain by basalt lavas forming part of a mafic to felsic volcanic suite present in the upper part of the sequence. Similar to Thalanga, the Benambra deposits formed at the waning stage of widespread rhyolitic volcanism in close spatial association with volcanic centres.

The footwall to the Tertiary Kuroko massive sulphide deposits in the Hokuroko basin (Japan) consists of dacitic lavas, domes and intrusions, basaltic lavas and associated volcaniclastic facies whereas a volcano-sedimentary succession dominated by mudstone, pumiceous volcaniclastic facies and minor dacite occurs in the hangingwall (Sato et al., 1974; Horikoshi, 1990; Cas, 1992). The environment of ore formation is a contentious issue, depending mainly on interpretation of the footwall volcaniclastic facies. A deep-water caldera setting has been proposed (eg. Ohmoto & Takahashi, 1983), based on the interpretation that the volcaniclastic units represent in situ pyroclastic facies derived from intrabasinal, deep-water explosive vents. However, other studies have found that volcaniclastic facies are mainly hyaloclastite and autobreccia (Takahashi & Suga, 1974; Cas et al., 1990b) and that pyroclast-rich units were emplaced by mass flows derived from sources in shallow settings (Matsukuma & Horikoshi, 1970; Guber & Green, 1983; Cas et al., 1990b). An alternative model for the geological setting of Kuroko deposits involves submarine lava and dome complexes which locally grewn into shallow water where explosive eruptions may have occurred, providing pyroclastic debris that was resedimented into deeper parts of the basin (Ishikawa, 1983; Yamagishi, 1987; Cas et al.,

1990b; Cas, 1992). This setting is similar to that of the Thalanga deposit, except that pyroclast-rich volcaniclastic units are absent in the Thalanga sequence.

Notwithstanding the association of massive sulphides and effusive, submarine volcanic centres, it should be stressed that VHMS deposits are known to occur in volcano-sedimentary successions of diverse character and lava-dominated facies associations may dominate either the footwall or the hangingwall (Cas, 1992). Furthermore, many deposits occur in host sequences which are composed mainly of volcaniclastic and sedimentary units. Prominent examples of massive sulphides in sequences dominated by volcaniclastic facies occur in Canada and have been termed 'Mattabi-type' by Morton and Franklin (1987) (eg. Mattabi, Ontario; Kidd Creek, Ontario; Detour, Quebec). The host rocks consist of variable facies including 'pumice-rich ash tuff', 'hyalotuff' and 'welded and non-welded ash tuff' of felsic to mafic composition, interpreted to represent the deposits of primary subaqueous pyroclastic flows and secondary mass flows. Morton & Franklin (1987) suggested that these volcaniclastic units and the enclosed massive sulphides accumulated in shallow-water environments (<500 m).

Although broadly similar to the Mattabi type, the pumice-rich host-rocks to the Rosebery and Hercules ore bodies (Tasmania, Australia) are interpreted to be deposits of mass-flows derived from subaerial or shallow marine sources, emplaced in a below-wave-base, submarine environment (Allen & Cas, 1990). The extremely high primary permeability of these units favoured formation of the Rosebery and Hercules massive sulphides by sub-seafloor replacement processes (Allen, 1994).

Massive sulphides in sequences dominated by fine-grained sedimentary and volcaniclastic facies and minor in situ volcanic facies are common in the Bathurst mining camp (New Brunswick, Canada; Lentz & Goodfellow, 1996; Lentz et al., 1997). These deposits share some characteristics with sediment-hosted massive sulphide deposits.

9.2 Alteration at Thalanga and a model for the hydrothermal system

9.2.1 Hydrothermal alteration of the footwall rhyolite

The Thalanga footwall alteration zone consists of a variety of alteration facies with a large range in mineralogical and geochemical characteristics. This diversity reflects the complexity of the Thalanga hydrothermal system and the influence of factors including fluctuation in the supply of hydrothermal fluids, fluid temperature and composition (including pH, f_{O_2} and a_{H_2S}), water/rock ratios and interaction of hydrothermal fluids with ambient seawater. Textural, mineralogical and geochemical evidence indicates that alteration in the footwall involved destruction of primary feldspar, silicification and formation of pyrite, carbonate, K-feldspar and hydrothermal phyllosilicates (Chapters 7 and 8).

The muscovite-, chlorite- and biotite-rich mineral assemblages in the altered footwall rhyolite are inferred to be the metamorphic equivalents of hydrothermal phyllosilicates. Comparison with mineral assemblages associated with modern, submarine hydrothermal systems suggests that the hydrothermal phyllosilicates were mainly sericite, chlorite and clay minerals such as illite and smectite. These phyllosilicates have been identified in hydrothermally altered submarine volcanics associated with actively forming massive sulphide mineralisation on the seafloor (Alt & Jiang, 1991; Goodfellow et al., 1993; Binns & Scott, 1993; Ridley et al., 1994; Turner et al., 1993; Honnorez et al., 1998).

Several different alteration facies have been identified in the Thalanga sequence on the basis of the dominant mineral assemblages and alteration intensity (Chapter 7). The bulk of the footwall alteration zone is occupied by the feldspar-destructive, phyllosilicate-rich mottled alteration facies with gradational lateral contacts to the surrounding least-altered rhyolite. This facies envelops discordant zones of quartz-pyrite alteration facies which commonly extend to massive sulphides in the Favourable Horizon. The quartz-pyrite alteration facies also occupies prominent strata-bound zones immediately below the Favourable Horizon. The chlorite-pyrite alteration facies is restricted to the immediate footwall below the East Thalanga ore lens. The quartz-K-feldspar alteration facies occurs preferentially on the fringes of the footwall alteration zone and shows complex, overprinting textural relationships with the mottled alteration

facies. The carbonate-chlorite-tremolite alteration facies is common in the Favourable Horizon and the upper part of footwall rhyolite in West Thalanga (section 2). In contrast, calcareous alteration is restricted to rare occurrences of the disseminated tremolite alteration facies in East Thalanga.

The bulk of the footwall alteration zone, represented by the mottled alteration facies, is characterised by Na- and Ca-loss and enrichment in Mg, Fe and S (Chapter 8). In addition, the quartz-pyrite alteration facies has also gained substantial Si and is enriched in several trace elements which are compatible in pyrite (eg. As, Bi and Mo). The chlorite-pyrite alteration facies has lost Si and gained large amounts of Mg, Fe and S. The disseminated tremolite and carbonate-chlorite-tremolite alteration facies are characterised by large gains in Ca and Mg. The quartz-K-feldspar alteration facies gained substantial amounts of Si and K.

The geometry of the footwall alteration zone and compositional characteristics of altered footwall rhyolite suggest that the Thalanga hydrothermal system may have evolved from dominantly calcareous alteration to phyllosilicate-dominated alteration before mineralising hydrothermal activity occurred. A conceptual model for this evolution is discussed below and summarised in Fig. 9.2. However, it should be noted that textural constraints on timing relationships are generally inconclusive and it is equally possible that alteration facies in the footwall formed more or less simultaneously from a spatially heterogeneous hydrothermal system.

Calcareous alteration

The disseminated tremolite and carbonate-chlorite-tremolite alteration facies represent calcareous alteration of moderate and strong intensity which introduced significant hydrothermal carbonate into the alteration zone. The genesis of the carbonate-chlorite-tremolite alteration facies has been examined in detail by Herrmann (1994) and Hill (1996) who concluded that this alteration facies represents the metamorphic equivalent of footwall rhyolite which experienced intense chlorite-carbonate alteration. In this facies, the tremolite-forming metamorphic reaction was mainly controlled by the availability of volcanic quartz providing SiO_2 for the reaction. In contrast, the disseminated tremolite alteration facies represents footwall rhyolite which experienced disseminated to patchy

Fig. 9.2: Model for the Thalanga hydrothermal system.

A model for the Thalanga hydrothermal system has been inferred based on the distribution of alteration facies and their geochemical characteristics.

(a) Calcareous alteration.

(b) Phyllosilicate-dominated and quartz-K-feldspar alteration.

(c) Quartz-pyrite and chlorite-pyrite alteration and mineralisation.

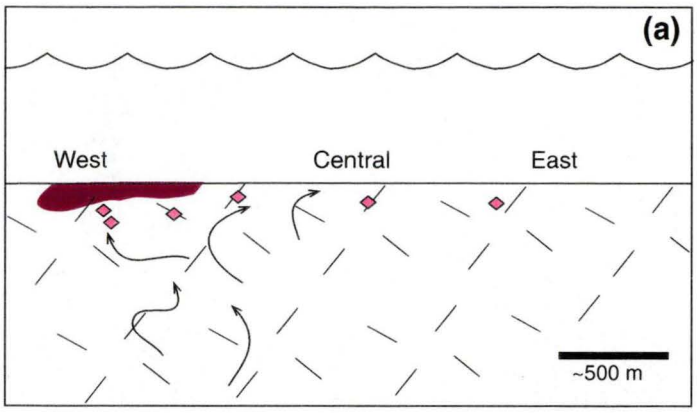

CALCAREOUS ALTERATION

=> formation of patchy carbonate-chlorite alteration within the footwall (precursor to disseminated tremolite alteration facies)

=> formation of intense carbonate-chlorite alteration at the top of footwall rhyolite in West Thalanga (precursor of carbonate-chlorite-tremolite alteration facies)

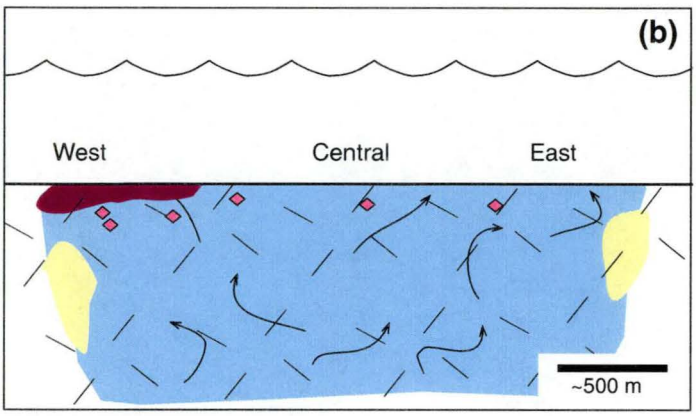

PHYLLOSILICATE-DOMINATED ALTERATION AND QUARTZ-K-FELDSPAR ALTERATION
diffuse unfocussed upflow of seawater-derived, evolved hydrothermal fluids

=> broad alteration zone characterised by destruction of primary feldspar, precipitation of pyrie and formation of hydrothermal phyllosilicate (mottled alteration facies)

=> formation of quartz-K-feldspar alteration on the fringes of the hydrothermal system

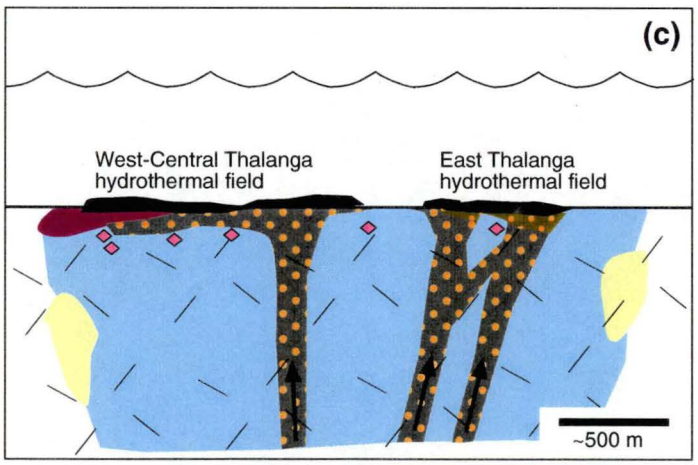

QUARTZ-PYRITE AND CHLORITE-PYRITE ALTERATION
focussed discharge of mineralising hydrothermal fluids (dominately evolved, seawater-derived fluids + ?magmatic component?)

=> formation of discordant and stratiform zones of quartz-pyrite alteration (silica addition, precipitation of disseminated pyrite and pyrite veins, formation of various hydrothermal phyllosilicates)

=> formation of chlorite-pyrite alteration in East Thalanga (silica leaching, formation of chlorite and pyrite)

=> mineralisation in West-Central and East Thalanga hydrothermal fields

Legend:

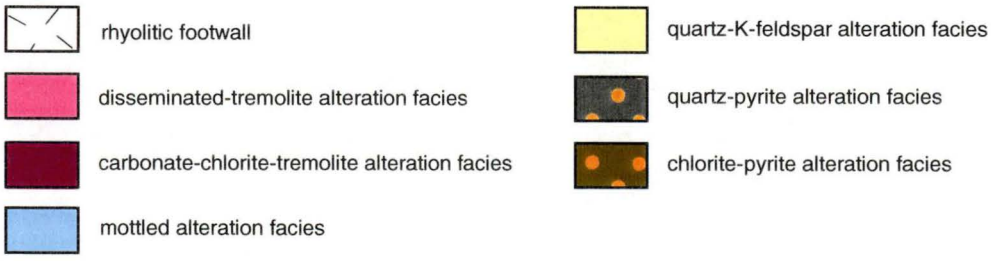

Fig. 9.2

chlorite-carbonate alteration. Consequently tremolite crystallisation was a function of the abundance, composition and relative proportions of pre-existing carbonate and chlorite.

The timing of this type of alteration at Thalanga is difficult to constrain due to substantial recrystallisation during metamorphism. However, Hill (1996) inferred that massive sulphides in West Thalanga formed predominantly by a mineralisation process involving sub-seafloor replacement of carbonate-chlorite-rich altered rhyolite. Consequently, carbonate-chlorite alteration must have occurred prior to mineralising hydrothermal activity.

Hill (1996) showed that C isotope data on calcite and dolomite in the carbonate-chlorite-tremolite alteration facies are consistent with the interpretation that CO_2 was predominantly derived from cool seawater. This suggests that hydrothermal carbonate precipitated during interaction of the hydrothermal fluid with ambient seawater, just below the palaeo-seafloor. The Mg required for the dolomite- and chlorite-forming reactions may have also been provided by seawater. It is possible that Ca was derived from the hydrothermal fluid which could have leached Ca from plagioclase during passage through the footwall rhyolites, or from the ambient seawater.

The abundance of the carbonate-chlorite-tremolite alteration facies in West Thalanga suggests that volcaniclastic units, which represent the top part of footwall rhyolite in section 2, provided favourable conditions for mixing of upwelling hydrothermal fluids with ambient seawater. In contrast, coherent rhyolite facies dominates in the top part of the footwall in East Thalanga and was probably less permeable to fluids and, consequently, calcareous alteration there is restricted to patchy occurrences of the disseminated tremolite alteration facies. However, it may also be argued that the hydrothermal discharge responsible for calcareous alteration was more concentrated in West than in East Thalanga.

Hydrothermal carbonate alteration is relatively common in the VHMS environment and has been described from several deposits in Tasmania (Australia) (Rosebery; Lees et al., 1990; Hercules; Zaw & Large, 1992; Hellyer; Gemmell & Large, 1992) and other VHMS districts (Chisel Lake, Canada; Galley et al., 1993; Kuroko, Japan; Shikazono et al., 1998). It has also been observed in modern, submarine hydrothermal systems (Middle Valley; Goodfellow et al., 1993). In general, carbonate alteration is interpreted to represent a low temperature (<100 °C to <200 °C) alteration process related to relatively

oxidised hydrothermal fluids. Ore-related carbonate alteration occurred early during hydrothermal activity at the weakly metamorphosed (lower greenschist facies) Rosebery deposit (Orth & Hill, 1994; Allen, 1997). Pumice and volcanic shard textures are preserved within carbonate nodules in the immediate ore environment whereas texturally destructive phyllosilicate-rich alteration has overprinted the remainder of the pumice-rich footwall rocks. Galley et al. (1993) also concluded that carbonate associated with massive sulphides at the strongly metamorphosed Chisel Lake deposits (amphibolite facies) were precipitated early during the evolution of the hydrothermal system, prior to intense, mineralising hydrothermal activity. In contrast, Shikazono et al. (1998) described hydrothermal carbonates at the Kuroko deposits which are interpreted to post-date massive sulphide formation.

Phyllosilicate-dominated alteration

The bulk of the footwall alteration zone is occupied by the mottled alteration facies which is characterised by destruction of primary feldspar, formation of hydrothermal phyllosilicates and precipitation of disseminated pyrite. The textural diversity of the mottled alteration facies and the predominance of apparent clastic textures, indicate that domainal and multi-stage alteration processes were common. These processes may have been related to variations in fluid compositions, temperature and pathways and water/rock ratio. The pervasive character and continuous lateral extent of the mottled alteration facies suggest that upwelling of hydrothermal fluids was diffuse and unfocused.

Mottled alteration facies is present down to a stratigraphic depth of >300 m below the Favourable Horizon, however, its full stratigraphic extent into the footwall is unknown due to limited drilling. Brauhart & Groves (1998) described broad, feldspar-destructive alteration zones (100's of m to ≤1 km in diameter) below Archean VHMS deposits in the Panorama district (Western Australia) which can be traced for up to 3 km into the footwall stratigraphy where they become narrower and more confined. It is possible that the apparently stratabound footwall alteration zone at Thalanga represents only the upper part of a similarly broad transgressive zone of unfocused hydrothermal fluid upflow which may become narrower at depth. Consequently, the true geometry of the footwall alteration zone may be discordant rather than strata-bound.

The Mg-rich composition of the mottled alteration facies is an indication for seawater-dominated hydrothermal alteration (Schmidt, 1988; Schade et al., 1989; Trägårdh, 1991; Shriver & MacLean, 1993; Barrett & MacLean, 1994a). The hydrothermal fluids may have evolved during fluid/rock interaction in the subsurface and formation of chlorite probably resulted in the acidic character of these fluids according to the reaction:

$$5\ Mg^{2+}_{(aq)} + 3\ SiO_2 + Al_2O_3 + 9\ H_2O \Rightarrow Mg_5Al_2Si_3O_{10}(OH)_8 + 10\ H^+_{(aq)}$$

(rock) (chlorite) (Reed, 1997).

Quartz-K-feldspar alteration

The quartz-K-feldspar alteration facies occurs locally on the fringes of the Thalanga footwall alteration zone and often shows complex overprinting textural relationships with the mottled alteration facies (section 7.3.2). This type of alteration seems to be generally uncommon in alteration zones associated with VHMS deposits. Nevertheless, K-feldspar has been observed in the outer parts of alteration systems associated with the Kuroko deposits in Japan (Shirozo, 1974) and the Que River deposit (Tasmania, Australia; McGoldrick & Large, 1992). At Que River, K-feldspar is associated with silicification and Au-rich mineralisation which are interpreted to have formed by mixing of ore fluids of moderate temperature (200 to 250 °C) and a near-neutral pH ambient seawater. In another study, numerical modelling of water/rock interaction in the footwall to the Hellyer deposit (Tasmania, Australia) predicted a K-feldspar-rich zone in the outer part of the discordant alteration pipe (Schradt et al., 1999). Although predicted, this type of alteration has not been recognised in the hydrothermal alteration zone associated with this deposit (Gemmell & Large, 1992).

The formation of the quartz-K-feldspar alteration facies at Thalanga probably took place under relatively low temperature conditions and low water/rock ratios because it occurs preferentially on the fringes of the footwall alteration zone. This alteration facies is relatively sulphide-poor, except for occasional occurrences of sphalerite, which is consistent with a comparatively low a_{H_2S} of the fluid. The formation of K-feldspar instead of K-rich white mica indicates that the pH of the hydrothermal fluids increased

from acidic in the central parts of the hydrothermal alteration system to near neutral on its fringes. Thus, mixing of hydrothermal fluids with ambient seawater on the margin of the hydrothermal system could have caused simultaneous cooling and neutralisation. This could have resulted in supersaturation of Si and K and precipitation of quartz and K-feldspar.

During the evolution of the hydrothermal system, the sites of quartz-K-feldspar alteration may have moved in response to variations in the influx rate, temperature, composition and pathways of the hydrothermal fluids. Consequently, overprinting textural relationships with the mottled alteration facies developed.

Mineralising alteration

The mottled alteration facies envelops discordant zones of the quartz-pyrite alteration facies which cross cut the footwall alteration zone. These zones are interpreted to represent the dominant pathways of hydrothermal fluids during the principal stage of mineralising hydrothermal activity and would have been characterised by high water/rock ratios. This interpretation is supported by the high abundance of disseminated pyrite and pyrite veins and substantially elevated concentrations of S, base metals and trace elements such as As, Mo and Bi in the quartz-pyrite alteration facies. Furthermore, massive sulphides in the Favourable Horizon are generally connected to discordant zones of the quartz-pyrite alteration facies in the footwall (Fig. 7.5 to 7.7).

The quartz-pyrite alteration facies also occupies stratiform zones immediately below the massive sulphides. These zones probably formed as a result of lateral flow of hydrothermal fluids below the palaeo-seafloor. This process appears to have been particularly important in West Thalanga (section 2; Fig. 7.5b) where this stratiform zone is up to 50 m thick. The top part of footwall rhyolite in section 2 consists of volcaniclastic facies that may have had relatively high primary permeability which facilitated lateral fluid migration. In addition, an impermeable cap could have formed over sites of fluid discharge due to precipitation of silica, pyrite and other sulphides, forcing ascending fluids sideways before reaching the seafloor. In time, successive sealing of discharge sites could have produced the stratiform zones of intense quartz-pyrite alteration facies. This process may be referred to as 'self choking' and is common in subaerial geothermal systems (Hodgson, 1990).

The quartz-pyrite alteration facies is characterised by silicification, precipitation of pyrite and formation of hydrothermal phyllosilicates. Mass balance calculations show that large amounts of Si, Fe and Mg were added. The gains in Mg suggest that evolved seawater was the main component in the mineralising hydrothermal fluids.

The Mg enrichment in quartz-pyrite alteration facies at Thalanga is contrary to expectations because the solubility of Mg is generally reduced in hot, acidic fluids and chlorite-rich alteration zones are widely regarded as the result of relatively low temperature alteration (Galley, 1993; Seyfried et al., 1988). Hence, it is unlikely that silicification, pyrite precipitation and chlorite formation were concurrent. Instead, the elevated Mg values could be related to chlorite alteration during the formation of mottled alteration facies which was then overprinted by intense quartz-pyrite alteration facies. However, unequivocal textural evidence for overprinting relationships of these alteration facies has not been recognised, having been obscured during metamorphic recrystallisation.

Biotites of the quartz-pyrite alteration facies, which formed during metamorphic recrystallisation of hydrothermal phyllosilicates (Chapter 3), has high fluorine concentrations (1.5 to 1.9 pfu; equal to 3.5 to 3.8 wt.%; Fig. 8.13c). In contrast, biotites in the mottled alteration facies contain 0.2 to 1 pfu F and biotites with <0.2 pfu F are restricted to least-altered rhyolite from the outcrop section. It is possible that the fluorine was incorporated into hydrothermal phyllosilicates during the alteration of rhyolite as a result of interaction with seawater-derived fluid. This interpretation is consistent with the observation that modern hydrothermal vent fluids are depleted in F relative to seawater (Von Damm et al., 1985) and the results of thermodynamic calculations which indicate that F-talc may form during alteration of seafloor basalt (Seyfried and Ding, 1995).

Alternatively, it could be argued that the high F contents of biotites suggest the involvement of a magmatic fluid component. Fluorine is a common volatile element in felsic magmas and may be partitioned into an aqueous phase during crystallisation (Burnham, 1997). At Thalanga, seawater-derived hydrothermal fluids may have mixed with F-rich magmatic fluids in the subsurface prior to intense hydrothermal activity. This interpretation is consistent with S isotope data from sulphides in the Thalanga ore body which indicate that S was derived from a mixture of seawater and an igneous source (Hill, 1996). However, the igneous sulphur component could have been obtained by leaching of

the footwall rhyolite and does not represent direct evidence for the involvement of a magmatic fluid during the mineralisation. Further fluid inclusion studies could help to clarify the source of hydrothermal fluids at Thalanga.

In contrast to the quartz-pyrite alteration facies, which is ubiquitous below the Thalanga deposit, the chlorite-pyrite alteration facies is restricted to a narrow zone underlying massive sulphides in East Thalanga (section 5). This alteration facies is distinctive in showing extreme enrichment in Mg, Fe and S and substantial loss of silica, in marked contrast to the large Si-gains in the quartz-pyrite alteration facies. Possibly, a relatively short-lived episode of hydrothermal alteration characterised by Mg-rich, Si-undersaturated fluids forming zones of chlorite-pyrite alteration facies occurred in East Thalanga. The conditions of alteration and/or the composition of the hydrothermal fluids may have changed and quartz-pyrite alteration facies was generated. This speculative model, involving a phase of silica-leaching, Mg-rich alteration in East Thalanga, implies that conditions of alteration were different in East and West Thalanga and that two separate hydrothermal fields may have co-existed during mineralising hydrothermal activity.

This interpretation is supported by the arrangement of massive pyrite lenses in the Favourable Horizon, the distribution of massive barite and barite-rich massive sulphides and variations in metal ratios of the massive sulphides along strike of the deposit (Fig. 9.3 from Hill, 1996). Parts of ore lenses with high Cu-ratios (Cu/Cu+Zn), low Zn-ratios (Zn/Zn+Pb) and basal zones of massive pyrite may be interpreted as discharge sites of hot, metal-rich fluids whereas barite-rich massive sulphides represent distal, low temperature zones (Huston & Large, 1987; Lydon, 1988). Accordingly, the Vomacka zone, located between East and Central Thalanga (Fig. 1.5), may be regarded as the western margin of the East Thalanga hydrothermal field and distal parts of the Central-West Thalanga hydrothermal field are marked by barite-rich zones along the up-dip and western termination of the central and western ore lenses (Hill, 1996).

9.2.2 Summary of hydrothermal alteration at Thalanga and comparison with other VHMS deposits

The Thalanga footwall alteration zone consists of a complex assemblage of diverse alteration facies. The hydrothermal system may have evolved from calcareous alteration to phyllosilicate-dominated alteration prior to intense, mineralising hydrothermal activity (Fig. 9.2). Chlorite-carbonate alteration of variable intensity was the pre-metamorphic precursor to the disseminated tremolite alteration facies and carbonate-chlorite-tremolite alteration facies which formed in the near-seafloor environment by mixing of low-temperature hydrothermal fluids and ambient seawater. Diffuse upwelling of acidic, seawater-derived, hydrothermal fluids caused destruction of primary feldspar, precipitation of pyrite and formation of hydrothermal phyllosilicates (now muscovite-chlorite-biotite-rich assemblages) in a broad zone below the palaeo-seafloor, presently occupied by the mottled alteration facies. Intense hydrothermal alteration, represented by quartz-pyrite alteration facies,occurs in both discordant zones cross cutting the footwall and in stratiform zones immediately below the massive sulphides. This alteration facies is inferred to have formed during the mineralising stage of hydrothermal activity and the discordant zone are interpreted as feeder zones supplying metal-rich fluids to two mineralising hydrothermal fields (East Thalanga and Central-West Thalanga).

The overall arrangement of alteration facies in the Thalanga footwall with siliceous, discordant zones enveloped by phyllosilicate-dominated alteration is characteristic for footwall alteration systems underlying many VHMS deposits of the Zn-Pb-Cu type (Franklin et al., 1981). Other examples of massive sulphides with footwall alteration zones consisting of siliceous central zones and phyllosilicate-rich outer parts include the Hellyer deposit (Tasmania, Australia; Gemmell & Large, 1992), Brunswick No.12 (Bathurst mining camp, Canada; Lentz & Goodfellow, 1996), the Chisel Lake deposits (Manitoba, Canada; Galley et al., 1993) and the Kuroko deposits (Japan; Shirozo, 1974; Iijima, 1974).

Fig. 9.3: Variations in the composition of Thalanga massive sulphides and interpretation of two separate hydrothermal fields during mineralisation.

The metal zonation, occurrences of massive pyrite and the distribution of barite-rich zones imply that two separate hydrothermal systems existed at Thalanga (from Hill, 1996).

(a) A long section of the Thalanga deposit shows the distribution of massive pyrite and massive sulphides with high Cu-ratios (Cu/Cu+Zn) and low Zn-ratios (Zn/Zn+Pb). These areas may be interpreted as discharge sites of relatively hot hydrothermal fluids (Huston & Large, 1987). Hill (1996) identified numerous D3-faults offsetting massive sulphide lenses and determined the relative sense of movement along these structures.

(b) When the movement along the D3 faults is reversed it becomes apparent that the Thalanga deposit consists of the products of two hydrothermal systems. Relative temperature gradients can be inferred for the East Thalanga and the Central-West Thalanga hydrothermal fields based on the distribution of massive pyrite and interpreted discharge sites and barite-rich zones on the fringes of the ore lenses (Hill, 1996).

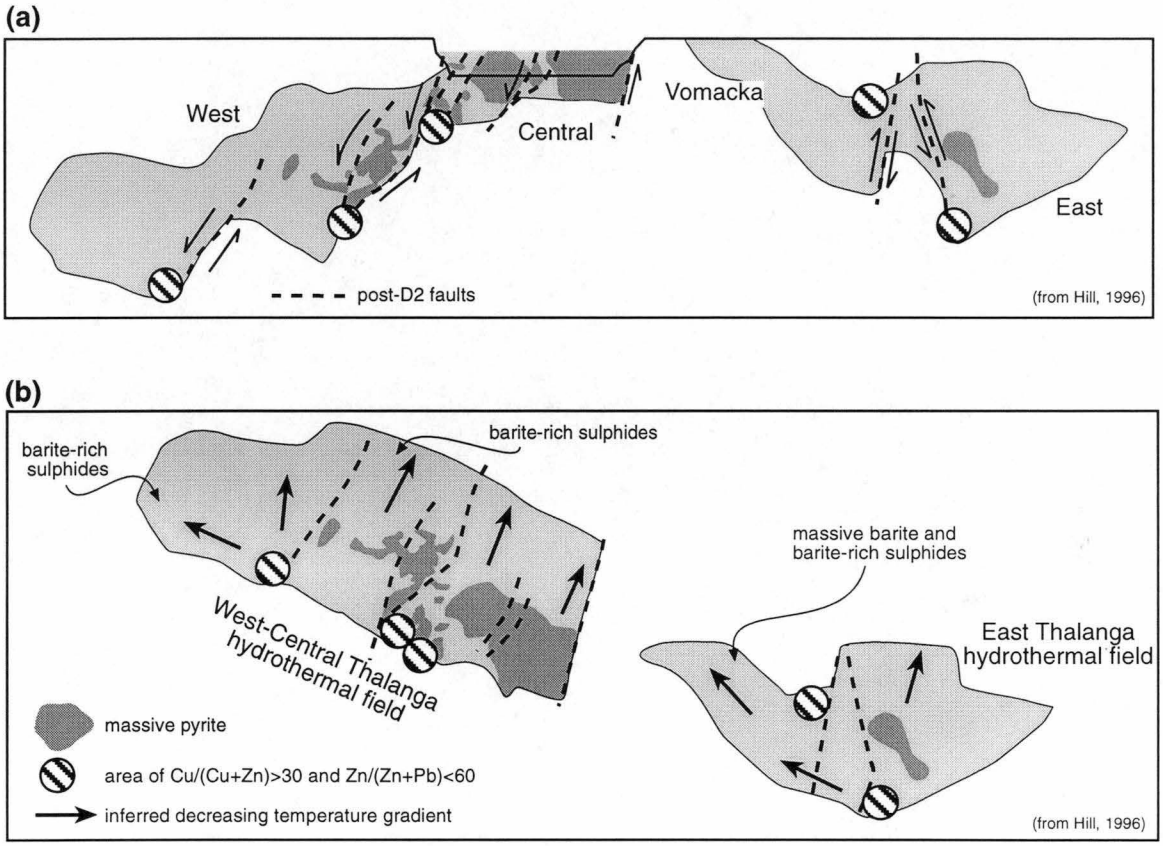
(a)
West
Central
Vomacka
East
post-D2 faults
(from Hill, 1996)
(b)
barite-rich sulphides
barite-rich sulphides
West-Central Thalanga hydrothermal field
massive barite and barite-rich sulphides
East Thalanga hydrothermal field
massive pyrite
area of Cu/(Cu+Zn)>30 and Zn/(Zn+Pb)<60
inferred decreasing temperature gradient
(from Hill, 1996)

Fig. 9.3

In contrast, VHMS deposits of the Cu-Zn type are generally underlain by alteration zones which lack intense silicification, and consist of a chloritic core and a sericitic outer zone (Franklin et al., 1981). Detailed geochemical studies on footwall alteration zones of Cu-Zn massive sulphide deposits in the Noranda mining camp have shown that Si loss is a ubiquitous feature of intense alteration in these systems (Barrett & MacLean, 1994a). The contrasting behaviour of Si in footwall alteration zones of Cu-Zn and Zn-Pb-Cu type VHMS deposits may be controlled by a variety of factors including temperature and composition of the fluids, composition of the footwall rocks and the physical and chemical conditions that prevailed during hydrothermal activity.

Enrichment in Mg and depletion in Na are prominent geochemical characteristics of footwall alteration at Thalanga, especially in the mottled and quartz-pyrite alteration facies. These are common geochemical features of alteration associated with VHMS deposits and have been interpreted as evidence for a seawater-origin of the mineralising hydrothermal fluids (Schmidt, 1988; Schade et al., 1989; Trägårdh, 1991; Shriver & MacLean, 1993; Barrett & MacLean, 1994a).

The source of metals contained in VHMS deposits has been the subject of debate with alternative scenarios including leaching of metals from the footwall volcanic pile by heated, evolved seawater (eg. Spooner & Fyfe, 1973; Solomon, 1976), direct derivation of metals from a magmatic volatile phase (eg. Urabe & Sato, 1978; Sawkins & Kowalik, 1981) or a process involving mixing of magmatic fluids with seawater-derived fluids (eg. Large, 1992). In general, the 'leaching model' is supported by calculations demonstrating that metals and sulphur required to generate particular massive sulphide deposits could be obtained by seawater convection in footwall rocks (eg. Solomon, 1976; Stolz & Large, 1992). However, other studies have presented evidence supporting a magmatic input in the hydrothermal system, at least for Cu-Au-rich VHMS deposits such as Mount Lyell (Tasmania, Australia; Large et al., 1996).). At Thalanga, the available analytical data are consistent with a seawater origin of the hydrothermal fluids and although plausible, no input of a magmatic fluid phase is required. The metals may have been obtained during interaction with the rhyolitic footwall, however, a detailed investigation of this question was beyond the scope of this study.

9.2.3 Hangingwall alteration: Background seafloor alteration or late stage hydrothermal activity?

Alteration in the hangingwall at Thalanga is weak and feldspar crystals in coherent dacite, volcaniclastic facies and sedimentary facies are preserved. Several distinctive facies of weak alteration (epidote alteration, albite alteration, phyllosilicate alteration and hematite dusting) have been recognised, which are typical of, but not exclusive to, the hangingwall dacites. These alteration facies are considered to be unrelated to the Thalanga mineralising hydrothermal system. Instead, they represent the effects of background seafloor alteration, including diagenetic processes and processes related to low-grade sub-seafloor metamorphism.

Alteration logging has shown that epidote alteration and hematite dusting in the hangingwall dacite show no consistent variations in abundance or intensity with distance from the Favourable Horizon (Fig. 7.5 to 7.7). Furthermore, syn-volcanic intrusions of siliceous footwall rhyolite that post-date the mineralising hydrothermal activity also show these alteration facies locally. These observations indicate that hematite dusting and epidote alteration occurred after hydrothermal activity at Thalanga had ceased, and are possibly related to background seafloor alteration processes characterised by low water/rock ratios. These alteration facies are typically developed in phyllosilicate-poor, siliceous volcanic facies. This facies may have contained Fe^{2+}-rich oxide microcrysts which were oxidised to form hematite, and plagioclase phenocrysts could have provided Ca for epidote formation during circulation of low temperature, oxidising fluids. However, epidote may have also formed during metamorphism, from reactions involving calcite and feldspar. Epidote veins and hematite dusting also occur locally in post-D2 diorite intrusions (section 6; Fig. 7.7b and Appendix) clearly indicating that these alteration facies developed at least in part after regional deformation. Therefore, it is possible that epidote alteration and hematite dusting have formed at several stages during diagenesis, low-grade sub-seafloor metamorphism, regional metamorphism or contact metamorphism.

Variations in the abundances of muscovite, chlorite and biotite in the weak phyllosilicate alteration facies in the hangingwall are broadly correlated with lithofacies composition. The coherent dacite facies may contain $\leq$5 vol.% biotite, muscovite and chlorite whereas volcaniclastic dacite units are often rich (up to ~50 vol.%) in these phyllosilicates indicating that primary composition (abundance of glassy volcanic

fragments?) is an important controlling factor (Fig. 4.2b and Fig. 4.3a). In contrast, there is no correlation between the amount and relative proportions of phyllosilicate minerals in the hangingwall dacite and proximity to the Favourable Horizon. Furthermore, minor (≤3 vol.%) interstitial muscovite ± biotite (± chlorite) are also present in the footwall rhyolite from the outcrop section, ~5 km to the west of the deposit. The low abundance of phyllosilicates, the scarcity of chlorite and biotite, their low X_{Mg} values, and the remoteness from massive sulphides indicate that the formation of these phyllosilicates was unrelated to mineralising hydrothermal activity. Thus, it is inferred that weak phyllosilicate alteration in the hangingwall and in areas of the footwall laterally equivalent to, but significantly removed from, the hydrothermal alteration zone, represents diagenetic alteration probably related to hydration of glass and formation of clay minerals.

Geochemical analyses of samples from drill hole TH382A (Fig. 8.12) show that albite alteration, reflected by Na-enrichment, is prominent in the top part of the dacite type 1 unit but decreases in intensity towards the Favourable Horizon. In fact, the sample closest to the massive sulphides (TH382A-400) has Na_2O and K_2O concentrations characteristic of fresh, modern felsic volcanics. This relationship clearly shows that albite alteration was unrelated to the Thalanga hydrothermal system. Albite is typical of low-grade sub-seafloor metamorphism, forming pseudomorphs of primary feldspar, and is common in altered volcanics of the modern ocean crust (Cann, 1969; Humphris & Thompson, 1978). It is inferred that albite alteration was related to an alteration process characterised by relatively low water/rock ratios and alkali exchange reactions between seawater and dacite in the shallow (? <100 m) sub-seafloor environment shortly after dacite emplacement. Seawater convection through the dacite may have been driven by conductive heat loss of the slowly cooling central parts of lavas or syn-volcanic intrusions.

The most prominent geochemical changes in the hangingwall dacite related to alteration include silicification, widespread Na-enrichment and localised Ca-enrichment associated with epidote alteration. Slightly elevated concentrations of Fe and Mg in the altered hangingwall dacite compared to least-altered equivalents are uncommon and S values are generally below detection limit (<0.01 wt.%). However, some samples of dacite directly overlying massive sulphide locally show somewhat elevated sulphur (≥0.01 wt.%), and base metal values (eg. sample TH382A-400; Fig. 8.12). Minor

occurrences of pyrite and sphalerite have also been noted (eg. TH40, section 1 and TH10, section 4; see Appendix). These features may indicate that weak hydrothermal activity continued locally after emplacement of the hangingwall dacite, generating traces of sulphides in the basal parts of some emplacement units.

9.3 Metamorphism

VHMS deposits may be subjected to various tectonic and metamorphic events after mineralisation. In fact, massive sulphides were widely interpreted as structurally controlled, epigenetic base metal replacement deposits until the 1960s because they commonly occur in deformed and metamorphosed ancient successions (Franklin et al., 1981 and Hodgson, 1993). However, the close association of these deposits with submarine volcanic successions and the recognition of a strong stratigraphic control on sulphide distribution prompted the development of syngenetic models for their genesis. The discovery of active hydrothermal systems, including black smokers discharging sulphide-rich particles, on the modern seafloor in the late 1970s further substantiated the interpretation of a syngenetic origin for ancient VHMS deposits.

VHMS deposits occur in successions of variable metamorphic grade, ranging from sub-greenschist to upper amphibolite facies. Lower greenschist facies metamorphism has affected many VHMS deposits (eg. in Canadian greenstone belts such as the Noranda mining camp) however, some deposits occur in successions affected only by diagenesis (eg. the Kuroko deposits, Japan). VHMS deposits in areas of high metamorphic grade (amphibolite facies) include the Montauban deposit (Grenville Province, Canada; Bernier et al., 1987), the Millenbach deposit (Noranda mining camp, Canada; Riverin & Hodgson, 1980) and the Boliden deposit (Skellefte district, Sweden, Allen et al., 1996b).

The Millenbach deposit (Noranda mining camp, Canada) is located within the amphibolite grade contact metamorphic aureole of a granodiorite pluton. Chlorite-rich alteration zones were recrystallised to cordierite-anthophyllite assemblages with a distinctive spotted appearance ('dalmatianite', Wilson, 1935). These minerals probably formed via a reaction of:

chlorite + quartz = cordierite + anthophyllite + H_2O

at temperatures of 550 to 600 °C (Riverin & Hodgson, 1980).

At Thalanga, cordierite is restricted to biotite-chlorite-rich pelitic hornfels in the contact metamorphic aureole and formed at significantly lower temperatures (~500 °C) probably via a reaction such as:

muscovite + chlorite = cordierite + biotite + quartz + H_2O

(Yardley, 1989; Harte & Hudson, 1979). The general paucity of cordierite in the Thalanga sequence is consistent with peak metamorphic temperatures of 450 to ~500 °C indicated by garnet-biotite and garnet-chlorite thermometry (Chapter 4).

Deposits which experienced metamorphic conditions similar to those at Thalanga (upper greenschist grade) include the Arctic deposit (Alaska, USA; Schmidt, 1988) and the Heath Steel B Zone deposit (Bathurst Mining Camp, Canada; Lentz et al., 1997). The footwall alteration zones of these deposits also contain abundant chlorite, biotite and muscovite that represent recrystallised hydrothermal phyllosilicates.

In general, metamorphic recrystallisation of fine-grained hydrothermal alteration minerals commonly forms coarser-grained assemblages which are readily identifiable in hand specimen. Metamorphic mineral assemblages that develop in alteration zones may differ significantly from adjacent, metamorphosed, least-altered country rock (Hodges & Manojlovic, 1993). Consequently, the mineralogy of metamorphosed successions may reveal the prior existence of particular hydrothermal alteration zones (Galley, 1995). Hodges & Manojlovic (1993) demonstrated that mapping of metamorphic mineral assemblages, in conjunction with appropriate lithogeochemical data, can be used to outline zones of increasing alteration intensity below the strongly metamorphosed Raindrop Lake deposit (Manitoba, Canada).

At Thalanga, biotite-muscovite-chlorite assemblages dominate in the footwall rhyolite. However, marked differences in the abundance of these minerals, their composition, the occurrences of disseminated pyrite and pyrite veins in the footwall alteration zone and the association with massive sulphide clearly indicate that biotite-muscovite-chlorite assemblages below the Thalanga deposit represent the metamorphic equivalents of hydrothermal phyllosilicates in variably altered rhyolite. This reflects the substantial hydratisation of footwall rhyolite and enrichment in Mg, Fe and S during hydrothermal alteration. In contrast, least-altered rhyolite experienced comparatively little geochemical modification during devitrification and diagenetic alteration and

consequently, the mineralogy is dominated by quartz and feldspar.

Most studies of metamorphosed alteration systems associated with VHMS deposits infer that metamorphism was isochemical (eg. Schmidt, 1988; Schade et al., 1989). However, Huston (1993) presented evidence for element mobility during high grade metamorphism (middle amphibolite facies) of the host-rock sequence to the Balcooma deposit (Queensland, Australia). At Thalanga, textural evidence indicates that metamorphism was isochemical on a cm- to mm-scale (Chapter 3). Therefore, geochemical differences between altered rhyolite in the footwall to the Thalanga deposit and least-altered equivalents can be confidently interpreted to be related to pre-metamorphic hydrothermal alteration processes.

9.4 Summary: Controls on mineralising processes at Thalanga

The Thalanga massive sulphide deposit occurs within the proximal facies association of a felsic submarine dome and lava complex which was elevated up to 500 m above the surrounding area. The sedimentary facies associations and considerations concerning the controls of water depth on massive sulphide genesis suggest that the Thalanga deposit formed in a deep-water setting (>1,000 m water depth). Mineralisation occurred during a period of relative volcanic quiescence at the waning stage of rhyolitic volcanism. The rhyolitic magma chamber that fed the thick and laterally extensive footwall rhyolite may have provided the heat required to sustain the hydrothermal activity.

The general Mg-rich character of the footwall alteration zone indicates that hydrothermal activity was dominated by evolved, seawater-derived hydrothermal fluids. However, hydrothermal alteration produced a complex, compositionally diverse footwall alteration zone. Carbonate-chlorite alteration was generated locally in the near-seafloor environment by mixing of low-temperature hydrothermal fluids with ambient seawater. Phyllosilicate-dominated alteration was the result of diffuse upwelling of acidic hydrothermal fluids which caused feldspar-destruction, precipitation of pyrite and formation of hydrothermal phyllosilicates in a zone which measures at least 3,000 m (strike extent) x 1,000 m (down-dip extent) x 300 m (stratigraphic thickness). More focussed and hotter hydrothermal discharge generated discordant zones of quartz-pyrite alteration feeding two separate mineralising hydrothermal fields. Mineralising

hydrothermal activity was associated with a fluid of distinctive composition which is reflected in the Si-, Fe- and S-rich composition of the quartz-pyrite alteration facies.

10 Conclusions

The Thalanga VHMS deposit formed on top of an elevated, felsic lava-dominated volcanic complex in a deep, submarine environment. Mineralisation was the result of hydrothermal activity which generated a compositionally diverse alteration zone in the footwall rhyolites below the massive sulphides prior to the emplacement of the hangingwall dacites. The geochemical evidence indicates that hydrothermal activity was mainly associated with evolved, seawater-derived, acidic hydrothermal fluids. The association of massive sulphides and the proximal facies association of a felsic, lava-dominated submarine volcanic centre suggests a link between magmatic processes and hydrothermal activity. It is possible that the magma chambers feeding the voluminous effusive rhyolite eruptions at Thalanga may have also provided the heat required to sustain a vigorous hydrothermal system. In the following, the principal conclusions related to the aims of this study are summarised (section 1.1).

Conditions of regional and contact metamorphism:

- The Thalanga sequence has been affected by isochemical upper greenschist facies metamorphism during regional deformation (D2) and contact metamorphism associated with the emplacement of a post-D2 diorite pluton to the east of the deposit;
- peak conditions during regional metamorphism were in the range of 480 to 500 °C and ≤3.5 kbar;
- contact metamorphism occurred under pressure conditions of 3 to 3.5 kbar and temperatures reached 500 to 530 °C in a ~1,200 m wide contact metamorphic aureole;
- temperatures reached up to 750 °C in the immediate contact zone with the diorite pluton;
- no significant uplift occurred between regional metamorphism and contact metamorphism.

Reconstruction of the volcanic facies architecture:

- Several types of rhyolite and dacite can be distinguished based on consistent differences in the mineralogy, abundance and size range of phenocrysts;
- the altered rhyolitic footwall to the massive sulphides consists dominantly of coherent facies in which apparent clastic textures due to domainal and/or multi-stage hydrothermal alteration processes are common;
- previously unrecognised palaeo-seafloor positions in the footwall are marked by mass-flow-emplaced volcaniclastic units;
- the Thalanga mine area was a topographic high during massive sulphide formation, rising up to 500 m above the surrounding seafloor;
- mineralisation occurred preferentially in localised, shallow depressions on top of the rhyolitic ridge/plateau and was largely synchronous with emplacement of Quartz-Eye Volcaniclastic units (facies F) in the Favourable Horizon;
- minor rhyolitic volcanism continued after intense hydrothermal activity had ceased;
- the Thalanga mine area remained a centre of effusive volcanic activity after mineralisation;
- lavas of dacite type 1 are restricted to East Thalanga whereas dacite type 2 lavas occur in West Thalanga; this distribution of particular dacite types is reflected in the systematic changes in the composition of polymictic breccia units in the hangingwall along strike;
- a modern analogue for the Thalanga deposit is represented by the PACMANUS hydrothermal field which is located at 1,600 m below sea level on top of a dacitic ridge rising 400 to 600 m above the seafloor in the Manus basin (Papua New Guinea).

Alteration at Thalanga:

- Ten different alteration facies can be distinguished at Thalanga based on mineralogical characteristics;
- moderate to intense alteration is restricted to the footwall alteration zone (mottled alteration facies, quartz-pyrite alteration facies, chlorite-pyrite alteration facies, quartz-K-feldspar alteration facies, disseminated tremolite alteration facies and carbonate-chlorite-tremolite alteration facies) and related to hydrothermal activity associated with mineralisation;
- the broad, laterally continuous footwall alteration zone below the massive sulphides is dominated by the mottled alteration facies which formed by hydrothermal alteration processes including feldspar-destruction, formation of hydrothermal phyllosilicates and precipitation of pyrite;
- the pathways of mineralising fluids, marked by discordant zones of quartz-pyrite alteration facies, developed independently of the volcanic facies arrangement in the footwall;
- the hangingwall dacites are typically weakly altered (epidote alteration, phyllosilicate alteration, hematite dusting and albite alteration), due to diagenetic alteration and low-grade sub-seafloor metamorphism.

Constraints on primary geochemistry of Thalanga volcanic units:

- The geochemical compositions of Thalanga volcanic units have been strongly modified due to alteration;
- high-field strength elements were immobile during alteration and ratios such as Ti/Zr and Ti/Th can be used to discriminate some of the petrographically distinctive volcanic rock types;
- the immobile element and REE data of volcanic units from the TCF and the MWF at Thalanga are similar to the compositional characteristics of these formations from other parts of the Mount Windsor Subprovince;

- the data from the Thalanga volcanic units are consistent with the inferred emplacement of the volcano-sedimentary succession of the Seventy Mile Range Group in a continental back-arc basin (Stolz, 1995).

Geochemical modifications associated with alteration:

- Hydrothermal alteration caused substantial gains of magnesium, iron and sulphur and loss of sodium in the footwall rhyolite below the Thalanga deposit;
- Substantial silica was added to quartz-pyrite alteration facies and silicification also occurred locally on the fringes of the hydrothermal system (quartz-K-felspar alteration facies);
- potassium was conserved or added during hydrothermal alteration;
- the concentrations of trace elements such as Ba, Rb, Sr, As and Bi vary according to mineralogical differences among alteration facies in the footwall (ie. abundances of barite, muscovite, alkali feldspar, plagioclase, epidote, tremolite and pyrite).
- LREE and Eu were mobile during hydrothermal alteration;
- several geochemical features of the footwall alteration zone show systematic changes with distance from ore; prospect-scale proximity indicators include: Na_2O loss and increases in MgO, S, Alteration Index, Carbonate-Chlorite-Pyrite Index; Rb/Sr ratio, Mo, Bi, As and increasing X_{Mg} of chlorite and biotite; mine-scale proximity indicators include: increases in Carbonate-Chlorite-Pyrite Index; Ba, Tl and X_{Mg} of chlorite and biotite;
- weak alteration of the hangingwall dacites is characterised by mobility of Si, Na-enrichment (albite alteration) and Ca-enrichment (epidote alteration);
- rare occurrences of sulphides in the basal parts of the hangingwall dacite are probably related to localised, late-stage hydrothermal activity.

References

Aitchinson, J. (1984) The statistical analysis of geochemical compositions. Journal of Mathematical Geology, *16*, 531-564.

Allen, R.L. (1988) False pyroclastic textures in altered silicic lavas, with implications for volcanic-associated mineralization. Economic Geology, *83*, 1424-1446.

Allen, R.L. (1992) Reconstruction of the tectonic, volcanic, and sedimentary setting of strongly deformed Zn-Cu massive sulfide deposits at Benambra, Victoria. Economic Geology, *87*, 825-851.

Allen, R.L. (1994) Synvolcanic, subseafloor replacement model for Rosebery and other massive sulphide ores. Geological Society of Australia, Tasmania Division, Contentious Issues in Tasmanian Geology Symposium, Hobart, Australia, Abstracts No. *39*, 107-108.

Allen, R.L. (1997) Rosebery alteration study and regional alteration studies in the Mount Read Volcanics: The record of diagenetic alteration in the strongly deformed, felsic volcaniclastic succession enclosing the Rosebery and Hercules massive sulphide deposits. In: Studies of VHMS-related alteration: Geochemical and mineralogical vectors to ore. AMIRA Project P439, Report *5*, CODES University of Tasmania, 135-147.

Allen, R.L. and Cas, R.F.A. (1990) The Rosebery controversy: Distinguishing prospective submarine ignimbrite-like units from true subaerial ignimbrites in the Rosebery-Hercules ZnCuPb massive sulphide district, Tasmania. Geological Society of Australia Abstracts, *25*, 31-32.

Allen, R.L., Lundström, I., Ripa, M., Simeonov, A. and Christofferson, H. (1996a) Facies analysis of 1.9 Ga, continental margin, back-arc, felsic caldera province with diverse Zn-Pb-Ag-(Cu-Au) sulfide and Fe oxide deposits, Bergslagen Region, Sweden. Economic Geology, *91*, 979-1008.

Allen, R.L., Weihed, P. and Svenson, S.-Å. (1996b) Setting of Zn-Cu-Au-Ag massive sulfide deposits in the evolution and facies architecture of a 1.9 Ga marine volcanic arc, Skellefte District, Sweden. Economic Geology, *91*, 1022-1053.

Alt, J.C. and Jiang, W.T. (1991) Hydrothermally precipitated mixed-layer illite-smectite in recent massive sulfide deposits from the sea-floor. Geology, *19*, 570-573.

Arth, J.G. and Barker, F. (1976) Rare earth partitioning between hornblende and dacitic liquid and implications for the genesis of trondhjemite-tonalite magmas. Geology, *4*, 534-536.

Barrie, C.T., Ludden, J.N. and Green, T.H. (1993) Geochemistry of volcanic rocks associated with Cu-Zn and Ni-Cu deposits in the Abitibi Subprovince. Economic Geology, *88*, 1341-1358.

Barrett, T.J., Cattalani, S. and MacLean, W.H. (1993) Volcanic lithogeochemistry and alteration at the Delbridge massive sulfide deposit, Noranda, Quebec. Journal of Exploration Geochemistry, *48*, 135-173.

Barrett T.J. and MacLean, W.H. (1994a) Mass changes in hydrothermal alteration zones associated with VMS deposits of the Noranda area. Exploration Mining Geology, *3*, 131-160.

Barrett, T.J. and MacLean, W.H. (1994b) Chemostratigraphy and hydrothermal alteration in exploration for VHMS deposits in Greenstones and younger volcanic rocks. In: Lentz, D.R. (ed.) Alteration and alteration processes associated with ore-forming systems, Short Course Notes, Geological Association of Canada, *11*, 433-467.

Barrett, T.J. and MacLean, W.H. (1997) Volcanic sequences, lithogeochemistry and hydrothermal alteration in some bimodal VMS systems. In: Barrie, C.T. and Hannington, M.D. (eds.) Volcanic-associated massive sulfide deposits, processes and examples in modern and ancient settings, GAC - MDD - SEG short course, 105-133.

Beams, S.D., Laurie, J.P. and O'Neill, D.M. (1990) Reward polymetallic sulphide deposit. In: Hughes, F.E. (ed.) Geology of the mineral deposits of Australia and Papua New Guinea. Australasian Institute of Mining and Metallurgy, Monograph *14*, 1539-1543.

Berman, R.G. (1990) Mixing properties of Ca-Mg-Fe-Mn garnets. American Mineralogist, *75*, 328-344.

Bernier, L., Pouliot, G. and MacLean, W.H. (1987) Geology and Metamorphism of the Montauban North Gold Zone: A metamorphosed polymetallic exhalative deposit, Grenville Province, Quebec. Economic Geology, *82*, 2076-2090.

Berry, R.F., Huston, D.L., Stolz, A.J., Hill, A.P., Beams, S.D., Kuronen, U. and Taube, A. (1992) Stratigraphy, structure and volcanic hosted mineralisation of the Mt. Windsor Subprovince, North Queensland, Australia. Economic Geology, *87*, 739-763.

Bhattacharya, A., Mohanty, L., Maji, A., Sen, S.K. and Raith, M. (1992) Non-ideal mixing in the phlogopite-annite binary: Constraints from experimental data on Mg-Fe partitioning and a reformulation of the biotite-garnet geothermometer. Contributions to Mineralogy and Petrology, *111*, 87-93.

Binns, R.A. and Scott, S.D. (1993) Actively forming polymetallic sulfide deposits associated with felsic volcanic rocks in the eastern Manus back-arc basin, Papua New Guinea. Economic Geology, *88*, 2226-2236.

Black, L.P., Seymour, D.B., Corbett, K.D., Cox, S.E., Streit, J.E., Bottrill, C.R., Calver, C.R., Everard, J.L., Green, G.R., McCenaghan, M.P., Pemberton, J., Taheri, J. and Turner, N.J. (1997) Dating Tasmania's oldest geological events. Australian Geological Service Organisation, Record 1997/15, 1-63.

Boynton, W.V. (1984) Geochemistry of the rare earth elements: meteorite studies. In: Henderson, P. (ed.) Rare earth element geochemistry. Elsevier, Amsterdam, 63-114.

Brauhart, C.W. and Groves, D.I. (1998) Regional alteration systems associated with volcanogenic massive sulfide mineralization at Panorama, Pilbara, Western Australia. Economic Geology, *93*, 292-302.

Burnham, C.W. (1997) Magmas and hydrothermal fluids. In: Barnes, H.L. (ed.) Geochemistry of hydrothermal ore deposits. Wiley, New York, 63-124.

Calvez, J.Y., Cochiere, A. and Oudin, E. (1988) Sr-Nd isotopes and REE signatures of the hydrothermal activity in the Red Sea. Chemical Geology, *70*, 133.

Campbell, I.H., Lesher, C.M., Coad, P., Franklin, J.M., Gorton, M.P. and Thurston, P.C. (1984) Rare-earth element mobility in alteration pipes below massive Cu-Zn-sulfide deposits. Chemical Geology, *45*, 182-202.

Cann, J.R. (1969) Spilites from the Carlsberg Ridge, Indian Ocean. Journal of Petrology, *20*, 244-267.

Cas, R.A.F. (1978) Silicic lavas in Paleozoic flyschlike deposits in New South Wales, Australia: Behavior of deep subaqueous silicic flows. Geological Society of America Bulletin, *89*, 1708-1714.

Cas, R.A.F. (1992) Submarine volcanism: Eruption styles, products, and relevance to understanding the host-rock successions to volcanic-hosted massive sulfide deposits. Economic Geology, *87*, 511-541.

Cas, R.A.F., Allen, R.L., Bull, S.W., Clifford, B.A. and Wright, J.V. (1990a) Subaqueous, rhyolitic dome-top tuff cones: A model based on the Devonian Bunga Beds, southeastern Australia and a modern analogue. Bulletin of Volcanology, *52*, 159-174.

Cas, R.A.F., Allen, R.L., Yamagishi, H., Ishikawa, Y. and Ohguchi, T. (1990b) Eruptive style, products and setting of Kuroko volcanics, Miocene Green Tuff belt, Japan. Geological Society of Autralia Abstracts, *25*, 34.

Courtois, C. and Treuil, M. (1977) Distribution des terres rares et de quelques éléments en trace dans les sédiments récents des fosses de la mer rouge. Chemical Geology, *20*, 57-72.

Day, R.W., Whitaker, W.G., Murray, C.G., Wilson, I.H. and Grimes, K.G. (1975) Queensland geology, a companion volume to the 1 : 2 500 000 scale geological map, Geological Survey of Queensland.

Deer, W.A., Howie, R.A. and Zussman, J. (1992) An introduction to the rock-forming minerals. Wiley, New York, 1-696.

De Rosen-Spence, A., Provost, G., Dimroth, E., Gochnauer, K. and Owen, V. (1980) Archean subaqueous felsic flows, Rouyn-Noranda, Quebec, Canada, and their Quarternary equivalents. Precambrian Research, *12*, 43-77.

Dickenson, M.P. and Hewitt, D. (1986) A garnet-chlorite geothermometer. Geological Society of America Abstracts with Programs, *18*, 584.

Doucet, P., Mueller, W. and Chartrand, F. (1994) Archean, deep-marine, volcanic eruptive products associated with the Coniagas massive sulfide deposit, Quebec, Canada. Canadian Journal of Earth Sciences, *31*, 1569-1584.

Doyle, M.G. (1997) A Cambro-Ordovician volcanic succession hosting massive sulphide mineralisation: Mount Windsor Subprovince, Queensland. University of Tasmania, Hobart, unpublished PhD thesis, 1-264.

Drummond, S.E. and Ohmoto, H. (1985) Chemical evolution and mineral deposition in boiling hydrothermal systems: Economic Geology, *80*, 126-147.

Dudàs, F., Campbell, I.H. and Gorton, M.P. (1983) Geochemistry of igneous rocks in the Hokoroku District, northern Japan. In: Ohmoto, H. and Skinner, B.J. (eds.) The Kuroko and related volcanogenic massive sulphide deposits. Economic Geology, Monograph *5*, 115-133.

Duffield, W.A. and Dalrymple G.B. (1990) The Taylor Creek Rhyolite of New Mexico: A rapidly emplaced field of lava domes and flows. Bulletin of Volcanology, *52*, 475-487.

Duhig, N.C., Stolz, J., Davidson, G.J. and Large, R.R. (1992) Cambrian microbial and silica gel textures in silica iron exhalites from the Mount Windsor Volcanic Belt, Australia: Their petrography, chemistry, and origin. Economic Geology, *87*, 764-784.

Ferry, J.M. and Spear, F.S. (1978) Experimental calibration of the partitioning of Fe and Mg between biotite and garnet. Contributions to Mineralogy and Petrology, *66*, 113-117.

Fink, J. (1980) Surface folding and viscosity of rhyolite flows. Geology, *8*, 250-254.

Finlow-Bates, T. and Stumpfl, E.F. (1981) The behaviour of so-called immobile elements in hydrothermally altered rocks associated with volcanogenic submarine-exhalative ore deposits. Mineralium Deposita, *16*, 319-328.

Franklin, J.M., Lydon, J.W. and Sangster, D.F. (1981) Volcanic-associated massive sulfide deposits. Economic Geology 75th Anniversary Volume, 485-627.

Galley, A.G. (1993) Characteristics of semiconformable alteration zones associated with volcanogenic massive sulfide districts. Journal of Geochemical Exploration, *48*, 175-200.

Galley, A.G. (1995) Target vectoring using lithogeochemistry: Applications to the exploration for volcanic-hosted massive sulphide deposits. CIM Bulletin, *88*, 15-27.

Galley, A.G., Bailes, A.H. and Kitzler, G. (1993) Geological setting and hydrothermal evolution of the Chisel Lake and North Chisel Zn-Pb-Cu-Ag-Au massive sulfide deposits, Snow Lake, Manitoba. Exploration and Mining Geology, *2*, 271-295.

Gemmell, J.B. and Large, R.R. (1992) Stringer system and alteration zones underlying the Hellyer volcanic-hosted massive sulfide deposit, Tasmania, Australia. Economic Geology, *87*, 620-649.

Ghent, E.D. and Stout, M.Z. (1981) Geobarometry and geothermometry of plagioclase-biotite-garnet-muscovite assemblages. Contributions to Mineralogy and Petrology, *76*, 92-97.

Gibson, H.L., Watkinson, D.H., Watkins, J.J., Labrie, M. and Doiron, G. (1993) Volcanological reconstruction of the Corbret Breccia Pile, and Cu-Zn massive sulphide deposit, Nodanda, Quebec. 1993, *2*, 1-16.

Goodfellow, W.D., Grapes, K., Cameron, B., and Franklin, J.M. (1993) Hydrothermal alteration associated with massive sulfide deposits, Middle Valley, northern Juan de Fuca ridge. The Canadian Mineralogist, *31*, 1025-1060.

Goto, Y. and McPhie, J. (1998) Endogenous growth of a Miocene submarine dacite cryptodome, Rebun Island, Hokkaido, Japan. Journal of Volcanology and Geothermal Research, *84*, 273-286.

Grant, J.A. (1986) The isocon diagram - a simple solution to Gresens' equation for metasomatic alteration. Economic Geology, *81*, 1976-1982.

Gregory, P.W., Hartley, J.S. and Wills, K.J.A. (1990) Thalanga zinc-lead-copper-silver deposit. In: Hughes, F.E. (ed.) Geology of the mineral deposits of Australia and Papua New Guinea, AIMM, Melbourne, 1527-1537.

Gresens, R.L. (1967) Composition-volume relationships of metasomatism. Chemical Geology, *2*, 47-55.

Guber, A.L. and Green, G.R. (1983) Aspects of the sedimentologic and structural development of the eastern Hokuroko district, Japan. Economic Geology Monograph *5*, 71-95.

Halbach, P., Pracejus, B. and Märten, A. (1993) Geology and mineralogy of massive sulfide ores from the Central Okinawa Trough, Japan. Economic Geology, *88*, 2210-2225.

Halley, S.W. and Roberts, R.H. (1997) Henty: A shallow-water gold-rich volcanogenic massive sulfide deposit in western Tasmania. Economic Geology, *92*, 438-447.

Harper, G.D. (1995) Pumpellyite and prehnite associated with epidosite in the Josphine ophiolite - Ca metasomatism during upwelling of hydrothermal fluids at a spreading axis. In: Schiffman, P. and Day, H.W. (eds.) Low-grade metamorphism of mafic rocks, Geological Society of America, *296*, 101-122.

Harte, B. and Hudson, N.F.C. (1979) Pelite facies series and the temperatures and pressures of Dalradian metamorphism in E. Scotland. In: Harris, C.H., Holland, C.H. and Leake, B.E. (eds.) Geological Society of London, Special Publication *8*, 323-337.

Hartley, J.S. (1984) Thalanga - exploration history [abs.]: Seventh Australian Geological Convention, 216-218.

Henderson, P. (1984) General geochemical properties and abundances of rare earth elements. In: Henderson, P. (ed.) Rare earth element geochemistry, developments in geochemistry, Elsevier, Amsterdam, *2*, 1-32.

Henderson, R.A. (1983) Early Ordovician faunas from the Mount Windsor Subprovince, northeastern Queensland. Memoirs of the Association of Australasian Palaeontologists, *1*, 145-175.

Henderson, R.A. (1986) Geology of the Mt Windsor Subprovince - a lower Palaeozoic volcano-sedimentary terrane in the northern Tasman Orogenic Zone. Australian Journal of Earth Science, *33*, 343-364.

Henley, R.W. and Ellis, A.J. (1983) Geothermal systems ancient and modern: A geochemical review. Earth Science Reviews, *19*, 1-50.

Herrmann, W. (1994) Immobile element geochemistry of altered volcanics and exhalites at the Thalanga Deposit, North Queensland. University of Tasmania, Hobart, unpublished M.Econ.Geol. thesis, 1-74.

Herrmann, W. (1995) Geochemical aspects of the Thalanga massive sulphide deposit, Mt Windsor Subprovince: 17. International Geochemical Exploration Symposium. Mineral Deposits of Northeast Queensland: Geology and Geochemistry, 155-170.

Hill, A.P. (1996) Structure, volcanic setting, hydrothermal alteration and genesis of the Thalanga massive sulphide deposit. University of Tasmania, Hobart, unpublished PhD thesis, 1-404.

Hodges, D.J. and Manojlovic, P.M. (1993) Application of lithogeochemistry to exploration for deep VMS deposits in high grade metamorphic rocks, Snow Lake, Manitoba. Journal of Geochemical Exploration, *48*, 201-224.

Hodges, K.V. and Crowley, P.D. (1985) Error estimation and empirical geothermobarometry for pelitic systems. American Mineralogist, *70*, 702-709.

Hodges, K.V. and Spear, F.S. (1992) Geothermometry, geobarometry and the Al_2SiO_5 triple-point at the Mt. Moosilauke, New Hampshire. American Mineralogist, *67*, 1118-1134.

Hodgson, C.J. (1990) Uses (and abuses) of ore deposit models in mineral exploration. Geo-science Canada, *17*, 79-89.

Hodgson, C.J. (1993) Mesothermal lode-gold deposits. In: Kirkham, R.V., Sinclair, W.D., Thorpe, R.I. and Duke, J.M. (eds.) Mineral deposit modeling. Special Paper - Geological Association of Canada, *40*, 635-678.

Hoisch, T.D. (1990) Empirical calibration of six geobarometers for the mineral assemblage quartz+muscovite+biotite+plagioclase+garnet. Contributions to Mineralogy and Petrology, *104*, 225-234.

Holdaway, M.J. (1971) Stability of andalusite and the aluminium silicate phase diagram. American Journal of Science, *271*, 97-131.

Holdaway, M.J., Dutrow, B.L. and Hinton, R.W. (1988) Devonian and Carboniferous meta-morphism in west-central Maine: The muscovite-almandine geobarometer and the staurolite problem revisited. American Mineralogist, *73*, 20-47.

Honnorez, J.J., Alt, J.C. and Humphris, S.E. (1998) Vivisection and autopsy of active and fossil hydrothermal alterations of basalt beneath and within the Tag hydrothermal mound. In: Herzig, P.M., Humphris, S.E. and Zierenberg, R.A. (eds.) Proceedings of the Ocean Drilling Program, Scientific Results, *158*, 231-254.

Horikoshi, E. (1969) Volcanic activity related to the formation of the Kuroko-type deposits in the Kosaka District, Japan. Mineralium Deposita, *4*, 321-345.

Horikoshi, E. (1990) Opening of the Sea of Japan and Kuroko deposit formation. Mineralium Deposita, *25*, 140-145.

Hughes, C.J. (1973) Spilites, keratophyres, and the igneous spectrum. Geological Magazine, *109*, 513-527.

Humphris, S.E. (1984) The mobility of the rare earth elements in the crust. In: Henderson, P. (ed.) Rare earth element geochemistry. Elsevier, Amsterdam, 315-341.

Humphris, S.E. and Thompson, G. (1978) Hydrothermal alteration of oceanic basalts by seawater. Geochimica et Cosmochimica Acta, *42*, 107-125.

Hunns, S.R. and Zaw, K. (1997) Mount Chalmers - a shallow water exhalative VMS deposit. GAC/MAC Annual meeting, Ottawa 1997, Abstract Volume, 70.

Huston, D.L. (1993) The effect of alteration and metamorphism on wall rocks to the Balcooma and Dry River South volcanic-hosted massive sulfide deposits, Queensland, Australia. Journal of Geochemical Exploration, *48*, 277-307.

Huston, D.L. and Large, R.R. (1987) Genetic and exploration significance of the zinc ratio (Zn/(Zn+Cu)) in massive sulfide systems. Economic Geology, *82*, 1521-1539.

Huston, D.L., Kuronen, U. and Stolz, J. (1995) Waterloo and Agincourt prospects, northern Queensland: contrasting styles of mineralization within the same volcanogenic hydro-thermal system. Australian Journal of Earth Science, *42*, 203-221.

Hutchinson, R.W. (1973) Volcanogenic sulfide deposits and their metallogenic significance. Economic Geology, *68*, 1223-1246.

Hutchinson, R.W., Spence, C.D. and Franklin, J.M. (eds.) (1982) Precambrian sulphide deposits. Special Paper - Geological Association of Canada, *25*, 1-791.

Hutton, L.J., Rienks, I.P., Tenison Woods, K.L., Hartley, J.S. and Crouch, S.B.S. (1994) Geology of the Ravenswood Batholith, North Queensland: Department of Minerals and Energy Queensland.

Ikramuddin, M., Asmeron, Y., Nordstrom, P.M., Kinart, K.P., Martin, W.M., Digby, S.J.M., Elder, D.D., Mijak, W.F. and Afemari, A.A. (1983) Thallium: A potential guide to mineral deposits. Journal of Geochemical Exploration, *19*, 465-490.

Iijima, A. (1974) Clay and zeolitic alteration zones surrounding Kuroko deposits in the Hokuroku district, northern Akita, as submarine hydrothermal-diagenetic alteration products. Society of Mining Geologists Japan, Special Issue *6*, 267-289.

Ishikawa, Y. (1983) Volcanic activities and mineralization of the Fukazawa-Ezuri Kuroko deposits area. Akita University, Mining College, Scientific and Technological Report *4*, 23-32.

Ishikawa, Y., Sawaguchi, T., Iwaya, S. and Horiachi, M. (1976) Delineation of prospecting targets for Kuroko deposits based on modes of volcanism of underlying dacite and alteration halos. Mining Geology, *26*, 105-117 (in Japanese with English abstract)

Kano, K., Takeuchi, K., Yamamoto, T. and Hoshizumi, H. (1991) Subaqueous rhyolite block lavas in the Miocene Ushikiri Formation, Shimane Peninsula, SW Japan. Journal of Volcanology and Geothermal Research, *46*, 241-253.

Kay, J.R. (1987) The Highway gold mine, Charters Towers-submarine volcanogenic gold-barite stringer mineralization, modified by laterite weathering. University of Queensland, Department of Geology Paper, *12*, 111-125.

Klau, W. and Large, D.E. (1980) Submarine exhalative Cu-Pb-Zn deposits - a discussion of their classification and metallogenesis. Geologisches Jahrbuch, *40*, 13-58.

Kleemann, U. and Reinhardt, J. (1994) Garnet-biotite thermometry revisited: The effects of AlVI and Ti in biotite. European Journal of Mineralogy, *6*, 925-941.

Kokelaar, B.P. (1982) Fluidization of wet sediments during implacement and cooling of various igneous bodies. Journal of the Geological Society of London, *139*, 21-33.

Laird, J. (1988) Chlorites: Metamorphic petrology. In: Bailey, S.W. (ed.) Hydrous phyllosilicates (exclusive of mica): Mineralogical Society of America, Reviews in Mineralogy *19*, 405-453.

Large, R.R. (1992) Australian volcanic hosted massive sulphide deposits: Features, styles and genetic models. Economic Geology, *87*, 855-872.

Large, R.R. (1996) The Hercules-Mount Read traverse: Relationships between volcanic mineralogy, alteration and geochemistry. In: Pongratz J. (ed.) Studies of VHMS-related alteration: Geochemical and mineralogical vectors to ore, Report *3*, 153-234. Centre for Ore Deposit Research - Special Research Centre, AMIRA project P439, University of Tasmania, Hobart.

Large, R.R., Doyle, M., Raymond, O., Cooke, D., Jones, A. and Heasman, L. (1996) Evaluation of the role of Cambrian granites in the genesis of world class VHMS deposits in Tasmania. Ore Geology Reviews, *10*, 215-230.

Larson, P.B. (1984) Geochemistry of the alteration pipe at the Bruce Cu-Zn volcanogenic massive sulfide deposit, Arizona. Economic Geology, *79*, 1880-1896.

Leat, P.T., Jackson, S.E., Thorpe, R.S. and Stillman, C.J. (1986) Geochemistry of bimodal basalt-subalkaline/peralkaline rhyolite provinces within the Southern British Caledonides. Journal of the Geological Society of London, *143*, 259-273.

Lees, T., Zaw, K., Large, R.R. and Huston, D.L. (1990) Rosebery and Hercules copper-lead-zinc deposits. In: Hughes F.E. (ed.) Geology of the mineral deposits of Australia and Papua New Guinea, AusIMM, 1241-1247.

Leitch, C.H.B. and Lentz, D.R. (1994) The Gresens approach to mass balance constraints of alteration systems: Methods, pitfalls, examples. In: Lentz, D.R. (ed.) Alteration and alteration processes associated with ore-forming systems, Short Course Notes, Geological Association of Canada, *11*, 161-192.

Le Maitre, R.W. (1976) The chemical variability of some common igneous rocks. Journal of Petrology, *17*, 589-637.

Le Maitre, R.W., Bateman, P., Dubek, A., Keller, J., Lameyre, J., Le Bas, M.J., Sabine, M.A., Schmid, R., Sorensen, H., Streckeisen, A., Wooley, A.R. and Zanettin, B. (1989) A classification of igneous rocks and glossary of terms: Recommendations of the International Union of Geological Sciences Subcommisson on the Systematics of Igneous rocks, Blackwell Scientific Publications, Oxford, 1-193.

Lentz, D.R. (1998) Petrogenetic evolution of felsic volcanic sequences associated with Phanerozoic volcanic-hosted massive sulphide systems: The role of extensional geodynamics. Ore Geology Reviews, *12*, 289-327.

Lentz, D.R. and Goodfellow, W.D. (1992) Re-evaluation of the petrochemistry of felsic volcanics and volcaniclastic rocks near the Brunswick No. 6 and 12 massive sulphide deposits, Bathurst Mining camp, New Brunswick. In: Current research, Part E, Geological Survey of Canada, Paper 92-1E, 340-350.

Lentz, D.R. and Goodfellow, W.D. (1996) Intense silicification of footwall sedimentary rocks in the stockwork alteration zone beneath the Brunswick No. 12 massive sulphide deposit, Bathurst, New Brunswick. Canadian Journal of Earth Sciences, *33*, 284 - 302.

Lentz, D.R., Hall, D.C. and Hoy, L.D. (1997) Chemostratigraphy, alteration, and oxygen isotopic trends in a profile through the stratigraphic sequence hosting the Heath Steele B zone massive sulfide deposit, New Brunswick. The Canadian Mineralogist, *35*, 841-874.

Lentz, D.R., Walker, J. and McCutcheon, S.R. (1999) Pyroclastic volcanism and VMS deposit genesis: Resolving the depth dilema. GAC-MAC Joint Annual Meeting Sudbury 1999, Abstract Volume *24*, 69-70.

Lesher, C.M., Goodwin, A.M., Campell, I.H. and Gorton, M.P. (1986) Trace-element geochemistry of ore-associated and barren, felsic metavolcanic rocks in the Superior Province, Canada. Canadian Journal of Earth Sciences, *23*, 222-237.

Lipman, P. W. (1965) Chemical comparison of glassy and crystalline rocks. Bulletin of the United States Geological Survey, No. 1201-D, 1-24.

Lofgren, G. (1971) Experimentally produced devitrification textures in natural rhyolitic glasses. Geological Society of America Bulletin, *82*, 111-124.

Ludden, J.N. and Thompson, G. (1979) An evaluation of the behaviour of the rare earth elements during weathering of sea-floor basalt. Earth and Planetary Science Letters, *43*, 85-92.

Lydon, J.W. (1988) Volcanogenic massive sulphide deposits, part 1 a descriptive model. In: Roberts, R.G. and Sheahan, P.A. (eds.) Ore deposit models, Geoscience Canada Reprint Series *3*, 145-154.

MacGeehan, P.J. and MacLean, W.H. (1980) Tholeiitic basalt-rhyolite magmatism and massive sulphide deposits at Matagami, Quebec. Nature, *283*, 153-157.

MacLean, W.H. (1988) Rare earth element mobility at constant inter-REE ratios in the alteration zone at the Phleps Dodge massive sulphide deposit, Matagami, Quebec. Mineralium Deposita, *23*, 231-238.

MacLean, W.H. (1990) Mass change calculations in altered rock series. Mineralium Deposita, *25*, 44-49.

MacLean, W.H. and Barrett, T.J. (1993) Lithogeochemical techniques using immobile elements. Journal of Geochemical Exploration, *48*, 109-133.

MacLean, W.H. and Kranidiotis, P. (1987) Immobile elements as monitors of mass transfer in hydrothermal alteration: Phleps Dodge massive sulfide deposit, Matagami, Quebec. Economic Geology, *82*, 951-962.

Madeisky, H.E. and Stanley, C.R. (1993) Lithogeochemical exploration of metasomatic zones associated with volcanic-hosted massive sulfide deposits using Pearch Element Ratio Analysis. International Geology Review, *35*, 1121-1148.

Marani, M.P., Gamberi, F. and Savelli, C. (1997) Shallow-water polymetallic sulfide deposits in the Aeloian island arc. Geology, *25*, 815-818

Matsukuma, T. and Horikoshi, E. (1970) Kuroko deposits in Japan: A review. In: Tatsumi, T. (ed.), Volcanism and ore genesis, University of Tokyo Press, Tokyo, 153-179.

McBirney, A.R. (1963) Factors governing the nature of submarine volcanism. Bulletin of Volcanology, *26*, 455-469.

McBirney, A.R. and Murase, T. (1984) Rheological properties of magmas. Annual Reviews in Earth and Planetary Science, *12*, 377-357.

McGoldrick, P.J. and Large, R.R. (1992) Geologic and geochemical controls on gold-rich stringer mineralization in the Que River deposit, Tasmania. Economic Geology, *87*, 667-685.

McPhie, J. and Allen, R.L. (1992) Facies architecture of mineralized submarine volcanic sequences: Cambrian Mount Read Volcanics, Western Tasmania. Economic Geology, *87*, 587-596.

McPhie, J., Doyle, M. and Allen, R. (1993) Volcanic Textures. A guide to the interpretation of textures in volcanic rocks. Codes, University of Tasmania, Hobart, 1-198.

Menzies, M., Seyfried, W. and Blanchard, D. (1979) Experimental evidence of rare earth mobility in greenstones. Nature, *282*, 398-399.

Michard, P.J. (1989) Rare earth element systematics in hydrothermal fluids. Geochimica et Cosmochimica Acta, *53*, 745-750.

Miller, C.R. (1996) Geological and geochemical aspects of the Liontown VHMS deposit, NE Queensland. University of Tasmania, Hobart, unpublished M.Econ.Geol. thesis, 1-90.

Möller, P., Dieterle, M.A., Dulski, P., German, K., Schneider, H.J. and Schütz, W. (1983) Geochemical proximity indicators of massive sulphide mineralization in the Iberian Pyrite Belt and the East Pontic Metallotect. Mineralium Deposita, *18*, 387-398.

Moore, J.G. (1965) Petrology of deep-sea basalt near Hawaii. American Journal of Science, *263*, 40-52.

Morton, R.L. and Franklin, J.M. (1987) Two-fold classification of Archean volcanic-associated massive sulfide deposits. Economic Geology, *82*, 1057-1063.

Morton, R.L., Walker, J.S., Hudak, G.J. and Franklin, J.M. (1991) The early development of an Archean submarine caldera complex with emphasis on the Mattabi ash-flow tuff and its relationship to the Mattabi massive sulfide deposit. Economic Geology, *86*, 1002-1011.

Mosier, D.L., Singer, D.A. and Salem, B.B. (1983) Geologic and grade-tonnage information on volcanic-hosted copper-zinc-lead massive sulfide deposits. United States Geological Survey Open File Report, *83-89*, 1-77.

Mulholland, I.R. (1991) The geology, petrology and alteration geochemistry of the Magpie volcanogenic massive sulfide deposit, north Queensland, Australia. Economic Geology, *86*, 1387-1400.

Murase, T. and McBirney, A.R. (1973) Properties of some common igneous rocks and their melts at high temperatures. Geological Society of America Bulletin, *84*, 3563-3592.

Norman, M.B. (1974) Improved techniques for selective staining of feldspar and other minerals using amaranth. Journal of Research of the U.S. Geological Survey, *2*, 73-79.

Ohmoto, H. and Skinner (eds.) (1993) The Kuroko and related volcanogenic massive sulfide deposits. Economic Geology Monograph *5*, 1-604.

Ohmoto, H. and Takahashi, T. (1983) Geological setting of the Koroko deposits, Japan: Part III. Submarine calderas and Kuroko genesis. Economic Geology Monograph *5*, 39 54.

Orth, K. and Hill, A.P. (1994) Textures and origins of carbonate associated with the Rosebery VHMS deposit. Geological Society of Australia, Tasmania Division, Contentious Issues in Tasmanian Geology Symposium, Hobart, Australia, Abstracts No. *39*, 105.

Paulick H. (1997) Volcanic facies analysis, alteration, and geochemistry of the host rock sequence to VHMS-style mineralisation at Thalanga (north Queensland). In: Pongratz J. (ed.) Studies of VHMS-related alteration: Geochemical and mineralogical vectors to ore, Report *4*, 185-223. Centre for Ore Deposit Research - Special Research Centre, AMIRA project P439, University of Tasmania, Hobart.

Paulick, H., McPhie, J. (1999) Facies architecture of the felsic lava-dominated host sequence to the Thalanga massive sulfide deposit, Lower Ordovician, northern Queensland. Australian Journal of Earth Sciences, *46*, 391-405.

Pearce, J.A. (1982) Trace element characteristics of lavas from destructive plate boundaries. In: Thorpe, R.S. (ed.) Andesites: Orogenic andesites and related rocks. Wiley, New York, 525-548.

Pearce, J.A. (1983) Role of sub-continental lithosphere in magma genesis at active continental margins. In: Hawkesworth, C.J. and Norry, M.J. (eds.) Continental basalts and mantle xenoliths, Shiva, Nantwich, 230-249.

Pearce, A.J. and Cann, J.R. (1973) Tectonic setting of basic volcanic rocks determined using trace element analysis. Earth and Planetary Science Letter, *19*, 290-300.

Peckover, R.S., Buchanan, D.J. and Ashby, D.E. (1973) Fuel-coolant interaction in submarine volcanism. Nature, *245*, 307-308.

Perkins C., McDougall, I. and Walshe, J. L. (1993) Isotopic dating of precious and base metal deposits and their host rocks in Eastern Australia, Final report. Research School of Earth Science, AMIRA project P334, Australian National University, Canberra.

Perchuk, L.L. and Lavrent'eva, I.V. (1983) Experimental investigation of exchange equilibria in the system cordierite-garnet-biotite. In: Saxena, S.K. (ed.) Kinetics and equilibrium in mineral reactions, Springer Verlag, New York, 199-240.

Peter, J.M. and Goodfellow, W.D. (1996) Mineralogy, bulk and rare earth element geochemistry of massive sulfide-associated hydrothermal sediments of the Brunswick Horizon, Bathurst Mining Camp, New Brunswick. Canadian Journal of Earth Sciences, *33*, 252-283.

Pichler, H. (1965) Acid hyaloclastites. Bulletin Volcanologique, *28*, 293-310.

Powell, R. and Holland, T.J.B. (1988) An internally consistent thermodynamic dataset with uncertainties and correlations: 3. Applications to geobarometry, worked examples and computer program. Journal of Metamorphic Geology, *6*, 173-204.

Reed, M.H. (1997) Hydrothermal alteration and its relationship to ore fluid composition. In: Barnes, H.L. (ed.) Geochemistry of hydrothermal ore deposits. Wiley, New York, 303-358.

Ridley, W.I., Perfit, M.R., Jonasson, I.R. and Smith, M.F. (1994) Hydrothermal alteration in oceanic ridge volcanics: A detailed study at the Galapagos fossil hydrothermal system. Geochimica Cosmochimica Acta, *58*, 2477-2494.

Riverin, G. and Hodgson, C.J. (1980) Wall-rock alteration at the Millenbach Cu-Zn Mine, Noranda, Quebec. Economic Geology, *75*, 424-444.

Robinson, P., Townsend, A.T., Zongshou, Y. and Münker, C. (1999) Determination of scandium, yttrium and rare earth elements in rocks by high resolution inductively coupled plasma-mass spectrometry. Geostandards Newsletter (in press)

Rollinson, H.R. (1993) Using geochemical data: Evaluation, presentation, interpretation. Wiley, New York, 1-352.

Rona, P.A. and Scott, S.D. (1993) A special issue on sea-floor hydrothermal mineralization: New perspectives - preface. Economic Geology, *88*, 1935-1976.

Sainty, R.A. (1992) Shallow-water stratigraphy at the Mount Chalmers volcanic-hosted massive sulfide deposit, Queensland, Australia. Economic Geology, *87*, 812-824.

Sampson, D.E. (1987) Textural heterogeneities and vent area structures in the 600-year-old lavas of the Inyo volcanic chain, eastern California. In: Fink, J.H. (ed.) The emplacement of silicic domes and lava flows, Special Paper *212*, Boulder, Colorado, Geological Society of America, 89-101.

Sato, T., Tanimura, S. and Ohtagaki, T. (1974) Geology and ore deposits of the Hokuroko district, Akita Prefecture. Society of Mining Geologists Japan, Special Issue *6*, 11018.

Saunders, A.D. and Tarney, J. (1984) Geochemical characteristics of basaltic volcanism within back-arc basins. In: Kokelaar, B.P. and Howells, M.F. (eds.) Marginal basin geology, Geological Society of London, Special Publication *16*, 56-76.

Sawkins, F.J. (1976) Massive sulphide deposits in relation to geotectonics. In: Strong, D.F. (ed.) Metallogeny and plate tectonics, Geological Association of Canada, Special Paper *14*, 221-240.

Sawkins, F.J. and Kowalik, J. (1981) The source of ore metals at Buchans: Magmatic versus leaching models. Geological Association of Canada, Special Paper *22*, 255-267.

Schade, J., Cornell, D.H. and Theart, H.F.J. (1989) Rare earth elements and isotopic evidence for the genesis of the Prieska massive sulfide deposit, South Africa. Economic Geology, *84*, 49-63.

Schandl, E.S., Gorton, M.P. and Wasteneys, H.A. (1995) Rare earth element geochemistry of the metamorphosed volcanogenic massive sulfide deposits of the Manitouwadge Mining Camp, Superior Province, Canada: A potential exploration tool?. Economic Geology, *90*, 1217-1236.

Seyfried, W.E., Berndt, M.E. and Seewald, J.S. (1988) Hydrothermal alteration processes at mid-ocean ridges: constraints from diabase alteration experiments, hot-spring fluids and composition of the oceanic crust. In: Martin, R.F. (ed.) Seafloor hydrothermal mineralization. Canadian Mineralogist, *26*, 787-804.

Seyfried, W.E. and Ding, K. (1995) The hydrothermal chemistry of fluoride in seawater. Geochimica et Cosmochimica Acta, 59, 1063-1071.

Schiffman, P., Bettison, L.A. and Smith, B.M. (1990) Mineralogy and geochemistry of epidosites from the Solea Graben, Troodos Ophiolite, Cyprus. In: Malpas, J., Moores, E.M., Panayiotou, A. and Xenophontos, C. (eds.) Ophiolites; oceanic crustal analogues; proceedings of the symposium "Troodos 1987". Ministery for Agriculture and Natural Resources, Nicosia, Cyprus, 673-683.

Schmidt, J.M. (1988) Mineral and whole-rock compositions of seawater-dominated hydrothermal alteration at the Arctic volcanogenic massive sulfide prospect, Alaska. Economic Geology, *83*, 822-842.

Schradt, C., Cooke, D.R., Gemmell, J.B. and Large, R.R. (1999) Geochemical modelling of the footwall alteration assemblages, Hellyer VHMS deposit, western Tasmania, Australia. GAC-MAC Joint Annual Meeting, Sudbury 1999, Abstract Volume *24*, 110.

Scott, S.D. (1997) Submarine hydrothermal systems and deposits. In: Barnes, H.L. (ed.) Geochemistry of hydrothermal ore deposits, Wiley, New York, 797-877.

Seaman, S.J, Scherer, E.E. and Standish, J.J. (1995) Multistage magma mingling and the origin of flow banding in the Aliso lava dome, Tumacacori Mountains, southern Arizona. Journal of Geophysical Research, B, Solid Earth and Planets, *100*, 8381-8398.

Shikazono, N., Hoshino, M., Utada, M., Nakata, M. and Ueda, A. (1998) Hydrothermal carbonates in altered wall rocks at the Uwamuki Kuroko deposits, Japan. Mineralium Deposita, *33*, 346-358.

Shirozo, H. (1974) Clay minerals in altered wall rocks of the Kuroko-type deposits. Society of Mining Geologists Japan, Special Issue *6*, 303-311.

Shriver, N.A. and MacLean, W.H. (1993) Mass, volume and chemical changes in the alteration zone at the Norbec mine, Noranda, Quebec. Mineralium Deposita, *28*, 157-166.

Sillitoe, R.H. (1973) Environments of formation of volcanogenic massive sulfide deposits. Economic Geology, *68*, 1321-1325.

Sillitoe, R.H. (1982) Extensional habitats of rhyolite-hosted massive sulphide deposits. Geology, *109*, 403-407.

Sisson, T.W. (1994) Hornblende-melt trace-element partitioning measured by ion microprobe. Chemical Geology, *117*, 331-344.

Slaughter, J., Kerrick, D.M. and Wall, V.J. (1975) Experimental and thermodynamic study of equilibria in the system CaO-MgO-SiO_2-H_2O-CO_2. American Journal of Science, *275*, 143-162.

Solomon, M. (1976) "Volcanic" massive sulphide deposits and their host rocks-a review and an explanation. In: Wolf, K.H. (ed.) Handbook of stratabound and stratiform ore deposits, Elsevier, Amsterdam, *2*, 21-50.

Smith, R.L. (1960) Zones and zonal variations in welded ash flows. US Professional Paper *354F*, 149-159.

Spear, F.S. (1993) Metamorphic phase equilibria and pressure-temperature-time paths, Mineralogical Society of America, Monograph, 1-788.

Spear, F.S. and Kohn, M.J. (1998) Program Thermobarometry, Version 2.1. November, 1998.

Spooner, E.T.C. and Fyfe, W.S. (1973) Sub-sea floor metamorphism, heat and mass transfer. Contributions to Mineralogy and Petrology, *42*, 287-304.

Stolz, A.J. (1995) Geochemistry of the Mount Windsor Volcanics: Implications for the tectonic setting of Cambro-Ordovician volcanic-hosted massive sulfide mineralization in northeastern Australia. Economic Geology, *90*, 1080-1097.

Stolz, A.J. and Large, R.R. (1992) Evaluation of the source-rock control on precious metal grades in volcanic-hosted massive sulfide deposits from western Tasmania. Economic Geology, *87*, 720-738.

Swinden, H.S. (1991) Paleotectonic settings of volcanogenic massive sulphide deposits in the Dunnage Zone, Newfoundland Appalachians. Canadian Mining and Metallurgical Bulletin, *84*, 59-69.

Syme, E.C. and Bailes, A.H. (1993) Stratigraphy and tectonic setting of Early Proterozoic volcanogenic massive sulphide deposits, Flin Flon, Manitoba. Economic Geology, *88*, 566-589.

Takahashi, T. and Suga, K. (1974) Geology and ore deposits of the Hanaoka Kuroko belt, Akita Prefecture. Society of Mining Geologists Japan, Special Issue *6*, 101-114.

Taylor, S.R. and McLennan, S.M. (1985) The continental crust: Its composition and evolution. Blackwell, Oxford, 1-312.

Thompson, A.J.B. and Thompson, J.F.H. (1996) Atlas of alteration - a field and petrographic guide to hydrothermal alteration minerals. Mineral Deposits Devision, Geological Association of Canada, 1-119.

Trägårdh, J. (1991) Metamorphism of magnesium-altered felsic volcanic rocks from Bergslagen, central Sweden: A transition from Mg-chlorite- to cordierite-rich rocks. Ore Geology Reviews, *6*, 485-497.

Turner, R.J.W., Ames, D.E., Franklin, J.M., Goodfellow, W.D., Leitch, C.H.B. and Höy, T. (1993) Character of active hydrothermal mounds and nearby altered hemipelagic sediments in the hydrothermal areas of Middle Valley, northern Juan de Fuca ridge: Data from shallow cores. The Canadian Mineralogist, *31*, 973-995.

Urabe, T. and Sato, T. (1978) Kuroko deposits of the Kosaka mine, northeast Honshu, Japan-products of submarine hot springs on the Miocene sea floor. Economic Geology, *73*, 161-179.

Vokes, F.M. and Craig, J.R. (1993) Post-recrystallisation mobilisation phenomena in metamorphosed stratabound sulphide ores. Mineralogical Magazine, *57*, 19-28.

Von Damm, K.L., Edmond, J.L., Grant, B., Measures, C.I., Walden, B. and Weiss, R.F. (1985) Chemistry of submarine hydrothermal solutions at 21°N, East Pacific Rise. Geochimica Cosmochimica Acta, *49*, 2221-2237.

Waters, J.C. and Wallace, D.B. (1992) Volcanology and sedimentology of the host succession to the Hellyer and Que River volcanic-hosted massive sulfide deposits, northwestern Tasmania. Economic Geology, *87*, 650-666.

Wedepohl, K.H. (1995) The composition of the continental crust. Geochimica et Cosmochimica Acta, *59*, 1217-1232.

Whitford, D.J., Korsch, M.J., Porritt, P.M. and Craven, S.J. (1988) Rare-earth element mobility around the volcanogenic polymetallic massive sulfide deposit at Que River, Tasmania, Australia. Chemical Geology, *68*, 105-119.

Wills, K.J.A. (1985) Thalanga Comprehensive Study - Final Report. Pennaroya Pty. Ltd. (Australia), No: 1551/10, unpublished company report.

Wilson, L. (1980) Relationships between pressure, volatile content and ejecta velocity in three types of volcanic explosions: Journal of Volcanology and Geothermal Research, *8*, 297-313.

Wilson, M. (1989) Igneous petrogenesis: A global tectonic approach. Chapman & Hall, London, 1-466.

Wilson, M.E. (1935) Rock alteration at the Amulet mine, Noranda district, Quebec. Economic Geology, *30*, 478-492.

Winchester, J.A. and Floyd, P.A. (1977) Geochemical discriminations of different magma series and their differentiation products using immobile elements. Chemical Geology, *20*, 325-343.

Yamagishi, H. (1987) Studies on the Neogene subaqueous lavas and hyaloclastites in southwest Hokkaido. Hokkaido Geological Survey Report *59*, 55-117.

Yamagishi, H. and Dimiroth, E. (1985) A comparison of Miocene and Archean rhyolite hyaloclastites: Evidence for a hot and fluid rhyolite lava. Journal of Volcanology and Geothermal Research, *23*, 337-335.

Yardley, B.W.D. (1989) An introduction to metamorphic petrology. Wiley, New York, 1-248.

Zaleski, E., Froese, E. and Gordon, T.M. (1991) Metamorphic petrology of Fe-Zn-Mg-Al alteration at the Linda volcanogenic massive sulfide deposit, Snow Lake, Manitoba. Canadian mineralogist, *29*, 995-1017.

Zaw, K. and Large, R.R. (1992) The precious metal rich Hercules mineralization, Western Tasmania: A possible sub-seafloor replacement volcanic-hosted massive sulfide deposit. Economic Geology, *87*, 931-952.

A1 Appendix

In this Appendix, geochemical analyses are tabulated including bulk rock and microprobe data. Relevant information concerning analytical procedures are given below Graphic logs for drill holes from section 1 to 6 and geological interpretations of these sections are located in the back pocket of the thesis. Drill hole logs illustrate the lithofacies and alteration facies, provide estimates for mineral abundances, and describe textural observations.

A1.1 Bulk rock geochemistry

Bulk rock geochemical data of 184 samples were obtained during this study. Major and trace element compositions were determined by XRF analysis at the School of Earth Sciences (SES, University of Tasmania) (Table A1). Analyses for some trace elements with low abundances (Ag, Bi, Cd, Sb, Cs, Tl and U) were performed by ICP-MS at the Central Science Laboratory (CSL, University of Tasmania) and at *Analabs*, an Australian company providing analytical services to the mining industry. The concentration of REE were measured for selected samples by ICP-MS at the CSL.

Sampled core intervals are 20 to 40 cm in length and quarter core off-cuts were used for geochemical analyses. Drill core samples were cut with a standard rock saw and weathered surfaces were removed where appropriate. Weathered parts of surface samples were also removed during this stage of sample preparation.

Sample preparation for XRF analyses and ICP-MS analyses at the CSL was undertaken at the facilities of the School of Earth Sciences (University of Tasmania). Sample splits selected for geochemical analysis were wrapped in a hard plastic bag and crushed manually with an iron hammer to fragment sizes <1 cm. Representative rock chips were milled in a common tungsten carbide mill for 2 to 3 minutes to produce about 20 to 40 g of rock powder.

Major elements and sulphur were measured by XRF on fusion discs as well as Ba, Cu, Pb and Zn for strongly altered or mineralised samples. A special method, designed for the measurement of sulphur by XRF was followed for disc preparation ('altered silicate method'). In order to prevent sulphur loss during fusion, 1 ml of 38.5% $LiNO_3$ solution was added to the platinum crucibles holding a mixture of 0.7700 g sample powder and 3.7125 g Nourish Flux. Crucibles were placed in a muffle furnace at 700 °C for 10 minutes

prior to fusion of the sample powder in a 'Fusilux' fusion bead casting machine where temperatures of 1000 to 1100 °C were applied for 10 minutes to produce homogeneous melts. Several standards (Tasbas, Tasdior, Tasmonz and Tasgran) and blank discs were produced to test the accuracy of the measurements.

The loss of ignition (LOI) of the samples has been determined on 1 to 2 g of rock powder weighed into platinum crucibles. The powders were subjected to 500 °C for 4 hours prior to ignition at 1000 °C for 12 hours in order to ensure that all volatiles (including sulphur) were driven off. Temperatures were reduced to 400 °C over a period of ~5 hours before the crucibles were moved to a drying cabinet with a temperature of 100 °C. After one hour the crucibles were placed in an exicator in order to cool to room temperature before weighing. Steel thongs were used for handling of the crucibles.

Trace element analysis by XRF was performed on pellets made from pressed sample powder. These were manufactured using 6 g of sample powder which had been mixed with 0.6 ml PVA solution prior to pressing.

XRF data was obtained from a Philips PW1480 x-ray spectrometer using modified X40 software (Robinson, personal communication, School of Earth Sciences, University of Tasmania). Trace elements were measured with a Sc-Mo tube and a Au tube (see Table A1). Several local and international standard samples were measured during trace element analysis including Tasgran, Tasbas, AGV1, RGM1, ENDV, G2, BIR-1, RSES(Cu) and AWQuartz.

Solutions for ICP-MS analyses at the CSL were prepared for 106 samples by acid digestion at the facilities of the School of Earth Sciences. Savillex beakers, which were cleaned by soaking in 6N HCl and 30%HNO_3 for 2 consecutive days, were filled with 100 mg of sample powder. High purity H_2O, HF (2 ml) and concentrated HNO_3 (0.5 ml) were added. After digestion of the powder for 48 hours in the closed beaker on a hotplate the solution was evaporated to incipient dryness. A second evaporation stage using 1 ml of concentrated HNO_3 was followed by the final preparation of the solution with high purity H_2O producing 100 ml of sample solution for ICP-MS analysis. The solutions were spiked with 10 ml of iridium solution and analysed with a Finnigan *ELEMENT* high-resolution ICP-MS at the Central Science Laboratory (University of Tasmania). Blank solutions were used to determine instrument drift and were analysed every eight to ten samples during each analysis sequence. Using the same solutions, REE data was obtained

for a sub-set of the samples at CSL. Details about the analytical procedures for REE analysis are described in Robinson et al. (1999).

Powders of samples which were not analysed at CSL were submitted to *Analabs* where they were digested and analysed according to standard procedures (GS201, OM612). Several standards and duplicates of samples previously analysed at CSL provided an independent control on the quality of the analytical data. Comparison of results from CSL and *Analabs* showed that the data from these laboratories is in good agreement. At Analabs, 0.2 g of sample powder was used for digestion involving a combination of perchloric and hydrofluoric acid and aqua regia (code: D201). The solutions were analysed for low abundance trace elements by ICP-MS analysis (code: GS201). Furthermore, samples submitted to *Analabs* were analysed for total carbon by infrared spectophotometry (OM612, Leco analysis).

Some analytical data from an extensive geochemical exploration study by RGC on the altered footwall rhyolite at Thalanga was made available for this research. Analyses from RGC were used exclusively to supplement the data-base in order to identify geochemical proximity indicators to the Thalanga deposit and are therefore only included in Figure 8.12.

Data from the RGC footwall study were obtained from samples of half core generally 20 cm to 40 cm long which were submitted to *Analabs* for geochemical analysis. The rocks were fragmented in a jaw crusher and pulverised to nominal 75 µm using a chrome steel mill (procedures GP009 and GP017). Instrumental neutron activation analysis (INAA) was carried out on 30 g of powder, analysing for a wide range of major, trace and rare earth elements (Table A2). Solutions for ICP analysis were prepared by digesting 0.2 g of sample material in aqua regia, hydrofluoric and perchloric acid. Optical emission techniques in ICP analysis were used to measure major elements and selected trace elements with relatively high concentrations. Trace elements with low concentrations were measured by ICP-MS. Zirconium was analysed by XRF with pressed powder pellets. Atomic absorption spectrophotometry (AAS) was used to measure Cu, Pb and Zn of sulphide-rich samples. The sulphur content of pyrite-rich samples was determined by infrared spectrophotometry in a Leco induction furnace.

Table A1: Bulk rock geochemical analysis(this study): Methods and laboratories

Laboratory	method	elements
SES	ignition	total volatiles
SES	XRF (fusion disc)	Si, Ti, Al, Fe, Mn, Ca, Na, K, P, S (also Zn, Pb, Cu and Ba for samples with high concentrations of these elements)
SES	XRF (pressed powder, ScMo tube)	Cu, Pb, Zn, Ni, Y, Rb, Th, As
SES	XRF (pressed powder, Au tube)	Nb, Zr, Sr, Cr, Ba, V
CSL and *Analabs* (GS201)	ICP-MS (solution)	Ag, Bi, Mo, Cd, Sb, Cs, Tl, U
CSL	ICP-MS (solution)	La, Ce, Pr, Nd, Sm, Eu, Gd, Tb, Dy, Ho, Er, Tm, Yb, Lu
Analabs (OM612)	Leco	C

SES. School of Earth Sciences, University of Tasmania

CSL: Central Science Laboratory, University of Tasmania

Table A2: Bulk rock geochemical analysis (RGC footwall alteration study): *Analabs* methods for analysis of altered footwall rhyolite

code	method	elements
GN801	INAA	Ag, As, Au, Ba, Ce, Cr, Cs, Eu, Fe, Hf, K, La, Lu, Mo, Na, Rb, Sb, Sc, Se, Sm, Ta, Th, U, Yb, Zn
GI201	ICP-OES	Al, Ca, Cu, Fe, K, Mn, Mg, Na, Ni, P, Pb, S, Sr, V, Zn
GI202	ICP-OES	Si
GS201	ICP-MS	Ag, Bi, Ga, Mo, Sc, Se, Ti, Tl
GX401	XRF (pressed powder)	Zr
GA104	AAS	Cu, Pb, Zn (for high concentrations)
OA601	AAS	Pb, Zn (for ore grade concentrations)
OM613	Leco	S (for high concentrations)

NB: results for Na, K and Fe by INAA and ICP-OES are in excellent agreement showing 1:1 correlations.

A1.2 Microprobe analysis

Microprobe analyses were obtained for a number of minerals at the Central Science Laboratory (CSL, University of Tasmania) and at the Technical University of Berlin (TUB, Germany). Microprobe analyses were performed with a Cameca SX50 at the CSL using an acceleration voltage of 15 kV, a beam current of 25 nA and a beam diameter of ~1 µm. Analyses at TUB were obtained with a Camebax-Microbeam instrument applying an acceleration voltage of 15 kV, a current of 16 nA and a beam diameter of ~3 µm. Elements analysed, standards used for analyses and the limits of detection are detailed in Table A3.

Calculated mineral composition of muscovite, biotite, chlorite and garnet are tabulated individually (Table A6 to A9). Furthermore, several other minerals such as epidote, calcite, feldspar and amphiboles were also analysed (Table A10 to A13). Samples with garnet crystals were analysed at TUB whereas samples from DDH TH247 and the outcrop section were analysed at CSL. All analysed crystals are individually labelled with a code consisting of a letter (identifying the thin section) and a number (identifying the crystal). Multiple analyses of one crystal have the same 'mineral' label. The locations of microprobe analyses were recorded on photomicrographs during the measurements. Analyses with numbers from 1 to 290 were obtained at TUB whereas analyses with numbers ≥ 300 identify data from CSL.

Table A3: Condition for microprobe analysis at CSL and TUB: elements analysed, standards and detection limits

	CSL		TUB	
	standard	detection limit [wt.%]	standard	detection limit [wt.%]
Si	quartz	0.05	wollastonite	0.1
Ti	ilmenite	0.05	rutile	0.1
Al	plagioclase	0.05	andalusite	0.1
Fe	fayalite	0.13	native iron	0.2
Mn	rhodonite	0.14	native manganese	0.2
Mg	forsterite	0.05	olivine	0.1
Ca	apatite	0.06	wollastonite	0.1
Na	carnegieite	0.05	albite	0.1
K	microcline	0.05	microcline	0.1
Ba	barite	0.13	na	
Zn	sphalerite	0.19	na	
F	lithiumflourite	0.28	na	
Cl	halite	0.05	na	

na not analysed

Table A4: Bulk rock geochemical data

sample	C2047-13	C2047-20	C2047-3 3	C2047-40	C2047-64	C2047-70	C2047-83	TH10-129	TH10-17	TH112-211	TH112-227	TH112-337	TH112-370	TH112-404	TH112-448	TH112-551	TH112-653	TH114B-170	TH114B-217	TH114B-226	TH114B-297
DDH	C2047SD46	C2047SD46	C2047SD46	C2047SD46	C2047SD46	C2047SD46	C2047SD46	TH10	TH10	TH112	TH112	TH112	TH112	TH112	TH112	TH112	TH112	TH144B	TH144B	TH144B	TH144B
depth from	13 1	20 1	3 3	40	64 1	70 3	82 9	129 3	17	211 3	227 3	236 8	370	404	448 5	550 8	652 6	169.7	217	225 5	296 7
depth to	13 35	20 3	3 5	40 2	64 45	70 6	83 15	129 65	17 25	211 5	227 65	237 1	370 4	404 4	448 75	551 1	652 9	170	217 2	225 75	296 95
lithofacies	D3	R1	D3	R1	R1	R1	R1	R1	D3	R1	R1	R1	R1	R1	R1	R1	D3	R1	R1	R1	R1
altn facies	W4	QP	W1	M	M	DT	W3	QP	LA	M	QP	QKF	W1,3	W1	QKF	W2	W2	M	QKF	QKF	M
SiO2 [wt %]	60 4	79 3	64 1	67.7	77 8	57 0	76 1	85 6	72 0	74.4	62 3	75 0	78 5	79 6	85 6	78 9	73 1	74 2	81 2	77 9	76 7
TiO2 [wt %]	0 50	0 06	0 40	0.11	0 07	0 10	0 09	0 05	0 45	0 10	0 08	0 10	0 08	0 08	0 05	0 09	0 45	0 11	0 06	0 08	0 07
Al2O3 [wt %]	14 9	8 7	12 3	15 7	10 3	14 9	13 2	6 7	14 2	13 7	11.9	13 4	11 0	9.7	7 6	11 8	13 7	13 8	9 4	11 5	10 0
Fe2O3 [wt %]	9 51	1 48	3 48	2 15	1 22	5 78	0 57	2 86	3 00	1 84	8 65	1 39	1 37	1 24	1 07	1 12	2 50	2 02	1 78	1 61	5 09
MnO [wt %]	0 13	0 02	0,14	0,03	0 02	0.49	<0 01	<0 01	0 04	0 09	0 18	0 06	0 04	0 06	0 02	0 03	0 04	0 04	<0 01	0 05	0.07
MgO [wt %]	4 87	3 42	1 49	4 46	1 10	2.13	0 09	0 51	0 72	3 47	7.31	3 62	0.16	0 18	1 45	0 49	0 58	1 75	0 45	1 61	2 47
CaO [wt %]	2.45	0 64	8 05	0 03	1 17	12 98	0 40	<0 01	0 97	0 01	0 01	<0 01	1 47	1 32	0 09	0 68	0 88	0 51	0 65	0 10	0 06
Na2O [wt %]	4 08	0 62	4 35	0 19	0.72	0 28	5 50	0 19	6 18	0 15	0 17	0 09	2.47	0 43	1 61	5 86	5 77	1 44	3 24	3 12	0 23
K2O [wt %]	0 93	2 53	1 04	5 76	5 29	3 06	2 94	2 18	2 26	3 61	2 12	3 62	4 30	6 84	1 82	0 43	2 02	4 54	1 51	2 05	2 23
P2O5 [wt.%]	0 11	0 01	0.10	0 02	0 03	0 02	0 02	0 01	0 11	0 01	0 01	0.01	0 01	0 02	0 01	<0 01	0 11	0 01	0 01	0 01	0 01
BaO [wt %]	0 05	0 87	0 11	0 32	0 46	0 28	0 11	0 04	0 05	0 06	0 02	0 02	0 07	0 11	0 02	0 01	0 06	0 07	0 05	0 04	0 01
CuO [wt %]	<0 01	0 05	<0 01	<0 01	<0 01	<0 01	<0 01	<0 01	<0 01	<0 01	<0 01	<0 01	<0 01	<0 01	<0 01	<0 01	<0 01	<0 01	<0 01	<0 01	0 01
PbO [wt %]	<0 02	0 08	<0 02	<0 02	<0 02	0 22	<0 02	<0 02	<0 02	<0 02	<0 02	<0 02	<0 02	<0 02	<0 02	<0 02	<0 02	<0 02	0 02	<0 02	<0 02
ZnO [wt %]	0 03	0 11	0 02	0 06	0 02	0 51	<0 01	<0 01	0 01	0 01	0 02	0 01	0 01	0 01	0 19	0 01	0 01	0 01	<0 01	0.01	0 01
LOI* [wt %]	2.26	2.39	3 28	3 17	2 00	2.17	0 39	2 33	0 46	2 96	6 42	2 82	0 33	0 33	1 22	0 36	0 50	1 52	1.72	1 33	2.58
Total [wt %]	100 18	100 32	98 86	99 68	100 10	99 95	99 40	100 50	100 50	100 38	99 21	100.10	99 80	99 90	100 72	99 76	99 68	99 98	100 11	99 47	99 58
S [wt %]	0.10	0 90	0 03	1 16	0 78	0 32	0 37	2 10	<0 01	0 61	4 68	0 24	0 01	<0 01	0 61	0 01	0.36	<0 01	1 21	0 42	0 77
CO2	0 2	0 3	2 9	0 1	0 7	1 1	0.2	0 3	0 2	0 1	<0.1	0 1	0 2	0 2	0 3	0 2	<0 1	<0 1	0 4	<0 1	<0 1
Ba [ppm]	529	8700	1250	3200	4600	2800	1080	509	741	364	260	405	866	994	280	99	697	740	584	267	199
Cu [ppm]	4	400	7	20	13	36	7	3	4	2	39	2	3	4	30	2	7	3	15	26	89
Pb [ppm]	19	894	12	38	101	2013	15	7	7	4	7	4	20	40	99	5	5	17	251	31	8
Zn [ppm]	311	968	134	515	177	4096	8	9	86	110	226	88	26	36	1839	40	36	62	49	110	73
Ag [ppm]	0 3	10 1	0 2	1 4	0 7	53 5	0 5	0 2	0 2	0 2	0 4	0,1	<0 1	<0.1	0 2	<0.1	<0 1	<0 1	0 4	<0 1	<0 1
As [ppm]	<3	<3	<3	<3	4	<3	<3	12	<3	<3	8	3	<3	<3	<3	<3	<3	<3	8	5	3
Bi [ppm]	<0 1	1.2	0 2	0 6	0 2	413 0	11 9	12 1	1 8	1 8	6 8	1 0	0 5	0 4	0 6	0 2	0 3	1 0	1 3	0 5	1 1
Cd [ppm]	0 3	2.8	0 2	3 2	0 6	48 9	0.4	0 2	0 3	0 2	0 3	0 2	0 1	0 1	5 2	0 1	0 2	0 2	0 3	0 2	0.1
Cr [ppm]	2	<2	4	2	<2	<2	<2	<2	3	2	2	<2	<2	<2	2	3	4	4	<2	<2	3
Cs [ppm]	3 5	3 4	0 4	2 8	1 3	0 5	0.1	0 4	1 0	0 6	0 5	0 8	0 4	0 5	0 9	0 3	0 6	1 1	0 4	0 9	0.5
Mo [ppm]	1.1	16 7	0 3	6.2	3 0	3 4	0 3	8 5	0 4	1 2	26 1	1 5	0 4	0 2	4 8	0 3	2 0	17 3	5 3	2 4	1 7
Nb [ppm]	10	11	8	21	13	13	14	9	8	17	15	16	13	12	9	16	8	20	11	14	13
Ni [ppm]	2	2	1	4	2	2	<1	1	1	1	2	1	1	2	<1	2	<1	1	1	<1	<1
Rb [ppm]	33	104	19	197	111	52	40	60	35	137	77	132	85	121	61	21	33	142	37	61	67
Sb [ppm]	1.1	5 5	0 8	1 1	1 2	2 2	0 5	1 2	0.3	0 2	0 3	0 4	0 5	0 4	0 4	0 3	0 4	0 2	0 4	0 2	0 2
Sr [ppm]	135	216	120	30	49	158	70	12	57	11	5	10	101	67	22	89	97	47	50	34	7
Th [ppm]	8	9	6	18	12	-	12	5	7	15	12	16	11	11	8	15	7	16	10	11	11
Tl [ppm]	0 8	2 9	<0 5	5 1	2 5	1 1	<0 5	2 5	<0 5	<0 5	<0 5	0 6	0 5	0 7	0 6	<0 5	<0 5	0 6	0 6	0 8	<0 5
U [ppm]	1.7	2 9	1.4	5 3	3 9	5 0	2.7	1 8	1 3	2 1	3 0	2 1	1 8	1 8	1 7	1 2	1 4	2 8	4 2	2 4	2.2
V [ppm]	35	11	22	5	15	38	6	2	22	<1 5	2	<1 5	<1 5	<1 5	<1.5	<1 5	26	<1 5	10	<1 5	<1 5
Y [ppm]	23	27	30	64	42	52	41	23	26	43	29	33	35	30	23	39	26	47	32	37	32
Zr [ppm]	160	99	133	196	125	151	125	79	146	150	129	145	118	111	77	149	147	159	97	119	111
La [ppm]	-	-	-	-	-	-	-	-	-	-	-	-	-	-	-	-	-	-	-	-	-
Ce [ppm]	-	-	-	-	-	-	-	-	-	-	-	-	-	-	-	-	-	-	-	-	-
Pr [ppm]	-	-	-	-	-	-	-	-	-	-	-	-	-	-	-	-	-	-	-	-	-
Nd [ppm]	-	-	-	-	-	-	-	-	-	-	-	-	-	-	-	-	-	-	-	-	-
Sm [ppm]	-	-	-	-	-	-	-	-	-	-	-	-	-	-	-	-	-	-	-	-	-
Eu [ppm]	-	-	-	-	-	-	-	-	-	-	-	-	-	-	-	-	-	-	-	-	-
Gd [ppm]	-	-	-	-	-	-	-	-	-	-	-	-	-	-	-	-	-	-	-	-	-
Tb [ppm]	-	-	-	-	-	-	-	-	-	-	-	-	-	-	-	-	-	-	-	-	-
Dy [ppm]	-	-	-	-	-	-	-	-	-	-	-	-	-	-	-	-	-	-	-	-	-
Ho [ppm]	-	-	-	-	-	-	-	-	-	-	-	-	-	-	-	-	-	-	-	-	-
Er [ppm]	-	-	-	-	-	-	-	-	-	-	-	-	-	-	-	-	-	-	-	-	-
Tm [ppm]	-	-	-	-	-	-	-	-	-	-	-	-	-	-	-	-	-	-	-	-	-
Yb [ppm]	-	-	-	-	-	-	-	-	-	-	-	-	-	-	-	-	-	-	-	-	-
Lu [ppm]	-	-	-	-	-	-	-	-	-	-	-	-	-	-	-	-	-	-	-	-	-
Tl/Zr	18 8	3 6	18 2	3 4	3 4	3 9	4 3	3 8	18 5	3 9	3 7	4 1	4.0	4 3	3 9	3 6	18 5	4 1	3 7	4 0	3.8
Altn Index	47	83	17	98	77	28	34	93	29	98	98	99	53	80	66	12	28	76	34	53	94
CCP Index	73	60	46	52	27	69	7	57	29	58	87	57	17	15	41	19	27	37	30	37	74

Table A4: Bulk rock geochemical data

sample	TH114B-67	TH144B-34	TH148-130	TH148-159	TH148-54	TH148-564	TH148-567	TH148-569	TH18-191	TH18-266	TH18-90	TH238-130	TH238-144	TH238-183	TH238-194	TH238-202	TH238-205	TH238-236	TH238-95	TH243-86	TH243A-425
DDH	TH144B	TH144B	TH148	TH148	TH148	TH148	TH148	TH148	TH18	TH18	TH18	TH238	TH238	TH238	TH238	TH238	TH238	TH238	TH238	TH243	TH243A
depth from	66 8	34 2	129 7	159 2	54	564	567	568 85	191 2	265.7	89 7	129 8	143 7	182 6	193.7	201 9	205 2	236	95 2	86	424 9
depth to	67.1	34 4	129 85	159 3	54 2	564 1	567 15	569 05	191 5	265 85	89 9	130 15	143 95	182 85	194	202 1	205 4	236 3	95 4	86 2	425
lithofacies	R2	R1	R1	R1	R2	QEV	QEV	QEV	R3	R1	D3	R1	R1	R1	R1	R1	R1	R1	R1	R2	D3
altn facies	W4	LA	W2	M	W4	W4	W4	W1	M	M	W2	QP	QP	QP	M	W2	M	M	QP	W4	W4
SiO2 [wt %]	77 5	77 3	82 5	82 0	80 1	59 7	65 2	62 6	62 4	66 8	73 5	68 1	72 4	67 0	74 4	79 6	70 9	74 6	81 8	77 4	70 2
TiO2 [wt %]	0 10	0 10	0 09	0 08	0 08	0 26	0 24	0 24	0 22	0 08	0 43	0 07	0 08	0 05	0 09	0 08	0 10	0 09	0 06	0.12	0 47
Al2O3 [wt %]	11 8	11 9	10 6	8 8	11 0	18 2	16 9	17 3	18 3	11 3	14 5	9 7	11 4	6 6	12 2	11 0	14 5	13 4	9 4	11 7	14 3
Fe2O3 [wt %]	1 30	2 09	0 33	0 68	1.32	4 69	3 37	3 71	3 27	2 46	1 76	10 20	4 61	14 34	1 42	1 04	1.69	1 40	1 94	1 33	3 44
MnO [wt %]	0 03	0 03	0 01	0 02	0 02	0 05	0 14	0 16	0 04	0 13	0 01	0 04	0 06	0 02	0 05	0 02	0 04	0 02	0 02	0 03	0 05
MgO [wt %]	0 57	0 68	0 33	1.05	0 68	2 73	3 44	4 16	2 64	9 88	0 42	2 55	4 57	1 67	4 16	0 23	3 94	3 54	2 25	0 63	1 55
CaO [wt %]	1 37	0 90	0 20	0 24	0 17	0 94	0 48	4 01	0 55	0 01	1 01	0 01	<0 01	0 05	0 07	0 84	0 12	0 12	<0 01	0 20	2 27
Na2O [wt %]	4 52	2 77	4 60	0 53	3 67	0 15	0 97	3 32	0 84	0 12	7 71	0 13	0 11	0 06	0 08	5 20	1 05	1 82	0 12	3 15	4 85
K2O [wt %]	1 14	3 60	1 97	5 33	2 48	6 67	5 95	2 98	6 90	5 08	0 11	2 62	2 47	1 99	3 57	0 37	3 92	2 23	2 61	3 99	1 69
P2O5 [wt %]	0 01	0 02	0 02	0 02	0 01	0 05	0 06	0 08	0 05	0 02	0 11	0 01	0 01	0 01	0 01	0 01	0 01	0 01	0 01	0 02	0.11
BaO [wt %]	0 03	0 10	0 06	0 09	0 04	0 58	0 31	0 27	0 22	0 46	0 01	0 15	0 03	0 26	0 12	0 02	0 08	0 03	0 02	0 18	0 06
CuO [wt %]	<0.01	<0 01	<0 01	<0 01	<0 01	<0 01	<0 01	<0 01	<0 01	<0 01	<0 01	<0 01	<0 01	<0 01	<0 01	<0 01	<0 01	<0 01	<0 01	<0.01	<0 01
PbO [wt.%]	<0 02	<0 02	<0 02	<0 02	<0 02	<0 02	<0 02	<0 02	<0 02	<0 02	<0 02	<0.02	<0 02	<0 01	<0 02	<0 02	<0 02	<0 02	<0 02	<0 02	<0 02
ZnO [wt %]	0 01	0 01	<0 01	<0 01	<0 01	<0 01	<0 01	<0.01	<0 01	<0 01	<0 01	0 02	0 01	0 01	0 01	<0 01	0 03	0 01	<0 01	<0 01	<0.01
LOI* [wt %]	0.47	0 77	0 35	1 03	0 75	5 25	2.36	1 25	3 83	2 65	0 38	5 98	3 84	8 24	2 79	0 42	2 67	2.49	2 21	0 95	0 92
Total [wt %]	98 85	100 23	101.04	99 93	100 32	99 23	99 40	100 02	99 33	98 97	99 86	99 74	99 49	100 23	98 96	98 77	98 95	99 78	100 39	99 68	99 90
S [wt %]	0 04	0 24	0 02	0 3	<0 01	2 75	0 01	0 03	1.66	0 53	<0 01	6 69	1 66	10 61	0 44	0 09	<0 01	<0 01	0 70	0 42	<0 01
CO2	<0.1	0 1	-	-	-	-	-	-	-	-	-	0 1	<0 1	<0 1	0.3	0 3	0 1	<0 1	<0 1	-	-
Ba [ppm]	201	956	403	740	351	5210	2835	2296	1969	4194	30	1930	433	2300	1210	230	952	584	393	1518	492
Cu [ppm]	2	3	<1	4	<1	87	4	8	10	5	1	10	6	22	5	3	3	1	3	347	3
Pb [ppm]	5	8	26	35	3	250	20	34	23	3	4	8	5	16	10	17	5	7	4	19	20
Zn [ppm]	34	51	10	74	54	520	178	181	163	521	17	139	142	74	113	31	231	72	47	1142	124
Ag [ppm]	<0.1	<0 1	< 0 5	< 0 5	< 0 5	12 5	< 0 5	< 0 5	< 0 5	< 0 5	< 0 5	<0 1	<0 1	0 2	<0 1	<0 1	<0 1	<0 1	<0 1	0 7	< 0 5
As [ppm]	<3	<3	3	<3	<3	68	<3	<3	8	<3	<3	6	6	25	5	<3	<3	4	7	<3	<3
Bi [ppm]	0 3	0 3	0 1	< 0 1	0 2	0 3	< 0 1	< 0 1	0 3	0 2	< 0 1	17 5	8 4	19 6	1 3	1 3	0 2	0,1	2 6	0 5	0 2
Cd [ppm]	0 1	0 2	< 0 1	0 3	< 0 1	1 0	0 1	0 2	0 7	1 3	1 6	0 3	0 3	0 3	0 2	0 1	0 1	0 1	<0 1	5 9	2 2
Cr [ppm]	2	3	2	3	1	2	2	2	1	2	2	<2	3	<2	<2	2	<2	3	<2	1	2
Cs [ppm]	0 4	0 7	0 1	0 9	0 5	6 1	5 0	6 3	1 9	4.7	< 0 1	1 2	0 6	1 2	1 3	0 2	1.7	0 6	0 5	0 5	1 2
Mo [ppm]	0 1	0 4	3 3	4 2	< 0.1	7 7	< 0 1	< 0 1	2 4	6 9	0 1	43 3	30 1	74 1	5 9	0 5	0.3	0.1	3 5	1.0	1.4
Nb [ppm]	14	12	12	11	13	19	20	19	23	15	8	13	14	7	16	12	19	13	12	16	9
Ni [ppm]	1	1	1	2	1	2	5	4	3	3	1	1	1	2	1	2	2	2	<1	2	1
Rb [ppm]	42	91	26	99	69	234	248	190	224	255	2	108	81	68	116	13	145	84	99	84	58
Sb [ppm]	0 3	0 2	0 3	0 5	< 0 1	6 2	0 3	0 4	1 1	0 6	0 3	0 5	0 5	1 1	0 3	0 5	0 2	0 4	0 4	0 4	0 2
Sr [ppm]	93	90	49	30	56	38	76	173	53	14	75	12	9	16	11	101	40	59	6	44	99
Th [ppm]	12	9	10	9	10	14	12	13	16	9	7	10	13	6	13	12	16	14	10	14	8
Tl [ppm]	<0 5	<0 5	0 2	0 8	0 3	5 1	4 8	4 9	8 7	14 6	< 0 1	1 0	0 8	1 9	1 8	<0 5	2 6	1 6	0 8	0 5	0 4
U [ppm]	2 3	1 5	3 5	3 0	2 3	4.9	1.1	2 8	4 1	5 7	1.6	2 6	2 7	2.2	3 2	1 4	1 5	0 8	2.3	3 9	3 5
V [ppm]	<1 5	<1 5	1	2	1	12	17	13	1	9	12	5	2	2	<1 5	<1 5	<1.5	3	<1 5	1	26
Y [ppm]	41	33	26	28	31	40	51	51	57	45	26	33	32	44	39	35	54	30	18	47	26
Zr [ppm]	147	141	127	114	123	235	248	252	322	132	139	107	129	79	138	113	162	140	102	174	155
La [ppm]	-	-	-	-	38 6	35 2	-	-	-	-	-	-	-	-	-	-	-	-	-	-	-
Ce [ppm]	-	-	-	-	70 0	68 2	-	-	-	-	-	-	-	-	-	-	-	-	-	-	-
Pr [ppm]	-	-	-	-	8 6	8 6	-	-	-	-	-	-	-	-	-	-	-	-	-	-	-
Nd [ppm]	-	-	-	-	31.7	33 5	-	-	-	-	-	-	-	-	-	-	-	-	-	-	-
Sm [ppm]	-	-	-	-	5 6	7 0	-	-	-	-	-	-	-	-	-	-	-	-	-	-	-
Eu [ppm]	-	-	-	-	0 8	2 2	-	-	-	-	-	-	-	-	-	-	-	-	-	-	-
Gd [ppm]	-	-	-	-	5 3	7.0	-	-	-	-	-	-	-	-	-	-	-	-	-	-	-
Tb [ppm]	-	-	-	-	0 9	1 2	-	-	-	-	-	-	-	-	-	-	-	-	-	-	-
Dy [ppm]	-	-	-	-	5 1	6 7	-	-	-	-	-	-	-	-	-	-	-	-	-	-	-
Ho [ppm]	-	-	-	-	1 2	1 6	-	-	-	-	-	-	-	-	-	-	-	-	-	-	-
Er [ppm]	-	-	-	-	3 3	4 8	-	-	-	-	-	-	-	-	-	-	-	-	-	-	-
Tm [ppm]	-	-	-	-	0 6	0 9	-	-	-	-	-	-	-	-	-	-	-	-	-	-	-
Yb [ppm]	-	-	-	-	3 6	5 8	-	-	-	-	-	-	-	-	-	-	-	-	-	-	-
Lu [ppm]	-	-	-	-	0 5	0 8	-	-	-	-	-	-	-	-	-	-	-	-	-	-	-
Ti/Zr	4 0	4 2	4 3	4 2	3 9	6 6	5 8	5 7	4 1	3 6	18 6	3 7	3.7	3 5	3 8	4 2	3 7	3 8	3 5	4 1	18 2
Altn Index	23	54	32	89	45	90	87	49	87	99	6	97	98	97	98	9	87	75	98	58	31
CCP Index	24	29	9	22	23	50	48	54	42	70	20	80	77	88	60	17	52	54	59	20	42

Table A4: Bulk rock geochemical data

sample	TH245-517	TH247-136	TH247-75	TH270-121	TH270-145	TH270-220	TH270-278	TH270-313	TH270-381	TH270-395	TH270-78	TH28-139	TH28-304	TH28-416	TH29-174	TH3-5	TH334-136	TH334-81	TH37-138 6	TH37-138 6	TH37-90
DDH	TH245	TH247	TH247	TH270	TH270	TH270	TH270	TH270	TH270	TH270	TH270	TH28	TH28	TH28	TH29	TH3	TH334	TH334	TH37	TH37	TH37
depth from	517 1	136 1	74 5	121 2	144 5	220 3	277 7	313 1	381 45	395	77 3	139	304 5	416	173 8	5	135 6	80 8	138 45	138 4	89 7
depth to	517 2	136 2	74 65	121 45	144 9	220 55	278	313 5	381 6	395 3	77 7	139 15	304 55	416 1	173 85	5 1	135 85	81 1	138 5	138 55	89 9
lithofacies	D3	R3	R2	R1	R1	R1	R1	R1	R1	D1	R1	D2	D2	D3	A	D3	D3	A	PH	PH	D2
altn facies	W4	M	LA	W4	M	QP	M	QP	QP	W2,4	W4	LA	LA	W4		W2	W2,4				W2
SiO2 [wt %]	69 9	72 0	77 6	79 0	72 7	63 4	64 4	72 6	55 4	76 6	78 9	79 5	77 9	67 9	50 1	74 5	71 7	50 4	59 8	63 1	75 4
TiO2 [wt.%]	0 46	0 12	0 11	0 08	0 09	0 05	0 12	0 10	0 10	0 32	0 07	0 33	0 29	0 48	0 68	0 44	0 48	0 46	0 99	1 07	0 29
Al2O3 [wt %]	14 2	13 0	11.7	10 0	12 2	8 0	17 6	12 6	13 9	12 5	10 6	11 8	11 3	14 7	16 5	13 6	15 1	15 2	13 4	13 9	12.7
Fe2O3 [wt %]	4.04	3 06	1 38	1 81	2 39	13 46	4 73	4 93	14 36	1 90	1 63	0 98	1 65	5 21	9 69	1 40	2 29	8 24	9 03	8 50	2 61
MnO [wt %]	0 06	0 10	0 04	0 05	0 09	0 13	0 07	0 07	0 14	0 04	0 02	0 01	0 02	0 07	0 16	0 02	0 02	0 31	0 33	0 21	0 05
MgO [wt %]	1.05	2 71	0 57	2 11	4.24	5 88	4 35	3 88	4 90	0 89	1 06	0 31	0 24	1 44	7 39	0 95	0 55	9.44	3 10	3 01	0 60
CaO [wt.%]	1 11	0 31	0 24	0 22	0 27	<0 01	0 01	<0 01	0 11	1 21	0 07	0 38	0 73	0 90	7 82	0 59	1 06	10 79	8 52	2.73	0 71
Na2O [wt %]	5 64	2 44	4 02	2 37	0.22	<0 05	0 24	0 03	0 18	5 50	1 90	5 25	4 55	6 25	4 66	6 81	8 36	3 06	2 82	3 23	6 58
K2O [wt %]	2 60	3 79	3 22	2 68	4 73	0 91	4 15	2 50	2 40	0 55	2 51	1 75	2 69	1 79	1 34	0 54	0 53	0 85	0 56	2 56	0 11
P2O5 [wt %]	0 11	0 02	0 02	0 01	0 01	0 01	0 02	0 01	0 02	0 05	0 01	0 06	0 05	0 11	0 10	0 10	0 11	0 10	0 50	0 42	0 06
BaO [wt %]	0.11	0.10	0.15	0 13	0 08	0 03	0 04	0 04	0 08	<0 01	0 12	0 09	0 11	0 06	0 03	0 03	0 02	0 08	0 03	0 08	<0 01
CuO [wt %]	<0 01	<0 01	<0 01	<0 01	<0 01	0 03	<0 01	<0 01	0 31	<0 01	0 01	<0 01	<0 01	<0 01	<0 01	0 01	<0 01	<0 01	<0 01	<0 01	<0 01
PbO [wt %]	<0 02	<0 02	<0 02	<0 02	<0 02	<0 02	<0 02	<0 02	<0 02	<0 02	<0 02	<0 02	<0 02	<0 02	<0 02	<0 02	<0 02	<0 02	<0 02	<0 02	<0 02
ZnO [wt %]	<0 01	<0 01	<0 01	0 03	0 02	0 05	0.02	0 04	0 12	0 01	0 68	<0 01	<0 01	<0 01	<0 01	0 10	0 01	0.04	<0 01	<0 01	<0 01
LOI* [wt %]	0 48	2 02	0 71	1 52	2 56	7 60	4 23	3.17	7.22	0 29	1 99	0 57	0 69	0 95	1 47	0 68	0 35	1 48	0 68	0 9	0 47
Total [wt %]	99 68	99 70	99 70	100 04	99 62	99 51	99 91	99 88	99 20	99 83	99 61	100 98	100 16	99 85	99 92	99 82	100 49	100 41	99 82	99 62	99 54
S [wt %]	0 02	0 56	0 2	0 82	0 84	7 64	1 08	0 44	5 92	<0 01	1 30	<0 01	0 04	<0 01	<0 01	0 01	<0 01	0 03	<0 01	0 04	0,03
CO2	-	-	-	-	-	-	-	-	-	-	-	-	-	-	-	-	0 1	1 9	-	-	-
Ba [ppm]	982	882	1395	1648	1067	89	429	451	945	120	1536	793	1006	539	245	402	141	673	174	813	23
Cu [ppm]	24	145	63	10	4	305	3	112	2477	2	77	3	5	3	29	148	1	72	5	22	19
Pb [ppm]	22	38	15	28	11	27	61	65	74	31	55	9	7	11	24	163	4	190	7	7	11
Zn [ppm]	100	142	36	301	164	446	184	358	1215	48	5462	36	58	121	108	912	56	427	137	128	43
Ag [ppm]	< 0 5	< 0 5	< 0 5	< 0 5	< 0 5	< 0 5	< 0 5	< 0 5	5 5	< 0 5	< 0 5	< 0 5	< 0 5	< 0 5	< 0 5	0 9	<0 1	0.2	< 0 5	< 0 5	< 0 5
As [ppm]	<3	<3	<3	4	4	42	<3	<3	39	<3	19	<3	<3	<3	<3	<3	<3	<3	<3	<3	<3
Bi [ppm]	< 0 1	2 5	0 2	1 2	0 4	6 5	1 5	17 5	5 2	0 2	1 5	< 0 1	< 0 1	< 0 1	0 1	0 3	0 1	0 5	0 6	< 0 1	0 1
Cd [ppm]	0 2	0 3	0 2	0 6	< 0.1	0 5	0 6	0 4	5 2	0 1	13 9	0 3	1 0	0.7	0 3	1 2	0 1	0 3	0 3	0 4	1 0
Cr [ppm]	2	2	1	3	<2	<2	2	<2	<2	<2	3	2	3	2	226	<2	2	482	2	3	3
Cs [ppm]	0 8	1.9	0 6	0 9	2 0	0 3	0 5	0 9	0 6	0 7	0 3	0 4	0 8	2 0	4.7	0 9	0 3	1 6	0 6	5 6	0 3
Mo [ppm]	0 8	11.3	0 4	2 5	1 7	2 6	3 4	< 0 1	1 9	0 2	1 3	0 1	0 6	1 1	< 0 1	0 2	0 2	0 1	0 7	0 9	0 1
Nb [ppm]	9	14	13	12	14	9	20	16	19	9	11	11	10	10	2	8	9	2	9	9	11
Ni [ppm]	2	2	1	2	1	1	1	1	2	<1	<1	2	2	1	52	6	1	75	5	3	2
Rb [ppm]	58	155	71	98	158	33	120	86	61	25	78	28	39	46	44	23	5	31	16	75	3
Sb [ppm]	0 3	0 1	< 0 1	< 0 1	0 2	0 3	0 2	0 2	0 8	0 7	0 2	0 2	0 2	0 1	0 2	1 2	0 4	0 8	0 2	< 0 1	< 0 1
Sr [ppm]	83	39	53	54	22	2	14	9	19	99	30	46	42	74	140	77	60	279	109	117	49
Th [ppm]	7	11	10	11	13	9	19	14	16	8	11	8	7	7	<1 5	6	7	2	3	4	7
Tl [ppm]	0 8	0 9	0 4	0 7	1.1	0.3	1.3	1.1	1 6	1 0	0 4	0 3	0 3	0 5	0 5	0 6	<0 5	<0 5	0 1	0 4	< 0 1
U [ppm]	2 0	2 9	2 9	2 8	3 5	2 1	4 8	3 4	2 4	2 3	2 0	2 3	2 0	2 0	0 2	1 9	0.7	0 4	0 8	0 8	2 1
V [ppm]	26	2	1	<1 5	<1 5	<1.5	<1 5	2	2	4	<1 5	3	6	28	284	18	27	230	69	68	9
Y [ppm]	26	31	34	28	36	19	46	39	63	26	31	31	28	29	13	147	27	9	53	43	33
Zr [ppm]	149	160	148	106	130	83	195	140	154	160	102	174	165	163	35	136	154	36	138	159	164
La [ppm]	-	20 6	-	34 1	33 6	29 0	51 5	39 4	45 9	18 8	17 7	-	12 6	-	4 5	-	-	-	-	-	-
Ce [ppm]	-	38 4	-	60 2	64 2	51 6	102 9	74 4	86 6	37 2	33,1	-	23 8	-	9 7	-	-	-	-	-	-
Pr [ppm]	-	4 9	-	7 3	8 1	6 3	12 7	9 3	10 9	5.0	4 2	-	3 3	-	1.4	-	-	-	-	-	-
Nd [ppm]	-	18 7	-	27 3	31 4	23 0	48 4	35 8	43 3	20 4	16 1	-	14 2	-	6.7	-	-	-	-	-	-
Sm [ppm]	-	4 1	-	5 3	6 8	4 2	9 4	7 4	9 1	4 5	3 5	-	3 9	-	1 8	-	-	-	-	-	-
Eu [ppm]	-	0 7	-	0 7	0 9	0 4	1.2	0 9	1 6	1 2	0 5	-	1 2	-	0 7	-	-	-	-	-	-
Gd [ppm]	-	4 2	-	5 0	7.0	3 9	8 6	7 3	9 4	4 9	3.5	-	4 5	-	2 1	-	-	-	-	-	-
Tb [ppm]	-	0 8	-	0 8	1 2	0 6	1 4	1 2	1.4	0 8	0 6	-	0 9	-	0.4	-	-	-	-	-	-
Dy [ppm]	-	4 6	-	4 4	6 6	3 0	7 6	6 4	7 3	4.7	3 3	-	5 1	-	2.1	-	-	-	-	-	-
Ho [ppm]	-	1 1	-	1 0	1.5	0.7	1 8	1 4	1 6	1 1	0 7	-	1.2	-	0 5	-	-	-	-	-	-
Er [ppm]	-	3 3	-	2 9	4.3	1 9	5 3	4 0	4 3	3 0	2 1	-	3,3	-	1 3	-	-	-	-	-	-
Tm [ppm]	-	0 6	-	0.5	0 8	0 4	1 0	0 7	0 8	0 5	0 4	-	0 6	-	0 2	-	-	-	-	-	-
Yb [ppm]	-	4 0	-	3 3	4 8	2 2	6 3	4 5	4 8	3 3	2 4	-	3 5	-	1 3	-	-	-	-	-	-
Lu [ppm]	-	0 6	-	0 5	0 7	0 3	0 9	0 7	0.7	0 5	0 3	-	0 5	-	0 2	-	-	-	-	-	-
Ti/Zr	18 5	4 5	4 5	4 5	4 1	3 3	3 7	4 2	3 9	12 1	4 1	11 4	10 5	17 7	116 6	19 5	18 7	76 6	43 0	40 4	10 6
Altn Index	35	70	47	65	95	100	97	100	96	18	64	27	36	31	41	17	10	43	24	48	9
CCP Index	36	47	20	43	56	95	66	77	87	30	36	15	19	43	73	23	23	81	77	65	31

Table A4: Bulk rock geochemical data

sample	TH38-191	TH38-260	TH38-421	TH38-54	TH382A-156	TH382A-157	TH382A-175	TH382A-213	TH382A-220	TH382A-297	TH382A-356	TH382A-400	TH394-114	TH394-142	TH394-197	TH394-198	TH394-293	TH394-44	TH394-455	TH40-348	TH40-450
DDH	TH38	TH38	TH38	TH38	TH382A	TH382A	TH382A	TH382A	TH382A	TH382A	TH382A	TH382A	TH394	TH394	TH394	TH394	TH394	TH394	TH394	TH40	TH40
depth from	191	260 3	421	54 2	156	156 8	174.75	212 5	220 15	297 1	356 3	399 9	113 8	142 1	196.1	197	293	43 8	454 7	348 1	449 4
depth to	191 2	260 4	421 2	54 35	156 25	156 95	175	212.75	220 35	297 4	356 5	400 1	114 1	142 4	197	197 9	293 3	44	454 9	348 2	449 8
lithofacies	R1	R3	D3	R1	DV	DV	ϕA	D3	D3	D1	D1	D1	R2	R1	R1	R1	R1	R2	R1	D2	D2
altn facies	M	M	W2	M	W2,4	W4		W2,4	W4	W4	LA	W1	M	LA	M	QKF	QP	W4	QP	W4	W1,4
SiO2 [wt %]	77 8	65 8	76 6	75 4	75 8	59 0	51 8	73 3	69 7	75 9	74 0	72 4	72 6	77 4	78 0	78 2	75 7	76 4	78 8	70 9	65 2
TiO2 [wt %]	0 07	0 13	0 40	0 08	0 46	0 71	0 46	0 42	0 51	0 36	0 33	0 35	0 13	0 09	0 08	0 08	0 07	0 11	0 05	0 23	0 40
Al2O3 [wt %]	10 5	18 9	12 6	10 7	11 2	18 0	14 1	13 2	14 5	12 3	12.7	14 1	14 6	11 9	11 3	11 7	11 4	11 9	6 6	14 3	14 6
Fe2O3 [wt.%]	1 51	1 54	1 90	4 47	1 44	7 31	9 44	2 70	2 49	2 23	1 47	1 61	1 83	1 13	1 40	1 35	5 14	1 64	7 03	0 67	7 34
MnO [wt.%]	0 09	0 05	0 01	0 02	0 03	0 07	0 16	0 02	0 06	0 04	0 03	0 10	0 03	0 02	0 04	0 01	0 08	0 04	<0 01	<0 01	0 15
MgO [wt %]	3 13	3 27	0 29	2 91	0.79	3 34	7 65	0 85	1 21	1 32	0 52	0 47	1 53	0 76	1.43	0 59	2 38	0 67	0 39	0 21	2 55
CaO [wt %]	0.25	0 05	0 57	<0 01	1 68	1 05	3 52	0 87	2 71	0 70	1 47	3 35	0 33	0 46	0 25	0 14	<0 01	1 42	0 03	0 52	1 29
Na2O [wt %]	0 90	0 36	6 10	0 12	5 30	6 90	2 22	6 81	6 17	5 70	4 10	4 44	1 41	4 79	2 49	2 74	0 21	2 27	0 19	0 89	4 64
K2O [wt %]	3 40	5 99	1 35	2 43	0 34	0 39	1 26	0 10	0 55	0 39	3 82	2 61	5 09	1 82	3 09	3 64	2 39	4 04	2 01	10 15	2 80
P2O5 [wt %]	0 01	0 02	0 10	0 01	0 09	0 14	0 04	0.10	0 11	0 05	0 06	0 06	0 02	0 01	0 01	0 01	0 01	0 02	0 01	0 06	0 06
BaO [wt %]	0 16	0 04	0 08	0 06	0 01	0 01	0 01	<0 01	0 02	0 01	0 12	0 07	0 05	0 04	0 08	0 11	0 02	0 08	0 03	0 94	0 07
CuO [wt %]	<0 01	<0 01	<0 01	<0 01	<0 01	<0 01	<0 01	<0 01	<0 01	<0 01	<0 01	<0 01	<0 01	<0 01	<0 01	<0 01	<0 01	<0 01	<0 01	<0 01	<0 01
PbO [wt %]	<0 02	<0 02	<0 02	<0 02	<0 02	<0 02	<0 02	<0 02	<0 02	<0 02	<0 02	<0 02	<0 02	<0 02	<0 02	<0 02	<0 02	<0 02	<0 02	<0 02	<0 02
ZnO [wt %]	<0 01	<0 01	<0 01	<0 01	0 01	0 02	0 02	<0 01	0 01	0 01	0 01	0 10	0 01	0 01	0 03	0 03	0 01	0 01	0 01	<0 01	<0 01
LOI* [wt.%]	2 08	3 39	0 42	3 54	3 07	2 48	7 66	0 91	1 86	0 62	0 47	0 34	1 60	0 49	1 36	1 29	2 75	0 60	4.43	1 08	1 24
Total [wt %]	99 95	99 47	100 37	99 71	100 27	99 42	98 38	99 31	99 94	99 60	99.14	100 00	99 23	98 86	99 55	99 93	100 09	99 24	99 58	100 01	100 34
S [wt %]	0 06	0 23	<0 01	1 61	0 08	0 04	<0 01	0 02	0 01	<0 01	<0 01	0 07	<0 01	<0 01	0 49	0.79	0 65	0 01	5 42	0 44	0 18
CO2	-	-	-	-	-	-	-	-	-	-	-	-	<0 1	0 1	0 2	<0 1	<0 1	<0 1	<0 1	-	-
Ba [ppm]	1461	373	740	554	21	17	125	18	155	50	1285	838	601	324	775	1178	326	1056	243	8311	632
Cu [ppm]	11	21	<1	34	4	15	4	4	3	2	3	6	3	3	22	13	18	5	63	5	46
Pb [ppm]	16	21	7	4	5	5	6	4	6	3	11	43	8	13	24	86	11	20	46	60	26
Zn [ppm]	279	76	18	48	149	20	160	34	53	48	29	934	57	40	258	312	77	48	43	3 3	239
Ag [ppm]	< 0 5	< 0 5	< 0 5	< 0 5	< 0 5	< 0 5	< 0 5	< 0 5	< 0 5	< 0 5	< 0 5	< 0 5	<0 1	0 1	<0 1	0 2	<0.1	<0 1	0.1	< 0 5	< 0 5
As [ppm]	<3	<3	<3	3	<3	<3	<3	<3	<3	<3	<3	<3	<3	<3	<3	<3	<3	<3	14	14	<3
Bi [ppm]	< 0 1	< 0.1	< 0 1	1 0	0 2	0 2	< 0 1	0 2	0 2	0 1	0 1	38 9	0 3	0 3	0 2	0 6	0 3	0 6	8 4	0 2	< 0 1
Cd [ppm]	0 3	0 9	3 1	0 7	0.2	0 6	< 0 1	0 1	0 2	0 9	0 1	11 9	0 2	0 2	0 9	1 4	0 2	0 2	0 2	0 1	0 2
Cr [ppm]	1	<1	1	2	4	<2	214	<2	<2	3	5	3	<2	<2	<2	<2	<2	<2	<2	1	4
Cs [ppm]	1 8	1 8	0 1	0 3	0 6	0 6	1 5	0.2	0 4	0 7	0 5	0 3	1 0	0 5	0 5	0 4	0 3	1 1	0 5	0 7	6 9
Mo [ppm]	3 2	3 0	0 2	1.1	9 6	0 5	< 0 1	< 0 1	0 5	< 0 1	0 2	0 3	0 2	<0 1	1.5	1 8	1 4	0 8	2 8	0 5	< 0.1
Nb [ppm]	13	25	8	14	12	8	3	8	8	10	9	9	19	14	14	15	14	13	8	6	13
Ni [ppm]	2	2	2	2	4	3	42	<1	2	<1	1	1	1	1	2	1	1	2	1	2	3
Rb [ppm]	118	262	16	79	12	10	60	3	15	13	64	38	135	54	92	81	64	110	57	123	130
Sb [ppm]	0 2	0 2	0 1	< 0 1	0 3	0 4	0 4	0 2	0 2	< 0 1	0 2	0 2	0 2	0 2	0.2	0 3	0 2	0 2	0 3	0 6	0 1
Sr [ppm]	22	18	76	11	61	54	94	46	109	89	76	97	47	49	34	41	8	82	5	156	73
Th [ppm]	12	22	6	6	11	6	3	7	7	9	8	-	15	14	11	14	13	11	7	1	11
Tl [ppm]	1 2	3 1	0 1	0 4	< 0 1	< 0 1	0 3	< 0 1	< 0 1	< 0 1	0 5	0 3	0 6	<0 5	1.9	1 4	<0 5	0 5	0 6	1 4	1 4
U [ppm]	4.0	4 9	1 8	2 2	2 8	1 9	0 7	1 9	1 9	2 4	2 2	2 4	3 1	2 6	3 6	3 2	2 2	2 2	1 5	1 3	2 7
V [ppm]	3	1	21	3	65	23	243	21	17	5	12	9	1	0	3	<1.5	<1 5	3	<1 5	9	8
Y [ppm]	41	51	24	27	35	25	14	25	28	32	26	27	45	34	38	43	36	40	20	18	35
Zr [ppm]	119	224	131	119	215	144	54	137	152	179	164	168	188	137	115	136	128	146	72	107	225
La [ppm]	-	-	14 4	-	-	-	-	11 7	23 2	100 1	35 3	36 5	-	-	-	-	-	-	-	-	-
Ce [ppm]	-	-	28 6	-	-	-	-	25 6	43 0	179 0	65 8	62 1	-	-	-	-	-	-	-	-	-
Pr [ppm]	-	-	3 8	-	-	-	-	3 6	5 6	19 9	7 9	7 6	-	-	-	-	-	-	-	-	-
Nd [ppm]	-	-	15 5	-	-	-	-	15 3	22.8	69 3	28.7	29 1	-	-	-	-	-	-	-	-	-
Sm [ppm]	-	-	3 6	-	-	-	-	4 0	4 4	10 7	5 2	5 3	-	-	-	-	-	-	-	-	-
Eu [ppm]	-	-	1 0	-	-	-	-	1 1	1 1	2 0	1 1	1 3	-	-	-	-	-	-	-	-	-
Gd [ppm]	-	-	4 0	-	-	-	-	4 5	4 8	8 8	5 2	5 4	-	-	-	-	-	-	-	-	-
Tb [ppm]	-	-	0 7	-	-	-	-	0 8	0 8	1 1	0 9	0 8	-	-	-	-	-	-	-	-	-
Dy [ppm]	-	-	4 1	-	-	-	-	4 7	4 7	5 6	4 8	4 5	-	-	-	-	-	-	-	-	-
Ho [ppm]	-	-	0 9	-	-	-	-	1.1	1 2	1 3	1 1	1.1	-	-	-	-	-	-	-	-	-
Er [ppm]	-	-	2 6	-	-	-	-	3 0	3 4	3 5	3 2	3 1	-	-	-	-	-	-	-	-	-
Tm [ppm]	-	-	0 5	-	-	-	-	0 5	0 6	0 7	0 6	0 6	-	-	-	-	-	-	-	-	-
Yb [ppm]	-	-	2.7	-	-	-	-	3 2	3 7	4 0	3 5	3 5	-	-	-	-	-	-	-	-	-
Lu [ppm]	-	-	0 4	-	-	-	-	0 5	0 5	0 6	0 5	0 5	-	-	-	-	-	-	-	-	-
Ti/Zr	3 5	3 5	18 3	4 0	12 9	29 6	51 9	18 5	20 2	12.2	12 2	12 6	4 1	3 9	4 1	3 5	3 3	4.4	4 0	12 9	10 7
Altn Index	85	96	20	98	14	32	61	11	17	21	44	28	79	33	62	59	96	56	92	88	47
CCP Index	51	42	21	73	27	58	82	32	34	35	19	21	33	21	33	22	73	25	75	7	55

Table A4: Bulk rock geochemical data

sample	TH40-506	TH401-111	TH401-120	TH401-89	TH402-103	TH402-113	TH402-123	TH402-176	TH402-219	TH402-321	TH402-398	TH402-88	TH410-121	TH410-131	TH410-131 2	TH410-132	TH410-150	TH410-313	TH410-323	TH410-323	TH410-390
DDH	TH40	TH401	TH401	TH401	TH402	TH402	TH402	TH402	TH402	TH402	TH402	TH402	TH410	TH410	TH410	TH410	TH410	TH410	TH410	TH410	TH410
depth from	505.6	111 2	120	89 4	102 6	113	123	175 5	219 1	320 8	398	88 3	121.4	131	131 2	131 4	150 1	312 8	322 8	323	389 8
depth to	505 7	111 45	121	89 6	102 85	113 15	123 2	175 75	219 4	321	399	88 5	121 5	131 2	131 4	131.6	150.3	313	322 9	323 1	389 85
lithofacies	QEV	R1	R1	D1	D3	D3	D1	D1	DIO	D1	R1	D3	RV	R1	R1	R1	R1	R1	R1	R3	R3
altn facies	W4	M	CP	LA	W2,3	W2	W3,4	W3,1		LA, W3,1	QP	W2	QKF	QKF	QKF	W4	M	QKF	M	QKF	LA	QKF
SiO2 [wt %]	63 7	62 0	32 1	73 9	76 4	65 4	77 1	74.4	48 5	73 7	51 6	76 1	85 5	73 3	78 6	81 1	79 2	78 2	75 8	80 8	83 4
TiO2 [wt %]	0 25	0 15	0 11	0 36	0 40	0 54	0 33	0 33	0 83	0 34	0 05	0 49	0 05	0 10	0 07	0 07	0 08	0 10	0.12	0 10	0 08
Al2O3 [wt %]	17.6	18 4	17 3	13 4	12 6	16 4	12 0	12 4	16 4	12 4	6 7	12 2	7.4	12 6	11 1	10 0	10 5	10 9	11 9	10.7	8 3
Fe2O3 [wt %]	3 46	1 82	17 67	2 47	1 92	4 62	2 13	1 67	10 57	2 44	23 96	2 52	0 61	2.09	1 05	0.78	0 59	1 46	1 25	0 40	1.00
MnO [wt %]	0 05	0 01	0 21	0 05	0 02	0 07	0 02	0 06	0 18	0 08	0 01	0 03	0 01	0 07	0.03	0 01	0 02	0 03	0 02	0 01	<0 01
MgO [wt %]	3 14	0.64	9 36	0 68	0 36	1 90	0 78	0 29	8 45	0 49	0 64	0 69	0 57	2 01	0.82	0 42	0 59	1 22	1 15	0 20	0.10
CaO [wt %]	0 74	0 67	0 07	0 91	0 82	1 54	0 99	3 68	9 90	1 87	0 07	1 11	0 01	0 05	0 20	0 24	0 09	0 19	0 29	1 08	0 19
Na2O [wt %]	1 81	0 71	0 24	5 63	5 83	7 00	5 25	3 54	2 24	3 15	0.12	5 02	0 12	0 19	3.13	3 42	0 38	1 90	1 49	4 06	0 42
K2O [wt %]	5 03	12 97	3 27	2 04	1 01	0 28	0 67	2 42	1 23	4 09	1 91	1 28	4 67	7.19	3 94	3 09	8 07	4 95	7 07	2 45	6.69
P2O5 [wt %]	0 06	0 05	0 03	0 06	0 10	0 13	0 06	0 06	0 15	0 06	0 01	0 11	0 01	0 02	0 01	0 01	0 02	0 02	0 02	0 01	0.06
BaO [wt %]	0 35	0 75	0 31	0 06	0 08	0 01	0 02	0 06	0 05	0 03	0 02	0 04	0 23	0 34	0 19	0 12	0 45	0 18	0.26	0.10	0 19
CuO [wt %]	<0 01	<0 01	3 79	<0 01	<0 01	<0 01	<0 01	<0 01	<0 01	<0 01	0 06	<0 01	<0 01	<0 01	<0 01	<0 01	<0 01	<0 01	<0 01	<0,01	<0 01
PbO [wt %]	<0 02	<0 02	0 17	<0 02	<0 02	<0 02	<0 02	<0 02	<0 02	<0 02	0 01	<0 02	<0 02	<0 02	<0 02	<0 02	<0 02	<0 02	<0 02	<0 02	<0 02
ZnO [wt.%]	<0 01	0 01	2 74	0 01	0 01	0 01	0 01	<0 01	0 01	0 01	0 09	0 01	<0 01	<0.01	<0 01	<0 01	<0 01	<0 01	<0 01	<0 01	<0 01
LOI* [wt.%]	3 33	1 60	13 19	0 37	0 41	1 78	0 56	1.41	2 13	0 63	15 67	0 62	0.98	1.7	0 94	0 81	0 6	0 91	0.75	0.77	0 75
Total [wt %]	99 47	99 83	100 57	99 95	99 90	99 62	99 91	100 27	100 66	99 34	100 91	100.18	100 24	99 67	100 05	100 14	100 59	100 01	100 12	100.70	101.12
S [wt %]	1.23	1 27	10 35	0 01	<0 01	<0 01	<0 01	<0 01	0 02	<0 01	18 24	<0 01	0 16	0 47	0 36	0 38	0 1	0 01	0 06	0 15	0 01
CO2	-	-	-	-	0 6	0 6	0 3	1 0	0 1	0 2	0 1	0 3	0 4	0 2	0 2	-	-	-	-	-	-
Ba [ppm]	3152	7500	2800	522	750	98	200	666	410	579	265	538	2071	2910	1664	1087	4039	1637	2222	912	1841
Cu [ppm]	11	7	30296	2	2	4	4	3	13	15	761	3	51	4	3	2	4	22	4	3	3
Pb [ppm]	31	38	1528	8	5	9	8	6	7	11	65	6	15	7	5	4	9	14	21	15	24
Zn [ppm]	111	62	22041	55	28	86	27	28	110	38	759	43	46	50	20	9	14	65	38	214	13
Ag [ppm]	0 7	< 0 5	31 8	< 0 5	<0.1	<0 1	<0 1	<0 1	<0 1	<0 1	0 5	<0 1	0 1	<0 1	<0 1	< 0 5	< 0 5	< 0 5	< 0 5	0 9	< 0 5
As [ppm]	58	17	26	<3	<3	<3	<3	<3	<3	<3	59	<3	<3	<3	<3	4	<3	<3	<3	6	<3
Bi [ppm]	0 8	0 5	23 9	0 2	0 1	<0 1	<0 1	0 3	0 3	0 2	23 7	0.4	0 5	0 6	0 5	0 4	0 4	< 0 1	0 2	6 8	< 0 1
Cd [ppm]	0 1	0 2	35 6	0 1	0 1	0 1	0 1	0 2	0 2	0 2	2 2	0 1	0 1	0.1	0 1	0 1	< 0 1	< 0 1	0 1	1 7	< 0 1
Cr [ppm]	3	<2	23	2	2	3	3	2	113	<2	189	2	2	1	2	2	1	2	2	3	2
Cs [ppm]	2 9	2 5	3 2	0 3	0 2	0 4	0.5	0 5	1 6	0 5	0 5	0 5	1 0	1 2	0 7	0 2	0 5	1 8	1 3	0 2	1 0
Mo [ppm]	0 4	0 1	5 9	0 2	0 3	<0 1	<0 1	0 3	<0 1	0 3	15 1	0 4	6 3	4 8	2 1	1 7	4 2	0 1	0 2	0 4	0 2
Nb [ppm]	20	25	15	10	7	10	9	9	4	10	9	8	10	18	12	11	13	15	17	13	12
Ni [ppm]	6	4	17	<1	1	1	1	1	43	<1	11	2	2	1	2	2	1	2	1	2	2
Rb [ppm]	178	204	108	36	16	9	27	39	34	59	44	23	95	152	69	47	145	129	150	41	106
Sb [ppm]	2 2	2 2	6 9	0 5	0 2	0 6	0 2	0 3	0 3	0 2	0 6	0 2	0 3	0 2	0 3	0 2	0 1	< 0 1	0.2	0 4	0 4
Sr [ppm]	72	108	31	64	132	190	143	112	732	132	16	151	42	47	54	50	33	42	66	42	40
Th [ppm]	13	21	17	9	6	10	8	8	5	8	11	7	7	14	9	9	10	12	13	10	8
Tl [ppm]	3 3	21 2	6 6	0 6	<0 5	<0 5	<0 5	<0 5	<0 5	<0 5	0 7	<0 5	0 6	0 8	<0 5	0 3	1 1	0 8	1 0	0 3	0 9
U [ppm]	1 9	5 0	3 9	2 4	1 7	0 9	1 7	1 5	1 0	1 6	1 8	1 6	1 7	2 8	1 9	2 5	3 0	2 9	4 0	3 2	2 1
V [ppm]	8	15	6	6	20	33	7	6	325	5	3	41	3	5	3	3	5	<1	3	2	3
Y [ppm]	51	60	79	28	26	33	25	26	17	26	39	30	19	47	28	23	33	38	41	34	20
Zr [ppm]	258	225	170	177	131	182	161	158	62	162	76	139	79	159	104	101	116	161	185	135	121
La [ppm]	-	-	-	-	-	-	-	-	-	-	-	-	-	-	-	-	-	-	-	-	4 4
Ce [ppm]	-	-	-	-	-	-	-	-	-	-	-	-	-	-	-	-	-	-	-	-	9 8
Pr [ppm]	-	-	-	-	-	-	-	-	-	-	-	-	-	-	-	-	-	-	-	-	1 3
Nd [ppm]	-	-	-	-	-	-	-	-	-	-	-	-	-	-	-	-	-	-	-	-	6 1
Sm [ppm]	-	-	-	-	-	-	-	-	-	-	-	-	-	-	-	-	-	-	-	-	2 1
Eu [ppm]	-	-	-	-	-	-	-	-	-	-	-	-	-	-	-	-	-	-	-	-	0 4
Gd [ppm]	-	-	-	-	-	-	-	-	-	-	-	-	-	-	-	-	-	-	-	-	2 8
Tb [ppm]	-	-	-	-	-	-	-	-	-	-	-	-	-	-	-	-	-	-	-	-	0 6
Dy [ppm]	-	-	-	-	-	-	-	-	-	-	-	-	-	-	-	-	-	-	-	-	3.5
Ho [ppm]	-	-	-	-	-	-	-	-	-	-	-	-	-	-	-	-	-	-	-	-	0 8
Er [ppm]	-	-	-	-	-	-	-	-	-	-	-	-	-	-	-	-	-	-	-	-	2 3
Tm [ppm]	-	-	-	-	-	-	-	-	-	-	-	-	-	-	-	-	-	-	-	-	0 4
Yb [ppm]	-	-	-	-	-	-	-	-	-	-	-	-	-	-	-	-	-	-	-	-	2 4
Lu [ppm]	-	-	-	-	-	-	-	-	-	-	-	-	-	-	-	-	-	-	-	-	0.3
Ti/Zr	5 8	3 9	4 0	12 3	18 5	17 8	12 2	12.4	80 0	12 7	4 0	21 3	3 8	3 8	4 0	4 2	4 1	3 7	3 9	4 4	4 0
Altn Index	76	91	98	29	17	20	19	27	44	48	93	24	98	97	59	49	95	75	82	34	92
CCP Index	48	14	88	27	23	45	31	23	84	27	92	32	19	35	20	15	12	27	21	8	12

Table A4: Bulk rock geochemical data

sample	TH410-94	TH410-97	TH412-145	TH412A-551	TH412A-558	TH412B-645	TH412B-676	TH412B-786	TH41A-439	TH41A-479	TH41A-575	TH41A-653	TH41A-713	TH471-104	TH471-228	TH5-104	TH5-166	TH5-178	TH5-22	TH5-256	TH5-301
DDH	TH410	TH410	TH412	TH412A	TH412A	TH412B	TH412B	TH412B	TH41A	TH41A	TH41A	TH41A	TH41A	TH471	TH471	TH5	TH5	TH5	TH5	TH5	TH5
depth from	93 7	97 4	145 2	550 6	557.7	645 4	674 4	785 7	439	479 2	575.1	653 25	713 4	104 1	228	104	165 5	178	21 5	255 5	301
depth to	93 8	97 45	145 45	550 75	557 8	645 5	674 5	785 9	439 15	479 3	575 2	653 3	713 55	104 3	228 35	104 35	165 75	178 25	21,7	255 8	301 4
lithofacies	R1	R3	R1	R1	R1	R1	R2	R1	RV	D3	R1	R1	R1	R1	DIO	D3	SBA	DV	D2	R1	RV
altn facies	M	QKF	M	W2	W1	QKF	W4	DT	M	W4	DT	M	QKF	M		W4		W4	W4	DT	M
SiO2 [wt %]	68 8	80 4	80 3	79 3	73 1	80 5	76 1	61 3	65 0	70 1	76 7	60 6	75 9	73 4	52 7	69 4	83 7	66 4	76 2	77 8	73 7
TiO2 [wt.%]	0 14	0 09	0 07	0 08	0 08	0 07	0 10	0 11	0 18	0 45	0 07	0 12	0 10	0 08	0 91	0.45	0 04	0 40	0 31	0 07	0 09
Al2O3 [wt %]	15 8	10 0	10 3	11 4	10 7	9 6	12 2	12 4	16 8	14 4	10 2	18 3	12 2	12 0	17 9	14 2	1 8	15 3	11 7	8 8	13 2
Fe2O3 [wt %]	1 83	0 39	2 51	0 96	1 95	0 67	0 47	3 92	2 68	4 10	0 99	2 32	1 70	5 74	10 02	4 63	0 29	3 39	2 96	1 90	1.79
MnO [wt %]	0.04	0 01	0 02	0 02	0 09	0 01	0 02	0 46	0 04	0 05	0 08	0 12	0 05	0 18	0 19	0 06	<0 01	0 03	0 05	0 06	0 02
MgO [wt %]	1.59	0 26	1 32	0 89	1 44	0 26	0 53	4 39	3 29	1 16	4 33	3 36	1 12	2 28	4 64	2 91	0 27	5.62	1 27	2.14	3.01
CaO [wt %]	0.01	0.22	0 02	1 58	5 21	0 06	0 19	11 61	0 85	1 38	1 75	0 12	0 08	0 01	8 23	0 90	0 13	0 10	1 16	3 08	0 13
Na2O [wt.%]	0 40	0 39	0 24	4 78	3.18	1 39	1 62	1.78	0 37	6 42	1 57	0 43	0 42	0 28	2.96	5 39	<0 05	0 18	4 32	0 84	2 45
K2O [wt %]	8 88	7 88	3 39	0 53	0 64	6 44	7 96	0 62	5 56	1 18	2 80	11 37	6 36	3 03	1 36	0 51	0 53	5 65	1 29	3 06	2 08
P2O5 [wt %]	0 03	0 02	0 02	0 01	0 03	0 02	0 02	0 05	0 04	0 11	0 02	0 03	0 02	0 01	0 26	0 09	0 08	0 04	0 05	0 05	0 01
BaO [wt.%]	0 28	0 20	0 08	0 02	0 01	0 21	0 21	0 03	1 11	0 06	0 06	0 25	0 20	0 06	0 06	0 01	6 52	0 44	0.02	0 15	0 03
CuO [wt %]	<0.01	<0 01	<0.01	<0 01	<0 01	<0 01	<0 01	<0 01	<0 01	<0 01	<0 01	<0 01	<0 01	0 01	<0 01	<0 01	<0 01	<0 01	<0 01	<0 01	<0 01
PbO [wt %]	<0 02	<0 02	<0 02	<0 02	<0.02	<0 02	<0 02	<0 02	<0 02	<0 02	<0.02	<0 02	<0 02	<0 02	<0 02	<0 02	<0 02	<0 02	<0 02	<0 02	<0 02
ZnO [wt %]	<0.01	<0 01	<0 01	<0 01	<0 01	<0 01	<0.01	<0 01	<0 01	<0 01	<0.01	<0 01	<0 01	0 01	0.01	0 01	0.01	0,03	0 01	0.01	0.01
LOI* [wt %]	1.98	0 55	2 27	0 73	3 47	0 72	0 65	2 85	3 73	0 64	1 38	2 02	1 71	2 71	1 20	1 49	1 63	2 46	0 51	2 12	2 26
Total [wt %]	99 83	100 35	100 54	100.36	99 90	99 99	100 08	99 48	99 65	100 01	99 94	99 11	99 80	99 74	100 41	100 00	94 98	100 07	99 83	100 11	98 73
S [wt %]	0 37	0 18	0 99	0.14	0.16	0 42	0 1	0 01	<0 01	<0 01	0 01	0 4	0 66	0 78	0 07	0 03	1 65	0 02	0.01	1.33	<0 01
CO2	<0 1	0 3	-	-	-	-	0 2	-	-	-	-	-	-	0.1	0 2	<0 1	0 1	<0 1	<0 1	1 0	0 4
Ba [ppm]	2440	1772	726	145	140	1927	1915	201	10225	490	510	2011	1773	633	331	143	65200	4400	204	1519	413
Cu [ppm]	2	3	8	1	3	4	16	3	9	2	6	8	10	109	34	3	33	38	3	25	2
Pb [ppm]	28	34	26	8	15	25	69	33	25	6	64	212	66	11	6	7	231	25	8	21	6
Zn [ppm]	109	20	108	41	64	11	70	230	176	92	209	267	145	103	102	77	21	233	111	98	78
Ag [ppm]	<0 1	<0 1	< 0 5	< 0 5	< 0 5	< 0 5	<0 1	< 0 5	< 0 5	< 0 5	< 0 5	< 0 5	0 5	<0 1	<0 1	<0 1	0 4	0 7	<0 1	1.1	<0 1
As [ppm]	5	7	10	<3	<3	<3	<3	<3	<3	<3	<3	6	13	<3	<3	<3	<3	<3	<3	21	<3
Bi [ppm]	0 3	0 4	2 8	0 2	0.6	0 1	0 2	3 4	0 1	< 0 1	< 0 1	0 3	0 6	3 0	0 3	<0 1	<0 1	<0 1	0 2	0 2	0.1
Cd [ppm]	0 1	0 2	0 4	< 0 1	0 7	< 0 1	0 3	0 6	0 1	< 0 1	0 2	0 5	0 4	0 2	0 1	0 2	<0 1	0 2	1 5	0 3	0 1
Cr [ppm]	1	2	2	2	2	2	2	1	3	2	1	1	2	1	8	3	<2	4	<2	<2	<2
Cs [ppm]	2 0	0 8	1 6	0 6	0 5	0 5	0 4	0 5	5.4	0 5	2 7	4 9	1 6	1 1	2 7	0 6	0.2	4 3	1 3	1 8	0 6
Mo [ppm]	2 3	31 3	2 8	0 8	0 2	1 6	7 0	< 0 1	< 0 1	0 2	1 8	3 6	8 0	1 8	1 0	<0 1	<0 1	0 2	<0 1	2 6	0.1
Nb [ppm]	19	13	14	15	15	12	13	24	25	9	12	22	17	15	6	9	3	13	9	13	16
Ni [ppm]	3	2	2	2	2	2	2	2	9	2	2	2	2	1	5	1	<1	2	2	2	1
Rb [ppm]	222	144	107	25	35	129	143	20	189	22	105	310	172	91	45	19	9	194	63	107	81
Sb [ppm]	0 5	0 5	0 2	0 8	0 6	0 2	0 2	0 2	0 2	0 5	0 2	0 3	0 6	0 2	0 2	0 3	0 4	0 4	0 2	6 5	0 3
Sr [ppm]	51	45	14	119	145	66	62	116	52	91	89	55	45	7	439	120	1070	31	104	77	65
Th [ppm]	15	11	11	12	13	10	13	16	14	7	11	23	15	13	7	8	-	10	7	10	15
Tl [ppm]	1 6	1 2	0 8	1 1	0 9	1 2	1 2	0 2	3 7	0 4	0 9	4 0	2 0	<0 5	<0 5	<0 5	<0 5	4 4	<0 5	4 8	1.1
U [ppm]	4 0	2 3	2 5	3 6	6 0	3 1	2 6	2 3	1 8	2 0	3 2	6 2	4 3	2 5	1 2	1 6	0 9	2 0	1 4	2 2	1 8
V [ppm]	4	3	2	1	2	2	2	11	32	25	2	4	2	<1 5	237	37	11	11	<1 5	4	<1.5
Y [ppm]	68	28	33	39	41	30	33	66	54	27	30	53	47	40	22	28	9	36	31	57	41
Zr [ppm]	201	139	115	131	131	107	149	155	256	150	113	211	157	135	70	156	20	202	160	114	147
La [ppm]	-	-	-	-	-	-	-	-	-	-	-	-	-	-	-	-	-	-	-	-	-
Ce [ppm]	-	-	-	-	-	-	-	-	-	-	-	-	-	-	-	-	-	-	-	-	-
Pr [ppm]	-	-	-	-	-	-	-	-	-	-	-	-	-	-	-	-	-	-	-	-	-
Nd [ppm]	-	-	-	-	-	-	-	-	-	-	-	-	-	-	-	-	-	-	-	-	-
Sm [ppm]	-	-	-	-	-	-	-	-	-	-	-	-	-	-	-	-	-	-	-	-	-
Eu [ppm]	-	-	-	-	-	-	-	-	-	-	-	-	-	-	-	-	-	-	-	-	-
Gd [ppm]	-	-	-	-	-	-	-	-	-	-	-	-	-	-	-	-	-	-	-	-	-
Tb [ppm]	-	-	-	-	-	-	-	-	-	-	-	-	-	-	-	-	-	-	-	-	-
Dy [ppm]	-	-	-	-	-	-	-	-	-	-	-	-	-	-	-	-	-	-	-	-	-
Ho [ppm]	-	-	-	-	-	-	-	-	-	-	-	-	-	-	-	-	-	-	-	-	-
Er [ppm]	-	-	-	-	-	-	-	-	-	-	-	-	-	-	-	-	-	-	-	-	-
Tm [ppm]	-	-	-	-	-	-	-	-	-	-	-	-	-	-	-	-	-	-	-	-	-
Yb [ppm]	-	-	-	-	-	-	-	-	-	-	-	-	-	-	-	-	-	-	-	-	-
Lu [ppm]	-	-	-	-	-	-	-	-	-	-	-	-	-	-	-	-	-	-	-	-	-
Ti/Zr	4 2	3 9	3.7	3 7	3 7	3 9	4 0	4 3	4 2	18 0	3 7	3 4	3 8	3 5	78 6	17 4	12 0	11 9	11 8	3 7	3.7
Altn Index	96	93	95	18	20	82	82	27	88	23	68	96	94	95	35	35	86	98	32	57	66
CCP Index	26	7	50	25	46	10	9	77	49	39	54	32	28	69	76	55	50	60	41	50	50

Table A4: Bulk rock geochemical data

sample	TH5-308	TH5-337	TH5-339	TH5-358	TH5-394	TH5-54	TH61-118	TH61-124	TH61-157	TH61-197	TH61-284	TH61-287	TH61-86	TH61-86	TH62C-142	TH62C-46	TH62C-510	TH62C-680	TH62C-825	TH85-125	TH85-159
DDH	TH5	TH5	TH5	TH5	TH5	TH5	TH61	TH61	TH61	TH61	TH61	TH61	TH61	TH61	TH62C	TH62C	TH62C	TH62C	TH62C	TH85	TH85
depth from	307 5	336 5	338 8	357 5	393 8	54	117 6	123 9	156 4	196 6	283 5	286 5	85 6	85 8	141 6	46	510 1	679 5	825 2	124 5	159 1
depth to	307.7	336 75	339	357 8	394 1	54 3	117 9	124 15	156 6	196 8	283 65	286 75	85 75	85 95	141.8	46 2	510 15	679 75	825 4	124.9	159 45
lithofacies	R1	R1	R1	R1	R1	DV	RV	R1	R1	R1	D1	D1	R1	R1	D2	R4	D2	D2	D2	R1	R1
altn facies	M	W1,3,4	LA	W1,3	QP	W4	M	M	QKF	W1	W3,2	W1	M	QKF	W2	W2	W2	W3,1	W1	M	M
SiO2 [wt %]	69 6	81 6	73 4	66 4	76 6	72 3	75 3	71 1	78 5	77 3	81 4	62 6	81 3	74 4	81 4	73 7	79.7	76 1	73 5	75 3	75 3
TiO2 [wt %]	0 13	0 06	0 12	0 14	0 07	0 48	0 09	0 11	0 08	0 06	0 27	0 49	0 07	0 11	0 18	0 35	0.27	0 21	0 25	0 07	0.09
Al2O3 [wt.%]	16 0	9 8	13 8	14 0	11 5	13 5	13 7	14 8	11 6	10 7	10,2	17 8	9 7	13 8	10 4	13 5	10 3	10 4	10 1	11.1	12 8
Fe2O3 [wt.%]	2 43	0 79	1.66	1 73	2 76	3 80	1 21	2 20	0 88	1 26	0 70	4 55	0 84	1 56	1 17	2 73	2 17	2 02	2 41	2 32	1 96
MnO [wt %]	0 02	<0 01	0 01	0 03	0 03	0 05	0 02	0 06	0 01	0 02	0 01	0 06	0 02	0 03	0 02	0 05	0 04	0.11	0 10	0 06	0 09
MgO [wt %]	3.21	0.14	0 70	0 48	2.75	1 92	1 05	2 54	0 61	0 50	0 32	4 68	0 60	1 19	0 23	0 78	0 26	0 43	0 66	1 90	2 51
CaO [wt %]	0.28	0 65	0 71	5 12	0 01	0 96	0 23	0 42	0 12	1 77	1 51	0.77	0 84	0 34	0 33	0 97	0 45	4 47	4 81	3.03	0 08
Na2O [wt.%]	2.72	3 49	4 97	3 50	0 22	4 62	0,90	0 36	0 37	0 59	4 35	1,42	1 76	0 95	5 56	6 23	5 12	3 76	2 42	0.59	0 10
K2O [wt %]	2.77	2 33	3 46	5.16	3 06	1 51	6 74	6 17	7 60	6.28	0 41	3 92	4 22	6 33	0 29	0 89	0 93	0 63	3 33	3 68	4 41
P2O5 [wt %]	0 02	0 01	0 02	0 02	0 01	0 11	0 02	0 02	0 02	0 03	0 05	0 07	0 01	0 01	0 03	0 07	0 04	0 05	0 06	0 02	0 01
BaO [wt %]	0 05	0 10	0 09	0 12	0 05	0 01	0 13	0 07	0 17	0 34	0 01	0 03	0 07	0.10	0.01	0 04	0 06	0 02	0 15	0 10	0 05
CuO [wt %]	<0 01	<0 01	<0 01	<0 01	<0 01	<0 01	<0 01	<0 01	<0 01	<0 01	<0 01	<0 01	<0 01	<0 01	<0 01	<0 01	<0 01	<0 01	<0 01	<0 01	<0 01
PbO [wt %]	<0 02	<0 02	<0 02	<0 02	<0 02	<0 02	<0.02	<0 02	<0 02	<0 02	<0 02	<0 02	<0 02	<0 02	<0 02	<0 02	<0 02	<0 02	<0 02	0 02	0 02
ZnO [wt %]	0 01	<0 01	0 01	0 01	<0 01	0 01	0 01	0 01	0 01	0 01	<0 01	0 02	0.01	0 01	<0 01	<0 01	<0 01	<0 01	<0 01	0 01	0 05
LOI* [wt %]	2 66	0.28	0 45	3 09	2 76	1 02	1 32	2 08	0 76	1 47	1 02	3 81	0 52	1 24	0 48	0 65	0 41	2 3	2 59	1.75	2 50
Total [wt %]	99 88	99 16	99.40	99 77	99 82	100 24	100 63	99 95	100 71	100 36	100,17	100 22	99 91	100 01	100.14	99 94	99 77	100 47	100 37	99 93	99 95
S [wt %]	<0 01	<0 01	<0 01	<0 01	0 69	<0 01	0 20	0 02	0 13	0 69	0 02	<0 01	<0 01	<0 01	<0 01	0 01	<0 01	0,02	0 04	1 39	0 81
CO2	0 3	0.2	0 2	3 0	<0 1	<0 1	0 1	0 2	0 2	0 5	0 7	0 6	0 2	<0,1	-	-	-	-	-	-	-
Ba [ppm]	545	1001	1020	1320	624	229	1273	758	1675	3400	107	399	766	808	78	427	502	165	1368	1028	588
Cu [ppm]	3	3	2	4	1	2	5	3	7	45	2	3	2	3	22	63	<1	35	9	11	24
Pb [ppm]	7	11	19	30	5	4	17	17	38	46	5	3	11	11	7	10	3	14	15	181	380
Zn [ppm]	82	10	94	54	48	62	41	89	85	72	16	108	28	49	31	46	34	44	118	133	483
Ag [ppm]	<0 1	<0 1	<0 1	<0 1	<0 1	<0 1	<0 1	<0 1	0 1	0 2	<0 1	<0 1	<0 1	<0.1	< 0 5	< 0 5	< 0 5	< 0 5	< 0 5	< 0 5	< 0 5
As [ppm]	<3	<3	<3	<3	<3	<3	<3	<3	<3	4	<3	<3	<3	<3	<3	<3	<3	<3	<3	3	5
Bi [ppm]	0 2	0.1	0 1	0 5	4 5	0 1	0 2	0.1	5 4	1 2	0 5	0 3	0 4	0.1	≤ 0 1	0 1	< 0 1	1 2	0 1	0 5	0.9
Cd [ppm]	0 1	<0 1	0 1	0 2	0 1	0 1	0 1	0 1	0 4	0 7	0 1	0.2	<0 1	0.4	< 0 1	0.1	0 1	0.1	0 2	0 2	1 9
Cr [ppm]	2	<2	2	<2	<2	<2	<2	<2	4	3	<2	2	<2	<2	3	3	4	3	2	3	<2
Cs [ppm]	0 7	0 2	1.1	0 7	0 5	0 7	1 1	1 7	0 7	1 0	0 4	1 9	0 5	0.9	0 4	1 3	0 2	1.3	0 7	1 4	1.3
Mo [ppm]	<0 1	<0 1	<0 1	<0.1	3 2	<0 1	1 8	0.2	1.9	1 6	<0.1	0 6	<0 1	<0 1	< 0 1	0 1	0 1	0 2	0 4	1 1	1.3
Nb [ppm]	21	11	19	16	16	9	17	19	13	12	8	15	11	18	7	9	9	7	9	12	16
Ni [ppm]	2	1	3	2	1	1	2	1	2	2	1	1	1	1	1	3	2	2	1	1	2
Rb [ppm]	111	42	80	113	100	63	178	206	165	120	16	110	93	167	5	19	13	24	55	110	164
Sb [ppm]	0 3	0 4	0 3	0 5	0 2	0 2	0 2	0 3	0 7	1 2	0 4	0 4	0 5	0.2	< 0 1	0 1	0 2	0 2	0 3	0 3	0 3
Sr [ppm]	78	81	120	128	8	87	36	30	28	85	110	57	49	33	40	59	48	85	76	48	11
Th [ppm]	19	9	18	16	12	8	14	16	12	11	6	12	9	15	4	7	7	6	6	11	14
Tl [ppm]	1 5	<0 5	0 9	1 0	0 7	<0 5	1 5	1 5	1 6	3 0	<0 5	<0 5	0 5	0 7	< 0 1	0 1	< 0 1	0 1	0 4	1 6	1.3
U [ppm]	2.1	1 2	2 0	1 3	2 5	1.2	2 9	4 2	2 4	3 2	1 4	2 5	2.0	3.1	1 6	2 6	1 9	1 7	1 8	3 3	3 6
V [ppm]	<1 5	<1 5	2	2	<1 5	21	2	4	<1 5	6	5	15	<1 5	<1 5	6	31	2	2	4	<1.5	<1 5
Y [ppm]	67	39	43	50	41	30	38	55	37	34	22	44	35	52	19	21	26	30	26	42	48
Zr [ppm]	194	100	178	161	131	155	143	163	122	122	128	255	95	158	116	134	151	112	142	116	137
La [ppm]	-	-	-	-	-	-	-	-	-	-	-	-	-	-	-	20 9	-	-	-	46 8	43 4
Ce [ppm]	-	-	-	-	-	-	-	-	-	-	-	-	-	-	-	37 5	-	-	-	91 6	81 8
Pr [ppm]	-	-	-	-	-	-	-	-	-	-	-	-	-	-	-	4 6	-	-	-	11 3	10 3
Nd [ppm]	-	-	-	-	-	-	-	-	-	-	-	-	-	-	-	18 1	-	-	-	43 1	40 5
Sm [ppm]	-	-	-	-	-	-	-	-	-	-	-	-	-	-	-	3 8	-	-	-	8 5	8 4
Eu [ppm]	-	-	-	-	-	-	-	-	-	-	-	-	-	-	-	0 9	-	-	-	1 4	1 2
Gd [ppm]	-	-	-	-	-	-	-	-	-	-	-	-	-	-	-	3 8	-	-	-	8 1	7 8
Tb [ppm]	-	-	-	-	-	-	-	-	-	-	-	-	-	-	-	0 6	-	-	-	1 2	1 2
Dy [ppm]	-	-	-	-	-	-	-	-	-	-	-	-	-	-	-	3 6	-	-	-	6 4	5 7
Ho [ppm]	-	-	-	-	-	-	-	-	-	-	-	-	-	-	-	0 8	-	-	-	1 4	1 2
Er [ppm]	-	-	-	-	-	-	-	-	-	-	-	-	-	-	-	2 4	-	-	-	3 8	3 1
Tm [ppm]	-	-	-	-	-	-	-	-	-	-	-	-	-	-	-	0 5	-	-	-	0 7	0 6
Yb [ppm]	-	-	-	-	-	-	-	-	-	-	-	-	-	-	-	2 7	-	-	-	4 3	3 4
Lu [ppm]	-	-	-	-	-	-	-	-	-	-	-	-	-	-	-	0 4	-	-	-	0 6	0 5
Ti/Zr	4 0	3 5	4 0	5 1	3 2	18 7	3 7	4 0	3 9	3 0	12 4	11 6	4 4	4 1	9 3	15 7	10 7	11 3	10 6	3 6	3 9
Altn Index	67	37	42	40	96	38	87	92	94	74	11	80	65	65	8	19	18	11	36	61	97
CCP Index	50	13	21	19	61	47	22	41	15	19	17	62	18	26	18	31	27	34	33	48	49

Table A4: Bulk rock geochemical data

sample	TH85-188	TH85-204	TH85-215	TH85-312	TH85-42	TH85-441	TH85-452	TH85-594	TH85-72	TH85A-241	TH85A-335	TH85A-348	TH85A-349	TH85A-384	TH85A-422	THFH2	THFH3	THFH4	THR2	THR3	THRC8-87
DDH	TH85	TH85	TH85	TH85	TH85	TH85	TH85	TH85	TH85	TH85A	TH85A	TH85A	TH85A	TH85A	TH85A	surface	surface	surface	surface	surface	THRC8
depth from	187 8	204	214 5	311 6	41 5	441	451 5	594 2	71 5	240 6	334 6	347 6	348 6	383.5	421 5						87
depth to	188 15	204 25	214 8	311 9	41 75	441 25	451 75	594 4	71 75	240 9	334 9	347 85	348 9	383.7	421.75						88
lithofacies	R1	R1	R1	R1	D3	RV	RV	D1	R1	R1	R1	R1	R1	R1	R1	QEV	RV	D2	R3	R2	GRA
altn facies	QP	QP	QP	M	LA	M	QP	W1	QKF	QP	QP	M	CP	CP	M	W2	W2	LA	QKF	QKF	
SiO2 [wt %]	74 5	71 2	67.1	72 7	73 1	57 9	66 7	73 0	84 2	71 6	78 0	66 9	40 2	49 3	70 0	74 6	82 6	75 7	78 6	82 3	75 7
TiO2 [wt %]	0 06	0 05	0 07	0.08	0 53	0 15	0 06	0 29	0 06	0 07	0 06	0 10	0 22	0.10	0 11	0 28	0 09	0 34	0 11	0 06	0.25
Al2O3 [wt.%]	8 4	8 3	10 4	12 3	13.7	22 0	9 1	11 1	7 4	11 0	9 5	14 6	20 1	13.5	13 1	13 6	10 4	13 4	11 0	8 3	12.9
Fe2O3 [wt %]	6 95	9 18	8 62	5 48	3 17	2 84	11 30	3.22	0 60	6 91	4 45	5 70	13 67	19 14	2 80	2 67	0 79	1.34	0 29	1 31	2 57
MnO [wt %]	0 05	0.09	0 13	0 01	0 04	0 10	0 03	0 15	<0 01	0 06	0 04	0 08	0 27	0 30	0 03	0 03	<0 01	0 01	<0 01	<0 01	0 05
MgO [wt %]	2.77	3 97	6 42	1 10	0 47	4 91	0 77	0.53	0 08	2 53	1 76	4 70	13 40	7 79	1 98	0 88	0 39	0 13	0 10	0 13	1.21
CaO [wt %]	<0 01	<0 01	0 01	<0 01	0 53	<0 01	0 99	6 44	0 11	0 08	0 02	<0 01	0 44	0.19	0 28	0 85	0 40	0 59	-0 01	0 03	1 04
Na2O [wt %]	0 09	0 15	0 12	0 17	5 56	0 24	0 06	1 82	0 34	0 11	0 16	0 09	0.20	0 08	0 38	5 67	5 24	4 81	0.15	0.70	4 86
K2O [wt %]	2.14	1 51	1.59	3 75	2 74	6 18	2 76	1 52	5 87	2 82	2 45	2 91	4 93	0 93	3 69	0 80	0 29	3 26	9 01	5 85	1 13
P2O5 [wt %]	0 01	0 01	0 01	0 01	0 12	0 02	0 01	0 09	0 01	0 02	0 01	0 01	0 02	0 02	0 05	0 06	0 01	0 06	0 03	0 02	0 04
BaO [wt %]	0 01	0.00	0 02	0 02	0 07	0 10	0 06	0 07	0 17	0 02	0 04	0 05	0 08	0 03	2 25	0 02	0 03	0.06	0 32	0 12	0 03
CuO [wt %]	0 08	0 01	<0 01	0 05	<0 01	<0 01	<0 01	<0 01	<0 01	<0 01	0 03	<0 01	0 01	0 06	0 09	<0 01	<0 01	<0 01	<0.01	0 01	<0 01
PbO [wt %]	<0 02	<0 02	<0 02	<0 02	<0 02	<0 02	<0 02	<0 02	<0 02	<0 02	0 02	<0 02	<0 02	0 02	0 52	<0 02	<0 02	<0 02	<0 02	0 02	<0 02
ZnO [wt %]	0.13	0.02	0 02	<0 01	0.04	0 01	0 01	0 27	0 02	0 01	0 08	0 02	0 07	0 37	0 95	0 01	<0 01	0 01	<0 01	<0 01	0 01
LOI* [wt %]	4 50	5 33	5 02	4 07	0 30	4 72	7 85	1 63	0 49	4 73	2 95	4 11	6.16	7 83	3 39	0 93	0 39	0 64	0 38	1.00	0 77
Total [wt %]	99.73	99 82	99 55	99 80	100 31	99 08	99 60	100 11	99 42	99 98	99 59	99 27	99 72	99 63	99 55	100 38	100 64	100 33	100 01	99 82	100 53
S [wt %]	4 36	4 97	2 89	3 47	<0 01	1 41	8 87	0.23	0 48	3 59	1 57	0 86	0 98	5 12	2 03	<0 01	<0 01	<0 01	0 02	1 04	0 08
CO2	-	-	-	-	-	-	-	-	-	-	-	-	-	-	-	-	-	-	-	-	-
Ba [ppm]	187	118	138	402	817	892	740	560	1936	315	515	579	643	336	>2500	296	225	580	3200	1361	239
Cu [ppm]	807	105	6	482	5	2	12	26	3	43	313	52	195	514	> 914	4	4	3	38	95	7
Pb [ppm]	37	23	20	33	214	29	32	116	70	25	245	35	22	70	4774	12	22	4	365	238	35
Zn [ppm]	1232	175	244	32	337	113	68	2169	118	100	836	172	648	2972	7606	43	25	43	6	32	51
Ag [ppm]	1 6	< 0 5	< 0 5	0 8	< 0 5	< 0 5	< 0 5	< 0 5	< 0 5	< 0 5	1 9	< 0 5	< 0 5	0.9	14 9	< 0 5	< 0 5	< 0 5	< 0 5	< 0 5	-
As [ppm]	9	20	14	12	<3	4	19	<3	<3	16	9	4	<3	23	19	<3	<3	<3	100	19	<3
Bi [ppm]	7 7	5 4	2 9	7 4	0 1	2 0	13 4	137 1	0 3	6 2	10 1	10 2	0 8	4 6	2 7	0 3	0 3	0 2	0 2	2.2	-
Cd [ppm]	3 8	0 1	< 0 1	0.1	1 1	0 1	0 2	30 4	0 5	0 1	2 2	0 1	0 2	0.5	24 4	0 1	0 1	0 3	0 3	1.6	-
Cr [ppm]	3	3	3	<2	2	<2	<2	4	<2	5	<2	4	3	<2	<2	3	2	2	<2	<2	2
Cs [ppm]	0 4	0 3	0 4	0 5	0 5	1 4	0 5	0 3	0 5	0 3	0 5	0 7	3 4	0 4	1 0	1.7	0 3	0 5	0 3	0.3	-
Mo [ppm]	3 0	3 2	2 4	0.2	0 9	6 0	8 0	2 1	2 1	3 4	3.7	2 2	0 9	1.8	2 6	0 1	0 1	0 2	3 7	6 7	-
Nb [ppm]	11	9	12	15	9	26	11	8	9	14	11	16	37	16	17	11	9	11	14	9	8
Ni [ppm]	<1	1	<1	1	1	2	<1	2	1	<1	<1	2	3	2	7	1	2	2	2	2	2
Rb [ppm]	67	41	51	112	41	221	85	25	94	79	76	89	259	32	113	38	8	84	137	105	32
Sb [ppm]	0 1	0 1	0 2	0 2	0 3	0 3	0 3	0 5	0 4	0 2	0 2	0 2	0 2	0 5	38.8	0 2	0 2	0 5	1 5	0 9	-
Sr [ppm]	7	7	11	8	70	20	16	113	42	16	7	12	9	7	392	202	77	48	32	32	129
Th [ppm]	9	9	12	11	7	23	10	-	8	12	10	18	21	14	-	11	16	9	10	8	14
Tl [ppm]	0 5	0 3	0 4	0 6	0 4	3 4	1 1	0 5	1 5	0 7	0 8	1 0	5 5	1.2	4 9	0 3	< 0 1	0 4	2 0	0 9	-
U [ppm]	3 0	2.1	2 7	3 1	1 8	7 2	2 5	2 9	2 3	2.7	2 4	4 0	4 5	2 5	5 3	2 1	4 4	1 6	2 3	2 0	-
V [ppm]	<1 5	<1 5	<1 5	<1 5	25	5	2	29	2	<1 5	<1 5	<1 5	5	3	28	20	2	<1.5	3	<1 5	42
Y [ppm]	29	17	29	35	32	36	28	27	20	37	30	46	78	44	49	29	27	32	23	18	15
Zr [ppm]	92	84	116	129	153	246	100	135	80	120	105	176	217	145	162	144	97	182	160	102	112
La [ppm]	-	-	-	18 7	-	-	-	18 9	57 3	39 8	28 7	49 5	64 6	44 0	44 4	38 5	-	-	-	-	-
Ce [ppm]	-	-	-	36 2	-	-	-	35 5	47 7	70 6	55 2	94 4	118 9	80 9	80 0	61 0	-	-	-	-	-
Pr [ppm]	-	-	-	4 5	-	-	-	4 6	6 0	8 5	7 0	11 6	14 2	9 9	9 7	8 3	-	-	-	-	-
Nd [ppm]	-	-	-	17 8	-	-	-	19 0	22 6	32 7	27 1	45 1	54 3	38 5	37 2	32 0	-	-	-	-	-
Sm [ppm]	-	-	-	4 0	-	-	-	4 5	4 4	6 6	5 6	8 9	10 4	7 9	7 5	6 3	-	-	-	-	-
Eu [ppm]	-	-	-	0 4	-	-	-	1 1	1 0	0 8	0 6	1 0	1 9	2 1	2 0	1 3	-	-	-	-	-
Gd [ppm]	-	-	-	4 5	-	-	-	5 1	4 4	7 0	5 5	8 3	9 9	8 6	7 7	6 6	-	-	-	-	-
Tb [ppm]	-	-	-	0 8	-	-	-	0 9	0 7	1 2	0 9	1.2	1 4	1 3	1 2	1 0	-	-	-	-	-
Dy [ppm]	-	-	-	4 6	-	-	-	4 9	3 8	6 5	4 6	6 1	7 4	7 2	6 6	5.6	-	-	-	-	-
Ho [ppm]	-	-	-	1 1	-	-	-	1 1	0 9	1 5	1 0	1 3	1 6	1 6	1 5	1 2	-	-	-	-	-
Er [ppm]	-	-	-	3 0	-	-	-	3 2	2 3	4 0	2 8	3 6	4 6	4 3	4 2	3 3	-	-	-	-	-
Tm [ppm]	-	-	-	0 6	-	-	-	0 6	0 4	0 7	0 5	0 7	0 9	0 8	0 8	0 6	-	-	-	-	-
Yb [ppm]	-	-	-	3 5	-	-	-	3 6	2 5	4 4	3 1	4 5	5 2	5 0	4 7	3 5	-	-	-	-	-
Lu [ppm]	-	-	-	0 5	-	-	-	0 5	0 4	0 6	0 5	0 7	0 8	0 7	0 7	0 5	-	-	-	-	-
Tl/Zr	3 9	3 6	3 6	3 7	20 9	3 7	3 3	13 1	4 4	3 5	3 4	3 3	6 0	4 1	3 9	11 5	5.6	11 2	4 0	3 5	13 2
Altn Index	98	97	98	97	35	98	77	20	93	97	96	99	97	97	90	20	11	39	98	89	28
CCP Index	80	88	89	61	29	54	80	51	9	75	69	77	83	96	53	34	17	14	4	17	37

Table A4: Bulk rock geochemical data

sample	THRW10	THRW11	THRW3	THRW4	THRW5	THRW6	THRW7	THRW8	THRW9	THWH1	THWH3	THWH4	RH1-95	RH1-96
DDH	surface	surface	surface	surface	surface	surface	surface	surface	surface	surface	surface	surface		
depth from														
depth to														
lithofacies	R3	R3	R3	R4	R3	R2	R4	R3	R1	R1	R1	R1	IRS	IRS
altn facies	LA	W4	LA	LA	LA	W4	W4	LA	LA	QKF	W4	LA		
SiO2 [wt %]	76 1	79 2	73 9	70 4	76 6	76 6	70 2	77 9	80 0	74 5	78 6	78 4	78 9	76 1
TiO2 [wt %]	0.13	0 13	0 18	0 27	0,14	0 08	0 32	0 14	0 11	0 14	0.11	0 11	0 07	0 08
Al2O3 [wt %]	13 4	11 0	13 6	15 0	12 4	12 1	15 5	11 3	11 2	12 4	11.2	11.6	10 7	11 2
Fe2O3 [wt %]	1 31	0 61	1 97	3 46	2 27	0 90	3 21	1 62	0 67	1 83	1 08	1,98	1 22	1 31
MnO [wt %]	0 02	0 01	0 05	0.04	0 05	0 02	0 06	0 04	<0 01	0 06	0 01	0 03	0 03	0 03
MgO [wt %]	0 46	0 28	0 80	2 21	0,72	0 47	1,17	0 63	0 22	0 85	0.42	0 31	0 85	1 20
CaO [wt %]	0.10	0 07	0 50	1 23	1,45	0 05	2 16	0 10	0 12	0 46	0,25	0 53	0 60	0 92
Na2O [wt %]	3.16	2.23	3.77	2 46	3 80	1 86	4 64	2 99	3,46	1,63	2.17	2 80	0 82	0 74
K2O [wt.%]	4 43	4 61	4 90	3 68	2,87	6 30	2 84	4 15	3 64	7,63	5 33	3 85	5 90	6 38
P2O5 [wt %]	0 02	0,01	0 02	0 05	0 02	0 02	0 05	0 02	0 01	0 02	0 01	0,01	0 02	0 01
BaO [wt.%]	0,06	0,06	0 06	0 05	0 06	0 12	0 08	0,07	0 05	0 08	0 05	0 04	0,16	0,11
CuO [wt %]	<0 01	<0 01	<0 01	<0 01	<0 01	<0 01	<0 01	<0 01	<0 01	<0 01	<0,01	<0 01	<0 01	<0 01
PbO [wt.%]	<0 02	<0 02	<0 02	<0 02	<0 02	<0 02	<0 02	<0 02	<0 02	<0 02	<0 02	<0 02	<0 02	<0 02
ZnO [wt.%]	0 01	<0 01	0 01	0 01	0 01	0,01	0 01	0,01	<0,01	0 01	<0 01	0 01	<0,01	0 03
LOI* [wt %]	0 94	0,76	0 57	1,68	0 63	0 75	0 72	0 62	0 58	0 35	0,53	0 54	1,18	1,26
Total [wt %]	100 17	98 95	100 38	100,54	101 04	99 29	100,93	99 58	100 07	100 01	99 68	100 25	100 42	99 36
S [wt %]	<0 01	<0 01	<0 01	<0 01	0 01	0 19	<0 01	0 14	0 19	0 01	0 01	<0 01	0 34	0 22
CO2	-	-	-	-	-	-	-	-	-	-	-	-	-	-
Ba [ppm]	502	531	579	596	597	1369	675	644	537	789	783	337	1343	1259
Cu [ppm]	3	2	5	3	3	10	3	5	1	3	6	2	8	15
Pb [ppm]	5	6	6	6	7	36	11	6	7	4	8	3	441	424
Zn [ppm]	31	23	66	53	37	64	71	37	9	48	22	54	721	286
Ag [ppm]	< 0 5	< 0 5	< 0 5	< 0 5	< 0 5	< 0 5	< 0 5	< 0 5	< 0 5	< 0 5	< 0 5	< 0 5	-	< 0 5
As [ppm]	<3	<3	<3	<3	<3	<3	<3	<3	5	<3	<3	<3	-	-
Bi [ppm]	1.0	< 0 1	0 5	0 5	0 2	0 3	0 2	0 3	0 1	< 0 1	0 3	0 1	-	0.4
Cd [ppm]	0 3	0,1	0 3	< 0 1	0,2	0,1	0 1	0 4	0 1	0 1	0 2	0 1	-	1,3
Cr [ppm]	<2	3	<2	5	<2	<2	2	6	<2	<2	3	4	2	2
Cs [ppm]	0 9	0 9	1 8	1 7	1 4	0,8	1 5	0 8	0 4	1 8	0 6	1 2	-	0 8
Mo [ppm]	0 3	0 6	0 3	< 0 1	0 5	< 0 1	0 1	1,2	0 2	0 2	0 9	0 4	-	1 0
Nb [ppm]	16	15	18	11	13	10	11	13	12	15	15	12	11	14
Ni [ppm]	<1	1	1	4	2	2	3	1	1	1	1	1	2	1
Rb [ppm]	120	115	146	129	67	162	89	92	67	127	105	87	130	139
Sb [ppm]	0 2	0,1	0 4	0 1	0,1	0 2	0 3	0 1	0 2	< 0 1	0 2	< 0 1	-	0 3
Sr [ppm]	43	37	84	83	79	43	144	38	61	33	83	39	40	48
Th [ppm]	12	13	16	17	10	15	16	11	11	13	12	11	16	12
Tl [ppm]	0 9	0 9	1.5	0 6	0,3	0 9	0 5	0 8	0.5	0 8	0.7	0 5	-	0.8
U [ppm]	3 4	3 6	3 5	1 4	5 9	2 9	2 0	2 2	2 3	3 1	3 4	2 4	-	5 3
V [ppm]	<1 5	<1 5	<1 5	14	<1.5	4	20	<1 5	<1 5	<1 5	<1 5	<1 5	3	2
Y [ppm]	39	37	47	33	45	27	32	30	25	44	27	41	36	36
Zr [ppm]	199	195	272	208	274	89	217	207	158	183	161	149	110	121
La [ppm]	-	-	-	-	34 3	18,7	56 9	-	15 8	-	-	22 0	-	30 6
Ce [ppm]	-	-	-	-	64 5	36 7	102 7	-	31 0	-	-	40 9	-	58 6
Pr [ppm]	-	-	-	-	8 2	4 6	11,9	-	3 8	-	-	5,3	-	7.5
Nd [ppm]	-	-	-	-	32 2	18 0	42 8	-	14 4	-	-	22 0	-	29 6
Sm [ppm]	-	-	-	-	6,8	4 2	7.4	-	2 9	-	-	5 7	-	6 2
Eu [ppm]	-	-	-	-	1 3	0 6	1 6	-	0 5	-	-	1 1	-	0 7
Gd [ppm]	-	-	-	-	7,2	4 6	7 0	-	3 0	-	-	6 8	-	6 5
Tb [ppm]	-	-	-	-	1 2	0 8	1.1	-	0 6	-	-	1 3	-	1.1
Dy [ppm]	-	-	-	-	7.4	4.4	6 1	-	3 5	-	-	7 6	-	6 3
Ho [ppm]	-	-	-	-	1 8	1 0	1 3	-	0 9	-	-	1,7	-	1,5
Er [ppm]	-	-	-	-	5,3	2 9	3 7	-	2 6	-	-	4 6	-	4 1
Tm [ppm]	-	-	-	-	1 0	0 5	0 7	-	0,5	-	-	0 8	-	0 8
Yb [ppm]	-	-	-	-	5 8	3,2	3 9	-	3,0	-	-	4,8	-	4 5
Lu [ppm]	-	-	-	-	0 8	0 5	0 6	-	0 5	-	-	0 7	-	0 7
Ti/Zr	3 9	3 9	3.9	7 6	3.0	5 4	8 9	4 0	4 1	4 6	4 0	4 3	3 8	3.9
Altn Index	60	68	57	61	41	78	37	61	52	80	70	56	83	82
CCP Index	18	11	23	46	29	14	35	23	10	21	16	24	22	25

Abbreviations in Table A4:

Lithofacies

R1	rhyolite type 1
R2	rhyolite type 2
R3	rhyolite type 3
R4	rhyolite type 4
D1	dacite type 1
D2	dacite type 2
D3	dacite type 3
A	andesite
Ph	phyllite
RV	rhyolitic volcaniclastic facies
DV	dacitic volcaniclastic facies
SBA	silica-barite rock
DIO	diorite
GRA	granite
IRS	internal rhyolite standard

Alteration facies

M	mottled alteration facies
QKF	quartz-K-feldspar alteration facies
DT	disseminated tremolite alteration facies
QP	quartz-pyrite alteration facies
CP	chlorite-pyrite alteration facies
W1	epidote alteration
W2	albite alteration
W3	hematite dusting
W4	phyllosilicate alteration
-	not analysed

Altn Index: Alteration Index
CCP Index: Chlorite-Carbonate-Pyrite Index
LOI*: Loss on ignition (includes sulphur)

Table A5: Bulk rock geochemical data (provided by RGC Exploration)

	TH270-49 5	TH270-89.6	TH270-130	TH270-158 1	TH270-187 5	TH270-213	TH270-252	TH270-243 1	TH270-292	TH270-323.1	TH270-368 2	TH247-57 7	TH247-98 8	TH247-169 8	TH247-219	TH247-238 8	TH247-279 8	TH247-300	TH247-347
DDH	TH270	TH270	TH270	TH270	TH270	TH270	TH270	TH270	TH270	TH270	TH270	TH247	TH247	TH247	TH247	TH247	TH247	TH247	TH247
depth from	49 5	89 6	130	158.1	187.5	212 65	251.75	243 1	291.8	323 1	368 2	57.7	98 6	169 8	219	238 8	274.8	300	347 2
depth to	49 8	89 8	130 3	158 4	187 8	213	252	243.35	292	323 4	368 4	57 9	98 8	170	219 2	238 95	275	300 2	347.35
SiO2 [wt.%]	63 60	60 60	61 90	64 80	68 70	78 00	79 40	34 70	73.90	78.10	41 10	78 90	75 40	75.10	79 60	80 80	65 50	68.30	62.90
TiO2 [wt.%]	0 09	0.13	0.09	0.10	0 07	0.07	0 07	0 05	0.06	0.06	0 06	0.08	0 13	0 10	0 08	0 05	0.13	0 12	0 18
Al2O3 [wt.%]	12.25	16.56	11.82	13.03	10 58	8.72	10 39	8 95	9.59	7 86	8 85	9 21	12 50	11.68	10 64	7 73	13 47	12 65	17.06
Fe2O3 [wt %]	1.70	2 37	3 47	2.04	2 04	2.97	4 39	29.27	5 26	4 93	2 43	1 24	2.69	2 07	1 70	1.47	2 70	1 79	3 53
MnO [wt %]	0 04	0.04	0 06	0.06	0.03	0 04	0 06	0.15	0.04	0.03	0 35	0 02	0 05	0 06	0 04	0.02	0 10	0.02	0.02
MgO [wt.%]	2 65	1 67	2 26	2 30	2 04	1 81	2 29	6 43	1.66	1.86	14 99	0 44	1 12	1.44	1 84	0 46	5.50	2 40	1 94
CaO [wt.%	0 19	0 03	0.17	0.34	0 04	0 01	0 01	0 05	0 03	0 01	8 72	0 24	0 15	0 36	0 11	0 15	0 17	0 01	0 05
Na2O [wt.%]	0 50	0 57	0 38	0 68	0 14	0.10	0 10	0 03	0.10	0.07	0 30	0 97	1.56	3.72	2 78	2.72	0.57	0.15	0.18
K2O [wt.%	6 00	5 32	4 91	4 58	3 57	2 30	2 63	1.04	2 43	1.83	1.40	5 18	5 52	1 83	1 90	0 93	4.48	4.34	5.70
P2O5 [wt.%]	<0 01	<0 01	<0 01	<0 01	<0 01	<0 01	<0 01	0 03	<0 01	<0.01	0.02	0 01	0 01	<0 01	<0.01	<0 01	0.01	0 01	0 02
BaO [wt %]	0.18	0.52	0.22	0.19	0.09	0.03	0 03	<0.01	0.04	0.04	9 96	0.33	0 29	0.07	0.10	0.03	0 39	0.15	0.24
CuO [wt %]	<0 01	<0 01	0.15	<0 01	0 01	<0 01	<0 01	<0.01	0 22	0 05	0 02	0 02	<0 01	0 05	<0 01	<0.01	<0 01	<0 01	<0 01
PbO [wt %]	<0 01	0 01	<0 01	<0 01	0 24	<0 01	<0.01	<0.01	0 02	<0 01	0 32	<0 01	0 01	0.05	<0 01	<0.01	<0.01	<0 01	0 01
ZnO [wt.%]	0.27	0 10	0 59	0 02	0.50	0.03	0.02	0.06	0.05	0.05	0 39	0 01	0 02	0 06	0 02	0.11	0.06	0.01	0.01
LOI [wt.%]	-	-	-	-	-	-	-	-	-	-	-	-	-	-	-	-	-	-	-
S [wt.%]	0.71	0 92	2.04	0 87	1 23	1 27	1 92	19 02	1 88	2.29	0 31	0 38	0 51	0 42	0 49	0 57	0 30	0 48	1.92
Total [wt %]	88.18	88 88	88 05	89.01	89.29	95 35	101 30	99 78	95 29	97 19	89 20	97.03	99 96	97.00	99 29	95.04	93.38	90 43	93 76
Zn [ppm]	2,150	830	4,700	141	4,050	214	126	515	424	385	3,170	82	145	513	146	911	463	75	101
Cu [ppm]	21	22	1,200	11	88	72	29	58	1,770	434	131	197	53	360	38	36	11	13	61
Pb [ppm]	50	100	< 25	50	1,900	< 25	< 25	< 25	150	< 25	2,550	< 25	100	400	< 25	50	< 25	< 25	100
Ba [ppm]	1,610	4,690	1,950	1,710	813	274	251	<100	329	330	89,200	2,920	2,600	622	914	225	3,530	1,370	2,120
Ag [ppm]	0 2	0 4	0 9	0.1	1.2	0 2	0 1	0.4	2.6	0 5	9 7	0.6	0 5	1.7	0 5	0 7	0 5	0 3	2 7
As [ppm]	6	8	11	20	12	19	13	101	96	28	34	15	8	2	<1	1	<1	2	57
Au [ppb]	<5	10	46	<5	6	<5	5	38	17	20	32	10	<5	<5	<5	5	<5	<5	41
Bi [ppm]	1.1	1.7	2.1	0 8	2.7	1 5	6 1	11 8	31.6	2 8	2.6	2 4	3 5	6.7	2	2 3	0 5	0 7	5 1
Cs [ppm]	1	<1	<1	1	1	<1	<1	1	<1	1	2	1	<1	<1	<1	<1	2	<1	1
Ga [ppm]	18 7	31	18 1	19 5	13 2	10 9	15 6	13 2	14	10 9	13 5	10 5	18 9	15 2	12	8 2	18	17 2	23.9
Hf [ppm]	5.0	7.2	5 2	5.6	4.0	3 7	4 1	2 7	3.4	2 8	3 6	3 8	5 2	4.6	4 1	2 9	5 8	5.7	8 2
Mo [ppm]	4 8	5 5	5.4	11 8	4.9	4.9	4 4	8 9	2 9	5.8	23 7	4 1	1 5	9	1.3	4 4	1 5	2	12
Ni [ppm]	<10	<10	<10	<10	<10	<10	<10	<10	<10	<10	<10	<10	<10	<10	<10	<10	<10	<10	<10
Rb [ppm]	141	175	155	135	115	66	74	30	73	66	58	92	112	80	77	25	166	157	175
Sb [ppm]	<0 2	<0 2	0 2	<0 2	0 7	<0 2	<0 2	0.3	1.8	0 3	25 2	1 0	0 4	<0 2	<0 2	<0.2	<0 2	<0 2	1 5
Sc [ppm]	7 2	11.0	7 5	8 4	6 3	5.1	6 7	3.9	5.7	4 9	5 0	5.0	7 5	6 7	6.0	4.1	8 5	8 9	12.3
Sr [ppm]	35	34	36	35	13	10	10	4	10	8	1550	65	51	64	51	33	47	18	21
Ta [ppm]	3	3	3	2	1	<1	2	<1	<1	1	1	2	3	3	2	1	1	3	3
Th [ppm]	13 9	20 6	14 0	16 1	11.9	10.2	11 6	7 5	10 7	8 9	9.7	9.2	12 4	12 0	12 2	8.1	13 3	13.1	18.6
Tl [ppm]	1.4	1 5	1	0 8	0 7	<0.5	0.5	<0 5	0.7	1 1	4 3	0 7	0 5	<0 5	<0 5	<0 5	0 5	0 6	3 3
U [ppm]	4	6	4	4	3	3	3	<2	2	3	9	3	3	2	4	2	5	3	5
V [ppm]	<2	2	2	2	<2	2	<2	3	<2	2	22	2	2	2	<2	3	2	2	5
W [ppm]	4	9	5	3	5	4	4	3	4	<2	<2	2	2	<2	3	<2	2	<2	3
Zr [ppm]	151	217	142	166	129	103	119	86	106	92	105	118	172	141	133	89	198	181	274
La [ppm]	28.9	41.1	52 4	33.8	39 8	25 5	32 7	155 0	31 1	20.7	29 8	22.6	31.5	21.5	27.3	14 3	31.5	34 0	48 3
Ce [ppm]	69 2	100.0	113 0	81 6	92.0	58 1	73.0	270 0	69 2	47 3	64.5	52 1	73 5	51 2	71.1	37 5	75 5	79 5	111.0
Sm [ppm]	6 3	10 1	9 0	8 2	7.6	5 4	7 0	13 4	6 2	4 5	6 6	4 7	7 6	5 4	7 3	4 6	7.2	7 2	10 3
Eu [ppm]	0 8	1 2	1.3	0 8	0.6	<0.5	0 7	1 6	<0 5	0 7	1.5	<0 5	0 9	0 8	0.8	<0 5	0 8	0.9	1.6
Yb [ppm]	5 4	7 1	4 8	5 2	4 0	2.6	4 0	4.1	3.4	2 9	5.8	2 7	4 3	3 6	4 5	2 4	4 6	4.2	6.4
Lu [ppm]	0 8	1 1	0 7	0 8	0 6	0 4	0 6	0.6	0 5	0 4	0 9	0 4	0.7	0 6	0 7	0.4	0 7	0 7	1 0

Table A6: Microprobe analyses - biotite

sample	TH247-136	TH247-136	TH247-169	TH247-169	TH247-169	TH247-169	TH247-169	TH247-169	TH247-219	TH247-219	TH247-219	TH247-219	TH247-219	TH247-219	TH247-219	TH247-238	TH247-238	TH247-238	TH247-238	TH247-238	TH247-274	TH247-274
mineral	bioAG4	bioAG3	bioAW6	bioAW5	bioAW4	bioAW3	bioAW2	bioAW1	bioAX8	bioAX7	bioAX6	bioAX4	bioAX3	bioAX2	bioAX1	bioAY4	bioAY3	bioAY3	bioAY2	bioAY1	bioAZ8	bioAZ7
Label	448	444	409	408	407	406	404	402	320	316	311	309	305	304	303	510	507	508	505	504	368	367
lab	CSL	CSL	CSL	CSL	CSL	CSL	CSL	CSL	CSL	CSL	CSL	CSL	CSL	CSL	CSL	CSL	CSL	CSL	CSL	CSL	CSL	CSL
[wt %]																						
SiO2	36 01	38 47	38 42	39.69	38 22	38.63	38 78	37.28	40.55	39 88	39 87	40 33	40 48	39 85	40 21	39 8	39.66	39 76	39 94	39 35	39 85	41.25
TiO2	0.39	0 56	0 82	0 9	0.84	0 82	0 79	0 86	0 53	0 7	0 65	0 56	0.69	0 49	0 59	0 81	0.84	0 79	0 74	0 76	0.36	0 34
Al2O3	17 24	17.77	18 07	18 42	17.74	17.63	17 29	17 8	18 18	17 44	18 19	18 26	18 23	18 56	17 73	17 8	17 4	17.75	17 6	17 91	18.65	17.14
FeO	13 73	11 69	11.13	11.43	11 08	11 55	10 79	11 13	6 89	6 71	6 83	6 72	6 65	6 94	6 83	7 52	7.46	7.31	7 61	7 9	5 97	5 66
MnO	0 67	0 68	0.55	0.62	0 54	0 65	0 6	0 59	0 39	0 39	0 46	0 43	0 35	0 46	0 4	0 38	0 34	0 34	0 35	0 38	0 43	0 44
MgO	17.4	16 23	16 58	17 09	16 32	16 83	17 07	16 03	20.19	19 89	20 12	19 71	19 05	19 67	20 12	19 65	19 4	19 44	19 59	19 34	20 22	21.05
CaO	0 05	0	0	0	0 02	0 04	0 01	0 05	0	0	0	0	0	0	0	0	0 01	0 06	0	0	0	0
Na2O	0 04	0 09	0 14	0 13	0.13	0.11	0.12	0 13	0 2	0 11	0.13	0 15	0 18	0 16	0 11	0 16	0 18	0 13	0 15	0 13	0 12	0.11
K2O	7 43	10 08	10 2	10 02	10 18	9 74	9 78	10	9 32	9 88	9.64	9.48	9.49	9 37	9 25	9 63	9 75	9 53	9.53	10	10.11	9 45
ZnO	0 06	0 08	0.17	0.09	0 15	0.11	0 17	0.19	0 16	0 18	0.17	0 16	0 17	0 04	0 15	0 24	0 18	0 25	0.24	0.22	0 24	0.11
BaO	0.04	0 06	0 14	0.13	0 09	0.13	0 08	0 14	0 13	0 18	0 12	0 13	0 23	0 2	0 2	0 09	0 08	0 02	0 03	0.05	0 21	0.17
F	1 01	1 17	1 29	1 45	1 42	1.48	1.49	1 17	1 65	1.6	1.59	1.6	1 5	1 42	1 78	1.99	1 82	2 19	2	2 04	1	1.02
Cl	0	0 01	0	0 02	0	0 01	0.03	0	0	0	0	0	0	0 01	0 01	0	0	0	0 01	0.01	0 01	0 01
H2O(c)	3 5	3 54	3 51	3 55	3 41	3 42	3 39	3 47	3 48	3 43	3 48	3 48	3 51	3.55	3 38	3 27	3 32	3.15	3 26	3.23	3 76	3 77
O=F	0 42	0 49	0 54	0 61	0 6	0.62	0.63	0 49	0.7	0 68	0 67	0.67	0 63	0 6	0 75	0 84	0.77	0.92	0 84	0.86	0.42	0 43
O=Cl	0	0	0	0	0	0	0.01	0	0	0	0	0	0	0	0	0	0	0	0	0	0	0
Sum Oxides [%]	93 06	95 71	96 22	98.52	95 31	96.24	95.48	94.2	96 54	95 36	96.18	95 93	95 52	95 74	95 59	96.08	95.3	95 38	95 78	96 04	96 16	95.72
# cations:	calculated on the basis of 22 oxygens																					
Si	5.427	5 63	5 586	5 616	5 609	5 611	5.657	5 55	5 699	5.703	5 644	5.706	5 749	5 656	5 711	5 66	5 69	5 683	5 692	5 623	5.637	5 815
Ti	0 044	0.062	0.09	0 096	0 093	0 09	0 087	0 096	0.056	0 076	0 069	0 059	0 073	0.053	0 063	0.087	0 09	0 085	0 079	0 082	0 039	0 036
Al [4]	2.573	2.37	2 414	2 384	2 391	2 389	2 343	2 45	2 301	2.297	2 356	2.294	2 251	2 344	2 289	2 34	2 31	2 317	2 308	2.377	2 363	2 185
Al [6]	0 491	0 694	0 682	0 688	0 678	0 629	0 629	0 674	0.711	0.642	0 678	0 75	0 801	0 76	0 68	0 644	0 632	0 672	0 648	0.64	0.746	0.663
Fe2+	1 73	1 43	1.353	1 352	1 36	1 403	1.317	1 385	0 809	0 802	0 809	0 795	0 789	0 824	0 812	0 895	0 895	0 874	0 906	0 944	0 706	0 668
Mn2+	0 086	0 084	0 067	0 074	0.067	0 08	0 074	0 075	0 047	0 047	0 055	0.051	0 042	0 056	0 048	0 045	0 042	0 041	0 043	0 046	0 052	0 052
Mg	3 91	3 539	3 592	3 604	3 57	3 644	3 712	3 556	4 23	4 239	4.246	4 156	4 032	4.161	4 26	4 165	4 147	4 142	4.161	4 119	4 263	4 422
Ca	0 007	0	0	0	0.003	0.006	0 001	0 009	0	0	0	0	0	0	0	0	0 002	0 009	0	0 001	0	0
Na	0 012	0 025	0.04	0.037	0 036	0.032	0 034	0 037	0 056	0 031	0.037	0 041	0 049	0 045	0 032	0 045	0 049	0 036	0.042	0.036	0 032	0 029
K	1.429	1.882	1.891	1.807	1.907	1 805	1.819	1 9	1 671	1.802	1 741	1.711	1.719	1.696	1 676	1.746	1 785	1.737	1.732	1.822	1 824	1.7
Zn	0 006	0 009	0 018	0 01	0 016	0 012	0 018	0 021	0 016	0 019	0 017	0 017	0 017	0 004	0.015	0 025	0 02	0 026	0 025	0 023	0 025	0 011
Ba	0 002	0 004	0 008	0 007	0 005	0.007	0 004	0 008	0 007	0 01	0.007	0 007	0.013	0 011	0 011	0 005	0.005	0.001	0 002	0 003	0 012	0 009
F	0 48	0 543	0 592	0 65	0.661	0 681	0.689	0 551	0.735	0 726	0 712	0 717	0 674	0 638	0.797	0 894	0 828	0 992	0 902	0 921	0 448	0.457
Cl	0 001	0 003	0	0 004	0 001	0 003	0 008	0	0	0	0	0	0	0 003	0 003	0	0	0 001	0 003	0.002	0 002	0 002
OH	3 519	3 454	3 408	3 346	3 338	3 317	3 303	3 449	3 265	3 274	3 288	3 282	3 326	3 359	3 199	3.106	3 172	3 008	3 095	3 076	3 551	3 542
Sum cations	15 717	15.729	15 741	15.675	15 735	15.708	15 695	15 761	15 603	15 668	15 659	15 587	15 535	15 61	15 597	15.657	15 667	15 623	15 638	15.716	15.699	15 59
Y-position [6]	6.266	5 819	5 802	5 823	5 784	5 859	5 837	5 807	5 868	5 825	5 874	5 829	5.755	5 858	5 877	5.861	5 825	5 841	5 862	5 854	5 83	5 851
X-position [12]	1.451	1.911	1 939	1 852	1.951	1.85	1 859	1 954	1 734	1 843	1 785	1 76	1 78	1 752	1 719	1 797	1 84	1.783	1.776	1 862	1 868	1 738
XMg	0 693	0 712	0 726	0 727	0 724	0 722	0 738	0.72	0 839	0 841	0 84	0 839	0 836	0 835	0 84	0 823	0 823	0 826	0 821	0 814	0 858	0 869

Table A6: Microprobe analyses - biotite

sample	TH247-274	TH247-274	TH247-274	TH247-274	TH247-274	TH247-274	TH247-274	TH247-300	TH247-300	TH247-300	TH247-322	TH247-322	TH247-322	TH247-322	TH247-322	TH247-322	TH247-347	TH247-347	TH247-347	TH247-347	TH247-347	TH247-57.7
mineral	bioAZ6	bioAZ5	bioAZ4	bioAZ3	bioAZ2	bioAZ1	bioAZ1	bioBA2	bioBA1	bioBA1	bioAK6	bioAK5	bioAK4	bioAK3	bioAK2	bioAK1	bioBB5	bioBB4	bioBB3	bioBB2	bioBB1	bioAU1
Label	366	361	360	359	358	356	357	330	325	326	471	470	466	465	464	459	441	440	439	434	433	453
lab:	CSL	CSL	CSL	CSL	CSL	CSL	CSL	CSL	CSL	CSL	CSL	CSL	CSL	CSL	CSL	CSL	CSL	CSL	CSL	CSL	CSL	CSL
[wt %]																						
SiO2	39 5	39 8	39 61	39 86	39 65	39 42	39 98	41.86	40 49	40 73	39 02	38 78	39 28	38 95	38 6	38 4	42 18	41 38	42 58	41 24	41 19	38 54
TiO2	0 35	0 31	0 36	0 35	0 32	0.37	0 34	0 41	0 43	0 45	0 91	0 82	0 91	0 89	1 15	0 84	0 31	0 3	0 26	0 33	0.31	1 29
Al2O3	18.14	18 46	17.75	18.18	18 56	18 01	18 49	17 46	19.04	18 55	18 12	18 23	18 09	18.28	18 5	18 84	15.71	15 92	15 31	16 55	16 24	15 98
FeO	6.06	5 83	5 97	5 98	5 95	6 01	5 88	4 96	4 87	5 15	8 22	8 34	8 05	7 92	8.14	8 51	3 09	3	3.29	2 93	2 6	11 25
MnO	0 37	0 35	0.43	0 44	0 37	0 34	0 51	0 22	0 21	0.16	0 56	0.75	0 75	0 66	0 62	0 79	0 3	0 27	0 27	0 31	0 3	0.82
MgO	20.41	20.31	21.16	20.52	20 12	20 12	20 08	22	20 14	21 26	18 02	18 57	18 67	18 21	18 37	19 07	24.12	24 13	24 54	23.98	23 74	16 1
CaO	0	0 03	0 01	0 03	0	0	0 01	0	0	0 06	0 06	0 02	0 01	0 04	0.35	0 05	0	0.03	0 03	0 01	0	0
Na2O	0 09	0 1	0 09	0 13	0.13	0 11	0.12	0.16	0 17	0 18	0 1	0 05	0 06	0 09	0 08	0 09	0 18	0.17	0.17	0 16	0.16	0.09
K2O	10 09	10 39	9 21	9 85	10.22	10 48	10 05	9.5	9 55	9 66	9 83	9 85	10 16	9 99	9.53	9 38	10.33	10 08	9 98	9 64	10 43	10 23
ZnO	0 17	0 2	0 22	0 18	0.18	0 21	0 2	0 17	0.07	0 08	0.17	0 11	0 19	0 16	0 18	0.15	0 2	0 15	0 07	0 13	0.08	0 16
BaO	0 21	0 27	0 24	0 22	0 25	0 23	0.22	0 08	0.14	0 06	0.15	0 12	0 1	0 13	0 18	0.12	0 11	0 11	0.07	0.09	0.12	0 06
F	1.07	1 09	1 08	0 98	1 03	0 95	1 02	1 95	1.37	1.72	0 74	0.6	0 7	0.79	0 71	0 65	4 11	3 92	3 8	3 62	3 43	2 03
Cl	0	0	0 01	0	0	0	0 01	0 01	0 01	0 01	0	0 01	0 01	0 01	0 01	0	0	0	0	0 01	0	0
H2O(c)	3 69	3 71	3 69	3.76	3 73	3.74	3 74	3.4	3 6	3 48	3 8	3 88	3 86	3 78	3 83	3 88	2 37	2 41	2 53	2 57	2 63	3 07
O=F	0.45	0.46	0 46	0 41	0.43	0 4	0 43	0 82	0 58	0.73	0 31	0 25	0 29	0 33	0 3	0 28	1.73	1.65	1 6	1 52	1 45	0.86
O=Cl	0	0	0	0	0	0	0	0	0	0	0	0	0	0	0	0	0	0	0	0	0	0
Sum Oxides [%	95.39	96 05	95 05	95 74	95 75	95 3	95 88	96.82	95 11	96 34	95 16	95 64	96.27	95 32	95.7	96 24	96 53	95 54	96.57	95 37	95 17	94 52
# cations:																						
Si	5 638	5 644	5 649	5 658	5 637	5 647	5 667	5 803	5 712	5 688	5 638	5 584	5 617	5 617	5 547	5 491	5 86	5 805	5 899	5.774	5.798	5 724
Ti	0.037	0 033	0.038	0 037	0 035	0 04	0 036	0 043	0 046	0 047	0 098	0 089	0 098	0 097	0 125	0 09	0 032	0.031	0 027	0.034	0 033	0 144
Al [4]	2 362	2 356	2 351	2 342	2 363	2.353	2.333	2 197	2 288	2 312	2 362	2 416	2 383	2 383	2 453	2 509	2.14	2 195	2 101	2 226	2.202	2 276
Al [6]	0 691	0 729	0 632	0.699	0 746	0 687	0 756	0 655	0 878	0 741	0.724	0 677	0 666	0 725	0 68	0 665	0 433	0.437	0 399	0 505	0 493	0 521
Fe2+	0 723	0 691	0.712	0.709	0 707	0 72	0 697	0 575	0.575	0.602	0 993	1.004	0 963	0.955	0.979	1.017	0.36	0 352	0.381	0 343	0 306	1 398
Mn2+	0 045	0 042	0.052	0 053	0.045	0.042	0 061	0 026	0 025	0 019	0 068	0 092	0 091	0 08	0 076	0 095	0.035	0 032	0 031	0.036	0 036	0 103
Mg	4 342	4 292	4 499	4 341	4 262	4.296	4.242	4.546	4.236	4 425	3.882	3 986	3 98	3 914	3 934	4.065	4 996	5.046	5 067	5.005	4 98	3 565
Ca	0	0 004	0 002	0 005	0	0.001	0.001	0	0	0.009	0 009	0 003	0 002	0 006	0 054	0 008	0	0 004	0 004	0.001	0	0
Na	0.025	0 028	0 024	0 035	0.036	0 029	0.033	0 043	0 047	0 05	0 028	0 015	0 016	0 026	0 023	0 024	0 048	0 046	0 046	0 044	0 042	0 025
K	1.838	1 88	1.676	1.784	1 853	1.915	1 818	1 68	1.718	1 72	1 811	1.809	1 853	1.837	1 747	1.711	1.83	1 804	1 763	1 722	1 872	1.938
Zn	0 018	0 021	0 023	0 019	0 019	0 022	0 021	0 017	0.007	0 008	0 018	0.012	0.02	0 017	0 019	0 016	0 02	0 015	0.007	0 014	0.008	0 018
Ba	0 012	0.015	0 014	0.012	0 014	0 013	0 012	0 004	0.008	0 003	0 009	0 007	0 006	0 008	0 01	0 007	0 006	0 006	0 004	0.005	0.007	0 003
F	0 485	0 487	0 488	0 442	0.463	0.431	0 456	0 856	0 612	0 761	0 337	0 272	0 316	0 36	0 321	0 295	1 806	1.741	1 665	1.601	1 529	0 954
Cl	0 001	0	0 001	0	0	0	0 004	0 003	0.003	0 002	0 001	0 002	0 001	0 003	0.003	0	0 001	0	0.001	0 002	0	0
OH	3 515	3 513	3 511	3 558	3 536	3 569	3 541	3.141	3 386	3 237	3 662	3.726	3 682	3 638	3 676	3.704	2.193	2 258	2 334	2.397	2 471	3 045
Sum cations	15.731	15.735	15 672	15 694	15.717	15 765	15.677	15 589	15 54	15 624	15 64	15 694	15 695	15 665	15 647	15 698	15 76	15 773	15.729	15 709	15 777	15 715
Y-position [6]	5.855	5 808	5 956	5 858	5.814	5 807	5 813	5 862	5 768	5 841	5.783	5 859	5 819	5.788	5 813	5.949	5 876	5 913	5 912	5.937	5.857	5.749
X-position [12]	1.874	1.927	1.715	1 836	1 904	1 958	1 864	1.728	1 773	1.783	1 857	1 833	1 877	1.876	1.834	1.75	1 885	1 86	1 817	1 772	1.922	1.966
XMg	0 857	0 861	0 863	0 86	0 858	0 856	0 859	0 888	0 88	0 88	0 796	0 799	0 805	0 804	0 801	0 8	0 933	0 935	0 93	0 936	0 942	0 718

Table A6: Microprobe analyses - biotite

sample	TH247-74.5(	TH247-74 5(	TH247-74 5(	TH247-74 5(	TH247-74 5(	TH247-74 5(	TH247-74 5(	TH247-98 8(	TH247-98 8(	TH247-98 8(	TH247-98 8(	TH247-98 8(	TH247-98 8(	TH247-98 8(	TH247-98 8(	TH40 - 67 0	TH40 - 67 0	TH40 - 67 0	TH40 - 67 0	TH40 - 67 0	TH40 - 67 0	TH40 - 67 0	TH40 - 67 0
mineral	bioAF5	bioAF4	bioAF3	bioAF2	bioAF1	bioAF1	bioAV8	bioAV7	bioAV6	bioAV5	bioAV4	bioAV3	bioAV2	bioAV1	bioF9	bioF9	bioF8	bioF7	bioF6	bioF5	bioF4	bioF3
Label	492	491	490	488	482	483	397	392	391	390	379	378	376	375	253	254	252	251	236	235	234	233
lab:	CSL	CSL	CSL	CSL	CSL	CSL	CSL	CSL	CSL	CSL	CSL	CSL	CSL	CSL	TUB	TUB	TUB	TUB	TUB	TUB	TUB	TUB
[wt.%]																						
SiO2	34.93	36 62	36 74	36 04	36 58	36 78	36.11	36 47	37 51	35 81	37 6	37.14	37 54	37 62	34 56	35 21	35 52	35.70	35 51	35 21	35.11	35.76
TiO2	1 62	1.83	1.77	1 57	1 78	1.81	0 96	0 88	1 03	0 85	1 04	1 06	1 02	1.07	1 02	1 00	1.07	0.80	0 84	0 83	0.83	0 96
Al2O3	16 75	15.78	15 99	16.38	16 05	16 01	16 16	17 34	17 16	17.07	17 36	17.13	17 38	17 58	18 56	18 37	17.78	18 70	18 36	18.43	18.73	17.64
FeO	20 18	18 4	18 12	18 49	18 09	17 79	16.91	16 66	15.38	17 57	15 86	15 67	16 37	15 93	22 47	22 35	22.58	20.62	22 18	21 82	21 91	22 59
MnO	0 96	1.04	0 98	0 84	1	0 99	0.65	0 81	0.71	0 66	0 66	0 72	0 75	0.73	0.52	0 53	0.55	0 41	0.44	0.44	0.63	0.51
MgO	11.63	10 81	11.48	11.75	11 38	11 39	13 28	13.57	13 26	13 66	13 45	13 2	13 29	13 31	7 43	7 69	7 71	8 56	7 92	8 05	7.90	8 25
CaO	0 06	0 04	0	0	0 02	0	0	0 04	0 01	0 03	0 03	0 02	0.02	0	0 12	0 07	0 08	0 02	0 04	0 01	0 11	0 01
Na2O	0 06	0 06	0 06	0 06	0 05	0 07	0 03	0.07	0 07	0 04	0 08	0 07	0 08	0 05	0.06	0 08	0 03	0 09	0 09	0 04	0 08	0 03
K2O	7 62	9 24	9 49	8 66	9 61	9 34	9 05	8 62	9 81	8.85	10 11	9 31	8.97	9 02	9.34	9.38	9 61	9 55	9.64	9.76	9.82	9.67
ZnO	0 08	0 09	0.12	0 07	0 1	0 12	0 06	0	0 12	0 2	0 02	0 09	0 08	0.09								
BaO	0 07	0.1	0.1	0 04	0.05	0.07	0 03	0 01	0 01	0 04	0 05	0 08	0.07	0 08								
F	0 84	1 11	1 24	1.07	1 23	1 56	1 04	0 94	1.23	0 93	1.2	1.28	1 09	1.03								
Cl	0 01	0	0 01	0 03	0 02	0 01	0	0 05	0 02	0 02	0 01	0 01	0.01	0.01								
H2O(c)	3 47	3 35	3.33	3.37	3 32	3 17	3 39	3 51	3 41	3 5	3 46	3 36	3 5	3 53								
O=F	0.35	0 47	0 52	0 45	0 52	0 66	0 44	0 4	0 52	0 39	0 51	0.54	0 46	0.43								
O=Cl	0	0	0	0 01	0	0	0	0.01	0	0 01	0	0	0	0								
Sum Oxides [%	93 96	94 01	94 85	93 9	94.71	94.37	93 24	94.47	95 07	94 78	96 26	94 49	95 57	95 48	94 09	94 38	94 94	94 44	95.02	94 60	95 12	95.44
# cations*																						
Si	5.412	5 659	5 623	5 555	5.61	5 642	5 573	5 52	5 63	5.45	5.593	5.609	5.604	5 608	5 43	5 49	5.54	5.52	5 51	5 49	5.45	5.54
Ti	0.189	0 212	0 204	0.182	0 205	0 209	0 111	0 1	0.117	0 097	0 117	0 12	0 114	0.12	0 12	0 12	0 13	0 09	0.10	0.10	0 10	0 11
Al [4]	2 588	2.341	2 377	2 445	2 39	2.358	2 427	2.48	2 37	2 55	2 407	2 391	2 396	2 392	2.57	2.51	2 46	2 48	2.49	2 51	2 55	2.46
Al [6]	0 47	0 533	0 507	0.531	0 511	0.535	0 511	0 612	0 667	0.512	0 636	0 658	0 662	0 695	0 87	0 86	0 80	0 93	0 87	0 87	0 88	0 76
Fe2+	2.615	2 378	2 32	2 383	2 32	2 282	2 182	2 109	1 93	2 236	1 973	1 979	2 044	1 986	2 95	2.91	2 94	2 67	2 88	2 84	2 85	2 93
Mn2+	0 126	0 136	0 127	0.109	0 13	0.129	0 084	0 104	0 09	0 085	0 083	0.093	0 094	0 092	0 07	0 07	0 07	0 05	0 06	0 06	0 08	0 07
Mg	2 686	2 49	2 619	2 699	2 602	2 604	3 054	3 062	2 967	3 097	2 982	2 971	2 957	2 956	1 74	1 79	1 79	1 97	1 83	1.87	1 83	1 91
Ca	0 01	0 006	0	0	0 004	0	0	0 006	0 002	0 005	0 004	0 004	0 003	0	0.02	0 01	0 01	0 00	0 01	0.00	0 02	0 00
Na	0.019	0 017	0 019	0.018	0.016	0 021	0 009	0.02	0 019	0 011	0 022	0 019	0.024	0 015	0 02	0 02	0 01	0.03	0.03	0 01	0 02	0 01
K	1.505	1.822	1 853	1 703	1 88	1 828	1 782	1 663	1 879	1.718	1.918	1.793	1.708	1 715	1.87	1 87	1.91	1 89	1.91	1.94	1 95	1 91
Zn	0.009	0.01	0 014	0 007	0 011	0 013	0 006	0	0 013	0 022	0 002	0 01	0 009	0 01								
Ba	0 004	0 006	0 006	0 002	0 003	0.004	0 002	0 001	0	0 002	0 003	0 005	0 004	0 004								
F	0.411	0 542	0 6	0 523	0.596	0 755	0 508	0 45	0 582	0 446	0 566	0 609	0 513	0 484								
Cl	0 003	0 001	0 003	0 008	0.005	0 003	0	0 012	0 004	0 006	0 002	0 003	0 004	0 002								
OH	3 586	3 456	3 397	3.469	3.398	3 241	3.492	3 539	3.414	3 548	3 432	3 388	3 484	3 514								
Sum cations	15.633	15 61	15 669	15 634	15 682	15 625	15 741	15 677	15 684	15 785	15 74	15 652	15 619	15 593	15 67	15.65	15 67	15 63	15.68	15.70	15.72	15.70
Y-position [6]	6 094	5 76	5 789	5 912	5.78	5 773	5 949	5 986	5 784	6 05	5 792	5 831	5 88	5 859	5 76	5 75	5 73	5.72	5 74	5 74	5 73	5.77
X-position [12]	1.539	1 851	1 878	1 724	1 902	1 854	1 794	1 69	1 9	1 736	1 948	1 821	1 739	1.734	1 89	1 89	1 92	1.91	1 94	1 95	1 97	1 92
XMg	0 507	0 511	0 53	0 531	0.529	0 533	0 583	0 592	0 606	0 581	0 602	0 6	0 591	0 598	0 37	0.38	0 38	0 43	0 39	0 40	0 39	0 39

Table A6: Microprobe analyses - biotite

sample	TH40 - 67.0	TH40 - 67 0	TH40 - 67 0	TH40 - 67 0	TH40 - 67 0	TH40 - 67.0	TH40 - 67 0	TH40 - 67.0	TH40 - 67 0	TH471 - 104	TH471 - 104	TH471 - 104	TH471 - 104	TH471 - 104	TH471 - 104	TH471 - 159	TH471 - 159	TH471 - 159	TH471 - 159	TH471 - 159	TH471 - 159	TH471 - 159
mineral	bioF2	bioF16	bioF15	bioF14	bioF13	bioF12	bioF11	bioF10	bioF1	bioD6	bioD5	bioD4	bioD3	bioD2	bioD1	bioC9	bioC8	bioC7	bioC6	bioC6	bioC5	bioC4
Label	232	280	279	261	260	259	258	255	231	186	184	162	161	160	159	1	92	90	86	87	82	81
lab.	TUB	TUB	TUB	TUB	TUB	TUB	TUB	TUB	TUB	TUB	TUB	TUB	TUB	TUB	TUB	TUB	TUB	TUB	TUB	TUB	TUB	TUB
[wt %]																						
SiO2	36 13	35.61	35 78	34.67	34 92	34 26	34 54	35 88	35 13	36 20	36 17	34 61	35 48	35 91	35 91	36 41	36 97	38 53	35 25	36 50	37 58	36 44
TiO2	0.81	1 47	1.67	1.48	1.47	1 44	1 38	1.05	0 78	0.58	0.77	0 73	0.65	0 99	0.78	1 6	1 66	1.10	1 38	1 57	1 81	1 43
Al2O3	18 46	17.32	17 42	17.96	18 05	17 92	17 54	17.99	18.74	18 89	18 79	18 53	18.39	17 54	17.90	18 54	18 06	18 47	18 40	18 30	17.16	18,70
FeO	21 57	22 23	21 89	23 46	23 84	24 20	23.18	21.14	22 46	17.36	18 40	19 51	18 58	18 55	18 43	14 51	14 60	6 73	13 11	12,52	12.29	15.31
MnO	0 49	0 52	0 44	0.58	0 57	0 59	0 53	0 53	0.66	0 32	0 32	0 38	0 33	0 29	0 32	0 58	0 61	0 44	0 68	0 63	0.50	0 49
MgO	7 31	7 75	7.72	6 64	6 33	6 26	6 50	7 91	7.90	11 45	10 90	11 37	11.04	11 04	11 20	13 02	13 30	19 44	17 83	17.69	16 15	13 43
CaO	2 07	0 04	0 02	0 00	0 03	0 00	0 00	0 02	0 06	0 03	0 00	0 06	0 02	0 04	0 03	0 03	0 01	0 01	0 00	0 01	0.00	0 03
Na2O	0 06	0 05	0.05	0,04	0 08	0.06	0 06	0 05	0 01	0 16	0 15	0.13	0 13	0 12	0 10	0 07	0.10	0 62	0 12	0.13	0 16	0,10
K2O	8 80	9 65	9.75	9.72	9.71	9 60	9 60	9 65	9 57	10.05	9.98	8 86	9.75	9.78	9 99	9 73	10.12	8 84	6.72	7.24	9 03	9 35
ZnO																						
BaO																						
F																						
Cl																						
H2O(c)																						
O=F																						
O=Cl																						
Sum Oxides [%]	95 70	94 65	94.75	94 55	95 00	94 34	93.33	94.22	95 31	95 04	95 48	94.16	94.37	94 26	94 66	94 49	95 43	94 18	93.49	94.59	94 68	95.28
# cations:																						
Si	5 54	5 56	5 57	5.47	5.48	5 44	5 51	5 59	5.45	5.49	5 48	5 34	5 46	5 53	5 50	5 47	5 52	5 55	5.25	5.36	5 55	5 44
Ti	0 09	0 17	0 20	0.18	0 17	0.17	0 17	0.12	0.09	0.07	0 09	0.08	0 08	0 11	0 09	0 18	0 19	0 12	0 15	0.17	0.20	0 16
Al [4]	2 46	2 44	2 43	2 53	2 52	2 56	2.49	2 41	2 55	2.51	2 52	2 66	2.54	2.47	2 50	2 53	2 48	2.45	2 75	2.64	2 45	2 56
Al [6]	0 88	0 75	0 77	0 80	0 82	0 79	0 81	0 89	0 87	0 86	0 84	0 72	0.79	0 71	0 74	0.76	0 69	0 69	0 48	0.53	0 54	0.73
Fe2+	2.77	2 90	2.85	3 09	3 13	3 21	3 09	2.75	2 91	2.20	2 33	2 52	2.39	2 39	2 36	1.82	1.82	0.81	1 63	1 54	1 52	1 91
Mn2+	0 06	0 07	0 06	0.08	0 08	0.08	0.07	0 07	0 09	0 04	0 04	0.05	0 04	0 04	0 04	0 07	0.08	0 05	0 09	0.08	0.06	0 06
Mg	1.67	1.80	1 79	1.56	1 48	1.48	1 55	1.84	1 83	2 59	2 46	2 62	2 53	2.53	2 56	2 92	2 96	4 18	3.96	3 87	3.56	2.99
Ca	0.34	0 01	0 00	0 00	0 01	0.00	0 00	0.00	0 01	0 00	0 00	0 01	0 00	0 01	0.01	0.00	0.00	0 00	0 00	0 00	0.00	0 00
Na	0 02	0 02	0 01	0 01	0 02	0 02	0 02	0 02	0.00	0 05	0 04	0 04	0 04	0 04	0.03	0 02	0 03	0 17	0 03	0 04	0 04	0 03
K	1.72	1.92	1 94	1.96	1 94	1 94	1.95	1 92	1.89	1 94	1 93	1.75	1.91	1 92	1 95	1 87	1 93	1 63	1.28	1.36	1.70	1 78
Zn																						
Ba																						
F																						
Cl																						
OH																						
Sum cations	15 56	15.64	15.61	15 67	15 66	15.70	15 66	15 61	15.70	15.75	15 74	15 78	15 78	15 75	15 78	15 64	15.70	15 65	15 62	15 59	15.62	15 66
Y-position [6]	5.48	5.70	5 66	5 71	5 68	5 73	5 69	5 67	5 79	5 76	5 76	5 98	5 83	5.78	5 79	5.76	5 74	5 85	6 31	6.19	5 88	5 85
X-position [12]	1.74	1.94	1.95	1.97	1.97	1.96	1.97	1 93	1 90	1 99	1.97	1 78	1 95	1.96	1 98	1 88	1.96	1.80	1 31	1 40	1.74	1 81
XMg	0 38	0 38	0 39	0 34	0 32	0 32	0 33	0 40	0 39	0 54	0 51	0 51	0 51	0 51	0 52	0 62	0 62	0 84	0 71	0 72	0 70	0 61

Table A6: Microprobe analyses - biotite

sample	TH471 - 159	TH471 - 159	TH471 - 159	TH471 - 159	TH471 - 159	TH471 - 159	TH471 - 159	TH471 - 159	TH471 - 159	TH471 - 159	TH471 - 159	TH471 - 159	TH471 - 159	TH471 - 159	TH471 - 159	TH471 - 159	TH471 - 159	TH471 - 159	TH471 - 159	TH471 - 159	TH471 - 159	TH471 - 159
mineral	bioC3	bioC3	bioC26	bioC25	bioC24	bioC23	bioC22	bioC21	bioC20	bioC2	bioC19	bioC18	bioC17	bioC16	bioC15	bioC14	bioC13	bioC12	bioC11	bioC10	bioC1	bioC1
Label	79	80	146	133	132	129	128	127	126	78	125	123	122	121	120	118	97	95	94	93	73	74
lab·	TUB	TUB	TUB	TUB	TUB	TUB	TUB	TUB	TUB	TUB	TUB	TUB	TUB	TUB	TUB	TUB	TUB	TUB	TUB	TUB	TUB	TUB
[wt.%]																						
SiO2	35 81	37.08	36 04	36 62	35 84	35 97	36 55	36 83	36 86	37.02	36 65	36 92	37 12	36 80	36 92	36 24	35 59	36 14	36 45	37.11	36 81	36 87
TiO2	1.59	1.72	1 63	1.62	1.62	1.61	1.48	1 58	1.57	1 64	1.64	1.63	1 67	1.74	1 62	1 64	1 53	1 61	1 52	1.58	1.47	1 51
Al2O3	17.98	18 22	18.26	18 26	18 49	18 70	18 34	17 83	18.45	18 21	18 65	18.09	18 64	18 68	18 62	17.74	18.15	18 20	18.57	18 07	18 02	18.27
FeO	14 88	14 10	14.74	15 01	14.82	14 64	14.86	14 58	14.85	14 49	15 04	15 00	15 01	15.22	14 31	14 96	14.56	14.37	14.85	14.15	14 85	14 95
MnO	0.67	0 52	0 57	0 51	0 46	0 52	0 60	0 59	0 61	0.55	0.45	0 63	0 46	0 57	0.52	0 63	0 55	0 64	0 58	0.48	0 79	0.67
MgO	12 54	13 21	13 00	13 30	13 11	13 04	13 29	13 63	13 23	13 33	13 23	13 22	13 29	13 25	13.14	12 89	12 98	13 04	13 21	13 52	13 55	13 44
CaO	0 05	0 00	0 02	0 00	0 04	0 01	0 02	0.01	0 04	0 03	0 02	0 04	0 03	0 01	0 03	0 04	0 01	0 02	0.02	0.02	0 05	0 02
Na2O	0 10	0.13	0 09	0.10	0 08	0 05	0 08	0.10	0 10	0 08	0 04	0 10	0 12	0.10	0.10	0 08	0 05	0 11	0.13	0 09	0 08	0.07
K2O	9.72	10 34	9 75	10 01	9 95	10.43	10.13	10.11	9 62	10.00	9 98	9.79	9 65	10.08	9 99	9.65	9 93	10 20	9.79	10 08	9,59	9.52
ZnO																						
BaO																						
F																						
Cl																						
H2O(c)																						
O=F																						
O=Cl																						
Sum Oxides [%	93 34	95.32	94.10	95 42	94 41	94 96	95 36	95 26	95 33	95 35	95 71	95.41	95 99	96.45	95 24	93.86	93 37	94.33	95 12	95 11	95 21	95 32
# cations·																						
Si	5.48	5 53	5.46	5 47	5.42	5 41	5.47	5 51	5.49	5 52	5 45	5 51	5 49	5.44	5.50	5 51	5.44	5 46	5.45	5 54	5.50	5.50
Ti	0.18	0 19	0 19	0 18	0.18	0.18	0 17	0 18	0.18	0 18	0 18	0 18	0 19	0 19	0 18	0.19	0.18	0.18	0.17	0 18	0.16	0 17
Al [4]	2.52	2 47	2.54	2 53	2 58	2.59	2.53	2.49	2 51	2 48	2 55	2 49	2 51	2.56	2 50	2 49	2 56	2 54	2 55	2 46	2 50	2 50
Al [6]	0.72	0 73	0 71	0 69	0 71	0 73	0 70	0 65	0 73	0 72	0 72	0 69	0 74	0.70	0 77	0 68	0 71	0 71	0 73	0.71	0 67	0 71
Fe2+	1 90	1 76	1 87	1 88	1 87	1 84	1.86	1 82	1 85	1 81	1 87	1 87	1 86	1 88	1 78	1 90	1 86	1 82	1 86	1 77	1.86	1 86
Mn2+	0 09	0.07	0 07	0.06	0 06	0.07	0 08	0.07	0 08	0 07	0 06	0 08	0 06	0 07	0 07	0 08	0 07	0 08	0 07	0 06	0 10	0 08
Mg	2.86	2.94	2 93	2 96	2 95	2.92	2.96	3 04	2 94	2.96	2 93	2.94	2 93	2 92	2.92	2 92	2.96	2 94	2 95	3 01	3 02	2 99
Ca	0.01	0 00	0 00	0 00	0.01	0.00	0.00	0 00	0 01	0 00	0 00	0 01	0.00	0.00	0.01	0 01	0 00	0 00	0 00	0 00	0.01	0 00
Na	0.03	0 04	0 03	0 03	0 02	0 01	0 02	0 03	0.03	0 02	0 01	0 03	0 04	0 03	0 03	0 02	0 02	0 03	0 04	0.03	0 02	0.02
K	1.90	1 97	1.88	1 91	1 92	2 00	1.93	1.93	1 83	1 90	1.89	1 86	1.82	1 90	1 90	1.87	1 93	1 97	1 87	1 92	1 83	1 81
Zn																						
Ba																						
F																						
Cl																						
OH																						
Sum cations	15.69	15 70	15 68	15.71	15.72	15 76	15 73	15.72	15 64	15 66	15 68	15 66	15 63	15 70	15.65	15 67	15 73	15 73	15.69	15 67	15 67	15 64
Y-position [6]	5.75	5 69	5 77	5 77	5 78	5.74	5.77	5 76	5.78	5 74	5.77	5 77	5 77	5.77	5 72	5.77	5 77	5.73	5.78	5.72	5 81	5 81
X-position [12]	1.93	2.01	1 91	1 94	1 94	2 01	1 96	1.96	1.86	1 92	1 91	1.89	1.86	1.93	1 93	1.89	1 95	2.00	1.91	1.95	1.85	1.83
XMg	0.60	0 63	0 61	0 61	0 61	0.61	0 61	0 62	0 61	0 62	0 61	0 61	0 61	0 61	0 62	0 61	0 61	0 62	0.61	0 63	0 62	0 62

Table A6: Microprobe analyses - biotite

sample	TH62C - 14	TH62C - 14	TH62C - 14	TH62C - 14	TH62C - 14	TH62C - 14	TH62C - 14	TH62C - 14	TH62C - 14	TH62C - 14	TH62C - 14	THRW1	THRW1	THRW1	THRW1	THRW1	THRW5	THRW5	THRW5	THRW5
mineral	bioA8	bioA8	bioA7	bioA6	bioA5	bioA4	bioA3	bioA3	bioA2	bioA2	bioA1	bioAE6	bioAE5	bioAE4	bioAE2	bioAE1	bioAD3	bioAD2	bioAD1	bioAD4
Label	28	29	24	23	22	20	15	16	13	14	12	427	426	425	423	420	339	338	337	355
lab.	TUB	TUB	TUB	TUB	TUB	TUB	TUB	TUB	TUB	TUB	TUB	CSL	CSL	CSL	CSL	CSL	CSL	CSL	CSL	CSL
[wt.%]																				
SiO2	33 75	34 83	34 49	32 27	32.87	33 51	34 25	34.13	33 11	33 91	33 94	37.02	37 21	36 84	40 16	37 93	35 69	35 65	35 86	39 59
TiO2	1.63	1.56	0 14	1 03	1.61	1.41	1 50	1 54	1 42	1.52	1 47	0 85	0 8	1 03	0 6	0 82	1 66	1 61	1.65	1 25
Al2O3	17 51	17.52	18 35	18 32	17 27	17 89	17 15	17.40	17 50	17 44	17 29	17 45	17.35	17 2	22 19	17 08	16 65	16 89	17.66	18 29
FeO	27 57	27 24	26 42	28 11	27 79	27 32	27 88	28.09	28 16	27 81	28.04	16 82	16.56	17 18	12.76	15 78	21 91	21 69	21 38	17 64
MnO	0.35	0 38	0 39	0 40	0.46	0.40	0.37	0.38	0 57	0 43	0 43	0.66	0 63	0.77	0 52	0 58	0 52	0.59	0 59	0 65
MgO	5 20	5.57	5 99	5 65	5 58	5 42	5 21	5 23	5 38	5 23	5 25	12.31	12 87	11.5	9 42	12 88	9 45	9 4	9 45	8 31
CaO	0 04	0 02	0.12	0 10	0.05	0 08	0 00	0 00	0 04	0 03	0 06	0.08	0 12	0.11	0 05	0 07	0 15	0 06	0.06	0 77
Na2O	0.05	0.08	0 07	0.03	0 04	0 06	0 05	0 06	0 04	0 11	0.10	0.04	0.06	0 04	0 09	0 06	0 04	0 05	0 06	1.62
K2O	8 26	9 10	8 61	7.18	7 68	8 27	9 45	9 31	8 20	9.35	8 84	9.04	8 91	8.76	9 06	9 58	9 2	9 49	9 08	6 51
ZnO												0 24	0 05	0 12	0 13	0.09	0 1	0 06	0 07	0 08
BaO												0	0 05	0 04	0	0	0 12	0.1	0 18	0 08
F												1.14	1 24	0 95	0 75	1 08	0 38	0 42	0 22	0 23
Cl												0.02	0.01	0 03	0 02	0 03	0 04	0 02	0 02	0
H2O(c)												3.41	3 38	3 46	3 77	3 48	3 69	3 68	3 81	3.92
O=F												0 48	0 52	0 4	0 32	0 45	0.16	0 18	0.09	0 1
O=Cl												0	0	0 01	0	0 01	0 01	0	0 01	0
Sum Oxides [%]	94 36	96 30	94 58	93.09	93 35	94.36	95 86	96 14	94 42	95 83	95.42	94 51	94.61	93 59	94 98	94 87	95 49	95 59	96 04	94 79
# cations:																				
Si	5 40	5 46	5 47	5 24	5 33	5 36	5 44	5 40	5 33	5 39	5 41	5 609	5 615	5 642	5 828	5 697	5 515	5 504	5.482	5.896
Ti	0 20	0 18	0 02	0 13	0 20	0 17	0 18	0 18	0 17	0.18	0.18	0.097	0 091	0 119	0 065	0 093	0.193	0 187	0 19	0 141
Al [4]	2 60	2 54	2.53	2 76	2 67	2 64	2 56	2 60	2 67	2 61	2 59	2 391	2.385	2 358	2 172	2 303	2 485	2 496	2 518	2.104
Al [6]	0 71	0 70	0 90	0.75	0 63	0 74	0 65	0 65	0 65	0 66	0 66	0 725	0 701	0 746	1 623	0 72	0.548	0 577	0 663	1 106
Fe2+	3 69	3.57	3 51	3 82	3.77	3.66	3 70	3 72	3 79	3 69	3 74	2 131	2 089	2 201	1 548	1 981	2 832	2 801	2 734	2 197
Mn2+	0 05	0 05	0 05	0 06	0 06	0 05	0 05	0 05	0 08	0 06	0 06	0 084	0 08	0 099	0 063	0 074	0 068	0.077	0 077	0 082
Mg	1 24	1 30	1.42	1.37	1.35	1 29	1 23	1 23	1.29	1 24	1 25	2 779	2 896	2.626	2 037	2 883	2 177	2 164	2.153	1 844
Ca	0.01	0 00	0 02	0.02	0 01	0 01	0 00	0 00	0 01	0 00	0 01	0.014	0 019	0 019	0 007	0 011	0 025	0 01	0 01	0.123
Na	0 02	0 02	0 02	0.01	0.01	0 02	0 01	0.02	0 01	0.03	0 03	0.01	0 017	0 012	0 025	0 018	0 013	0 015	0 017	0 468
K	1.69	1.82	1.74	1.49	1 59	1 69	1 91	1 88	1 68	1 90	1.80	1.748	1 715	1.712	1 678	1.835	1.813	1.87	1.771	1 237
Zn												0 027	0 006	0 013	0 014	0 01	0 011	0 007	0 008	0 009
Ba												0	0 003	0 002	0	0	0 007	0 006	0.011	0 005
F												0 546	0 591	0 458	0 346	0 512	0 183	0 206	0 108	0 107
Cl												0 005	0 002	0 008	0 004	0 007	0 01	0 004	0.006	0.001
OH												3 449	3 407	3 533	3 65	3 481	3 807	3 79	3 886	3 892
Sum cations	15 61	15 64	15 68	15 65	15 62	15 63	15.73	15 73	15 68	15.76	15.73	15 615	15 617	15 549	15.06	15 625	15.687	15 714	15 634	15 212
Y-position [6]	5 89	5 80	5 90	6 13	6 01	5 91	5 81	5 83	5 98	5 83	5 89	5 843	5 863	5.804	5 351	5 761	5 829	5 813	5 824	5 378
X-position [12]	1 71	1.84	1.76	1 50	1 60	1.71	1.92	1 90	1 69	1 93	1 83	1 772	1.755	1.745	1.709	1 864	1 859	1 901	1 808	1 833
XMg	0 25	0 27	0 29	0 26	0 26	0 26	0 25	0 25	0 25	0 25	0 25	0 566	0 581	0 544	0 568	0 593	0 435	0.436	0.441	0 456

Table A7: Microprobe analyses - chlorite

sample	THRW5	THRW5	THRW5	THRW5	THRW5	TH247-74 5C	TH247-74 5C	TH247-74 5C	TH247-322	TH247-322	TH247-322	TH247-361 3	TH247-361.3	TH247-361 3	TH247-361 3	TH247-98 8C	TH247-98 8C	TH247-98 8C	TH247-98 8C	TH247-98 8C
mineral	chlAD1	chlAD1	chlAD2	chlAD3	chlAD4	chlAF1	chlAF1	chlAF1	chlAK1	chlAK2	chlAK3	chlAL1	chlAL2	chlAL3	chlAL4	chlAV1	chlAV1	chlAV1	chlAV1	chlAV1
analysis no.	343	344	347	349	354	493	494	495	467	468	469	473	474	476	478	380	381	382	383	384
lab:	CSL	CSL	CSL	CSL	CSL	CSL	CSL	CSL	CSL	CSL	CSL	CSL	CSL	CSL	CSL	CSL	CSL	CSL	CSL	CSL
[wt %]																				
SiO2	25.53	26 16	27 63	25 88	27.51	26.02	25 08	27 89	27.96	28 24	28 6	32 66	32.62	33.2	33.7	27 35	27.25	27.11	27.07	26.95
TiO2	0.07	0 09	0.11	0.06	0.16	0.06	0 04	0.04	0.04	0	0 06	0 04	0.01	0.05	0.03	0.06	0.06	0.03	0.02	0.06
Al2O3	20.36	20 62	18.07	20.45	17.66	19 24	19 86	17.03	22 04	21.95	22.03	18.34	18 29	17.13	16.19	19.26	19.56	19.8	19.3	19.26
FeO	29.12	29.41	29.24	28.39	28.92	30 61	29.76	29.43	9 8	10.07	9.69	1.91	2 01	3.53	3 25	23 41	23.59	23 96	23 58	24.34
MnO	1.08	1.11	0.83	1.13	0.74	1.84	1 97	0.97	1.18	1.01	1.1	0.14	0.09	0.12	0.12	0 88	0 84	0 97	0.77	1
MgO	12.14	12	12.87	12.87	13.58	10 62	10	12 54	24.95	25.6	25.89	34.06	33.48	33.18	33.18	16.88	16.86	16.65	16.9	16.3
CaO	0.05	0.1	0 08	0.02	0.16	0 02	0.08	0.03	0.04	0	0 03	0.01	0 06	0.06	0.03	0 02	0.02	0	0.05	0
Na2O	0.02	0.01	0	0.01	0.01	0.02	0.02	0.04	0	0	0.01	0.01	0.01	0	0	0.02	0	0.01	0	0
K2O	0.01	0	0 19	0.01	0 26	0.03	0.05	0 04	0	0 01	0.02	0 03	0.03	0	0.11	0	0.02	0.02	0.01	0.01
ZnO	0 04	0.15	0.07	0 01	0.03	0.11	0 06	0 03	0 22	0.23	0.11	0 04	0.12	0.47	0.14	0.15	0.08	0	0 04	0.13
H2O(c)	11.19	11.36	11 31	11.3	11 3	11.08	10.87	11.15	12.12	12.24	12.34	12 88	12 8	12.82	12.73	11 52	11.55	11 56	11.47	11.45
Sum Oxides [%	88.38	89.5	89.02	88.82	89	88.46	86 86	88.01	86.01	86.88	87.43	87.2	86.6	87.27	86.61	87 88	88 2	88.55	87.7	87.92
# cations:	calculated on the basis of 28 oxygens																			
Si	5.473	5.526	5 861	5 493	5.84	5 637	5 531	5 999	5 532	5.534	5.562	6.081	6.112	6 21	6.352	5 694	5.66	5.624	5 66	5 646
Ti	0 011	0.014	0.017	0 01	0.026	0 009	0.006	0.006	0 007	0	0 008	0.006	0.001	0 007	0 005	0 01	0 009	0.005	0.003	0 009
Al [4]	2.527	2.474	2.139	2.507	2.16	2.363	2.469	2 001	2.468	2.466	2 438	1.919	1.888	1.79	1 648	2.306	2 34	2.376	2.34	2 354
Al [6]	2 617	2.659	2 381	2.608	2.257	2.549	2.693	2 315	2.671	2.602	2.609	2.106	2.151	1.988	1.95	2.42	2.447	2.465	2.414	2.403
Fe2+	5 221	5.195	5.188	5.038	5.134	5.544	5.49	5 293	1.622	1 651	1.576	0 298	0 316	0.552	0.513	4.076	4.097	4.157	4.123	4.264
Mn2+	0.196	0.198	0.149	0.203	0.133	0.337	0.369	0.177	0.198	0 168	0.181	0.022	0.015	0 019	0 019	0.156	0.148	0.17	0 136	0.178
Mg	3.878	3.778	4.071	4 07	4 296	3 427	3.266	4.021	7 356	7.477	7.504	9.454	9.35	9.251	9.32	5 24	5.218	5.149	5.265	5.089
Ca	0 011	0.022	0.019	0.006	0.037	0.005	0.018	0.006	0.008	0	0.007	0.003	0.012	0.012	0.006	0.004	0.004	0	0.011	0.001
Na	0.007	0 003	0	0 004	0 005	0.009	0.007	0 015	0	0	0.005	0.004	0 004	0	0	0 006	0	0.002	0	0
K	0.002	0	0.052	0.004	0.07	0.008	0.014	0.012	0 001	0.002	0 004	0.008	0.007	0	0 026	0.001	0.005	0.005	0.002	0.003
Zn	0.006	0.024	0.011	0.001	0 005	0.018	0 009	0.004	0 032	0 034	0 016	0.005	0 017	0.064	0 019	0.023	0.012	0	0.007	0.021
OH	16	16	16	16	16	16	16	16	16	16	16	16	16	16	16	16	16	16	16	16
Sum cations	19 94	19.89	19.836	19.936	19 888	19.889	19 871	19.822	19.894	19.932	19.901	19 894	19.862	19 893	19.832	19.929	19.935	19.946	19.959	19.965
Y-position [6]	11.94	11.89	11.836	11.936	11 888	11 889	11 871	11.822	11.894	11 932	11.901	11.894	11 862	11.893	11.832	11 929	11.935	11.946	11.959	11.965
XMg	0 426	0.421	0 44	0.447	0.456	0.382	0 374	0.432	0 819	0 819	0 826	0 969	0 967	0 944	0 948	0 562	0.56	0 553	0 561	0.544

Table A7: Microprobe analyses - chlorite

sample	TH247-98 8(	TH247-98 8(	TH247-98 8(	TH247-169 8	TH247-169 8	TH247-169 8	TH247-169 8	TH247-169 8	TH247-169 8	TH247-169 8	TH247-219	TH247-219	TH247-219	TH247-219	TH247-219	TH247-219	TH247-238 8	TH247-238 8	TH247-238 8	TH247-238.8
mineral	chlAV1	chlAV1	chlAV1	chlAW1	chlAW2	chlAW3	chlAW4	chlAW5	chlAW6	chlAW7	chlAX1	chlAX1	chlAX1	chlAX2	chlAX3	chlAX4	chlAY1	chlAY2	chlAY3	chlAY3
analysis no	385	386	387	398	399	400	415	416	417	418	300	301	302	315	318	321	506	509	511	512
lab:	CSL	CSL	CSL	CSL	CSL	CSL	CSL	CSL	CSL	CSL	CSL	CSL	CSL	CSL	CSL	CSL	CSL	CSL	CSL	CSL
[wt %]																				
SiO2	26.93	28.01	27.61	26.7	27.35	27.98	26.59	26.47	26 72	27 06	27 94	27.68	27.56	29.6	29 1	28 99	29.34	30.46	27.79	27.84
TiO2	0 04	0.06	0 03	0 04	0	0 05	0.02	0.07	0.03	0 04	0.04	0.03	0.07	0.08	0.02	0.04	0 04	0 1	0.05	0.06
Al2O3	19.75	17.31	17.99	22.72	23.42	21.78	23.44	23.39	22 51	22.35	23.6	23 39	23.64	22 42	23 06	22 64	21.4	20 2	23 21	22.96
FeO	24.46	24.78	25.83	14.84	15.4	16 51	15 11	15.05	16 01	15.78	9.38	9 34	9.2	9.18	9.2	8.96	10.24	10 9	10.14	9.96
MnO	0 99	1	1.22	0 95	1.05	0.78	1.03	1.14	1.03	1.05	0.54	0.7	0.78	0.7	0 61	0.77	0.66	0.44	0.61	0 61
MgO	16.25	16.31	15.25	21.61	22.15	20.5	21 5	21.77	21.09	21.68	26 05	25.65	25.76	25.8	27.31	26 47	25.98	25 76	25.55	25.44
CaO	0.02	0.02	0.04	0.03	0.02	0.01	0.01	0.01	0.02	0	0.03	0.04	0	0 04	0.02	0	0.01	0.05	0.04	0 04
Na2O	0	0.02	0	0.02	0.01	0.02	0	0	0	0	0	0	0.01	0.02	0 01	0.05	0	0.02	0.04	0.02
K2O	0	0.01	0 01	0	0	0.02	0.01	0	0	0	0.01	0.03	0	0.77	0.03	0.17	0.02	0.41	0.01	0.01
ZnO	0.06	0 08	0 01	0.19	0.17	0.14	0 21	0 3	0.11	0 24	0.25	0.29	0.14	0.09	0 3	0 2	0 23	0.22	0.24	0.25
H2O(c)	11.51	11.37	11.35	11.93	12.26	11 97	12.03	12 05	11.91	12 02	12 42	12.31	12 33	12.53	12 69	12.5	12 39	12.44	12.34	12 28
Sum Oxides [%	88.44	87.52	87 98	86.91	89.4	87.65	87.71	87.9	87.41	87.96	87.59	86 86	87.02	88.61	89 36	88.09	87.69	88.34	87.44	86 94
# cations:																				
Si	5 61	5 91	5.834	5.369	5 354	5 607	5.304	5.27	5.38	5 402	5 394	5.395	5.363	5 865	5.498	5 561	5.68	5 875	5.402	5.437
Ti	0.006	0 009	0 005	0.006	0.001	0.008	0.003	0.011	0 004	0.006	0.006	0.005	0.011	0 012	0.003	0 006	0.005	0 014	0 007	0.008
Al [4]	2 39	2.09	2.166	2 631	2 646	2 393	2 696	2.73	2 62	2.598	2.606	2 605	2.637	2 335	2.502	2.439	2.32	2.125	2.598	2.563
Al [6]	2.459	2.216	2 316	2.753	2.757	2.752	2.813	2 759	2.721	2 66	2 765	2.767	2.785	2.723	2.633	2 678	2.564	2.467	2.72	2.721
Fe2+	4.261	4.373	4.566	2.496	2.521	2.767	2.52	2 507	2 695	2.633	1.515	1.523	1.497	1 469	1.454	1.437	1.658	1.759	1.649	1.626
Mn2+	0.175	0.179	0 219	0.162	0.174	0.133	0.175	0 192	0.176	0.177	0 088	0.115	0.128	0.113	0 097	0.125	0.108	0.072	0.101	0.101
Mg	5 045	5.131	4 802	6.475	6.46	6.124	6.393	6 46	6.329	6.451	7.496	7.449	7.472	7.36	7 693	7.569	7.499	7 407	7.403	7.405
Ca	0.005	0 004	0.008	0.007	0.004	0.002	0.001	0 001	0 003	0 001	0.006	0 009	0	0.008	0.003	0	0.002	0.01	0.008	0.009
Na	0	0 007	0	0 009	0.004	0.007	0 002	0	0	0	0	0.001	0 002	0.007	0 005	0 017	0	0.006	0 016	0 009
K	0	0.002	0 002	0	0.001	0.006	0.001	0	0	0	0.002	0 008	0	0 188	0.006	0 041	0 006	0.1	0.002	0.003
Zn	0.009	0 012	0.002	0 029	0.025	0.021	0 031	0.045	0.017	0 036	0.036	0 041	0 02	0 013	0.042	0 028	0 034	0 032	0.034	0.036
OH	16	16	16	16	16	16	16	16	16	16	16	16	16	16	16	16	16	16	16	16
Sum cations	19.96	19 924	19.918	19.928	19 942	19 807	19.936	19.975	19.945	19 964	19.912	19.909	19 913	19.698	19 925	19.843	19.87	19.761	19.922	19.906
Y-position [6]	11.96	11.924	11.918	11.928	11.942	11.807	11.936	11.975	11.945	11 964	11.912	11.909	11.913	11 698	11.925	11.843	11.87	11.761	11.922	11 906
XMg	0.542	0 54	0.513	0 722	0.719	0.689	0 717	0.72	0.701	0.71	0.832	0.83	0 833	0.834	0.841	0 84	0 819	0.808	0.818	0 82

Table A7: Microprobe analyses - chlorite

sample	TH247-238 8	TH247-238 8	TH247-274 8	TH247-274 8	TH247-274.8	TH247-274.8	TH247-300	TH247-300	TH247-300	TH247-347	TH247-347	TH247-347	TH247-347	TH62C - 141	TH62C - 141	TH62C - 141	TH62C - 141	TH62C - 141	TH62C - 141	TH85A - 383
mineral	chlAY3	chlAY3	chlAZ1	chlAZ2	chlAZ3	chlAZ3	chlBA1	chlBA1	chlBA2	chlBB1	chlBB1	chlBB2	chlBB3	chlA1	chlA1	chlA1	chlA2	chlA2	chlA2	chlB1
analysis no.	513	514	362	363	364	365	327	328	329	428	429	430	435	17	18	19	25	26	27	36
lab:	CSL	CSL	CSL	CSL	CSL	CSL	CSL	CSL	CSL	CSL	CSL	CSL	CSL	TUB	TUB	TUB	TUB	TUB	TUB	TUB
[wt.%]																				
SiO2	28.26	28 1	28.76	28.47	28.39	28.81	29.46	29 97	28.89	30.25	31 04	30 82	30.89	23.89	24.01	23.69	24.02	24.11	23.58	24.47
TiO2	0 06	0.04	0.03	0.04	0 04	0.03	0 03	0.05	0.02	0.03	0 04	0.05	0.02	0.04	0.07	0 06	0 07	0.07	0.07	0.05
Al2O3	23 23	23 37	22.95	22.84	22.65	23.27	21.91	22.03	23.47	21.67	20 08	20 51	20.36	20.61	20.14	20.52	20 41	20.40	20 52	23 25
FeO	10.21	10.73	8.19	8.02	8.13	7.88	7.34	6 82	6.99	4.78	4.78	4.8	4.91	35 56	35.54	35 94	36.03	35.60	35.74	22 24
MnO	0.69	0.71	0.63	0.67	0.58	0.69	0 29	0.37	0.24	0.46	0.55	0 42	0.53	0.74	0.70	0.78	0.73	0.72	0.71	0 66
MgO	25 9	25.68	27.32	27.15	26.68	27.42	28.1	28.67	28.06	30 6	30 32	30 29	30 65	7.10	7.45	6.90	7.27	7.18	7.23	16.70
CaO	0.04	0.02	0.03	0.02	0 02	0 03	0.01	0.02	0 02	0	0.04	0.03	0	0.01	0.00	0 01	0.02	0.02	0.02	0.00
Na2O	0.04	0.03	0.01	0	0	0	0.01	0	0	0	0	0.01	0	0.00	0.00	0.03	0.00	0 00	0.01	0.00
K2O	0.01	0.01	0	0.01	0.01	0.01	0.05	0.04	0.01	0	0.13	0.02	0.01	0.00	0.02	0.00	0 03	0 00	0.04	0.00
ZnO	0 25	0.23	0.14	0.26	0.27	0.24	0 02	0.19	0.19	0.19	0.1	0 05	0 21							
H2O(c)	12.48	12.48	12.54	12.45	12.35	12.6	12.51	12.67	12.62	12.76	12 64	12.64	12 7							
Sum Oxides [%	88.44	88 69	87.92	87.22	86.5	88.14	87.2	87.97	87.7	87.79	86.98	86 95	87.37	87.95	87.93	87.93	88.58	88.10	87.92	87.37
# cations:																				
Si	5.431	5 402	5.501	5 484	5.514	5 484	5.649	5 675	5.49	5.685	5.893	5.847	5 836	5 34	5 36	5 32	5.34	5.38	5 28	5 10
Ti	0 009	0 006	0 005	0 006	0.006	0 005	0.004	0 006	0.003	0 004	0 006	0.007	0 003	0.00	0 02	0 01	0.02	0.02	0.02	0 00
Al [4]	2.569	2 598	2.499	2 516	2.486	2 516	2.351	2.325	2.51	2 315	2.107	2.153	2.164	2.66	2.64	2.68	2.66	2.62	2.72	2.90
Al [6]	2 694	2.696	2.674	2.67	2.699	2.706	2.601	2.591	2.746	2.484	2 385	2 434	2.369	2.78	2.68	2.74	2.70	2.74	2.70	2.82
Fe2+	1.641	1.726	1.31	1.292	1.32	1.255	1.176	1.079	1 11	0.751	0.759	0.762	0.775	6.64	6.64	6.74	6.70	6.64	6.70	3.88
Mn2+	0.113	0.116	0 102	0.11	0 095	0.11	0.046	0 059	0.038	0.074	0.089	0 068	0.086	0.14	0.14	0.15	0.14	0.14	0.14	0.12
Mg	7.42	7 357	7.789	7.796	7.725	7.781	8.03	8 09	7 948	8.572	8.578	8.565	8 63	2.36	2.48	2.31	2.42	2 38	2.42	5 20
Ca	0.008	0 004	0 005	0 005	0.004	0 007	0 002	0 004	0 004	0	0.008	0.006	0	0.00	0.00	0.00	0.00	0 00	0.00	0.00
Na	0.015	0.01	0.005	0	0	0	0.002	0	0	0	0	0.003	0	0 00	0 00	0 01	0.00	0.00	0.00	0.00
K	0.001	0 004	0 001	0.002	0.001	0.003	0.012	0 01	0 003	0	0.031	0 005	0.002	0.00	0 00	0.00	0.00	0 00	0 02	0.00
Zn	0.035	0 033	0 02	0.037	0.038	0 034	0 003	0 026	0.027	0.027	0.014	0.007	0.03							
OH	16	16	16	16	16	16	16	16	16	16	16	16	16							
Sum cations	19.92	19.938	19.905	19.916	19.887	19.898	19 862	19 855	19.876	19.912	19.839	19.849	19.893	19 92	19.96	19.97	19 98	19.92	20.00	20.02
Y-position [6]	11.92	11.938	11.905	11.916	11.887	11.898	11.862	11.855	11.876	11.912	11.839	11.849	11.893	11.92	11.94	11 94	11 96	11.90	11.96	12.02
XMg	0 819	0.81	0.856	0 858	0.854	0.861	0 872	0 882	0.877	0.919	0 919	0.918	0 918	0 26	0 27	0 26	0 27	0.26	0.27	0 57

Table A7: Microprobe analyses - chlorite

sample	TH85A - 383	TH85A - 383	TH85A - 383	TH85A - 383	TH85A - 383	TH85A - 383	TH85A - 383	TH85A - 383	TH85A - 383	TH85A - 383	TH85A - 383	TH85A - 383	TH471 - 159	TH471 - 159	TH471 - 159	TH471 - 104	TH471 - 104	TH471 - 104	TH471 - 104	TH471 - 104
mineral	chlB2	chlB2	chlB2	chlB2	chlB3	chlB4	chlB4	chlB5	chlB6	chlB7	chlB8	chlB9	chlC1	chlC1	chlC2	chlD1	chlD2	chlD3	chlD3	chlD4
analysis no.	37	38	39	40	41	50	51	56	57	58	59	60	83	84	89	157	158	163	164	165
lab:	TUB	TUB	TUB	TUB	TUB	TUB	TUB	TUB	TUB	TUB	TUB	TUB	TUB	TUB	TUB	TUB	TUB	TUB	TUB	TUB
[wt.%]																				
SiO2	25.24	25 36	25.48	25 27	24.29	24 71	24 74	24.91	24 92	25 51	25.48	24.97	27 25	27.67	27.57	24.86	25.80	25.24	25.55	25.80
TiO2	0 03	0 04	0 06	0.00	0.04	0.07	0.06	0.06	0.02	0.06	0.08	0.06	0.22	0 13	0.12	0.06	0.09	0.05	0.07	0.04
Al2O3	22.36	21 83	21.91	22.61	21.76	22.77	21.85	21 87	22.33	22 54	22 83	22.42	22.34	21 91	22.16	22.64	21 89	22 21	22.57	22.03
FeO	22.12	22 01	24 97	23 29	23 81	23 30	24.18	24 54	23 22	22.15	22 37	24 38	13.74	13.81	12.28	21 15	21 99	20 86	21 66	20 52
MnO	0 69	0.65	0.61	0.56	0.55	0 61	0 68	0 63	0 58	0 58	0 59	0.57	0.74	0.79	0.79	0.79	0.69	0.63	0.62	0.72
MgO	16.87	17.27	15.56	15.85	15.21	15.83	15.22	14.78	16.16	17.19	17.10	14.70	22.78	22.93	23 99	16 92	16.92	17.32	17.13	17.42
CaO	0.01	0 01	0 00	0 02	0.00	0 02	0.03	0.02	0.03	0 00	0.00	0.00	0.01	0.01	0.00	0 01	0.00	0.00	0.01	0.03
Na2O	0.01	0.02	0 00	0.01	0.00	0 00	0.00	0.00	0.01	0.01	0.00	0.01	0.00	0.00	0.02	0.00	0.02	0.01	0.03	0.00
K2O	0.00	0.00	0.01	0.01	0.03	0.00	0.00	0.00	0.00	0.00	0.00	0.01	0.01	0 04	0.07	0 00	0.00	0.00	0.01	0.01
ZnO																				
H2O(c)																				
Sum Oxides [%	87.33	87.19	88 60	87 62	85.69	87.31	86.76	86 81	87 27	88 04	88 45	87 12	87.09	87.29	87.00	86.44	87 40	86.32	87.66	86.58
# cations:																				
Si	5 26	5 30	5.30	5 28	5.22	5.18	5.26	5.30	5 24	5.26	5 24	5.28	5.44	5 50	5.46	5.22	5.37	5 29	5 29	5.38
Ti	0 00	0 00	0.00	0 00	0.00	0.02	0 02	0 00	0.00	0 00	0.02	0.00	0.04	0.02	0 02	0 01	0.01	0.01	0.01	0 01
Al [4]	2.74	2.70	2 70	2.72	2.78	2 82	2.74	2 70	2 76	2.74	2.76	2.72	2.56	2.50	2.54	2.78	2.63	2.71	2.71	2.62
Al [6]	2 76	2.68	2.68	2 84	2.74	2.82	2.74	2.78	2.76	2.74	2.78	2.86	2.70	2 64	2 64	2.82	2 73	2.77	2.79	2.79
Fe2+	3.86	3 84	4.36	4.06	4.28	4 10	4.30	4.36	4 08	3.82	3.84	4.30	2 30	2.30	2.04	3.71	3 82	3.66	3.75	3.58
Mn2+	0.12	0.12	0.10	0 10	0.10	0.10	0.12	0.12	0 10	0 10	0.10	0 10	0.12	0 14	0.14	0.14	0.12	0.11	0.11	0.13
Mg	5.24	5.38	4 84	4.94	4.88	4.96	4 82	4 68	5 06	5.30	5 24	4.64	6.78	6 80	7 08	5.29	5.24	5.41	5.28	5 41
Ca	0.00	0.00	0.00	0.00	0 00	0.00	0 00	0 00	0.00	0.00	0.00	0 00	0 00	0.00	0.00	0.00	0.00	0 00	0.00	0.01
Na	0.00	0.00	0.00	0.00	0.00	0 00	0.00	0.00	0 00	0 00	0 00	0 00	0 00	0.00	0.00	0.00	0.01	0 00	0.01	0 00
K	0.00	0.00	0 00	0.00	0.00	0.00	0.00	0.00	0.00	0.00	0 00	0 00	0.00	0.02	0.02	0.00	0.00	0.00	0.00	0 00
Zn																				
OH																				
Sum cations	19.98	20 02	19 98	19 94	20.00	20 00	20.00	19 94	20.00	19.96	19 98	19 90	19.94	19.92	19.94	19.97	19.94	19.96	19.96	19.91
Y-position [6]	11.98	12 02	11.98	11 94	12.00	11.98	11.98	11.94	12 00	11.96	11.96	11.90	11.90	11.88	11.90	11 96	11 92	11 95	11 93	11.90
XMg	0.58	0 58	0.53	0 55	0 53	0 55	0 53	0.52	0 55	0.58	0 58	0.52	0.75	0.75	0 78	0 59	0 58	0.60	0 59	0 60

Table A7: Microprobe analyses - chlorite

sample	TH471 - 104	TH471 - 104	TH471 - 104	TH471 - 104	TH471 - 104	TH394 - 262	TH394 - 262	TH394 - 262	TH394 - 262	TH394 - 262	TH40 - 67 0	TH40 - 67 0	TH40 - 67.0	TH40 - 67.0	TH40 - 67 0
mineral	chlD5	chlD6	chlD7	chlD8	chlD9	chlE1	chlE2	chlE3	chlE4	chlE5	chlF1	chlF2	chlF3	chlF4	chlF5
analysis no.	166	188	190	191	195	210	211	212	213	214	277	278	268	270	274
lab:	TUB	TUB	TUB	TUB	TUB	TUB	TUB	TUB	TUB	TUB	TUB	TUB	TUB	TUB	TUB
[wt.%]															
SiO2	25.26	24.81	25 68	27.12	26.63	24 62	24 71	24.92	24.15	24 79	24.20	24 60	29.47	26.53	29.36
TiO2	0 04	0 03	0 04	0.05	0.01	0 04	0 07	0.04	0.03	0 02	0.02	0.11	0 08	0.06	0.12
Al2O3	21.74	21.77	22 30	21.08	21 18	22.81	22.90	22 52	23 06	22 12	19 70	20.37	15.60	17.33	15.22
FeO	24.90	22.31	21.72	22 92	20.98	24.04	24.12	23.50	24.09	24 95	32.54	32 83	29.02	29.16	29.18
MnO	0.58	0.50	0.62	0 50	0.62	0.86	0.83	0.77	0.78	0 86	1 06	1.06	0.65	0.94	0 76
MgO	14.79	16.15	16.87	15.10	17.71	15.03	14.88	15.55	14 47	14.33	9.42	9.15	10.99	11.02	11.50
CaO	0.00	0.01	0 03	0 02	0.04	0.02	0 00	0 01	0.00	0.00	0.05	0.13	0.44	0.15	0 48
Na2O	0 00	0 02	0 02	0.03	0 00	0.05	0.01	0 00	0 02	0.00	0 03	0.01	0 05	0.04	0.06
K2O	0 00	0 03	0.00	1.20	0.01	0.02	0.06	0 00	0.04	0.01	0.00	0.00	0.04	0 00	0.04
ZnO															
H2O(c)															
Sum Oxides [%	87.31	85.62	87.29	88.01	87.18	87.48	87.60	87.31	86 65	87.09	87.03	88 26	86.34	85 23	86.72
# cations:															
Si	5.34	5 29	5.34	5 65	5.51	5.19	5.20	5.24	5.14	5 27	5.40	5.40	6.43	5.92	6.39
Ti	0 01	0.01	0.01	0 01	0.00	0 01	0 01	0 01	0 01	0 00	0.00	0 02	0 01	0.01	0.02
Al [4]	2.66	2.71	2.66	2.35	2.49	2 81	2 80	2 76	2 86	2.73	2 60	2 60	1.57	2.08	1 61
Al [6]	2.76	2 76	2 80	2.82	2.68	2.85	2.87	2 82	2.93	2 81	2 58	2.67	2 44	2.47	2.30
Fe2+	4.41	3 98	3.78	3 99	3.63	4.23	4.24	4.13	4.29	4.44	6.07	6.03	5.29	5.44	5.31
Mn2+	0 10	0.09	0.11	0.09	0.11	0.15	0.15	0.14	0 14	0.15	0.20	0 20	0 12	0.18	0.14
Mg	4.66	5 13	5 23	4.69	5.47	4.72	4.67	4.87	4 59	4.54	3.13	2.99	3 57	3.66	3 73
Ca	0.00	0 00	0.01	0.00	0 01	0.00	0 00	0.00	0 00	0.00	0 01	0 03	0.10	0.04	0 11
Na	0.00	0 01	0.01	0.01	0 00	0.02	0 00	0 00	0 01	0.00	0 01	0.00	0.02	0.02	0.03
K	0.00	0 01	0 00	0.32	0.00	0.01	0 02	0.00	0.01	0 00	0 00	0.00	0.01	0.00	0.01
Zn															
OH															
Sum cations	19 94	19.98	19.93	19 92	19 90	19.99	19.96	19.97	19 97	19 95	20 01	19.95	19 57	19 81	19 66
Y-position [6]	11.93	11.96	11.91	11 58	11.89	11.96	11.93	11.96	11 95	11.95	11.98	11.90	11.42	11.74	11.48
XMg	0.51	0 56	0 58	0 54	0.60	0 53	0.52	0.54	0 52	0 51	0 34	0 33	0 40	0.40	0.41

Table A8: Microprobe analyses - muscovite

sample	THRW5	THRW5	THRW5	THRW5	THRW5	THRW5	THRW1	THRW1	TH247-74 5C	TH247-74 5C	TH247-74 5C	TH247-74 5C	TH247-136 1	TH247-136 1	TH247-136 1	TH247-322	TH247-322	TH247-322	TH247-57 7C	TH247-57 7C	TH247-98 8C	TH247-98 8C	TH247-98 8C	TH247-98 8C	TH247-169 6
mineral	musAD1	musAD1	musAD2	musAD3	musAD5	musAD6	musAE1	musAE2	musAF1	musAF1	musAF2	musAF3	musAG1	musAG2	musAG3	musAK1	musAK2	musAK5	musAU2	musAU3	musAV1	musAV6	musAV7	musAV8	musAW2
analysis no	335	336	340	342	351	353	421	422	485	486	487	489	445	446	447	458	460	463	455	456	371	393	394	395	403
lab	CSL	CSL	CSL	CSL	CSL	CSL	CSL	CSL	CSL	CSL	CSL	CSL	CSL	CSL	CSL	CSL	CSL	CSL	CSL	CSL	CSL	CSL	CSL	CSL	CSL
[wt %]																									
SiO2	49 19	49 31	48 78	49 56	48 9	48 57	46 27	49 17	50 49	48 96	49 84	49.74	47 45	49 01	46 04	48 54	49 03	46 47	49 92	48 96	49 42	48 5	47 57	45 63	49.31
TiO2	0 71	0 21	0.2	0 23	0.27	0 22	0 33	0 17	0 6	0 59	0 58	0 56	0 25	0 19	0 24	0 43	0 47	0 46	0 72	0 61	0.33	0 32	0 4	0 32	0.23
Al2O3	30.99	32 29	31 98	31 82	31 11	30 81	30 82	34 36	31 45	31.02	33 2	32.98	31 84	34.19	30 94	34 28	35 05	33 33	33.7	31 55	33.4	33 6	31.75	37 91	32.15
FeO	5 16	4 82	5 35	4 91	5 6	5 88	6	2 15	3 23	3.77	3 59	3 81	4 32	2 52	4 07	2 21	1.78	1 67	2 53	2 4	3 52	3.16	4 86	2 54	2 15
MnO	0 04	0 08	0 06	0 04	0 03	0 02	0 19	0 01	0	0.08	0 09	0.14	0 13	0 08	0 15	0 04	0.09	0 03	0 07	0 05	0 08	0 02	0.21	0 07	0 03
MgO	1.81	1 6	1 81	1.79	1 81	1 93	3 95	1.49	1 58	1 74	1 72	1 85	4 23	2 26	4	3 33	1.58	1.77	1 84	1.97	2.09	1 72	3 34	1 7	2 81
CaO	0 05	0	0 03	0	0 11	0 01	0 01	0 03	0 04	0 03	0	0 02	0 02	0	0 03	0 04	0.04	0 02	0 02	0 05	0	0	0 04	0 12	0 06
Na2O	0.17	0 18	0 19	0.21	0.17	0 14	0 17	0 22	0 89	0 28	0 24	0 24	0 23	0 24	0 22	0 34	0 3	0 35	0 24	0 26	0 26	0 28	0 28	0 69	0 28
K2O	8 61	8 55	9 51	9 46	8 99	8 57	8 72	9 02	8 72	9 05	8 32	8 37	9 75	9 87	9 9	8 06	8 95	9 78	9 2	9 39	9 01	9 62	8 8	8 73	9 5
ZnO	0 07	0	0 05	0	0 05	0 07	0 05	0	0 05	0	0	0 02	0 07	0 08	0	0 04	0	0 09	0 01	0 07	0 05	0 05	0	0 03	0
BaO	0.14	0 12	0 14	0 04	0 17	0 12	0 02	0 07	0 15	0.19	0 2	0 29	0 19	0.28	0 21	0 72	0.86	0.87	0.22	0 2	0.2	0 23	0 19	0 15	0 4
F	0 28	0 25	0 36	0.21	0 16	0 17	0 44	0.22	0 3	0 23	0 52	0 33	0 38	0 19	0 31	0 06	0	0 06	0 29	0 34	0 24	0.22	0 43	0 18	0 64
Cl	0 01	0 02	0	0	0	0	0 01	0	0.21	0.12	0 03	0 02	0	0 01	0.01	0	0 01	0 01	0	0 01	0	0	0 02	0	0.01
H2O(c)	4 42	4.46	4 41	4 5	4 47	4 43	4 27	4 51	4 41	4.37	4 39	4 48	4 41	4 57	4 3	4 63	4.66	4 43	4 54	4 36	4 54	4 49	4 34	4 54	4 28
O=F	0.12	0 11	0 15	0 09	0 07	0 07	0 18	0 09	0 12	0 1	0 22	0 14	0 16	0 08	0 13	0 02	0	0 03	0.12	0 14	0 1	0 09	0 18	0 08	0 27
O=Cl	0	0	0	0	0	0	0	0	0 05	0 03	0 01	0	0	0	0	0	0	0	0	0	0	0	0	0	0
Sum Oxides [%	96 94	97 16	98 1	98 06	97 21	96 34	96 53	96 69	97.2	95.71	97 78	98 02	98 48	98 72	95 8	98 03	98.15	94 84	98 47	95 51	98 36	97 5	97 44	97 89	96 92
# cations:	calculated on the basis of 22 oxygens																								
Si	6 476	6 45	6 389	6 459	6 453	6 458	6 193	6 386	6 569	6 504	6.431	6 422	6 206	6 306	6.204	6 245	6 307	6.249	6 399	6 488	6 373	6 328	6 264	5.907	6 443
Ti	0 071	0 021	0 019	0 023	0 027	0 022	0 033	0 016	0 059	0 059	0 056	0 054	0 025	0 018	0 025	0 041	0 046	0 046	0 07	0 061	0 032	0 031	0 039	0 031	0 022
Al [4]	1 524	1 55	1 611	1 541	1.547	1 542	1 807	1 614	1 431	1 496	1.569	1.578	1 794	1 694	1 796	1.755	1.693	1 751	1 601	1 512	1.627	1 672	1 736	2.093	1 557
Al [6]	3 285	3 428	3 325	3 347	3 291	3 286	3 055	3 646	3 39	3 361	3 479	3 44	3 116	3 491	3 116	3 444	3 619	3 531	3 49	3 415	3 448	3 494	3 191	3 692	3 394
Fe2+	0 569	0 527	0 586	0 536	0 618	0 653	0.672	0 234	0 352	0 419	0 387	0 411	0.472	0 272	0 459	0 238	0 191	0 188	0 271	0 266	0 38	0 345	0 535	0.275	0 235
Mn2+	0 005	0 009	0 006	0 004	0 003	0 002	0 021	0 001	0	0 009	0 009	0 015	0 014	0 008	0 017	0 005	0 01	0 003	0.008	0 006	0 009	0 002	0 023	0 007	0 004
Mg	0.355	0 313	0 353	0 348	0 356	0 382	0 788	0 288	0 306	0 345	0 331	0 357	0 825	0 433	0 804	0 638	0 303	0 354	0 352	0 389	0.401	0 334	0 655	0 328	0 548
Ca	0.007	0	0 004	0	0 015	0 002	0 001	0 004	0 006	0 004	0	0 003	0 003	0 001	0 004	0 005	0 006	0 003	0 002	0 007	0	0	0 005	0 017	0 009
Na	0 044	0 045	0 048	0 054	0 043	0 037	0 045	0 056	0 224	0 071	0 06	0 059	0 059	0 059	0 058	0 086	0 076	0 092	0 059	0 067	0 065	0 072	0 07	0.174	0 071
K	1 446	1 427	1 588	1 573	1 512	1 454	1.489	1 495	1 447	1.534	1 37	1 378	1 627	1 619	1 701	1 322	1 469	1 677	1 504	1 586	1 482	1 6	1 479	1 441	1 583
Zn	0 007	0	0 005	0	0 005	0.007	0 005	0	0.005	0	0	0 001	0 006	0 008	0	0 003	0	0 009	0 001	0 006	0 005	0 005	0	0 003	0
Ba	0 007	0 006	0 007	0 002	0 009	0 006	0 001	0 004	0 008	0 01	0 01	0 015	0 01	0 014	0 011	0 036	0 043	0 046	0 011	0 01	0 01	0 012	0 01	0 007	0 02
F	0.115	0 103	0.149	0 088	0.066	0 073	0 184	0 089	0.122	0 097	0 213	0.136	0 156	0 079	0 134	0 024	0 002	0 028	0.117	0 141	0 096	0 089	0.181	0 075	0 265
Cl	0 003	0 004	0	0	0	0	0 003	0	0 047	0 026	0 006	0 004	0	0 002	0 003	0	0 001	0 003	0	0 003	0 001	0 001	0 004	0	0 003
OH	3 883	3.893	3 851	3 912	3 933	3 927	3 812	3 91	3 831	3 876	3 781	3 86	3 844	3 919	3 863	3 976	3 997	3 969	3 883	3 855	3 903	3 91	3 816	3 925	3 732
Sum cations	13 91	13 88	14 09	13 98	13.95	13 92	14 30	13 83	13 97	13 94	13 92	13 87	14.31	14 00	14 33	13 84	13 77	13 98	13 89	13 96	13 93	13 99	14 19	14 05	14 15
Y-position [6]	4.29	4 30	4 29	4 26	4 30	4 35	4 57	4 19	4.11	4.19	4.26	4.28	4 46	4 23	4 42	4 37	4.17	4 13	4 19	4.14	4 28	4 21	4 44	4 34	4 20
X-position [12]	1 51	1.48	1 65	1 63	1 58	1 50	1 54	1 56	1 68	1 62	1.44	1.46	1 70	1 69	1 77	1.45	1 59	1 82	1 58	1 67	1 56	1 68	1.56	1.64	1 68
XMg	0.38	0 37	0 38	0 39	0 37	0 37	0 54	0.55	0 47	0 45	0 46	0 47	0 64	0 61	0 64	0 73	0 61	0 65	0 57	0 59	0 51	0 49	0 55	0 54	0 70

Table A8: Microprobe analyses - muscovite

sample	TH247-169 8	TH247-169 8	TH247-169 8	TH247-219	TH247-219	TH247-219	TH247-219	TH247-219	TH247-219	TH247-219	TH247-238 8	TH247-238 8	TH247-238 8	TH247-238 8	TH247-238 8	TH247-238 8	TH247-274 8	TH247-274 8	TH247-300	TH247-300	TH247-300	TH247-300	TH247-347	TH247-347	TH247-347
mineral	musAW3	musAW4	musAW8	musAX1	musAX2	musAX3	musAX4	musAX5	musAX6	musAX9	musAY1	musAY1	musAY1	musAY3	musAY5	musAY6	musAZ1	musAZ2	musBA1	musBA2	musBA3	musBA4	musBB1	musBB2	musBB3
analysis no.	405	410	414	306	307	308	312	313	314	324	496	497	503	499	501	502	369	370	331	332	333	334	431	432	436
lab:	CSL	CSL	CSL	CSL	CSL	CSL	CSL	CSL	CSL	CSL	CSL	CSL	CSL	CSL	CSL	CSL	CSL	CSL	CSL	CSL	CSL	CSL	CSL	CSL	CSL
[wt %]																									
SiO2	48 08	47 16	47 31	45 34	48 18	50.23	47 34	44 73	44 8	47 76	49 07	48 59	48 42	49 23	48 27	48 49	46 47	43 92	52 72	49 21	49 73	48 69	49 51	50 46	49 31
TiO2	0.24	0 28	0 24	0.41	0 22	0 31	0 37	0 31	0.28	0 29	0 46	0 52	0 52	0 45	0 49	0 56	0 2	0 21	0 21	0 22	0 26	0.21	0 3	0 3	0.4
Al2O3	36 37	30 45	35 28	31 42	36 72	33 75	35.59	30 53	34 58	36 79	35 75	36 5	36 82	37.2	35 02	36 59	30 76	28 96	33 06	35 71	36.04	35 97	33.44	35.11	34 29
FeO	1 92	5 35	2 42	3 3	1 57	1 57	1.45	2 75	1 94	1.45	1.46	1 4	1.49	1 33	2 03	1 4	2 72	3 12	1.21	1 63	1 64	1 31	1 07	0 8	0 73
MnO	0 02	0 01	0 08	0 14	0 06	0	0	0 1	0 03	0	0 01	0 02	0 04	0	0 09	0	0 1	0 04	0 01	0 04	0	0 05	0	0 03	0
MgO	1 11	2 96	1.74	6 91	1	2 37	1 35	5 81	1 89	1 06	1 41	1 08	1.05	1 03	2 86	1 07	7 57	8 58	2 73	2 16	1 63	1 71	2 77	2 62	2 16
CaO	0 02	0.19	0	0	0	0 01	0	0 04	0	0 02	0 04	0 03	0	0 03	0 05	0	0	0.01	0 01	0 02	0 01	0 06	0 02	0 03	0 02
Na2O	0 93	2.26	0 62	0 71	0 86	0 46	0 62	0 47	0 69	0 81	0 7	0 7	0 66	0 92	0 68	0 6	0 33	0 33	0 33	0 35	0 4	0 41	0.28	0 32	0 33
K2O	8 84	6 37	8 64	8 63	8 23	8 65	8 76	8 85	8 41	8 99	8 06	8 72	8 84	8 35	8 56	9 09	8 51	9.74	8 93	9 07	9 75	9 99	9 39	8 77	9 97
ZnO	0 02	0 04	0 42	0 04	0 02	0 05	0	0 07	0	0	0 02	0	0 04	0	0	0 12	0 1	0 06	0 01	0 01	0	0.03	0 09	0 04	0 02
BaO	0 6	0.43	0 56	0 68	0 82	0.67	0.78	0 62	0 83	0 84	0 22	0 32	0 35	0 32	0.25	0 32	1.03	0 96	0 53	0 38	0 4	0 5	0.28	0.45	0 47
F	0 16	0 13	0 09	0 57	0 09	0 29	0 1	0 73	0 18	0 16	0 11	0 21	0 14	0 14	0 28	0 05	0 33	0 46	0.22	0 03	0.13	0 11	0 56	0 36	0 27
Cl	0	0 02	0	0	0	0 01	0 01	0	0	0	0 01	0	0	0	0	0	0	0	0 01	0	0	0 01	0	0 01	0
H2O(c)	4 58	4.41	4 56	4 27	4 61	4 54	4.53	4 05	4 33	4.58	4 62	4 58	4 62	4 67	4 54	4 66	4 41	4 19	4 68	4.7	4 68	4 63	4 37	4 57	4 52
O=F	0 07	0 05	0 04	0.24	0 04	0 12	0 04	0 31	0 07	0 07	0 05	0 09	0 06	0 06	0 12	0 02	0 14	0.19	0 09	0 01	0 05	0 05	0 24	0.15	0.12
O=Cl	0	0	0	0	0	0	0	0	0	0	0	0	0	0	0	0	0	0	0	0	0	0	0	0	0
Sum Oxides [%	98.15	95 5	97 31	97 58	97 68	98 07	96 26	94 28	93 45	98 01	97 2	97.88	98 23	98 86	98 3	98 24	97.79	95 93	99 75	98 8	99 86	98 93	97.15	98 93	97.7
# cations																									
Si	6 189	6.322	6 171	5 991	6.203	6 435	6.204	6 098	6 085	6 156	6 3	6 227	6 194	6 228	6 192	6 207	6 103	5 973	6 608	6 265	6 282	6 227	6 405	6 374	6.36
Ti	0 024	0 029	0 024	0 041	0 021	0 03	0 037	0 032	0 028	0 028	0.045	0.05	0 05	0 043	0 047	0 054	0 02	0 022	0 02	0 021	0 025	0 02	0 029	0.029	0 039
Al [4]	1.811	1.678	1.829	2 009	1 797	1 565	1.796	1 902	1 915	1 844	1 7	1.773	1 806	1 772	1 808	1.793	1 997	2 027	1.392	1 735	1 718	1 773	1 595	1 626	1 64
Al [6]	3 707	3 132	3 593	2 884	3 775	3 531	3 701	3 002	3 62	3 746	3 711	3 739	3 745	3 772	3 488	3 727	2 366	2 616	3 492	3 623	3 649	3 649	3 503	3 6	3 572
Fe2+	0 206	0.6	0 264	0 365	0 169	0 169	0.158	0 314	0.221	0 156	0.157	0 15	0 159	0 141	0 218	0 15	0 298	0 354	0 126	0.174	0 173	0 141	0 116	0 084	0 079
Mn2+	0 002	0 001	0 009	0 015	0 006	0	0	0 012	0 003	0	0 001	0 002	0.004	0	0 01	0	0 011	0 005	0 001	0 004	0	0 005	0	0 003	0
Mg	0 213	0 591	0 338	1 361	0 193	0 453	0 264	1.18	0 382	0 204	0 271	0 207	0 2	0 194	0 548	0 205	1.482	1 739	0 509	0.411	0 306	0 326	0 534	0 493	0 416
Ca	0 002	0 027	0	0	0	0 001	0	0 006	0	0 003	0 006	0 004	0	0 005	0 006	0	0	0 001	0 002	0 003	0 002	0 008	0 003	0 004	0 002
Na	0.233	0 588	0 156	0.181	0.214	0.115	0 159	0 124	0.182	0 202	0 173	0 174	0 163	0 225	0 169	0 148	0 085	0 088	0 081	0 086	0 097	0 102	0 069	0 077	0 083
K	1 452	1.09	1 438	1 454	1 351	1.413	1 464	1.539	1 457	1.479	1 32	1 425	1 442	1 347	1.401	1 485	1 426	1 689	1 427	1 473	1 571	1 629	1 549	1 413	1 641
Zn	0 002	0 004	0 041	0.004	0 002	0 005	0	0 007	0	0	0 001	0	0 003	0	0	0 011	0 01	0 006	0 001	0 001	0	0 003	0 008	0 004	0 001
Ba	0 03	0 023	0 029	0 035	0 041	0 034	0 04	0 033	0 044	0 042	0 011	0 016	0 017	0 016	0 012	0 016	0 053	0 051	0 026	0 019	0 02	0 025	0 014	0 022	0 024
F	0 066	0 055	0 035	0 239	0 037	0 118	0 042	0 316	0 076	0 064	0 044	0 084	0 055	0 057	0 114	0 02	0 135	0 198	0 086	0 011	0 052	0 046	0 229	0 144	0.112
Cl	0	0.004	0 001	0	0	0 002	0 001	0	0	0 001	0 002	0	0 001	0 001	0	0	0	0	0 001	0.001	0	0 002	0 001	0 002	0
OH	3 934	3 941	3 964	3 761	3 963	3 88	3 956	3 683	Φ° 3 924	3 936	3 953	3 916	3 944	3 943	3 885	3 98	3 864	3 802	3 913	3 988	3 947	3 952	3 77	3 854	3 888
Sum cations	13 94	14.14	13 93	14 58	13 81	13 87	13 87	14 57	14 01	13 93	13 74	13 85	13 84	13 80	14 01	13 82	14.39	14 77	13 77	13 83	13 90	13 96	14 06	13 88	13 97
Y-position [6]	4.15	4 36	4.27	4 67	4 17	4 19	4 16	4 55	4 26	4 14	4 19	4.15	4 16	4.15	4 31	4.15	4 69	4 74	4.15	4.23	4 15	4 14	4 19	4 21	4.11
X-position [12]	1.72	1.73	1.62	1 67	1 61	1 56	1 66	1 70	1 68	1.73	1.51	1 62	1 62	1.59	1 59	1 65	1 57	1.83	1.54	1 58	1.69	1.76	1 64	1 52	1 75
XMg	0 51	0 50	0 56	0.79	0 53	0 73	0 63	0.79	0 63	0 57	0 63	0 58	0 56	0 58	0.72	0 58	0.83	0 83	0 80	0 70	0 64	0 70	0 82	0 85	0 84

Table A8: Microprobe analyses - muscovite

sample	TH247-347	TH247-347	TH85A - 383	TH85A - 383	TH85A - 383	TH85A - 383	TH471 - 159	TH471 - 159	TH471 - 159	TH471 - 104	TH471 - 104	TH471 - 104	TH471 - 104	TH471 - 104	TH471 - 104	TH471 - 104	TH471 - 104	TH471 - 104	TH471 - 104	TH394 - 262	TH394 - 262	TH394 - 262	TH394 - 262	TH394 - 262
mineral	musBB4	musBB5	musB1	musB2	musB3	musB5	musC1	musC2	musC3	musD1	musD2	musD2	musD3	musD4	musD5	musD6	musD7	musD8	musD9	musE1	musE2	musE3	musE4	musE5
analysis no.	437	438	44	43	61	63	130	131	134	168	169	170	180	181	182	183	192	193	194	215	216	217	220	221
lab:	CSL	CSL	TUB	TUB	TUB	TUB	TUB	TUB	TUB	TUB	TUB	TUB	TUB	TUB	TUB	TUB	TUB	TUB	TUB	TUB	TUB	TUB	TUB	TUB
[wt.%]																								
SiO2	50 34	49 24	48 73	48 05	47 23	48 63	47 38	45 57	47 00	46.29	46 41	45 63	47 59	48 67	46 80	46 77	45 69	46 04	48 83	45 88	45 26	45 50	46 51	45 58
TiO2	0 33	0 36	0 03	0	0 01	0	0 49	0 42	0 42	0.21	0.29	0 12	0 00	0 01	0 10	0.23	0.11	0.10	0 03	0.24	0 16	0.29	0.10	0 11
Al2O3	35 47	34 17	36 06	35 63	34 9	34 09	35 02	35 02	35 38	34 71	34 36	33 30	36 28	36 43	34 27	34.03	32 95	34 63	34.66	34 78	33 62	33.86	33.79	34 19
FeO	0 65	0 88	0 67	2 7	3 65	2 42	2.26	2.16	2 02	2 47	2 46	3 45	3 00	1 04	3 07	3 04	5 38	3 35	2 08	2 54	3 50	3.07	2.45	2 71
MnO	0	0 03	0 1	0 06	0 08	0 1	0 00	0 02	0 01	0.02	0 04	0.00	0 20	0 06	0 01	0 06	0 06	0 01	0 07	0 00	0 03	0.01	0.04	0 05
MgO	2 01	2.33	0 03	0 08	0,31	0 58	0 87	0 80	0 67	0 72	0 74	0.69	1 51	0 64	0 84	0 92	2.29	1.33	0 72	0 69	0 80	0 87	0 97	0 57
CaO	0 02	0 02	0	0.05	0 04	0 05	0.00	0 00	0 00	0 00	0 03	0 00	0 05	0.09	0 00	0.00	0 02	0.00	0.00	0 00	0 00	0 01	0 00	0.00
Na2O	0 33	0 3	0 02	0 03	0 02	0.02	0 61	0 81	0 69	0 93	1.03	0 96	0 65	4 48	0 72	0 91	0 52	0 84	1 01	0 55	0 56	0 48	0 53	0 64
K2O	9.22	9 66	7 46	10 75	10.4	10 28	7 89	9 99	8 68	9 99	9.51	8 78	7 35	3 70	9 41	9 03	8.74	10 09	9 88	10 90	10 78	10 57	10 92	10 86
ZnO	0 02	0																						
BaO	0 47	0 37																						
F	0 35	0 45																						
Cl	0	0.01																						
H2O(c)	4 57	4.42																						
O=F	0 15	0.19																						
O=Cl	0	0																						
Sum Oxides [%	98 86	97 36	93 1	97.35	96 64	96.17	94 53	94 82	94.88	95 35	94 86	92 93	96 64	95.11	95 23	94.99	95 77	96 39	97 29	95 58	94 71	94.68	95 30	94.71
# cations:																								
Si	6 371	6.361	6 43	6.27	6 24	6 4	6 271	6 118	6 226	6.183	6 215	6.245	6 172	6 282	6.245	6.249	6 135	6 120	6 351	6.146	6 156	6 163	6.243	6.172
Ti	0 031	0 035	0	0	0	0	0 049	0 043	0 042	0 021	0 029	0 012	0 000	0.001	0.010	0 023	0 011	0 010	0 003	0 024	0 016	0 030	0 010	0 012
Al [4]	1 629	1 639	1 57	1.73	1 76	1 6	1 730	1.882	1 774	1 817	1 785	1 755	1 828	1 718	1.755	1.751	1 865	1.880	1 649	1.854	1 845	1 837	1 757	1.828
Al [6]	3 661	3 564	4 04	3 75	3 68	3 69	3 734	3 658	3 749	3 648	3 638	3 617	3.718	3 825	3 635	3 608	3 348	3 545	3 665	3.637	3 544	3.571	3.588	3 627
Fe2+	0 069	0 095	0.07	0 29	0 4	0 27	0 251	0.245	0 224	0.277	0 276	0 395	0 325	0 112	0 343	0 339	0 605	0 373	0 226	0.284	0 398	0 348	0 275	0 307
Mn2+	0	0 004	0 01	0.01	0 01	0 01	0.000	0 003	0 001	0 003	0.005	0 000	0 022	0.006	0 001	0 006	0 007	0 001	0 008	0 000	0 003	0 001	0.004	0 006
Mg	0.378	0.449	0 01	0 02	0 06	0.11	0.171	0.161	0 132	0.144	0 147	0 140	0 293	0.123	0 167	0 182	0 458	0.264	0.140	0 137	0.163	0 176	0 193	0 115
Ca	0.003	0 003	0	0 01	0	0.01	0 000	0.001	0 000	0 000	0 004	0 000	0 007	0.013	0 001	0 000	0 003	0 000	0 000	0 000	0 000	0.002	0.000	0 000
Na	0.081	0 075	0 01	0 01	0 01	0	0.157	0 210	0 176	0 241	0 267	0 254	0 163	1.122	0 185	0 237	0 136	0 216	0 254	0 142	0.147	0.125	0 138	0 169
K	1.488	1.591	1.26	1.79	1 75	1.73	1 332	1.711	1 468	1 703	1 624	1 532	1.216	0.609	1 602	1 539	1.496	1.710	1.640	1 862	1.871	1.826	1 870	1.876
Zn	0 002	0																						
Ba	0.023	0.019																						
F	0.14	0 185																						
Cl	0	0 002																						
OH	3.86	3 813																						
Sum cations	13 88	14 02	13 40	13 88	13 91	13 82	13.69	14 03	13 79	14 04	13 99	13 95	13 74	13 81	13 94	13.94	14.06	14.12	13 94	14.09	14.14	14.08	14 08	14.11
Y-position [6]	4.14	4.15	4 13	4 07	4.15	4 08	4 20	4.11	4.15	4 09	4.10	4.16	4.36	4 07	4 16	4.16	4 43	4 19	4 04	4 08	4.12	4 13	4 07	4 07
X-position [12]	1.60	1 69	1.27	1 80	1.76	1 73	1.49	1 92	1.64	1 94	1 89	1.79	1 38	1 73	1.79	1.78	1 63	1 93	1 89	2 00	2 02	1.95	2 01	2 04
XMg	0 85	0 83	0.13	0 06	0 13	0 29	0 41	0 40	0 37	0 34	0 35	0.26	0 47	0 52	0 33	0 35	0.43	0 41	0 38	0 33	0 29	0 34	0 41	0 27

Table A9: microprobe analyses - garnet

sample	TH62C - 14	TH62C - 14	TH62C - 14	TH62C - 14	TH62C - 14	TH62C - 14	TH62C - 14	TH62C - 14	TH62C - 14	TH85A - 383	TH85A - 383	TH85A - 383	TH85A - 383	TH85A - 383	TH85A - 383	TH85A - 383	TH85A - 383	TH85A - 383	TH85A - 383	TH85A - 383	TH85A - 383
mineral	gtA1	gtA1	gtA1	gtA1	gtA1	gtA1	gtA1	gtA1	gtA1	gtB1	gtB1	gtB1	gtB1	gtB1	gtB2	gtB2	gtB2	gtB2	gtB3	gtB3	gtB3	gtB3
analysis no	2	3	4	5	6	7	8	9	10	31	32	33	34	35	45	46	47	49	52	53	54	55
location [µm]	10 (rim)	114	193	263	351	527	632	711	820 (rim)	5 (rim)	54	125	170	220 (rim)	5 (rim)	77	125	155 (rim)	8 (rim)	89	155	185 (rim)
lab:	TUB	TUB	TUB	TUB	TUB	TUB	TUB	TUB	TUB	TUB	TUB	TUB	TUB	TUB	TUB	TUB	TUB	TUB	TUB	TUB	TUB	TUB
wt.%																						
SiO2	36.55	36.51	36 47	36 35	36.40	36.31	36 58	36 84	37 32	37 21	36 99	37.52	37.06	36 86	35.19	35.44	35.53	38 19	37 24	36 87	37.15	37.64
TiO2	0 04	0 07	0 10	0 20	0 04	0.08	0 10	0.14	0 02	0 00	0 04	0 05	0 05	0 01	0.02	0 07	0 07	0 00	0 01	0 04	0 03	0.03
Al2O3	20.20	20 61	20 36	20 32	20 33	20.82	20.81	20 63	20 22	20 70	21.06	20 81	20 83	21.09	20 93	20 96	20.75	20 71	20.58	20.76	20 90	19.72
FeO	26 72	28.12	28.30	29 02	28 02	28 05	28 48	28 44	26 77	22 50	22 27	22 49	22 45	22 14	22 65	22 46	22.48	22 09	22 53	22 33	22 66	22.32
MnO	12 91	12 14	11 87	12 37	12 29	11 92	12 15	12 17	13 33	16 11	15.36	16 04	15 57	15 95	16.39	15 48	15 45	16 34	15 82	15 38	15 82	16.26
MgO	0 53	0 67	0 63	0 59	0 63	0.64	0 66	0 64	0 58	1 64	1.91	1 86	1 81	1 66	1.61	1.96	1 95	1.47	1 83	1 84	1 81	1.59
CaO	2.21	2.11	2.14	1 92	1.93	1 79	1 91	1 89	1 99	1 85	2 11	1 82	1 99	1 85	2 04	2.13	2 16	2.05	1.97	2 27	2 00	2 11
Na2O	0 07	0 02	0 02	0 03	0 02	0 05	0.02	0 01	0 01	0.01	0 04	0 00	0 03	0.02	0 02	0 03	0 00	0 02	0 02	0 03	0 02	0 04
K2O	0 00	0 00	0 01	0 00	0.00	0.00	0.00	0 00	0 01	0 00	0 00	0 00	0.00	0 00	0 00	0 00	0 00	0 00	0 00	0 00	0 01	0.01
Sum Oxides [%	99 23	100.25	99 90	100.80	99.66	99 66	100 71	100 76	100 25	100.02	99.78	100 59	99 79	99 58	98 85	98 53	98.39	100 87	100.00	99 52	100.40	99 72
# cations:	calculated on the basis of 12 oxygens																					
Si 4+	3 02	2 99	3	2 97	3	2 98	2 98	3	3.04	3 02	3	3 02	3 01	3	2.92	2 93	2.94	3 06	3 02	3	3	3 07
Ti 4+	0	0	0 01	0 01	0	0	0 01	0 01	0	0	0	0	0	0	0	0	0	0	0	0	0	0
Al [6]	1 96	1.99	1 97	1.96	1 97	2 02	2	1 98	1.94	1 98	2 01	1.98	1 99	2 02	2.04	2 04	2 02	1 96	1.97	1 99	1.99	1 89
Fe 2+	1.84	1.92	1 94	1.99	1.93	1.93	1 94	1.94	1.83	1 53	1.51	1.51	1 52	1.51	1 57	1.55	1.56	1 48	1.53	1 52	1 53	1 52
Mn 2+	0.9	0 84	0 83	0 86	0 86	0 83	0 84	0 84	0 92	1.11	1 05	1 09	1 07	1.1	1.15	1 08	1.08	1.11	1 09	1.06	1 08	1 12
Mg 2+	0 07	0 08	0 08	0 07	0 08	0 08	0.08	0 08	0 07	0 2	0 23	0 22	0 22	0 2	0 2	0 24	0.24	0.18	0 22	0 22	0 22	0 19
Ca 2+	0 2	0.19	0 19	0.17	0.17	0 16	0 17	0 16	0 17	0.16	0.18	0.16	0 17	0.16	0 18	0.19	0.19	0.18	0 17	0 2	0.17	0 18
Na 1+	0 01	0	0	0	0	0 01	0	0	0	0	0 01	0	0	0	0	0	0	0	0	0 01	0	0 01
K 1+	0	0	0	0	0	0	0	0	0	0	0	0	0	0	0	0	0	0	0	0	0	0
Total	8	8 01	8 02	8 03	8 01	8 01	8 02	8 01	7 97	8	7 99	7 98	7.98	7 99	8 06	8.03	8 03	7 97	8	8	7.99	7 98
X position [8]	3 01	3 03	3 04	3 09	3 04	3	3 03	3 02	2 99	3	2 97	2 98	2 98	2 97	3.1	3.06	3 07	2 95	3 01	3	3	3 01
mol per cent end-members:																						
pyrope	2	3	3	2	3	3	3	3	2	7	8	7	7	7	6	8	8	6	7	7	7	6
almandine	61	63	64	64	63	64	64	64	61	51	51	51	51	51	51	51	51	50	51	51	51	50
spessartine	30	28	27	28	28	28	28	28	31	37	35	37	36	37	37	35	35	38	36	35	36	37
grossular	7	6	6	6	6	5	6	Φ° 5	6	5	6	−5	6	5	6	6	6	6	6	7	6	6
	100	100	100	100	100	100	100	100	100	100	100	100	100	100	100	100	100	100	100	100	100	100

Table A9: microprobe analyses - garnet

sample	TH471 - 159	TH471 - 159	TH471 - 159	TH471 - 159	TH471 - 159	TH471 - 159	TH471 - 159	TH471 - 159	TH471 - 159	TH471 - 159	TH471 - 159	TH471 - 159	TH471 - 159	TH471 - 159	TH471 - 159	TH471 - 159	TH471 - 159	TH471 - 159	TH471 - 159	TH471 - 159	TH471 - 159
mineral	gtC1	gtC1	gtC1	gtC1	gtC1	gtC1	gtC1	gtC1	gtC1	gtC2	gtC2	gtC2	gtC2	gtC2	gtC3	gtC3	gtC3	gtC3	gtC3	gtC4	gtC4	gtC4
analysis no	64	65	66	67	68	69	70	71	72	98	96	99	100	101	102	103	104	105	106	109	110	111
location [µm]	10 (rim)	477	282	141	635	777	935	1068	1225 (rim)	5 (rim)	106	282	441	590 (rim)	10 (rim)	141	177	300	430 (rim)	5 (rim)	195	407
lab:	TUB	TUB	TUB	TUB	TUB	TUB	TUB	TUB	TUB	TUB	TUB	TUB	TUB	TUB	TUB	TUB	TUB	TUB	TUB	TUB	TUB	TUB
wt %																						
SiO2	37.38	37 24	37.52	37 41	38.02	37 86	37 63	37.37	36 69	35 59	36 66	37.46	37.66	37 37	37 00	35 47	36 13	36 12	36 42	37 45	37.67	37.69
TiO2	0 04	0 08	0 13	0 01	0.18	0 08	0 05	0 05	0 09	0.10	0 06	0 30	0 09	0 08	0 10	0.18	0.19	0 09	0.13	0 04	0.05	0 08
Al2O3	20 98	21 02	21 03	21 07	20.83	21.10	21.14	20 97	20.72	21.07	21.19	20 59	20 93	20 97	20 97	20 72	20 90	21.15	21.06	20 96	20.87	20 51
FeO	17.96	15 70	16 91	18 20	15 10	15 54	15 50	16 83	17 25	17.15	17.19	16 28	17 58	17 38	17 11	16 68	16 68	16 36	17 61	18.07	18 29	16 04
MnO	20 40	18 91	19 64	19 45	20 03	19 68	18 48	19 33	21.42	22 42	19 20	18 97	19 11	20 84	21 89	19.12	19 13	18 89	21.10	20.40	19 38	19 25
MgO	2.18	5.08	4 40	3.75	5 34	4 99	5 83	4 38	2 09	2 24	3 94	4 94	3 89	1 96	1.93	4.70	4.81	4 78	1 72	2 14	3 75	5 10
CaO	1.32	0 95	0 80	0.46	0.79	0.82	0 92	0.76	1.31	0.66	0 93	0.83	0 87	1.32	1.14	0 85	0 84	0 91	1.23	1.26	0 53	0 85
Na2O	0 01	0 04	0 00	0 00	0.02	0 01	0 01	0.02	0 00	0 03	0 03	0 00	0 04	0 01	0 01	0 03	0 04	0 02	0 01	0 00	0 02	0 04
K2O	0.04	0 00	0 00	0 01	0 01	0 00	0 00	0 00	0 00	0.02	0 00	0 00	0 01	0 02	0 01	0 00	0 00	0 00	0 01	0 00	0 00	0.00
Sum Oxides [%	100.31	99 02	100 43	100 36	100 32	100 08	99 56	99.71	99 57	99 28	99 20	99 38	100.18	99 95	100 15	97.75	98.72	98 33	99 29	100 32	100 55	99 56
# cations																						
Si 4+	3.01	2 99	2.99	3	3 01	3.01	2 99	3	2 99	2.93	2 96	3.00	3 01	3 02	3 00	2.92	2 93	2 94	2 98	3 02	3 01	3.01
Ti 4+	0	0	0.01	0	0.01	0	0	0	0 01	0 01	0 00	0.02	0 01	0 01	0.01	0 01	0.01	0 01	0.01	0.00	0 00	0 01
Al [6]	1 99	1 99	1 97	1 99	1 94	1.97	1 98	1 98	1 99	2 04	2 02	1 95	1.97	2 00	2 00	2 01	2 00	2 03	2.03	1.99	1.97	1 93
Fe 2+	1.21	1 05	1.13	1 22	1	1.03	1 03	1.13	1.18	1 18	1 16	1 09	1 18	1 17	1 16	1.15	1.13	1 11	1 20	1 22	1.22	1.07
Mn 2+	1.39	1 29	1.33	1 32	1.34	1.32	1.24	1 31	1.48	1 56	1 31	1 29	1 29	1 43	1.50	1.33	1 32	1.30	1 46	1.39	1 31	1 30
Mg 2+	0.26	0 61	0 52	0 45	0 63	0 59	0 69	0.52	0 25	0 27	0 47	0.59	0 46	0 24	0.23	0 58	0.58	0 58	0 21	0 26	0 45	0 61
Ca 2+	0.11	0.08	0 07	0 04	0 07	0.07	0.08	0 07	0.11	0 06	0 08	0 07	0 07	0 11	0 10	0 07	0 07	0 08	0 11	0.11	0 05	0 07
Na 1+	0	0 01	0	0	0	0	0	0	0	0 00	0.00	0 00	0 01	0 00	0.00	0 00	0 01	0 00	0 00	0 00	0 00	0 01
K 1+	0	0	0	0	0	0	0	0	0	0 00	0 00	0 00	0 00	0 00	0 00	0 00	0 00	0 00	0 00	0 00	0 00	0 00
Total	7.97	8 02	8 02	8 02	8	7.99	8 01	8 01	8 01	8 05	8 02	8.01	8 00	7.98	8.00	8 07	8 06	8 05	8 00	7 99	8 01	8 02
X position [8]	2 97	3.03	3 05	3 03	3 04	3 01	3 04	3 03	3 02	3 07	3 03	3 04	3 01	2 95	2 99	3 13	3 11	3.07	2 98	2 98	3 03	3 06
mol per cent e																						
pyrope	9	20	17	15	21	20	23	17	8	9	16	19	15	8	8	18	19	19	7	9	15	20
almandine	41	35	37	40	33	34	34	37	39	38	38	36	39	40	39	37	36	36	40	41	40	35
spessartine	47	43	44	44	44	44	41	43	49	51	43	42	43	48	50	43	42	42	49	47	43	43
grossular	4	3	2	1	2	2	3	2	4	2	3	2	2	4	3	2	2	3	4	4	1	2
	100	100	100	100	100	100	100	100	100	100	100	100	100	100	100	100	100	100	100	100	100	100

Table A9: microprobe analyses - garnet

sample	TH471 - 159	TH471 - 159	TH471 - 159	TH471 - 159	TH471 - 159	TH471 - 159	TH471 - 159	TH471 - 159	TH471 - 159	TH471 - 159	TH471 - 159	TH471 - 159	TH471 - 159	TH471 - 159	TH471 - 159	TH471 - 159	TH471 - 104	TH471 - 104	TH471 - 104	TH471 - 104	TH471 - 104	TH471 - 104
mineral	gtC4	gtC4	gtC4	gtC4	gtC4	gtC5	gtC5	gtC5	gtC6	gtC6	gtC6	gtC6	gtC7	gtC7	gtC7	gtC7	gtD1	gtD1	gtD1	gtD1	gtD1	gtD1
analysis no	112	113	114	115	116	135	136	137	138	139	140	141	142	143	144	145	147	148	149	150	151	152
location [µm]	584	814	956	1115	1320 (rim)	5 (rim)	60	115 (rim)	10 (rim)	137	222	370 (rim)	5 (rim)	248	393	645 (rim)	5 (rim)	306	612	850	1122	1428
lab.	TUB	TUB	TUB	TUB	TUB	TUB	TUB	TUB	TUB	TUB	TUB	TUB	TUB	TUB	TUB	TUB	TUB	TUB	TUB	TUB	TUB	TUB
wt %																						
SiO2	37 35	37 34	37.76	36 82	37 04	36 95	37 06	37.30	37 46	37 49	37.51	36 96	37 33	37 62	37.76	36 42	37 45	37 41	37 39	37 08	37 19	37 21
TiO2	0 27	0 22	0 06	0 03	0 09	0 05	0 04	0.04	0 03	0 08	0 05	0 08	0 09	0 13	0 17	0 06	0 00	0.16	0 03	0.05	0 00	0.07
Al2O3	20 57	20 20	20 82	21 14	20 54	20 57	20 85	20 87	21 00	20 88	20 92	21.06	20 89	20 79	21.13	21 05	21 04	20.74	20 81	20 75	20 60	21 33
FeO	16 78	15.93	15 86	16 67	17 69	17.45	18 07	17 81	17 67	18 02	17 83	17 37	17.90	15 90	16 06	17.95	20 59	20.06	20 00	19 67	19 24	18 91
MnO	19 68	19 29	18 72	19 66	21.21	21 25	20 54	21 01	20 61	19.32	19 27	21 10	20 78	18 62	19 33	20 04	18.54	19 86	19.90	20.10	19 83	20.19
MgO	4 11	4.96	5 08	4 13	2 08	2.09	2 60	2 18	2 01	3 83	3 83	1 98	2 00	5.12	4.71	2 02	1.58	1 78	1 77	1 83	1 90	1.73
CaO	0 83	0 86	0 89	0.78	1 24	1.21	0 45	0 67	1 34	0 47	0 72	1 24	1.19	0 95	0 91	1 41	1 80	1.12	1 10	1.17	1 07	1 00
Na2O	0 03	0.01	0 00	0 00	0 00	0 03	0 02	0 04	0 02	0 03	0 03	0 04	0 00	0 04	0 02	0 05	0 00	0 03	0 01	0 02	0 00	0 00
K2O	0 01	0 00	0 00	0 01	0 00	0 01	0 00	0 03	0 01	0 00	0.00	0 03	0 01	0 00	0.00	0 01	0 00	0 00	0 00	0 01	0 00	0.00
Sum Oxides [%	99 64	98 80	99 20	99 24	99 89	99 62	99.63	99 95	100.15	100.12	100 15	99 85	100 20	99.17	100.09	99 00	101 01	101.18	101.00	100.70	99 83	100 43
# cations																						
Si 4+	3 00	3 01	3 02	2 97	3 01	3 01	3 01	3 02	3 02	3 01	3 00	3 00	3.01	3 01	3 00	2 98	3 01	3 01	3.01	3 00	3 02	3 00
Ti 4+	0 02	0 01	0.00	0 00	0 01	0.00	0 00	0.00	0 00	0 00	0 00	0 00	0 01	0 01	0 01	0 00	0 00	0 01	0 00	0 00	0 00	0.00
Al [6]	1 95	1.92	1 96	2.01	1.97	1.97	1 99	1 99	2 00	1 97	1.98	2 01	1.99	1.96	1 98	2 03	1.99	1 97	1 98	1 98	1.97	2 03
Fe 2+	1 13	1.08	1.06	1.13	1 20	1.19	1 23	1 21	1.19	1 21	1.19	1.18	1.21	1.06	1 07	1.23	1 38	1.35	1.35	1 33	1 31	1.28
Mn 2+	1.34	1 32	1 27	1 34	1.46	1.47	1 41	1 44	1 41	1 31	1.31	1 45	1.42	1 26	1 30	1 39	1 26	1.35	1 36	1 38	1 37	1 38
Mg 2+	0 49	0 60	0 61	0 50	0 25	0 25	0 31	0 26	0 24	0 46	0 46	0 24	0 24	0 61	0 56	0 25	0.19	0 21	0 21	0 22	0 23	0 21
Ca 2+	0 07	0 07	0 08	0.07	0.11	0.11	0 04	0 06	0 12	0 04	0 06	0 11	0 10	0 08	0 08	0.12	0 15	0 10	0 09	0 10	0 09	0 09
Na 1+	0 00	0 00	0.00	0 00	0.00	0 00	0 00	0 01	0.00	0 00	0.00	0 01	0 00	0 01	0 00	0 01	0.00	0 01	0 00	0 00	0 00	0 00
K 1+	0 00	0 00	0 00	0 00	0 00	0 00	0 00	0 00	0 00	0 00	0 00	0 00	0 00	0 00	0 00	0 00	0 00	0 00	0.00	0 00	0 00	0 00
Total	8 01	8 01	8 00	8 02	8 00	8 00	8 00	7 99	7 98	8.01	8 01	8 00	7 99	8 00	8 00	8 01	7 99	8 00	8 00	8 01	7.99	7 98
X position [8]	3 03	3 06	3 01	3 03	3.02	3 01	2 99	2 97	2 96	3 02	3 02	2 97	2 97	3 02	3 00	2 99	2.99	3 01	3 01	3 03	3 00	2 95
mol per cent e																						
pyrope	16	19	20	16	8	8	11	9	8	15	15	8	8	20	19	8	6	7	7	7	8	7
almandine	37	35	35	37	40	39	41	41	40	40	40	40	41	35	36	41	46	45	45	44	44	43
spessartine	44	43	42	44	48	49	47	49	48	43	43	49	48	42	43	46	42	45	45	45	46	47
grossular	2	2	3	2	4	4	1	2	4	1	2	4	3	3	3	4	5	3	3	3	3	3
	100	100	100	100	100	100	100	100	100	100	100	100	100	100	100	100	100	100	100	100	100	100

Table A9: microprobe analyses - garnet

sample	TH471 - 104	TH471 - 104	TH471 - 104	TH471 - 104	TH471 - 104	TH471 - 104	TH471 - 104	TH471 - 104	TH471 - 104	TH471 - 104	TH471 - 104	TH471 - 104	TH394 - 262	TH394 - 262	TH394 - 262	TH394 - 262	TH394 - 262	TH394 - 262	TH394 - 262	TH394 - 262	TH394 - 262
mineral	gtD1	gtD1	gtD1	gtD1	gtD2	gtD2	gtD2	gtD2	gtD2	gtD2	gtD2	gtD2	gtE1	gtE1	gtE1	gtE1	gtE1	gtE1	gtE1	gtE1	gtE1	gtE1
analysis no	153	154	155	156	171	187	172	175	176	177	178	179	197	198	199	200	201	202	203	204	205	206
location [µm]	1632	1904	2200	2205 (rim)	10 (rim)	15	406	744	963	1318	1555	1820 (rim)	5 (rim)	270	473	811	1217	1656	2028	2400	2805	3245
lab:	TUB	TUB	TUB	TUB	TUB	TUB	TUB	TUB	TUB	TUB	TUB	TUB	TUB	TUB	TUB	TUB	TUB	TUB	TUB	TUB	TUB	TUB
wt.%																						
SiO2	37.15	36.79	36 72	36 38	37 26	36 81	36 92	37 13	37 46	37 35	37 53	37 53	37 06	36 87	36 91	37 18	37 08	36 96	37.11	37 08	36 73	37.07
TiO2	0 07	0 07	0 04	0 04	0 11	0 04	0 08	0 08	0 03	0 02	0 00	0.04	0 02	0 06	0 06	0 11	0 02	0 03	0 03	0.08	0.07	0 06
Al2O3	20 80	20 94	20 99	20 81	19 67	20.85	21 02	20.35	20 74	20 83	21 10	20 64	20.52	20 55	20 61	20 67	20 93	20 89	20 76	20 72	20.90	20 62
FeO	19 70	20 20	20 13	19.78	20 34	19.45	19 39	18 89	19 22	18 91	19 52	20 23	20 70	18 54	17 99	18 66	19 43	20 04	19 64	19 11	17 94	18.77
MnO	20 34	19 32	19 02	20.14	18 45	18 63	19 98	20 78	20 69	20.41	19 25	18 48	18 14	20 10	20 62	20 27	19 61	18 93	18 96	19 25	20.75	19 93
MgO	1.85	1 90	1.46	1.30	1.71	1 36	1 78	1 81	1.76	1,71	2.16	1 52	1.58	1 41	1 44	1.55	1 55	1 57	1 55	1 66	1 45	1.35
CaO	1.33	1.21	1 34	1.11	1 89	1 09	1.19	1 17	1 08	1 03	1.19	1 56	1 99	2 15	2 15	2 23	1.94	2 01	2 38	2.15	1 91	2.39
Na2O	0 00	0 00	0 00	0 00	0 02	0 01	0 01	0 00	0 03	0 00	0 01	0 01	0 03	0 02	0 00	0 02	0 00	0 02	0.00	0 01	0 02	0 01
K2O	0 00	0 00	0 00	0 00	0 01	0 00	0 01	0 00	0.00	0 00	0 00	0 01	0 00	0 00	0 00	0 00	0 00	0 00	0 00	0 00	0 00	0 00
Sum Oxides [%	101 24	100 43	99 71	99 58	99 45	98 25	100.37	100 21	101.00	100 28	100.76	100.01	100 05	99 71	99 78	100 69	100 57	100 45	100.44	100 06	99.78	100 21
# cations:																						
Si 4+	2 99	2 98	2 99	2 98	3 05	3 03	2 99	3.02	3 02	3.02	3 01	3 04	3 01	3 01	3 01	3 00	3 00	2 99	3 00	3 01	2 99	3 01
Ti 4+	0 00	0.00	0 00	0 00	0.01	0 00	0 00	0 00	0 00	0.00	0 00	0 00	0.00	0 00	0 00	0 01	0 00	0 00	0.00	0 01	0 00	0 00
Al [6]	1 97	2.00	2 02	2 01	1 90	2 02	2 01	1.95	1 97	1.99	2 00	1.97	1.97	1.98	1.98	1 97	1.99	1 99	1 98	1 98	2.01	1.97
Fe 2+	1 33	1.37	1.37	1.36	1.39	1.34	1 31	1.28	1 29	1 28	1.31	1.37	1.41	1 26	1 23	1 26	1 31	1.36	1 33	1.30	1 22	1 27
Mn 2+	1 39	1.33	1.31	1.40	1 28	1.30	1.37	1.43	1.41	1 40	1 31	1 27	1 25	1 39	1 42	1 39	1 34	1 30	1 30	1.32	1.43	1 37
Mg 2+	0 22	0 23	0.18	0 16	0 21	0 17	0 21	0 22	0 21	0 21	0 26	0 18	0.19	0 17	0.17	0 19	0 19	0.19	0.19	0 20	0.18	0.16
Ca 2+	0 11	0 11	0.12	0 10	0.17	0 10	0.10	0.10	0 09	0 09	0 10	0 14	0 17	0 19	0 19	0 19	0 17	0 17	0 21	0 19	0 17	0 21
Na 1+	0 00	0 00	0 00	0 00	0 00	0.00	0.00	0 00	0.00	0 00	0 00	0 00	0 01	0 00	0 00	0.00	0 00	0 00	0 00	0.00	0.00	0 00
K 1+	0.00	0 00	0 00	0 00	0 00	0 00	0.00	0 00	0.00	0 00	0.00	0 00	0 00	0 00	0 00	0.00	0 00	0 00	0 00	0.00	0 00	0.00
Total	8 02	8 02	8.00	8 01	8 00	7 96	8 00	8 00	8 00	7 98	7 99	7 97	8 01	8 00	8 00	8.01	8 00	8 01	8 01	8 00	8 00	8 00
X position [8]	3 05	3.03	2 98	3 01	3 04	2 90	3 00	3 03	3 01	2 97	2 98	2 96	3 02	3 01	3 01	3 03	3 01	3 02	3 02	3 01	3.00	3.02
mol per cent e–																						
pyrope	7	8	6	5	7	6	7	7	7	7	9	6	6	6	6	6	6	6	6	7	6	5
almandine	43	45	46	45	46	46	44	42	43	43	44	46	47	42	41	42	44	45	44	43	41	42
spessartine	45	44	44	46	42	45	46	47	47	47	44	43	41	46	47	46	45	43	43	44	48	45
grossular	4	3	4	3	5	3	3	3	3	3	3	5	6	6	6	6	6	6	7	6	6	7
	100	100	100	100	100	100	100	100	100	100	100	100	100	100	100	100	100	100	100	100	100	100

Table A9: microprobe analyses - garnet

sample	TH394 - 262	TH394 - 262	TH394 - 262	TH40 - 67 0	TH40 - 67 0	TH40 - 67 0	TH40 - 67 0	TH40 - 67.0	TH40 - 67 0	TH40 - 67 0	TH40 - 67.0	TH40 - 67.0	TH40 - 67 0	TH40 - 67.0	TH40 - 67 0	TH40 - 67 0	TH40 - 67.0	TH40 - 67 0	TH40 - 67 0
mineral	gtE1	gtE1	gtE1	gtF1	gtF1	gtF1	gtF1	gtF1	gtF1	gtF1	gtF2	gtF2	gtF2	gtF2	gtF2	gtF2	gtF2	gtF2	gtF2
analysis no	207	208	209	222	224	225	226	227	229	230	238	239	242	243	244	246	247	249	250
location [µm]	3617	3887	4010 (rim)	10 (rim)	245	123	385	543	718	915 (rim)	10 (rim)	138	310	587	863	932	1173	1208	1300 (rim)
lab:	TUB	TUB	TUB	TUB	TUB	TUB	TUB	TUB	TUB	TUB	TUB	TUB	TUB	TUB	TUB	TUB	TUB	TUB	TUB
wt.%																			
SiO2	37 00	36 90	37 28	37 98	38 02	37 98	37 86	38 00	37 77	37 41	38 96	38 11	37.57	37 94	38 31	37 56	37 23	37 85	37.60
TiO2	0 09	0 04	0 02	0 03	0 15	0.09	0 06	0.09	0.09	0 02	0.11	0 15	0 21	0 20	0 23	0 23	0.13	0.10	0 07
Al2O3	20 53	20 80	20 94	21.18	20 57	20 51	20 52	20 34	20.68	20 64	20 37	20.74	20.53	20 60	20 51	20 44	20 59	20.79	21 07
FeO	18 95	20 72	20 74	16 01	15 73	16 31	18.36	18 85	16 34	15.81	15 90	17 07	16 70	16 97	16 64	17 37	16 62	17 00	15.48
MnO	19 04	17 87	17.99	13.48	10 38	11.88	10.41	10 19	11 93	13 27	13.73	11 39	9.50	9 90	9 66	9 55	11.35	11 92	13 29
MgO	1 45	1 63	1.31	0 37	0 40	0 46	0.43	0 43	0 43	0 34	0.38	0 41	0 35	0 40	0 04	0 41	0 47	0 48	0 31
CaO	2 41	2.14	1 99	11.20	14 33	12.74	12 10	12.15	12 99	11.48	10 55	12 60	14 35	13 92	13 78	14 06	12 22	12 52	12 17
Na2O	0 01	0 03	0 00	0 01	0 01	0 00	0 00	0 00	0.00	0.01	0 01	0 00	0 00	0.01	0.02	0 03	0.01	0 02	0.02
K2O	0 00	0 00	0 02	0.02	0 00	0.00	0 00	0 00	0 00	0 00	0 04	0 00	0 00	0.00	0 18	0.00	0 00	0 02	0 01
Sum Oxides [%	99 48	100 11	100 29	100 28	99 59	99 97	99 74	100 05	100 24	98 97	100 03	100 47	99 23	99 92	99 35	99 66	98 63	100 69	100 02
# cations:																			
Si 4+	3 02	3 00	3 02	3 02	3 03	3 03	3.03	3.04	3 01	3 02	3 10	3 03	3 01	3 02	3 06	3 01	3 01	3 01	3 00
Ti 4+	0 01	0 00	0 00	0.00	0 01	0 01	0.00	0 01	0 01	0 00	0 01	0 01	0.01	0 01	0.01	0 01	0 01	0 01	0 00
Al [6]	1 97	1 99	2 00	1 99	1.93	1 93	1 94	1.92	1 94	1 96	1 91	1 94	1.94	1.93	1 93	1.93	1.96	1 95	1 98
Fe 2+	1 29	1.41	1.40	1 07	1.05	1 09	1.23	1 26	1 09	1 07	1.06	1.13	1 12	1.13	1 11	1.16	1.12	1.13	1.03
Mn 2+	1.32	1 23	1.23	0 91	0.70	0.80	0.71	0 69	0.81	0 91	0 92	0 77	0.65	0 67	0 65	0 65	0 78	0.80	0 90
Mg 2+	0 18	0 20	0 16	0 04	0 05	0.06	0 05	0 05	0 05	0 04	0 04	0 05	0 04	0 05	0 00	0 05	0 06	0 06	0.04
Ca 2+	0 21	0 19	0 17	0 96	1.22	1.09	1 04	1.04	1 11	0 99	0 90	1.07	1 23	1.19	1.18	1 21	1 06	1.07	1 04
Na 1+	0 00	0 00	0.00	0 00	0 00	0 00	0.00	0 00	0 00	0 00	0 00	0.00	0 00	0.00	0 00	0 01	0 00	0 00	0 00
K 1+	0 00	0 00	0.00	0 00	0 00	0 00	0 00	0 00	0.00	0 00	0 00	0 00	0.00	0.00	0 02	0 00	0.00	0 00	0 00
Total	7.99	8 01	7.98	7.98	7 99	8 00	8 00	8 00	8 01	8 00	7 94	8 00	8 01	8.00	7 97	8 02	8 00	8 02	8 00
X position [8]	2 99	3.02	2 97	2 97	3 02	3 04	3 02	3 04	3 05	3 01	2 93	3 02	3 04	3.03	2 95	3 07	3.02	3.05	3 01
mol per cent e																			
pyrope	6	7	5	1	2	2	2	2	2	1	2	2	1	2	0	2	2	2	1
almandine	43	47	47	36	35	36	41	41	36	35	36	38	37	37	38	38	37	37	34
spessartine	44	41	42	31	23	26	23	23	26	30	32	25	21	22	22	21	26	26	30
grossular	7	6	6	32	41	36	34	34	36	33	31	35	41	39	40	39	35	35	35
	100	100	100	100	100	100	100	100	100	100	100	100	100	100	100	100	100	100	100

Table A10: Microprobe analyses - amphibole

sample	TH247-361.3	TH247-361.3	TH40 - 67 0	TH40 - 67.0	TH40 - 67 0
mineral	ampAL1	ampAL2	ampF1	ampF2	ampF3
analysis no.	472	475	269	272	273
lab:	CSL	CSL	TUB	TUB	TUB
[wt.%]					
SiO2	58 2	57.94	42 37	39.99	41.18
TiO2	0.04	0.05	0 35	0.30	0.35
Al2O3	1.04	0.74	11.99	13.01	11.89
FeO	0.89	1.07	21 67	21 86	22 25
MnO	0.16	0.32	0.76	0.84	0.76
MgO	23.9	23.94	6 12	5.51	5 97
CaO	13.91	13.75	11.48	11.51	11.50
Na2O	0.13	0 15	0 84	0.92	0.98
K2O	0.05	0 09	0 88	0 98	1.00
F	0.29	0.35			
Cl	0	0.01			
H2O(c)	2.08	2.04			
O=F	0.12	0.15			
O=Cl	0	0			
Sum Oxides [%	98.32	98 05	96.45	94.92	95 88
# cations:					
Si	7.881	7.879	6.58	6.37	6.49
Ti	0.004	0.005	0 04	0.04	0.04
Al [4]	0.119	0 118	1.42	1 63	1 51
Al [6]	0.046	0	0.78	0.81	0.70
Fe2+	0.101	0.11	2.82	2 91	2.93
Mn2+	0.018	0.037	0.10	0 11	0.10
Mg	4.824	4.851	1.42	1.31	1.40
Ca	2 018	2 004	1.91	1.96	1 94
Na	0 033	0.04	0 25	0 29	0 30
K	0.009	0 016	0 18	0 20	0.20
F	0.123	0.15			
Cl	0	0.001			
OH	1.877	1.849			
T position [4]	8	7.997	8	8	8
C position [8]	5	5	5	5	5
B position [8]	2	2	2	2	2
A position [12]	0.053	0.06	0 43	0 48	0.50
Sum cations	15 053	15.06	15 49	15.62	15.62
XMg	0.979	0.988	0.33	0.31	0 32

Table A11: Microprobe analyses - epidote

sample	TH40 - 67.0	TH40 - 67.0	TH40 - 67.0	TH40 - 67.0	TH40 - 67.0	TH40 - 67.0
mineral	epiF1	epiF1	epiF2	epiF3	epiF4	epiF5
analysis no.	262	263	264	265	281	282
lab:	TUB	TUB	TUB	TUB	TUB	TUB
[wt.%]						
SiO2	38.26	38.11	38.72	38.34	38.61	37.94
TiO2	0.18	0.07	0.15	0.07	0.11	0.10
Al2O3	25.30	25.54	25.48	25 69	25.60	25 60
FeO	9.26	9.50	9.29	9.11	9.19	9 26
MnO	0.30	0 30	0.29	0.31	0.26	0 28
MgO	0.01	0.00	0 00	0.00	0.00	0.00
CaO	23.21	23.36	23.18	23 47	22.90	23.01
Na2O	0.01	0 02	0.01	0 00	0.01	0.00
K2O	0.01	0.00	0.00	0.02	0.02	0.01
Sum Oxides [%	96.53	96 88	97.12	97.01	96 72	96.20
# cations:	calculated on the basis of 12.5 oxygens					
Si	2 97	2.96	2.99	2.96	2.99	2 96
Ti	0.01	0 00	0.01	0.00	0.01	0.01
Al [6]	2.32	2.33	2.32	2.34	2.33	2.35
Fe 3+	0.67	0.68	0.67	0 65	0 66	0.67
Mn 2+	0 02	0.02	0.02	0 02	0 02	0.02
Mg	0.00	0.00	0 00	0.00	0.00	0.00
Ca	1.93	1 94	1.92	1.94	1.90	1.92
K	0 00	0.00	0.00	0.00	0.00	0.00
Na	0.00	0.00	0.00	0.00	0.00	0.00
Total	7.93	7.94	7.91	7.93	7.91	7.93
mole per cent pistacite end-member.						
pistacite:	66 8	68 5	66.6	65 5	66.1	67.1

Table A12: Microprobe analyses - carbonate

sample	TH247-361.3	TH247-361.3	TH40 - 67 0
mineral	carAL1	carAL1	carbF1
analysis no.	479	480	237
lab:	CSL	CSL	TUB
[wt.%]			
SiO2	0.03	0.03	0.00
FeO	0 14	0.15	1.24
MnO	0.41	0.35	2 71
MgO	0.32	1.46	0 21
CaO	64.88	63.56	58.85
BaO	0 02	0 01	
Sum Oxides [%	65 8	65.56	63.03
# cations:			
Fe2+	0.004	0.004	0.03
Mn2+	0.016	0.016	0 06
Mg	0.014	0 062	0 01
Ca	1.966	1.916	1.90

Table A13: Microprobe analyses - feldspar

sample	TH471 - 159	TH40 - 67.0
mineral	fspC1	fspF1
analysis no	124	256
lab:	TUB	TUB
[wt.%]		
SiO2	66 79	63.76
TiO2	0.02	0.00
Al2O3	21.58	18 29
Fe2O3	0.14	0.76
MnO	0.00	0.23
MgO	0.00	0.00
CaO	2 24	0.78
Na2O	9.24	0.81
K2O	0 11	15 30
Sum Oxides [w	100.13	99.92
# cations:		
calculated on the basis of 32 oxygens		
Si	11.662	11.896
Al	4.437	4.019
Fe	0.006	0.036
Ca	0.419	0.155
Na	3.127	0.294
K	0 024	3.640
Z position	16.099	15.950
X position	3.577	4.089
mol per cent end-members:		
anorthite	11 74	3.79
albite	87.57	7.18
orthoclase	0.68	89 03

Table A14: Rock catalogue

UTas#	Field#	Rock Name	Rock description	AMG Northing	AMG Easting	Lithostratigraphy	Preps	Comments
140677	C2047-3 3	dacite	mod ep-carb-act alt, mod fspr phyric f/ dac	7750141N	371418E	Trooper Creek Formation	R,PD,TS	
140678	C2047-4 5	dacite	intrusive top contact of dac	7750141N	371418E	Trooper Creek Formation	R	
140679	C2047-13	andesite	chloritised, px-(fspr)-phyric andt intrusion	7750141N	371418E	Trooper Creek Formation	R,PD,TS	
140680	C2047-18 6	breccia	ser-chl-bt alt, monomictic rhy bx	7750141N	371418E	Mount Windsor Formation	R,TS	
140681	C2047-20	rhyolite	str qz-ser-py alt, qz phyric rhy	7750141N	371418E	Mount Windsor Formation	R,PD,TS	
140682	C2047-40	rhyolite	pervasive ser-py alt, qz phyric rhy	7750141N	371418E	Mount Windsor Formation	R,PD,TS	
140683	C2047-64	rhyolite	mod ser(-py)+carb-ep alt, qz (fspr) phyric rhy	7750141N	371418E	Mount Windsor Formation	R,PD,TS	
140684	C2047-70	rhyolite	domainal ep-tm(-carb) alt, qz phyric rhy	7750141N	371418E	Mount Windsor Formation	R,PD,TS	
140685	C2047-83	rhyolite	sil'd, hem alt, qz fspr phyric rhy	7750141N	371418E	Mount Windsor Formation	R,PD,TS	
140686	C2047-99 1	breccia	monomictic dac bx w perlitic dac clasts	7750141N	371418E	Trooper Creek Formation	R,TS	
140687	C2047-112 75	breccia	polymictic bx w perlitic fspr phyric dac clasts	7750141N	371418E	Trooper Creek Formation	R,TS	
140688	E3204SD50-57 9	hornfels	crd-rich pelitic hornfels	7750267N	372367E	Mount Windsor Formation	R,TS	
140689	TH10-17	dacite	least alt, high fspr phyric f/ dac	7750179N	371357E	Trooper Creek Formation	R,PD,TS	
140690	TH10-129	rhyolite	pervasive qz-ser-py alt, qz phyric rhy	7750179N	371357E	Mount Windsor Formation	R,PD,TS	
140691	TH112-211	rhyolite	pervasive qz-ser-py alt, qz phyric rhy	7750383N	371573E	Mount Windsor Formation	R,PD,TS	
140692	TH112-227	rhyolite	strong pervasive ser-chl-py alt, qz phyric rhy	7750383N	371573E	Mount Windsor Formation	R,PD,TS	
140693	TH112-237	rhyolite	white sil'd overprinting ser-py alt, qz phyric rhy	7750383N	371573E	Mount Windsor Formation	R,PD,TS	
140694	TH112-370	rhyolite	least alt, qz-fspr phyric rhy, minor hem+ep alt	7750383N	371573E	Mount Windsor Formation	R,PD,TS	
140695	TH112-388 6	rhyolite	ep and hem alt, sillc qz-fspr phyric rhy	7750383N	371573E	Mount Windsor Formation	R	
140696	TH112-404	rhyolite	mod ep(+chl-act-carb) alt, qz (fspr) phyric rhy	7750383N	371573E	Mount Windsor Formation	R,PD,TS	
140697	TH112-420	rhyolite	least alt, qz fspr rhy	7750383N	371573E	Mount Windsor Formation	R	
140698	TH112-436	breccia	monomictic rhy bx	7750383N	371573E	Mount Windsor Formation	R,TS	
140699	TH112-448	rhyolite	white sil'd overprinting ser-py alt, qz phyric rhy	7750383N	371573E	Mount Windsor Formation	R,PD,TS	
140700	TH112-551	rhyolite	alb alt, fspr qz phyric rhy	7750383N	371573E	Mount Windsor Formation	R,PD,TS	
140701	TH112-653	dacite	least alt, high fspr phyric f/ dac	7750383N	371573E	Trooper Creek Formation	R,PD,TS	
140702	TH144B-54	rhyolite	wk ser-bt alt, qz-fspr phyric rhy	7750458N	372877E	Mount Windsor Formation	R,PD,TS	
140703	TH144B-67	rhyolite	wk ser-chl-bt alt, qz fspr phyric rhy	7750458N	372877E	Mount Windsor Formation	R,PD,TS	
140704	TH144B-151 7	sandstone	crse qz CRVS	7750458N	372877E	Mount Windsor Formation	R	
140705	TH144B-170	rhyolite	mod pervasive ser-bt alt, qz phyric rhy	7750458N	372877E	Mount Windsor Formation	R,PD,TS	
140706	TH144B-217	rhyolite	white sil'd qz phyric rhy	7750458N	372877E	Mount Windsor Formation	R,PD,TS	
140707	TH144B-226	rhyolite	sil'd domains in ser-chl-bt alt, qz (fspr) phyric rhy	7750458N	372877E	Mount Windsor Formation	R,PD,TS	
140708	TH144B-297	rhyolite	mottled, ser-chl-bt alt, qz phyric	7750458N	372877E	Mount Windsor Formation	R,PD,TS	
140709	TH144B-392.8	diorite	ep and hem alt, diorite	7750458N	372877E	Lolworth-Ravenswood Batholith	R,PS	
140710	TH144B-586 4	sandstone	crse qz CRVS	7750458N	372877E	Mount Windsor Formation	R	
140711	TH148-34	rhyolite	least alt, qz-fspr phyric rhy	7750877N	370640E	Mount Windsor Formation	R,PD,TS	
140712	TH148-130	rhyolite	sil'd and ?alb alt, qz fspr phyric rhy	7750877N	370640E	Mount Windsor Formation	R,PD,TS	
140713	TH148-159	rhyolite	mottled, ser-chl-bt alt, qz phyric	7750877N	370640E	Mount Windsor Formation	R,PD,TS	
140714	TH148-564	rhyolite	ser-py-chl alt + carb-ep alt, ?v'clastic qz-eye rhy	7750877N	370640E	Mount Windsor Formation	R,PD	
140715	TH148-567	rhyolite	str pervasive ser alt, ?v'clastic qz-eye porph rhy	7750877N	370640E	Mount Windsor Formation	R,PD,TS	
140716	TH148-569	rhyolite	ser + ep-act + bt-chl alt, qz-eye porph rhy	7750877N	370640E	Mount Windsor Formation	R,PD,TS	
140717	TH18-90	dacite	alb alt, dac	7749927N	371692E	Trooper Creek Formation	R,PD,TS	
140718	TH18-139 8	dacite	bt alt, fspr phyric dac	7749927N	371692E	Trooper Creek Formation	TS	
140719	TH18-191	rhyolite	str pervasive ser-py alt, qz (fspr) phyric rhy	7749927N	371692E	Mount Windsor Formation	R,PD,TS	
140720	TH18-266	rhyolite	pervasive ser alt, qz phyric rhy	7749927N	371692E	Mount Windsor Formation	R,PD,TS	
140721	TH238-95	rhyolite	pervasive qz-ser-py(chl-bt) alt, qz phyric rhy	7750305N	371497E	Mount Windsor Formation	R,PD,TS	
140722	TH238-130	rhyolite	py-rich pervasive qz-ser-py(chl-bt) alt, qz phyric rhy	7750305N	371497E	Mount Windsor Formation	R,PD,TS	
140723	TH238-144	rhyolite	pervasive ser-chl-py alt, qz phyric rhy	7750305N	371497E	Mount Windsor Formation	R,PD,TS	
140724	TH238-183	rhyolite	str py(-qz-ser) alt, qz phyric rhy	7750305N	371497E	Mount Windsor Formation	R,PD,TS	
140725	TH238-194	rhyolite	pervasive ser-py(-bt) alt, qz phyric rhy	7750305N	371497E	Mount Windsor Formation	R,PD,TS	
140726	TH238-202	rhyolite	alb alt, qz fspr phyric rhy	7750305N	371497E	Mount Windsor Formation	R,PD,TS	
140727	TH238-205	rhyolite	str pervasive ser alt, qz fspr phyric rhy	7750305N	371497E	Mount Windsor Formation	R,PD,TS	
140728	TH238-236	rhyolite	str pervasive ser alt, qz fspr phyric rhy	7750305N	371497E	Mount Windsor Formation	R,PD,TS	
140729	TH243-86	rhyolite	wk ser-bt alt, qz-fspr phyric rhy	7750606N	371203E	Mount Windsor Formation	R,PD,TS	
140730	TH243A-249 2	rhyolite	ser-chl-bt alt, qz phyric rhy	7750606N	371203E	Mount Windsor Formation	R,TS	
140731	TH243A-425	dacite	str pervasive bt(-ser-ep) alt, poor fspr phy f/ dac	7750606N	371203E	Trooper Creek Formation	R,PD,TS	
140732	TH245-224 4	rhyolite	mottled, ser-bt-chl alt, qz phyric	7750537N	371254E	Trooper Creek Formation	R,TS	
140733	TH245-399 1	breccia	ser-chl alt, rhy bx	7750537N	371254E	Trooper Creek Formation	R,TS	
140734	TH245-517	dacite	mod bt-chl(-ep) alt, mod fspr phyric f/ dac	7750537N	371254E	Trooper Creek Formation	R,PD,TS	
140735	TH245-674 8	calc-silicate	msve carb-chl-tm alt, ?rhy	7750537N	371254E	Mount Windsor Formation	R	
140736	TH245-675 8	calc-silicate	diop + tm bearing, msve calc-	7750537N	371254E	Mount Windsor Formation	TS	
140737	TH245-713	breccia	monomictic rhy bx	7750537N	371254E	Mount Windsor Formation	R	
140738	TH245-755 8	dacite	least alt, fspr phyric dac	7750537N	371254E	Trooper Creek Formation	R	
140739	TH247-57 7	rhyolite	wk ser alt, mod qz fspr phyric rhy	7750627N	371254E	Mount Windsor Formation	R,PS	RGC sample
140740	TH247-75	rhyolite	least alt, qz-fspr phyric rhy	7750627N	371254E	Mount Windsor Formation	R,PD,PS	
140741	TH247-98 8	rhyolite	ser-chl alt, wk py alt, highly qz (fspr) phyric rhy	7750627N	371254E	Mount Windsor Formation	R,PS	RGC sample
140742	TH247-136	rhyolite	chl-bt alt, qz phyric rhy	7750627N	371254E	Mount Windsor Formation	R,PD,PS	
140743	TH247-169 8	rhyolite	ser-bt-chl alt, mod qz phyric rhy	7750627N	371254E	Mount Windsor Formation	R,PS	RGC sample
140744	TH247-219	rhyolite	chl-bt alt, qz phyric rhy ?v'clastic	7750627N	371254E	Mount Windsor Formation	R,PS	RGC sample
140745	TH247-230 5	rhyolite	wk ser-chl alt, qz phyric rhy	7750627N	371254E	Mount Windsor Formation	R	
140746	TH247-238 8	breccia	sillc, py alt, qz phyric rhy bx	7750627N	371254E	Mount Windsor Formation	R,PS	RGC sample
140747	TH247-251 7	breccia	mudst intraclasts in rhy bx	7750627N	371254E	Mount Windsor Formation	R	
140748	TH247-256	breccia	lam sillc mudst top of normal graded monomictic rhy bx	7750627N	371254E	Mount Windsor Formation	R	
140749	TH247-274 8	breccia	str ser alt, mod qz phyric rhy bx w interbedded sed	7750627N	371254E	Mount Windsor Formation	R,PS	RGC sample
140750	TH247-300	breccia	sillc, wk alt (ser-py), monomict rhy	7750627N	371254E	Mount Windsor Formation	R,PS	RGC sample
140751	TH247-322	rhyolite	ser-bt alt, qz (fspr) rhy	7750627N	371254E	Mount Windsor Formation	R,PS	
140752	TH247-325 2	rhyolite	tm ep-carb alt, qz phyric rhy	7750627N	371254E	Mount Windsor Formation	R	
140753	TH247-347 2	rhyolite	intense qz-py-ser alt, qz phyric rhy	7750627N	371254E	Mount Windsor Formation	R,PS	RGC sample
140754	TH247-361 3	calc-silicate	rare remnant qz xl, calc-chl-tm-py-sph rich alt rhy	7750627N	371254E	Mount Windsor Formation	R,PS	
140755	TH270-49 5	rhyolite	sillc, ser alt, highly qz phyric rhy ?v'clastic	7750331N	372496E	Mount Windsor Formation	R	RGC sample
140756	TH270-78	rhyolite	wk ser alt, qz phyric rhy	7750331N	372496E	Mount Windsor Formation	R,PD,PS	
140757	TH270-121	rhyolite	wk ser-bt-py alt, qz phyric rhy	7750331N	372496E	Mount Windsor Formation	R,PD,PS	
140758	TH270-145	rhyolite	pervasive ser-bt-py alt, qz phyric	7750331N	372496E	Mount Windsor Formation	R,PD,PS	
140759	TH270-220	rhyolite	str pervasive chl/bt-ser-py alt, qz phyric rhy	7750331N	372496E	Mount Windsor Formation	R,PD,PS	
140760	TH270-278	rhyolite	str pervasive ser-chl-bt-py alt, qz phyric rhy	7750331N	372496E	Mount Windsor Formation	R,PD,PS	
140761	TH270-313	rhyolite	str pervasive qz phyric rhy	7750331N	372496E	Mount Windsor Formation	R,PD,PS	

Table A14: Rock catalogue

UTas#	Field#	Rock Name	Rock description	AMG Northing	AMG Easting	Lithostratigraphy	Preps	Comments
140762	TH270-368 2	rhyolite	ser-chl-carb alt, mod qz phyric rhy	7750331N	372496E	Mount Windsor Formation	R PS	RGC sample
140763	TH270-381	rhyolite	str pervasive chl-ser-py alt, qz phyric rhy	7750331N	372496E	Mount Windsor Formation	R,PD,TS	
140764	TH270-395	dacite	mod bt alt, + ?alb alt, mod fspr phyric f/ dac	7750331N	372496E	Trooper Creek Formation	R,PD,PS	
140765	TH28-80 6	dacite	bt alt, fspr phyric dac	7750187N	371045E	Trooper Creek Formation	R,TS	
140766	TH28-139	dacite	least alt (wk hem alt), dac	7750187N	371045E	Trooper Creek Formation	R,PD TS	
140767	TH28-304	dacite	least alt, dac	7750187N	371045E	Trooper Creek Formation	R,PD,TS	
140768	TH28-416	dacite	mod bt-chl alt, dac	7750187N	371045E	Trooper Creek Formation	R PD TS	
140769	TH28-502 85	calc-silicate	carb-chl - tm, msve calc-silicate	7750187N	371045E	Mount Windsor Formation	R TS	
140770	TH29-56 5	breccia	polymictic rhy dac bx	7750271N	371055E	Trooper Creek Formation	R	
140771	TH29-174	andesite	str pervasive act-bt-chl alt, poor px fspr phyric andt	7750271N	371055E	Trooper Creek Formation	R,PD,TS	2 TS
140772	TH3-5	dacite	alb alt, dac	7750011N	371752E	Trooper Creek Formation	R PD TS	
140773	TH3-46	rhyolite	perlitic ser alt, qz phyric rhy	7750011N	371752E	Mount Windsor Formation	TS	
140774	TH334-59 1	breccia	polymictic dac rhy bx	7750080N	371344E	Trooper Creek Formation	R,TS	
140775	TH334-61 6	breccia	polymictic bx w. rhy + dac clasts	7750080N	371344E	Trooper Creek Formation	R	
140776	TH334-81	andesite	mod ep-carb alt, high hbl phyric f/ andt	7750080N	371344E	Trooper Creek Formation	R,PD,TS	
140777	TH334-136	dacite	mod bt(-chl-ep)+alb alt, high fspr phyric f/ med dac	7750080N	371344E	Trooper Creek Formation	R,PD,TS	
140778	TH37-22 3	sandstone	fspr-qz CRVS	7750433N	370353E	Trooper Creek Formation	R	
140779	TH37-70 7	sandstone	normal graded, fspr-rich turbidite	7750433N	370353E	Trooper Creek Formation	R	
140780	TH37-80	dacite	act and alb alt, mod/high fspr phyric dac	7750433N	370353E	Trooper Creek Formation	R,PD,TS	
140781	TH37-138 5	mudstone	phyllitic mudst w act-qz-rich interval	7750433N	370353E	Trooper Creek Formation	R,PD,PS	separate XRF analyses of phyllitic mudst (140781A) and act-qz-rich
140782	TH37-152 8	sandstone	fspr CRVS w dac pum clasts	7750433N	370353E	Trooper Creek Formation	R,TS	
140783	TH37-184 5	sandstone	qz fspr CVVS w mudst interclasts	7750433N	370353E	Trooper Creek Formation	R	
73244	TH37-189 1	calc-silicate	qz-calc-ep-act, msve calc-silicate	7750433N	370353E	Trooper Creek Formation	TS	sample catalogued by J Stolz no.
73245	TH37-190 2	calc-silicate	carb-rich, chl-ep-qz, msve calc-silicate	7750433N	370353E	Trooper Creek Formation	TS	sample catalogued by J Stolz no 73245
140784	TH37-193	calc-silicate	bt-rich, qz-calc-ep-act-chl, msve calc-silicate	7750433N	370353E	Trooper Creek Formation	TS	
140785	TH38-54	rhyolite	domainal ser-chl-py alt, qz phyric	7750205N	371735E	Mount Windsor Formation	R,PD,TS	
140786	TH38-58	breccia	monomictic rhy bx w rotated flow lam clasts	7750205N	371735E	Mount Windsor Formation	R	
140787	TH38-191	rhyolite	str pervasive ser alt, qz phyric rhy	7750205N	371735E	Mount Windsor Formation	R PD,TS	
140788	TH38-260	rhyolite	str ser-chl-bt alt, qz phyric rhy	7750205N	371735E	Mount Windsor Formation	R,PD TS	
140789	TH38-403 4	mudstone	foliated bt+musc+ch-rich mudst	7750205N	371735E	Trooper Creek Formation	TS	
140790	TH38-404 5	breccia	polymictic bx w rhy + dac clasts	7750205N	371735E	Trooper Creek Formation	R	
140791	TH38-406 4	breccia	polymictic bx w sil'd dac pum	7750205N	371735E	Trooper Creek Formation	TS	
140792	TH38-421	dacite	least alt, mod fspr phyric med dac	7750205N	371735E	Trooper Creek Formation	R,PD TS	
140793	TH382A-156	sandstone	mod pervasive chl alt, + alb alt, dacitic fspr-rich sst	7749918N	372565E	Trooper Creek Formation	R,PD PS	
140794	TH382A-157	dacite	wk chl alt, v high fspr phyric f/ med dac w carb veins	7749918N	372565E	Trooper Creek Formation	R,PD,TS	
140795	TH382A-175	andesite	str pervasive chl-ser-carb alt amp/px phyric andt	7749918N	372565E	Trooper Creek Formation	R,PD,TS	
140796	TH382A-213	dacite	mod chl alt, +alb alt, high fspr phyric f/ dac	7749918N	372565E	Trooper Creek Formation	R,PD,PS	
140797	TH382A-220	dacite	mod chl(-ser) alt, v high fspr phyric med dac	7749918N	372565E	Trooper Creek Formation	R,PD,PS	
140798	TH382A-297	dacite	chl alt, poorly fspr phyric f/ dac	7749918N	372565E	Trooper Creek Formation	R PD,PS	
140799	TH382A-356	dacite	least alt w, minor dissem act + rare carb veins, dac	7749918N	372565E	Trooper Creek Formation	R,PD,PS	
140800	TH382A-400	dacite	act-ep alt, poor fspr phyric f/ dac	7749918N	372565E	Trooper Creek Formation	R PD,PS	
140801	TH382A-426 8	breccia	bt-chl-ser-rich polymictic bx	7749918N	372565E	Trooper Creek Formation	R TS	
140802	TH394-44	rhyolite	least alt, qz fspr phyric rhy	7750466N	372776E	Mount Windsor Formation	R PD,TS	
140803	TH394-114	rhyolite	mottled, ser-bt alt, qz phyric rhy	7750466N	372776E	Mount Windsor Formation	R,PD TS	
140804	TH394-142	rhyolite	least alt, qz fspr phyric rhy	7750466N	372776E	Mount Windsor Formation	R PD,TS	
140805	TH394-197	rhyolite	pervasive ser-bt alt, qz (fspr) phyric rhy	7750466N	372776E	Mount Windsor Formation	R,PD,TS	
140806	TH394-198	rhyolite	sil'd domains in ser(-py) alt, qz (fspr) phyric rhy	7750466N	372776E	Mount Windsor Formation	R,PD,TS	
140807	TH394-262 8	rhyolite	gn-bearing, domainal chl alt, qz phyric rhy	7750466N	372776E	Mount Windsor Formation	R,PS	
140808	TH394-293	rhyolite	pervasive chl-ser alt, qz phyric rhy	7750466N	372776E	Mount Windsor Formation	R,PD,TS	
140809	TH394-455	rhyolite	pervasive qz-ser-py alt, qz phyric rhy	7750466N	372776E	Mount Windsor Formation	R,PD,TS	
140810	TH40-37 4	mudstone	foliated bt+musc+ch-rich mudst	7750428N	370349E	Trooper Creek Formation	TS	
140811	TH40-44	mudstone	lam mudst	7750428N	370349E	Trooper Creek Formation	R	
140812	TH40-67	mudstone	gn+bt+calc laminae, mudst	7750428N	370349E	Trooper Creek Formation	R PS	
140813	TH40-68 5	breccia	bt alt, silic dac bx	7750428N	370349E	Trooper Creek Formation	R TS	
140814	TH40-236 6	sandstone	qz fspr CRVS w mudst interclasts	7750428N	370349E	Trooper Creek Formation	R,TS	
140815	TH40-348	dacite	qz-ser + patchy bt-py alt, mod fspr phyric dac	7750428N	370349E	Trooper Creek Formation	R,PD,TS	
140816	TH40-358 7	breccia	dac pum bx	7750428N	370349E	Trooper Creek Formation	R	
140817	TH40-450	dacite	patchy act-ep + bt alt, mod fspr phyric dac	7750428N	370349E	Trooper Creek Formation	R,PD,TS	
140818	TH40-506	rhyolite	pervasive ser-py-chl alt, ?v'clastic qz-eye porph rhy	7750428N	370349E	Mount Windsor Formation	R,PD	
140819	TH401-89	dacite	least alt (wk bt alt), dac	7750122N	372515E	Trooper Creek Formation	R PD,TS	
140820	TH401-101.1	sandstone	semi-MS overprinting qz-fspr-	7750122N	372515E	Mount Windsor Formation	R	
140821	TH401-103 7	semi-massive sulphide	semi-MS in crse qz-rich v'clastic	7750122N	372515E	Mount Windsor Formation	R	
140822	TH401-111	rhyolite	pervasive qz-ser-py alt, qz phyric rhy	7750122N	372515E	Mount Windsor Formation	R,PD,TS	
140823	TH401-120	rhyolite	str pervasive py-sph-bt-chl alt, qz phyric rhy (semi MS)	7750122N	372515E	Mount Windsor Formation	R,PD,TS	
140824	TH401-121	rhyolite	pervasive qz-ser-py alt, qz phyric rhy	7750122N	372515E	Mount Windsor Formation	R,PD,TS	
140825	TH402-88	dacite	least alt, high fspr phyric med dac	7750020N	372932E	Trooper Creek Formation	R PD,TS	
140826	TH402-103	dacite	least alt (hem alt), high fspr phyric f/ dac	7750020N	372932E	Trooper Creek Formation	R,PD,TS	
140827	TH402-113	dacite	mod chl-bt alt + alb alt, high fspr phyric f/ dac	7750020N	372932E	Trooper Creek Formation	R,PD,TS	
140828	TH402-119.2	dacite	musc, chl, foliated bt, dac	7750020N	372932E	Trooper Creek Formation	R,TS	
140829	TH402-123	dacite	mod bt-chl alt + hem alt, poor fspr phyric f/ dac	7750020N	372932E	Trooper Creek Formation	R,PD,TS	
140830	TH402-176	dacite	mod ep-act alt + str hem alt, poor fspr phyric f/ dac	7750020N	372932E	Trooper Creek Formation	R,PD,PS	
140831	TH402-219	diorite	med, eqgr hbl-plag (sericitised) diorite	7750020N	372932E	Lolworth-Ravenswood Batholith	R,PD,TS	
140832	TH402-321	dacite	least alt (wk hem and ep alt), dac	7750020N	372932E	Trooper Creek Formation	R,PD,TS	
140833	TH402-330 1	dacite	hem alt, dac in contact w diorite	7750020N	372932E	Trooper Creek Formation	R TS	
140834	TH402-348 9	breccia	sil'd dac pum clast in polymictic bx	7750020N	372932E	Trooper Creek Formation	R	
140835	TH402-366	diorite	med, eqgr hbl-plag diorite	7750020N	372932E	Lolworth-Ravenswood Batholith	R	large sample for future radiometric
140836	TH402-366 4	diorite	med, eqgr hbl-pleg diorite	7750020N	372932E	Lolworth-Ravenswood Batholith	R	
140837	TH402-398	rhyolite	str pervasive qz-ser-py alt, qz phyric rhy	7750020N	372932E	Mount Windsor Formation	R,PD,TS	
140838	TH410-94	rhyolite	pervasive ser-bt alt, qz fspr phyric rhy	7750798N	370600E	Mount Windsor Formation	R,PD,TS	
140839	TH410-97	rhyolite	K-fspr alt, qz phyric rhy	7750798N	370600E	Mount Windsor Formation	R PD	
140840	TH410-121	mudstone	str sil'd, rhy'c, lam mudst	7750798N	370600E	Mount Windsor Formation	R PD,TS	
140841	TH410-125 1	rhyolite	ser alt, qz (fsp) rhy	7750798N	370600E	Mount Windsor Formation	R,TS	
140842	TH410-131	rhyolite	white sil'd domain + ser-bt alt, qz (fspr) phyric rhy	7750798N	370600E	Mount Windsor Formation	R,PD,TS	3 separate XRF analyses and 3 TS of (1) white, sil'd rhy (140842A) (2) ser-bt alt rhy (140842C) and (3)
140843	TH410-150	rhyolite	K-fspr alt, qz (?fspr) phyric rhy	7750798N	370600E	Mount Windsor Formation	R,PD,TS	
140844	TH410-169 9	rhyolite	ser-chl alt, qz phyric rhy	7750798N	370600E	Mount Windsor Formation	R,TS	

Table A14: Rock catalogue

UTas#	Field#	Rock Name	Rock description	AMG Northing	AMG Easting	Lithostratigraphy	Preps	Comments
140845	TH410-192 8	rhyolite	wk ser(-chl-bt) alt, qz (fspr) phyric rhy	7750798N	370600E	Mount Windsor Formation	R	
140846	TH410-278	breccia	normal graded rhy'c bx	7750798N	370600E	Mount Windsor Formation	R	
140847	TH410-295	mudstone	str sil'd, rhy'c, lam mudst w ep-act domains	7750798N	370600E	Mount Windsor Formation	R,TS	
140848	TH410-313	rhyolite	mottled, ser-chl-bt alt, qz phyric	7750798N	370600E	Mount Windsor Formation	R,PD,TS	
140849	TH410-323	rhyolite	least alt and K-fspr alt domain, qz (fspr) phyric rhy	7750798N	370600E	Mount Windsor Formation	R,PD,TS	separate XRF analyses of least alt (140849A) and K-fspr alt
140850	TH410-337 8	breccia	rhy'c bx w sl-chl vein	7750798N	370600E	Mount Windsor Formation	R	
140851	TH410-390	rhyolite	K-fspr, ep and hem alt, qz phyric	7750798N	370600E	Mount Windsor Formation	R,PD,TS,PS	
140852	TH410-398	rhyolite	intrusive top contact of rhy	7750798N	370600E	Mount Windsor Formation	R	
140853	TH410-503 1	calc-silicate	qz + calc + ep, msve calc-silicate	7750798N	370600E	Mount Windsor Formation	R,TS	
140854	TH412-145	rhyolite	chl-bt-ser-py alt, rhy	7750317N	371802E	Mount Windsor Formation	R PD,TS	
140855	TH412A-490	breccia	monomictic rhy bx	7750317N	371802E	Mount Windsor Formation	R	
140856	TH412A-551	rhyolite	alb alt qz fspr phyric rhy	7750317N	371802E	Mount Windsor Formation	R,PD TS	
140857	TH412A-558	rhyolite	mod ep-musc-chl-carb alt, qz phyric rhy	7750317N	371802E	Mount Windsor Formation	R,PD TS	
140858	TH412B-645	rhyolite	K-fspr alt, qz fspr phyric rhy	7750317N	371802E	Mount Windsor Formation	R,PD,TS	
140859	TH412B-674	rhyolite	wk ser(-chl-py) + ?K-fspr alt, qz-eye porph rhy	7750317N	371802E	Mount Windsor Formation	R,PD,TS	
140860	TH412B-786	rhyolite	pervasive ep-tm-carb alt, qz phyric rhy	7750317N	371802E	Mount Windsor Formation	R,PD,TS	
140861	TH412B-899 5	breccia	polymictic dac rhy bx	7750317N	371802E	Mount Windsor Formation	R	
140862	TH41A-439	sediment	mod pervasive ser alt, rhy v'clastic sed	7750167N	371069E	Mount Windsor Formation	R,PD,TS	
140863	TH41A-479	dacite	wk chl-bt alt, f/ dac	7750167N	371069E	Trooper Creek Formation	R PD,TS	
140864	TH41A-575	rhyolite	domainal ser-bt-carb and ser-tm-ep alt, qz phyric rhy	7750167N	371069E	Mount Windsor Formation	R,PD,TS	
140865	TH41A-653	rhyolite	pervasive ser-chl/bt-py alt, qz phyric rhy	7750167N	371069E	Mount Windsor Formation	R,PD,TS	
140866	TH41A-713	rhyolite	K-fspr alt, qz phyric rhy	7750167N	371069E	Mount Windsor Formation	R PD,TS	
140867	TH471-104	rhyolite	chl-ser-py alt, qz phyric rhy, minor gn	7750900N	373975E	Mount Windsor Formation	R,PD,PS	
140868	TH471-159 5	garnet-hornfels	gn hornfels w. bt+musc+qz-rich mtx	7750900N	373975E	Mount Windsor Formation	R,PS	
140869	TH471-228	diorite	crse, eqgr plag-hbl-bt diorite	7750900N	373975E	Lolworth-Ravenswood Batholith	R,PD,TS	
140870	TH5-22	dacite	mod bt-chl alt, mod fspr phyric med dac	7750051N	371301E	Trooper Creek Formation	R,PD,TS	
140871	TH5-28	breccia	polymictic, dacitic bx	7750051N	371301E	Trooper Creek Formation	TS	2 TS
140872	TH5-28.25	breccia	mtx-supported dacitic bx	7750051N	371301E	Trooper Creek Formation	R,TS	
140873	TH5-54	dacite	mod pervasive bt alt, v'clastic dac	7750051N	371301E	Trooper Creek Formation	R PD TS	
140874	TH5-104	dacite	mod pervasive chl alt, mod/high fspr phyric med dac	7750051N	371301E	Trooper Creek Formation	R,PD,TS	
140875	TH5-166	exhalite	msve sl-bar ?exhalite	7750051N	371301E	Mount Windsor Formation	R,PD TS	
140876	TH5-178	sediment	str pervasive qz-ser(-chl) alt, dacitic sed?	7750051N	371301E	Trooper Creek Formation	R,PD,TS	
140877	TH5-256	rhyolite	qz-ser-py alt + tm-carb-ep alt, qz phyric rhy	7750051N	371301E	Mount Windsor Formation	R,PD,PS	
140878	TH5-301	breccia	ser alt, rhy v'clastic w qz fspr phyric rhy clasts	7750051N	371301E	Mount Windsor Formation	R,PD,TS	
140879	TH5-308	rhyolite	mod pervasive ser-chl alt, qz fspr phyric rhy	7750051N	371301E	Mount Windsor Formation	R,PD,TS	
140880	TH5-337	rhyolite	sil'd, hem (carb-ep + chl-bt) alt, qz fspr phyric rhy	7750051N	371301E	Mount Windsor Formation	R,PD,TS	
140881	TH5-339	rhyolite	least alt, qz fspr phyric rhy	7750051N	371301E	Mount Windsor Formation	R PD,TS	
140882	TH5-358	rhyolite	hem alt, qz phyric rhy w. patchy carb-ep alt	7750051N	371301E	Mount Windsor Formation	R,PD,PS	
140883	TH5-394	rhyolite	pervasive qz-ser-py alt, qz phyric rhy	7750051N	371301E	Mount Windsor Formation	R,PD,TS	
140884	TH61-86	rhyolite	ser-bt alt + white sil'd, qz (fspr) phyric rhy	7750363N	372855E	Mount Windsor Formation	R,PD,TS	2 separate XRF analyses of ser-bt-chl alt part (140884A) and white,
140885	TH61-118	rhyolite	pervasive ser alt, rhy qz bearing ?v'clastic	7750363N	372855E	Mount Windsor Formation	R,PD,TS	
140886	TH61-124	rhyolite	pervasive ser alt, qz fspr phyric	7750363N	372855E	Mount Windsor Formation	R,PD,TS	
140887	TH61-157	rhyolite	K-fspr alt, qz phyric rhy	7750363N	372855E	Mount Windsor Formation	R,PD,TS	
140888	TH61-197	rhyolite	K-fspr alt, qz phyric rhy w. ep-carb veins	7750363N	372855E	Mount Windsor Formation	R,PD,PS	
140889	TH61-216.2	sandstone	crse blue qz CRVS w. mudst intraclasts	7750363N	372855E	Mount Windsor Formation	R	
140890	TH61-237.5	sandstone	crse blue qz CRVS w. mudst intraclasts	7750363N	372855E	Mount Windsor Formation	R,TS	
140891	TH61-284	dacite	sil'd, hem and alb alt, poor fspr phyric f/ dac	7750363N	372855E	Trooper Creek Formation	R,PD,TS	
140892	TH61-287	dacite	str pervasive chl-ser-bt alt, poor fspr phyric f/ dac	7750363N	372855E	Trooper Creek Formation	R,PD,TS	
140893	TH62C-46	rhyolite	wk bt alt + alb alt, qz-eye porph	7750409N	370338E	Trooper Creek Formation	R,PD,TS	
140894	TH62C-142	dacite	sil'd, mod bt(-chl) and alb alt, highly fspr phyric dac	7750409N	370338E	Trooper Creek Formation	R,PD,PS	
140895	TH62C-261 2	mudstone	gn-hbl-rich interval in phyllite	7750409N	370338E	Trooper Creek Formation	R,TS	
140896	TH62C-510	dacite	sil'd + alb alt, dac	7750409N	370338E	Trooper Creek Formation	R,PD	
140897	TH62C-680	dacite	str ep(carb-act) alt, + hem alt, mod fspr phyric dac	7750409N	370338E	Trooper Creek Formation	R,PD,TS	
140898	TH62C-793 1	breccia	dac clasts in qz fspr bearing phyllitic mtx	7750409N	370338E	Trooper Creek Formation	R,TS	
140899	TH62C-825	dacite	mod ep-carb-act alt, poor fspr phyric f/ dac	7750409N	370338E	Trooper Creek Formation	R,PD,TS	
140900	TH62C-882 05	rhyolite	least alt, qz fspr phyric rhy w. relict perlitic texture	7750409N	370338E	Mount Windsor Formation	R,TS	
140901	TH85-42	dacite	least alt, high fspr phyric med dac	7750275N	372542E	Trooper Creek Formation	R,PD,TS	
140902	TH85-72	rhyolite	white sil'd qz fspr phyric rhy	7750275N	372542E	Mount Windsor Formation	R PD,TS	
140903	TH85-100 9	breccia	monomictic rhy bx	7750275N	372542E	Mount Windsor Formation	R	
140904	TH85-125	rhyolite	mottled bt-ser-ep-py alt, qz (fspr) phyric rhy	7750275N	372542E	Mount Windsor Formation	R,PD,TS	
140905	TH85-159	rhyolite	pervasive qz-ser-py-bt alt, qz phyric rhy	7750275N	372542E	Mount Windsor Formation	R,PD,TS	
140906	TH85-188	rhyolite	intense domainal ser-chl/bt-py alt, qz phyric rhy	7750275N	372542E	Mount Windsor Formation	R,PD,TS	
140907	TH85-204	rhyolite	vein controlled py-chl alt, qz phyric rhy	7750275N	372542E	Mount Windsor Formation	R,PD,TS	
140908	TH85-215	rhyolite	pervasive chl-bt-ser(-py) alt, qz phyric rhy	7750275N	372542E	Mount Windsor Formation	R,PD,TS	
140909	TH85-312	rhyolite	intense domainal ser-chl/bt-py alt, qz phyric rhy	7750275N	372542E	Mount Windsor Formation	R,PD,TS	
140910	TH85-441	rhyolite	domainal ser and ser-chl-py, qz bearing rhy ?v'clastic	7750276N	372542E	Mount Windsor Formation	R,PD,PS	
140911	TH85-452	rhyolite	domainal ser-chl-py alt, qz bearing rhy ?v'clastic	7750275N	372542E	Mount Windsor Formation	R,PD,TS	
140912	TH85-594	dacite	str pervasive ep alt, fspr phyric	7750275N	372542E	Trooper Creek Formation	R,PD,TS	
140913	TH85A-241	rhyolite	intense domainal ser-chl/bt-py alt, qz phyric rhy	7750275N	372542E	Mount Windsor Formation	R,PD,TS	
140914	TH85A-335	rhyolite	intense domainal ser-chl/bt-py alt, qz phyric rhy	7750275N	372542E	Mount Windsor Formation	R,PD,TS	
140915	TH85A-348	rhyolite	pervasive qz-ser + domainal chl alt, qz phyric rhy	7750275N	372542E	Mount Windsor Formation	R,PD,TS	
140916	TH85A-349	rhyolite	str, pervasive chl-bt alt, qz phyric	7750275N	372542E	Mount Windsor Formation	R,PD,PS	
140917	TH85A-384	rhyolite	pervasive chl-ser-py alt, qz phyric rhy	7750275N	372542E	Mount Windsor Formation	R,PD,PS	
140918	TH85A-422	rhyolite	pervasive ser-chl-sph alt, rhy	7750275N	372542E	Mount Windsor Formation	PD,TS	
140919	TH85A-444 4	breccia	dac clasts in qz fspr bearing phyllitic mtx	7750275N	372542E	Mount Windsor Formation	R,TS	
140920	THFH1	sandstone	qz fspr CVRS	7753175N	367140E	Mount Windsor Formation	R TS	
140921	THFH2	rhyolite	crse v highly qz-fsrp phyric rhy	7753180N	367145E	Mount Windsor Formation	R,PD,TS	

Table A14: Rock catalogue

UTas#	Field#	Rock Name	Rock description	AMG Northing	AMG Easting	Lithostratigraphy	Preps	Comments
140922	THFH3	rhyolite	f/ poorly qz phyric rhy	7753170N	367130E	Mount Windsor Formation	R,PD,TS	
140923	THFH4	dacite	mod fspr phyric f/ dac	7753150N	367110E	Trooper Creek Formation	R,PD TS	
140924	THR2	rhyolite	silic, mod-highly qz phyric rhy	7750820N	370330E	Mount Windsor Formation	R PD,TS	
140925	THR3	rhyolite	silic, qz-fspr phyric rhy	7750915N	370380E	Mount Windsor Formation	R,PD,TS	
140926	THRC8-87	granite	blue qz, fspr, bt, granite	7752325N	371060E	Lolworth-Ravenswood Batholith	R PD,TS	
140927	THRW1	breccia	monomictic rhy bx	7753350N	367550E	Mount Windsor Formation	R PS	
140928	THRW2	breccia	monomictic rhy bx	7753330N	367510E	Mount Windsor Formation	R TS	
140929	THRW3	rhyolite	silic, mod qz phyric rhy	7753290N	367470E	Mount Windsor Formation	R,PD,TS	
140930	THRW4	rhyolite	v highly qz phyric, mod fspr phyric med rhy	7753450N	367720E	Mount Windsor Formation	R,PD,TS	
140931	THRW5	rhyolite	f/ mod qz-fspr phyric rhy	7753430N	367680E	Mount Windsor Formation	R,PD,PS	
140932	THRW6	rhyolite	v highly qz phyric, mod fspr phyric med rhy	7753470N	367750E	Mount Windsor Formation	R PD,TS	
140933	THRW7	rhyolite	crse v highly fsp-qz phyric rhy w abundant bt	7753445N	367710E	Mount Windsor Formation	R,PD,TS	
140934	THRW8	rhyolite	silic, mod qz phyric rhy	7753380N	367605E	Mount Windsor Formation	R,PD TS	
140935	THRW9	rhyolite	f/ mod qz phyric rhy	7753355N	367580E	Mount Windsor Formation	R,PD,TS	
140936	THRW10	rhyolite	silic, mod qz phyric rhy	7753330N	367525E	Mount Windsor Formation	R,PD TS	
140937	THRW11	rhyolite	silic, mod qz phyric rhy	7753310N	367500E	Mount Windsor Formation	R,PD,TS	
140938	THRW20	silica-ironstone	sil-ironstone	7753369N	367800E	Puddler Creek Formation	R	
140939	THWH1	rhyolite	fresh mod qz-fspr phyric rhy	7750685N	371375E	Mount Windsor Formation	R,PD TS	
140940	THWH3	rhyolite	mod qz-fspr phyric rhy	7750770N	370900E	Mount Windsor Formation	R PD TS	
140941	THWH4	rhyolite	silic, mod-highly qz fspr phyric rhy	7750820N	371460E	Mount Windsor Formation	R,PD,TS	
140942	RH1	rhyolite	silic, qz fspr phyric rhy	see comments	see comments	Mount Windsor Formation	R PD	Internal geochemical standard provided by RGC of least alt rhy form East Thalanga, exact
140943	HPTH-1	calc-silicate	msve tm	see comments	see comments	Mount Windsor Formation	R	hand specimen from West Thalanga Favourable Horizon, provided by Walter Herrmann,
140944	92-314	rhyolite	least alt, qz (fspr) phyric rhy	see comments	see comments	Mount Windsor Formation	R	hand specimen of sample dated by SHRIMP at ANU; northwestern end of railway cutting through Thalanga Range (outcrop section), exact

Abbreviations for rock description in sample catalogue					
Mineral abbreviations			Word abbreviations		
Abbreviation	Expansion		Abbreviation	Expansion	
act	actinolite		alt	alteration / altered	
alb	albite		alk	alkaline	
amp	amphibole		andt	andesite	
ap	apatite		assoc	association	
apy	arsenopyrite		bx	breccia	
Au	gold		bx'd	brecciated	
aug	augite		cong	conglomerate	
bar	barite		C'ous	carbonaceous	
bn	bornite		crse	coarse	
bornn	bournonite		dac	dacite	
boul	boulangerite		dep	deposit	
bt	biotite		dissem	disseminated	
bx	breccia		evap	evaporite	
calc	calcite		f/	fine	
carb	carbonate (general)		ferromag	ferromagnesian	
cct	chalcocite		fm	formation	
chl	chlorite		frag	fragment	
chr	chromite		g'diorite	granodiorite	
cov	covellite		grnd	grained	
cpx	clinopyroxene		lam	laminated	
cpy	chalcopyrite		lamn	lamination	
ct	chert		leucog	leucogranite	
dig	digenite		lith	lithic	
diop	diopside		med	medium	
dol	dolomite		min'd	mineralised	
ep	epidote*		minn	mineralisation	
fl	fluorite		mod	moderately / moderate	
fld	fluoride*		MS	massive sulphide	
fspr	feldspar		msve	massive	
fuch	fuchsite		mudst	mudstone	
gal	galena		porph	porphyry / porphyritic	
gn	garnet		Pnt	Point	
gyp	gypsum		Port	Pt	
hem	haematite		pum	pumice	
hbl	hornblende		pumic	pumiceous	
jam	jamesonite		repl	replacing, replacement of	
K	potassium		Rd	Road	
kal	kalsilite		sandst	sandstone	
leuc	leucite		sed	sediment	
mag	magnetite		sed'd	sedimented	
Mg	magnesium		sedn	sedimentation	
mel	melilite		sedry	sedimentary	
ml	millerite		sil	silica	
molyb	molybdenite		sil'd	silicified	
ol	olivine		silic	siliceous	
per	perovskite		siltst	siltstone	
phlog	phlogopite		str	strong	
plag	plagioclase		supp	supported	
pn	pentlandite		u'mfc	ultramafic	
po	pyrrhotite		v	very	
prn	prehnite		v'clast	volcaniclast	
py	pyrite		v'clastic	volcaniclastic	
px	pyroxene		w.	with	
pyx	?pyroxenite		wk	weak	
qz	quartz		xl	crystal	
sal	salite				
sch	scheelite		R	hand specimen	
ser	sericite		TS	thin section	
serp	serpentine		PS	polished thin section	
sid	siderite		PD	rock powder	
si	silica				
sp	sphene				
sph	sphalerite				
sulf	sulphate				
tet	tetrahedrite				
to	tourmaline				
tm	tremolite				
ves	vesuvianite				
wol	wollastonite				

Pages 363 to 377 have been removed as they are equivalent to the published version of the Taylor and Francis article

H. Paulick & J. McPhie (1999) Facies architecture of the felsic lava-dominated host sequence to the Thalanga massive sulfide deposit, Lower Ordovician, northern Queensland, Australian Journal of Earth Sciences, 46:3, 391-405, DOI: 10.1046/j.1440-0952.1999.00713.x